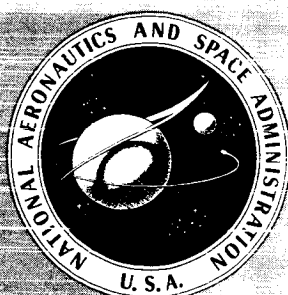


# PERFORMANCE AND DYNAMICS OF AEROSPACE VEHICLES

**CASE FILE  
COPY**



# PERFORMANCE AND DYNAMICS OF AEROSPACE VEHICLES

By the Staff of Langley Research Center

*Prepared at Langley Research Center*



*Scientific and Technical Information Office*

NATIONAL AERONAUTICS AND SPACE ADMINISTRATION

*Washington, D.C.*

1971



## PREFACE

This publication consists of a series of lectures prepared by personnel of the NASA Langley Research Center. Collectively, they were presented as a graduate seminar at Rensselaer Polytechnic Institute, Troy, New York, under the auspices of Professor Robert E. Duffy. The lectures summarize theoretical and experimental work in a number of areas of current interest in the design of aeronautical and space vehicles and were intended as an extension of general academic studies toward applications to solutions of practical problems.

The material presented is not intended to be a comprehensive survey of the state of the art but rather a series of résumés of work in several areas, some of which represent fairly recent developments and others in which the significant contributions are distributed in various publications. The material covered reflects the specialties and viewpoints of the individual lecturers and little effort has been made to provide continuity between the different papers. The topics are, nevertheless, grouped under three general headings, as follows:

1. Aerodynamics of vehicles in various speed ranges
2. Problems involving aeroelasticity and unsteady aerodynamics
3. Methods and application of analytical techniques in dynamic stability problems

The material is considered suitable for providing aeronautical engineering students with background information and working knowledge in a number of specialized fields which are usually omitted or discussed only briefly in an undergraduate curriculum.

## CONTENTS

PREFACE . . . . .	iii
-------------------	-----

### AERODYNAMICS OF VEHICLES IN VARIOUS SPEED RANGES

1. STABILITY AND CONTROL CHARACTERISTICS OF STOL AND V/STOL AIRPLANES . . . . .	1
Joseph R. Chambers	
2. METHODS OF OBTAINING STABILITY DERIVATIVES . . . . .	71
M. J. Queijo	
3. DESIGN OF BODIES FOR LOW DRAG AND HIGH PERFORMANCE IN PRACTICAL HYPERSONIC FLIGHT . . . . .	103
E. S. Love	
4. PROBLEMS OF ATMOSPHERIC ENTRY . . . . .	175
Percy J. Bobbitt	

### PROBLEMS INVOLVING AEROELASTICITY AND UNSTEADY AERODYNAMICS

5. FLUTTER AND UNSTEADY-LIFT THEORY . . . . .	289
E. Carson Yates, Jr.	
6. EFFECTS OF AEROELASTICITY ON STATIC AERODYNAMIC DERIVATIVES . . . . .	375
John E. Lamar	
7. RESPONSE OF FLEXIBLE AIRPLANES TO ATMOSPHERIC TURBULENCE . . . . .	439
Kermit G. Pratt	
8. GUST ALLEVIATION . . . . .	505
William H. Phillips	

METHODS AND APPLICATION OF ANALYTICAL TECHNIQUES  
IN DYNAMIC STABILITY PROBLEMS

9. HUMAN RESPONSE IN CLOSED-LOOP CONTROL OF DYNAMIC SYSTEMS . . . . .	555
James J. Adams	
10. INTRODUCTION TO LINEAR SYSTEM ANALYSIS AND DESIGN BY USE OF STATE VECTOR APPROACH . . . . .	579
Raymond C. Montgomery	
11. OPTIMIZATION TECHNIQUES . . . . .	629
Ernest S. Armstrong	



# 1. STABILITY AND CONTROL CHARACTERISTICS OF STOL AND V/STOL AIRPLANES

By Joseph R. Chambers  
Langley Research Center

## ABSTRACT

Some of the stability and control characteristics common to most V/STOL airplanes are discussed. In particular, specific stability and control problems of deflected slipstream, tilt-wing, ducted-propeller, and jet-powered vehicles are covered. The contents include a variety of experimental and analytical techniques presently used to analyze the stability and control characteristics of V/STOL airplanes.

## INTRODUCTION

Since the earliest days of manned flight, emphasis has usually been placed on obtaining the maximum speed capability for advanced airplane configurations. This emphasis has not diminished today, as evidenced by flight tests of supersonic transports and studies of hypersonic cruise vehicles. In contrast to this emphasis on speed, however, recent military and commercial aviation experience has led to a pronounced interest in vehicles that can attain lower minimum operating speeds. From an operational point of view, lower approach and take-off speeds result in a more versatile airplane that requires a minimum amount of take-off and landing distance. As a result of interest in attaining lower operating speeds, a number of new types of airplanes having vertical and/or short take-off and landing capabilities are being actively developed. This paper describes some of the more promising short take-off and landing (STOL) and vertical/short take-off and landing (V/STOL) concepts and points out some of their associated stability, control, and handling quality characteristics.

At this point, the abbreviations used to identify the airplane configurations to be studied are defined. First, the basic definitions of VTOL, STOL, and V/STOL airplanes are explained.

(1) A VTOL airplane has a capability for vertical take-off and landing; as a result it does not require a runway for normal operations.

(2) STOL airplanes are capable of extremely short take-offs and landings, but they have no VTOL capability, and therefore require a take-off and landing ground run for normal operation.

(3) The V/STOL airplane has the capability to perform either vertical or short take-offs and landings. It should be noted that a V/STOL airplane may operate a majority of the time in the STOL mode of operation due to economic and safety considerations.

This paper is concerned with the stability and control characteristics of STOL and V/STOL airplanes with the exception of the helicopter. The material presented was taken from the technical publications given in the Bibliography.

An outline of the principal topics of this paper is as follows: First, the basic characteristics of STOL and V/STOL airplanes are described. The next section discusses the stability and control characteristics of STOL airplanes. Past research on stability and control characteristics of STOL concepts is discussed by using results obtained during flight tests of a jet transport equipped with boundary-layer control. The current status of STOL airplane development is discussed; then a projection of future STOL concepts powered by the external-flow jet flap is presented. The next major section of the lecture covers the general area of V/STOL airplanes. In that section, stability and control characteristics of airplanes employing typical V/STOL propulsive concepts such as the tilt-wing, ducted-propeller, and vectored-thrust jet engine are examined. The final section of the paper is devoted to a discussion of the principles and application of several specialized test techniques commonly used at the NASA Langley Research Center to evaluate the stability and control characteristics of V/STOL designs.

## SYMBOLS

$a_y$	lateral acceleration
$b$	wing span
$\bar{c}$	mean aerodynamic chord
$C_L$	lift coefficient
$C_{L\alpha}$	lift-curve slope
$C_l$	rolling-moment coefficient
$C_{l\beta}$	effective dihedral parameter
$C_{lp}$	damping-in-roll parameter

$C_m$	pitching-moment coefficient
$C_n$	yawing-moment coefficient
$C_{np}$	yawing moment due to roll
$C_{nr}$	damping-in-yaw parameter
$C_{n\beta}$	directional stability parameter
$C_{n\dot{\beta}}$	yawing moment due to rate of change of sideslip
$C_{n\delta_a}$	yawing moment due to aileron deflection
$C_T$	thrust coefficient
$C_{Y\beta}$	lateral force coefficient due to sideslip
$D$	drag; also propeller diameter
$F_X$	axial force
$F_{Xq} = \frac{\partial F_X / \partial q}{m}$	
$F_{Xu} = \frac{\partial F_X / \partial u}{m}$	
$F_{Xw} = \frac{\partial F_X / \partial w}{m}$	
$F_Z$	vertical force
$F_{Zq} = \frac{\partial F_Z / \partial q}{m}$	
$F_{Zu} = \frac{\partial F_Z / \partial u}{m}$	
$F_{Zw} = \frac{\partial F_Z / \partial w}{m}$	
$g$	gravity



$h$  distance from lower surface of fuselage to ground

$i_w$  wing incidence

$I_X$  moment of inertia about  $X$  body axis

$I_Y$  moment of inertia about  $Y$  body axis

$l$  characteristic length

$L$  lift

$L_\infty$  lift out of ground effect

$m$  mass

$M_X$  rolling moment

$$M_{X_\phi} = \frac{\partial M_X}{\partial \phi}$$

$M_Y$  pitching moment

$$M_{Y_q} = \frac{\partial M_Y / \partial q}{I_Y}$$

$$M_{Y_u} = \frac{\partial M_Y / \partial u}{I_Y}$$

$$M_{Y_w} = \frac{\partial M_Y / \partial w}{I_Y}$$

$$M_{Y_{\dot{w}}} = \frac{\partial M_Y / \partial \dot{w}}{I_Y}$$

$$M_{Y_\alpha} = \frac{\partial M_Y}{\partial \alpha}$$

$$M_{Y_\theta} = \frac{\partial M_Y}{\partial \theta}$$

$M_Z$  yawing moment

$M_{Z_\infty}$  yawing moment out of ground effect

$N_{Fr}$  Froude number

$q$	pitching velocity
$\dot{r}_{\max}$	maximum yawing acceleration
$s$	LaPlace operator
$t$	time
$T$	thrust
$T_s$	static thrust
$u$	perturbation velocity along $X$ body axis
$v_i$	induced velocity
$V$	airspeed
$V_j$	slipstream velocity
$w$	velocity perturbation along $Z$ body axis
$\dot{w}$	time derivative of $w$
$W$	weight
$\alpha$	angle of attack
$\beta$	angle of sideslip
$\dot{\beta}$	time derivative of sideslip
$\delta_n$	nozzle deflection
$\theta$	pitch attitude
$\sigma$	real part of root of characteristic equation
$\omega$	imaginary part of root of characteristic equation

$\rho$	density
$\phi$	roll attitude

## BASIC CHARACTERISTICS OF STOL AND V/STOL AIRPLANES

Before specific details are discussed, consideration should be given to some basic aerodynamic characteristics of STOL and V/STOL configurations which determine to a great extent their stability, control, and handling-quality characteristics.

Shown in figure 1 are some fundamental relationships between lift and power required for a conventional airplane and for a typical V/STOL airplane. Plotted along the vertical scales are the variations with airspeed of the lift (in percent of weight) and the power required for level flight for both airplanes. On the lower plot, the solid line represents the classical variation of power required for the conventional airplane. The upper plot shows that the conventional airplane is supported solely by aerodynamic lift as speed is reduced from cruising flight down to the stall. On the other hand, the plots show that the aerodynamic lift supporting a V/STOL airplane is gradually replaced by powered lift as an airspeed of zero, or hovering flight, is approached. In the speed range where powered lift must be used – the so-called transition speed range – the power required for the V/STOL airplane rises rapidly up to a maximum value at hovering flight. This characteristic leads to flight operations on the so-called "back side" of the power-required curve, which in turn may require the use of unconventional piloting techniques and stability augmentation. The STOL airplane is usually operated over a more limited portion of the back side of the power-required curve, but it also may experience some of the problems associated with back-side operation.

The V/STOL airplane is also subject to stability and control deficiencies at low airspeeds, as illustrated in figure 2. Shown are typical variations of aerodynamic stability and control with airspeed for a V/STOL airplane from hovering flight through the transition to cruising flight. The V/STOL airplane is assumed to have satisfactory aerodynamic stability and control in cruising flight. Naturally, since all the parameters vary with dynamic pressure in the airstream, their relative magnitudes drop off rapidly as airspeed is reduced. The top plot shows that no aerodynamic control is available from conventional airplane control surfaces in hovering flight unless the control surfaces are located in a high-velocity slipstream. As a consequence, V/STOL airplanes are usually equipped with special control systems which do not rely on airstream dynamic pressure for effectiveness; these systems are exemplified by reaction jets powered by compressed air bled from compressor stages of jet engines. The middle plot of figure 2 indicates that all V/STOL airplanes have neutral static stability with respect to attitude in hovering



flight. This characteristic is often eliminated by the use of artificial attitude stabilization, as will be discussed in a later section of this paper. As for dynamic stability, the lower plot shows that most V/STOL designs are dynamically unstable in hovering flight. These inherent instabilities are usually composed of unstable pitching and rolling oscillations. The lack of static and dynamic stability does not prevent V/STOL airplanes from being flown under ideal visual flight conditions, but it does lead to unacceptable handling characteristics during instrument flight conditions which must be improved by artificial stability augmentation before satisfactory operation can be obtained. These inherent deficiencies and limitations indicate that a typical V/STOL airplane will in general have stability, control, and handling-quality characteristics which steadily deteriorate as airspeed is decreased. These important deficiencies should be kept in mind during the following sections of this paper.

## STABILITY AND CONTROL CHARACTERISTICS OF STOL AIRPLANES

### Airport Congestion

Interest in airplanes designed for short take-off and landing (STOL) has been expressed since the invention of the airplane, but within the last few years this interest has become increasingly intense. Perhaps the most important factor behind the active studies of STOL airplanes has been recent experience with congestion of our commercial airway system. Studies of passenger destinations have shown that more than half of the daily traffic at most of our major airports is bound for destinations involving trips of less than 300 miles. A concentrated effort is therefore being made to develop additional airway systems which could make use of secondary airports to relieve the major airports of some of the congestion created by this so-called "short-haul" traffic. Of course, most secondary airfields currently available for use are of insufficient length for conventional transport airplanes with nominal passenger loads of 120 or more. As a result of these and other associated operating limitations, the STOL airplane is envisioned as a possible solution to the congestion problems of commercial airways. In general, STOL airplanes have been developed from modifications to more or less conventional airplane configurations. Recent STOL designs, for example, have employed full-span flaps with the wing partially or completely immersed in the slipstream of the propulsion units to achieve the high lift augmentation required for STOL operation. As a result of their conventional airframe geometry, most STOL airplanes do not exhibit unsatisfactory or unconventional flying qualities in cruising flight. A discussion of the stability and control characteristics of STOL airplanes will therefore consist of a consideration of the normal deterioration of handling qualities of conventional airplanes as airspeed is reduced and the types of artificial stability and control augmentation necessary to ensure satisfactory flying qualities.

## Problems of STOL Operation

For a number of years, the NASA has investigated several STOL airplanes to obtain information relating to the performance, handling qualities, and operational characteristics of airplanes during STOL operation. These investigations have made it possible to document and in most cases to improve the basic stability and control characteristics of this type of airplane. The results of the studies have pointed out several stability and control problem areas that appear to be common to most STOL designs. This part of the paper presents some of the results obtained during a series of flight tests to evaluate a powered-lift swept-wing jet transport in the landing approach at high lift coefficients and low airspeed. Although not capable of true STOL performance, the airplane tested was, in general, found to have flying qualities quite typical of large STOL airplanes and therefore is used to point out some of the stability and control characteristics peculiar to these vehicles.

Airplane and evaluation procedures. - One method of improving the low-speed lift capabilities of high performance aircraft is boundary-layer control or "blown flaps." Recent flight test experience with a boundary-layer-control (BLC) jet transport at the Langley Research Center and the Ames Research Center has led to a better understanding of the stability and control characteristics of large STOL aircraft. The test airplane used in the investigations was a modified Boeing 707 prototype shown in figure 3. The airplane incorporated a powered-lift BLC system which used compressed air bled from the four engines. The wing was modified with a fixed leading-edge slat so as to avoid stall induced by the upwash associated with BLC operation. A simple hinged-flap system was used, and the maximum flap deflection tested was  $85^\circ$ . An enlarged horizontal tail having 25 percent larger area was used to improve the longitudinal stability and trim characteristics and an inverted leading-edge slat was fitted to the horizontal tail for improved trim capability at high negative lift conditions.

The BLC system used by the airplane is illustrated in figure 4. Compressed air was bled from each of the four engine compressors into a dual ducting system. As shown in the sketch in the upper left-hand corner, nozzles through which the compressed air was ejected were alternated along the entire length of the trailing-edge flaps to minimize lift loss in the event of engine failure. A typical cross section (section A-A) of the nozzle-ejector-flap system is shown in the lower right-hand sketch.

The airplane also employed a thrust-modulation system to permit high power settings on the jet engines for BLC operation while simultaneously reducing the net thrust of the engines to the lower levels normally associated with the landing approach. As shown in figure 5, the thrust-modulation system consisted of continuously controllable clamshell-type thrust reversers located in each of the four engine tailpipes. The thrust-modulation system was used in place of the normal throttle control during all BLC flight

conditions. As shown in figure 6, the thrust-modulation system proved to have rapid response in comparison to normal throttle control. The rapid response obtained with the thrust modulators permitted the pilot to maintain more precise control of airspeed during the landing approach. The thrust-modulation system was also used as a unit of an automatic airspeed-control system to be discussed in a subsequent section of this paper.

Pilot opinions of the flying qualities of the airplane were obtained under simulated instrument flight rules (IFR) during landing approaches in which the BLC system was in operation. These evaluation conditions provided a reasonable requirement for precise piloting techniques similar to actual IFR flight operations. The pilot's evaluation task consisted of first intercepting the localizer at about 8 miles from the runway at an altitude of 1500 feet (457 meters). At the intercept of the glide slope, approximately 5 miles from the runway, the pilot initiated the descent and flew the glide path as closely as possible. Following a simulated IFR breakout at 200 feet (61 meters), the pilot continued visually to touchdown.

Pilot's rating. - A summary of pilot opinions of the test airplane during approaches with BLC is shown in figure 7. Pilot numerical ratings for the longitudinal and lateral-directional axes are plotted as functions of airspeed, which was varied from the normal approach speed of about 140 knots down to 80 knots. Increasing (numerically larger) values of pilot rating correspond to less acceptable handling-quality characteristics. The data indicate that, for the approach speeds normally used by present-day jet transports (above 130 knots), the longitudinal and lateral-directional characteristics were acceptable. When the approach speed was lowered by the use of BLC, however, the pilot ratings became steadily worse, and at the minimum approach speed of 80 knots, the lateral-directional characteristics became unacceptable for IFR operation. As stated previously, the steady deterioration of handling qualities as airspeed is reduced is an inherent characteristic of STOL and V/STOL airplanes. Now, some of the specific reasons for the marked loss of acceptable flying characteristics will be examined.

Longitudinal stability and control. - The degradation of longitudinal stability was related primarily to pitch attitude requirements and trim changes in ground effect. Illustrated in figure 8 are test results showing the pitch attitude during approach for the basic airplane and for the airplane with BLC. The shaded area indicates the desired pitch attitude range for operation of the airplane whereas the vertical dashed lines represent physical limits on touchdown attitude. Within the shaded area the airplane would not touch down nose wheel first nor tail skid first during the landing flare. It can be seen that the pitch attitude varied from slightly high for the basic airplane to too low for the powered-lift airplane. During the approach and landing, the combination of flap setting and power condition used resulted in a nose-down attitude and concern that the airplane would touch down nose wheel first.



During powered-lift operation, the airplane exhibited large nose-down pitching moments as it neared touchdown. As shown in figure 9, this characteristic required considerably larger elevator deflections during the landing flare for the powered-lift airplane than those required for the basic airplane. The large trim change increased the pilot workload considerably. The trim change experienced in ground effect appears to be related to a large change in downwash angle at the tail in ground effect. Because of the relatively large angles of downwash associated with slow-speed flight at high lift coefficients, this characteristic will probably be an inherent problem with this type of airplane.

It should also be mentioned that the powered-lift airplane was flown on the back side of the power required curve, but the amount of speed instability was not sufficient to cause major adverse pilot comment.

Lateral-directional stability and control. - The two primary reasons for the unacceptable lateral-directional characteristics at low speeds were lack of adequate lateral-directional damping and problems of turn coordination. Shown in figure 10 are the variations of the damping characteristics of the classical roll and Dutch roll modes with approach speed. Values of the roll mode time constant greater than 1 second are considered to be excessive and indicative of low roll damping. Negative values of the Dutch roll damping ratio are indicative of unstable lateral-directional oscillations. The data indicate that as the approach speed was reduced, the damping of the roll mode and the Dutch roll mode was correspondingly reduced and that the Dutch roll oscillation actually became unstable at an approach speed of about 108 knots. This instability was caused by a combination of excessive dihedral effect and the nose-down attitude during approach. As might be expected, the unstable Dutch roll mode was found to be very troublesome and considerably degraded the lateral-directional handling characteristics. The second major lateral-directional problem, related to what pilots call "turn coordination," is illustrated in figure 11 which shows the variation with airspeed of the directional stability (in terms of the Dutch roll frequency) and the ratio of sideslip angle to bank angle for rudder-fixed turns. Poor turn coordination generally accompanies low levels of directional stability because large values of sideslip will be generated in rudder-fixed turn entries. The ratio  $\Delta\beta/\Delta\phi$  is therefore usually used as a measure of turn coordination. The data of figure 11 show that the test airplane at 80 knots had a value of  $\Delta\beta/\Delta\phi$  of about 0.8; that is, for a rudder-fixed bank angle of  $10^\circ$  during a turn, a peak sideslip angle of  $8^\circ$  was developed. Previous research and flight test studies have shown that when  $\Delta\beta/\Delta\phi$  is above about 0.3, turn coordination will be a problem.

Effects of stability augmentation. - Much effort was directed at improving the lateral-directional problem areas and relieving the pilot of a major portion of his workload during powered-lift operation. Most of this work was concerned with development of adequate forms of stability augmentation and automatic speed control. A block diagram

of the stability-augmentation system used is shown in figure 12. The augmentation system consisted of a sideslip rate damper, a turn coordination programmer, and a roll decoupler which were connected in parallel to the rudder. The sideslip rate damper, commonly known as a  $\dot{\beta}$  (sideslip rate) damper, consisted of a vane under the nose of the airplane to produce an electronic signal proportional to sideslip angle and an electronic differentiator to operate on the sideslip signal to produce a signal proportional to  $\dot{\beta}$ . The electronic output of the differentiator was then used to drive the rudder in proportion to  $\dot{\beta}$ , the end product of the unit being the creation of an artificial stability derivative  $C_{n\dot{\beta}}$  (rate of change in yawing moment coefficient with time derivative of sideslip). The turn coordination programmer consisted of an interconnect between aileron deflection and rudder deflection. With this type of mechanization, it was possible to change artificially the value and direction of the yawing moment due to aileron deflection  $C_{n\delta_a}$ . The roll decoupler consisted of a roll rate gyro, the output of which was used to deflect the rudder; with this device, it was possible to vary the magnitude and direction of the yawing moment due to roll rate  $C_{nr}$ . The effects of the entire stability-augmentation system on the lateral-directional dynamic motions of the airplane are illustrated in figures 13 and 14.

Shown in figure 13 are time histories of the control-fixed airplane roll rate following a disturbance for the basic airplane, the powered-lift airplane, and the powered-lift airplane with the  $C_{n\dot{\beta}}$  damper operating. The time histories show that the Dutch roll oscillation was lightly damped for the basic airplane and unstable for the airplane with BLC. Incorporation of the  $C_{n\dot{\beta}}$  damper, however, increased the damping of the Dutch roll markedly. As might be expected, the pilot rating of the lateral-directional characteristics improved considerably with the  $C_{n\dot{\beta}}$  damper. It might also be expected that variations of any stability derivative such as the damping-in-yaw  $C_{nr}$  to produce a stable Dutch roll mode would accomplish the gains afforded by the addition of sideslip rate damping. Research has shown, however, that  $\dot{\beta}$  damping is more versatile than yaw rate damping for control of sideslip on STOL airplanes. The response of the airplane to a conventional yaw damper and to a  $\dot{\beta}$  damper differs because of the different sense of the yawing moment applied by the two stability augmentation systems during turn entries. In the  $\dot{\beta}$  case, as the airplane banks and moves laterally due to bank angle, the positive yawing moment due to  $\dot{\beta}$  damping is in the direction of the turn, while the moment due to a yaw damper is in a direction opposite to the turn. As a result, the peak sideslip angle generated by the turn is reduced considerably and a steady-state turn rate is built up more rapidly with a  $\dot{\beta}$  damper in comparison with a conventional yaw damper.

The effects of the  $\dot{\beta}$  damper, turn coordination programmer, and roll decoupler on turn entry characteristics are presented in figure 14, which shows the angle of sideslip

generated in turn entries for the powered-lift airplane with and without stability augmentation. As illustrated by the time histories, the powered-lift airplane without augmentation had undesirably large amounts of adverse sideslip during turn entries. It can be seen that the adverse sideslip combined with the positive effective dihedral to change the sense of roll rate (roll reversal) even though the pilot held the roll control. With the stability-augmentation system in operation, the adverse sideslip was essentially eliminated and there was no tendency toward roll reversal.

During the course of the study, the effects of an automatic speed control were also evaluated in an effort to reduce the pilot workload required during powered-lift operation. The automatic speed system compared the airspeed to a reference speed selected by the pilot and automatically manipulated the thrust modulation to obtain the desired reference speed. The effect of automatic speed operation of pilot workload during approaches is illustrated in figure 15, which shows plots of approach speed and wheel position with auto-speed inoperative and operative. The use of automatic speed control provided a marked improvement in flying qualities. This improvement shows up in figure 15 in two ways: First, the airspeed deviation from the desired reference speed is seen to be much less with the automatic speed control in operation. Second, the lateral-control wheel inputs indicate that the pilot was using smaller control inputs when flying with automatic speed control. As a result of the reduced workload, the pilot could pay more attention to precise control of the flight path during the approach.

The improvement in handling qualities realized with lateral-directional augmentation of the powered-lift airplane is shown in figure 16. The pilot ratings of the unaugmented airplane are those previously presented in figure 7. The addition of stability augmentation improved the flying characteristics to the point that satisfactory ratings of 3 to  $3\frac{1}{2}$  were obtained at 80 knots.

These flight tests with a BLC-equipped jet transport have illustrated some of the stability and control problem areas common to most STOL airplanes. The principal stability and control problem areas appear to be lateral-directional in nature and consist of inadequate lateral-directional damping and poor turn coordination characteristics. If these problems are to be minimized, most STOL airplanes will require stability augmentation in the form of sideslip-rate damping, rudder-aileron interconnect, and artificial variation of yaw due to rate of roll.

### Current Status of STOL Airplanes

As previously pointed out, the most significant driving force behind the development of STOL airplanes has been the desire to improve the airway system of the nation by relieving the congestion problem. A number of so-called "shuttle" flights have been introduced at some of the larger airports to serve a portion of the short-haul traffic

demand. These flights are usually conducted with small, light airplanes having extremely limited passenger capabilities. At this time a true STOL transport is not operational, although progress is being made to the extent that many of the major airlines are issuing requirements for an STOL airplane. In particular, two major U.S. airlines have recently conducted an evaluation of STOL intra-city operations using the Breguet 941 airplane shown in figure 17. The Breguet 941 is an unpressurized transport utilizing the deflected-slipstream STOL technique. In this system the slipstream of the four propellers blows over the entire span of the wing which is equipped with extensive slotted flaps. The four engines are interconnected with shafting so that all propellers will continue to rotate in event of an engine failure. The airplane also incorporates a number of interconnect features between control surfaces so as to minimize trim changes and adverse yaw during STOL operation. Although not as large as desired, the airplane provided the airlines with an existing design by which they might evaluate the STOL system concept. In effect the tests conducted were made in crowded terminal areas such as the New York-Boston-Washington triangle in an effort to determine whatever STOL traffic could be segregated out from regular airway and terminal area users. The results of the evaluation were promising, and one of the significant effects has been to set in motion in-house design studies by the major airlines aimed at formulating specifications which they consider to be practical for an STOL transport. A cross section of the major airlines indicates an STOL transport must meet the following specifications:

- (1) A seating capacity of 100 to 200 passengers
- (2) Cruising speed of about 320 knots
- (3) Maximum range of 500 nautical miles

In addition, the vehicle must be capable of operation from a 1500-foot (457-meter) runway with climb-out angle and approach angle of  $7^{\circ}$  to  $10^{\circ}$ . Current demands indicate such an airplane would enter operational service in this decade.

#### Future STOL Concepts

Several concepts are being developed to meet these specifications, and it appears that a jet-powered STOL airplane may be one of the leading candidates. One particular concept receiving considerable research attention is the external-flow jet-flap concept. An airplane using this system might resemble a conventional jet transport with podded engines. As shown in figure 18, however, the jet engines are inclined slightly downward so that the exhaust from the engines impinges on a trailing-edge flap system. This arrangement results in a considerable increase in the circulation about the wing and large increases in lift. Although this configuration appears promising from performance considerations, a number of stability and control problems are inherent in this concept. First, the large downwash associated with the high lift coefficients strongly influences

the geometric design of the airplane. As shown in figure 19, the horizontal tail must be sufficiently removed from the downwash field to remain effective and ensure stability at low speeds.

The provision of adequate control power to maneuver the airplane is also a serious problem on this design. Obviously, as the minimum operational airspeed is reduced to zero, a point is reached at which unorthodox control systems, such as boundary-layer control on control surfaces and reaction jet controls, must be used.

The last and perhaps most important problem of the jet-flap concept is the provision of adequate control to cope with an engine-out condition. Without mechanical interconnect, loss of an engine on this type of airplane would pose a serious trim problem in roll and yaw which may be catastrophic.

In addition to the stability and control problems unique to the jet-flap system, it should be kept in mind that this configuration is subject to the problems discussed earlier for the BLC transport and therefore requires an artificial stabilization system.

## STABILITY AND CONTROL CHARACTERISTICS OF V/STOL AIRPLANES

The information presented in the previous section provided an insight as to the stability and control characteristics of airplanes as the approach and landing speed is reduced. This part of the paper extends the airspeed region of interest down to hovering flight by a discussion of the stability and control characteristics of V/STOL airplanes which employ several different propulsive concepts to achieve vertical take-offs and landings.

### Performance of V/STOL Airplanes

Over the last decade a bewildering array of various types of V/STOL airplanes has been proposed. Some of these concepts are shown in figure 20. The various types of V/STOL vehicles might logically be classified by the propulsive concept which powers the machine; for example, concepts powered by rotors, propellers, ducted fans, and turbojets. In addition, the various concepts can be grouped according to the method by which they perform the transition to forward flight. For example, the aircraft tilting types use pitch attitude changes, the thrust-tilting vehicles rotate the propulsion units, the thrust-deflection types deflect or rotate the slipstream of the propulsion unit, and dual-propulsion types use two separate power units for vertical take-off and for cruise. With such a large number of designs available, the question naturally arises as to which concept is best. A considerable amount of research and development has therefore been directed at answering this question. The result of this research indicates that no one design is best, but the various types have different applications depending on the type of

V/STOL mission under consideration. To illustrate this point, consider two phases of a typical V/STOL mission – the hovering phase and the cruise phase. Two important factors which govern to a large extent the hovering capability of a V/STOL airplane are shown in figure 21. Plotted in figure 21 is the variation with propeller diameter of the amount of power required to hover. The first important point to be noted is that the amount of power required for the airplane of a given weight to hover decreases markedly as the diameter of the lifting element increases. This power decrease results from the fact that for a given value of thrust to be produced, a large-diameter propeller must take a relatively large mass of air at rest and impart a relatively small induced velocity  $v_i$  to the air, whereas a small-diameter propeller produces this value of thrust by accelerating a relatively small mass of air and imparting a large velocity to the air. Inasmuch as the power required is proportional to the induced velocity, the power required for small-diameter lifting elements is extremely high. Of course, the large amount of power required also results in large fuel consumption for hovering flight. The second important factor to note in figure 21 is that smaller lifting elements tend to have high-velocity slipstreams, which may pose a problem with respect to ground erosion, foreign object ingestion, and injury to ground-based personnel.

The results of this analysis of hovering capability are shown in figure 22, which presents a plot of hovering efficiency (which may be thought of as thrust produced for a given power input) and slipstream velocities for several V/STOL concepts. As can be seen, the large-diameter lifting element (rotor) is easily the most advantageous choice for a V/STOL airplane if the mission calls for a great deal of hover time. The least efficient design is the turbojet for the reasons previously discussed, and hovering time with this type of machine must be kept to an absolute minimum. In summary, the analysis of performance characteristics in hovering flight indicates that a rotor-powered machine or helicopter is best suited for a mission involving hovering flight of long duration.

An analysis of the cruise portion of the V/STOL mission is now considered. Shown in figure 23 is the variation of power required with forward speed for a helicopter and a propeller-driven V/STOL transport of the same weight. Note that at a forward speed of zero, or hovering flight, the helicopter requires far less power than the propeller design for reasons previously discussed. As the forward speed is increased, however, the helicopter experiences a sharp rise in power required due to compressibility and stall effects on the rotor blades while the propeller-driven transport requires far less power. A jet-powered design would show an even greater speed advantage over that of the helicopter. This characteristic increase in power required for the helicopter places severe restrictions on the maximum speed capability of the helicopter and results in consideration of other V/STOL concepts for missions involving high cruise speeds.

The results of an analysis of the applications of various V/STOL concepts is shown in figure 24, which shows a plot of hovering capability and cruising speed for several concepts. Note that the helicopter has the greatest hovering capability and the lowest cruising speed, whereas the turbojet-powered design has the greatest cruising speed with little hovering capability. Note also that a variety of V/STOL concepts have capabilities within these two extremes.

This paper now considers the stability and control characteristics of three of the most promising V/STOL concepts: the propeller-driven tilt-wing airplane, the ducted-propeller or tilt-duct airplane, and the jet-powered V/STOL airplane.

### Tilt-Wing V/STOL Airplane

If cruise speeds of about 400 knots, or less, are acceptable, the tilt-wing propeller-driven V/STOL airplane can be used to great advantage. Over 60 years of development have been devoted to making the conventional airplane configuration an efficient cruising vehicle, and the tilt-wing concept adds VTOL capability to it with a minimum of compromise.

An example of the tilt-wing design is shown in figure 25. This design utilizes the deflected slipstream and tilting-wing concepts to avoid wing stall during the transition to forward flight. The airplane employs full-span double-slotted flaps to deflect the slipstream produced by 15-foot-diameter (5-meter-diameter) propellers. The total immersion of each wing semispan in the propeller slipstreams together with interconnected propellers is similar to the Breguet 941, but the tilt-wing design produces VTOL capability. An 8-foot-diameter (2.44-meter-diameter) tail rotor is provided for pitch control.

Because of extensive wind-tunnel and flight research and development, the propeller-powered V/STOL airplane represents a more advanced state of development than any other class except the helicopter. Since this type of V/STOL airplane is effectively a conventional propeller-driven airplane in cruising flight, it displays, for all practical purposes, no new stability and control problems in this flight regime. It does, however, exhibit a number of unconventional stability and control characteristics in hovering, transition, and STOL flight.

Stability and control in hovering.- As pointed out previously, in hovering flight the conventional aerodynamic control surfaces of V/STOL airplanes usually become ineffective. As a result, most V/STOL designs use separate control systems for hovering and conventional flight. The tilt-wing airplane is a typical example of a design employing a dual control system. Roll control for hovering flight is usually provided at little expense of airplane performance by differential variation of the blade angles of the right and left propellers. This type of control system produces a very powerful control which is usually more than adequate in terms of angular acceleration capability. Yaw control in

hovering flight is normally provided by differential deflection of ailerons located in the propeller slipstream. The ailerons are the sole aerodynamic control surfaces which do not totally lose all effectiveness in hover due to the high velocities in the propeller slipstream. Provision of adequate yaw control capability has proven to be somewhat troublesome in the past and has led to use of large aileron deflections to meet minimum control requirements. When hovering in ground effect, the ailerons also tend to lose effectiveness as shown in figure 26. This figure shows a plot of aileron effectiveness relative to effectiveness out of ground effect for various values of  $h/D$ . The data show that the ailerons lose almost one-half their effectiveness in ground effect as the airplane nears touchdown. This loss in yaw control effectiveness is caused by the fact that the propeller slipstream spreads as it approaches the ground, and the ailerons are less effective in turning the larger slipstream. Pitch control for the tilt-wing airplane in hovering flight is not obtained without significant penalties in terms of weight, performance, and mechanical complexity. Designers have, in the past, favored tail propellers or fans for pitch control on present-day tilt-wing designs.

Perhaps the most outstanding stability characteristics displayed by tilt-wing airplanes in hovering flight are dynamically unstable oscillations about the roll and pitch axes. Typical examples of these unstable oscillations are presented in figure 27. The data shown were obtained during hovering flights of a model of a four-propeller tilt-wing vehicle. Time histories are presented of control-fixed motions obtained separately in pitch and roll. The oscillations are very unstable, but the periods are relatively long and the unstable motions can be easily controlled by a pilot under visual flight conditions. The airplane would, however, be uncontrollable under instrument flight conditions without artificial stabilization. These unstable oscillations are typical of V/STOL vehicles employing rotors or propellers. In fact, unstable oscillations similar to these are exhibited by most present-day helicopters.

Dynamic analysis of the unstable oscillatory modes of hovering flight has pointed out the cause and possible remedies for the instabilities. A unique aspect of static stability that is important for most V/STOL airplanes is normally referred to as velocity stability -- that is, the variation of pitching moment with airspeed at constant angle of attack and power. This characteristic is illustrated in figure 28, which shows typical variations of nondimensional pitching-moment coefficient  $C_m$  with airspeed for a conventional airplane and for a V/STOL airplane. For constant values of power and angle of attack, the value of  $C_m$  is constant with airspeed for the conventional airplane with the exception of flight in the transonic speed range. On the other hand, the V/STOL airplane typically exhibits large nose-up variations of  $C_m$  with airspeed. Although this variation of moment with airspeed is statically stabilizing, excessive magnitudes can cause handling problems in gusty air and, in addition, excessive speed stability contributes to the dynamically unstable oscillations of hovering flight.



The linearized longitudinal equations of motion for a V/STOL airplane in hovering flight are as follows:

Vertical force:

$$-\underline{F_{Z_u}}u + (s - F_{Z_w})w - \underline{F_{Z_q}}s\theta = 0 \quad (1)$$

Longitudinal force:

$$(s - F_{X_u})u - \underline{F_{X_w}}w + (g - \underline{F_{X_q}}s)\theta = 0 \quad (2)$$

Pitching moment:

$$-M_{Y_u}u - (\underline{M_{Y_w}} + \underline{M_{Y_{\dot{w}}}}s)w + (s^2 - M_{Y_q}s - M_{Y_{\theta}})\theta = 0 \quad (3)$$

The values of the stability derivatives underlined in the equations of motion are normally negligible for V/STOL vehicles in hovering flight. As a result of the elimination of several stability derivatives, the characteristic equation describing the dynamic stability of the airplane becomes

$$(s - F_{Z_w}) \left[ s^3 - (F_{X_u} - M_{Y_q})s^2 + (F_{X_u}M_{Y_q} - M_{Y_{\theta}})s + (F_{X_u}M_{Y_{\theta}} + M_{Y_u}g) \right] = 0 \quad (4)$$

One root of the characteristic equation is immediately known and is equal in magnitude to the vertical-velocity damping derivative  $F_{Z_w}$ . The mode of motion described by this root is the convergence of the vertical motion of the vehicle to disturbances, in other words, the "heave" stability of the airplane in hovering flight. The remaining cubic equation in the brackets defines fore and aft and pitch stability of the airplane.

Typical solutions to the characteristic equation are shown in figure 29, which shows the four roots of the complete characteristic equation (4) plotted on the complex plane. Roots having positive real parts denote dynamically unstable modes of motion; therefore, the entire right half of the complex plane is associated with dynamic instability. The root at the origin is the real root equal to  $F_{Z_w}$ , which for simplicity in this case is assumed equal to zero. The solutions of the cubic equation usually consist of (1) a large negative real root describing a convergence of pitch and horizontal velocity displacements and (2) a complex pair with a positive real part describing the typical unstable oscillation involving pitch and horizontal translation. It may be shown mathematically that the unstable oscillation is brought about by excessive speed stability and lack of sufficient values of aerodynamic damping in pitch.

Stability-augmentation systems for hovering flight normally consist of both pitch-rate and pitch-attitude stabilization. The variations of the complex roots describing the unstable oscillation with these forms of stability augmentation are shown in figure 30. Presented in figure 30 are the effects of pitch-rate augmentation  $M_{Yq}$  and pitch-attitude augmentation  $M_{Y\theta}$  on the unstable pitch oscillation for a four-propeller tilt-wing airplane in hovering flight. When only pitch-rate augmentation is used  $\left(\frac{M_{Y\theta}}{M_{Yq}} = 0\right)$ , the path of the roots indicates that the oscillation can be made dynamically stable if the augmentation system gain is increased sufficiently. Large increases in damping in pitch, however, tend to decrease the effectiveness of the pitch control. In addition, a significant part of the pilot workload would still be devoted to attitude control. Addition of pitch-attitude stabilization without rate augmentation  $\left(\frac{M_{Y\theta}}{M_{Yq}} = \infty\right)$  makes the oscillation less unstable, but the major effect is an undesirable increase in the frequency of the oscillation. When rate and attitude stabilization are used simultaneously, almost any desired level of stability can be achieved with significant improvements in handling qualities, particularly in gusty air.

Although the preceding discussion emphasized dynamic characteristics of a tilt-wing airplane about the pitch axis in hovering flight, it should be pointed out that a similar situation exists about the roll axis. Consequently, tilt-wing vehicles will normally require roll-rate and roll-attitude stability augmentation for satisfactory handling characteristics in hovering flight.

Another unique characteristic of V/STOL airplanes is ground effect on lift and stability in hovering flight. The general character of the flow pattern around a tilt-wing airplane when hovering near the ground is shown in figure 31. The propeller slipstreams tend to spread out radially as they impinge on the ground, and as they meet in the plane of symmetry they tend to flow upward and may produce a positive, or lifting, pressure increment on the bottom of the fuselage. Presented in figure 32 are representative values of increases in lift due to ground effect. The ratio of lift in ground effect to lift out of ground effect ( $L/L_\infty$ ) is plotted in figure 32 as a function of the distance between the bottom of the fuselage and the ground in terms of propeller-diameter lengths ( $h/D$ ). The additional lift in ground effect is due to a combination of positive pressure increments on the bottom of the fuselage and the well-known increase of propeller thrust in ground effect.

Stability and control in transition. - As forward speed is increased and the transition to conventional flight has begun, the conventional aerodynamic control surfaces begin to regain effectiveness. Consequently, tilt-wing vehicles usually incorporate a form of

control-mixing mechanism which progressively changes the control functions so that the ailerons, rudder, and elevator become the primary controls at higher speeds.

When forward speed is increased, the aerodynamic pitching moment acting on the airplane becomes a function of the airplane angle of attack. The variation of pitching moment per degree angle of attack with airspeed is shown in figure 33 for several different propeller-driven V/STOL configurations. Positive values of the parameter  $-M_{Y_\alpha}$  represent a stable condition, whereas negative values represent an unstable condition. These data show that all configurations tend to be unstable at low speeds and become stable at higher forward speeds as the airplane approaches conventional flight conditions. As mentioned previously, the speed stability derivative  $M_{Y_u}$  tends to have positive (stable) values in the transition flight range. The overall static stability of the airplane is composed of the contributions of both the stabilizing  $M_{Y_u}$  and the destabilizing  $M_{Y_\alpha}$ .

The root-locus sketch in figure 34 shows a typical variation of longitudinal-stability characteristics as forward speed is increased. The solid symbols represent the stability roots for hovering flight, and the open symbols denote the roots for cruising flight. The unstable oscillation in hovering flight becomes less unstable with lower frequency as airspeed is increased until, in cruising flight, it becomes the conventional long-period phugoid oscillation. The two stable real roots of hovering flight combine as airspeed is increased to form the classical short-period oscillation displayed by a conventional airplane.

The variation of dynamic longitudinal stability as airspeed is increased is further illustrated in figure 35, which shows time histories of pitching velocity obtained during flight tests of a tilt-wing airplane following pulse inputs at various wing-tilt angles  $i_w$  corresponding to several values of forward speed. The data for  $85^\circ$  wing incidence indicate that the airplane displayed the unstable oscillation previously discussed. At a wing incidence of  $40^\circ$ , the oscillation became dynamically stable, and as the wing incidence was reduced further (airspeed was increased), the pitching-velocity time history is indicative of the conventional highly damped short-period oscillation. Because the airplane becomes dynamically stable as forward speed is increased, it is obvious that the need for artificial stability augmentation diminishes as cruising flight is approached. It has become normal practice, therefore, to program the gains of the stability-augmentation system with wing-incidence angle in such fashion that the system gains are reduced during the transition and are finally eliminated at high speeds.

Similar variations of lateral-directional stability with increasing airspeed are normally encountered, resulting in programmed variation of the lateral-directional stability-augmentation system.

Stability and control characteristics in STOL flight. - A tilt-wing V/STOL airplane, when operating at low airspeeds near the ground, can run into some of its own propeller

slipstream which has been deflected forward. As illustrated in figure 36, the deflection of the propeller slipstream by the ground creates a turbulent region through which the airplane must fly. Impingement of the turbulence on the airframe in an unsymmetrical manner results in large values of yawing acceleration. At the left in the figure is plotted the yaw acceleration for wing incidence angles between  $30^{\circ}$  and  $80^{\circ}$  corresponding to landing speeds up to 40 knots. The open symbols denote accelerations measured in actual flight tests of a tilt-wing airplane. The solid symbol represents the maximum yaw acceleration capability of the airplane control system in hovering flight. Obviously, this area of operation is potentially dangerous and should be avoided if at all possible. Actually, this phenomenon was encountered by an XC-142 airplane during a landing at about 20 knots. The airplane sustained considerable damage when control was lost and one wing tip struck the ground.

Other stability and control problems of tilt-wing V/STOL airplanes during STOL operation are related to wing stall, particularly in descending flight at partial power. This area of difficulty is discussed in a subsequent section of this paper.

In summary, the tilt-wing V/STOL airplane exhibits stability and control characteristics similar to present-day propeller-driven airplanes in cruising flight. It does, however, exhibit several undesirable stability and control characteristics at low airspeeds which can be alleviated by use of artificial stabilization equipment. The technology required to solve the stability and control problems of the tilt-wing vehicle is well in hand and it presently represents the most advanced V/STOL concept.

### Tilt-Duct V/STOL Airplane

A number of V/STOL designs powered by tilting ducted propellers have been evaluated as potential candidates for the long-range V/STOL mission in competition with the tilt-wing designs. In competition with the propeller, the ducted propeller offers the advantages of compactness and the possibility of increased static thrust efficiency. As shown in figure 37, the addition of a shroud around a conventional propeller prevents contraction of the propeller slipstream. Preventing contraction of the slipstream permits the ducted propeller to produce the same slipstream cross-sectional area as that produced by a conventional propeller of larger physical dimensions. In fact, for a given amount of power a ducted propeller will produce the same amount of thrust as a conventional propeller having a diameter 1.4 times as large as the duct exit. The ducted propeller is therefore a relatively compact propulsion unit. In addition, the duct walls produce a beneficial end-plate effect which reduces the blade-tip losses experienced by unshrouded propellers.

The advantages of the ducted fan are produced at the expense of the added weight and complexity of the duct and the performance losses in cruising flight associated with the extra drag of the duct.

An example of a tilt-duct V/STOL airplane is the X-22A transport shown in figure 38. Tandem tilt-duct configurations such as this one are powered by four ducted propellers arranged in pairs fore and aft. The tandem layout offers several advantages in control-system simplicity and results in a compact airplane that might be particularly suitable for shipboard or carrier-based operations. The tandem tilt-duct airplane has received a significant amount of research and development, and its stability and control characteristics have become fairly well documented. The tilt-duct design has been found to have many of the stability and control characteristics exhibited by tilt-wing designs in hovering, transition, and STOL flight. In addition, however, the fact that the tilt-duct vehicle does not resemble a conventional airplane during cruising flight produces additional stability and control problems as airspeed is increased. Most of these problems are related to the aerodynamic characteristics of the ducted propeller.

One of the fundamental characteristics of ducted propellers, as shown in figure 39, is that they produce a high drag in a side wind or crossflow. This characteristic results from the fact that when a ducted propeller moves horizontally, it must turn the air  $90^\circ$  down through the duct. A drag force is therefore produced which is equal in magnitude to the product of the mass flow of air through the propeller per second times the velocity of the crosswind. As can be seen in figure 39, the drag force produced by a ducted-propeller arrangement is much greater than that produced by an unshrouded propeller since the air can go through the free propeller at a relatively small deflection angle rather than at  $90^\circ$ . Obviously, a V/STOL configuration employing ducted propellers will be much more responsive to atmospheric gusts. If the inlets of the ducts are displaced from the center of gravity of the airplane, the forces generated normal to the inlet can produce sizable moments – for example, yawing moments in response to side gusts and pitching moments in response to head winds.

Another characteristic of ducted propellers, as shown in figure 40, is the development of large moments about an axis perpendicular to the duct center line when subjected to side winds. The moments are produced primarily by an effective change in the location of the thrust vector relative to the propeller shaft of such magnitude that greater lift is produced on the upwind lip of the duct than on the downwind lip. These moments are much greater for a ducted propeller than for a free propeller as shown by the test data at the bottom of the figure. It can therefore be rationalized that ducted-propeller airplanes will exhibit large values of the speed stability derivative  $M_{Y_u}$  due to the preceding aerodynamic characteristics.

Stability and control in hovering flight. – The general arrangement of the tandem ducted-propeller airplane results in powerful controls for roll and pitch by differential

changes in the pitch angle of the ducted propellers. Yaw control in hovering flight is provided by elevons mounted at the duct exit so that they are in the high-velocity propeller slipstream. When hovering in ground effect, the tandem configuration experiences the increase in lift and decrease in yaw control effectiveness previously discussed for the tilt-wing V/STOL airplane. As shown in figure 41, a typical configuration may experience a 20-percent increase in lift at touchdown. The data of figure 42 show that a decrease of about 40 percent in yaw control effectiveness occurred near the ground. This decrease in elevon effectiveness is partly explained by the decrease in thrust required in ground effect as shown in figure 41.

When hovering out of ground effect, the tilt-duct configuration experiences unstable pitch and roll oscillations similar to those discussed for tilt-wing airplanes in figure 32. The periods of the oscillations are long enough to be controllable by the pilot in visual flight, but artificial stabilization similar to the systems discussed for the tilt-wing airplane will be required to stabilize the oscillations for satisfactory all-weather operation. As might be expected, the airplane will be neutrally stable with respect to yaw displacement in hovering flight.

As the tilt-duct vehicle nears the ground, the slipstream impingement on the bottom of the fuselage produces natural variations of pitching and rolling moments with attitude as illustrated in figure 43. Plotted in figure 43 are the variations with distance above the ground of the pitching moment due to pitch attitude  $M_{Y_\theta}$  and rolling moment due to roll attitude  $M_{X_\phi}$ . It can be seen that the positive values of  $M_{X_\phi}$  produced in ground effect are statically unstable – that is, banking to right produces a rolling moment tending to further increase the bank angle. Because the tandem configuration is unsymmetrical within the plane of symmetry, the pitch attitude stability produced in ground effect is different for nose-up or nose-down attitudes.

During flight tests of model and full-scale tilt-duct airplanes, considerable difficulty has been experienced trying to control the airplane when hovering in ground effect. The moment changes brought about in ground effect, particularly the bank instability, may have contributed to the problems, but it is believed that the principal difficulty is caused by erratic disturbances produced by the random recirculation of the propeller slipstreams. Near the ground, the propeller slipstreams meet and form a strong upward flow between the fore and aft ducts that tends to flow erratically into one fan or another. These disturbances cause a considerable increase in pilot workload in hovering flight near the ground for a vehicle without artificial stability augmentation.

Stability and control in transition. - As the ducted propellers are tilted forward and the airplane begins to pick up speed, a control-system mixing unit varies the functions of the elevons so that roll and pitch control at high speeds are provided by differential elevon deflections, whereas yaw control is provided by differential propeller thrust.

As the transition to forward flight progresses, the large drag and moments generated by the ducted propellers produce large longitudinal trim changes as illustrated by the data of figure 44. Plotted in figure 44 is the variation with airspeed of untrimmed pitching moment in terms of angular acceleration about the pitch axis. These data indicate that large nose-up pitching moments are generated and reach a peak value of about  $1 \text{ radian/sec}^2$  midway through the transition to cruising flight. For a typical design, the margin between the trim requirement shown in figure 44 and the pitch control available may become critical in terms of excess control available for maneuvering requirements. The trim requirement can be reduced by differential deflection of the front and rear ducts; for example, reducing the incidence of the front ducts by  $10^\circ$  relative to the rear-duct incidence angle may reduce the trim requirement to about half the value obtained without differential deflection of the ducts. The dynamic longitudinal stability of the tilt-duct vehicle has been found to change from unstable oscillations in hovering flight to the classical phugoid and short-period oscillations in a manner similar to that of the tilt-wing airplane.

Studies of the lateral-directional stability characteristics of tandem tilt-duct vehicles have indicated several stability and control problem areas at high transition speeds. For example, shown in figure 45 are typical variations of yawing-moment coefficient  $C_n$  and rolling-moment coefficient  $C_l$  with sideslip angle for a high-speed flight condition. The variation of  $C_n$  with angle of sideslip is stable ( $C_{n\beta}$  positive) but is typically low in magnitude. The airplane also exhibits positive effective dihedral ( $C_{l\beta}$  negative) and the magnitude of  $C_{l\beta}$  is typically large – on the order of 3 to 4 times as large as  $C_{n\beta}$ . These characteristics tend to produce Dutch roll problems in cruising flight. Free-flight tests of a tandem tilt-duct model in the transition speed range have indeed exhibited Dutch roll oscillations that were unstable in the low-speed range and were still lightly damped to relatively high speeds corresponding to a duct angle of about  $20^\circ$ . During the course of the study, artificial stabilization supplied by a conventional yaw rate damper was found to be sufficient to stabilize the Dutch roll oscillation and eliminate this problem.

The free-flight model had another characteristic which contributed to poor lateral-directional behavior. The test results indicated that the model was experiencing stall on the upper outside surfaces of the ducts over a fairly large range of level-flight conditions for duct angles from about  $60^\circ$  to  $20^\circ$ . At the higher duct angles in this range (about  $60^\circ$  to  $30^\circ$ ), the resultant disturbances to the model were small, because of the low airspeeds, and were experienced mostly in yaw. At the lower duct angles (about  $30^\circ$  to  $20^\circ$ ), the dynamic input of the disturbances due to stalling was larger because of the higher dynamic pressure and was mostly about the roll axis because of the low duct angles. In these cases, the model experienced erratic and very objectionable rolling motions or wing dropping.

A series of tuft studies made with the model showed that, in some flight conditions, there was intermittent, erratic stalling of the upper surfaces of the ducts, and that over

an angle-of-attack range, these duct upper surfaces did not stall symmetrically. It was found in these tests that there was an intermittent stall condition on each duct surface so that at a given test condition there might be an unstalled duct, an intermittently stalling duct, and a stalled duct on the model all at the same time.

In an attempt to delay the stall of the duct upper surfaces, a set of leading-edge slats were fitted to the model as shown in figure 46. Tuft tests, made with the slats mounted as shown, indicated that the slats delayed the stall to a fuselage angle of attack of at least  $10^\circ$  for all duct incidence angles, and to angles of attack as much as  $20^\circ$  at low duct-incidence angles where the disturbances due to the stalling had been the most objectionable. With the slats mounted on the ducts, the model was again tested in flight throughout the transition range. As expected, the model with slats did not experience the erratic and objectionable rolling motions or wing dropping.

It should be noted that although the slats solved the wing dropping, the model still had the Dutch roll tendency and artificial damping in yaw was still required for satisfactory flight characteristics.

One additional area of concern during the high-speed flight of the tilt-duct airplane is the rather large magnitude of lateral force produced by sideslip. In fact, as shown in figure 47, the magnitude of the side-force-due-to-sideslip derivative  $-C_{Y\beta}$  for a duct incidence of  $15^\circ$  is about 40 percent as large as the lift-curve slope  $C_{L\alpha}$ . These data indicate that the airplane would experience large lateral accelerations in gusty air. For example, presented in figure 48 are the variations with airspeed lateral acceleration produced by a crosswind gust of 50 ft/sec (17 m/sec) for a tandem tilt-duct configuration and a conventional subsonic jet transport. As can be seen, the tilt-duct vehicle would experience lateral accelerations from about 0.6g to over 1.0g in this flight condition. Because the pilot tolerance to lateral accelerations is known to be very low, the large lateral accelerations shown in figure 48 suggest a critical problem area which will be typical of tilt-duct V/STOL airplanes.

In summary, the tilt-duct V/STOL airplane exhibits stability and control characteristics similar to those of most propeller-driven V/STOL designs in hovering flight. In high-speed flight, however, the tilt-duct vehicle does not exhibit conventional stability and control characteristics because of its unique physical layout. The significant stability and control problems appear to be duct stall, which can be eliminated by flow-control devices; unstable or lightly damped Dutch roll oscillations, which can be eliminated by artificial stabilization; and undesirably high lateral response to gusts, which appears to be an inherent characteristic of the design and is not easily solved.



## Jet V/STOL Airplanes

When the requirements for a V/STOL mission call for supersonic capability, a jet-powered V/STOL design becomes necessary. This type can be designed to obtain low volume and frontal area and thereby to permit maximum speed potential and is therefore ideally suited for fighter or attack missions. A large amount of flight experience with these airplanes has been accumulated. The two jet concepts presently under evaluation are the lift-engine concept, which uses separate jet engines for hovering and cruising flight and the vectored-thrust concept in which the thrust of a single jet engine is deflected for hovering flight. One of the more advanced vectored-thrust V/STOL airplanes is the P.1127 fighter shown in figure 49. The operational version of this airplane is the Harrier, and it has logged more V/STOL flight time than any other design and is currently in service.

The jet-powered configurations exhibit conventional airplane flying qualities in cruising flight. Unlike the tilt-wing and tilt-duct vehicles, the jet-powered designs are not subject to unstable oscillations in hovering flight, but they do encounter some unique stability and control problems in transition flight.

Stability and control in hovering. - The general layout of a high-speed configuration does not permit the conventional aerodynamic control surfaces to be placed in high-velocity slipstream as was the case for the ailerons of the tilt-wing airplane. Instead, the jet machine is usually provided with a jet reaction control system. These usually take the form of reaction jets in which the roll and pitch nozzles are located at the front, rear, and wing tips of the airplane, and an additional nozzle facing sideways at the tail is used for yaw control. High-pressure air bled from the engine compressor is ducted to the control valves. The reaction controls are usually linked mechanically to the aerodynamic control surfaces. When the control stick is moved to the right, for example, the left aileron deflects downward and the reaction jet at the left wing tip is opened downward to raise the wing.

It has been found that jet V/STOL airplanes do not exhibit the unstable oscillations displayed by machines of lower disk loading in hovering flight. As a consequence, some jet designs such as the P.1127 have been flown without artificial stabilization under visual flight rules (VFR) conditions. The lack of artificial stabilization does not, however, ease the control burden during precise maneuvers or gusty air. Without artificial stabilization, actuation of the jet reaction control system will result in roll acceleration rather than the roll rate normally produced by a conventional-airplane aileron control.

The problems involved in achieving precise translational maneuvers with a jet V/STOL airplane in hovering flight are illustrated in figure 50. Presented in figure 50 are time histories of the lateral control inputs required to produce roll rate and bank angle for a conventional airplane and a jet V/STOL airplane in hovering flight. When the

pilot of a conventional airplane applies lateral control, the rolling moment produced by the ailerons accelerates the airplane about its roll axis. As the roll rate increases, the natural aerodynamic damping moment increases until it is equal and opposite to the moment due to aileron deflection. The airplane then maintains a steady rate of roll until the pilot neutralizes the stick. When the forcing moment of the ailerons is eliminated, the aerodynamic damping slows the airplane to a constant bank angle.

In contrast, the sketch on the right of figure 50 shows that if the pilot of the V/STOL airplane in hovering flight applies lateral stick, the rolling moments caused by the reaction controls will also accelerate the airplane, but lack of natural aerodynamic damping results in an ever-increasing angle of roll unless opposite roll control is given. The control-input time history clearly illustrates that the pilot of the hovering jet V/STOL airplane has more work to do and more decisions to make for precise control during lateral translations. Because of the considerable amount of pilot workload involved, some form of stability augmentation – at least in the form of rate stabilization – will be required for operational aircraft.

During hovering flight out of ground effect, the P.1127 has been noted to have neutral directional stability in still air. In the presence of crosswinds, however, the airplane exhibited a tendency to turn away from the crosswind. This directional instability is associated with the side force produced at the nose of the airplane, created by turning a large mass flow of air into the engine inlets. As illustrated in figure 51, the side force created at the nose is much larger than that created by the vertical tail at low speeds. Since the engine inlet is located some distance forward of the center of gravity, a sizable destabilizing yawing moment is created. Under gusty conditions, or during turns away from headwinds, control of the airplane can become critical if large sideslip angles are produced by the instability.

Stability and control in transition. – The control system of the jet V/STOL airplane is perhaps the simplest of all the V/STOL designs. As forward speed is increased, the compressed air supply to the control jets is cut off, and the airplane uses conventional surfaces for control.

During the transition to forward flight, the jet airplane may encounter serious stability and control problems brought about by aerodynamic interference between the jet wake and the free-stream air. The basic principle of jet interference is shown schematically in figure 52. The sketch shows the pressure distribution induced on the lower fuselage and wings of a wing-body combination by a jet issuing perpendicular to the free-stream flow. As the jet flows from the airplane, it changes from a cylindrical-type flow to a kidney-shaped vortex field. The resulting pressure distribution consists of positive pressures ahead of the jet and larger negative pressures behind the jet. The total pressure distribution results in a net loss of lift and nose-up pitching moment. The effect of

interference between the free-stream and jet wake can affect (1) the stability and control characteristics of the basic wing-body combination, (2) the horizontal tail contribution to stability, and (3) lateral stability and control characteristics.

The effect of jet interference on the lift and pitching-moment characteristics of a wing-body combination is shown in figure 53. Nondimensional pitching moment and lift are plotted against nondimensional velocity ratio for three jet configurations: a single large nozzle and two arrangements of four small nozzles. The total jet exit area is the same for all three configurations. As shown on the left side of the figure, at  $0^\circ$  angle of attack, the jet-interference effects produce a large lift loss and nose-up pitching moment as forward speed is increased (conversion to conventional wingborne flight would typically occur at  $\frac{V}{V_j} \approx 0.25$ ). The effect of various jet arrangements is also shown in figure 53. The diamond arrangement on the right appears to be the best of the three since it shows higher lift and less pitching moment for a given angle of attack and velocity ratio. The better characteristics of this configuration are believed to be caused by the more effective "streamlining" of the jet wake. This streamlining probably reduces the obstruction to the free-stream flow and, consequently, produces less induced effect on the airframe.

The previous discussion was restricted to considerations of jet-interference effects on the wing-body combination with the horizontal tail off. Lifting jets can also induce large values of downwash at the horizontal tail, which result in additional nose-up pitching-moment variations. As shown in figure 54, in cruising flight, a contemporary variable-sweep fighter V/STOL configuration having a fixed forewing or glove will experience vortices shed by the lifting glove. It is, of course, highly desirable to locate the horizontal tail as low as possible so as to prevent impingement of the trailing vortex system on the horizontal tail as angle of attack is increased. Experience with conventional airplanes has shown that impingement of these vortices can cause serious longitudinal stability and control problems. Figure 55 shows the path of the trailing vortices for the jet V/STOL airplane in transition. The vortices can be pulled down by the flow field induced by the jet wake to such an extent that the horizontal tail will enter the vortex region as angle of attack is increased. An example of a jet-induced downwash problem is presented in figure 56. Pitching-moment variations with lift coefficient are shown for a vectored-thrust V/STOL configuration for several horizontal-tail positions and thrust conditions. The data in the left-hand plot show that the configuration is unstable with the horizontal tail off and that the instability increases with lift coefficient. Addition of a horizontal tail in a high position does not eliminate the instability, but moving the tail to a low position provides stability over the entire lift range. When power is increased, the data on the right side of figure 56 indicate that large changes in trim and stability occur with the exit nozzles in the  $30^\circ$  to  $60^\circ$  range. A marked instability or pitchup is shown for a nozzle angle of  $60^\circ$ . Obviously, considerable concern must be given to placement of the horizontal tail on this type of configuration.

The problems caused by jet interference are, unfortunately, not limited to longitudinal characteristics. For example, shown in figure 57 is an illustration of the rolling moments generated by propulsive effects when the airplane is sideslipped. Plotted at the top of the figure is the sideslip angle generated by a 30-knot crosswind as airspeed is reduced. Plotted at the bottom of the figure is the nondimensional rolling moment produced by these sideslip angles. The data points indicate the moment produced by a combination of flow into the inlets and jet-interference effects which must be trimmed by the available roll control. The control available is the sum of the contributions of the ailerons and jet reaction controls. The most critical region occurs at the lowest speeds, where control required for trim may approach the total control available from the tip jets. The problem is further aggravated by the fact that the reaction controls lose effectiveness as speed is increased due to the interference effects between the control jets and the wing. It is apparent that some limitation of sideslip excursions during low-speed flight will likely exist. Excursions in sideslip are easily produced at low speeds from several causes. First, when flying in close proximity to the ground, pilots tend to use the ground as a yaw reference with little regard for wind direction. As a result, during maneuvers large unintentional sideslip angles can be produced. Because of the low dynamic pressures involved, large sideslip excursions are not accompanied by the large lateral accelerations normally used as sideslip cues by the pilots of conventional airplanes. In addition, inherent yaw instabilities such as those exhibited by the P.1127 can produce a tendency toward generation of large values of sideslip.

In summary, the jet-powered V/STOL airplane is likely to be a high-speed fighter design which exhibits conventional stability and control characteristics in cruising flight. During the transition to forward flight, large aerodynamic-interference effects on stability and control can occur; these jet-interference effects can seriously limit the operational capability of the airplane. With proper consideration to these effects during early design stages, jet V/STOL airplanes are particularly suited to military missions, and they have consequently become the first fully operational class of V/STOL airplanes.

## STABILITY AND CONTROL TEST TECHNIQUES FOR V/STOL AIRPLANES

Several test techniques commonly used in investigations of the stability and control characteristics of V/STOL airplanes are now discussed. Because of the increased importance of propulsion-system effects in this type of vehicle, it has been very difficult or even impossible to predict stability and control characteristics based on estimation procedures commonly used for conventional airplanes. For this reason, the following five techniques have been used by NASA for investigations of the stability and control characteristics of V/STOL airplanes:

- (1) Free-flight technique
- (2) Static force tests
- (3) Dynamic force tests
- (4) Simulation
- (5) Flight tests

In the free-flight technique the motions of a powered, dynamically scaled model are the output. A properly scaled model may be thought of as an analog computer which produces motions identical to those of the full-scale airplane. In static and dynamic force tests the aerodynamic forces and moments are measured to obtain quantitative values for the static and dynamic stability derivatives necessary for computer or simulator studies. Perhaps the most promising of the techniques appears to be the use of in-flight or ground-based simulators to obtain quantitative pilot evaluations of V/STOL vehicles. Lastly, the end product or end point of the previous techniques is actual flight-test evaluation of the airplane.

#### Free-Flight Technique

The free-flight technique is based upon the principle of dynamic similarity. It can be shown through the use of dimensional analysis that the flight paths of a model and a full-scale airplane will be similar if certain nondimensional quantities have the same values for both vehicles. These scaling parameters for rigid body motions are:

- (1) The relative density, which is expressed as

$$\mu = \frac{m}{\rho l^3}$$

- (2) The Froude number, which is given by

$$N_{Fr} = \frac{V^2}{l g}$$

Disregarding the effects of Reynolds number and Mach number on aerodynamic characteristics, it can be shown that equivalence of the relative density parameter  $\mu$  and the Froude number  $N_{Fr}$  is sufficient to ensure dynamic similarity between two rigid bodies. This result has been applied to wind-tunnel testing in which airplane models are scaled in a similar fashion. A typical test setup for free-flight testing of V/STOL models is shown in figure 58. As depicted in the sketch, the model is flown in free flight in the 30- by 60-foot (9.14- by 18.29-meter) test section of the Langley full-scale tunnel, remotely controlled about all three axes by human pilots. The cable attached to the model serves two purposes: First, a portion of the cable is composed of wires and light plastic

tubes which supply electric power and control signals to the model control surfaces as well as pneumatic power to the model propulsion unit. The cable also includes a 1/8-inch (0.31-cm) steel cable that passes through a pulley above the test section. This cable serves as a safety cable to catch the model in the event of loss of control. During flights, the cable is kept slack so as not to influence the model motions by a safety cable operator situated in a balcony at the side of the test section. Seated alongside the safety-cable operator are the pitch pilot and power operator. The pilots who control the model about its roll and yaw axes are located in an enclosure at the rear of the test section where they can best view the lateral-directional motions of the model. Output data from flight tests usually consist of motion-picture records and qualitative pilot evaluations of the stability and control characteristics displayed by the model.

The flight tests usually are restricted to studies of level flight, but the technique has been modified to permit tests of descending flight, which has proved to be a particularly troublesome operational area for some V/STOL designs. The factors involved in the simulation of descending flight are illustrated in figure 59. Shown on the left-hand side of the figure is the balance of aerodynamic and gravitational forces during descent. For a descent condition, the airplane must have a net aerodynamic drag, and the lift, drag, and weight forces are in balance, with the drag being balanced by the forward component of the weight acting along the flight path. For the simulated descent condition shown on the right-hand side of figure 59, the model is flown with the same values of lift and drag, but the drag cannot be balanced by a component of the weight and must now be balanced by an auxiliary thrust force, which is independent of the normal propulsion system. This input is usually accomplished by use of a small compressed-air jet at the rear of the model. With this modification, the aerodynamic effects of descending flight can be simulated with the model in level flight in the wind tunnel. Obviously, this method of simulation does not account for the effects of descent angle on lateral-directional stability, but these effects are small compared with the aerodynamic effects that can be properly simulated.

The free-flight technique can be used to study a variety of stability, control, and handling-quality problems ranging from studies of the uncontrolled (stick-fixed) motions of V/STOL designs to studies of control requirements for satisfactory handling qualities. A particularly appropriate application of the technique is the study of the maximum descent capability of tilt-wing V/STOL airplanes. A typical tilt-wing design is limited in descent capability for reasons illustrated in figure 60. Shown in figure 60 is an illustration of the effect of descent condition on effective wing angle of attack. In the case of the tilt-wing airplane, the effective angle of attack of the wing is not merely the wing-tilt angle; it is also a function of the forward velocity and both the direction and velocity of the propeller slipstream. This point is illustrated by two flight conditions. On the left side of the figure, the upper sketch shows that the velocity of the airplane and the

slipstream velocity combine vectorially to produce an effective angle of attack  $\alpha$  which, through proper geometric design, will be less than the stall angle of attack for the wing aerodynamic section. As the airplane begins to descend, as shown on the right-hand part of figure 60, the power is reduced, and this reduction in power in turn reduces the magnitude of the slipstream velocity and changes the relative direction of the free-stream velocity. Both effects combine to produce an increase in effective angle of attack at the wing. As the descent is steepened by further reduction of power, a limiting condition is reached where the effective wing angle of attack exceeds the stall angle of the wing section so that major flow separation accompanied by buffet, wing dropping, and wallowing lateral-directional motions results. Figure 61 is presented as an example of the results obtained during free-flight tests of a model of the XC-142 airplane. The results of the tests are shown in the form of boundaries on a plot of flight-path angle against wing-incidence angle. The data show a  $6^\circ$  descent capability with no degradation in pilot rating. As the descent angle was increased into the dotted area, the model required more and more pilot attention to the controls, and flow separation on the wing was indicated by tufts. At the higher descent angles in the crosshatched area, the model experienced abrupt wing dropping, abrupt losses in height, and generally sloppy, wallowing motions. The characteristics in this region were considered completely unacceptable.

Normally, small-scale tests would not be suitable for flight conditions involving separated flow because of the discrepancy in Reynolds number. Experience has shown, however, that the stall of a small-scale model usually occurs at a lower angle of attack than that for the full-scale airplane, and also, when the stall does occur, the motions are generally similar. In the case of descent tests, therefore, it would be expected that the effect of low Reynolds number would tend to give conservative results. This expectation has indeed proven to be verified for the descent capability of the XC-142; that is, the full-scale airplane does have greater descent capability than that indicated in figure 61.

### Forced-Oscillation Force Tests

Quantitative values of the dynamic-stability derivatives are normally required for computer and simulator studies of stability and control characteristics. Over a period of years, estimation procedures have been developed with which to estimate derivatives for conventional airplanes. The V/STOL airplane, however, operates in a flow environment where the effects of propulsive devices on stability derivatives assume an order of magnitude of more importance. Dynamic-force test techniques are usually necessary, therefore, to measure values of dynamic stability derivatives. The basic principles of dynamic force testing are shown in figure 62. As illustrated by the sketch on the left, a model mounted to a strain-gage balance is forced to oscillate at fixed values of amplitude and frequency. The test setup illustrated would be used to obtain dynamic derivatives due to rolling velocity. Tests are also conducted to obtain derivatives due to pitching and

yawing; however, the basic method of data reduction is similar in all cases. The plot at the top of figure 62 illustrates the variation of roll angle as a function of time. Immediately below the variation of roll angle is a typical return signal from the strain-gage balance. For a model with stable values of aerodynamic damping, the balance voltage will lag behind the roll displacement by a time increment  $t$ . The damping moment is, of course, the component of return signal  $90^\circ$  out of phase with the displacement signal. In actual testing, the displacement and balance-return signals are fed into an analog-type analyzer which performs a Fourier analysis on the return signal, separating it into components in phase and  $90^\circ$  out of phase with displacement. The voltage magnitudes are then multiplied by appropriate geometric constants to obtain conventional dynamic derivatives.

An example of the application of the forced-oscillation technique to V/STOL airplanes is shown in figure 63. This figure shows the variations of the damping-in-roll derivative  $C_{l_p}$  and the damping-in-yaw derivative  $C_{n_r}$  with descent angle for a powered tilt-wing model. The increase in descent angle (decrease in power) is shown to reduce the aerodynamic damping greatly and to compound a piloting task already made formidable by flow separation.

### CONCLUDING REMARKS

The material presented in this paper has concentrated on several factors which influence the stability and control characteristics of V/STOL airplanes. Only a few of these factors are emphasized in the following remarks to illustrate some of the characteristics.

The first part of the paper described in detail some of the problems inherent in flight at low speeds. It was shown that most STOL powered-lift airplanes will require artificial stabilization, automatic speed control, and rapid thrust response for satisfactory flying qualities. It appears that the technology required to develop this type of vehicle is well in hand at the present time.

Next, some of the stability and control characteristics of tilt-wing airplanes were discussed. These airplanes also require artificial piloting aids for satisfactory characteristics, and in addition require a sophisticated flight control system. These vehicles have, however, progressed through a second generation and are relatively advanced V/STOL types. The tilt-wing airplane therefore represents an extremely promising concept.

The characteristics of ducted-propeller V/STOL airplanes were then outlined. Although a relatively compact vehicle can be designed with ducted propellers, it may be subject to extreme sensitivity to gusts and turbulence in cruising flight. Because of this



limitation, the ducted-propeller types require more research and development to ensure adequate flying qualities.

The jet-powered V/STOL airplane has shown considerable promise, particularly for fighter designs. This type displays relatively few stability and control deficiencies when proper consideration is given to interference effects between the jet efflux and the tail surfaces. With the recent advent of the Hawker-Siddeley Harrier, this type of vehicle has become the first operational V/STOL concept.

In the final section of the paper, some rather unique test techniques presently used by the NASA for analysis of the stability and control characteristics of V/STOL airplanes are described. These techniques supply pertinent information which consists of stability derivatives for use in analytical and simulator studies and flight motions of dynamically scaled models. The results of these tests are shown to have direct application to the design of V/STOL airplanes.

## BIBLIOGRAPHY

- Campbell, John P.: Operating Problems Peculiar to V/STOL and STOL Aircraft. Conference on Aircraft Operating Problems, NASA SP-83, 1965, pp. 275-280.
- Campbell, John P.: Vertical Takeoff and Landing Aircraft. Macmillan Co., c.1962.
- Campbell, John P.: V/STOL Session Introductory and Review Paper. Ann. N.Y. Acad. Sci., vol. 154, art. 2, Nov. 22, 1968, pp. 843-855.
- Chambers, Joseph R.; and Grafton, Sue B.: Static and Dynamic Longitudinal Stability Derivatives of a Powered 1/9-Scale Model of a Tilt-Wing V/STOL Transport. NASA TN D-3591, 1966.
- Goodson, Kenneth W.: Comparison of Wind-Tunnel and Flight Results on a Four-Propeller Tilt-Wing Configuration. Conference on V/STOL and STOL Aircraft, NASA SP-116, 1966, pp. 51-62.
- Hall, Albert W.; Grunwald, Kalman J.; and Deal, Perry L.: Flight Investigation of Performance Characteristics During Landing Approach of a Large Powered-Lift Jet Transport. NASA TN D-4261, 1967.
- Innis, Robert C.; Holzhauser, Curt A.; and Gallant, Richard P.: Flight Tests Under IFR With an STOL Transport Aircraft. NASA TN D-4939, 1968.
- McKinney, Marion O.; and Kirby, Robert H.: Dynamic Tests of V/STOL Transport Models. AIAA Pap. 64-619, Aug. 1964.
- McKinney, M. O., Jr.; Kuhn, R. E.; and Reeder, John P.: Aerodynamics and Flying Qualities of Jet V/STOL Airplanes. [Preprint] 864A, Soc. Automot. Eng., Apr. 1964.
- Newsom, William A., Jr.; and Freeman, Delma C., Jr.: Flight Investigation of Stability and Control Characteristics of a 0.18-Scale Model of a Four-Duct Tandem V/STOL Transport. NASA TN D-3055, 1966.
- Newsom, William A., Jr.; and Kirby, Robert H.: Flight Investigation of Stability and Control Characteristics of a 1/9-Scale Model of a Four-Propeller Tilt-Wing V/STOL Transport. NASA TN D-2443, 1964.
- Parlett, Lysle P.; and Kirby, Robert H.: Test Techniques Used by NASA for Investigating Dynamic Stability Characteristics of V/STOL Models. J. Aircraft, vol. 1, no. 5, Sept.-Oct. 1964, pp. 260-266.
- Parlett, Lysle P.; and Shivers, James P.: Wind-Tunnel Investigation of an STOL Aircraft Configuration Equipped With an External-Flow Jet Flap. NASA TN D-5364, 1969.

- Quigley, Hervey C.; Vomaske, Richard F.; and Innis, Robert C.: Lateral-Directional Augmentation Criteria for Jet Swept-Wing Transport Airplanes Operating at STOL Airspeeds. Conference on V/STOL and STOL Aircraft, NASA SP-116, 1966, pp. 295-310.
- Schade, R. O.; and Crane, H. L.: Low-Speed Flight Investigation of a Jet Transport With a Powered-Lift Boundary-Layer Control System. AGARD Rep. 503, June 1965.
- Seckel, Edward: Stability and Control of Airplanes and Helicopters. Academic Press, Inc., c.1964.

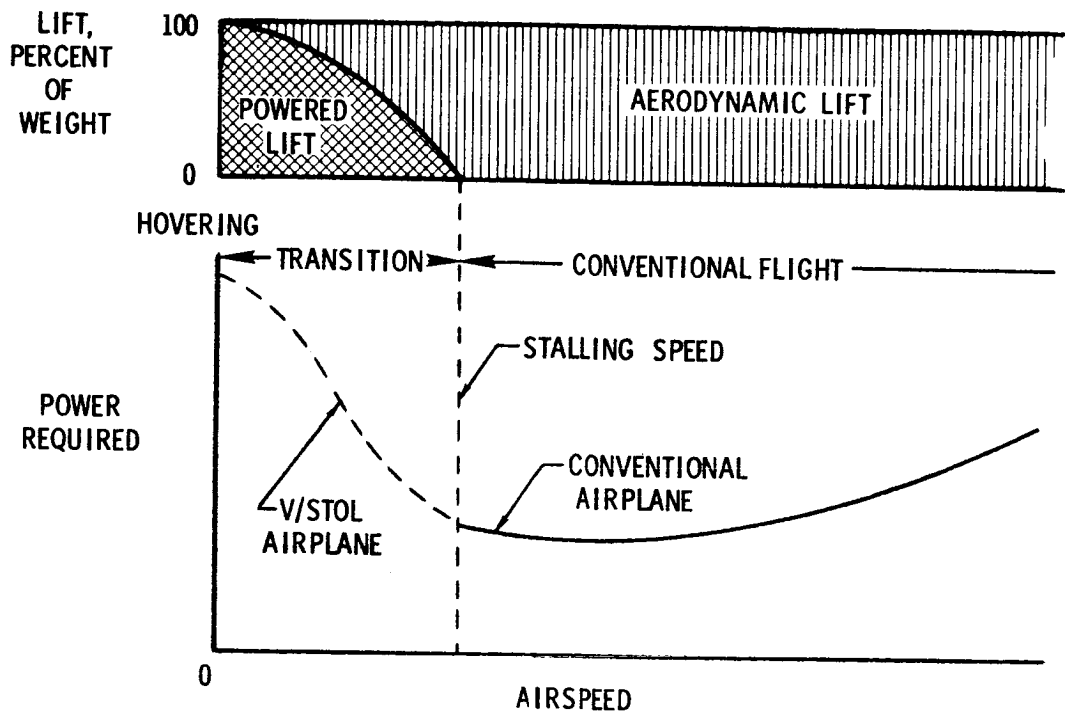


Figure 1.- Power and lift required for conventional and V/STOL airplanes.

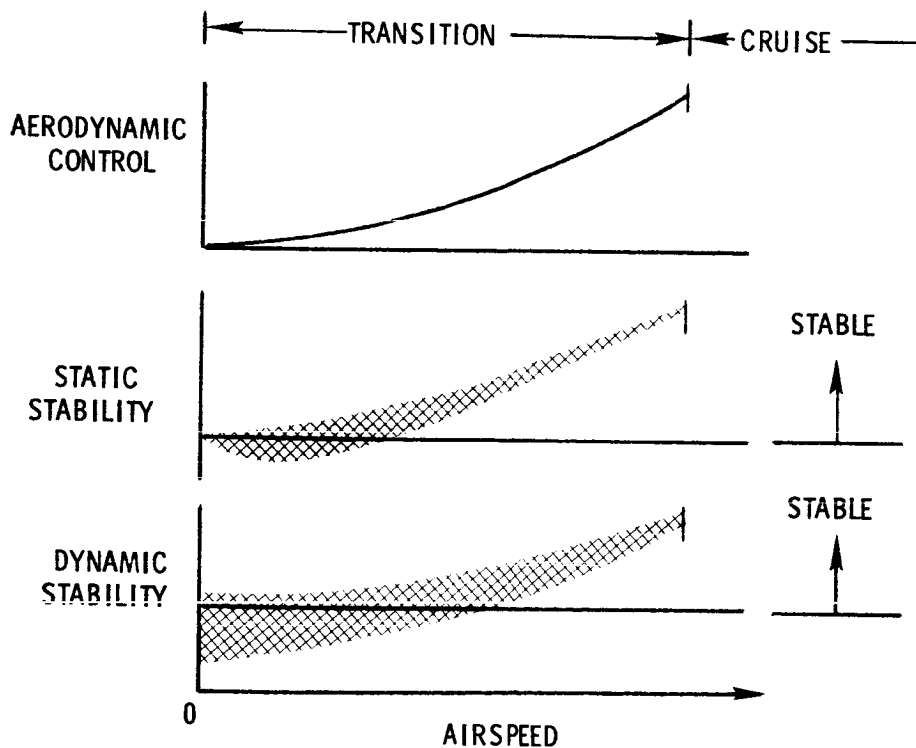


Figure 2.- Variations of V/STOL stability and control characteristics with airspeed.



Figure 3.- Jet transport modified for testing.

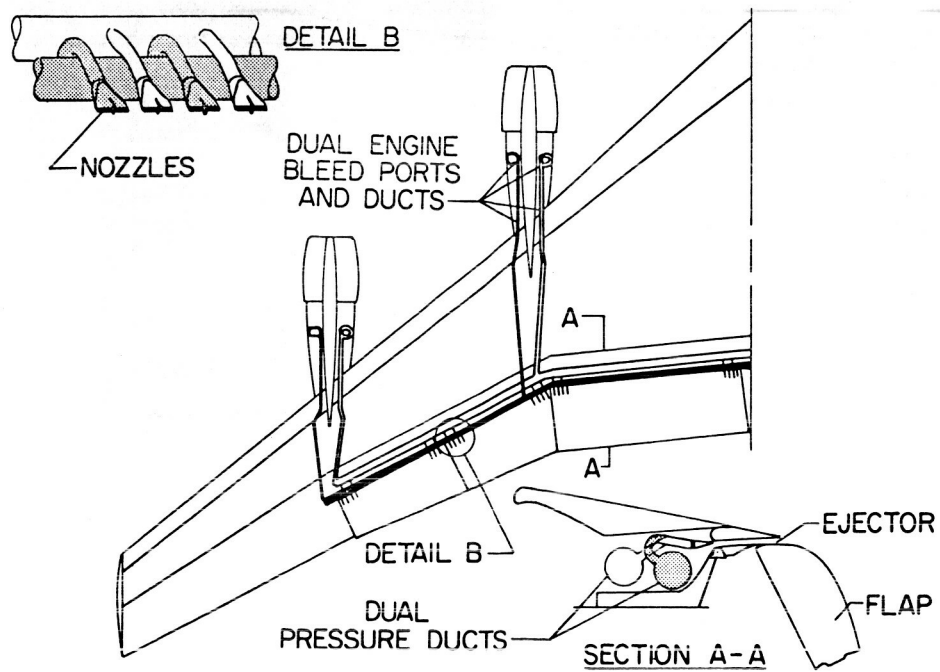


Figure 4.- Boundary-layer control of test airplane.

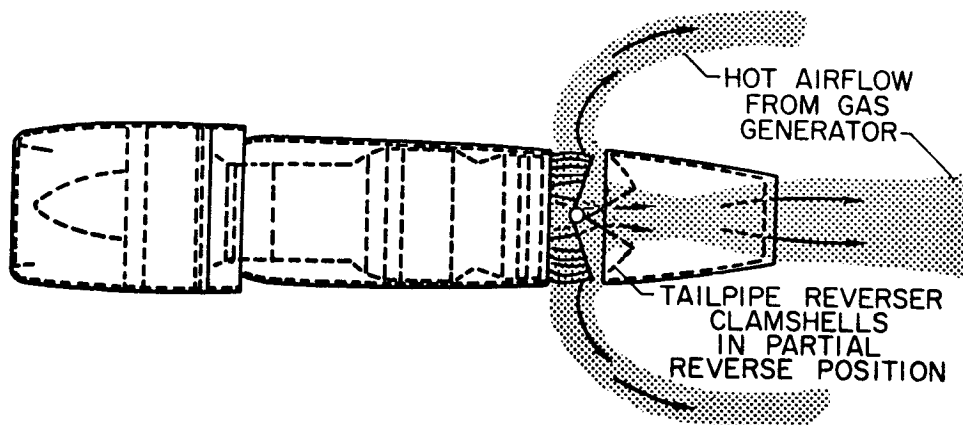


Figure 5.- Thrust-modulation system.

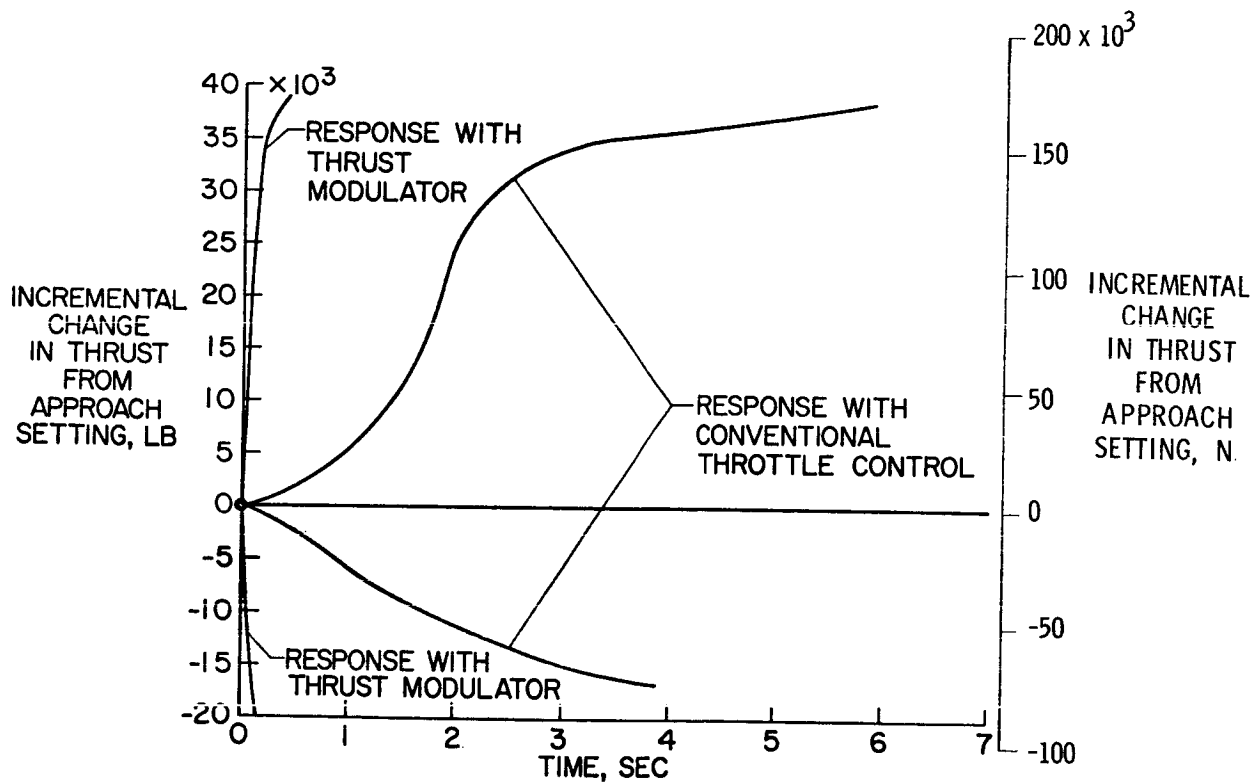


Figure 6.- Effect of thrust modulation system on thrust response.

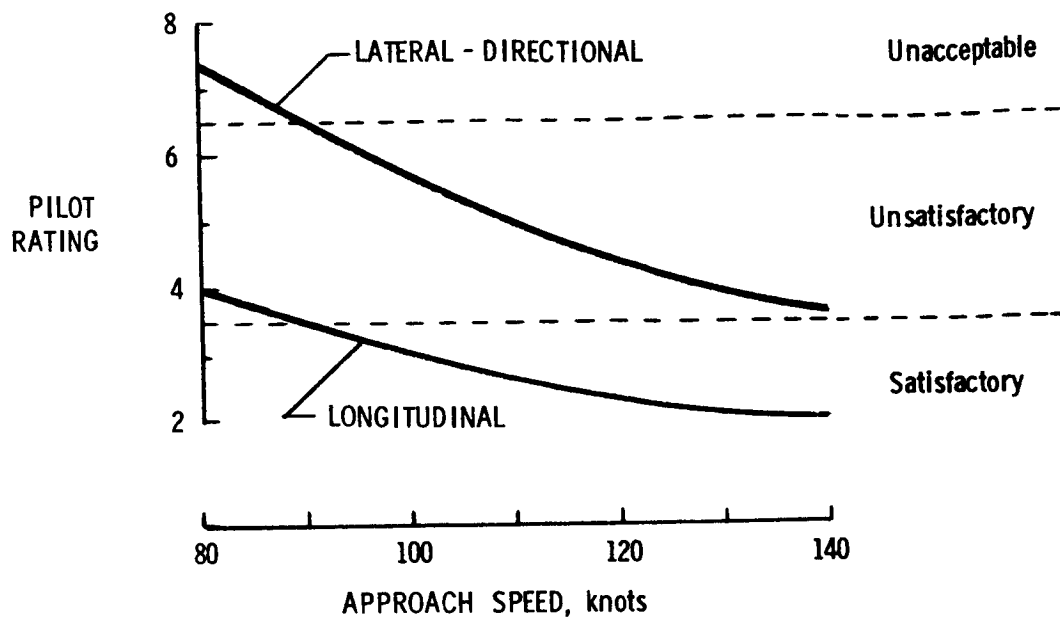


Figure 7.- Handling qualities of test airplane.

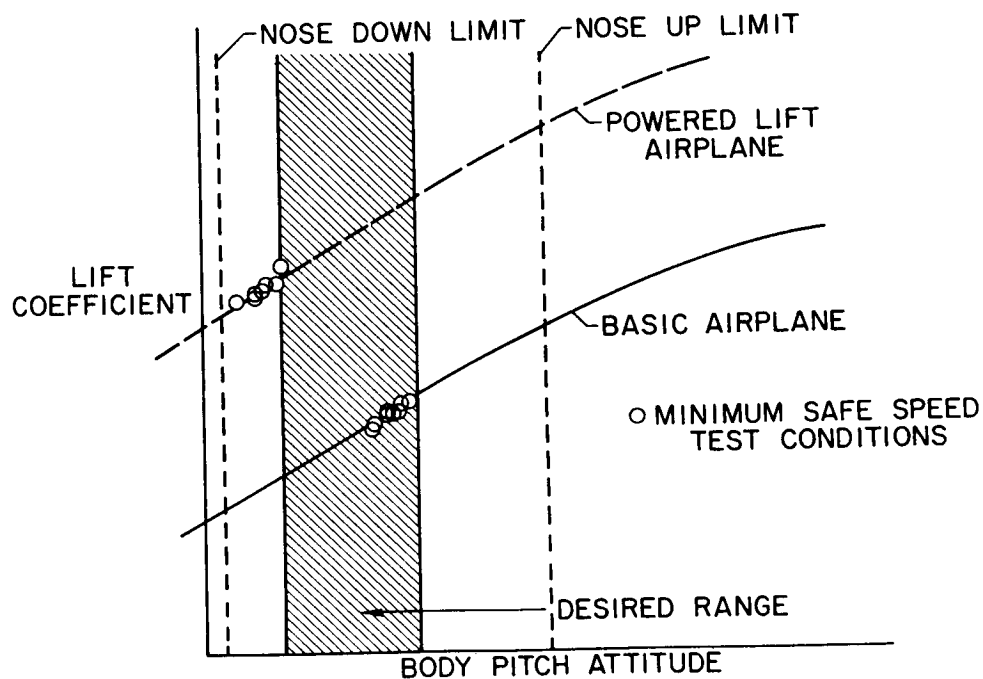


Figure 8.- Comparison of pitch attitude of basic airplane and airplane with BLC.

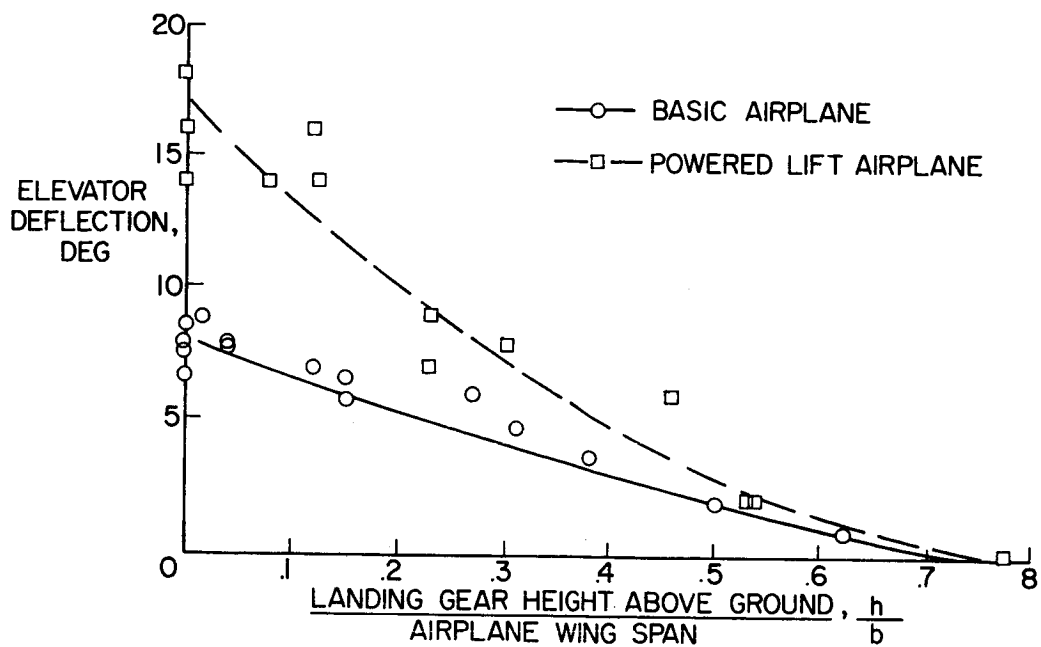


Figure 9.- Effect of powered lift on elevator deflection during landing flare.

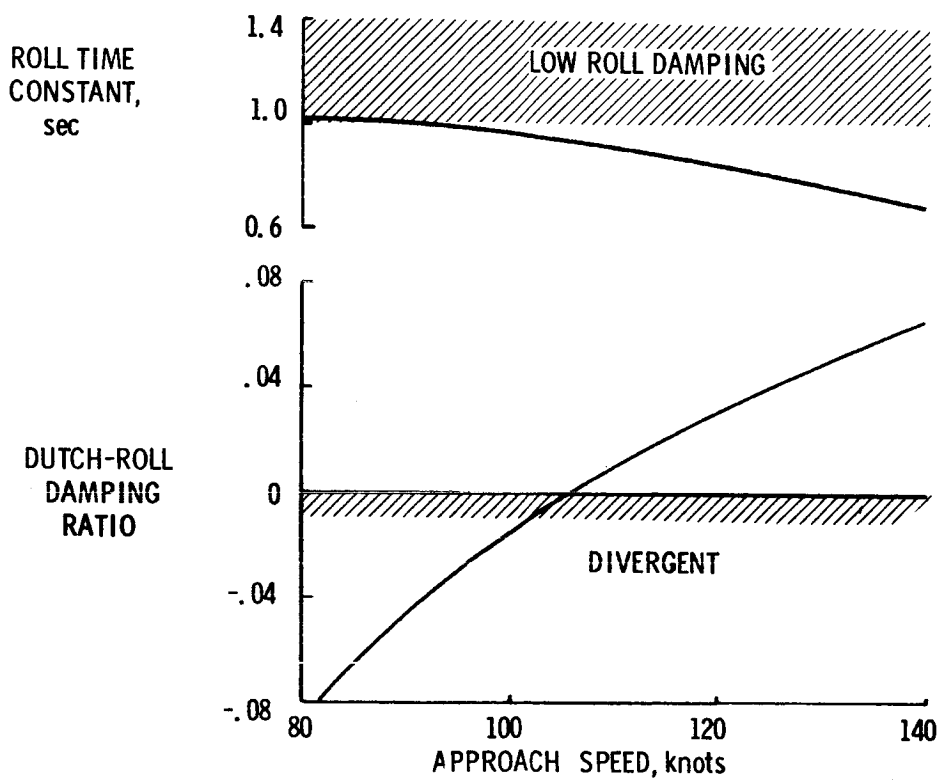


Figure 10.- Lateral-directional damping.



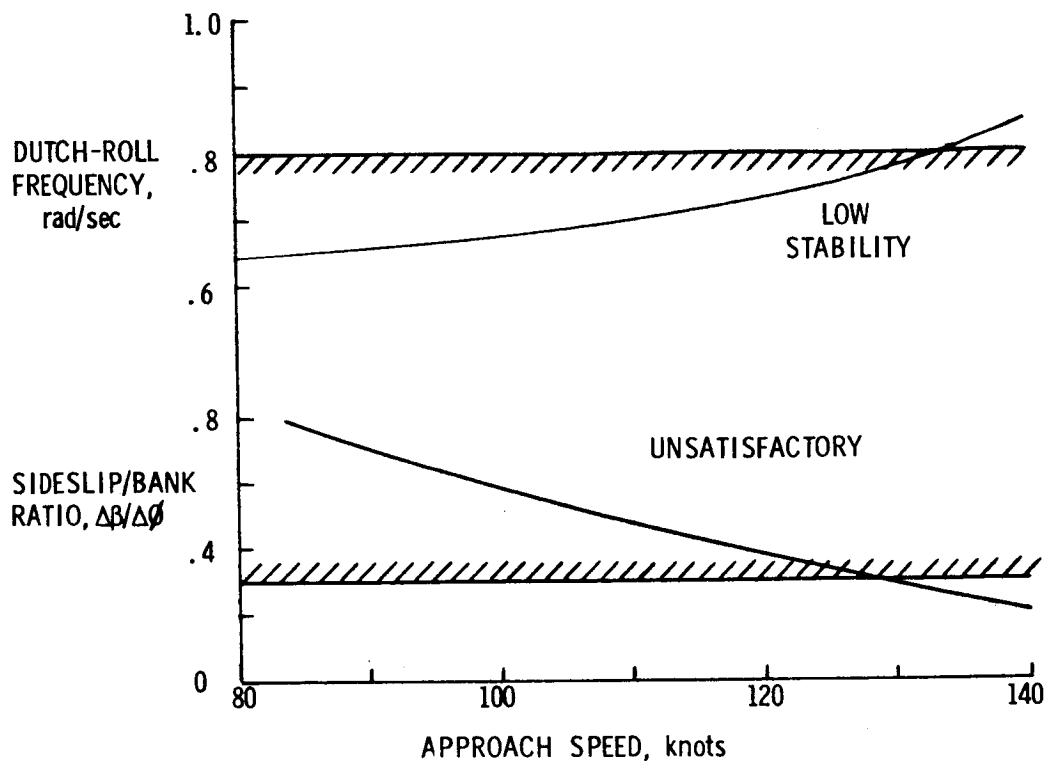


Figure 11.- Lateral-directional characteristics during landing approaches.

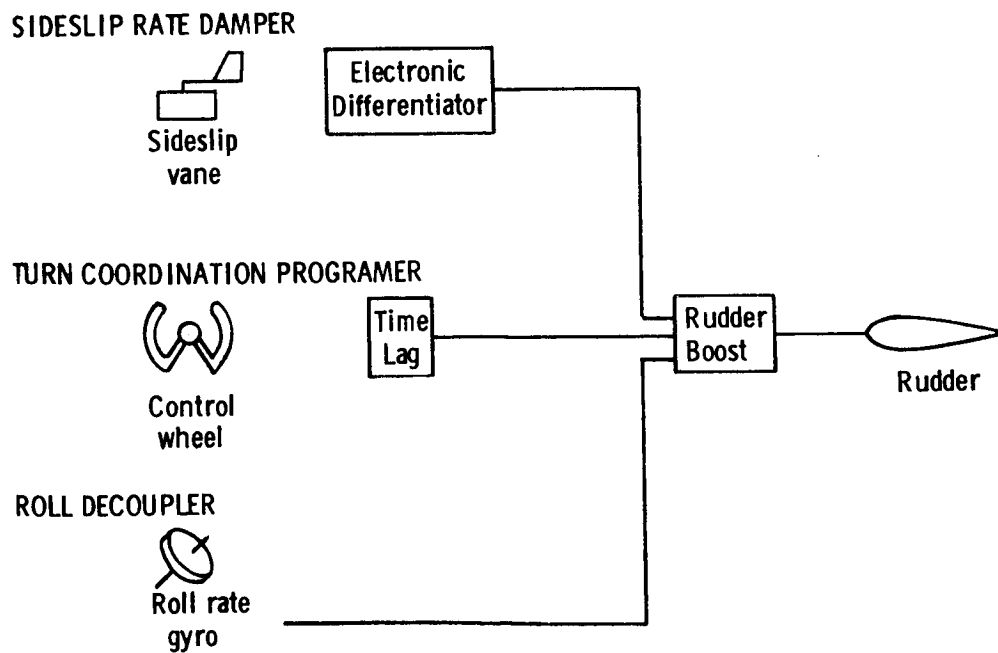


Figure 12.- Stability-augmentation system.

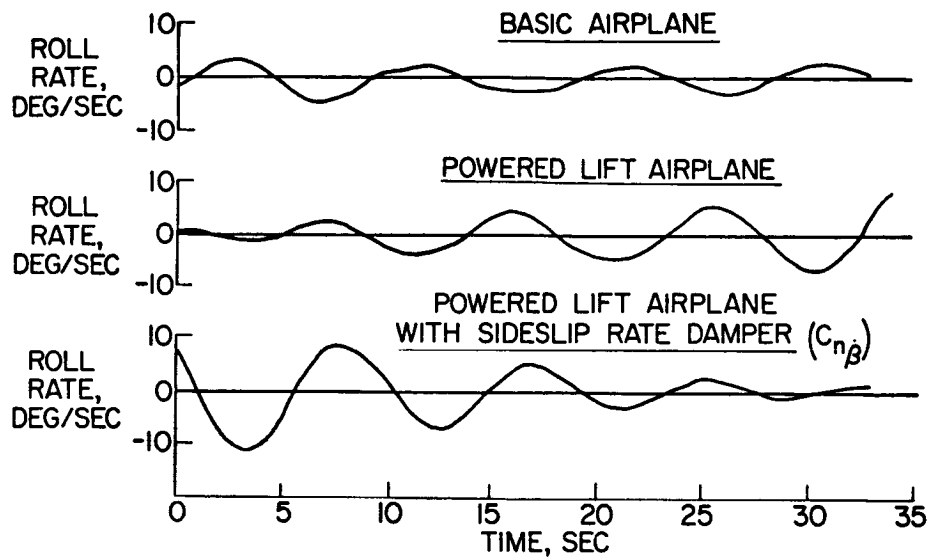


Figure 13.- Effect of stability augmentation on roll rate following a disturbance.

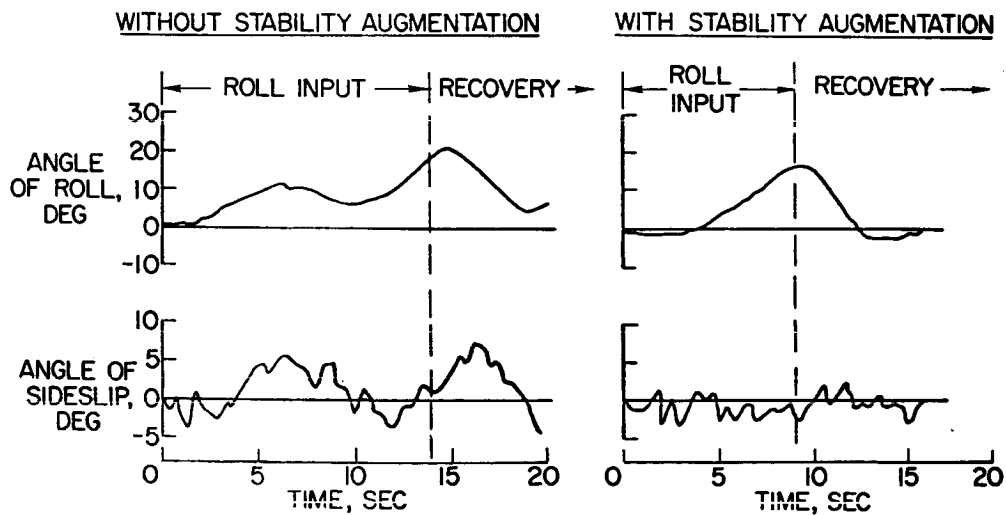


Figure 14.- Effect of stability augmentation on turn coordination.

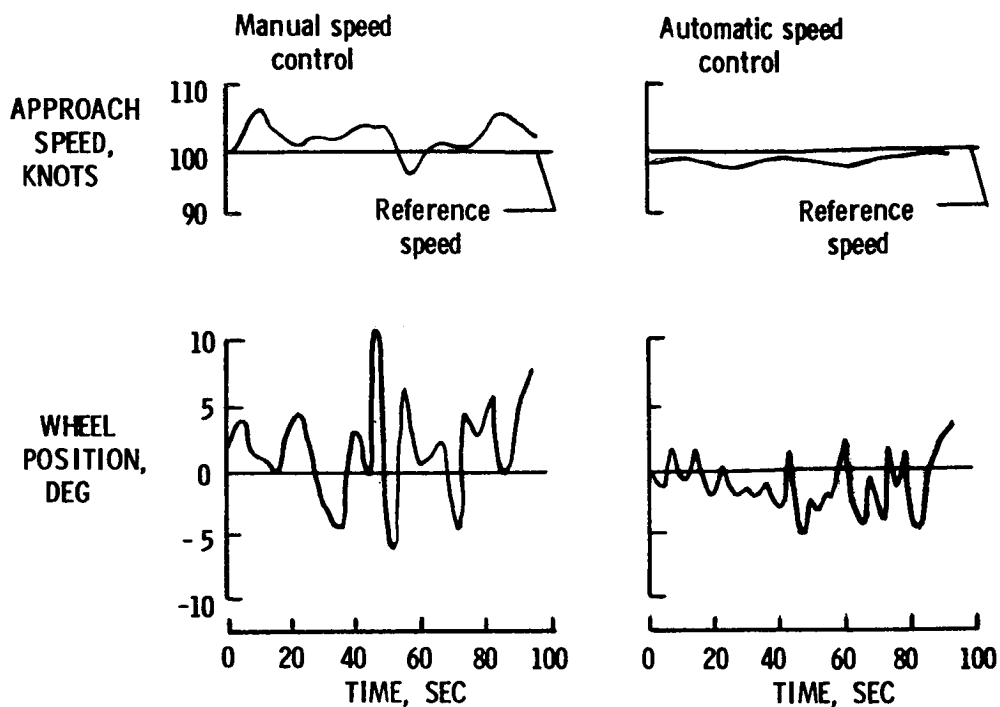


Figure 15.- Effect of automatic speed control on pilot workload.

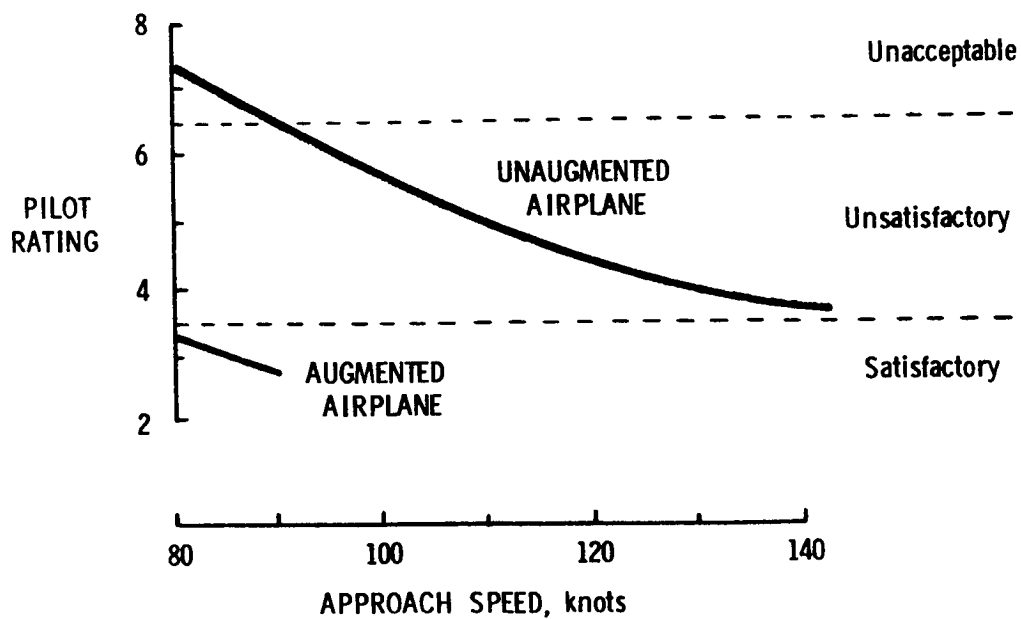


Figure 16.- Lateral-directional handling qualities.

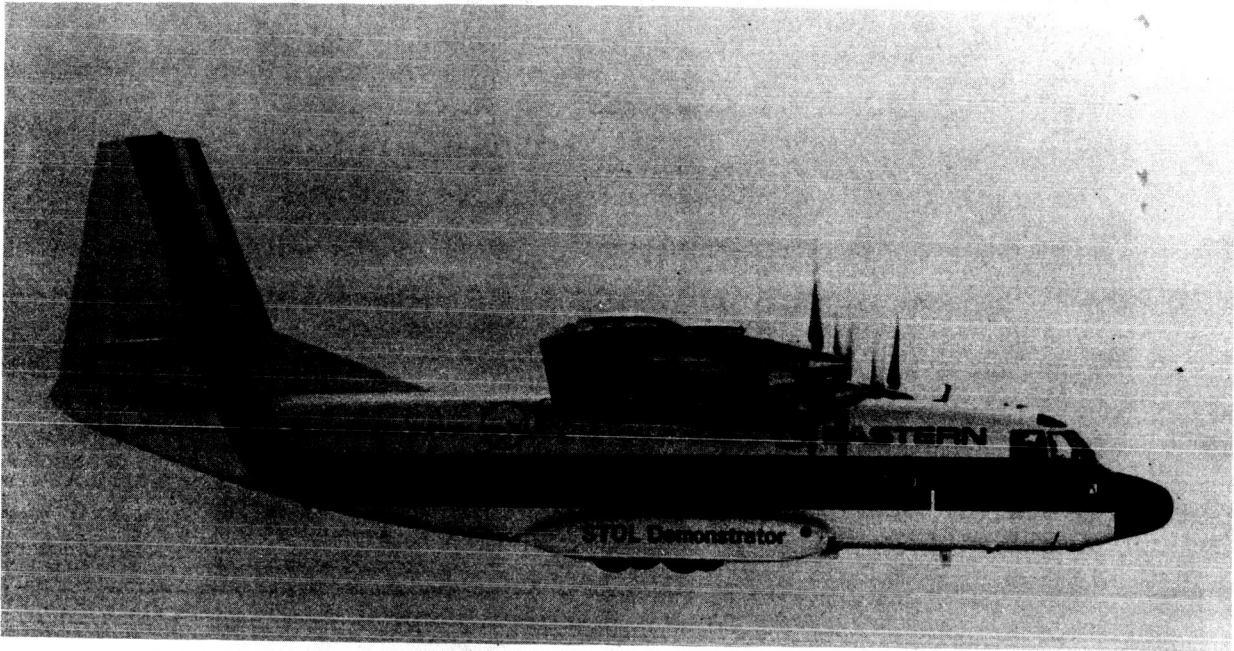


Figure 17.- Breguet 941 airplane.

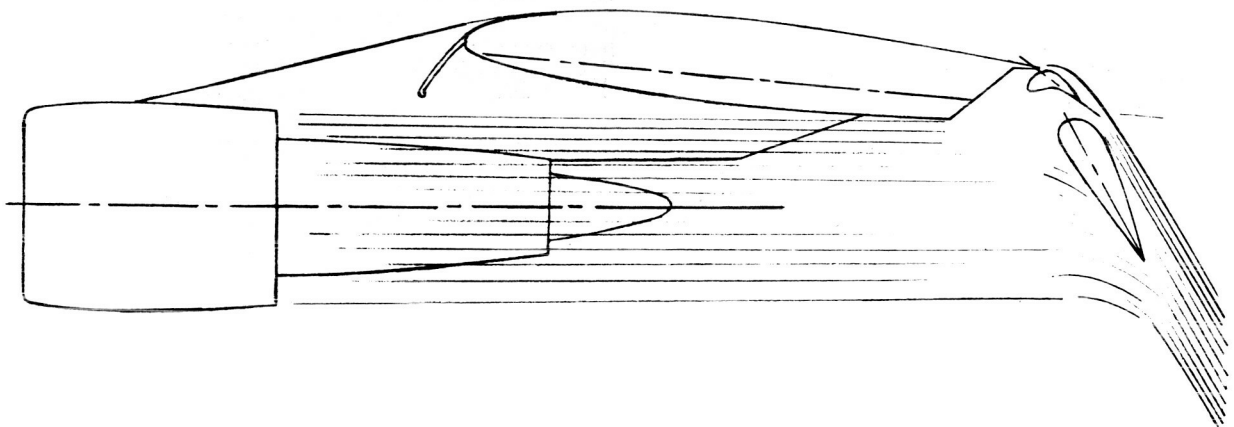


Figure 18.- Jet-flap concept.

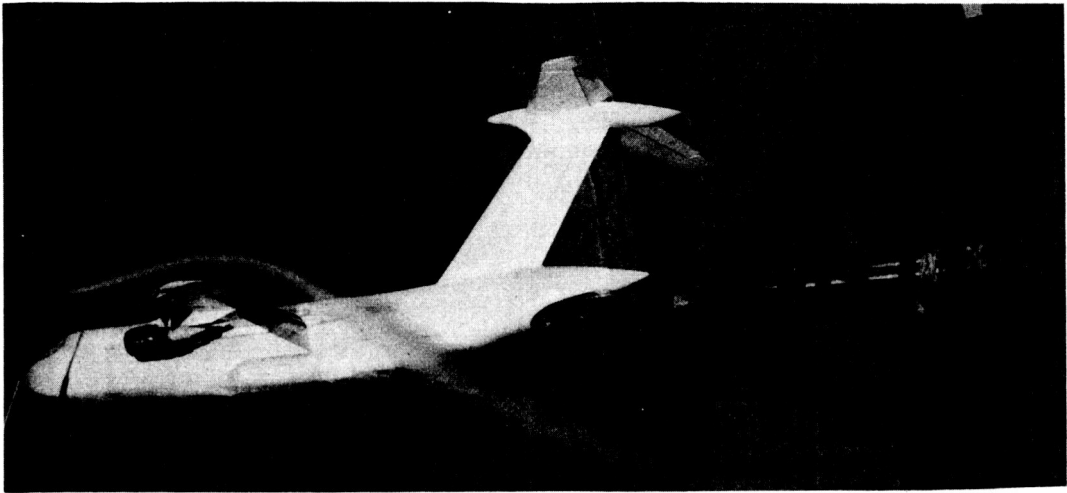


Figure 19.- High tail position required for STOL concept.

ROTOR	PROPELLER	DUCTED FAN	TURBOJET
AIRCRAFT TILTING 			
THRUST TILTING 			
THRUST DEFLECTION 			
DUAL PROPULSION 	<div>           THE V/STOL AIRCRAFT FAMILY         </div>		

Figure 20.- V/STOL airplane family.

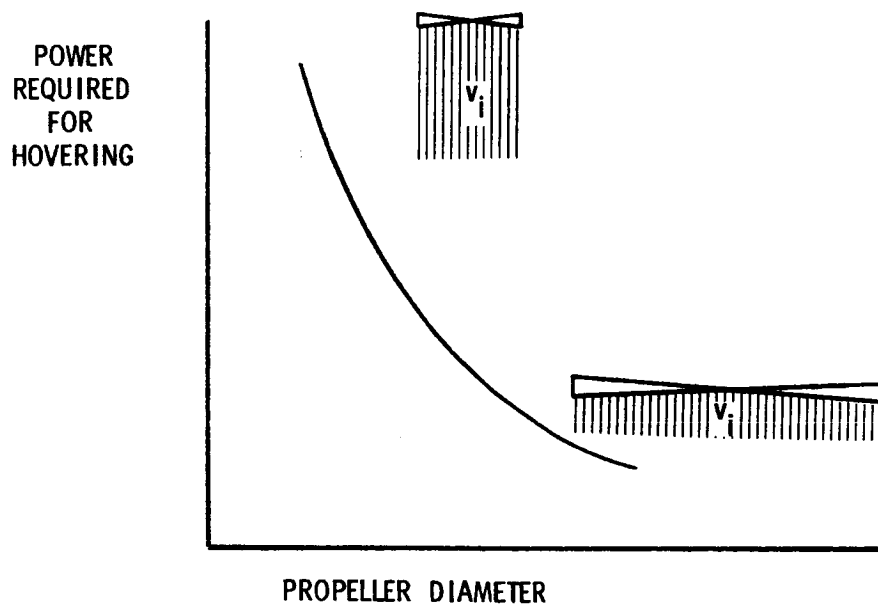


Figure 21.- Variation of power required to hover with propeller diameter.

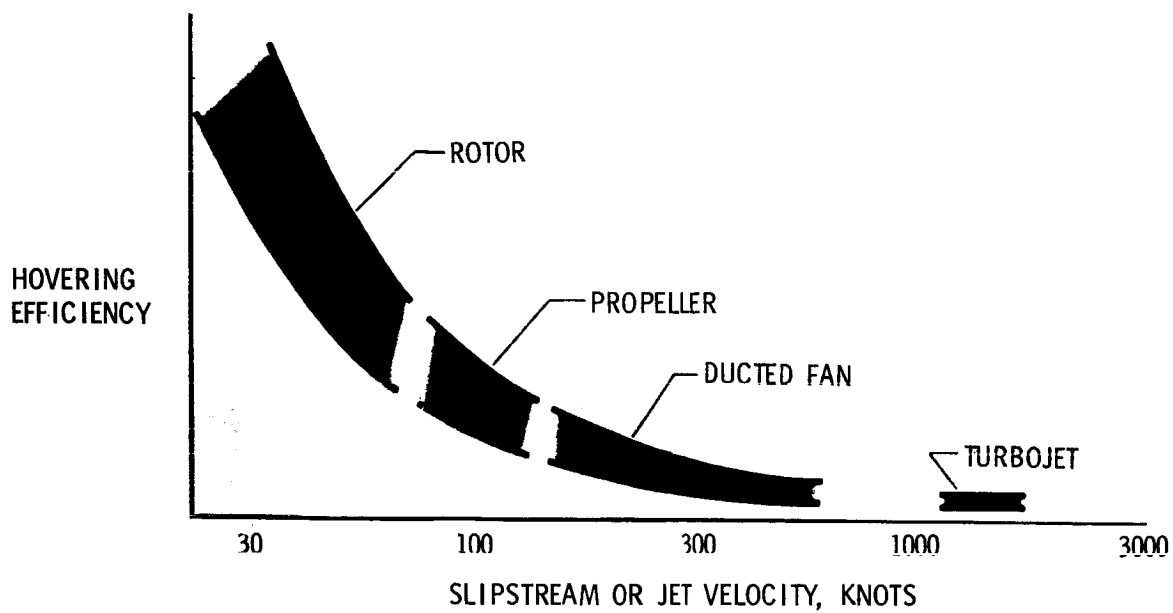


Figure 22.- Hovering efficiency of various V/STOL concepts.

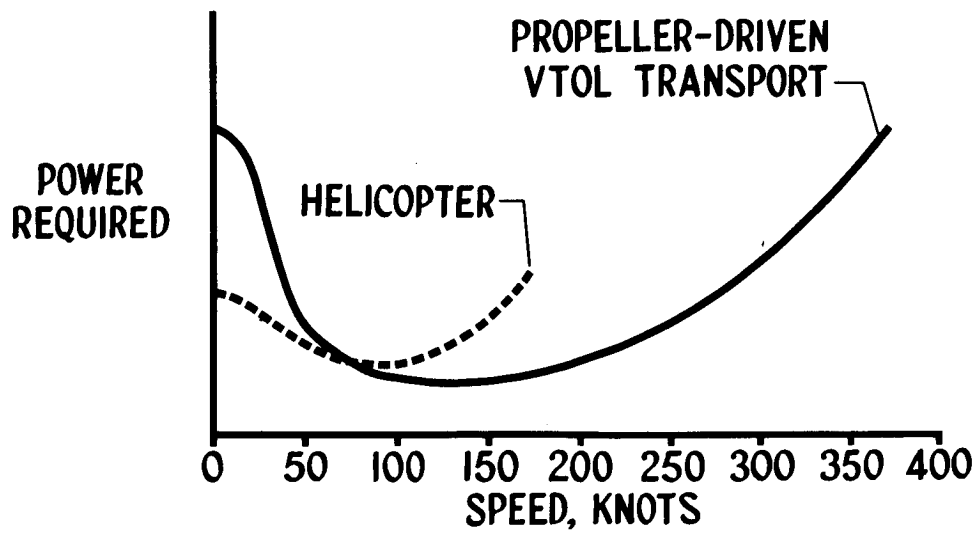


Figure 23.- Power required for helicopter and propeller-driven V/STOL transport.

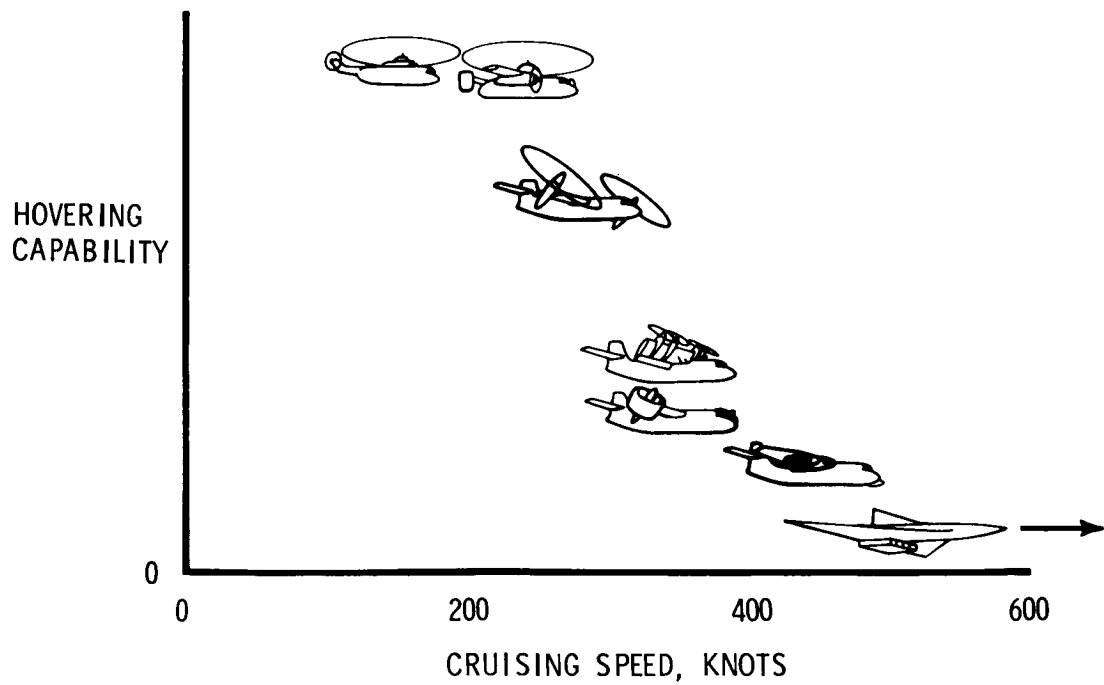


Figure 24.- Mission capability of various V/STOL concepts.

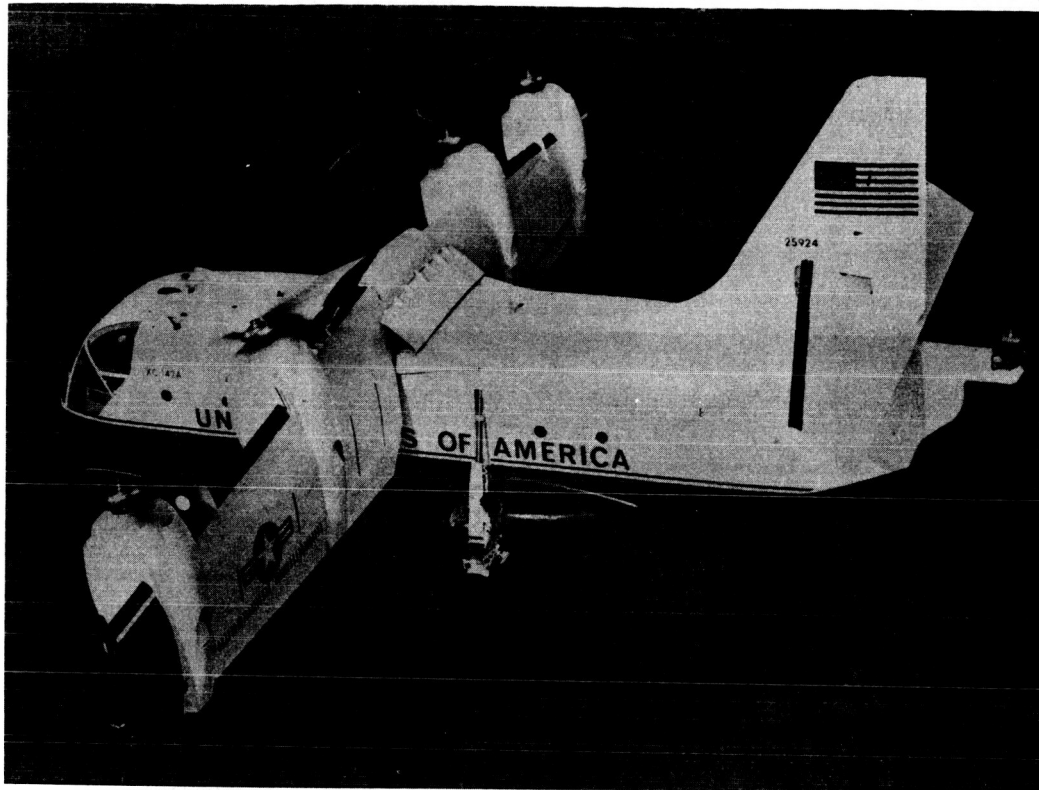


Figure 25.- Tilt-wing transport design.

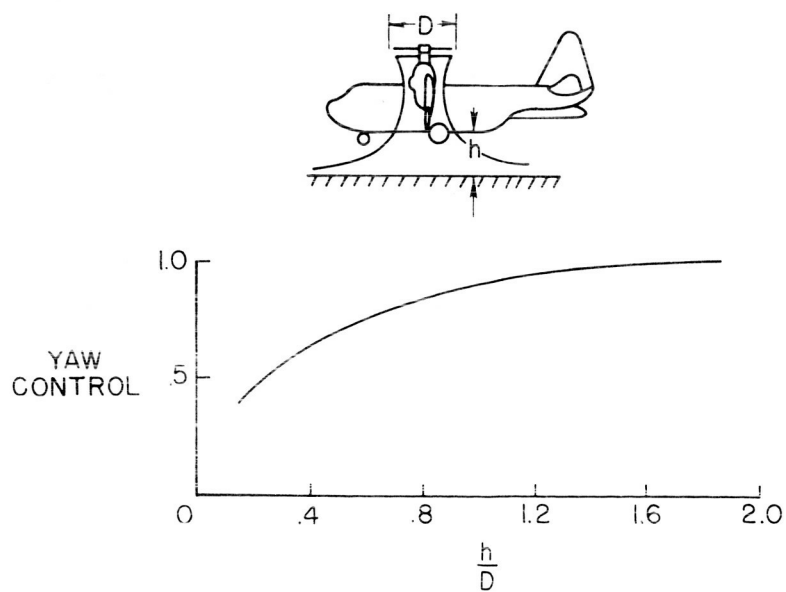


Figure 26.- Effect of ground proximity on yaw-control effectiveness.



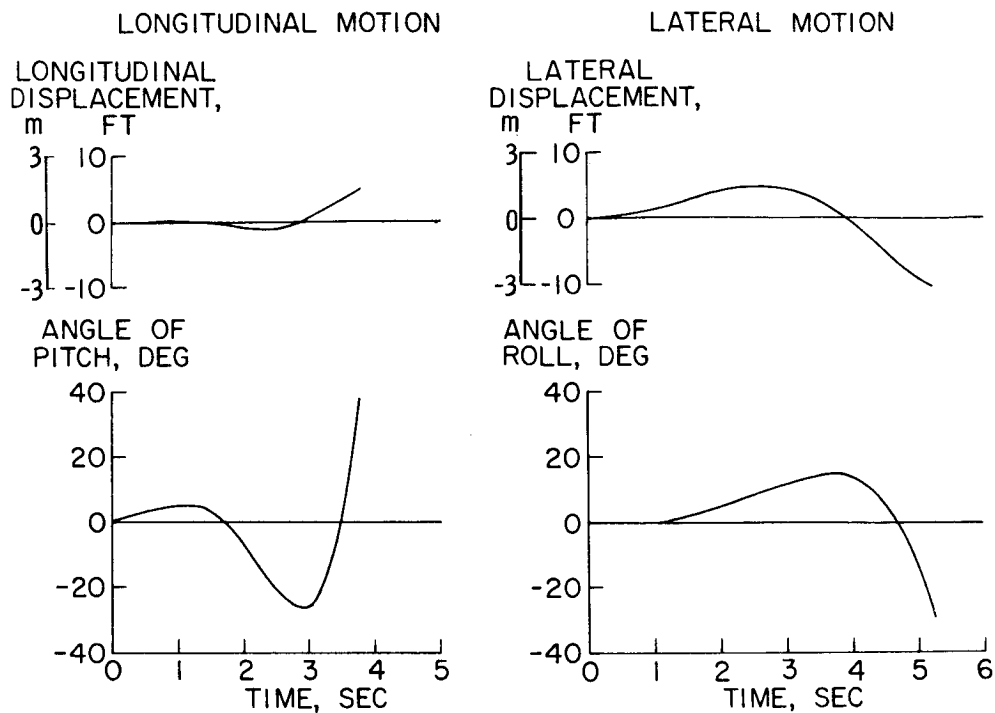


Figure 27.- Illustration of controls-fixed pitch and roll motions of tilt-wing airplane.

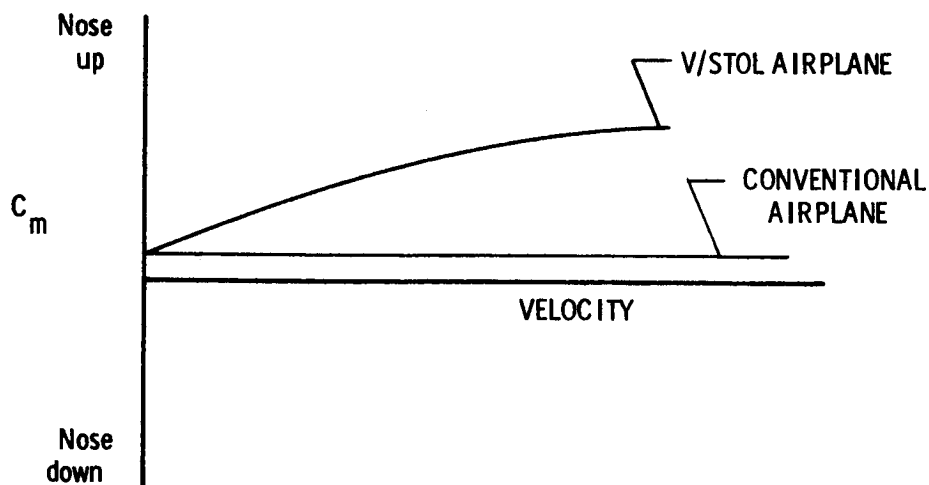


Figure 28.- Typical variation of pitching-moment coefficient with velocity for conventional and V/STOL airplanes.

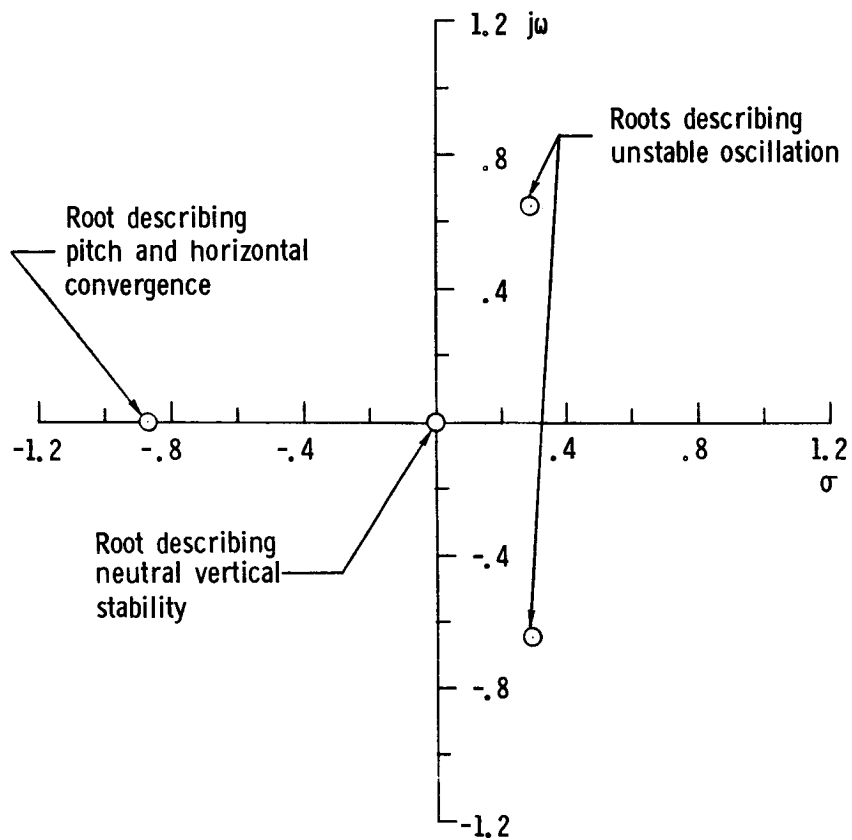


Figure 29.- Typical solution of characteristic equation (4).

	$M_{Y\theta}$ per rad-sec <sup>2</sup>	$M_{Yq}$ per rad-sec
○	0.0	0.0 (Basic unaugmented configuration)
□	0.0	-2.0 (Pitch-rate stabilization)
◇	-1.0	0.0 (Pitch-attitude stabilization)
△	-2.0	-2.0
▽	-4.0	-2.0

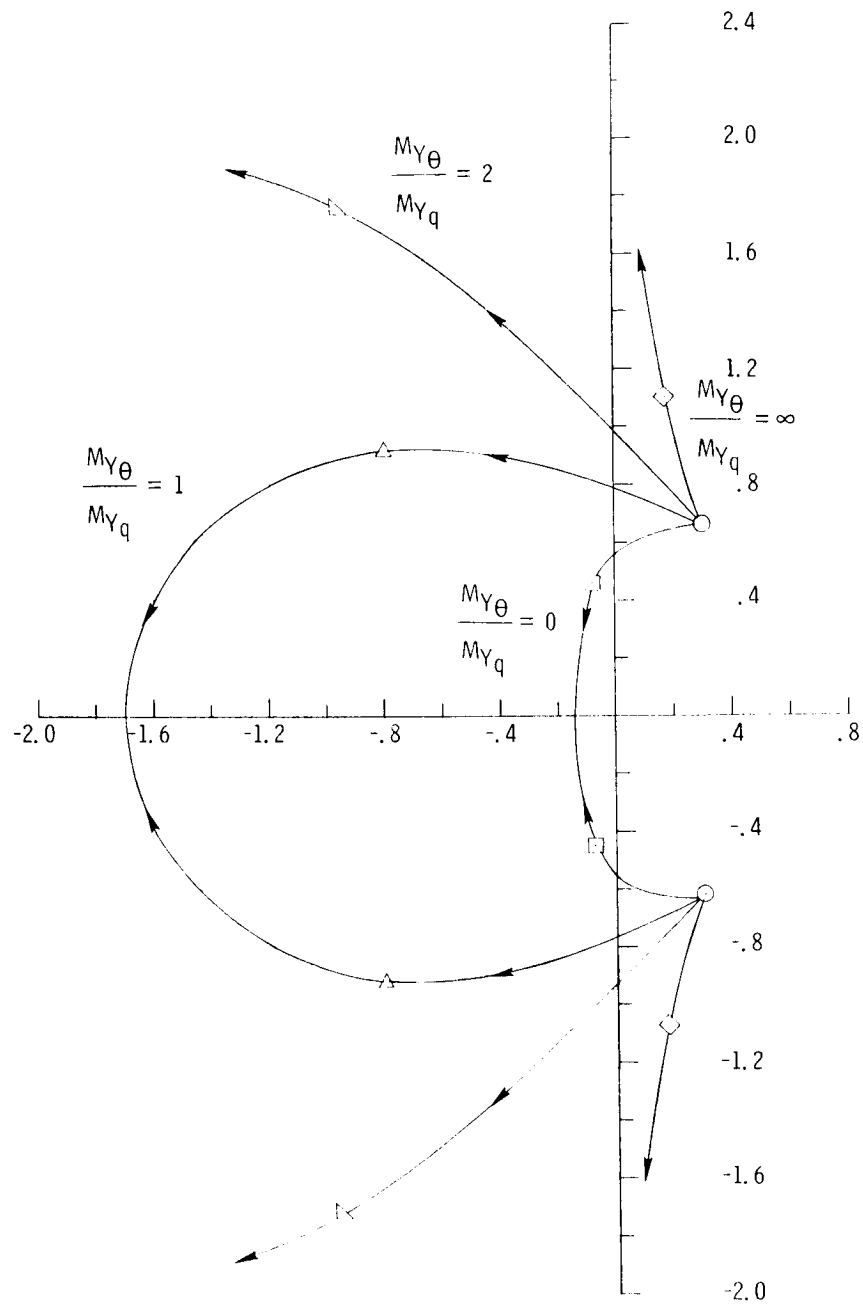


Figure 30.- Illustration of effects of pitch-rate and pitch-attitude augmentation.

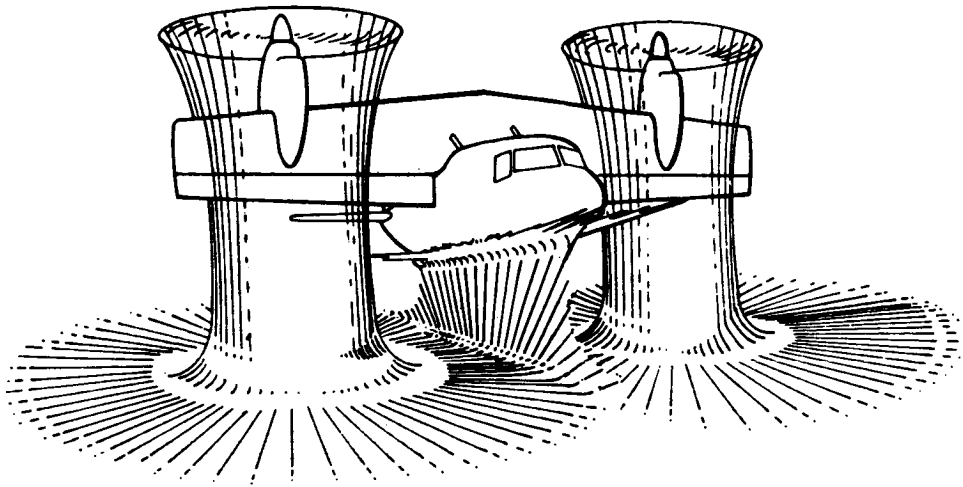


Figure 31.- Flow pattern about a tilt-wing configuration in ground effect.

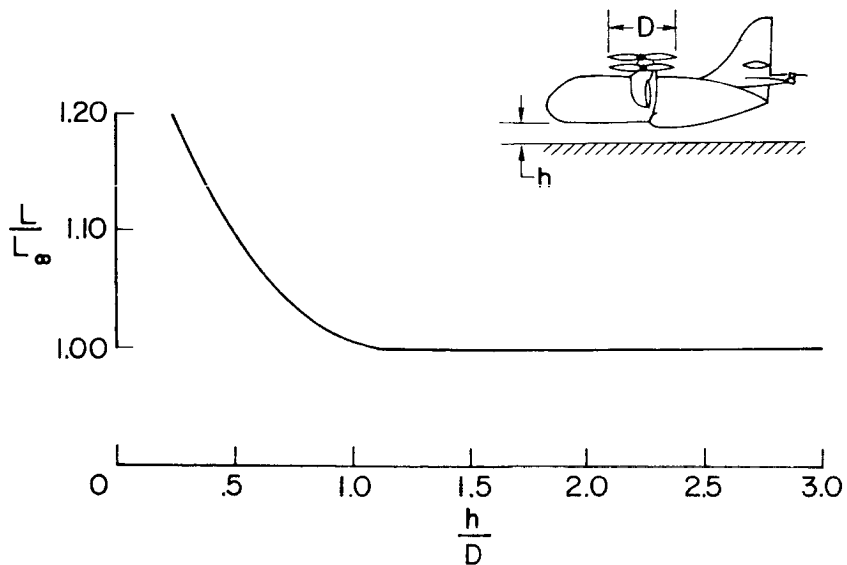


Figure 32.- Effect of ground proximity on lift for tilt-wing configuration.

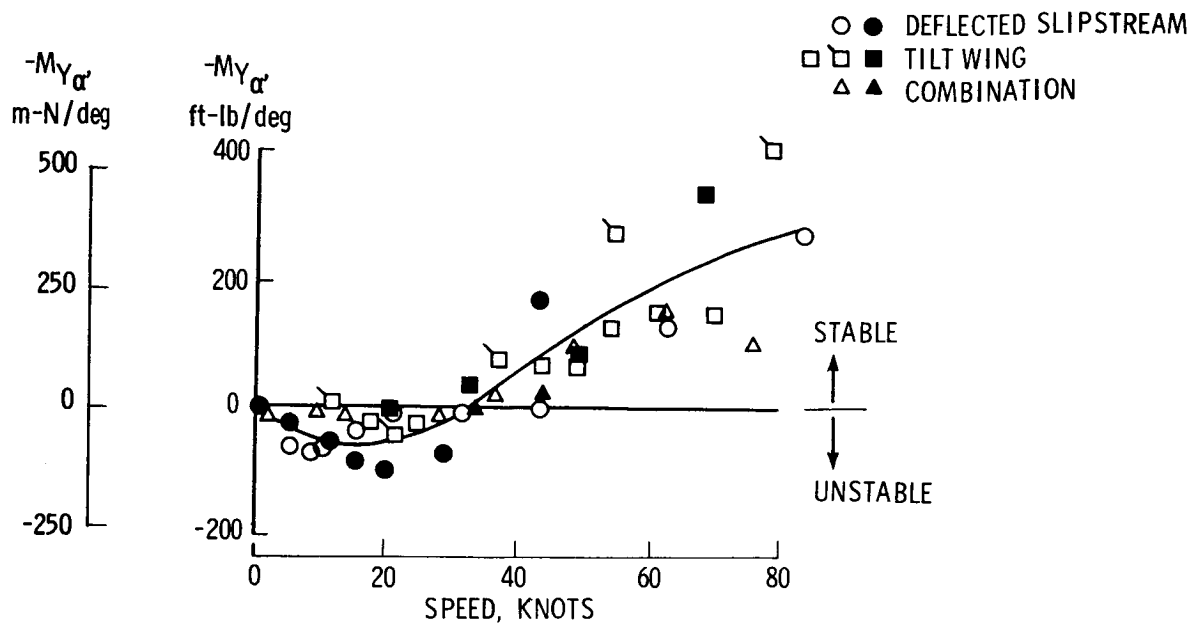


Figure 33.- Variation of angle-of-attack stability with airspeed of various V/STOL configurations.

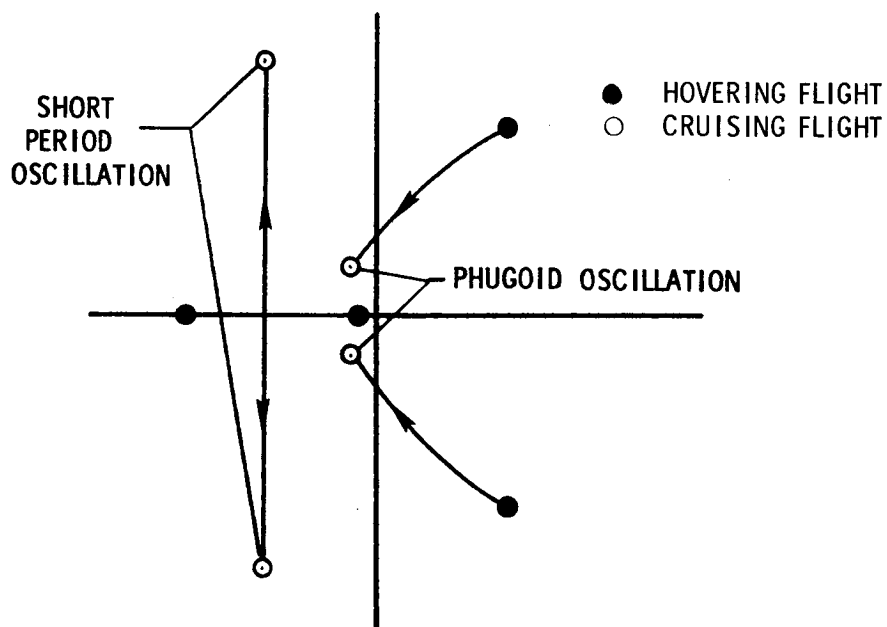


Figure 34.- Locus of roots with increasing speed.

ANGULAR PITCHING VELOCITY,  
RAD/SEC

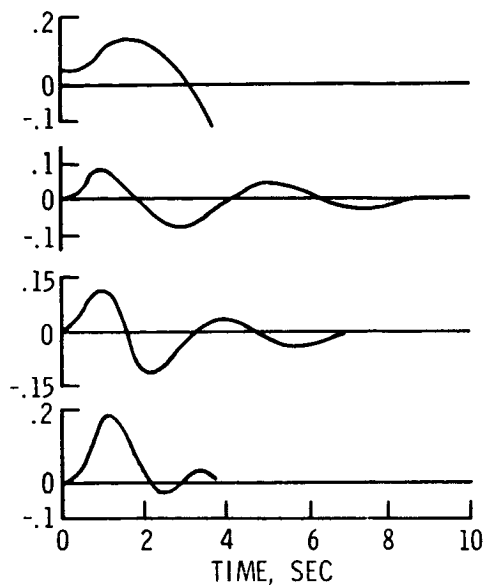
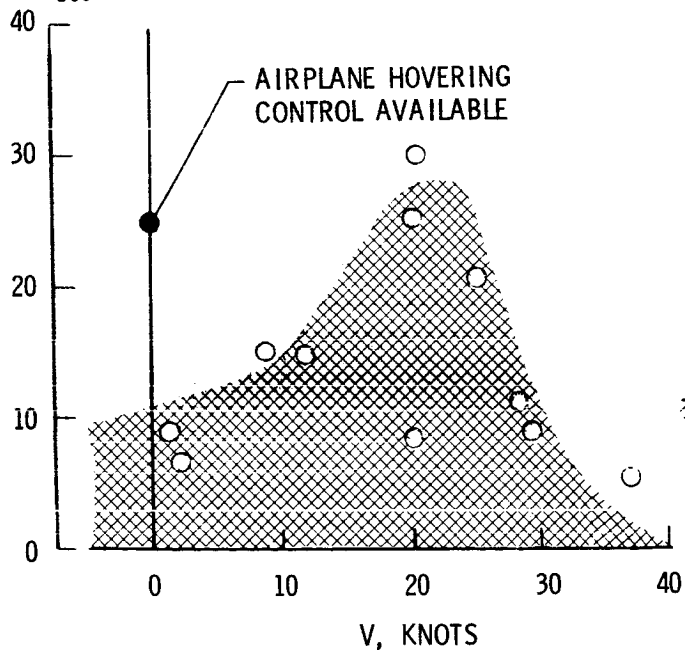


Figure 35.- Pitching velocity of tilt-wing airplane following disturbances at various wing tilt angles.

$\dot{r}_{max}, \frac{\text{deg}}{\text{sec}^2}$



○ FLIGHT TESTS

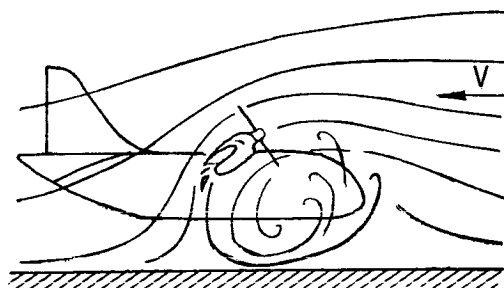


Figure 36.- Yaw disturbances of tilt-wing airplane in ground effect.

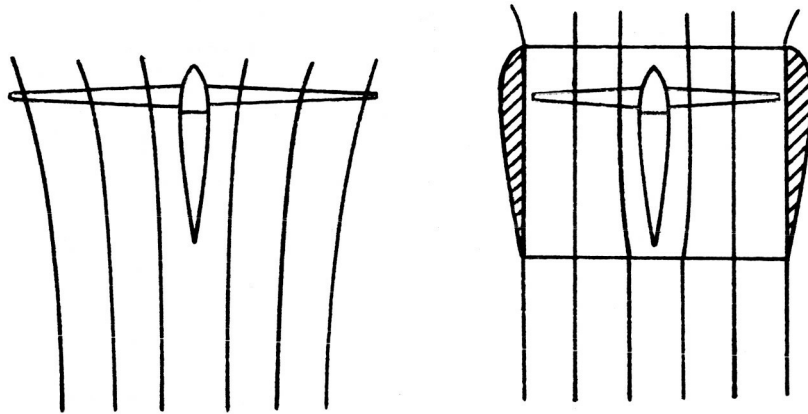


Figure 37.- Flow patterns for unshrouded and shrouded propellers.

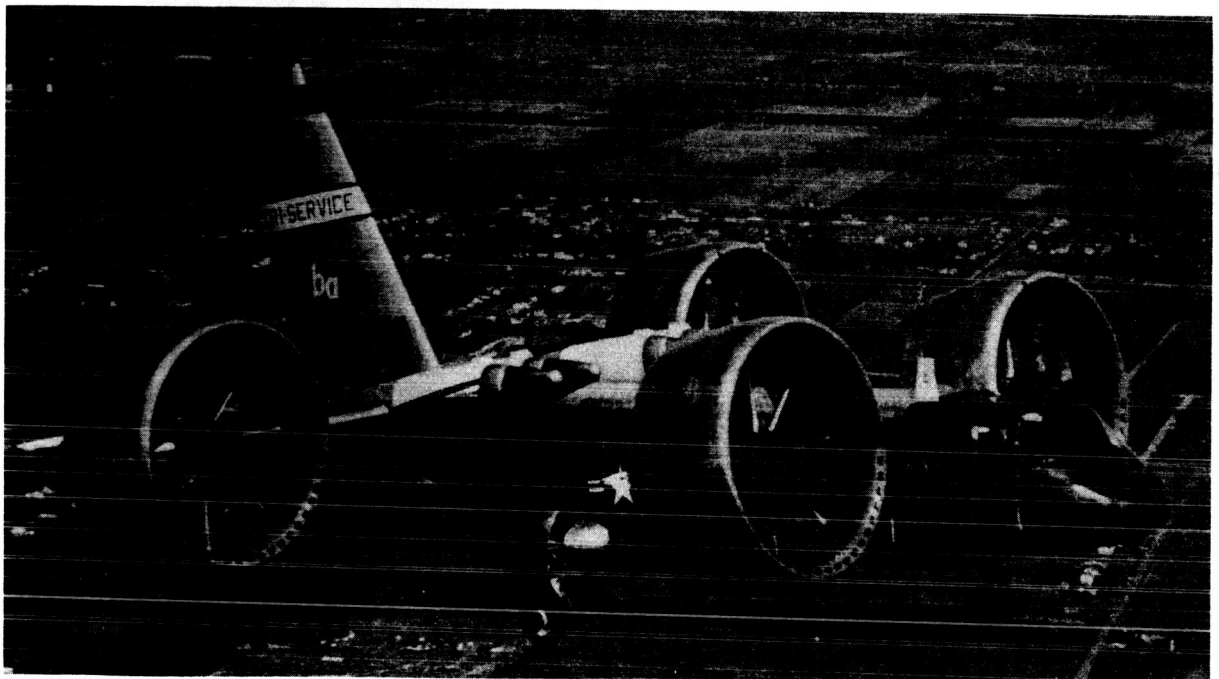


Figure 38.- Tilt-duct V-STOL airplane.

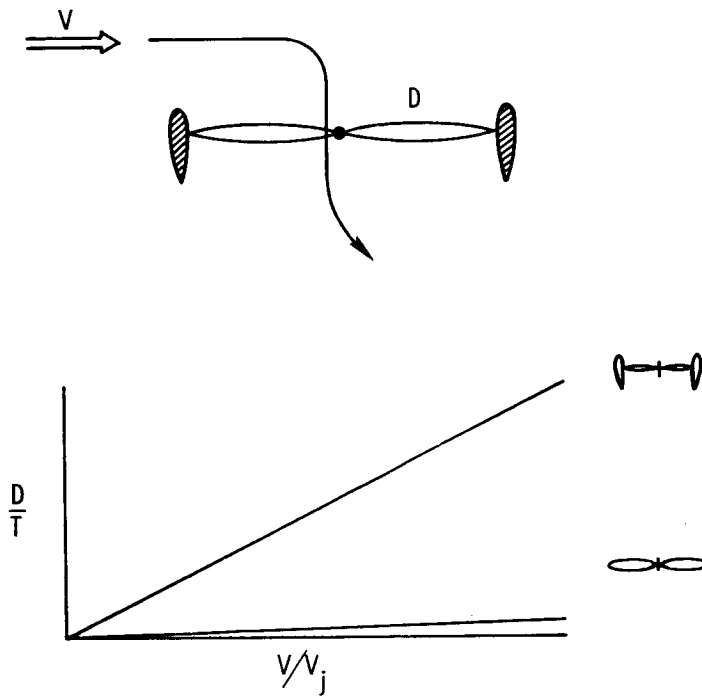


Figure 39.- Effect of crosswind on drag of ducted propellers.

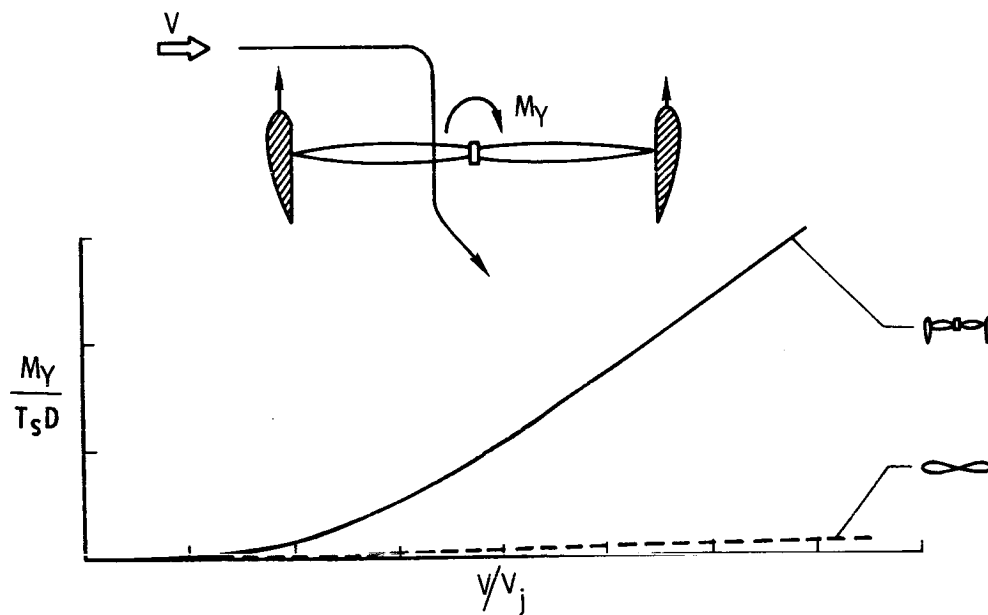


Figure 40.- Effect of cross flow on moments of ducted propellers.



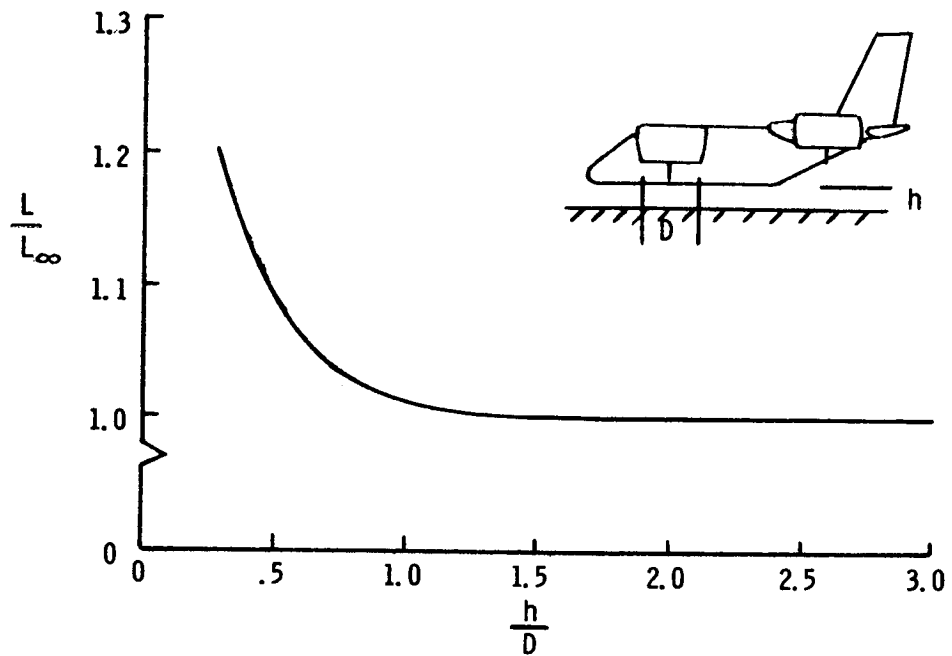


Figure 41.- Effect of ground proximity on lift of tandem ducted-propeller configuration.

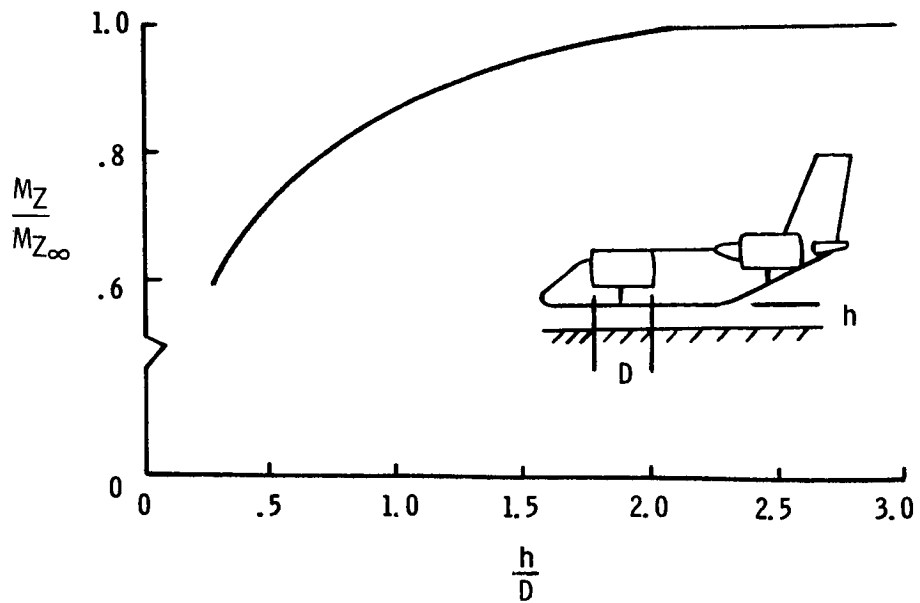


Figure 42.- Effect of ground proximity on yaw control of tilt-duct configuration.

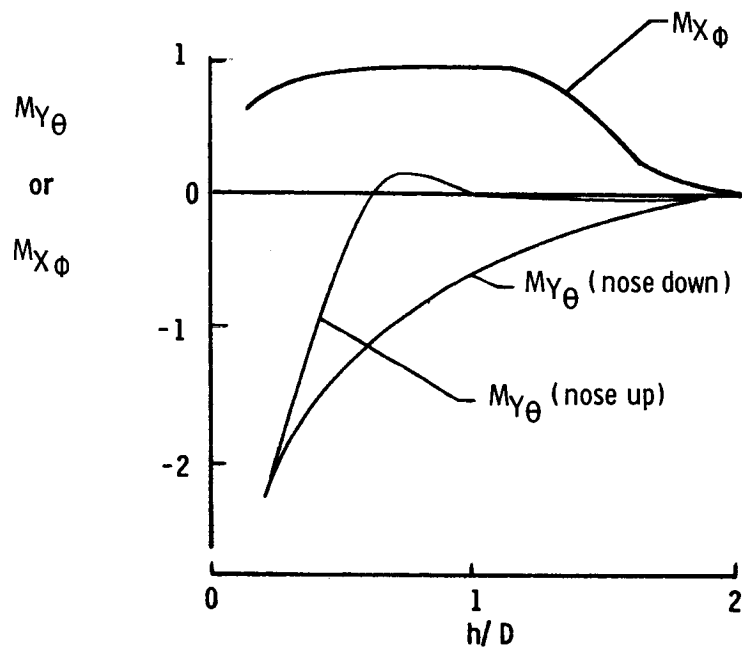


Figure 43.- Effect of ground proximity on pitch and roll derivatives with attitude.

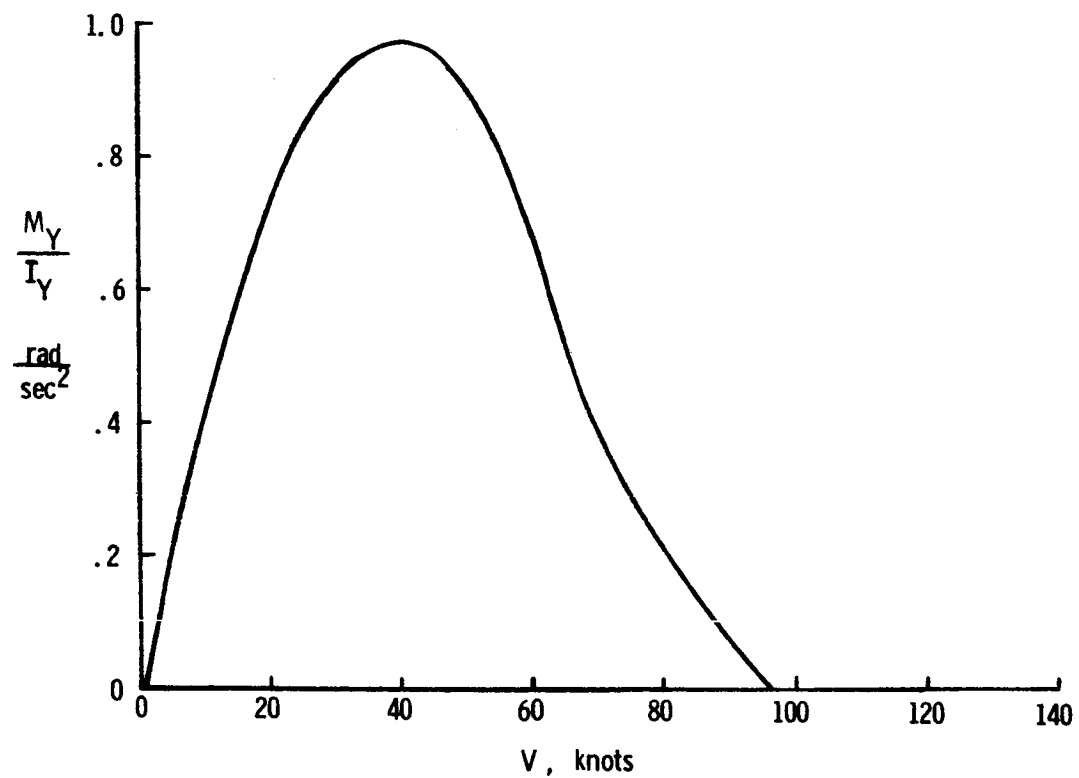


Figure 44.- Variation with airspeed of untrimmed pitching-moment parameter  $M_Y/I_Y$ .

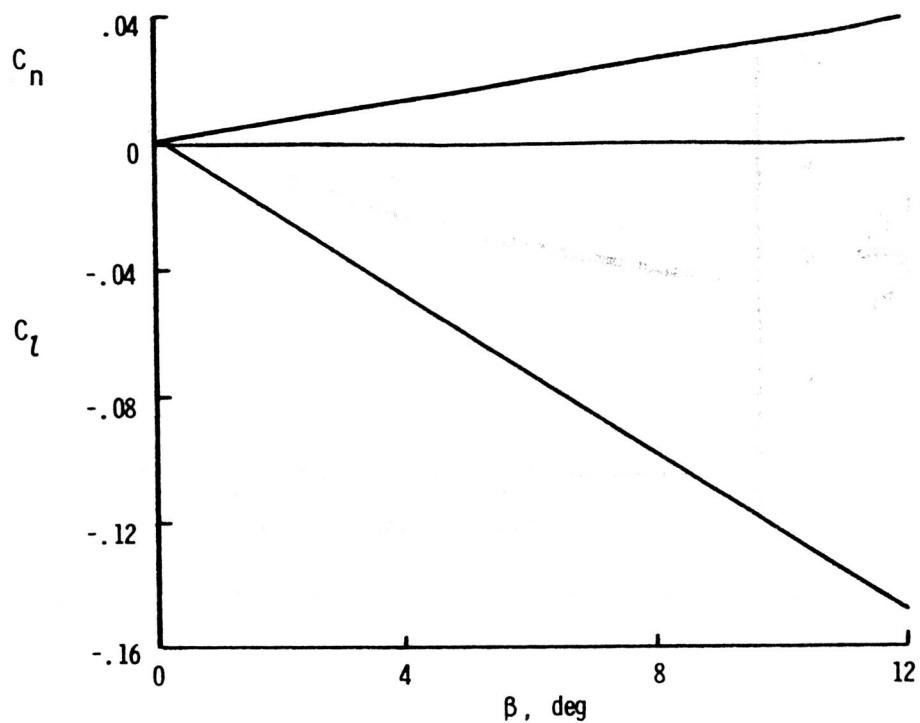


Figure 45.- Variation of  $C_n$  and  $C_L$  with  $\beta$  for tandem tilt-duct V/STOL airplane.

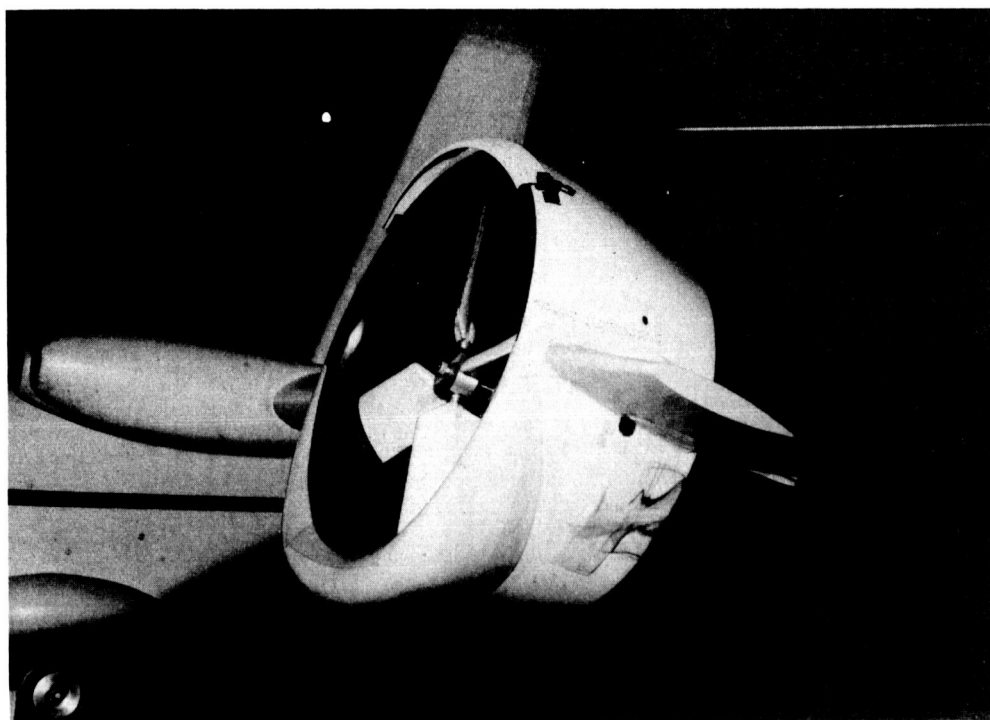


Figure 46.- Leading-edge slats fitted to duct upper surface.

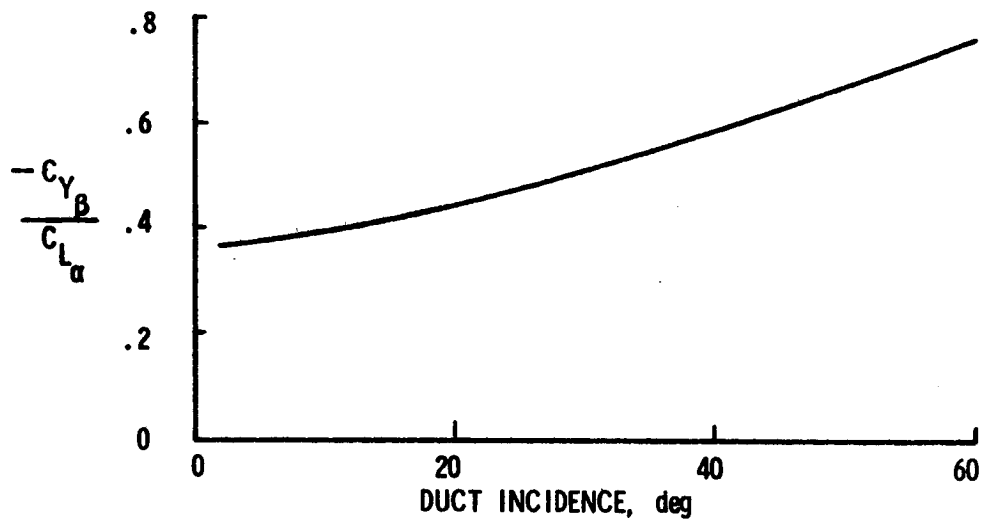


Figure 47.- Side-force characteristics of tilt-duct airplane.

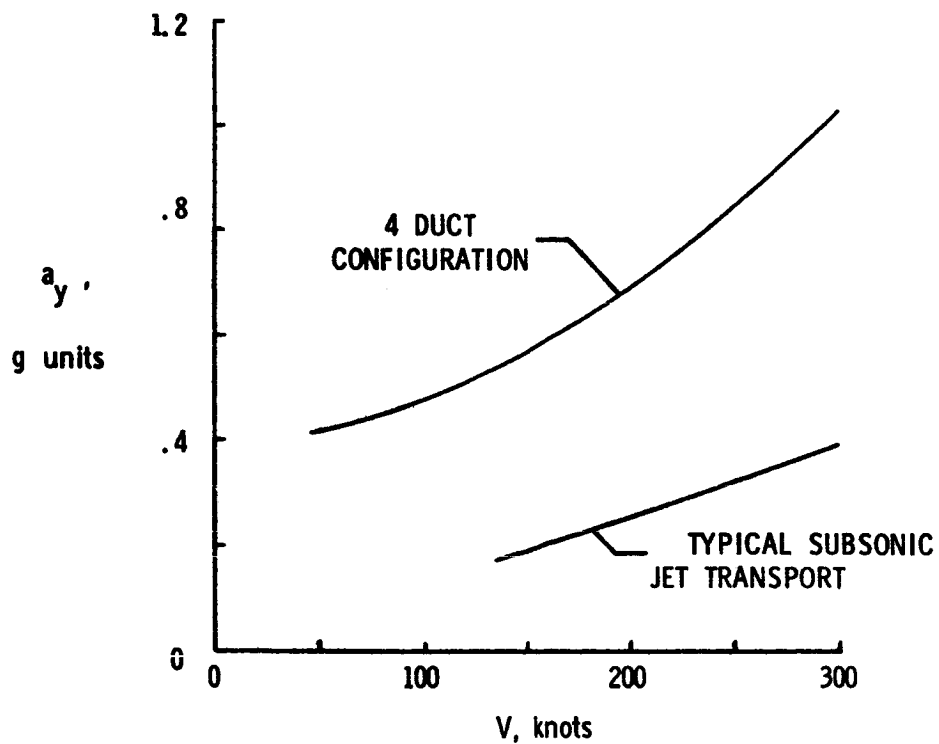


Figure 48.- Response to crosswind gust of 50 ft/sec (15.24 m/sec).

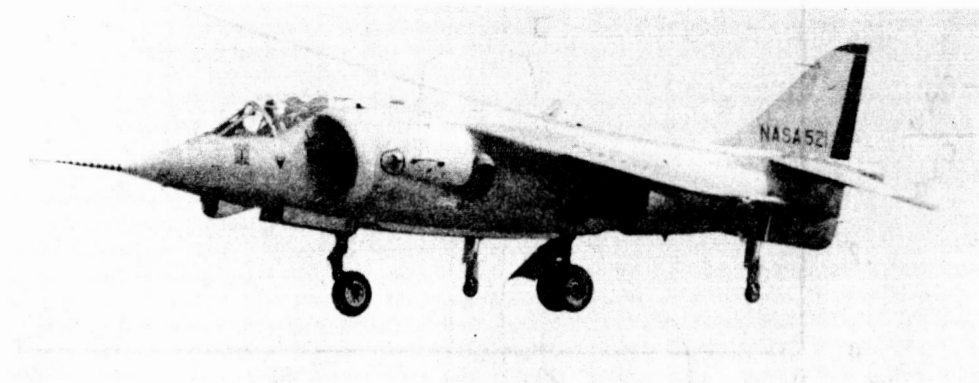


Figure 49.- Jet V/STOL airplane.

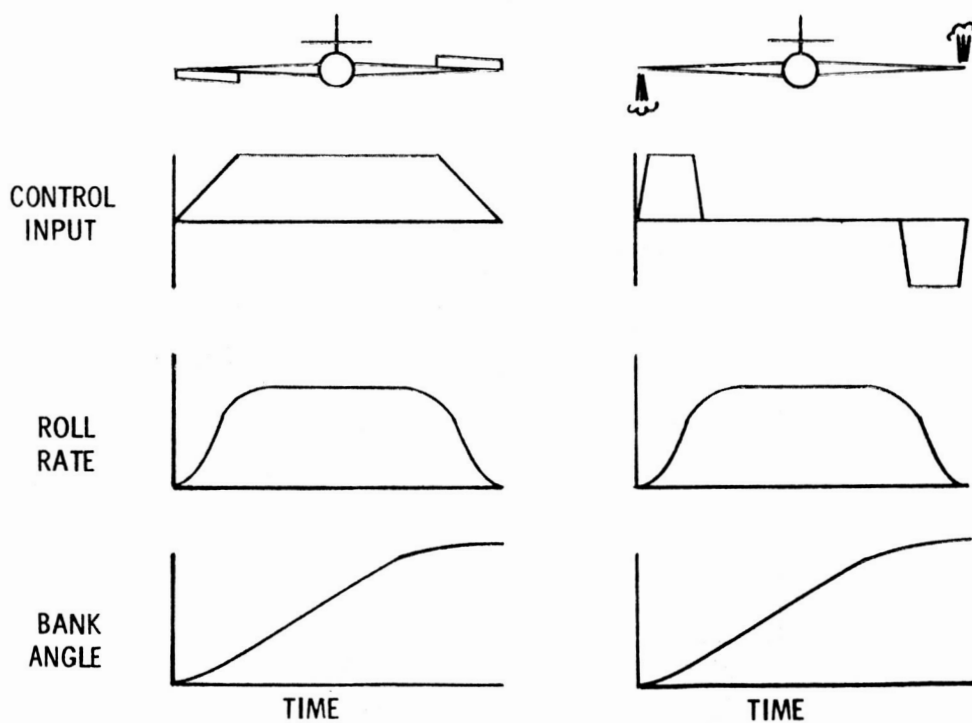


Figure 50.- Comparison of time histories of lateral control inputs of jet V/STOL and conventional airplanes.

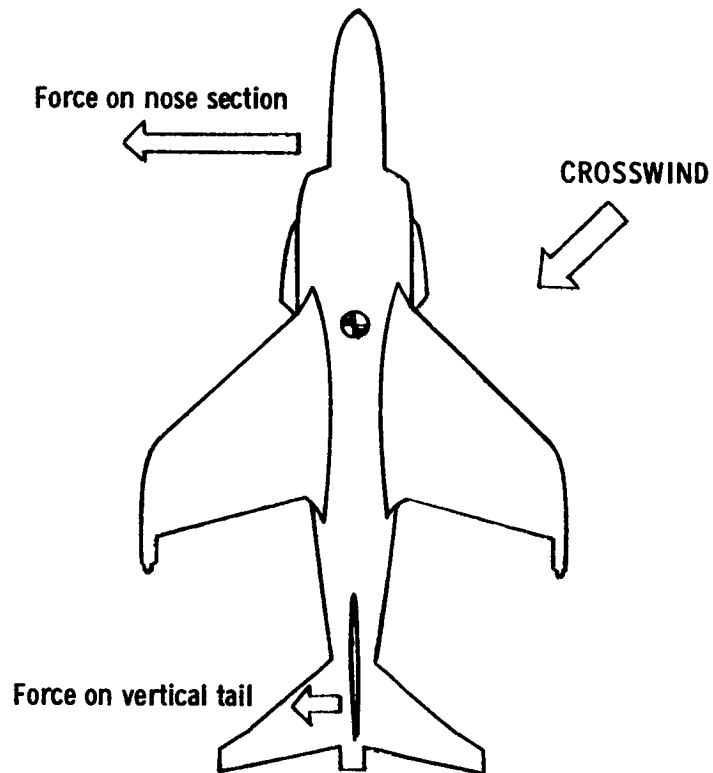


Figure 51.- Effect of crosswind on directional stability of jet V/STOL airplane.

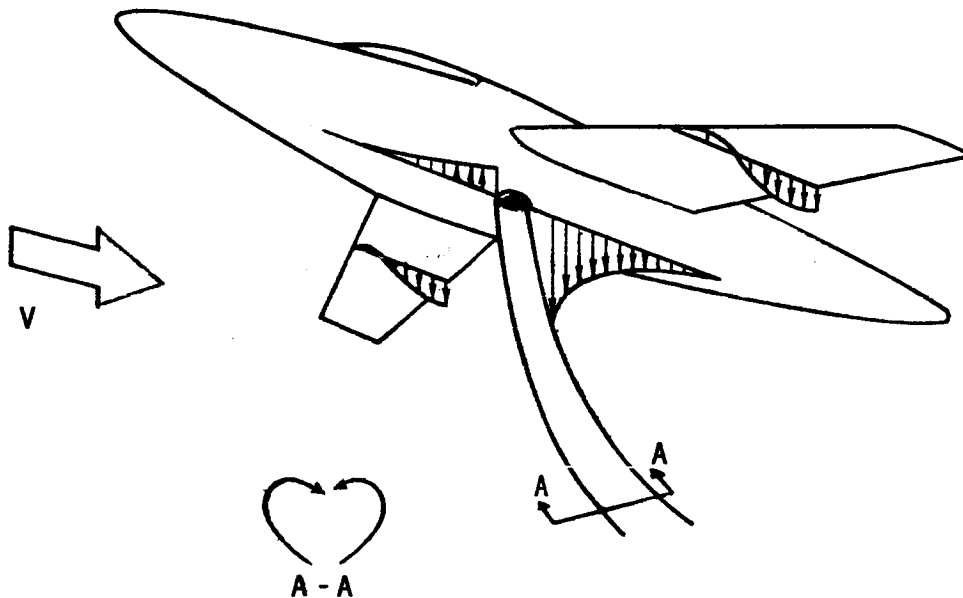


Figure 52.- Jet interference in transition flight.

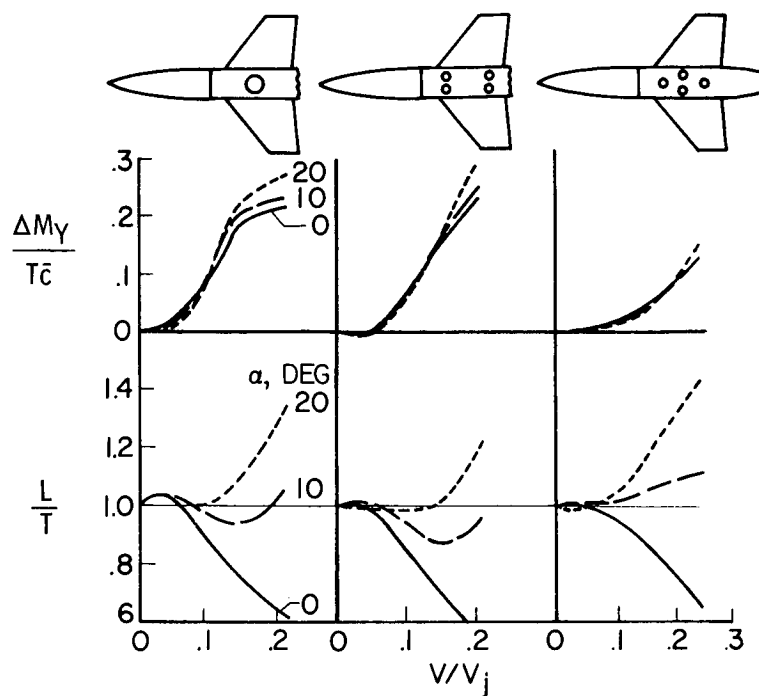


Figure 53.- Effect of jet interference on lift and pitching-moment characteristics.

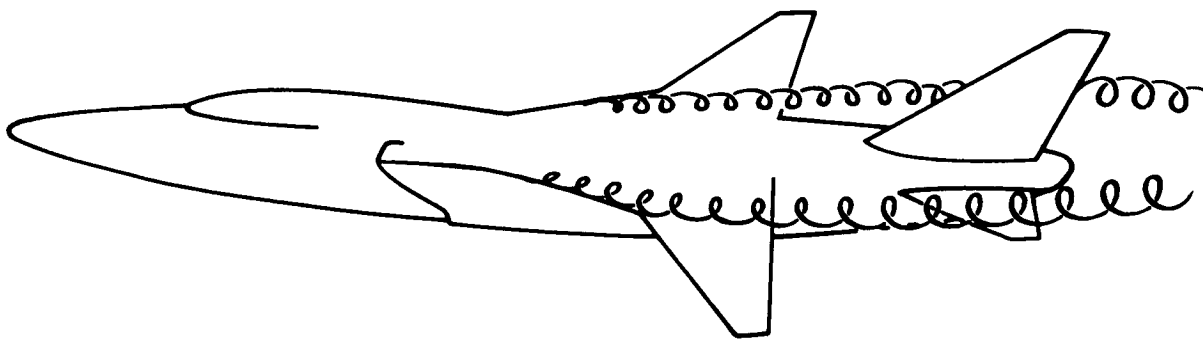


Figure 54.- Sketch of path of trailing vortices for contemporary fighter V/STOL configuration in cruising flight.

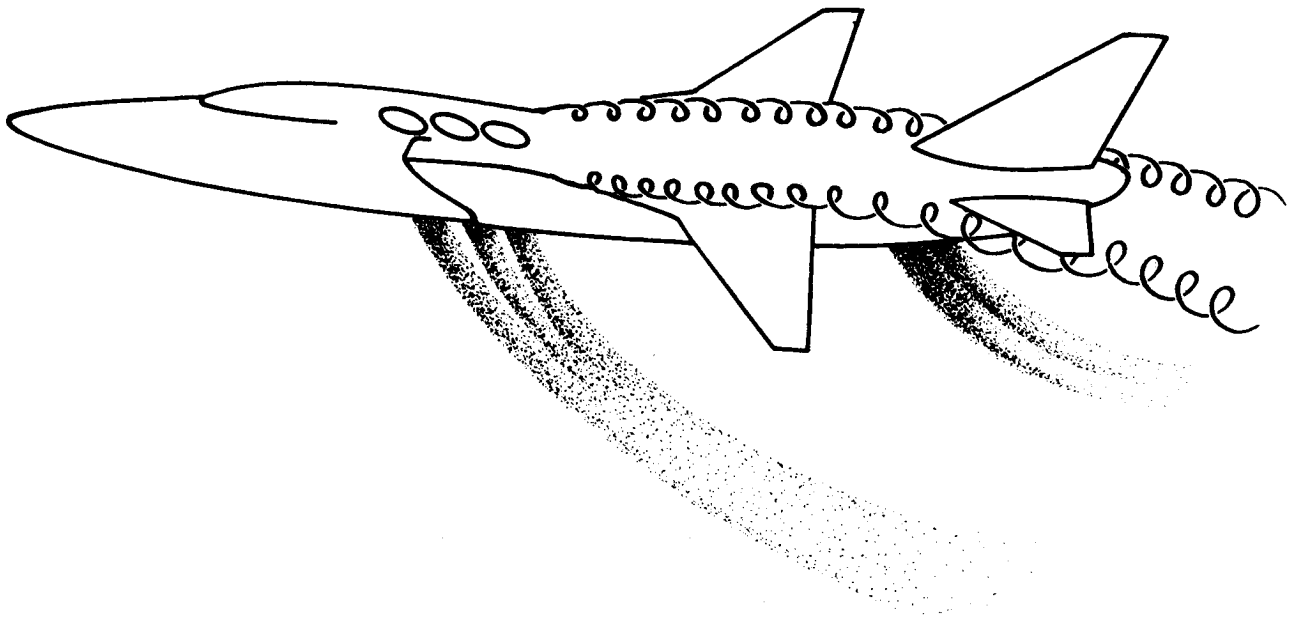


Figure 55.- Path of trailing vortices for jet V/STOL in transition.

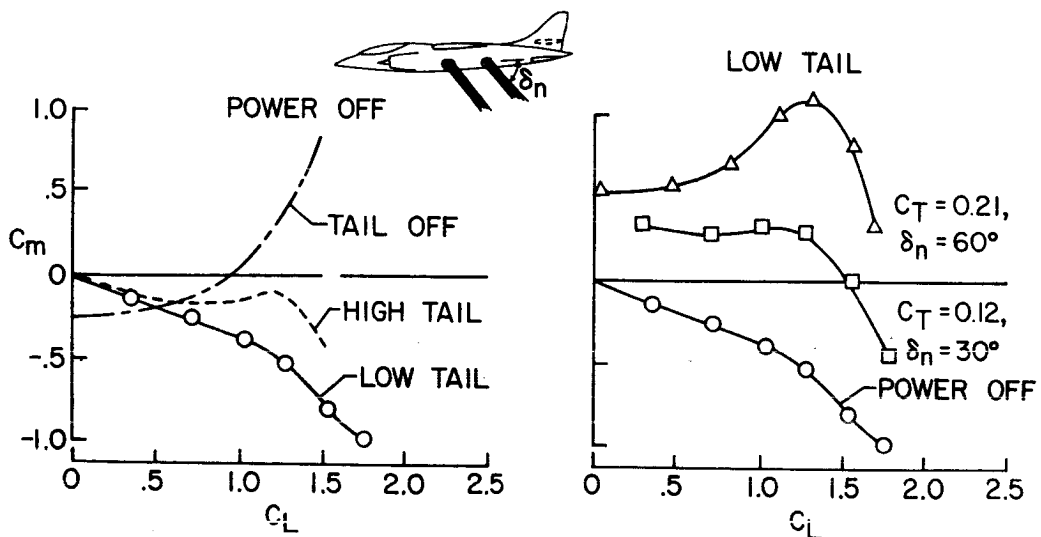


Figure 56.- Jet-induced-downwash effects for vectored-thrust V/STOL configuration.



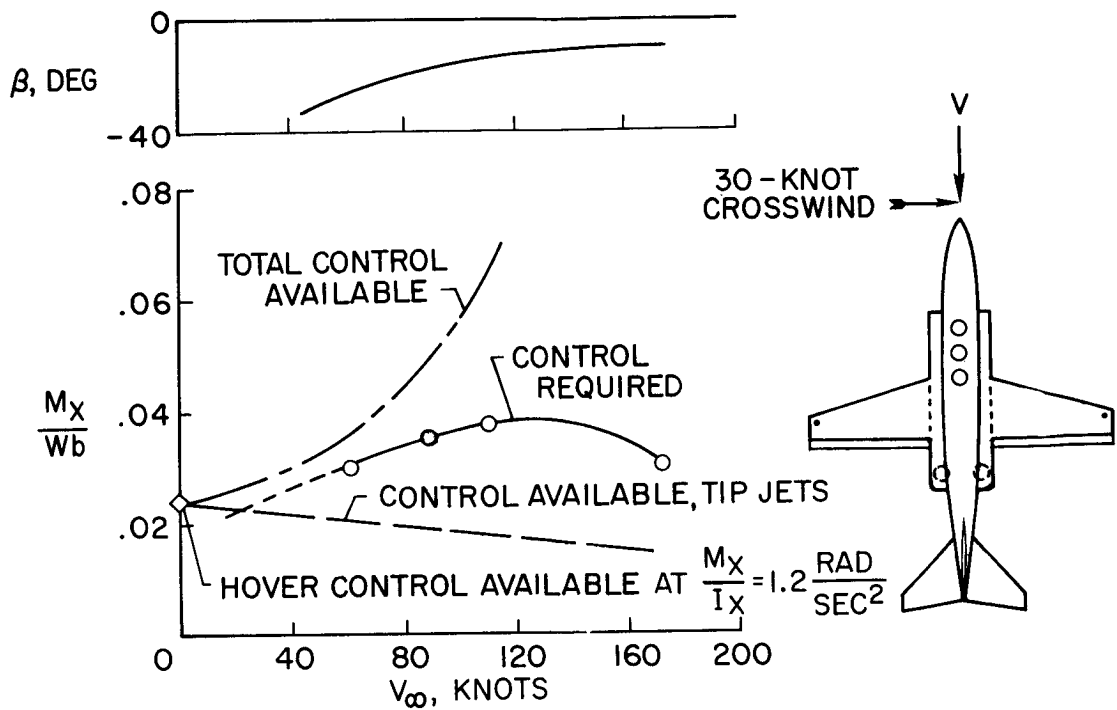


Figure 57.- Rolling moments generated by aerodynamic interference effects of jet V/STOL in sideslip.

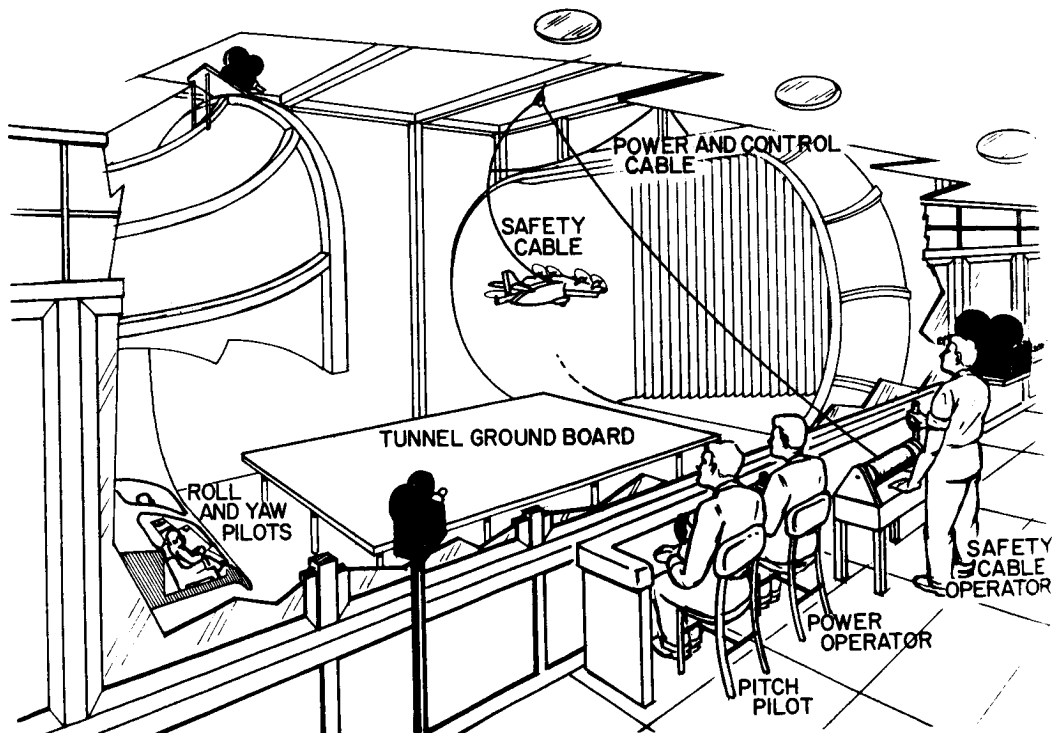


Figure 58.- Setup for free-flight testing.

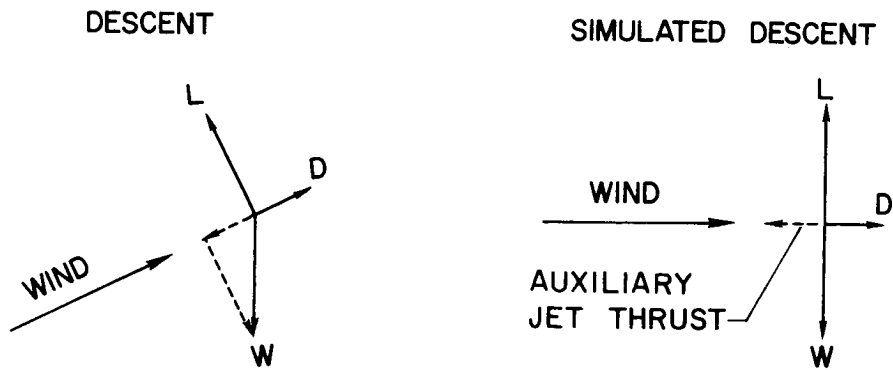


Figure 59.- Simulation of descending flight in free-flight technique.

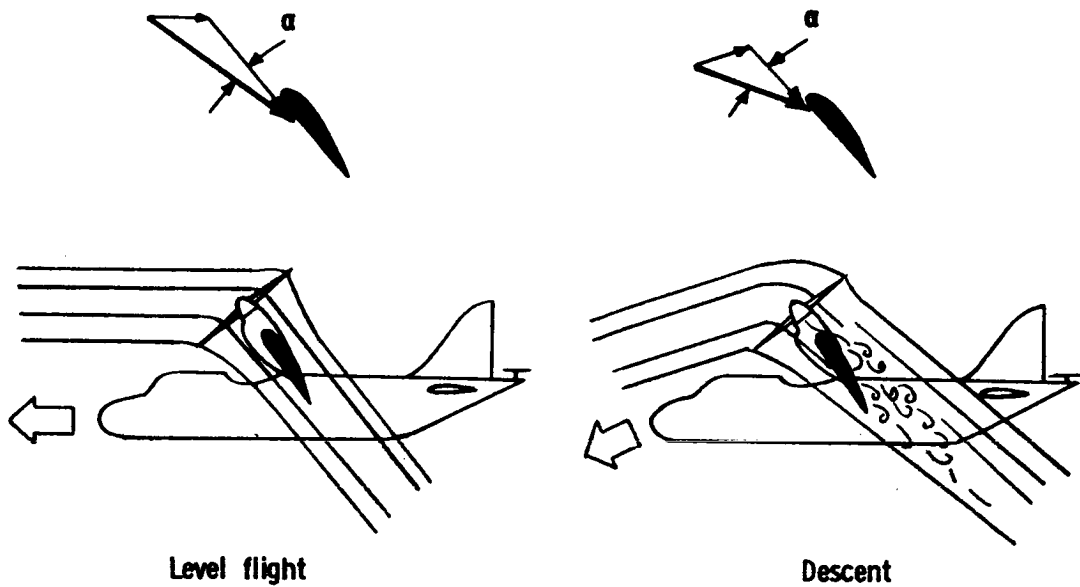


Figure 60.- Effect of descent on wing angle of attack.

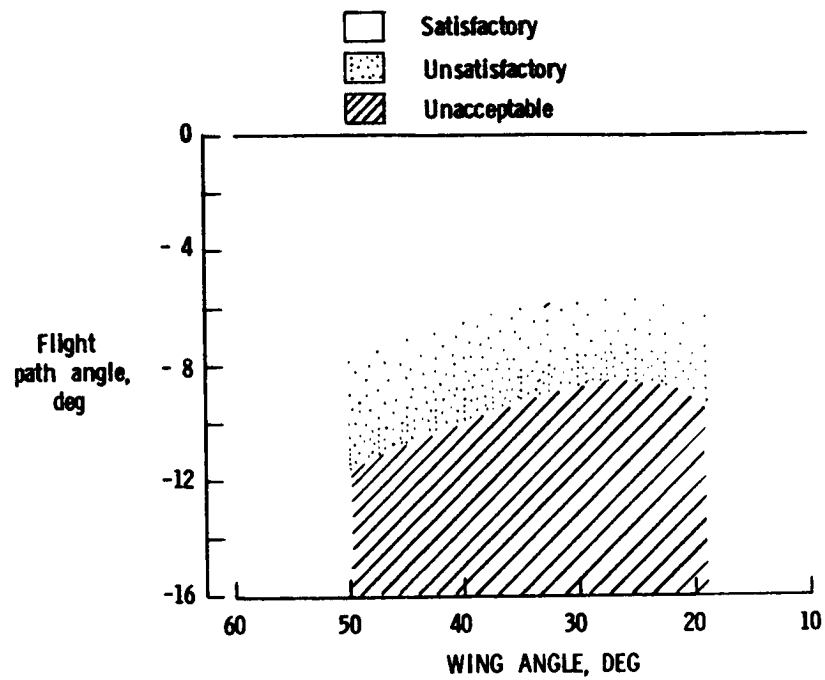


Figure 61.- Descent capability of XC-142 model.

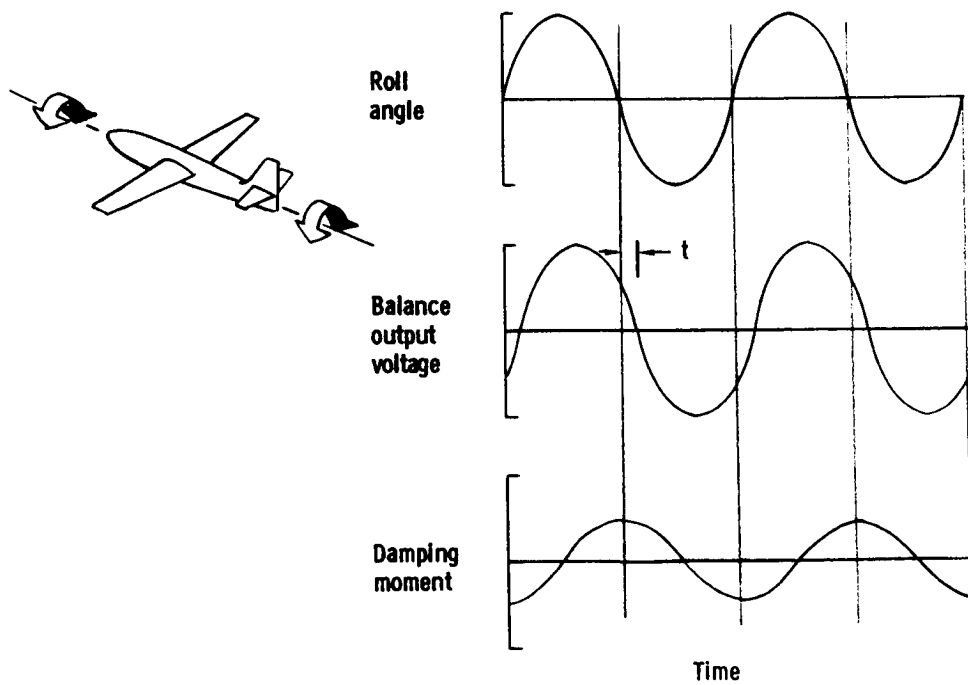


Figure 62.- Forced-oscillation data reduction.

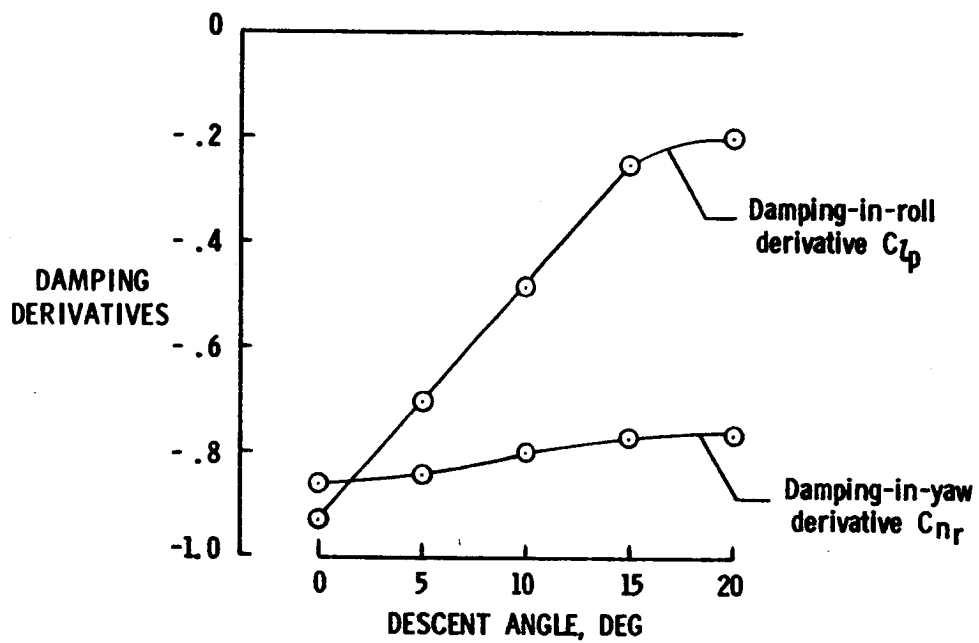


Figure 63.- Effect of descent on damping derivatives.  $i_w = 30^\circ$ .

## 2. METHODS OF OBTAINING STABILITY DERIVATIVES

By M. J. Queijo  
Langley Research Center

### ABSTRACT

Various methods of obtaining aerodynamic derivatives are reviewed. These methods include wind-tunnel tests, aerodynamic theory, and extraction from flight tests, with the emphasis being on flight tests. Two techniques for extracting derivatives from flight are covered in sufficient detail to indicate the procedures involved. These methods are a strict least-squares approach and an iteration technique. References are listed for additional background and details of various techniques.

### INTRODUCTION

The design of an airplane is a very complex problem because of the many and often conflictive requirements that have to be met. Many factors must be considered, such as total weight, payload, armament, speed, stability and control, acceleration capability, landing and take-off speed, and so forth. The final aircraft configuration is a compromise, and the items given priority are dependent on the primary function of the aircraft. In all cases, however, the stability and control, and the handling characteristics are quite important. Early in the design, an attempt is made to determine the stability and control characteristics of the airplane for two primary reasons:

- (1) To determine the inherent stability and control
- (2) To determine what stability augmentation, if any, is required to make the stability satisfactory

Such determinations can be made by estimating the response of the airplane to various disturbances, that is, by determining the motion of the aircraft for various force and moment disturbances. The motion can be studied by use of the equations of motion of the aircraft. Such equations generally are written in a form that includes a number of parameters that are referred to as stability derivatives. The purpose of this paper is to indicate several methods of obtaining such derivatives for use in stability or motion calculations.

## SYMBOLS

$a_X, a_Y, a_Z$     accelerations along body axes X, Y, and Z, respectively

$b$                 wing span

$C_l$               rolling-moment coefficient,  $\frac{M_X}{Q S b}$

$C_m$               pitching-moment coefficient,  $\frac{M_Y}{Q S \bar{c}}$

$C_n$               yawing-moment coefficient,  $\frac{M_Z}{Q S b}$

$C_X$               longitudinal-force coefficient,  $\frac{F_X}{Q S}$

$C_{X_0}$             trim value of  $C_X$

$C_Y$               lateral-force coefficient,  $\frac{F_Y}{Q S}$

$C_Z$               normal-force coefficient,  $\frac{F_Z}{Q S}$

$$C_{l_\beta} = \frac{\partial C_l}{\partial \beta}$$

$$C_{l_{\dot{\beta}}} = \frac{\partial C_l}{\partial \frac{\dot{\beta} b}{2V}}$$

$$C_{l_p} = \frac{\partial C_l}{\partial \frac{pb}{2V}}$$

$$C_{l_r} = \frac{\partial C_l}{\partial \frac{rb}{2V}}$$

$$C_{l_{\delta_a}} = \frac{\partial C_l}{\partial \delta_a}$$

$$C_{l\delta_r} = \frac{\partial C_l}{\partial \delta_r}$$

$$C_{m\alpha} = \frac{\partial C_m}{\partial \alpha}$$

$$C_{m\dot{\alpha}} = \frac{\partial C_m}{\partial \frac{\dot{\alpha} \bar{c}}{2V}}$$

$$C_{mq} = \frac{\partial C_m}{\partial \frac{q \bar{c}}{2V}}$$

$$C_{m\delta_e} = \frac{\partial C_m}{\partial \delta_e}$$

$$C_{n\beta} = \frac{\partial C_n}{\partial \beta}$$

$$C_{n\dot{\beta}} = \frac{\partial C_n}{\partial \frac{\dot{\beta} b}{2V}}$$

$$C_{np} = \frac{\partial C_n}{\partial \frac{pb}{2V}}$$

$$C_{nr} = \frac{\partial C_n}{\partial \frac{rb}{2V}}$$

$$C_{n\dot{r}} = \frac{\partial C_n}{\partial \frac{\dot{r} b}{2V}}$$

$$C_{n\delta_r} = \frac{\partial C_n}{\partial \delta_r}$$

$$\dot{C}_{X\alpha} = \frac{\partial C_X}{\partial \alpha}$$

$$C_{Xq} = \frac{\partial C_X}{\frac{q\bar{c}}{\partial \frac{2V}{\partial}}}$$

$$C_{X\delta_a} = \frac{\partial C_X}{\partial \delta_a}$$

$$C_{X\delta_e} = \frac{\partial C_X}{\partial \delta_e}$$

$$C_{X\delta_r} = \frac{\partial C_X}{\partial \delta_r}$$

$$C_{Y\beta} = \frac{\partial C_Y}{\partial \beta}$$

$$C_{Y\dot{\beta}} = \frac{\partial C_Y}{\frac{\dot{\beta}b}{\partial \frac{2V}{\partial}}}$$

$$C_{Yp} = \frac{\partial C_Y}{\frac{pb}{\partial \frac{2V}{\partial}}}$$

$$C_{Yr} = \frac{\partial C_Y}{\frac{rb}{\partial \frac{2V}{\partial}}}$$

$$C_{Y\delta_r} = \frac{\partial C_Y}{\partial \delta_r}$$

$$C_{Z\alpha} = \frac{\partial C_Z}{\partial \alpha}$$

$$C_{Zq} = \frac{\partial C_Z}{\frac{q\bar{c}}{\partial \frac{2V}{\partial}}}$$

$$C_{Z\delta_e} = \frac{\partial C_Z}{\partial \delta_e}$$



$c$	local wing chord
$\bar{c}$	wing mean aerodynamic chord
$c_l$	section lift coefficient
$F$	downwash function
$F_X, F_Y, F_Z$	forces along body axes $X$ , $Y$ , and $Z$ , respectively
$f$	frequency
$g$	acceleration due to gravity
$\text{Im}( )$	imaginary part
$I_X, I_Y, I_Z$	moments of inertia about body axes $X$ , $Y$ , and $Z$ , respectively
$I_{XZ}$	product of inertia
$J$	cost function as defined in equation (25)
$k$	arbitrary constant or spring constant
$l = \rho V \Gamma$	
$l_\beta$	lift on vortex due to sideslip velocity
$M_X$	rolling moment
$M_Y$	pitching moment
$M_Z$	yawing moment
$M_\psi$	yawing moment due to flexures
$m$	mass
$p$	rate of rotation about body axis $X$

Q	dynamic pressure, $\frac{1}{2}\rho V^2$
q	rate of rotation about body axis Y
Re( )	real part
r	rate of rotation about body axis Z
S	wing area
s	semispan of horseshoe vortex
t	time
$t_{1/2}$	time to damp to half amplitude
u	velocity in direction of body axis X
V	total velocity
v	velocity in direction of body axis Y
w	velocity in direction of body axis Z
X,Y,Z	body axes
$X_i, Y_i, Z_i$	inertial axes
$x', y'$	coordinates relative to horseshoe vortex
$\alpha$	angle of attack
$\beta$	angle of sideslip
$\Gamma$	circulation strength of vortex

$\Delta$	incremental change
$\delta_a$	aileron deflection
$\delta_e$	elevator deflection
$\delta_r$	rudder deflection
$\lambda$	damping coefficient
$\theta$	angle between body axis X and horizontal plane
$\rho$	air density
$\phi$	roll angle about body axis X
$\chi$	linear displacement
$\psi$	heading angle
$\omega$	circular frequency

Subscripts:

n	nth value or iteration
o	initial value

A dot over a symbol denotes a time derivative; that is,  $\dot{\beta} = \frac{\partial \beta}{\partial t}$ .

## EQUATIONS OF MOTION

Figure 1 shows a system of axes fixed relative to the airframe. The equations of motion are simply expressions of Newton's laws for translation and rotation along and around each axis. A typical set of the six equations of motion is

$$\left. \begin{aligned}
m\ddot{a}_X &= m(\dot{u} + qw - rv) = -mg \sin \theta + QS \left( C_{X_0} + C_{X_\alpha} \alpha + C_{X_q} \frac{q\bar{c}}{2V} + C_{X_{\delta_a}} \delta_a + C_{X_{\delta_e}} \delta_e + C_{X_{\delta_r}} \delta_r \right) \\
m\ddot{a}_Y &= m(\dot{v} + ru - pw) = mg \cos \theta \sin \phi + QS \left( C_{Y_\beta} \beta + C_{Y_{\dot{\beta}}} \frac{\dot{\beta}\bar{b}}{2V} + C_{Y_p} \frac{pb}{2V} + C_{Y_r} \frac{rb}{2V} + C_{Y_{\delta_r}} \delta_r \right) \\
m\ddot{a}_Z &= m(\dot{w} + pv - qu) = mg \cos \theta \cos \phi + QS \left( C_{Z_\alpha} \alpha + C_{Z_q} \frac{q\bar{c}}{2V} + C_{Z_{\delta_e}} \delta_e \right) \\
\dot{p}I_X + qr(I_Z - I_Y) - (pq + \dot{r})I_{XZ} &= QSb \left( C_{l_\beta} \beta + C_{l_{\dot{\beta}}} \frac{\dot{\beta}\bar{b}}{2V} + C_{l_p} \frac{pb}{2V} + C_{l_r} \frac{rb}{2V} + C_{l_{\delta_a}} \delta_a + C_{l_{\delta_r}} \delta_r \right) \\
\dot{q}I_Y + pr(I_X - I_Z) + (p^2 - r^2)I_{XZ} &= QS\bar{c} \left( C_{m_\alpha} \alpha + C_{m_{\dot{\alpha}}} \frac{\dot{\alpha}\bar{c}}{2V} + C_{m_q} \frac{q\bar{c}}{2V} + C_{m_{\delta_e}} \delta_e \right) \\
\dot{r}I_Z + pq(I_Y - I_X) + (qr - \dot{p})I_{XZ} &= QSb \left( C_{n_\beta} \beta + C_{n_{\dot{\beta}}} \frac{\dot{\beta}\bar{b}}{2V} + C_{n_p} \frac{pb}{2V} + C_{n_r} \frac{rb}{2V} + C_{n_{\delta_r}} \delta_r \right)
\end{aligned} \right\} \quad (1)$$

The equations are not derived in this presentation; however a complete derivation can be found in any good text on aircraft dynamics. (See ref. 1, for example.) One major problem involved with the equations of motion is the determination of aerodynamic derivatives. The aerodynamic derivatives are the items of concern in this presentation. Note that an aerodynamic derivative is simply a nondimensional coefficient which relates a force or moment to linear and angular velocities and accelerations; for example,

$$C_{X_\alpha} = \frac{\partial C_X}{\partial \alpha} = \frac{1}{\frac{1}{2}\rho V^2 S} \frac{\partial F_X}{\partial \alpha} \quad (2)$$

The force in the x-direction, owing to a change in angle of attack, is given by

$$\Delta F_X = \frac{1}{2}\rho V^2 S C_{X_\alpha} \Delta \alpha \quad (3)$$

Note that a basic assumption is involved here; that is, the force varies linearly with angle of attack. This assumption is generally valid only for small perturbations from equilibrium. The remainder of this presentation covers the following methods of determining aerodynamic derivatives:

- (1) Wind-tunnel tests
- (2) Aerodynamic theory
- (3) Flight testing

The emphasis is on flight testing.

## DETERMINATION OF AERODYNAMIC DERIVATIVES

There are several methods of determining aerodynamic derivatives. The most commonly used method is that of wind-tunnel testing. The specific procedure used depends on the derivative to be measured.

### Wind-Tunnel Testing

Static derivatives. - The static aerodynamic derivatives are the ones most easily determined in wind-tunnel tests. These derivatives are those associated with angle of attack and angle of sideslip. The forces and moments are measured for a range of angles, and the data are then used to obtain the derivatives. For example,  $C_{m_\alpha}$  is determined by plotting pitching moment as a function of angle of attack; the slope of the data is measured close to  $\alpha = 0$  and nondimensionalized. The procedure is simply

$$C_{m_\alpha} = \frac{1}{\frac{1}{2}\rho V^2 S \bar{c}} \frac{\partial M_Y}{\partial \alpha}$$

The static lateral derivatives are slightly more complicated because they are functions of angle of attack and sideslip. In measuring sideslip derivatives the procedure generally is to fix the angle of attack and to vary sideslip over some small range around zero. This procedure is followed for several values of angle of attack. At each value of  $\alpha$ , a value of the sideslip derivative is obtained; for example,

$$(C_{n_\beta})_{\alpha=0} = \frac{1}{\frac{1}{2}\rho V^2 S b} \left( \frac{\partial M_Z}{\partial \beta} \right)_{\alpha=0}$$

Rotary derivatives. - The rotary derivatives are those associated with rotary motion; that is, with the angular rates  $p$ ,  $q$ , and  $r$ . Measurement of these derivatives requires special facilities or techniques. These techniques are mentioned briefly; however, suitable references are cited for more detailed explanations. Three basic problems associated with experimental determination of rotary derivatives are as follows:

- (1) Obtaining the correct airflow distribution
- (2) Measurement of forces and moments
- (3) Isolation of the pertinent derivatives

One rather unique facility designed specifically to measure rotary derivatives is the stability tunnel, which was originally at the Langley Research Center of NASA and is now at the Virginia Polytechnic Institute in Blacksburg, Virginia. This facility can be used

to simulate rolling, pitching, and yawing motion by actually curving the airstream. The basic mechanisms involved are illustrated in figures 2 to 4.

In the rolling-flow setup, roll rate can be varied by changing the speed of the rotor blades ahead of the model. In this manner the simulated rolling velocity  $p$  can be varied. The rolling derivatives can be measured; for example,

$$C_{l_p} = \frac{\partial C_l}{\partial \frac{pb}{2V}} = \frac{\partial}{\partial \frac{pb}{2V}} \left( \frac{M_X}{\frac{1}{2} \rho V^2 S b} \right)$$

In the yawing- and pitching-flow setup, the angular velocities  $q$  and  $r$  are varied by physically changing the tunnel-wall curvature and adding screens upstream of the model to obtain the correct flow distribution. Detailed descriptions of the facility are given in references 2 and 3 for rolling and yawing flow, respectively.

A more popular method of measuring aerodynamic derivatives is that of oscillating a model in a rectilinear airstream. The oscillatory motion can be forced or free. Of the two, the free-oscillation technique is the simpler. The basic procedure is outlined in reference 4, and only the concepts involved are mentioned in this paper. In the free-oscillation technique the model is mounted rigidly on a strut in a wind tunnel. The strut is attached to a tube by means of several flexure pivots (fig. 5). When the tunnel is in operation, the model is deflected, and a continuous record is made of time and displacement. The method of extracting derivatives is illustrated in figure 6 for a yawing oscillation and should be referred to in the following discussion. A curve is drawn to connect the peaks of successive oscillations. By starting at some point on this envelope, preferably in the early part of the time history, the amplitude and time are noted. The time is noted again when the envelope has reduced to one-half the initial amplitude. The time difference is noted as  $t_{1/2}$ . The period of the oscillatory motion is also noted. The entire procedure is repeated at several angles of attack for wind-on and wind-off conditions.

The basis for extracting certain derivatives from oscillation tests is outlined in terms of a simple yaw oscillation. The equation of motion for this case is

$$Q S b \left( C_{n\dot{r}} \frac{\dot{r} b^2}{4V^2} + C_{nr} \frac{r b}{2V} + C_{n\dot{\beta}} \frac{\dot{\beta} b}{2V} + C_{n\beta} \beta \right) + M_{\psi} \psi = I_Z \ddot{\psi} \quad (4)$$

In a wind tunnel  $\beta = -\psi$ ; also, by definition  $r = \dot{\psi}$ . Making use of these relations in equation (4) results in

$$\left( \frac{I_Z}{Q S b} - \frac{b^2}{4V^2} C_{n\dot{r}} \right) \ddot{\psi} - \left( C_{nr} - C_{n\dot{\beta}} \right) \frac{b}{2V} \dot{\psi} + \left( C_{n\beta} - \frac{M_{\psi}}{Q S b} \right) \psi = 0 \quad (5)$$

Equation (5) is a second-order linear differential equation with a well-known solution

$$\psi = Ae^{\lambda t} \quad (6)$$

Substituting equation (6) into equation (5) results in a quadratic in  $\lambda$  which can be solved to yield  $\lambda$  in the form

$$\lambda = \frac{\left(C_{n_r} - C_{n_{\dot{\beta}}}\right) \frac{b}{2V}}{2\left(\frac{I_Z}{Q S b} - \frac{b^2}{4V^2} C_{n_{\dot{r}}}\right)} \pm \frac{\left[\left(C_{n_r} - C_{n_{\dot{\beta}}}\right)^2 \frac{b^2}{4V^2} - 4\left(\frac{I_Z}{Q S b} - \frac{b^2}{4V^2} C_{n_{\dot{r}}}\right)\left(C_{n_{\beta}} - \frac{M_{\psi}}{Q S b}\right)\right]^{1/2}}{2\left(\frac{I_Z}{Q S b} - \frac{b^2}{4V^2} C_{n_{\dot{r}}}\right)} \quad (7)$$

In general, the terms under the radical will be negative so that equation (7) will be of the form

$$\lambda = a + i\omega$$

It is then apparent that the first term of equation (7) (real part of  $\lambda$ ) determines the rate of decay of the oscillation, whereas the second term (imaginary part of  $\lambda$ ) defines the frequency of the oscillation. A convenient method of determining the real part of  $\lambda$  is to measure the time required for the amplitude of the oscillation to decay by some factor, usually taken as the time to reach half amplitude. In such a case

$$\frac{\psi}{\psi_0} = \frac{1}{2} = e^{\lambda t_{1/2}}$$

and

$$\text{Re}(\lambda) = \frac{\ln\left(\frac{1}{2}\right)}{t_{1/2}} = \frac{-0.693}{t_{1/2}} \quad (8)$$

From equations (7) and (8)

$$\frac{\left(C_{n_r} - C_{n_{\dot{\beta}}}\right) \frac{b}{2V}}{2\left(\frac{I_Z}{Q S b} - \frac{b^2}{4V^2} C_{n_{\dot{r}}}\right)} = \frac{-0.693}{t_{1/2}} \quad (9)$$

Since generally

$$\frac{I_Z}{Q S b} \gg \frac{b^2}{4V^2} C_{n_{\dot{r}}} \quad (10)$$

equation (9) yields

$$C_{n_r} - C_{n_{\dot{\beta}}} = \frac{-2.772 I_Z V}{Q S b^2 t_{1/2}} \quad (11)$$

The frequency of the oscillation is given by the second term of equation (7) (the imaginary part of  $\lambda$ ). Since in general the first term under the radical is much smaller than the second term,

$$\omega = \text{Im}(\lambda) = \left( \frac{C_{n_{\beta}} - \frac{M_{\psi}}{Q S b}}{\frac{I_Z}{Q S b} - \frac{b^2}{4 V^2} C_{n_{\dot{r}}}} \right)^{1/2}$$

from which

$$C_{n_{\beta}} + \left( \frac{\omega b}{2 V} \right)^2 C_{n_{\dot{r}}} = \frac{1}{Q S b} \left[ (2 \pi f)^2 I_Z + M_{\psi} \right] \quad (12)$$

Note that in oscillation tests it is generally not possible to measure an individual derivative because derivatives are generally obtained in combinations such as indicated in equations (11) and (12). However, in the case of a few derivatives, it has been possible to obtain isolated derivatives under oscillation conditions. (See refs. 5 and 6, for example.)

### Theory

Aerodynamic theory has been used extensively to develop methods for estimating aerodynamic derivatives of isolated lifting surfaces or fuselages. The work in this area is well documented for all flight regimes – subsonic, transonic, supersonic, and hypersonic. Analytical methods to account for mutual interference effects when components are assembled to form a complete aircraft are not well defined. However some empirical methods have been developed for estimating interference effects. Several papers which present methods for estimating the aerodynamics of complete aircraft have been published. References 7 and 8 are good examples of such papers. The list of references in reference 8 is a good indication of the amount of theoretical and experimental work which has been done on methods of estimating aerodynamic derivatives.

In theoretical aerodynamics the basic task is to develop a suitable analytical model for the wing, body, or combination and to use that model to obtain forces and moments. The analytical models generally consist of suitable distributions of sources, sinks,



doublets, vortices, or combinations of these depending on the problem under study. As an elementary example, consider a plane wing in subsonic flow.

It is well known that a wing can be represented by a suitable distribution of vortices in a windstream. One possible distribution of vortices is illustrated in figure 7. In forward flight the lift per unit length of bound vortex is given by the Kutta-Joukowski equation

$$l = \rho V \Gamma \quad (13)$$

or, in nondimensional form

$$c_l = \frac{2\Gamma}{Vc} \quad (14)$$

If the circulation distribution  $\Gamma$  is known, the lift distribution is determined from equation (14). The distribution  $\Gamma$  is determined by the following concept (refer to fig. 8). The circulation gives rise to a downwash velocity according to the Biot-Savart law. For a horseshoe vortex as shown in figure 8, the downwash velocity is given by

$$w \frac{4\pi s}{\Gamma} = \frac{1}{x'} \left( \frac{y' + 1}{\sqrt{x'^2 + (y' + 1)^2}} - \frac{y' - 1}{\sqrt{x'^2 + (y' - 1)^2}} \right) + \frac{1}{y' - 1} \left( 1 + \frac{x'}{\sqrt{x'^2 + (y' - 1)^2}} \right) + \frac{1}{y' + 1} \left( 1 + \frac{x'}{\sqrt{x'^2 + (y' + 1)^2}} \right) \quad (15)$$

Because there can be no flow through the wing, the total downwash at any point on the wing must be equal to the normal velocity component of the airstream relative to the wing plane. In representing the wing by a vortex system as illustrated in figure 7, the boundary condition is usually satisfied at only one point inside each horseshoe - at the 3/4-chord point. A set of simultaneous equations for the wing can be written as

$$\left. \begin{aligned} F_{11}\Gamma_1 + F_{12}\Gamma_2 + \dots + F_{1n}\Gamma_n &= V \sin \alpha_1 \\ F_{21}\Gamma_1 + F_{22}\Gamma_2 + \dots + F_{2n}\Gamma_n &= V \sin \alpha_2 \\ &\cdot \\ &\cdot \\ &\cdot \\ F_{n1}\Gamma_1 + F_{n2}\Gamma_2 + \dots + F_{nn}\Gamma_n &= V \sin \alpha_n \end{aligned} \right\} \quad (16)$$

The factors  $F$  for a horseshoe vortex can be found by application of the Biot-Savart law. However values of  $F$  have been published in a number of papers. (See ref. 9, for example.) Solution of the set of simultaneous equations (16) yields the circulation distribution and, therefore, also the lift distribution.

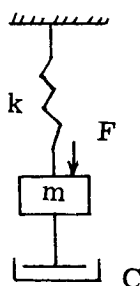
Now a method is needed to estimate the aerodynamic parameters other than lift or, more specifically, a method to estimate some of the sideslip or rotary derivatives. Again, several math models have been proposed. Only one model is mentioned herein. The basis for the model is simply this: It appears that the circulation strength is primarily a function of the flow perpendicular to the wing surface, and is, for practical purposes, independent of the flow direction in the plane of the wing; that is, the circulation for a wing appears to be nearly independent of sideslip and yawing. The circulation distribution is well documented for wings at angle of attack. Therefore, in order to obtain sideslip and yawing derivatives, the circulation due to angle of attack is used, and the velocity components in slideslip or yawing are allowed to react with the circulation. The concept is illustrated in figure 9. The circulation distribution is symmetric for the angle-of-attack case. However note that the lateral velocity reacts with corresponding vortices in such a manner as to produce an antisymmetric loading and therefore results in a rolling moment. This concept is worked out in reference 10 which shows that several derivatives can be calculated based on the concept.

#### Extraction of Derivatives From Flight Data

Various methods of estimating aerodynamic parameters by use of wind-tunnel data or from theory have been examined. The derivatives can be used to compute motions for the aircraft. It is important to realize that the computed motions and stability are meaningless unless the equations of motion and the aerodynamic derivatives are truly representative of the aircraft under consideration. Wind-tunnel measurements are usually made with small models, and Reynolds number, roughness, tunnel-wall effects, Mach number, and so forth, generally are not properly scaled to simulate the full-scale aircraft. Questions therefore arise relative to the correctness of the derivatives and subsequent calculations. It is desirable to check the derivatives by some other means. One method is to obtain the derivatives in controlled flight of the full-scale aircraft. A totally new problem arises – that of extracting aerodynamic parameters from flight tests. The basic problem now becomes: Given a group of measurements of velocities, positions, and accelerations taken over a time interval, determine whether the aerodynamic parameters can be estimated.

This problem is basically one of a type which falls under the general category of parameter identification. As a simple example, assume that a spring-dashpot-mass

system exists, as shown in the following sketch, but the spring constant, damping coefficient, or mass are not known:



where

$k$             spring constant

$C$             damping coefficient

$F$             force

$m$             mass

By observing the oscillatory system and by making measurements of velocities and displacements  $k$ ,  $C$ , and  $m$  can be determined provided that an equation, which adequately describes this motion of the system, can be written.

Several methods of determining the aerodynamic parameters are examined. In this discussion the measured or observed velocities, displacements, and accelerations are referred to as the state variables because they define the state of the system. The aerodynamic coefficients are called the aerodynamic parameters, or simply the parameters.

Analog-matching technique.- This method involves obtaining flight data for specific series of control inputs. The aircraft response, in terms of accelerations, angular rates, and angular displacements, is measured. Equations of motion are then written for the aircraft, and estimated aerodynamic derivatives are put into the equations. Measured or estimated mass and inertia characteristics for the aircraft are required and should be quite accurate. In the analog-matching technique, motions are computed for the same control inputs as those used in the flight tests. Comparisons are made between computed and flight-measured responses. If any of the responses do not compare favorably, some of the derivatives are changed, and the motions are computed again. The process is repeated until satisfactory agreement is obtained between estimated and flight responses. The ability to converge on a set of acceptable derivatives, or of even defining acceptable agreement between computed and flight motions, is largely a matter of experience.

Sometimes a particular computed response characteristic can be varied by altering a specific derivative. In many instances, however, a single derivative may alter several responses.

Some studies have been made to determine the effect of parameters on motions of an aircraft. Results of studies of this type have shown, for example, that:  $C_{n\beta}$  largely governs the period of the lateral oscillation;  $C_{l_p}$  largely governs the damping of the rolling motion;  $C_{n_r}$  largely governs the damping of the yawing motion;  $C_{m_q}$  largely governs the damping in pitch; and  $C_{m_\alpha}$  largely governs the period of the pitch oscillation.

It is generally convenient to perform the matching on an analog computer where derivatives can be varied at will by simply turning potentiometers, and where visual presentations of modes of motion can be obtained on oscilloscopes or paper records. By use of overlays, which give the actual aircraft motion, a comparison of computed and flight motions can be observed.

Analog matching depends quite heavily on the experience of the operator; however, it can be a very useful technique and has given very good results in many cases. One drawback is that this technique lacks a clearly defined measure of how well the estimated motion, obtained by using the extracted parameters, matches the flight records. More details of the analog-matching technique can be obtained from reference 11.

Simplified flight tests. - This technique requires that the aircraft motions be single degree of freedom. The technique for parameter identification is identical to that given earlier for wind-tunnel tests. For example, for a single-degree-of-freedom oscillation the rate of damping is related to a damping derivative, and the frequency is related to a directional-stability parameter. The total number of parameters which can be determined from such simple maneuvers is quite limited. Derivatives such as  $C_{l_r}$  or  $C_{n_p}$  are difficult to measure.

Least-squares technique. - This technique is rather fundamental in dealing with the correlation of data and is applied to a simple case to illustrate its use. A detailed explanation of the method can be found in references 12 and 13. The problem to be solved can be stated as follows: Given the time histories of some state variables of the aircraft and an analytical expression for one or more of these variables, find the set of parameters that gives the best agreement between the measured data and the flight data in the least-squares sense. In order to see what this means, assume that the equations applicable are those of equation (1) and consider the first equation

$$m\ddot{\alpha} = -mg \sin \theta + QS \left( C_{X_0} + C_{X_\alpha} \alpha + C_{X_q} \frac{q\bar{c}}{2V} \right) \quad (17)$$

simplified (for illustrative purposes) to the case with neutral controls. Assume that an aircraft is properly instrumented with accelerometers, rate gyros, velocity indicators, and control-position indicators so that the quantities  $\theta$ ,  $V$ ,  $\alpha$ , and  $q$  are measured. Assume also that the air density is known. All of these state variables could be plotted as functions of time as indicated in figure 10. Equation (17) contains three unknown parameters  $C_{X_0}$ ,  $C_{X_\alpha}$ , and  $C_{X_q}$ . Assume that for the small amplitudes of motion the parameters are constants. If the data were perfect (that is, free of noise), three sets of numbers (at  $t_1$ ,  $t_2$ , and  $t_3$ ) could be taken from the plots and substituted into equation (17) to obtain three simultaneous equations. In theory these equations could be solved simultaneously to obtain the desired parameters. However a number of practical problems arise in the application of the method. In general the data are not perfect, so that the answers obtained would depend on which three sets of data were used. The problem is that of determining one set of derivatives which, when used in the equations of motion, provides the best approximation to the flight records in the least-squares sense; that is, the set minimizes the square of the difference between computed curves and the flight data (fig. 11). Proceed as follows, and use as much good data as are available. If a set of aerodynamic derivatives and computed motion are available, differences as illustrated in figure 11 would be expected. Equation (17) would then be rewritten in the form

$$a_X + g \sin \theta - \frac{\rho S}{2m} V^2 \left( C_{X_\alpha} \alpha + C_{X_q} \frac{q\bar{c}}{2V} + C_{X_0} \right) = R \quad (18)$$

where  $R$  is the difference between the measured  $a_X$  and the sum of the aerodynamic terms (computed by using the measured values of  $\alpha$  and  $q$ ). One such equation for each time would be obtained so that

$$\left. \begin{aligned} a_{X_1} + g \sin \theta_1 - \frac{\rho S}{2m} V_1^2 \left[ C_{X_\alpha} \alpha_1 + C_{X_q} \left( \frac{q\bar{c}}{2V} \right)_1 + C_{X_0} \right] &= R_1 \\ a_{X_2} + g \sin \theta_2 - \frac{\rho S}{2m} V_2^2 \left[ C_{X_\alpha} \alpha_2 + C_{X_q} \left( \frac{q\bar{c}}{2V} \right)_2 + C_{X_0} \right] &= R_2 \\ a_{X_n} + g \sin \theta_n - \frac{\rho S}{2m} V_n^2 \left[ C_{X_\alpha} \alpha_n + C_{X_q} \left( \frac{q\bar{c}}{2V} \right)_n + C_{X_0} \right] &= R_n \end{aligned} \right\} \quad (19)$$

Squaring each of equations (19) results in

$$\left. \begin{aligned} R_1^2 &= \left\{ a_{X_1} + g \sin \theta_1 - \frac{\rho S}{2m} V_1^2 \left[ C_{X_\alpha} \alpha_1 + C_{X_q} \left( \frac{q\bar{c}}{2V} \right)_1 + C_{X_0} \right] \right\}^2 \\ R_2^2 &= \left\{ a_{X_2} + g \sin \theta_2 - \frac{\rho S}{2m} V_2^2 \left[ C_{X_\alpha} \alpha_2 + C_{X_q} \left( \frac{q\bar{c}}{2V} \right)_2 + C_{X_0} \right] \right\}^2 \\ R_n^2 &= \left\{ a_{X_n} + g \sin \theta_n - \frac{\rho S}{2m} V_n^2 \left[ C_{X_\alpha} \alpha_n + C_{X_q} \left( \frac{q\bar{c}}{2V} \right)_n + C_{X_0} \right] \right\}^2 \end{aligned} \right\} \quad (20)$$

Addition of equations (20) results in

$$\sum_i R_i^2 = \sum_i \left\{ a_{X_i} + g \sin \theta_i - \frac{\rho S}{2m} V_i^2 \left[ C_{X_\alpha} \alpha_i + C_{X_q} \left( \frac{q\bar{c}}{2V} \right)_i + C_{X_0} \right] \right\}^2 \quad (21)$$

To obtain the set of parameters which will minimize the summation of equation (21), perform the following operation:

$$\frac{\partial \sum_i R_i^2}{\partial C_{X_0}} = \frac{\partial \sum_i R_i^2}{\partial C_{X_\alpha}} = \frac{\partial \sum_i R_i^2}{\partial C_{X_q}} = 0$$

The result of performing this operation results in

$$\left. \begin{aligned} \frac{\partial \sum_i R_i^2}{\partial C_{X_\alpha}} &= 2 \sum_i \left\{ a_{X_i} + g \sin \theta_i - \frac{\rho S}{2m} V_i^2 \left[ C_{X_\alpha} \alpha_i + C_{X_q} \left( \frac{q\bar{c}}{2V} \right)_i + C_{X_0} \right] \right\} \left( -\frac{\rho S}{2m} V_i^2 \alpha_i \right) = 0 \\ \frac{\partial \sum_i R_i^2}{\partial C_{X_q}} &= 2 \sum_i \left\{ a_{X_i} + g \sin \theta_i - \frac{\rho S}{2m} V_i^2 \left[ C_{X_\alpha} \alpha_i + C_{X_q} \left( \frac{q\bar{c}}{2V} \right)_i + C_{X_0} \right] \right\} \left[ -\frac{\rho S}{2m} V_i^2 \left( \frac{q\bar{c}}{2V} \right)_i \right] = 0 \\ \frac{\partial \sum_i R_i^2}{\partial C_{X_0}} &= 2 \sum_i \left\{ a_{X_i} + g \sin \theta_i - \frac{\rho S}{2m} V_i^2 \left[ C_{X_\alpha} \alpha_i + C_{X_q} \left( \frac{q\bar{c}}{2V} \right)_i + C_{X_0} \right] \right\} \left( -\frac{\rho S}{2m} V_i^2 \right) = 0 \end{aligned} \right\} \quad (22)$$

For simplicity assume that the velocity remains constant during the measurements, and let

$$Q = \frac{1}{2} \rho V^2$$

Equation (22) becomes

$$\left. \begin{aligned} \sum_i a_{X_i} \alpha_i + g \sum_i \alpha_i \sin \theta_i - \frac{QS}{m} \left( C_{X_\alpha} \sum_i \alpha_i^2 + C_{X_q} \sum_i \alpha_i \left( \frac{q\bar{c}}{2V} \right)_i + C_{X_o} \sum_i \alpha_i \right) &= 0 \\ \sum_i a_{X_i} \left( \frac{q\bar{c}}{2V} \right)_i + g \sum_i \left( \frac{q\bar{c}}{2V} \right)_i \sin \theta_i - \frac{QS}{m} \left[ C_{X_\alpha} \sum_i \alpha_i \left( \frac{q\bar{c}}{2V} \right)_i + C_{X_q} \sum_i \left( \frac{q\bar{c}}{2V} \right)_i^2 + C_{X_o} \sum_i \left( \frac{q\bar{c}}{2V} \right)_i \right] &= 0 \\ \sum_i a_{X_i} + g \sum_i \sin \theta_i - \frac{QS}{m} \left( C_{X_\alpha} \sum_i \alpha_i + C_{X_q} \sum_i \left( \frac{q\bar{c}}{2V} \right)_i + n C_{X_o} \right) &= 0 \end{aligned} \right\} (23)$$

Each summation results in a number, so that there are three equations and the three unknown parameters  $C_{X_\alpha}$ ,  $C_{X_q}$ , and  $C_{X_o}$ . If there were more unknown parameters, there would be more equations. The equations are solved simultaneously to obtain the unknown parameters. Although the general approach used appears to be straightforward, there are a number of problems which can arise, as are now noted. Suppose that equations (23) were solved (by using Kramer's rule) for  $C_{X_\alpha}$ . The solution is given by

$$C_{X_\alpha} = \frac{\begin{vmatrix} \sum_i a_{X_i} \alpha_i + g \sum_i \alpha_i \sin \theta_i & \sum_i \alpha_i \left( \frac{q\bar{c}}{2V} \right)_i & \sum_i \alpha_i \\ \sum_i a_{X_i} \left( \frac{q\bar{c}}{2V} \right)_i + g \sum_i \left( \frac{q\bar{c}}{2V} \right)_i \sin \theta_i & \sum_i \left( \frac{q\bar{c}}{2V} \right)_i^2 & \sum_i \left( \frac{q\bar{c}}{2V} \right)_i \\ \sum_i a_{X_i} + g \sum_i \sin \theta_i & \sum_i \left( \frac{q\bar{c}}{2V} \right)_i & n \end{vmatrix}}{\begin{vmatrix} \sum_i \alpha_i^2 & \sum_i \alpha_i \left( \frac{q\bar{c}}{2V} \right)_i & \sum_i \alpha_i \\ \sum_i \alpha_i \left( \frac{q\bar{c}}{2V} \right)_i & \sum_i \left( \frac{q\bar{c}}{2V} \right)_i^2 & \sum_i \left( \frac{q\bar{c}}{2V} \right)_i \\ \sum_i \alpha_i & \sum_i \left( \frac{q\bar{c}}{2V} \right)_i & n \end{vmatrix}} \frac{QS}{m}$$

Some potential problem areas can now be indicated. Suppose that, for the flight record being studied,  $\left(\frac{q\bar{c}}{2V}\right)_i$  varied linearly with  $\alpha_i$ ; that is,

$$\left(\frac{q\bar{c}}{2V}\right)_i = k\alpha_i$$

By substituting  $k\alpha_i$  for  $\left(\frac{q\bar{c}}{2V}\right)_i$  in the denominator and by factoring out the constant  $k$  where possible, it can be shown that the first two columns in the denominator are identical. From the properties of determinants, the denominator becomes zero and the value of  $C_{X_\alpha}$  is absurdly large.

This problem is one of linear dependence; that is, two or more of the measured responses are linearly related. In this simple problem such a dependence probably can be seen by examination of the recorded data. In a practical situation, where many response quantities are being obtained, the problem shows up as an absurd solution, or no solution, because the determinant in the denominator (or its equivalent) is zero. If certain responses are suspected to be linearly dependent, it is sometimes possible to express one in terms of the other, and thereby reduce the number of unknowns and the number of simultaneous equations.

Take a look at another possible difficulty. Suppose that in a general case no measurable response occurs in one of the modes of motion following the application of a control input. Obviously an indeterminant situation again occurs. In working with flight data, it is best to examine the response records and to analyze those sections (time intervals) where there is motion in all of the variables of interest.

Other difficulties associated with analysis of data occur when using equations of the form given in equation (1). Several angular accelerations, which must be obtained from flight data, exist in the equations; however, these are generally not measured. These accelerations can be obtained by differentiation of angular-rate measurements; however, this increases inaccuracies in estimating derivatives. This problem can be overcome to some extent by numerically integrating the measured data. The procedure for this method is given in reference 13.

The example considered in this section is a very simple one where the concern has been with obtaining a good match between measured and computed accelerations. In dealing only with matching of accelerations, no coupling of the equations of motion exists; therefore, each equation can be treated by itself to determine the derivatives appearing in that equation. In practice it is often found that, when the aerodynamic derivatives are determined in such a manner, there may be poor matching between measured velocities and displacements and those computed by using the derivatives. Some techniques to improve the data fit are mentioned subsequently in conjunction with another method of



extraction of derivatives. Note that in applying the least-squares technique it was assumed that an equation was available relating all the measured state variables. The parameters were obtained by solving sets of algebraic equations.

Iteration techniques. - Various iteration techniques are being used for parameter identification. Detailed expositions of techniques, such as the modified Newton-Raphson technique of reference 14, are available in various publications. The principles of a typical iteration technique can be illustrated by reference to a simple example. Consider a spring-mass-dashpot system performing an oscillation. The equation of motion of the system is

$$\ddot{\chi} + \frac{c}{m} \dot{\chi} + \frac{k}{m} \chi = 0 \quad (24)$$

Suppose that the parameters  $\frac{c}{m}$  and  $\frac{k}{m}$  are unknown and that the displacement  $\chi$  can be measured at discrete intervals over a time period. The problem is to estimate the parameters  $\frac{c}{m}$  and  $\frac{k}{m}$  of the system, such that the differences between the measured displacement  $\chi_m$  and computed displacements  $\chi_c$ , using equation (24) and measured initial conditions, are minimized in the least-squares sense. The quantity to be minimized is the cost function

$$J = \sum_i (\chi_{m_i} - \chi_{c_i})^2 \quad (25)$$

The problem is to determine the parameters  $\frac{c}{m}$  and  $\frac{k}{m}$  that will minimize the cost function. The procedure is to roughly estimate or guess values of the parameters, compute displacements, form the cost function, and then use the cost function to determine incremental changes in the parameters to cause the cost function to be reduced. The development of the procedure starts by assuming that the displacement can be written in terms of a truncated Taylor series as follows:

$$\chi_c = \chi_{c_0} + \frac{\partial \chi_c}{\partial \left(\frac{c}{m}\right)} \Delta \left(\frac{c}{m}\right) + \frac{\partial \chi_c}{\partial \left(\frac{k}{m}\right)} \Delta \left(\frac{k}{m}\right) \quad (26)$$

The cost function then becomes

$$J = \sum_i \left\{ \chi_{m_i} - \left[ \chi_{c_0} + \frac{\partial \chi_c}{\partial \left(\frac{c}{m}\right)} \Delta \left(\frac{c}{m}\right) + \frac{\partial \chi_c}{\partial \left(\frac{k}{m}\right)} \Delta \left(\frac{k}{m}\right) \right]_i \right\}^2 \quad (27)$$

The cost function is minimized at this step by taking partial derivatives of equation (27) with respect to  $\Delta\left(\frac{c}{m}\right)$  and  $\Delta\left(\frac{k}{m}\right)$  and setting the partials equal to zero. The resulting equations are

$$\left. \begin{aligned} \sum_i \left[ \chi_m \frac{\partial \chi_c}{\partial \left(\frac{c}{m}\right)} - \chi_{c_0} \frac{\partial \chi_c}{\partial \left(\frac{c}{m}\right)} \right]_i &= \sum_i \left[ \frac{\partial \chi_c}{\partial \left(\frac{c}{m}\right)} \right]_i^2 \Delta\left(\frac{c}{m}\right) + \sum_i \left[ \frac{\partial \chi_c}{\partial \left(\frac{k}{m}\right)} \frac{\partial \chi_c}{\partial \left(\frac{c}{m}\right)} \right]_i \Delta\left(\frac{k}{m}\right) \\ \sum_i \left[ \chi_m \frac{\partial \chi_c}{\partial \left(\frac{k}{m}\right)} - \chi_{c_0} \frac{\partial \chi_c}{\partial \left(\frac{k}{m}\right)} \right]_i &= \sum_i \left[ \frac{\partial \chi_c}{\partial \left(\frac{c}{m}\right)} \frac{\partial \chi_c}{\partial \left(\frac{k}{m}\right)} \right]_i \Delta\left(\frac{c}{m}\right) + \sum_i \left[ \frac{\partial \chi_c}{\partial \left(\frac{k}{m}\right)} \right]_i^2 \Delta\left(\frac{k}{m}\right) \end{aligned} \right\} \quad (28)$$

Equations (28) can, in principle, be solved simultaneously to determine the conditions  $\Delta\left(\frac{c}{m}\right)$  and  $\Delta\left(\frac{k}{m}\right)$  to minimize the cost function. However, it is first necessary to evaluate the partial derivatives appearing in equations (28). The partial derivatives are generally referred to as sensitivity coefficients.

The sensitivity coefficients are obtained by use of equation (24). Taking partial derivatives with respect to  $\left(\frac{c}{m}\right)$  and  $\left(\frac{k}{m}\right)$  results in

$$\left. \begin{aligned} \frac{\partial \ddot{\chi}}{\partial \left(\frac{c}{m}\right)} + \frac{c}{m} \frac{\partial \dot{\chi}}{\partial \left(\frac{c}{m}\right)} + \dot{\chi} + \frac{k}{m} \frac{\partial \chi}{\partial \left(\frac{c}{m}\right)} &= 0 \\ \frac{\partial \ddot{\chi}}{\partial \left(\frac{k}{m}\right)} + \frac{c}{m} \frac{\partial \dot{\chi}}{\partial \left(\frac{k}{m}\right)} + \chi + \frac{k}{m} \frac{\partial \chi}{\partial \left(\frac{k}{m}\right)} &= 0 \end{aligned} \right\} \quad (29)$$

Since  $\left(\frac{c}{m}\right)$  and  $\left(\frac{k}{m}\right)$  are independent of time, the order of differentiation can be changed in equations (29) to obtain

$$\frac{d^2}{dt^2} \left[ \frac{\partial \chi}{\partial \left(\frac{c}{m}\right)} \right] + \frac{c}{m} \frac{d}{dt} \left[ \frac{\partial \chi}{\partial \left(\frac{c}{m}\right)} \right] + \frac{k}{m} \left[ \frac{\partial \chi}{\partial \left(\frac{c}{m}\right)} \right] = -\dot{\chi} \quad (30)$$

$$\frac{d^2}{dt^2} \left[ \frac{\partial \chi}{\partial \left( \frac{k}{m} \right)} \right] + \frac{c}{m} \frac{d}{dt} \left[ \frac{\partial \chi}{\partial \left( \frac{k}{m} \right)} \right] + \frac{k}{m} \left[ \frac{\partial \chi}{\partial \left( \frac{k}{m} \right)} \right] = -\chi \quad (31)$$

Equations (30) and (31) are second order linear differential equations and can be solved numerically to obtain the sensitivity coefficients as function of time. In these equations,  $\dot{\chi}$  and  $\chi$ , which act as forcing functions, are values obtained from integrating equation (24) with the first estimates of  $\left( \frac{c}{m} \right)$  and  $\left( \frac{k}{m} \right)$ . Also note that the initial values (at  $t = 0$ ) of  $\frac{d}{dt} \left[ \frac{\partial \chi}{\partial \left( \frac{c}{m} \right)} \right]$ ,  $\frac{d}{dt} \left[ \frac{\partial \chi}{\partial \left( \frac{k}{m} \right)} \right]$ ,  $\frac{\partial \chi}{\partial \left( \frac{c}{m} \right)}$ , and  $\frac{\partial \chi}{\partial \left( \frac{k}{m} \right)}$  to be used in solving equations (30) and (31) are equal to zero.

The sensitivity coefficients, which are functions of time, are used in equations (28), which can then be solved simultaneously to obtain  $\Delta \left( \frac{c}{m} \right)$  and  $\Delta \left( \frac{k}{m} \right)$ .

The updated parameters are then simply

$$\left. \begin{aligned} \left( \frac{c}{m} \right) &= \left( \frac{c}{m} \right)_0 + \Delta \left( \frac{c}{m} \right) \\ \left( \frac{k}{m} \right) &= \left( \frac{k}{m} \right)_0 + \Delta \left( \frac{k}{m} \right) \end{aligned} \right\} \quad (32)$$

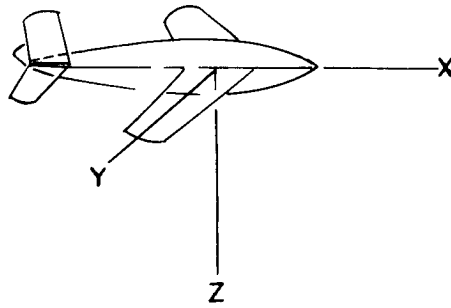
The revised parameters are used with equation (24) to evaluate  $\chi_c$  for comparison with  $\chi_m$ , and if necessary the iteration process is repeated.

It should be emphasized that the discussion presented here on iteration techniques is a very simple introduction to the subject. The process becomes quite complicated if there are several degrees of freedom and numerous parameters are to be extracted.

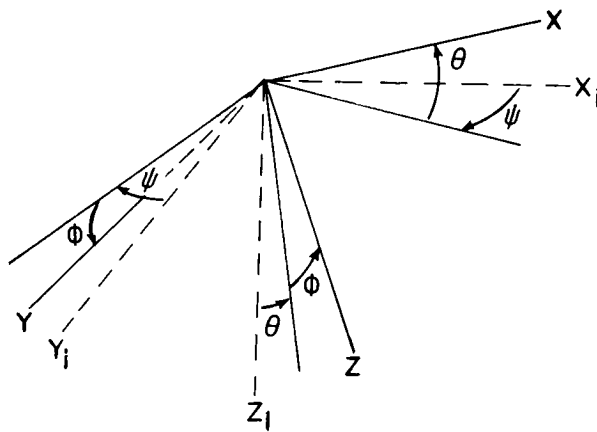
## REFERENCES

1. Anon.: Fundamentals of Design of Piloted Aircraft Flight Control Systems. Vol. II - Dynamics of the Airframe. Rep. AE-61-4, Bur. Aero., Feb. 1953.
2. MacLachlan, Robert; and Letko, William: Correlation of Two Experimental Methods of Determining the Rolling Characteristics of Unswept Wings. NACA TN 1309, 1947.
3. Bird, John D.; Jaquet, Byron M.; and Cowan, John W.: Effect of Fuselage and Tail Surfaces on Low-Speed Yawing Characteristics of a Swept-Wing Model as Determined in Curved-Flow Test Section of Langley Stability Tunnel. NACA TN 2483, 1951. (Supersedes NACA RM L8G13.)
4. Bird, John D.; Fisher, Lewis R.; and Hubbard, Sadie M.: Some Effects of Frequency on the Contribution of a Vertical Tail to the Free Aerodynamic Damping of a Model Oscillating in Yaw. NACA Rep. 1130, 1953. (Supersedes NACA TN 2657.)
5. Riley, Donald R.; Bird, John D.; and Fisher, Lewis R.: Experimental Determination of the Aerodynamic Derivatives Arising From Acceleration in Sideslip for a Triangular, a Swept, and an Unswept Wing. NACA RM L55A07, 1955.
6. Queijo, M. J.; Fletcher, Herman S.; Marple, C. G.; and Hughes, F. M.: Preliminary Measurements of the Aerodynamic Yawing Derivatives of a Triangular, a Swept, and an Unswept Wing Performing Pure Yawing Oscillations, With a Description of the Instrumentation Employed. NACA RM L55L14, 1956.
7. Campbell, John P.; and McKinney, Marion O.: Summary of Methods for Calculating Dynamic Lateral Stability and Response and for Estimating Lateral Stability Derivatives. NACA Rep 1098, 1952. (Supersedes NACA TN 2409.)
8. McDonnell Douglas Corp.: USAF Stability and Control Datcom. Air Force Flight Dyn. Lab., U.S. Air Force, Oct. 1960. (Revised Aug. 1968.)
9. Diederich, Franklin W.: Charts and Tables for Use in Calculations of Downwash of Wings of Arbitrary Plan Form. NACA TN 2353, 1951.
10. Queijo, M. J.: Theory for Computing Span Loads and Stability Derivatives Due to Sideslip, Yawing, and Rolling for Wings in Subsonic Compressible Flow. NASA TN D-4929, 1968.
11. Rampy, John M.; and Berry, Donald T.: Determination of Stability Derivatives From Flight Test Data by Means of High Speed Repetitive Operation Analog Matching. FTC-TDR-64-8, U.S. Air Force, May 1964. (Available from DDC as AD 440 785.)

12. Donegan, James J.; and Pearson, Henry A.: Matrix Method of Determining the Longitudinal-Stability Coefficients and Frequency Response of an Aircraft From Transient Flight Data. NACA Rep. 1070, 1952. (Supersedes NACA TN 2370.)
13. Donegan, James J.: Matrix Methods for Determining the Longitudinal-Stability Derivatives of an Airplane From Transient Flight Data. NACA Rep. 1169, 1954. (Supersedes NACA TN 2902.)
14. Taylor, Lawrence W., Jr.; and Iliff, Kenneth W.: A Modified Newton-Raphson Method for Determining Stability Derivatives From Flight Data. Paper presented at 2nd International Conference on Computing Methods in Optimization Problems (Sanremo, Italy), Sept. 1968.



(a) Aircraft body axes.



(b) Orientation of body axes in space.

Figure 1.- Axes systems.

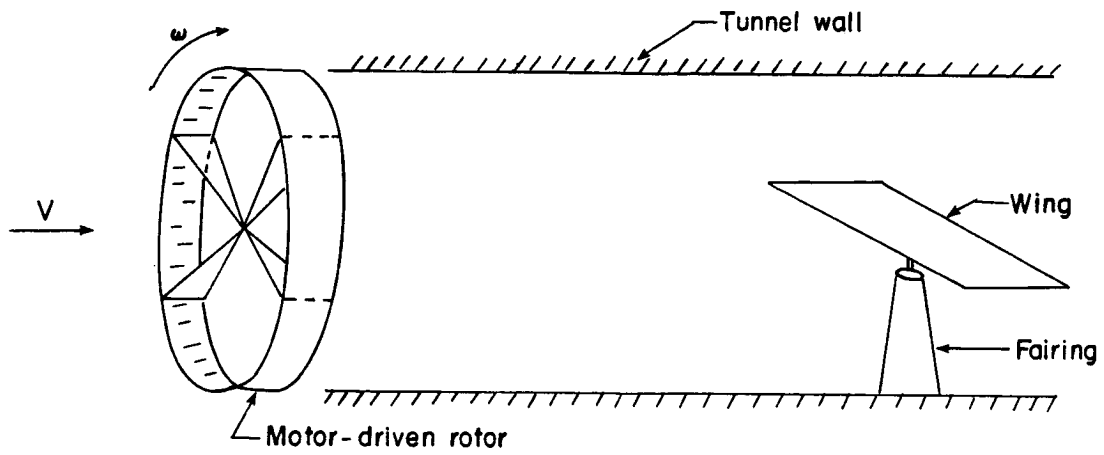


Figure 2.- Method of simulating rolling flow.

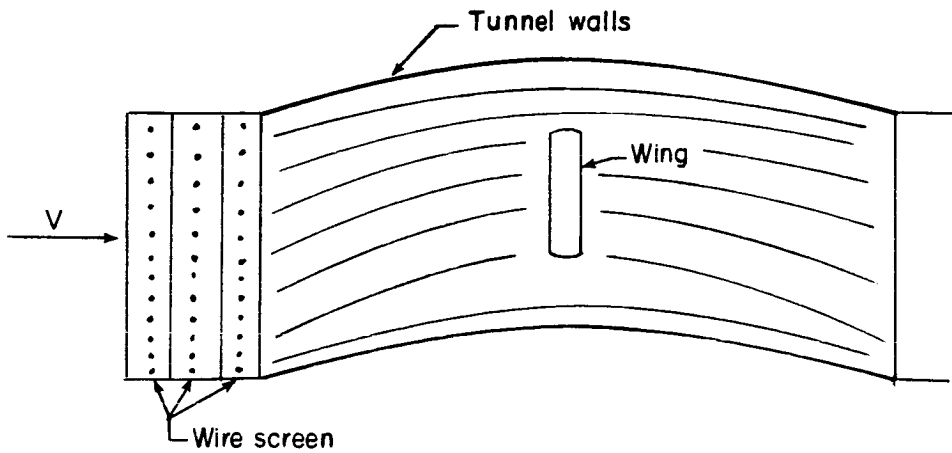


Figure 3.- Method of simulating yawing flow.

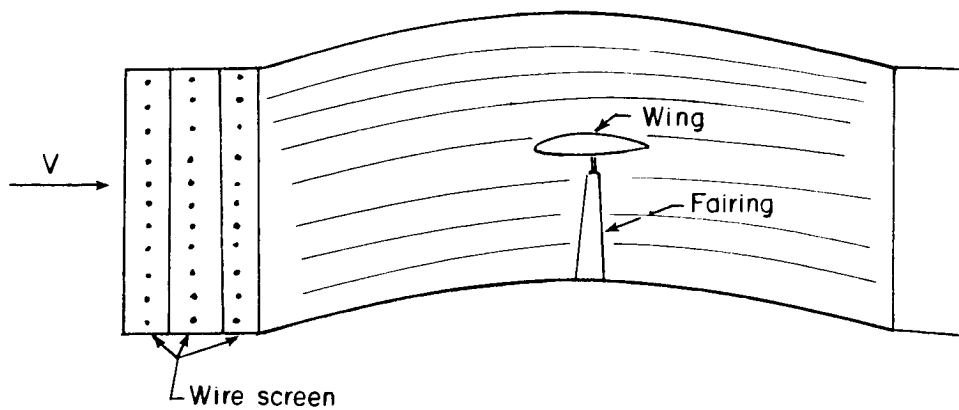
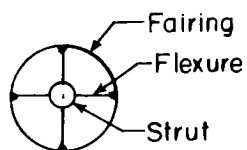


Figure 4.- Method of simulating pitching flow.



Section A-A

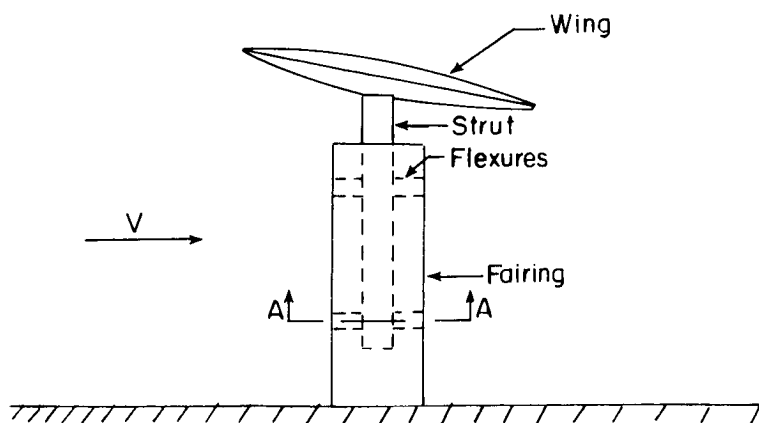
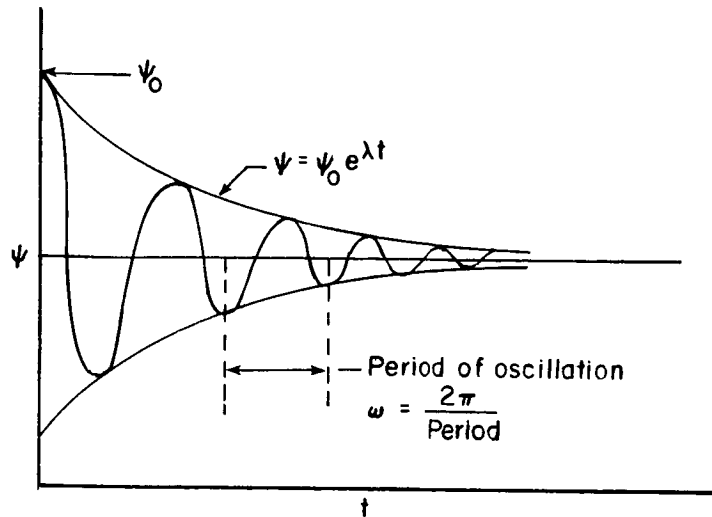


Figure 5.- Wing mounted for free-oscillation test.





$$C_{n_r} - C_{n_{\dot{\beta}}} = \frac{-2.772 I_Z V}{Q S b^2 t_{1/2}}$$

$$C_{n_{\beta}} + \left(\frac{\omega b}{2V}\right)^2 C_{n_{\dot{\beta}}} = \frac{1}{Q S b} \left[ (2\pi f)^2 I_Z + M \psi \right]$$

Figure 6.- Extraction of derivatives from single-degree-of-freedom oscillation tests.

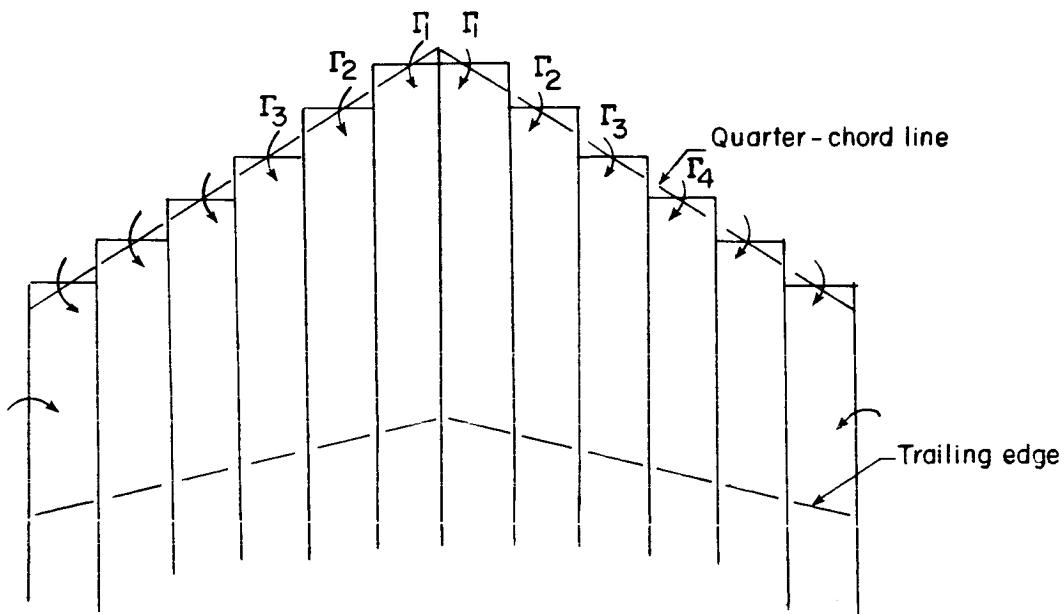


Figure 7.- Vortex distribution for representing a wing.

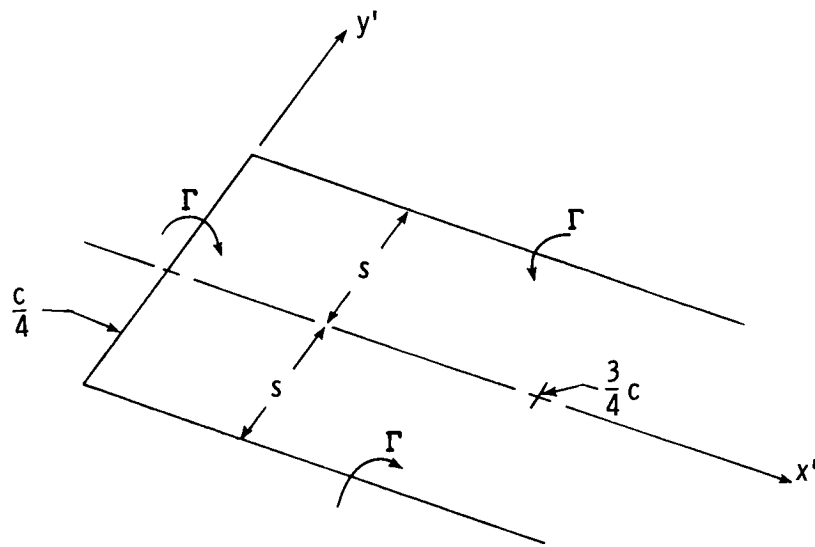


Figure 8.- Horseshoe vortex.

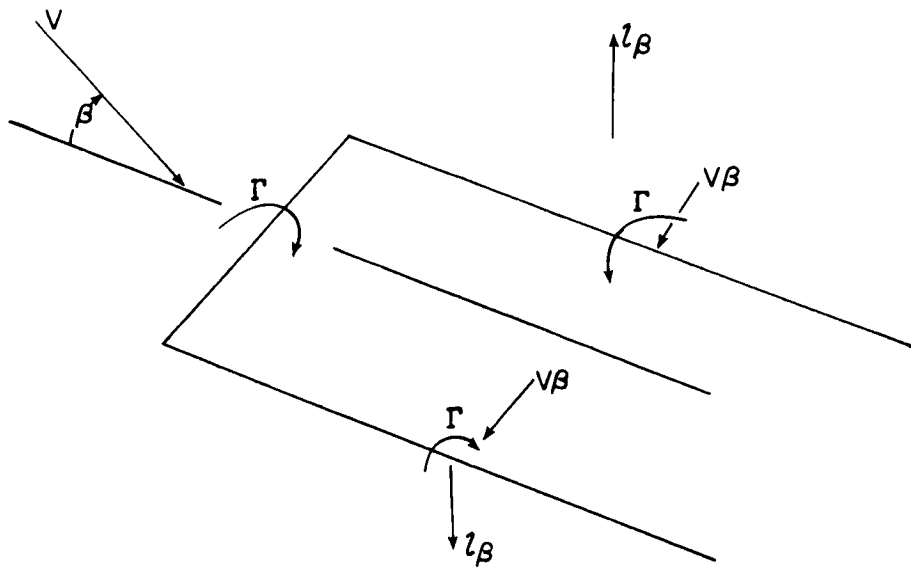


Figure 9.- Interaction of lateral-velocity component with angle-of-attack circulation.

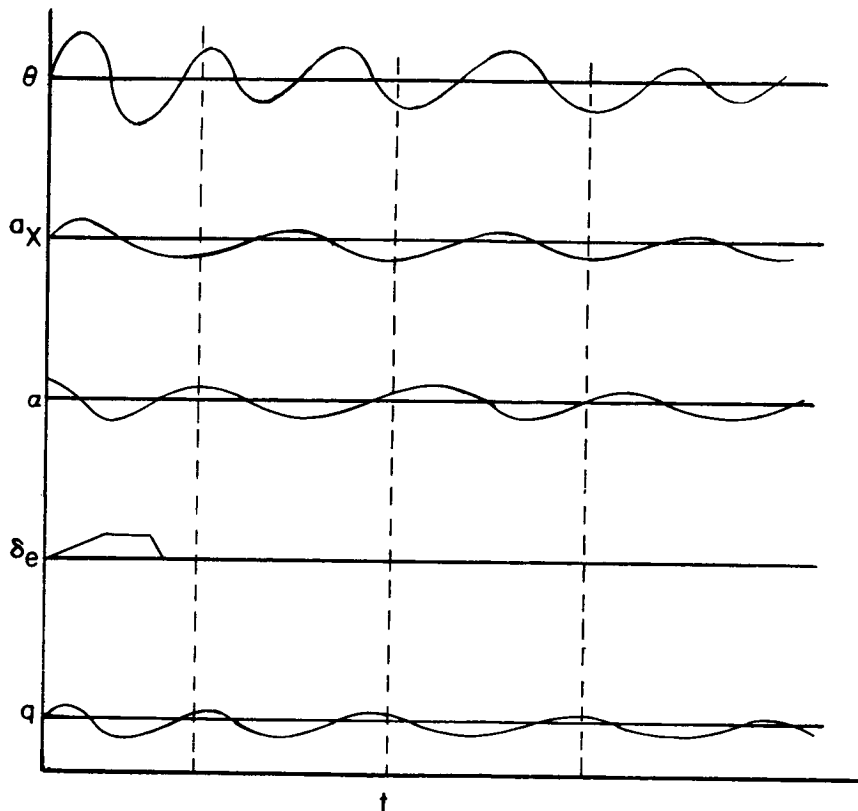


Figure 10.- Illustration of quantities measured in flight tests.

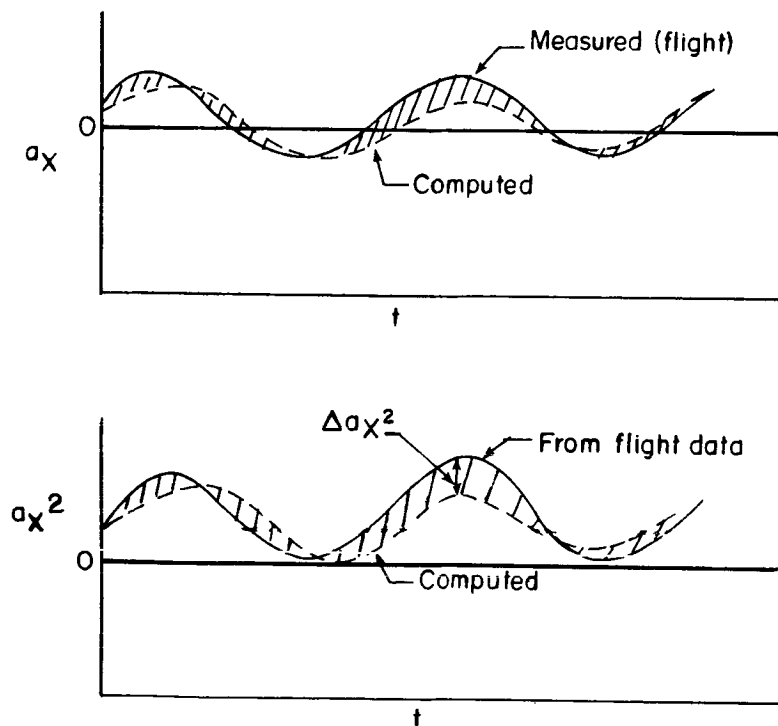


Figure 11.- Illustration of differences between measured and computed response.

### 3. DESIGN OF BODIES FOR LOW DRAG AND HIGH PERFORMANCE IN PRACTICAL HYPERSONIC FLIGHT\*

By E. S. Love  
Langley Research Center

#### ABSTRACT

Some topics related to body shaping for minimum drag and improved performance at hypersonic speed are presented. Implications of the most frequently assumed pressure laws are reviewed from the view of practical flight regimes, and solutions expressed in exponential residuals are presented for inviscid minimum-drag power-law bodies (simple and complex) for a wide range of fineness ratio. Analytical results and comparisons with experiment are given for constraints of length-and-diameter and length-and-volume. Experimental results from Mach numbers of 6 to 20 are presented for a series of trapezoidal bodies; the cross section of the body giving best lift-drag ratio differs from that indicated in earlier work. A simple " $\sin^2$ -deficiency method" is presented for predicting pressures on blunt shapes; the method appears to yield results comparable to more elaborate methods requiring machine computation.

#### INTRODUCTION

The history and breadth of our subject necessitates some bounds on the discussion. The topics and approach outlined in figure 1 have therefore been chosen.\*\* In recent years increased interest in advanced reusable concepts of transportation systems to and from earth orbit has been a major factor in the revival of studies in hypersonic body shaping. For many of these concepts, bodies of moderate to large fineness ratio appear to offer system compatibility advantages. This feature also suggests the possibility for significant hypersonic performance. Accordingly, gains in performance that might be achieved through body shaping without overly penalizing the total system and mission goals are receiving attention. This in turn has led to a critical examination of methods for minimizing drag and increasing performance and a reassessment of the validity and practical value of past solutions for optimum shapes.

---

\*A portion of this material was presented at the AIAA 7th Aerospace Sciences Meeting, New York, N.Y., Jan. 20-22, 1969, in a paper by E. S. Love, W. C. Woods, R. W. Rainey, and G. C. Ashby, Jr.

\*\*To expedite publication, figures prepared for the original lectures have been used herein. This accounts for repetition between the content of some figures and the text.

The mid-1950's saw notable original contributions and improvements in earlier minimum-drag solutions and optimization theory, such as the work of Eggers, Resnikoff, and Dennis (ref. 1, referred to hereinafter as the ERD solution), Hayes and Probstein (ref. 2), Cole (ref. 3), and Gonor and Chernyi (ref. 4). More recently additional analyses and refinements have been presented (e.g., refs. 5 to 10). With no less appreciation for the considerable contribution that these and other studies represent, observe that for practical application the shapes concluded to be optimum in much of this work rest on insecure ground, primarily because of the pressure laws employed. It is commonly accepted that some comparisons of experimental pressure distributions with the assumed pressure law do not show the satisfactory agreement claimed, for example, as concluded in reference 5 from comparison of Gonor's data (for a free-stream Mach number of 4 and a ratio of specific heats of 7/5) with the Newton-Busemann law. Concerns for similar questionable and/or fortuitous confirmations were frequently voiced in the late 1950's. At that time work focusing on these points was underway, but with the advent of the "space age" this effort was deemphasized. The purpose of this paper is to document a few results of this effort of a decade ago not heretofore published and to present some selected results of recent and current hypersonic research conducted in related fields.

## SYMBOLS

$$a = \frac{2}{5} + \frac{1}{20} \left( \frac{x}{l} \right)^2$$

A            local cross-sectional area of body

$$b = \frac{10}{33} + \frac{13}{8} F^{-4/5}$$

$\bar{C}_L$             ratio of lift coefficient at  $(L/D)_{\max}$  for given  $N$  to that for  $N = 8$  with positive camber

$\frac{C_{D_{\min}}}{C_{D,C_{\min}}}$             ratio of minimum-drag coefficient of body to that of pointed cone

$\left. \begin{array}{l} (C_{D,l^2})_{\min} \\ (C_{D,P})_{\min} \\ (C_{D,B})_{\min} \end{array} \right\}$             minimum-drag coefficient based on length squared, planform area, and base area, respectively

$C_p$  pressure coefficient,  $\frac{2(p - p_\infty)}{\gamma p_\infty M_\infty^2}$

$\overline{C_p}$  ratio of local pressure coefficient to pressure coefficient at stagnation point

$d$  base diameter (equals maximum diameter)

$F$  fineness ratio,  $l/d$

$$f = F(1 + F^2)^{-1/2}$$

$$g = 1 \text{ or } 1 + \frac{7}{9}f^3 \quad (\text{see text})$$

$$k = \frac{96}{5}(F^{20/61} + 85)^{-1/2}$$

$l$  body length

$(L/D)_{\max}$  maximum lift-drag ratio

$(\overline{L/D})_{\max}$  ratio of  $(L/D)_{\max}$  for given  $N$  to that for  $N = 8$  with positive camber

$$m = 1 + \frac{9}{44}F^k$$

$M_\infty$  free-stream Mach number

$n$  exponent in shape equation for power-law bodies,  $\frac{r}{R} = \left(\frac{x}{l}\right)^n$

$n_1, n_2, n_3, \dots$  optimum values of  $n$  for specified constraints

$N = \pi \left( \frac{\text{Span}}{\text{Height}} \right)$ , for trapezoidal family

$p, p_s, p_\infty$  local, stagnation-point, and free-stream pressures, respectively

$\bar{p}, \bar{p}_*, \bar{p}_{FD}$  ratio of local pressure to pressure at stagnation point, value of this ratio at sonic point, and values on flat disk, respectively

$$q = \frac{3}{4} + \frac{1}{4} \tan \left( \frac{\pi}{2} \frac{x}{l} \right)$$

$R$  base radius (equals maximum radius)

$Re_{\infty, l}, Re_{\infty, d}$  Reynolds numbers based on free-stream conditions and length and diameter, respectively

$r, x$  coordinates of point on meridian curve of body (origin of coordinate system coincides with nose of body, and  $x$ -axis coincides with axis of symmetry)

$r_{45}, x_{45}$  radius of body at point where  $\delta = 45^\circ$  and axial length of conical tip with  $45^\circ$  half-angle, respectively

$S, S_*$  distance measured along body surface from stagnation point, and value to sonic point, respectively

$V$  volume of body

$\alpha$  angle of attack

$\gamma$  ratio of specific heats

$\delta_c$  half-angle of cone

$\delta, \delta_*, \delta_{*0}$  inclination of body surface with respect to free stream, value at sonic point, and value at sonic point for  $M_\infty = \infty$ , respectively

$\Delta x_1, \Delta x_2$  axial distance between points 1 or 2 and point for which  $\delta = 0^\circ$ , all on same streamline (or on conformal extension thereto if  $\delta > 0^\circ$  at base)

$\epsilon, \epsilon_0$  nose radius and maximum nose radius, respectively, of spherically blunted cone for given  $\delta_c$ , radius being tangent to cone surface (see fig. 35)

$$\lambda = 4 \left[ \ln \left( \frac{S_*}{S} \right) \right]^{1/2}$$

$\phi$  constant in  $\sin^2$  pressure law

Subscripts:

eff effective

geom geometric

max maximum

## DISCUSSION

### Bodies of Revolution

Body types. - The bodies to be considered are limited to smoothly contoured convex types with maximum diameter at the base, unless otherwise noted. Bodies referred to as power-law types conform to

$$\frac{r}{R} = \left(\frac{x}{l}\right)^n \quad (1)$$

Figure 2 illustrates the body shapes and basic parameters. The practical significance of accurately defining the optimum value of  $n$  is demonstrated in figure 3. The ability to package equipment internally so as to move the center of gravity forward directs interest toward the lower values of  $n$ ; for large vehicles the difference in shape between  $n = 2/3$  and  $3/4$  suggests more than academic motivation for resolution of debates over optimum  $n$ . Minimum-drag examinations are limited to two isoperimetric constraint pairs: length-and-diameter and length-and-volume. Shapes dependent upon the existence of free layers are excluded. Here reference is to Newtonian free layers of inviscid flow concepts. As depicted by the sketches in figure 4, the Newtonian free layer is a Newtonian shock layer the position of which is determined, not by the geometry of the body, but by the fact that the pressure must be zero beneath the layer (see right-hand sketch).

Pressure laws. - With rare exception, optimization analyses to determine minimum-drag bodies at hypersonic speeds have employed either of two Newton-type inviscid pressure laws (or approximation thereto), a brief review of which follows. One of these laws may be expressed as

$$C_p = 2 \sin^2 \delta + 2 \sin \delta \frac{d\delta}{dA} \int_0^A \cos \delta dA \quad (2)$$



where the second term accounts for centrifugal effects. In effect, it states that the pressure coefficient is determined not only by the slope of the surface but also by the upstream shape. This law is variously referred to as the complete Newton, limiting Newton, corrected Newton, or Newton-Busemann and has been much publicized in optimization studies of recent years. Solutions based upon it are prominently described in the literature as the "correct solutions," the inference being at the expense of analyses based upon the Newton law that omits centrifugal effects. In the context of exactness at  $M_\infty = \infty$ , low  $\gamma$ , and application to bodies not restricted to small curvature, the "correct" claim poses little difficulty as illustrated at the right in figure 5. However, for larger values of  $\gamma$  at  $M_\infty = \infty$  (at the left in fig. 5) and particularly when the usual evaluations of hypersonic pressure-prediction methods are applied, such as for  $1 \ll M_\infty \ll \infty$  and values of  $\gamma$  likely to occur in practical flight regimes (typical examples shown in fig. 6), the pressure distributions predicted by the Newton-Busemann law are found to be grossly inadequate.\* Accordingly, use of this law in deriving optimum shapes can be expected a priori to provide only limiting solutions, albeit a possibility that some fortuitous combination of factors not anticipated in the choice of the law could, in the light of examination of the results, suggest broader application.

Recognition of this situation has led many investigators to abandon the Newton-Busemann law for one more adequate for predicting pressures on smoothly contoured bodies under conditions of practical hypersonic flight, for example, as in the ERD solutions (ref. 1). Almost invariably the choice has been the simple Newton or impact pressure law

$$C_p = 2 \sin^2 \delta \quad (3)$$

From the preceding discussion, it is perhaps obvious that this law has often been chosen, not because the conditions needed for it to be applicable via Newton concepts (see ref. 11) are more closely realized, but because of the considerable empirical evidence that it offers better pressure predictions for the bodies and flow conditions of interest than given by the Newton-Busemann law. Thus, viewed only from the degree of Newton compliance, the general success of equation (3) must be regarded as fortuitous and empirically justified. But there must be reason for this success, restricted though it may be. In pursuit

---

\*This long-recognized deficiency is no reflection upon the validity of Busemann's conclusion (ref. 11) that centrifugal effects should be included whenever (1) the body curvature is not small, and (2) the necessary conditions prevail that otherwise admit the use of Newtonian concepts. The confusion continues because conclusions derived through use of the Newton-Busemann law continue to be suggested for regimes in which this law is inappropriate by either analytical or empirical evaluation and for which Busemann never advocated its use.

of this, and following a brief examination of the merits of a generalized form of the Newton law (ref. 12), the flow fields and pressure distributions for a number of smoothly contoured bodies of revolution with attached shock and with maximum diameter at the base were obtained through the method of characteristics (including rotational effects). The scope of the parametric coverage of these calculations is shown in figure 7 along with amplifying details of the flow field. Examination of the pressures in the flow fields indicated that for  $M_\infty/F \gtrsim 2$  and bodies having constant radius of curvature, the ratio of the values of  $C_p$  for any two points on the same streamline, say 1 and 2, converges closely toward  $(\Delta x_1/\Delta x_2)^2$  as the observer proceeds from the field streamlines toward the body surface. This observation held up to the maximum nose angles of the study (near that for sonic flow on the body surface in close vicinity of the tip). Some minor exceptions occurred at the lower values of  $\gamma$ , and significant exceptions occurred when  $\delta$  closely approached zero. Provided these limitations are recognized,

$$C_{p2}/C_{p1} = (\Delta x_2/\Delta x_1)^2 \quad (4)$$

may generally be applied, and by noting that for bodies of constant curvature

$$(\Delta x_2/\Delta x_1)^2 = \sin^2 \delta_2 / \sin^2 \delta_1 \quad (5)$$

it may be concluded that\*

$$C_{p2}/C_{p1} = \sin^2 \delta_2 / \sin^2 \delta_1 \quad (6)$$

For the bodies having varying radius of curvature (increasing from nose to base) the relation given by equation (4) was generally evident over the forward portion of the body and, in fact, over most of the body; however, over the rearmost portion significant departure frequently occurred and was greatest when high curvature was concentrated near the nose. This observation is similar to that reported by Stocker (ref. 13) for shock-expansion theory in his analysis of two-dimensional hypersonic flows.

While this examination by the method of characteristics was somewhat pedestrian, it shows that without any resort to Newton principles, exact solutions indicate that for certain classes of bodies and flow conditions a pressure law of the form of equation (6) should give reasonable prediction of pressure distributions if an exact value of

---

\*This conclusion may be reached directly via shock-expansion, tangent-wedge, or tangent-cone approximations, but the reasons for the success of these approximations hinge upon a similar examination; for example, see reference 2.

$C_{p1}/\sin^2 \delta_1$  is employed. Evidence of this is shown in reference 12. Thus if equation (6) is expressed as simply

$$C_p = \varphi \sin^2 \delta \quad (7)$$

referred to hereafter as the  $\sin^2$  law, with the constant  $\varphi$  determined exactly and in accordance with application, then by analogy the success of the Newton law, equation (3), is not always fortuitous. The point to be emphasized is that if optimization conclusions are derived through proper use of the  $\sin^2$  law plus a subsequent examination to insure that the derived shape still conforms to reasonable use of this law, then fair confidence is assured in the conclusions as approximate guides for practical use. On the other hand, these observations offer no explanation for the success of the  $\sin^2$  law on the forward portion of certain blunt bodies,\* except in the sense that the shock shape may be similar to the body shape. Pressure prediction in this region is examined in more detail subsequently herein.

Certain optimization analyses employing variational methods, such as the ERD solutions (ref. 1), are based upon the Newton law. While such results in terms of drag are affected by the constant 2, this constant need not appear in the integral to be minimized. (See fig. 8.) Accordingly, the shape of the body concluded to be optimum is, in terms of the  $\sin^2$  law, unaffected by the value of  $\varphi$  so long as it is assumed to be the same for the entire body family. In some respects, this feature lends more weight to the ERD solutions and others. On the other hand, different values of  $\varphi$  in a given body family, or for a given shape, may be chosen to improve the accuracy of the results. This modification is of interest if the body family includes pointed and blunted bodies, and if both small and large fineness ratio are treated. Finally, for bodies of varying radius of curvature, such as most power-law bodies, the value of  $\varphi$  must be continually changing. This is the major factor casting suspicion upon solutions derived through use of the  $\sin^2$  law with  $\varphi$  constant.

With regard to modification of the synoptic pressure laws, it may be possible to weight the centrifugal term in equation (2), but this has not been explored herein.

Description of exponential residual solutions. - The following discussion presupposes some familiarity with exponential residual mathematical procedures. Figure 9 briefly summarizes the purpose and utility of residual procedures and notes three of the more prominent. The method of averages generally develops values for the constants in a series expression, but different values of the constants are possible. The method of

---

\*The reader is also referred to the work of J. C. South, Jr. (see, e.g., AIAA J., Feb. 1969, pp. 369-371). South calls attention to the importance of the nose region and the inadequacy of the similarity solutions in this region.

least squares has wide utility and the advantage of giving a unique set of values to the constants; it is assumed that the residuals follow a Gaussian law of error. The exponential residual solutions admit different values of constants; they are attractive for relations that must handle extensive plateaus in the dependent variable and have come into prominent use with the advent of versatile computers. The chosen equation is always of exponential form. These factors, combined with the power-law form of the bodies being considered, and other objectives described subsequently and summarized in figure 10, led to the choice of exponential residuals to express the results of the analytical studies discussed next.

In the late 1950's the author obtained (for  $\gamma = 7/5$ ) several minimum-drag solutions restricted to simple and complex power-law bodies, complex denoting that the power is a function of  $x$  as well as  $F$ . This restriction was deliberate so as to obtain a smooth transition from the blunt nose to the flanks of the body, in contrast to the sharp corner that occurs at the flat nose of the shapes given by the variational solutions — a prominent feature at small  $F$  and undesirable for practical application. These solutions covered a broad range of  $F$ , and the results were transformed to power expressions by use of exponential residuals in which the value of the simple or complex power in the optimum shape is explicit in  $F$ . This had the additional advantage of affording direct comparisons between complex power-law shapes resembling the ERD shapes (at moderate to large  $F$ ) and simple power-law shapes. These exponential residual solutions were never published in the open literature, and are presented here and compared with earlier and more recent work. Convergence of the exponential residual expressions was examined for  $0.1 < F < 100$  and was found satisfactory, as was the case of  $F \rightarrow \infty$ . Details of the calculations are omitted except as they depart noticeably from earlier work.

The exponential residual solutions for the length-and-diameter constraint were confined to simple power-law bodies. The two solutions,  $n_1$  and  $n_2$ , for the value of  $n$  in equation (1) that give minimum drag are

$$n_1 = \frac{3}{4}f \quad (8)$$

$$n_2 = \frac{3}{4}f^m \quad (9)$$

The solution  $n_1$  employed the  $\sin^2$  pressure law at large  $F$  with the value of  $\varphi$  taken as  $2(\gamma + 1)(\gamma + 7)/(\gamma + 3)^2$ , following the hypersonic approximation of Lees for sharp cones (ref. 14). At small  $F$ , the deficiency of the  $\sin^2$  law increases as the nose region bounded by the sonic circle becomes flatter (as for power-law bodies with low  $n$ ). In

this regime the approximation of Probstein (ref. 15) for the pressure distribution on a flat disk close to the stagnation point

$$\frac{C_p}{C_{p_s}} = 1 - \frac{16}{9\pi^2} \left( \frac{S}{S_*} \right)^2 \quad (10)$$

was employed ahead of the point for which it gave lower values of  $C_p$  than the  $\sin^2$  law with  $\varphi = C_{p_s} = (\gamma + 3)/(\gamma + 1)$ , this value of  $\varphi$  following the approximation of Lees (ref. 14) for the stagnation point of blunt bodies.\* The value of  $S_*$  was approximated by the  $\sin^2$  law, as were the pressures over the remaining portion of the body.

In the preceding manner, the solution  $n_1$  employed values of  $C_p$  at the nose that closely approximated the exact values, both for bodies with large bluntness and bodies that were essentially sharp. In the intermediate range of  $F$ , the point of transition from one value of  $\varphi$  to the other was roughly approximated by assuming that induced pressures from blunting became insignificant beyond a point on the body 40 nose radii downstream of the sonic point, the nose radius being taken as the body radius at the sonic point. This limit of 40 radii was chosen after evaluating the decay of induced pressures at  $M_\infty \gtrsim 20$  by an approximation (ref. 17) for spherical blunting based upon blast-wave pressure decay laws.\*\* Thus, for certain combinations of  $n$  and  $F$ , the solution  $n_1$  involves pressure distributions with discontinuities, but the variation of drag with  $F$  or  $n$  is orderly. These discontinuities in pressure distribution are clearly in no way related to the discontinuities in pressure distribution that occur on bodies derived via free-layer concepts and the Newton-Busemann pressure law.

The solution  $n_2$  used the same approach as the solution  $n_1$ , except that at large  $F$  the prediction of the pressure decay over the body employed the unmodified shock-expansion method of Eggers, Savin, and Syvertson (ref. 19). In applying this method, the small, blunt tip of the body was replaced with a conical tip tangent at the point where  $\delta = 45^\circ$ .

Figure 12 summarizes the calculations for the length-and-diameter constraint and simple power-law bodies.

---

\*This blunt-nose modification for  $\varphi$  may have been recognized prior to 1945. A 1945 document (ref. 16, p. 10), hints of this, and a recent survey by the author of related documents of that period appears to confirm this. Lee's result, however, was derived independently.

\*\*An evaluation of this approximation appearing in literature subject to dissemination controls (brought to the author's attention via ref. 18) is misleading since the approximation was applied to shapes for which it was not proposed, and incorrect shoulder pressure ratios were employed in some examples. Properly used, the approximation gives a reasonable prediction as illustrated in figure 11.

The solutions for the length-and-volume constraint were also confined to power-law bodies defined by equation (1). For this constraint, however, the value of  $n$  is complex (as defined previously). The solutions obtained were

$$n_3 = \frac{3}{4} f^{mg} \left(1 - \frac{x}{l}\right)^a \quad (11)$$

$$n_4 = \frac{3}{4} \left( \frac{2F^b}{1 + 2F^b} \right)^g \left(1 - \frac{x}{l}\right)^a \quad (12)$$

and three pseudo-slender-body forms of equations (11) and (12), including a trigonometric transformation, that apply from  $5 \lesssim F \lesssim 100$ ; that is,

$$n_5 \approx \frac{2}{3} \left(1 - \frac{x}{l}\right)^a \quad (g = 1) \quad (13)$$

$$n_6 \approx \frac{14}{23} \left(1 - \frac{x}{l}\right)^a \quad \left(g = 1 + \frac{7}{9} f^3\right) \quad (14)$$

$$\frac{r}{R} \approx \sin^q \left( \frac{\pi x}{2l} \right) \quad (g = 1) \quad (15)$$

where

$$q = \frac{3}{4} + \frac{1}{4} \tan \left( \frac{\pi}{2} \frac{x}{l} \right)$$

The solution  $n_3$  employed planform area in the drag coefficient. With  $g = 1$ , the solution  $n_3$  used the  $\sin^2$  pressure law throughout. With  $g = 1 + \frac{7}{9} f^3$ , the solution  $n_3$  combined the  $\sin^2$  law at small  $F$  with the second-order shock-expansion method (ref. 20) at large  $F$ , with intermediate  $F$  handled as described earlier. With regard to shock-expansion predictions, the unmodified method assumes that two-dimensional techniques apply to a three-dimensional field. Thus, the continuity law is only roughly approximated. With the second-order or modified shock-expansion method, a correction is applied to the stream tube to satisfy the continuity relation. The typical improvement given by the second-order method is demonstrated in figure 13.

The solution  $n_4$  employed  $l^2$  as the reference area in the drag coefficient. With  $g = 1$ , the solution  $n_4$  used the approach of  $n_1$  to the pressure distribution, and with  $g = 1 + \frac{7}{9} f^3$ , it employed the approach of  $n_2$ , but with second-order shock-expansion at

large  $F$ . The solutions  $n_3$  and  $n_4$  with  $g = 1 + \frac{7}{9}f^3$  were thus regarded to be more accurate at large  $F$ , and the solutions  $n_4$  to be more accurate at small  $F$ .

The different reference areas in these calculations were selected to demonstrate the significance of a proper choice of reference area, inasmuch as some of the conflicting results in the published literature can be traced to this factor.

Figures 14 and 15 summarize the calculations for the length-and-volume constraint and complex power-law bodies.

The shape factor  $\left(1 - \frac{x}{l}\right)^a$  was chosen so that when the  $\sin^2$  law was employed, the derived shape would agree essentially with the optimum shapes for large  $F$  as derived through variational methods (e.g., ERD shapes (ref. 1)). As mentioned earlier, this provided both a basis for relating the effects of other pressure laws to earlier work, and a body family free of the flat nose and sharp corners that become so prominent at small  $F$  for the variational shapes. The variation of this shape factor with  $x/l$  is shown in figure 16.

Method-of-characteristics solutions.- Although it was felt that the exercise with the exponential residual solutions gave values of optimum  $n$  that were fair approximations of the correct values, it also strengthened the conviction that the correct value of inviscid optimum  $n$  for practical flight regimes was not likely to be conclusively settled either by experiment\* or by analyses that employ approximate pressure laws, and the work of the past decade has not altered that view. Therefore the method of characteristics (including rotational effects) is now being applied to the problem by others at the Langley Research Center. The first phase of these calculations is confined to simple power-law bodies. While an accurate treatment of the blunt-nose region will be included, a study is first being made of bodies with  $F$  sufficiently large such that in the region of  $n$ -values where the optimum will fall (the exponential residual solutions provide a guide in this respect), a pointed cone tangent at the point where  $\delta = 45^\circ$  may be substituted for the blunt tip, with reasonable confidence that the resulting change in drag will be minor, if not negligible. Figure 17 illustrates the minute portions of bodies of moderate  $F$  that are changed in terms of the ratio of body radius at the  $45^\circ$  point to the base radius, and the ratio of axial length of the conical tip to the length of the unmodified body. The change in downstream induced pressures must also be considered, but here too the percentage of the body that would be significantly affected is small. The values of optimum  $n$  derived through the characteristics calculations will be shown subsequently for these two examples.

---

\*The value of experimental work as a rough confirmation is undisputed; it is essential, particularly in establishing viscous effects and practical guides.

### Comparison of exponential residual solutions with other solutions and experiment.-

The results of the exponential residual solutions for the  $l$ -and- $d$  constraint are shown in figure 18 and compared with other solutions. The horizontal ticks at the right are slender-body solutions for simple power-law bodies obtained independently by several authors (e.g., refs. 1 to 8) using the Newton and/or Newton-Busemann pressure laws. The agreement of the solution  $n_1$  at large  $F$  with the slender-body Newton solution should be expected. To date no satisfactory explanation for the agreement of the slender-body Newton-Busemann solution with the solution  $n_2$  at large  $F$  exists; the pressure distributions for these solutions are quite dissimilar. Since the unmodified\* shock-expansion method (ref. 19) was employed at large  $F$  in the solution  $n_2$ , the pressures on the body are significantly less than the exact toward the rear of the body; the Newton-Busemann pressures exhibit even greater disparity and marked difference in gradient. Also shown is a solution obtained by using the  $\sin^2$  law with  $\varphi$  constant. The marked departure of the solution  $n_2$  (and the solution  $n_1$  at small  $F$ ) from this solution indicates that the optimum bodies are likely blunter than the  $\sin^2$  law predicts.

The several points obtained from the characteristics solutions cast further doubt upon solutions based upon either the Newton or Newton-Busemann laws. While further output must be awaited to place these points in proper perspective, it is tentatively concluded that the correct solution (in the moderate to large range of  $F$ ) is neither the oft quoted  $2/3$ - and  $3/4$ -power bodies but somewhere between the solutions  $n_1$  and  $n_2$  presented herein. The characteristic solutions and the solutions  $n_1$  and  $n_2$  indicate that the decay in the value of  $n$  with decreasing  $F$  will take place at a significantly higher value of  $F$  than given by the  $\sin^2$  law.

Some comparisons of these predictions with experimental data (refs. 21 and 22 and unpublished results) are shown in figure 19. Figure 19(a) presents a compilation of experimental data for  $F \leq 5$  and  $3.5 \leq M_\infty \leq 24.5$ . The values of  $Re_{\infty,l}$  for these data ranged between about  $1/4$  to 3 million. The data for  $M_\infty = 24.5$  were obtained in helium ( $\gamma = 5/3$ ); all other data were obtained in air ( $\gamma = 7/5$ ). The  $n_1$ ,  $n_2$ , and  $\sin^2$  law predictions are indicated by the vertical ticks. The primary interest here is in the data for  $F = 1/2$  and 1, for which viscous effects are less likely to affect the identification of optimum inviscid  $n$  because of the predominant role of inviscid drag in the total drag. There is considerable latitude in fairing curves through the data; nevertheless, it would appear that for  $F = 1/2$  and 1 the solutions  $n_2$  and  $n_1$  agree more closely with the probable minimums than the  $\sin^2$  law predictions. The data for  $F = 3$  and 5 are too sparse to be used as criteria for closely evaluating the predictions, and the shapes in the optimum range are becoming slender enough to require an evaluation of viscous effects. Accordingly, it seems reasonable to conclude only that all of the predictions fall within the general area of the experimental minimum.

---

\*Without the Syvertson-Dennis second-order modification (ref. 20).



Figures 19(b) and 19(c) present recent results at  $M_\infty = 6.0$  and  $10.4$ , respectively, for a series of simple power-law bodies with the  $l$ -and- $d$  constraint and  $F = 6.63$ . While the analysis of the results at  $M_\infty = 6.0$  is incomplete, it is reasonably certain that major viscous effects are reflected in the data; preliminary study suggests that transition occurs on the bodies for  $Re_{\infty,l} \gtrsim 5 \times 10^6$ , and that the location of transition differs from body to body at constant  $Re_{\infty,l}$ . The drag data for  $Re_{\infty,l} = 2 \times 10^6$  exhibit a peculiar trend that analyses to date have not explained satisfactorily. The value of  $n$  in the vicinity of the prominent minimum in the drag curves for the higher Reynolds numbers is considerably less than that given by the inviscid predictions. Values of  $(L/D)_{\max}$  are shown at the top. The peak value of  $(L/D)_{\max}$  for  $5 \times 10^6 \leq Re_{\infty,l} \leq 10 \times 10^6$  occurs at a value of  $n$  larger than that for minimum drag. Additional analyses have given no reason to expect these values of  $n$  to coincide, and it has been concluded that values of  $n$  for minimum drag are not reliable indicators of peak  $(L/D)_{\max}$ .

The variation of  $(L/D)_{\max}$  for  $Re_{\infty,l} = 2 \times 10^6$  at  $M_\infty = 6.0$  is noticeably less than that for the higher Reynolds numbers. This lower sensitivity to  $n$  also occurs for the data at  $M_\infty = 10.4$  (fig. 19(c)) at comparable Reynolds numbers, for which the flow over the bodies is laminar at all test values of  $Re_{\infty,l}$ . The drag curves for  $M_\infty = 10.4$  are accordingly more orderly than at  $M_\infty = 6.0$ . The difference between the Newton law estimate of inviscid drag and the experimental data roughly indicates the major role that friction drag is playing in the total drag. Here again it can only be said that the predictions of optimum  $n$  are in the vicinity of the experimental minimums, and that for these all-laminar results the experimental value of optimum  $n$  may be lower at the higher Reynolds numbers, or a lower  $n$  may be admitted with negligible drag penalty. In any event, the overall results call for caution in using experimental results to evaluate inviscid optimum  $n$  and point up the need for additional study of the effect of viscosity. While past analytical studies of viscous effects have given significant insight (e.g., ref. 10), future studies in this area should be based upon more accurate pressure laws for practical regimes than the Newton or Newton-Busemann laws.

The results of the exponential residual solutions for the  $l$ -and- $V$  constraint are shown in figure 20 and compared with other solutions. Note that the value of  $n$  shown for the complex power-law bodies of the exponential residual solutions is for  $x/l = 0$  only. The ticks at the right are slender-body solutions for simple power-law bodies as derived by several authors (e.g., ref. 8). To date, no satisfactory explanation has been found for the general level of agreement of the exponential residual solutions for the shape of complex power-law bodies in close proximity of the stagnation point only, and the shape of simple power-law bodies. This might be associated with the prominent role that nose shape plays in defining the optimum shape. In this regard, studies such as those

of Rossow (ref. 23) have indicated that the nose vertex is a critical point for hypersonic similarity. (See also South's work mentioned earlier.) Note the agreement of the points obtained herein to date by characteristics solutions for simple power-law bodies with the exponential residual solutions for complex power-law bodies and  $g = 1 + \frac{7}{9}t^3$ .

Also shown in figure 20 are the results of recent solutions for simple power-law bodies obtained by using the  $\sin^2$  law with  $\varphi$  constant. The difference between the results that can occur when using a reference area that differs for each body in the family and one that is the same for all bodies in the family – the proper approach – is illustrated by the two curves, one employing base area, the other employing  $l^2$  (one of several proper reference indices within this family). While the percentage changes in planform area between bodies in a given  $l$ -and- $V$  constraint family are much less than the percentage changes in base area, it may yet be enough to affect the value of optimum  $n$ ; this should be recognized in employing the solutions  $n_3$ .

While the exponential residual expressions generally conformed to the calculated optimum values of  $n$  within less than  $\pm 0.01$ , the solutions  $n_4$  exceeded this slightly at  $F = 100$ . The degree of upward trend in the solutions  $n_4$  at large  $F$  may therefore be unrealistic. It is important to recall that the exponential residual solutions were based on calculations for  $F \leq 100$ , and thus may not apply for  $100 < F < \infty$ . However, as  $F \rightarrow \infty$  the exponential residual expressions give  $n = 3/4$  (as do the ERD variational solutions); the values of  $n$  must therefore eventually increase above those indicated at  $F = 100$ . The difference between the solutions  $n_3$  and  $n_4$  for  $F \lesssim 0.8$  perhaps poses an unresolved question, although it is felt that the solution  $n_4$  is more realistic in view of the pressure laws employed. No experimental data of sufficient scope could be found for comparison. A simple method for accurately predicting pressure distributions on blunt bodies is currently being applied to this regime of small  $F$ . A brief description of this  $\sin^2$ -deficiency method is given subsequently.

At moderate  $F$ , the experimental results of Spencer and Fox (ref. 24) are available. These results were obtained at  $M_\infty = 10.03$  and  $Re_{\infty, l}$  of  $1.4 \times 10^6$  for a family of simple power-law shapes conforming to an  $l$ -and- $V$  constraint. The left portion of figure 21(a) presents, as a function of  $n$ , the values of minimum-drag coefficient (including base drag) based on planform area and on  $l^2$  (to give the bodies a common reference) and values of  $(L/D)_{\max}$ . The solid-line curves are the fairings reproduced from reference 24; the dashed-line curves are the present fairings added to illustrate the difficulty in resolving by experimental measurements the questions relating to the confirmation of optimum  $n$ . At the bottom right of figure 21(a) the zero-base-drag data are shown; the fairing is original herein since these data were not presented in this format in reference 24. It is well known that the Newton law gives much better prediction of pressure distribution for these bodies and test conditions than the Newton-Busemann law,

but within the latitude of data fairing, it is not possible to conclude which law yields better prediction of the  $n$  for minimum drag (see vertical ticks). The value of  $n_3 \approx n_4$  with  $g = 1 + \frac{7}{9}f^3$  for  $F = 6$  (the midrange  $F$  of this family) is also indicated; this might be a reasonable index in the sense noted earlier with respect to nose region similarity, but recall that it is derived on the basis of complex power-law shapes. From these results, it is tentatively concluded that optimum  $n$  for minimum drag is in the neighborhood of 0.6, recognizing that the values of  $F$  in this family and the test conditions are such that viscous effects might be present that would alter this observation.

The values of  $(L/D)_{\max}$  shown at the top left of figure 21(a) indicate a peak value in the vicinity of  $n = 2/3$ . The ticks for the theoretical values of optimum  $n$  for minimum drag are shown for reference only. As observed for the  $l$ -and- $d$  results, without further analysis, there is no reason to expect the optimum  $n$  for  $(L/D)_{\max}$  and that for minimum drag to be the same. Moreover, it is now suggested that these data may indicate that the former lies to the right of the latter, although the evidence is not sufficiently convincing to negate the conclusion for correspondence in reference 25.

Recently additional experimental data have been obtained on the similar series of simple power-law bodies tested in helium at  $M_\infty \approx 20$  with varying Reynolds number, which also changes  $M_\infty$  since  $Re_\infty$  was varied by changing the stagnation pressure of the tunnel. The results (zero base drag) shown in figure 21(b) indicate that the optimum  $n$  for  $(L/D)_{\max}$  is much greater than that for minimum drag, in contrast to the results for  $M_\infty = 10.03$  in figure 21(a). Increasing the Reynolds number (laminar flow existed on the bodies for all test conditions), aside from decreasing the drag coefficient and increasing the  $(L/D)_{\max}$ , appears to increase the optimum  $n$  for  $(L/D)_{\max}$  and to flatten the drag curves in the region of optimum  $n$ . The latter precludes precise identification of optimum  $n$ ; however, for practical applications in which it may be desirable to distribute the volume more toward the front of the body, the possibility that values of  $n$  as low as 0.5 may be used with negligible drag penalty is attractive. The reference ticks shown in figure 21(a) for the theoretical solutions are repeated here.\* Recall that the  $n_3 \approx n_4$  solutions and the point derived from the characteristics solutions are for  $\gamma = 7/5$ , whereas the experimental results are for  $\gamma = 5/3$ .

Shape comparisons.- The results of the exponential residual solutions and their relation to other predictions can be placed in better perspective if the effect of differences

---

\*There is a possibility that the agreement of the  $n_3$  and  $n_4$  solutions ( $g = 1 + \frac{7}{9}f^3$ ) with the point from the characteristics solutions is partly due to the common use of the  $45^\circ$  tip. While it is felt that this possibility is remote for reasons given earlier, the ongoing calculations should resolve this question. At large  $F$ , use of the  $45^\circ$  tip should arouse no concern. Also, comparison of the  $n_2$  and characteristics solutions for the  $l$ -and- $d$  constraint reveals differences that reflect other than the tip question.

in the value of  $n$  upon body shape can be visualized. Toward this end, figure 22 presents in normalized dimensions some comparisons of shapes for selected values of  $F$  and for both  $l$ -and- $d$  and  $l$ -and- $V$  constraints. In figures 22(a) and 22(b) the prominent flat nose and sharp corner for the ERD solutions (ref. 1) are illustrated for  $F = 1/2$  and 1, respectively, and compared with the power-law shapes (simple and complex). According to the exponential residual solutions, a significantly larger volume is permissible for the  $l$ -and- $d$  constraint at small  $F$  than is predicted for the same class of bodies through the use of the  $\sin^2$  law only, or for the bodies given by the ERD variational solution employing the same pressure law (designated "impact" in ref. 1 since  $\varphi = 2$  was used). For the  $l$ -and- $V$  constraint and  $F = 1/2$ , the solutions  $n_4$  also indicate that larger volume is available than that realized by the  $\sin^2$  law referenced to  $l^2$ ; here recall that complex power-law shapes are being compared with simple power-law shapes. For  $F = 1$  and the  $l$ -and- $V$  constraint, note that the simple power-law body based upon the  $\sin^2$  law referenced to  $l^2$  gives greater bluntness near the nose than that given by what are believed to be the more accurate of the exponential residual bodies at this  $F$ , that is,  $n_4$  ( $\approx n_3$ ) with  $g = 1 + \frac{7}{9}F^3$ ; note also the agreement of these bodies with the ERD body at the downstream stations. As expected, the profiles of these complex power-law bodies exceed that of the simple power-law body (referenced to  $l^2$ ) at downstream stations. Overall, these comparisons (particularly of the profiles near the nose) may hint of a deficiency in the better of our exponential residual solutions for the  $l$ -and- $V$  constraint in the vicinity of  $F = 1$ .

Figure 22(c) presents comparisons at moderate and large  $F$  of available ERD variational solutions (refs. 1 and 24) and the exponential residual solutions. For  $5 \lesssim F \lesssim 100$ , only the pseudo-slender-body approximations (eqs. (13) to (15)) to the exponential residual solutions for the  $l$ -and- $V$  constraint are shown. Whether or not these approximations hold for  $F$  substantially greater than 100 is not known; but for reasons already indicated, the values  $n_4$  and  $n_3$  for  $F > 100$  are not recommended without further examination. These examples illustrate the typical accuracy with which the selected shape factor  $\left(1 - \frac{x}{l}\right)^a$  of the exponential residual solutions (that are based upon the  $\sin^2$  law at large  $F$ ) affords a power-law duplication of the ERD profiles at large  $F$ . The ERD "modified impact" shape refers to the variational solution in which an approximation was made of centrifugal effects (ref. 1); its agreement with the  $n_2$  shape is not fully understood. The pseudo-slender-body profiles,  $n_5$  and  $\sin^q\left(\frac{\pi x}{2l}\right)$ , agree closely; however, this may prove to be of secondary interest in the light of the  $n_6$  profile which is believed to be based upon better pressure laws. Here too is illustrated the volumetric advantage\* (as exhibited in the original ERD analysis (ref. 1) for

---

\*At no expense in inviscid drag.

the variational shapes) of the complex power-law shapes over the simple power-law shapes, the blunter of the latter exemplified by the slender-body solution for simple power-law shapes based on the Newton-Busemann law.

### Trapezoidal Bodies

Interest in the hypersonic aerodynamics of bodies with polygonal cross sections extends back a number of years, one of the foremost stimulants being the work of Sänger and Bredt in the early 1940's,\* who also suggested possible performance advantages for flat-bottom bodies. In the United States widespread interest in this area began in the late 1940's with the flood of documents reporting research conducted in European countries in the late 1930's to mid 1940's. Among these documents were fragmentary reports of experimental research at supersonic speeds on bodies of revolution, polygonal bodies, and half-bodies, the last being halves of a few of the former. Some of the data for the complete bodies have been published elsewhere; for example, see references 26 and 27. To the present author's knowledge, no reliable authorship was ever determined for a portion of the remaining data and several other documents, and as some will recall, most of the polygonal and half-body data became referred to as the GUS data (see appendix). The test conditions of the GUS data were never confidently determined, variously indicated to be between  $M_\infty = 3$  and 5, but more likely near 3, and if so, probably at  $Re_{\infty,l}$  near  $10^6$ . This lack of definitive test conditions, combined with the growing output from new facilities, soon caused interest in these data to wane. Nevertheless, it is felt that the GUS data for one series of polygonal half-bodies deserve one more exposure and a comparison with recent results for a series of trapezoidal bodies because of the close similarity in geometric features.

The GUS half-bodies, or trapezoidal family of interest here, consisted of seven bodies all having the same length, volume, planform area, longitudinal distribution of cross-sectional area, and width (or span). The longitudinal distribution of cross-sectional area corresponded to half of an ogival body of revolution of  $F = 3.5$ . The ratio of span to height at the base was equated to  $N/\pi$ , this form apparently chosen for convenience, since  $4 \leq N \leq 8$  embraces the series, and the value of  $N = 2\pi$  represents the reference ogival half-body and its trapezoidal equivalent. This use of  $N$  is adopted herein.

In recent years Spencer (refs. 25 and 28) has tested a similar series of five bodies at  $M_\infty = 10.03$  and  $Re_{\infty,l}$  of  $1.4 \times 10^6$ . These bodies had a longitudinal cross-sectional-area distribution conforming to the ERD variational solution for a body of revolution with the  $l$ -and- $V$  constraint, as derived via Newton's pressure law. Each of

---

\*See, for example, reference 16, pages 103-106.

the bodies had an equivalent fineness ratio (i.e., ratio of length to equivalent circular base diameter) of 5. This value corresponds to half of a body of revolution of  $F = 3.54$ , and thus is close to the  $F = 3.5$  of the GUS bodies. Figure 23 depicts the trapezoidal body family, lists their identical features, and notes the reference bodies of past studies now to be compared.

Figure 24(a) presents a comparison of the GUS data and Spencer's data in terms of  $(\overline{L/D})_{\max}$ . A similar comparison is shown in figure 24(b) for  $\overline{C}_L$ . The trends and values of Spencer's data and the GUS data for  $(\overline{L/D})_{\max}$  generally agree; some secondary differences occur for  $\overline{C}_L$ , dependent upon whether the data is read directly from figure 4 of reference 28\* or from figure 8 of reference 25. The general agreement may indicate that the small difference between the shape of the ogival reference body for the GUS data and  $l$ -and- $V$  constraint ERD body of Spencer's data has little effect upon the parameter ratios shown; however, more effect would be expected than indicated from increasing  $M_\infty$  from about 3 to 10. It is possible that compensating effects of shape and  $M_\infty$  could result in the agreement shown, although this seems unlikely. Camber appears to have only small effect upon  $(\overline{L/D})_{\max}$  within the N-overlap of these data, as contrasted to the advantage exhibited for positive camber for  $\overline{C}_L$ . Discussion of pitching-moment characteristics will be omitted herein except to note that the general characteristics for positive and negative camber for the two sets of data were similar, and negative camber may be more attractive from the view of trim, as has long been observed in numerous studies of hypersonic configurations. From a performance view only, these data draw attention to the triangular shape ( $N = 4$ ) at the left end of the curves for which the peak  $(\overline{L/D})_{\max}$  and  $\overline{C}_L$  is indicated to occur.

Recently tests have been conducted at  $M_\infty \approx 6, 10$ , and 20 ( $M_\infty \approx 20$  in helium) of a series of bodies similar to Spencer's and the effects of Reynolds number in a limited range have been examined. Spencer's body series was chosen in preference to the GUS series since the basic data for the former are available, and a direct comparison could be made of results from two different facilities at essentially the same Mach number ( $M_\infty = 10$ ) and Reynolds number ( $Re_{\infty,l} = 1.4 \times 10^6$ ). The series consisted of seven models, however, so as to obtain camber coverage over the full range of  $N$ . The tests required two sets of models because of tunnel test conditions and Reynolds number objectives, composite wood-and-plastic models for the tests in helium at high  $M_\infty$ , and metal models for the tests at  $M_\infty = 6$  and 10. Postconstruction measurements indicated that both sets closely conformed to the shape specifications. At the time of this writing the tests at  $M_\infty = 6$  had carried the negative camber to  $\alpha = 4^\circ$  only because of a model

---

\*Values as read by four observers. There is some latitude in arriving at  $\overline{C}_L$  since the tests were conducted at  $4^\circ$  increments in  $\alpha$ . Whether data-smoothing techniques have been applied to the GUS data is not known.

support problem. However, since this  $\alpha$  is approximately that for  $(L/D)_{\max}$  for the case of negative camber, the data have been included herein and are so designated.

The results for  $(\bar{L}/\bar{D})_{\max}$  and  $\bar{C}_L$  are presented in figures 25 to 27. No data-smoothing technique has been applied to the basic data in arriving at the values shown; some of the data for  $M_\infty = 6.0$  involve  $4^\circ$  increments in  $\alpha$ , twice that of the data for  $M_\infty \approx 10$  and 20. Comparison of three tentative points for  $Re_{\infty,l} = 1.4 \times 10^6$  at  $M_\infty = 6.0$  (fig. 25) with the data for  $Re_{\infty,l} = 6 \times 10^6$  indicates that significant viscous effects can occur with fairly modest changes in Reynolds number, if the values of  $M_\infty$  and  $Re_{\infty,l}$  are such as to introduce transition. For the data at  $M_\infty \approx 10$  and 20 (figs. 26 and 27), the flow over the bodies is primarily (if not all) laminar, and the effects of Reynolds number within the range indicated are small. (For  $M_\infty = 10.4$ ,  $Re_{\infty,l}$  was varied between  $0.6$  and  $1.8 \times 10^6$ ; preliminary checks indicate that the data for  $Re_{\infty,l} = 1.4 \times 10^6$  are representative.) The trends in  $(\bar{L}/\bar{D})_{\max}$  with  $N$  are significantly consistent at all three Mach numbers in indicating an advantage for placing the maximum span at the bottom, and in showing that the span-height ratio for peak  $(\bar{L}/\bar{D})_{\max}$  is greater than that for the triangular shape ( $N = 4$ ). The latter result is in opposition to the results of figure 24, which indicate the triangular shape to give peak  $(\bar{L}/\bar{D})_{\max}$ .\* This is of special interest inasmuch as the departure from the triangular shape toward  $N \approx 5$  to 6 (with maximum span on bottom) that has been frequently advocated in recent design studies of advanced spacecraft configurations apparently does not involve the sacrifice in  $(L/D)_{\max}$  previously thought to accompany this departure. Rather, a gain may well be the result, and there appears to be a fairly wide choice of  $N$  open to the designer in which this gain can be realized. In general, positive camber gives better  $(L/D)_{\max}$  although there are exceptions when the maximum span is at the top.

The variation in  $\bar{C}_L$  with  $N$  is generally similar at the three Mach numbers (figs. 25(b), 26(b), and 27(b)), a prominent decay usually occurring as the maximum span shifts from bottom to top. With positive camber and maximum span at the bottom, the peak  $\bar{C}_L$  occurs for the triangular shape ( $N = 4$ ). In this latter respect the present data agree with the results of figure 24(b); however, the present data consistently disagree with those results in the magnitude of  $\bar{C}_L$  for this shape, except as is read from the value of figure 4 in reference 28. (Again, there is considerable latitude in arriving at  $\bar{C}_L$ .) The present data indicate that the topmost area of this triangular shape ( $N = 4$ ) may be a major source of its loss in performance, but this bears further study.

Lest the foregoing discussion has overly emphasized the advantages of positive camber, attention is called to the earlier remarks on the merits of negative camber for

---

\*The present results are also in opposition to recent analyses of Huang and Miele (e.g., see J. Optimization Theory and Appl., vol. 2, no. 5, Sept. 1968); however, this is of less concern since it may be shown that the Newton law used in Huang's analysis introduces greater error than the effect of shape for shapes in the vicinity of the optimum.

trim. With negative camber, distinct advantage is found in  $(\overline{L/D})_{\max}$  in moving away from the triangular shape ( $N = 4$ ) toward larger values of  $N$  and, thereby as before, gaining performance with considerable freedom to the designer as to choice of  $N$  (reference is to the case of maximum span at bottom).

### The $\sin^2$ -Deficiency Method

In the discussion of the optimum bodies of revolution, several areas were noted in which the  $\sin^2$  law can introduce significant deficiencies in the prediction of pressures, one being on the blunt noses of power-law bodies of small  $F$ . The following is a summary of a simple method developed to alleviate this deficiency for that portion of smoothly contoured blunt shapes between the stagnation point and sonic point. In numerous comparisons with experiment made to date, the method has given good results, comparable to those achieved by numerical procedures generally requiring programmed machine computing; for examples of the latter, see reference 29.

If the deficiency of the  $\sin^2$  law can be identified and expressed simply but accurately for some basic blunt shapes, such as those shown in figure 28, then application of it to various blunt shapes by an approximation routine should be possible. A logical candidate shape for identifying this deficiency is the flat disk normal to the flow, for which of course  $\delta = 90^\circ$ . As depicted in figure 29 the value of the deficiency of the  $\sin^2$  law in this case is simply  $(1 - \bar{p}_{FD})$ , where  $\bar{p}_{FD}$  is the ratio of the local pressure to the pressure at the stagnation point on a flat disk. Assume, therefore, that an approximation for the pressure distribution in terms of the  $\sin^2$  law and its deficiency may, as the shape approaches a flat disk, be expressed as

$$\bar{p} = \sin^2 \delta - (1 - \bar{p}_{FD}) \quad (16)$$

This relation recognizes that for  $M_\infty \gg 1$ ,  $\frac{C_p}{C_{p_s}} \approx \frac{p}{p_s} \equiv \bar{p}$ .

For blunt bodies having local slopes such that the flow everywhere adjacent to the surface is subsonic ahead of a convex sharp corner sufficient to expand the flow to supersonic conditions, the sonic point is located at this corner, and the value of  $\bar{p}$  there is

$$\bar{p} = \bar{p}_* = \left( \frac{2}{\gamma + 1} \right)^{\frac{\gamma}{\gamma - 1}} \quad (17)$$

For smoothly contoured blunt bodies with sonic corners as described (for example, varying from a flat disk to spherical caps, or roughly so), the pressure distribution can be approximated by assuming that values of the  $\sin^2$ -deficiency term  $(1 - \bar{p}_{FD})$  apply to



the curved-body surface between the stagnation point and sonic point at corresponding values of  $S/S_*$ , but in proportion to the ratio  $\Delta \sin^2 \delta / (\Delta \sin^2 \delta)_{\max}$  or  $\Delta \bar{p} / \Delta \bar{p}_{\max}$ . For such bodies, equation (16) becomes as shown in figure 30

$$\bar{p} = \sin^2 \delta - (1 - \bar{p}_{\text{FD}}) \left( \frac{\sin^2 \delta - \bar{p}_*}{1 - \bar{p}_*} \right) \quad (18)$$

The key to this approximation thus becomes a solution for  $\bar{p}_{\text{FD}}$ , the pressure on the flat disk. In searching for a simple but adequate analytical solution, the author performed both variable-stream-tube-area approximations and Garabedian-Lieberstein calculations for  $\gamma = 7/5$ , and guided by equation (18) to look for an expression in terms of the ratio  $(1 - \bar{p}_{\text{FD}}) / (1 - \bar{p}_*)$ , observed from both approaches that at least to first order this ratio equals  $e^{-\lambda}$ . However, no direct solution could be found for  $\lambda$ . Nevertheless, this observation promised solution through numerical calculations, and these were performed for a flat disk for several values of  $\gamma$ . The results expressed in the ratio  $(1 - \bar{p}_{\text{FD}}) / (1 - \bar{p}_*)$  and shown in figure 31 as a function of  $S/S_*$  exhibited no conclusive effects of  $\gamma$ . Accordingly, let  $(1 - \bar{p}_{\text{FD}}) / (1 - \bar{p}_*) = e^{-\lambda}$  be the general solution and proceed to evaluate  $\lambda$  as a function of  $S/S_*$ . By plotting the results in this form (fig. 32) the relation is observed to be similar to an error function curve, and by adopting this type of expression, the following equation can be derived through graphical or exponential residual solution

$$\bar{p}_{\text{FD}} = 1 - e^{-\lambda} (1 - \bar{p}_*) \quad (19)$$

where

$$\lambda = 4 \left[ \ln \left( \frac{S}{S_*} \right) \right]^{1/2} \quad (20)$$

For  $\gamma = 7/5$

$$\bar{p}_{\text{FD}} = 1 - 0.472e^{-\lambda} \quad (21)$$

The prediction given by equation (21) is compared in figure 33 with a prediction by Belotserkovskii's method (ref. 30) and a compilation of experimental data (ref. 18); it appears adequate for engineering purposes. (A tabulation of values of  $\bar{p}_{\text{FD}}$  in fine increments of  $S/S_*$  facilitates rapid calculations for other shapes.) Use of equation (21) with equation (18) gives good results for smoothly contoured blunt bodies with sonic corners, as illustrated by the comparison with experiment (ref. 31) in figure 34, and appears

to at least equal the prediction accuracy of the method of integral relations, as machine computed by the program in reference 29.

Cones with half-angles exceeding that for sonic flow at the nose have received attention in recent years as candidate shapes for planetary entry probes. Consider first the application of equation (18) to sharp cones with  $\delta_c < 90^\circ$  but greater than that for sonic flow at the tip ( $\delta_c \approx 55^\circ$  for  $\gamma = 7/5$ ). By inspection, equation (18) would give a value of  $\bar{p}$  at the cone tip that is deficient by the amount  $(1 - \sin^2 \delta)$ . As a first step then equation (18) can be modified by the addition of  $(1 - \sin^2 \delta)$  in proportion to  $(1 - S/S_*)$ . The correct stagnation- and sonic-point values of  $\bar{p}$  are thus retained, but the resulting pressure decay is inadmissible for some conditions (e.g., consider large  $S/S_*$  and low  $\delta_c$ ). To resolve this difficulty, it may be reasoned that at large  $S/S_*$  an admissible decay should lie roughly midway between the  $\sin^2$ -deficiency decay of the flat disk and that resulting from the modification  $(1 - \sin^2 \delta)$  to equation (18); therefore a term is added that in effect averages the two as  $S/S_* \rightarrow 1$ . The resulting more complete form of equation (18) follows

$$\begin{aligned} \bar{p} = \sin^2 \delta - (1 - \bar{p}_{FD}) \left( \frac{\sin^2 \delta - \bar{p}_*}{1 - \bar{p}_*} \right) + \left( 1 - \frac{\epsilon}{\epsilon_0} \right) \left\{ (1 - \sin^2 \delta) \left( 1 - \frac{S}{S_*} \right) \right. \\ \left. + \frac{S/S_*}{2} \left[ \bar{p}_{FD} - 1 + \frac{S}{S_*} (1 - \sin^2 \delta) + (1 - \bar{p}_{FD}) \left( \frac{\sin^2 \delta - \bar{p}_*}{1 - \bar{p}_*} \right) \right] \right\} \end{aligned} \quad (22)$$

The term  $\left( 1 - \frac{\epsilon}{\epsilon_0} \right)$  is simply a linear approximation of the effect of tangential spherical blunting of the tip of the cone (see fig. 35).

Figure 36(a) compares the present method with the machine-computed numerical solutions of South (ref. 29) and the experimental data of Stallings and others (see ref. 29) for blunted cones. Figure 36(b) gives further comparisons with South's calculations. Figure 36(c) compares the present method with the modified Newtonian estimate and test results of Kurz (ref. 32). (Note that  $\bar{p}$  closely approximates  $\bar{C}_p$  for  $M_\infty \gg 1$ . A value of  $(\gamma + 3)/(\gamma + 1)$  was used in the present method for  $C_p$  at the stagnation point. Reference 32 quotes  $\epsilon/R$  as 0.46, but the model drawings and the Newtonian calculation therein conform to  $\epsilon/R$  of 0.412, which was used herein.) In these and other comparisons with data for  $M_\infty > 20$ , the present method is found to be adequate for predicting the pressure on sharp and blunted cones with sonic corners. For sharp cones, the method cannot be expected to give reliable results for  $\delta_c$  close to or less than that for which sonic flow occurs at the tip or to predict the cusp in the pressure distribution that occurs at the tangency point under these conditions. For spherically blunted cones the method

may be expected to hold to slightly lower values of  $\delta_c$ . In this regard the author found in early analyses for  $\gamma = 7/5$  that the following hypersonic approximation for the surface inclination at the sonic point  $\delta_*$  on a sphere

$$\delta_* = \delta_{*0} \left( 1 - \frac{3}{2M_\infty^2} \right) \quad (23)$$

is a reasonable guide, where  $\delta_{*0}$  is the surface inclination at the sonic point for infinite Mach number, taken as  $49.3^\circ$ .

The calculation of the pressure distribution over the entire surface of a hemisphere (and other smoothly contoured blunt bodies) can be made by applying the present method from the stagnation point to the sonic point, the  $\sin^2$  law matched at sonic point by equation (6) for  $\delta \leq \delta_*$ , and the Prandtl-Meyer approximation matched to the  $\sin^2$  law by the usual procedure, for example, Wagner's results (ref. 33). The results of a combined calculation of this type are shown in figure 37; ahead of the sonic point the  $\sin^2$ -deficiency method compares favorably with Van Dyke's numerical solutions (ref. 34) at  $M_\infty = 5.8$  and  $\infty$ , and with experimental results (ref. 18). The matched  $\sin^2$  law plus matched Prandtl-Meyer gives equally satisfactory results over the remainder of the body.

Good agreement has also been found between this combined approach and experimental distributions over bodies of the type reported by Ashby and Goldberg (ref. 35), others by Stallings (ref. 31), and for bodies with gross changes in curvature ahead of the sonic point, such as those having sizable flat regions in the vicinity of the stagnation point, followed by rounded shoulders (see fig. 38). The last require an iterative approximation for the location of the sonic point  $S_*/R$ . This iteration is necessary since for such shapes the surface pressure has decreased significantly at stations near the outer periphery of the flat region, even in the absence of the upstream relieving effect of the rounded shoulder. Accordingly, less expansion of the flow is required beyond the tangency point on the flat face to reach the sonic point. By use of equation (23) and the flat-disk solution, equation (19), and by interpreting the value of  $\bar{p}_{FD}$  at the tangency point on the face as the  $\sin^2$  of an effective  $\delta$  at the tangency point, an approximation for  $S_*/R$  can be determined by iteration. For the type of body shown in figure 38, and dependent upon the ratio of shoulder radius to  $R$ , one iteration may give a fair estimate of the geometric value of  $\delta_*$  that is obtained by the number of iterations necessary to yield negligible change as illustrated by the following tabulation for  $M_\infty \approx 20$ :

Ratio of shoulder radius to $R$	Geometric $\delta_*$ , deg	
	One iteration	Full iteration
0.10	72.2	80.6
.25	65.0	69.6
.50	57.5	59.3
.90	50.5	50.5
1.00	49.0	49.0

As the ratio of shoulder radius to  $R$  becomes small (but nonzero), use of only one iteration gives large error in  $\delta_*$ , but in terms of  $S_*/R$  this error is subdued.

Two approaches have been examined for applying the value of  $S_*/R$  thus determined with the present method (eq. (18)). The first uses the geometric values of  $\delta$ , the values of  $S/S_*$  being determined simply by  $(S/R)(R/S_*)$ . The second employs the same approach to  $S/S_*$ , but uses the effective value of  $\delta$  at the tangency point on the flat face (determined in the iterative calculation). The effective values of  $\delta$  ahead of the tangency point are varied between  $90^\circ$  and the value at the tangency point, and the corresponding values of the effective  $\Delta\delta$  are used with the shoulder radius to obtain  $\Delta(S/R)$ . The results of these two approaches are shown in figure 38. Either is a considerable improvement over the modified Newton method, the second giving a greater relieving effect from the rounded shoulder on the pressures ahead of the tangency point ( $S/R = 0.75$ ). The sonic point appears to be adequately predicted, and the matched  $\sin^2$  law and the matched Prandtl-Meyer give good prediction over the remainder of the nose.

### CONCLUDING REMARKS

In these selected topics on body shaping for minimum drag and improved performance at hypersonic speeds, the emphasis has been from the view of practical flight regimes. For both simple and complex power-law bodies of revolution, the optimum value of the exponent for inviscid minimum drag derived through the synoptic pressure laws (Newton type) appears to be no more exactly defined today than approximately a decade ago. The major source of uncertainty stems from the use of the synoptic and other approximate pressure laws having significant deficiencies. Experimental results roughly confirm several inviscid predictions, but the experimental approach is not likely to indicate a preferred prediction without exceptionally accurate measurement of viscous effects which, as shown by experimental results, can be major. Ongoing exact calculations are clarifying the issue on inviscid optimums. The present experimental results

indicate that the value of the exponent for minimum drag is not a reliable indicator of the value for maximum lift-drag ratio.

Since recent analytical attempts at defining optimum shapes with viscous effects included are based upon the same approximate pressure laws that have led to the uncertainty in the inviscid solutions, the quantitative predictions for the viscous optimums are equally suspect, if not more so, particularly when the assumed inviscid pressure law introduces pressure gradients markedly different from the correct. This emphasizes the need for accurate inviscid solutions as the essential base for accurate boundary-layer solutions.

Recent experimental results for Mach numbers of 6 to 20 for a family of trapezoidal bodies reinforces the substantial case already established for orienting the body such that the maximum width is at the bottom. Contrary to earlier results, the present results indicate that the maximum lift-drag ratio is obtained for bodies with some width at the top, rather than for a triangular cross section; this occurred for both positive and negative camber. These and similar experimental studies need to be extended to the case of transitional and turbulent boundary layers.

A simple method developed for predicting the pressure distribution ahead of the sonic point on smoothly contoured blunt shapes, the " $\sin^2$ -deficiency method," appears to yield results comparable in accuracy to those of more elaborate methods requiring machine computation. It thus offers a simple means for more accurate calculation of optimum shapes of small fineness ratio and of the drag contribution of a blunt nose on bodies of large fineness ratio. The method hinges upon a solution derived for the pressure distribution on a flat disk, for which related work showed no conclusive effects of the ratio of specific heats. However, the latter does not assure that the normalized pressure distributions for other shapes are equally insensitive to the ratio of specific heats and suggests the need for further study of these effects.

Several areas in need of improvement are summarized as follows:

Inviscid predictions:

- (1) Nonlifting
- (2) Lifting
- (3) Arbitrary longitudinal and transversal contours

Optimization analyses based upon reliable pressure laws ( $0 \leq F \leq \infty$ ):

- (1) Inviscid
- (2) Viscous with sound inviscid base
- (3) Items of inviscid predictions

Impact of practical factors:

- (1) Shape, volume distribution, and so forth
- (2) Environment

Innovation (analytical)

The last noted, analytical innovation, applies to all the preceding items and more. Over the past decade increasing concern has been expressed for the lack of a satisfactory method for predicting the aerodynamic characteristics of asymmetric lifting shapes in the portion of the hypersonic entry environment where viscous effects are prominent. This deficiency still exists.

## APPENDIX

### ADDITIONAL REMARKS ON GUS DATA

For those unfamiliar with GUS data, the incomplete source documents displayed little clue to authorship or origin except the letters G.U.S. on each page, bottom right, hence, the epithet. When the author first saw the documents containing the polygonal and half-body data, they were packaged with others relating to A4 and A5 missile research, alongside reports by Erdmann. (See refs. 1 and 3 of ref. 36.) In a recent second effort to shed light on the GUS data, it has been reasonably established that the GUS data shown in the present paper are not part of the A4 or A5 history, nor products of Erdmann. The author wishes to acknowledge the aid of A. Busemann, H. H. Kurzweg, C. E. Coleman, L. T. Bright, and others in this effort. It now appears that the original documents are either filed under some as yet unidentified listing at the Washington National Records Center, Suitland, Maryland, or were possibly destroyed several years ago with quantities of old documents rated as nonarchival. The GUS data herein are taken from notes recorded in 1949.

## REFERENCES

1. Eggers, A. J., Jr.; Resnikoff, Meyer M.; and Dennis, David H.: Bodies of Revolution Having Minimum Drag at High Supersonic Airspeeds. NACA Rep. 1306, 1957. (Supersedes NACA TN 3666.)
2. Hayes, Wallace D.; and Probstein, Ronald F.: Hypersonic Flow Theory. Academic Press, Inc., 1959.
3. Cole, J. D.: Newtonian Flow Theory for Slender Bodies. J. Aeronaut. Sci., vol. 24, no. 6, June 1957, pp. 448-455.
4. Gonor, A. L.; and Chernyi, G. G.: On Minimum Drag Bodies at Hypersonic Speeds. G-141, Morris D. Friedman, Inc. (Needham Heights 94, Mass.). (From Izvestiia, AN USSR, O. T. N., no. 7, 1957, pp. 89-93.)
5. Chernyi, G. G. (Ronald F. Probstein, trans.): Introduction to Hypersonic Flow. Academic Press, Inc., 1961.
6. Miele, Angelo: Theory of Optimum Aerodynamic Shapes. Academic Press, Inc., c.1965.
7. Kondo, J.: The Minimum Drag Problem of Axial Symmetric Body. Proceedings of the Sixth International Symposium on Space Technology and Science, AGNE Pub. Inc. (Tokyo), c.1965, pp. 129-140.
8. Lusty, Arthur H., Jr.: Slender, Axisymmetric Power Bodies Having Minimum Zero-Lift Drag in Hypersonic Flow. D1-82-0275, Flight Sci. Lab., Boeing Sci. Res. Lab., July 1963.
9. Ellinwood, John Webster: Minimum-Drag Body With Specified Center of Pressure. AIAA J., vol. 5, no. 4, Apr. 1967, pp. 826-827.
10. Kennet, H.: The Effect of Skin Friction on Optimum Minimum-Drag Shapes in Hypersonic Flow. J. Aerospace Sci., vol. 29, no. 12, Dec. 1962, pp. 1486-1487.
11. Busemann, A.: Flüssigkeits-und-Gasbewegung (The Motion of Liquids and Gases). Handwörterbuch der Naturwissenschaften, Vol. IV, Second ed., Gustav Fischer (Jena), 1933, pp. 244-279.
12. Love, E. S.: Generalized-Newtonian Theory. J. Aero/Space Sci. (Readers' Forum), vol. 26, no. 5, May 1959, pp. 314-315.
13. Stocker, P. M.: Hypersonic Flow - Part I: General Considerations and Two Dimensional Inviscid Flow Theory. A.R.D.E. Rep. (B) 22/25, Min. Supply (Brit.), Aug. 1955.



14. Lees, Lester: Hypersonic Flow. Fifth Int. Aeronaut. Conf. (Los Angeles, Calif.), Inst. Aeronaut. Sci., Inc., June 1955, pp. 241-276.
15. Probst, Ronald F.: Inviscid Flow in the Stagnation Point Region of Very Blunt-Nosed Bodies at Hypersonic Flight Speeds. WADC TN 56-395 (Contract No. AF 33(616)-2798), U.S. Air Force, Sept. 1956. (Available from DDC as AD 97273.)
16. Clauser, F. H.; Peebles, G. H.; Krueger, R. W.; and Osman, K. R.: Exploitation of German Aerodynamic Science (Field Notes). Rep. No. SM-20039, Douglas Aircraft Co., Inc., Nov. 26, 1945.
17. Love, E. S.: Prediction of Inviscid Induced Pressures From Round Leading Edge Blunting at Hypersonic Speeds. ARS J. (Tech. Notes), vol. 29, no. 10, pt. 1, Oct. 1959, pp. 792-794.
18. Matthews, R. K.; and Eaves, R. H., Jr.: Private Communication. ARO, Inc., Arnold Engineering Development Center, Arnold Air Force Station, Tennessee.
19. Eggers, A. J., Jr.; Savin, Raymond C.; and Syvertson, Clarence A.: The Generalized Shock-Expansion Method and Its Application to Bodies Traveling at High Supersonic Air Speeds. J. Aeronaut. Sci., vol. 22, no. 4, Apr. 1955, pp. 231-238.
20. Syvertson, Clarence A.; and Dennis, David H.: A Second-Order Shock-Expansion Method Applicable to Bodies of Revolution Near Zero Lift. NACA Rep. 1328, 1957. (Supersedes NACA TN 3527.)
21. McDearmon, Russell W.; and Lawson, Warren A.: Investigation of the Normal-Force, Axial-Force, and Pitching-Moment Characteristics of Blunt Low-Fineness-Ratio Bodies of Revolution at a Mach Number of 3.55. NASA TM X-467, 1961.
22. Witcofski, Robert D.; and Woods, William C.: Static Stability Characteristics of Blunt Low-Fineness-Ratio Bodies of Revolution at a Mach Number of 24.5 in Helium. NASA TN D-2282, 1964.
23. Rossow, Vernon J.: Applicability of the Hypersonic Similarity Rule to Pressure Distributions Which Include the Effects of Rotation for Bodies of Revolution at Zero Angle of Attack. NACA TN 2399, 1951.
24. Spencer, Bernard, Jr.; and Fox, Charles H., Jr.: Hypersonic Aerodynamic Performance of Minimum-Wave-Drag Bodies. NASA TR R-250, 1966.
25. Spencer, Bernard, Jr.; and Fox, Charles H., Jr.: Experimental Studies of Optimum Body Shapes at Hypersonic Speeds. J. Astronaut. Sci., vol. XIV, no. 5, Sept.-Oct. 1967, pp. 237-240.
26. Ferri, Antonio: Supersonic-Tunnel Tests of Projectiles in Germany and Italy. NACA WR L-152, 1945. (Formerly NACA ACR L5H08.)

27. Benecke, Th.; and Quick, A. W., eds.: History of German Guided Missile Development. AGARDograph No. 20, Verlag E. Appelhans & Co. (Brunswick, Germany), 1957.
28. Spencer, Bernard, Jr.: Hypersonic Aerodynamic Characteristics of Minimum-Wave- Drag Bodies Having Variations in Cross-Sectional Shape. NASA TN D-4079, 1967.
29. South, Jerry C., Jr.: Calculation of Axisymmetric Supersonic Flow Past Blunt Bodies With Sonic Corners, Including a Program Description and Listing. NASA TN TN D-4563, 1968.
30. Gold, Ruby; and Holt, Maurice: Calculation of Supersonic Flow Past a Flat-Headed Cylinder By Belotserkovskii's Method. AFOSR TN-59-199, AD 211-525, U.S. Air Force, Mar. 1959.
31. Stallings, Robert L., Jr.: Experimentally Determined Local Flow Properties and Drag Coefficients for a Family of Blunt Bodies at Mach Numbers From 2.49 to 4.63. NASA TR R-274, 1967.
32. Kurz, Donald W.: Detailed Pressure Distribution on a Blunted 60-deg Half-Angle Cone at Mach Numbers of 6.08 and 9.46. Tech. Mem. 33-404 (Contract No. NAS 7-100), Jet Propulsion Lab., California Inst. Technol., Sept. 1, 1968.
33. Wagner, Richard D., Jr.: Some Aspects of the Modified Newtonian and Prandtl-Meyer-Expansion Method for Axisymmetric Blunt Bodies at Zero Angle of Attack. J. Aero/Space Sci. (Readers' Forum), vol. 26, no. 12, Dec. 1959, pp. 851-852.
34. Van Dyke, Milton D.: The Supersonic Blunt-Body Problem - Review and Extension. J. Aerosp. Sci., vol. 25, no. 8, Aug. 1958, pp. 485-496.
35. Ashby, George C., Jr.; and Goldberg, Theodore J.: Application of Generalized Newtonian Theory to Three-Dimensional Sharp-Nose Shock-Detached Bodies at Mach 6 for Angles of Attack up to  $25^{\circ}$ . NASA TN D-2550, 1965.
36. Love, Eugene S.: Aerodynamic Investigation of a Parabolic Body of Revolution at Mach Number of 1.92 and Some Effects of an Annular Supersonic Jet Exhausting From the Base. NACA TN 3709, 1956. (Supersedes NACA RM L9K09.)

## REVIVAL OF INTEREST - STIMULUS

### HISTORY OF MINIMUM-DRAG SOLUTIONS (INVISCID)

- PRESSURE LAWS (SYNOPTIC, OTHER)
- PRIOR TO MID-1950's
- MID AND LATE 1950's
- THE 1960's

### EXPERIMENTAL EVIDENCE (NONLIFTING, LIFTING)

### RATIONALISTIC METHOD (E.G., $\sin^2$ -DEFICIENCY METHOD)

### AREAS NEEDING IMPROVEMENT

Figure 1.- Design of bodies for low drag and high performance in practical hypersonic flight.

#### PROBLEM: SHAPE FOR MINIMUM WAVE DRAG

$$\frac{r}{R} = \left(\frac{x}{l}\right)^n$$

SIMPLE,  $n = f(F)$

COMPLEX,  $n = f(F, \frac{x}{l})$

#### SIMPLE POWER-LAW BODIES

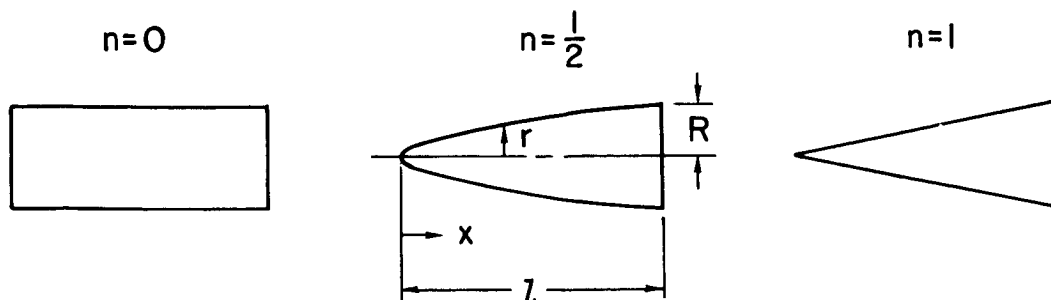


Figure 2.- Bodies of revolution; power-law types.

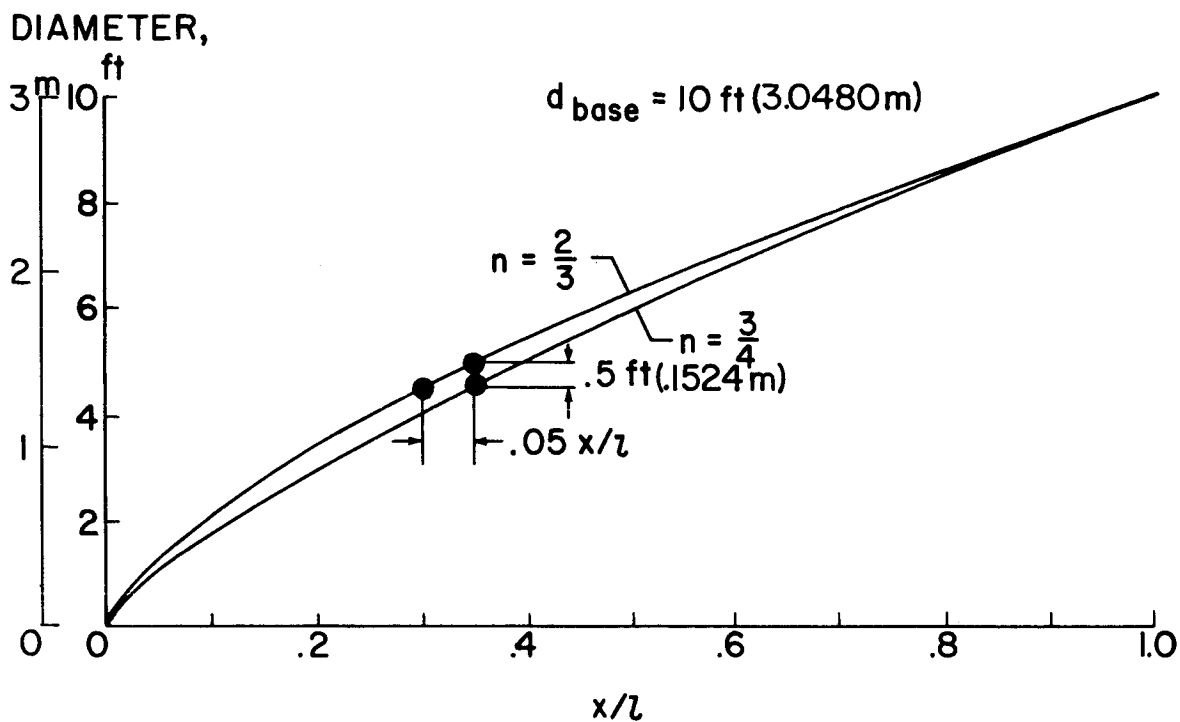


Figure 3.- Packaging significance of optimum value of  $n$ .

### PRESSURE LAWS

- NEWTON:  $C_p = 2 \sin^2 \delta$
- NEWTON-BUSEMANN:  $C_p = 2 \sin^2 \delta + 2 \sin \delta \frac{d\delta}{dA} \int_0^A \cos \delta dA$

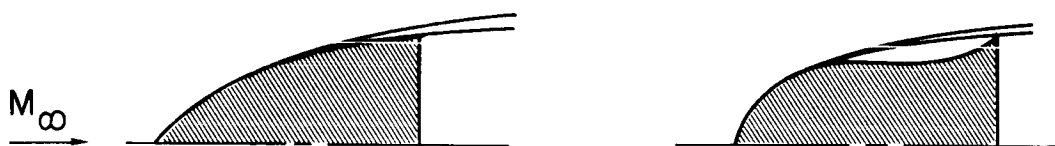


Figure 4.- Newtonian shock layers and free layers.

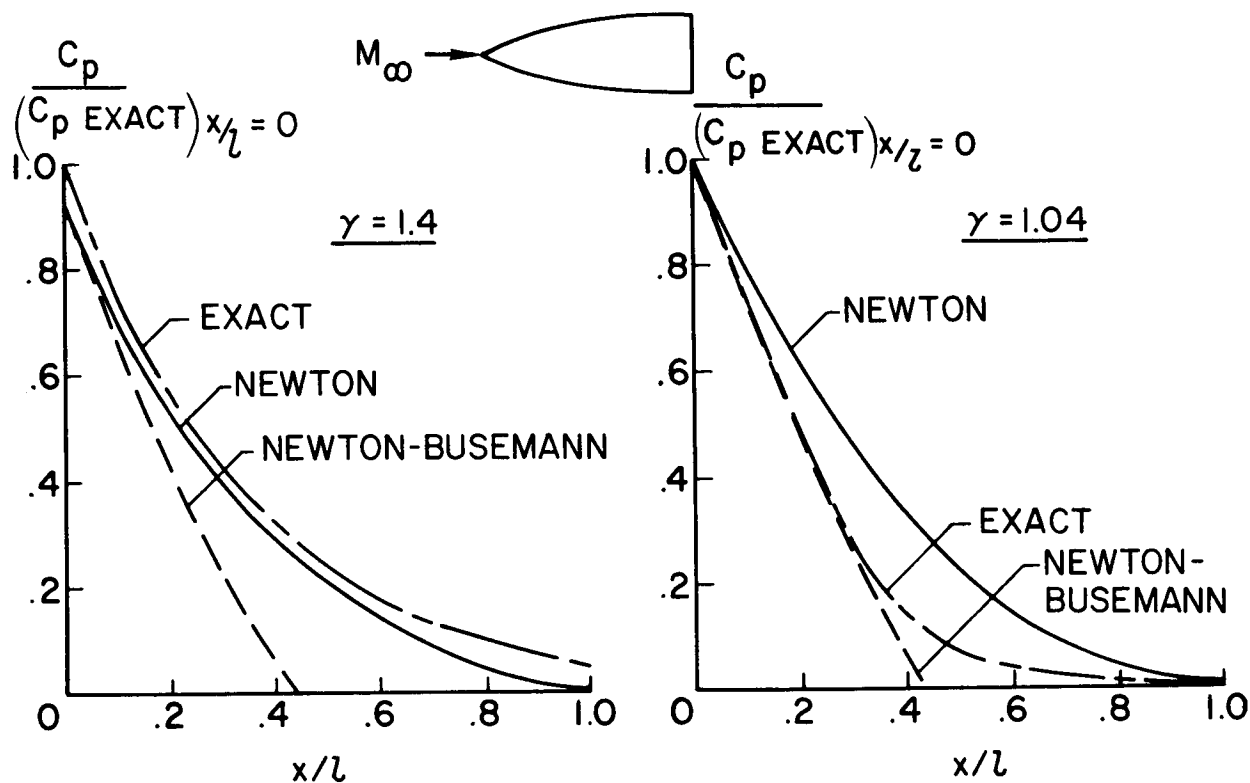


Figure 5.- Effect of  $\gamma$  on evaluation of Newton and Newton-Busemann pressure laws at  $M_\infty = \infty$ .

(CHERNYI, SHUL'GIN)

(GRIMMINGER, WILLIAMS, YOUNG)

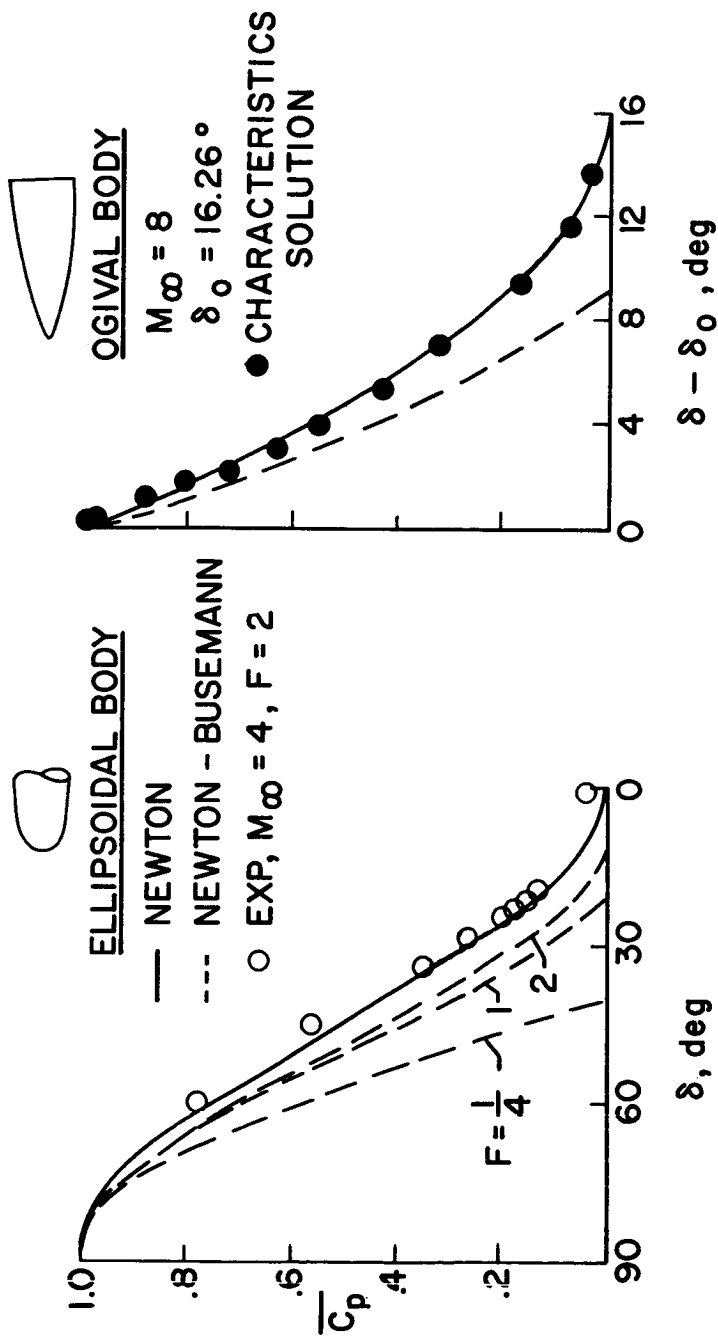
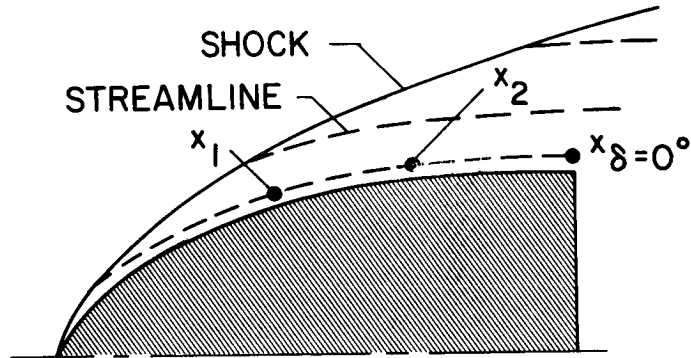


Figure 6.- Evaluation of Newton and Newton-Busemann pressure laws at moderate hypersonic speeds.  
 $\gamma = 7/5$ .

$$\begin{aligned} 9/7 \leq \gamma \leq 5/3 \\ 6 \leq M_\infty \leq 30 \\ 1/4 \leq F \leq 12 \end{aligned}$$

# BODY PROFILES: CONSTANT AND VARYING RADIUS OF CURVATURE



$$C_{p2}/C_{p1} = (\Delta x_2 / \Delta x_1)^2 \quad \text{FOR } M_\infty / F \geq 2$$

$$\begin{aligned} \text{FOR CONSTANT CURVATURE: } (\Delta x_2 / \Delta x_1)^2 &= \sin^2 \delta_2 / \sin^2 \delta_1 \\ C_{p2}/C_{p1} &= \sin^2 \delta_2 / \sin^2 \delta_1 \end{aligned}$$

Figure 7.- Flow-field examination by method of characteristics.

$$C_p = \varphi \sin^2 \delta$$

VARIATIONAL CALCULUS → MINIMUM-DRAG BODIES  
E.G., EGGERS, RESNIKOFF, DENNIS SOLUTIONS — ERD

$$I = \int_0^l \frac{\varphi y y'^3}{1 + y'^2} dx$$

ERD:  $\varphi = 2$  (NEWTON LAW)

Figure 8.- The  $\sin^2$  law and optimization analyses.

TO DETERMINE CONSTANTS THAT APPEAR IN THE EQUATION CHOSEN TO REPRESENT THE GIVEN DATA (EMPIRICAL OR THEORETICAL)

- PAIRS OF GIVEN VALUES:  $x_i, y_i$
- CHOSEN EQUATION:  $y = f(x)$
- RESIDUALS:  $R_i = f(x_i) - y_i$

METHOD OF AVERAGES:

- $\sum R_i = 0$ , DIFFERENT VALUES OF CONSTANTS POSSIBLE

METHOD OF LEAST SQUARES:

- BEST CURVE IS THAT FOR WHICH THE SUM OF THE SQUARES OF THE RESIDUALS IS A MINIMUM; UNIQUE SET OF VALUES FOR CONSTANTS

EXPONENTIAL RESIDUALS:

- $\sum R_i = 0$ , DIFFERENT VALUES OF CONSTANTS POSSIBLE
- ATTRACTIVE FOR RELATIONS THAT MUST HANDLE EXTENSIVE PLATEAUS. THE CHOSEN EQUATION IS ALWAYS IN EXPONENTIAL FORM
- $r/R = (x/L)^n$

Figure 9.- Residual procedures.



- (1) RESTRICTED TO SIMPLE AND COMPLEX POWER-LAW BODIES  
(COMPLEX:  $n$  IS A FUNCTION OF  $x$  AS WELL AS  $F$ )
- (2) PURPOSE: AVOID SHARP CORNERS OF VARIATIONAL BODIES  
AT SMALL  $F$
- (3) ISOPERIMETRIC CONSTRAINTS: LENGTH AND DIAMETER  
LENGTH AND VOLUME
- (4) PRESSURE LAWS: VARIED
- (5) ENVIRONMENT: PRACTICAL FLIGHT REGIMES,  $1 < M_{\infty} < \infty$
- (6)  $0.1 \lesssim F \lesssim 100$ , ALSO  $F \rightarrow \infty$  (LIMITED)
- (7) SHAPE FACTOR FOR COMPLEX POWER-LAW BODIES ( $z$ -AND- $v$  CONSTRAINT)  
 $(1 - \frac{x}{l})^a$  WHERE  $a = \frac{2}{5} + \frac{1}{20} (\frac{x}{l})^2$

BASIS FOR CHOICE:

- WHEN  $\sin^2$  LAW USED, DERIVED SHAPE TO AGREE ESSENTIALLY WITH  
OPTIMUM SHAPE FOR LARGE  $F$  AS DERIVED BY  
VARIATIONAL SOLUTION WITH  $\sin^2$  LAW
- A CONNECTING LINK FOR RELATING EFFECTS OF OTHER PRESSURE  
LAWS TO EARLIER WORK, AND ACHIEVES ITEM (2)

Figure 10.- Exponential residual solutions for minimum-drag power-law bodies.

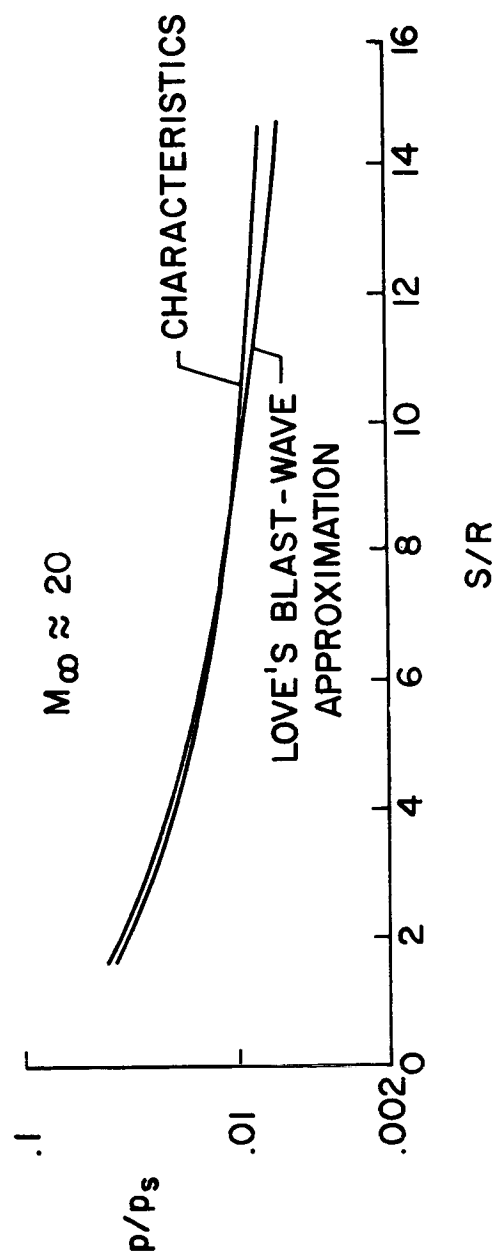


Figure 11.- Induced pressures from spherical blunting, hemisphere-cylinder.

$n_1 = \frac{3}{4} f$	$n_2 = \frac{3}{4} f^m$
<p><u>AT LARGE F:</u></p> <p>SIN<sup>2</sup> LAW</p> <p><math>\varphi = 2(\gamma + 1)(\gamma + 7)/(\gamma + 3)^2</math></p> <p><u>AT SMALL F:</u></p> <p>PROBSTEIN APPROX. NEAR STAGNATION POINT, WHERE IT GIVES LOWER <math>C_p</math> THAN SIN<sup>2</sup> LAW WITH</p> <p><math>\varphi = (\gamma + 3) / (\gamma + 1)</math></p> <p><u>AT INTERMEDIATE F:</u></p> <p>BLAST-WAVE PRESSURE LAW FOR ESTIMATING LIMIT OF INDUCED PRESSURES FROM BLUNTING</p>	<p><u>AT LARGE F:</u></p> <p>UNMODIFIED SHOCK - EXPANSION WITH SUBSTITUTION OF CONICAL TIP (<math>\delta = 45^\circ</math>)</p> <p><u>AT SMALL F:</u></p> <p>SAME AS <math>n_1</math></p>
<p><u>CONSTANTS:</u></p> <p><math>m = 1 + \frac{9}{44} F^k</math></p> <p><math>k = \frac{96}{5} \left( F^{\frac{20}{61}} + 85 \right)^{-\frac{1}{2}}</math></p>	<p><u>CONSTANT:</u></p> <p><math>f = F(1 + F^2)^{-\frac{1}{2}}</math></p>

Figure 12.- Exponential residual solutions; 1-and-d constraint; simple power-law bodies.

$$\frac{C_p}{(C_p \text{ EXACT})_{x/l=0}}$$

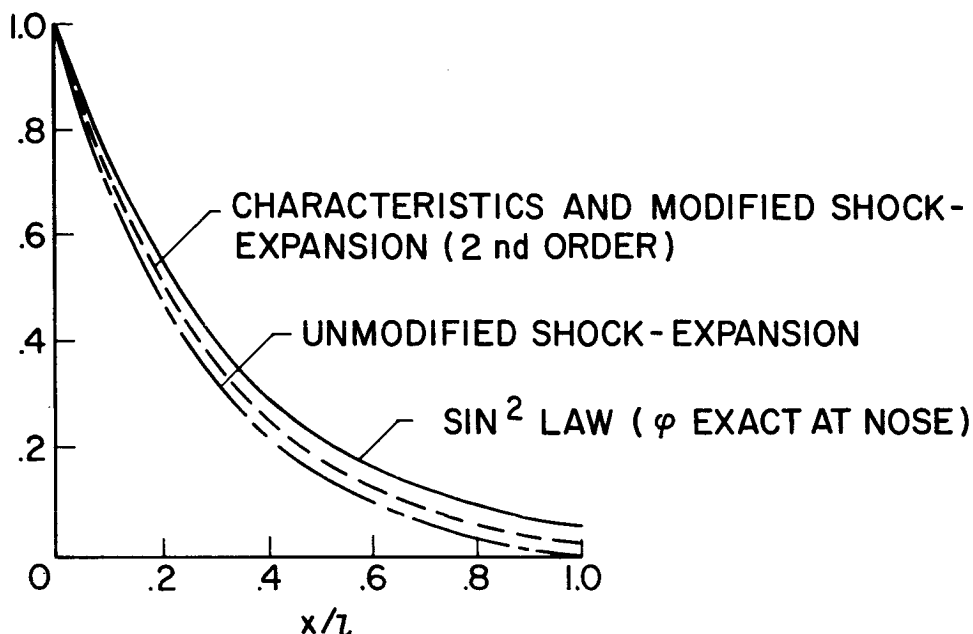


Figure 13.- Comparison of pressure-prediction methods.

$$n_3 = \frac{3}{4} f^{mg} \left(1 - \frac{x}{l}\right)^a$$

$$n_4 = \frac{3}{4} \left(\frac{2Fb}{1+2Fb}\right)^g \left(1 - \frac{x}{l}\right)^a$$

REF. AREA: PLANFORM  
CONSTANTS:

$g=1$ :  $\text{SIN}^2$  LAW THROUGHOUT

$g=1 + \frac{7}{9} f^3$ :

$\text{SIN}^2$  LAW AT SMALL  $F$

2<sup>nd</sup> ORDER SHOCK -

EXPANSION AT LARGE  $F$

INTERMEDIATE  $F$  HANDLED  
AS IN  $n_1$

REF. AREA:  $l^2$

CONSTANTS:

$g=1$ :  $n_1$  APPROACH

$g=1 + \frac{7}{9} f^3$ :  $n_2$  APPROACH BUT  
WITH 2<sup>nd</sup> ORDER  
SHOCK-EXPANSION  
AT LARGE  $F$

$$b = \frac{10}{33} + \frac{13}{8} F^{-\frac{4}{5}}$$

Figure 14.- Exponential residual solutions;  $l$ -and- $V$  constraint;  
complex power-law bodies.

LIMITS:  $5 \lesssim F \lesssim 100$

$$n_5 \approx \frac{2}{3} \left(1 - \frac{x}{l}\right)^q \quad (g=1)$$

$$\frac{r}{R} \approx \text{SIN}^q \left( \frac{\pi x}{2l} \right) \quad (g=1)$$

$$n_6 \approx \frac{14}{23} \left(1 - \frac{x}{l}\right)^q \quad \left(g = 1 + \frac{7}{9} f^3\right)$$

$$\text{WHERE: } q = \frac{3}{4} + \frac{1}{4} \text{TAN} \left( \frac{\pi x}{2l} \right)$$

Figure 15.- Pseudo-slender-body exponential residual solutions;  
l-and-V constraint; complex power-law bodies.

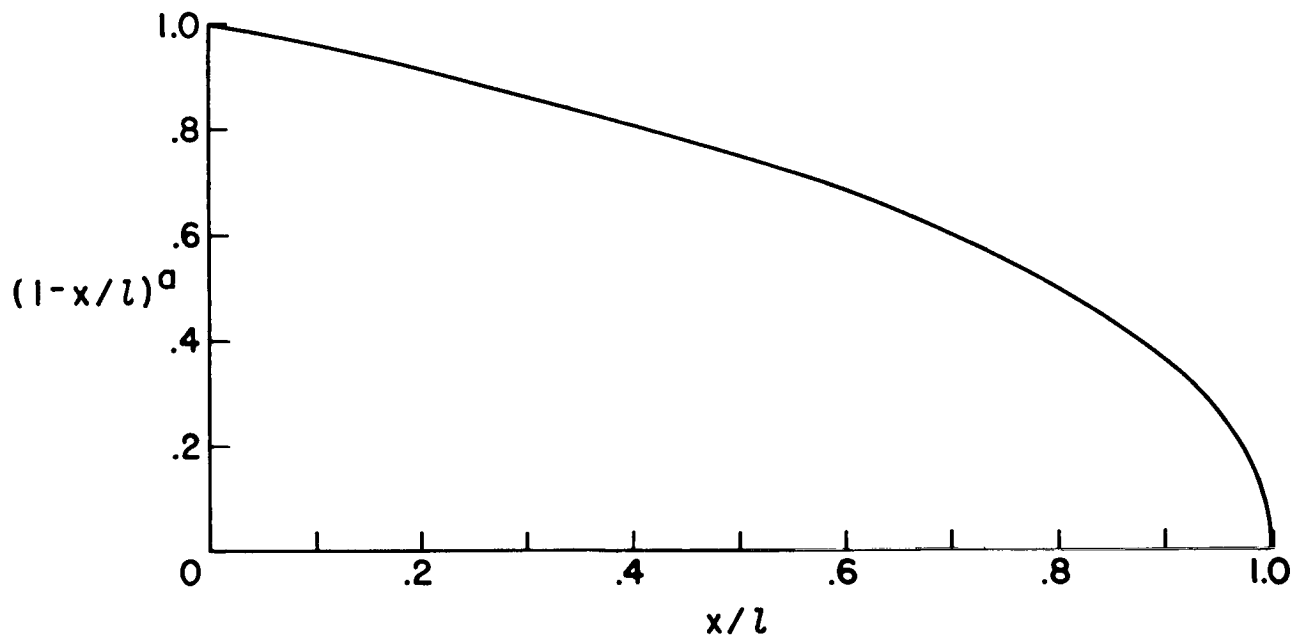


Figure 16.- Variation of shape factor with  $x/l$ ; l-and-V constraint.

CONSTRAINT	F	$\frac{r_{45}}{R}$	$\frac{x_{45}}{L}$
$l$ - AND - $d$	3.00	0.0123	0.002
$l$ - AND - $V$	5.84	0.0116	0.001

$r_{45}$  RADIUS AT POINT ON BODY WHERE  $\delta = 45^\circ$

$x_{45}$  AXIAL LENGTH OF CONICAL TIP WITH  $\delta = 45^\circ$

Figure 17.- Portion of body affected by substitution of conical tip.

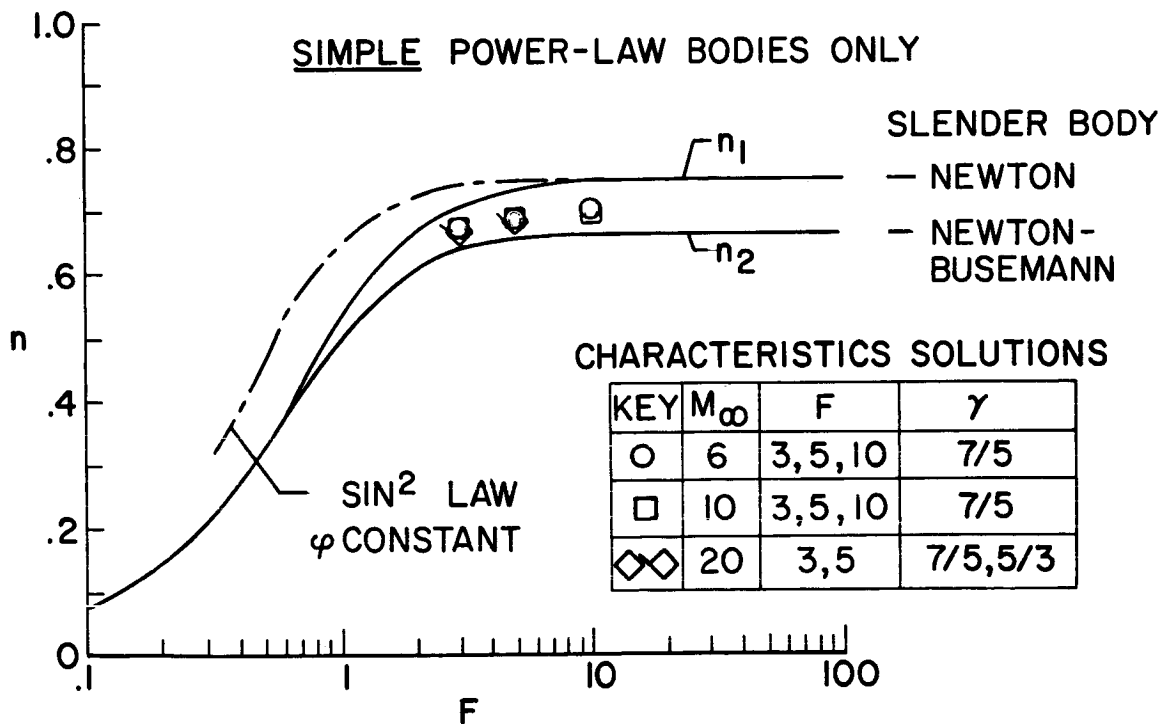
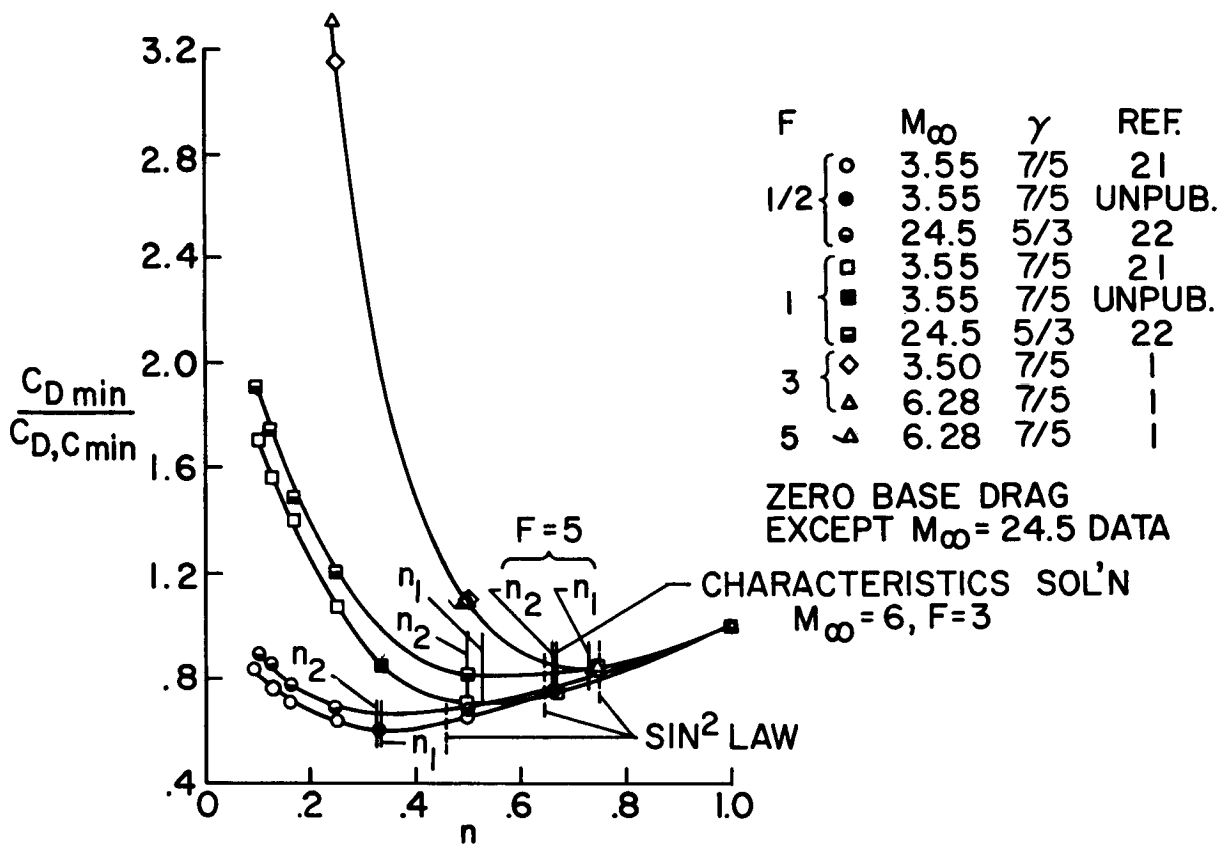
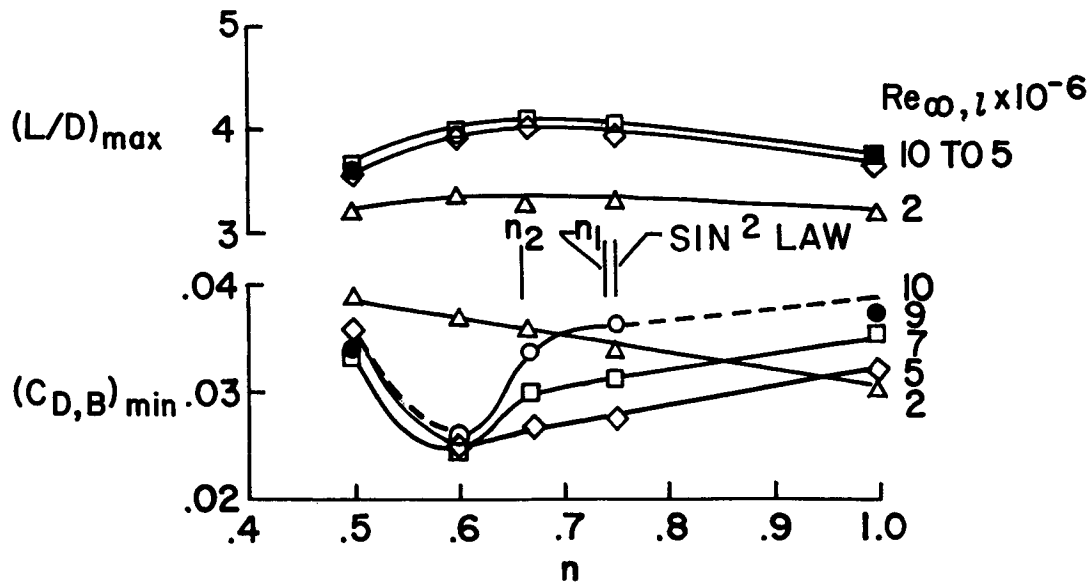


Figure 18.- Variation of optimum value of exponent with fineness ratio;  $l$ -and- $d$  constraint.

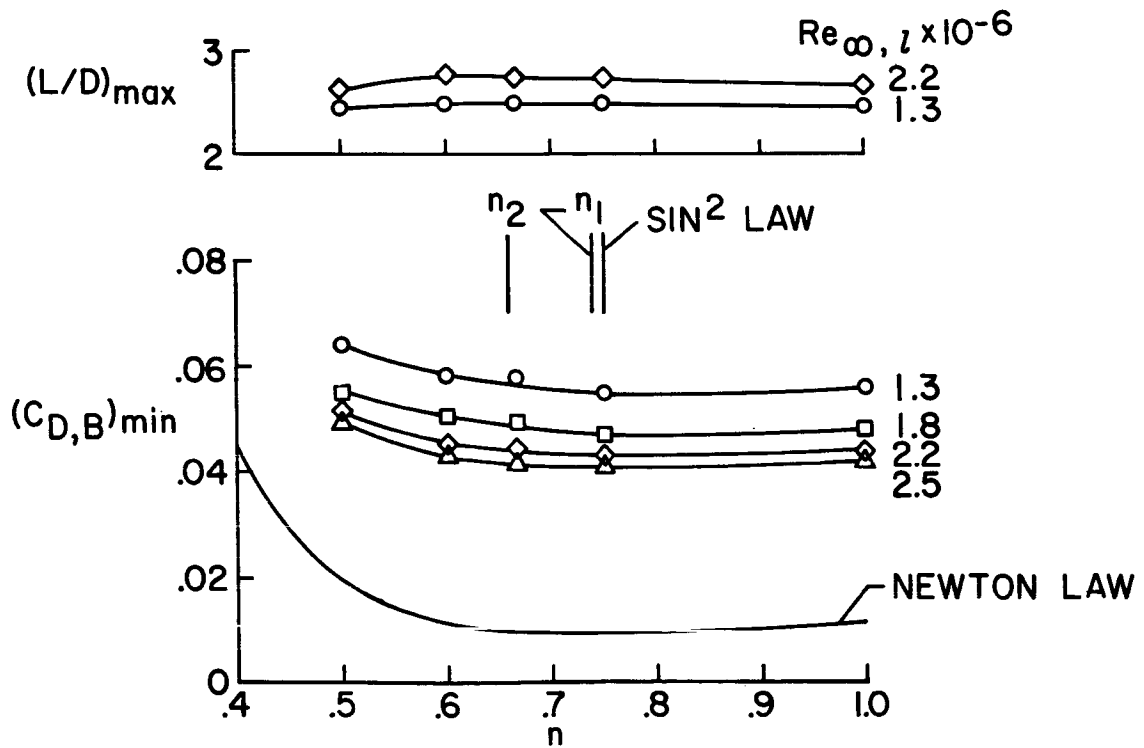


(a)  $F \leq 5$ ;  $3.5 \lesssim M_\infty \lesssim 24.5$ .

Figure 19.- Comparison of predictions of optimum exponent with experiment;  
l-and-d constraint.



(b)  $F = 6.63$ ;  $M_{\infty} = 6.0$ ;  $\gamma = 7/5$ .



(c)  $F = 6.63$ ;  $M_{\infty} = 10.4$ ;  $\gamma = 7/5$ .

Figure 19.- Concluded.



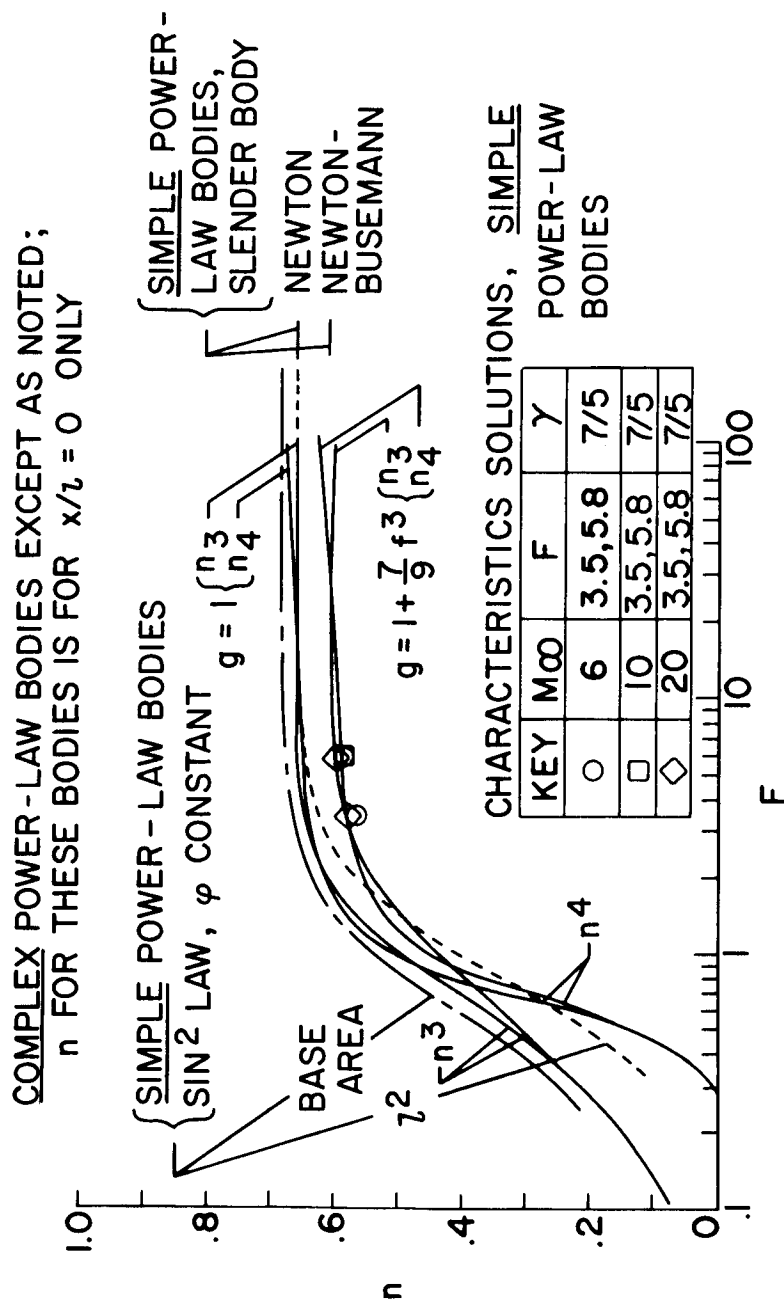


Figure 20.- Variation of optimum value of exponent with fineness ratio,  $l$ -and- $V$  constraint.

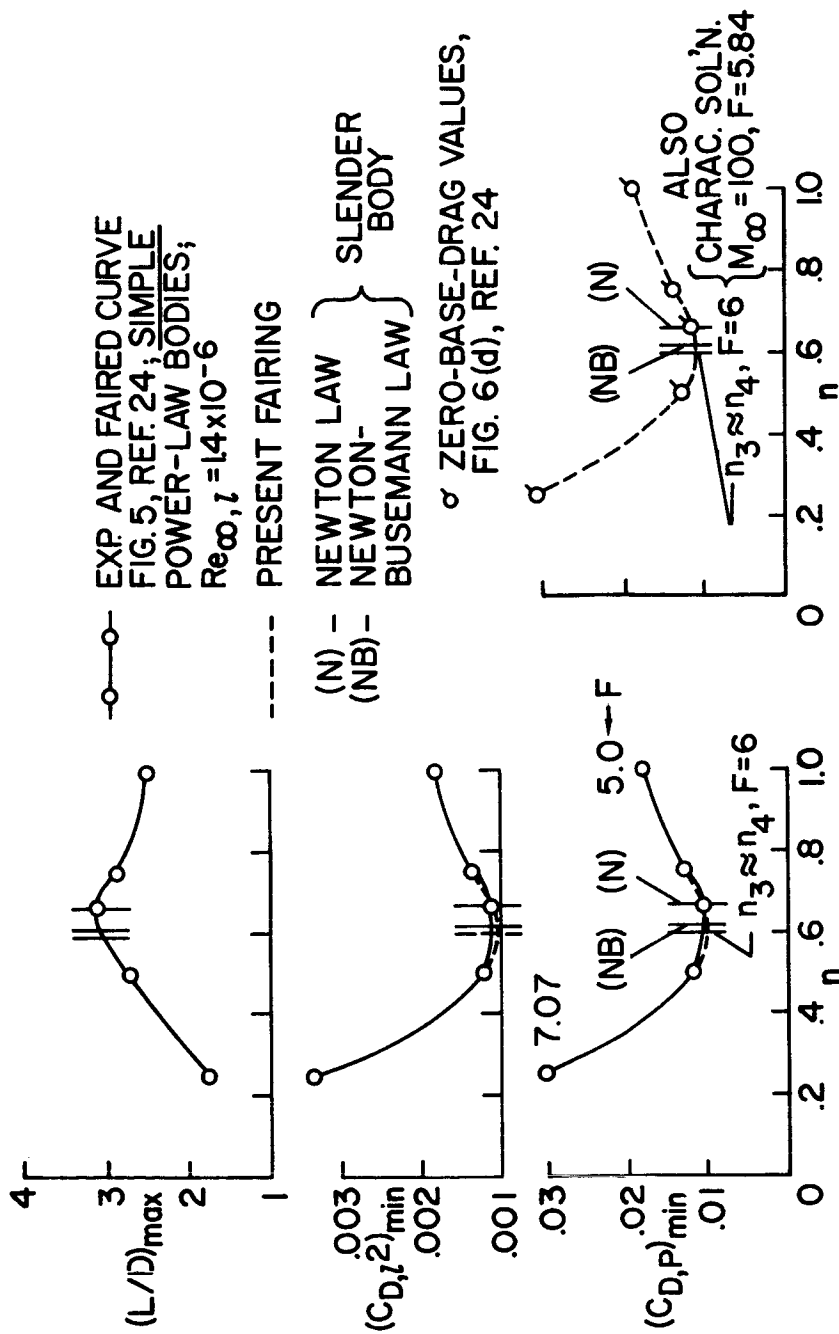
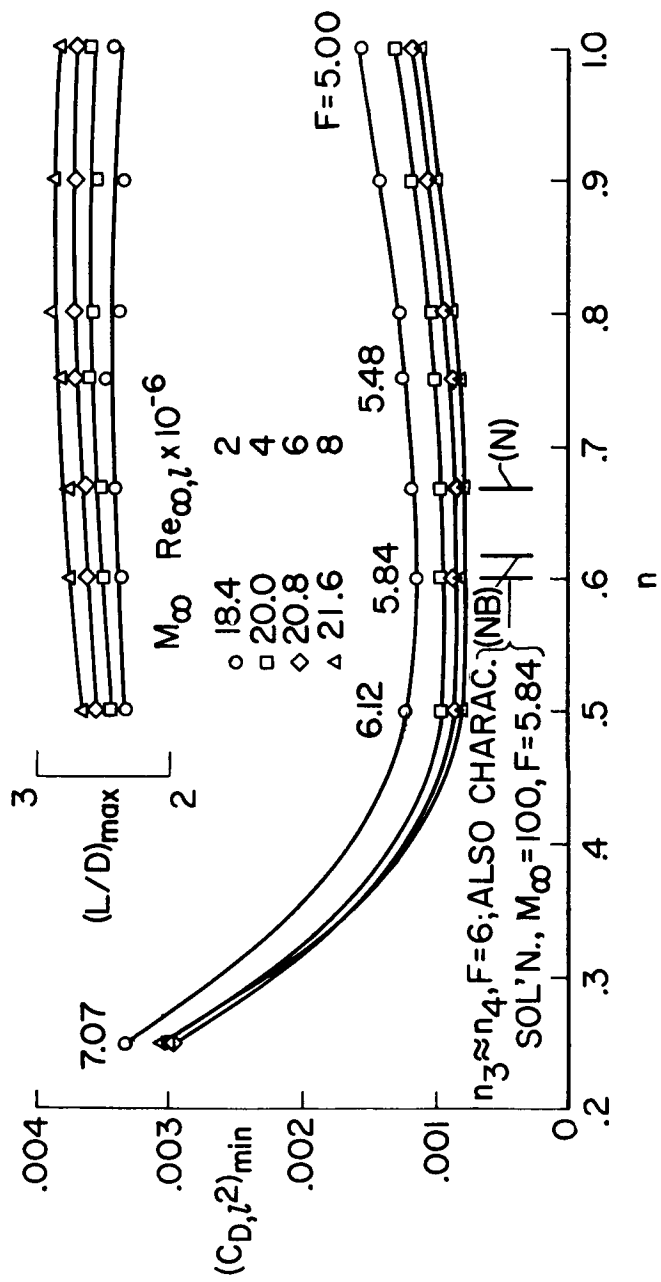
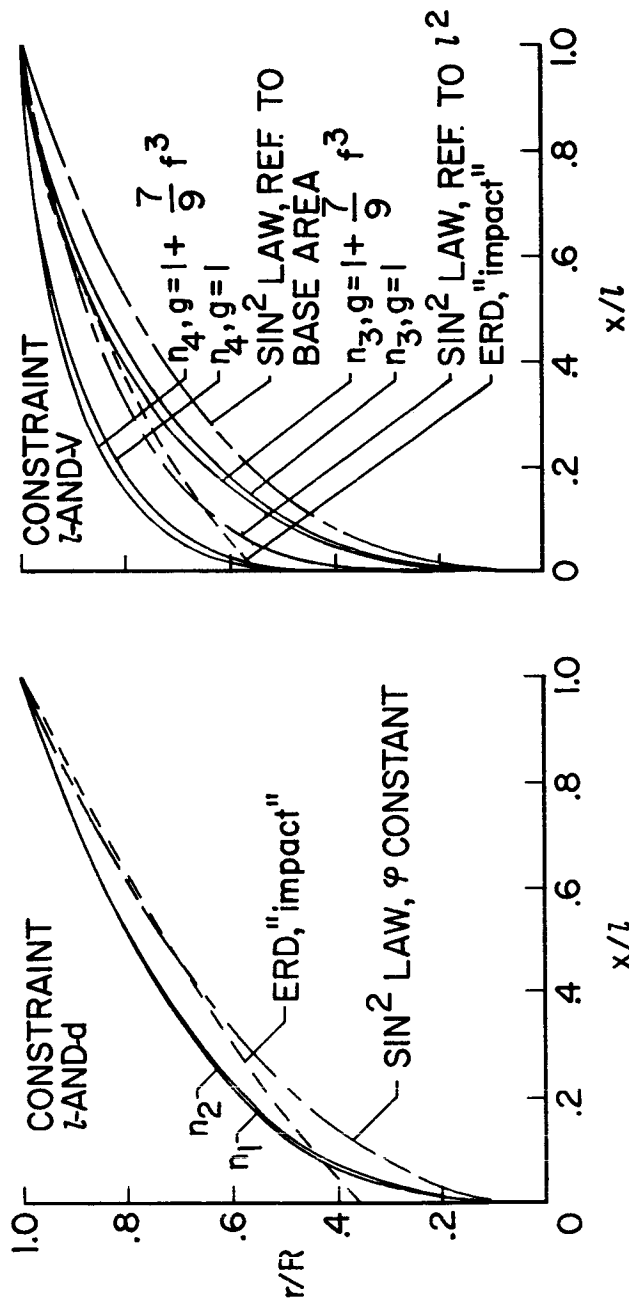


Figure 21.- Comparison of predictions of optimum exponent with experiment; l-and-V constraint.



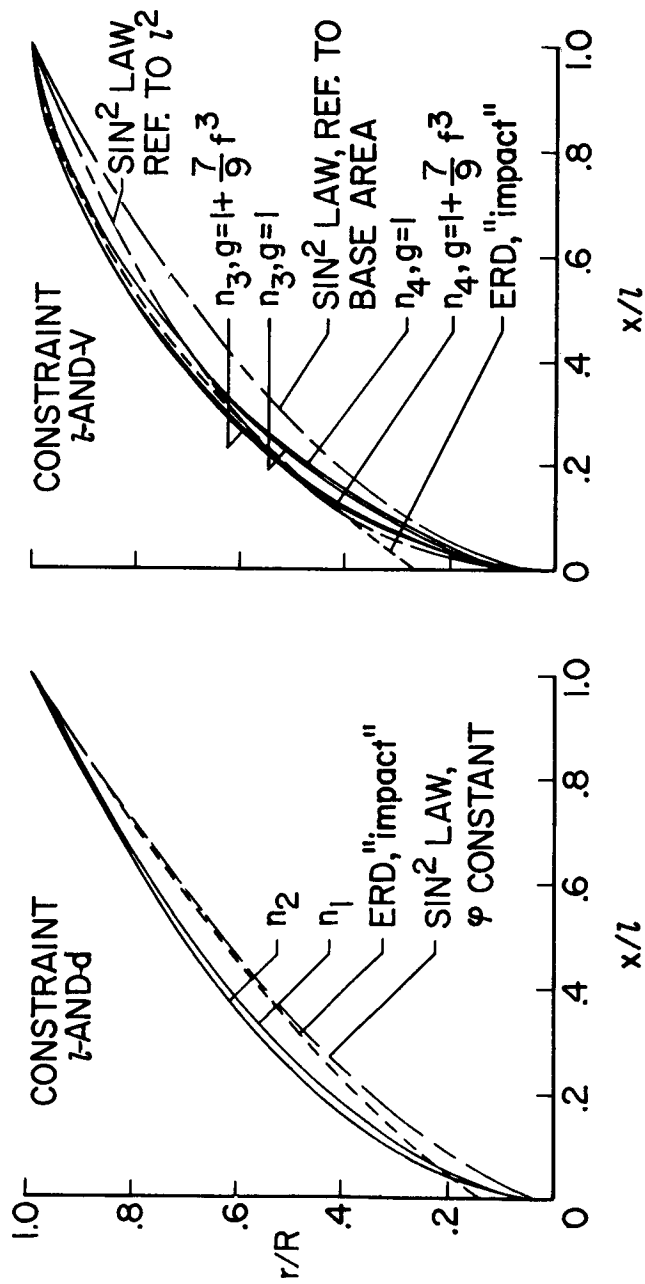
(b)  $M_\infty \approx 20; \gamma = 5/3.$

Figure 21.- Concluded.



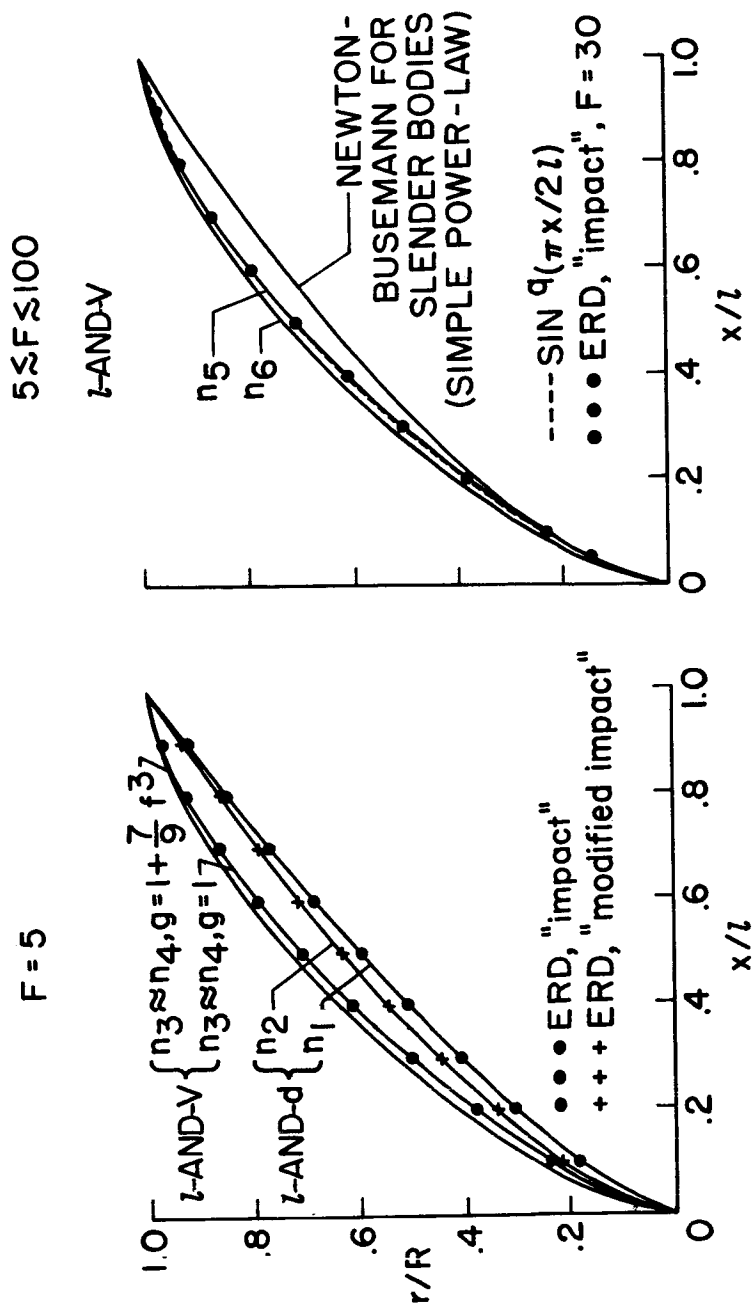
(a)  $F = 1/2$ .

Figure 22.- Comparison of body shapes.



(b)  $F = 1.$

Figure 22.- Continued.



(c)  $5 \lesssim F \lesssim 100$ .

Figure 22.- Concluded.

# FEATURES IDENTICAL FOR ALL BODIES:

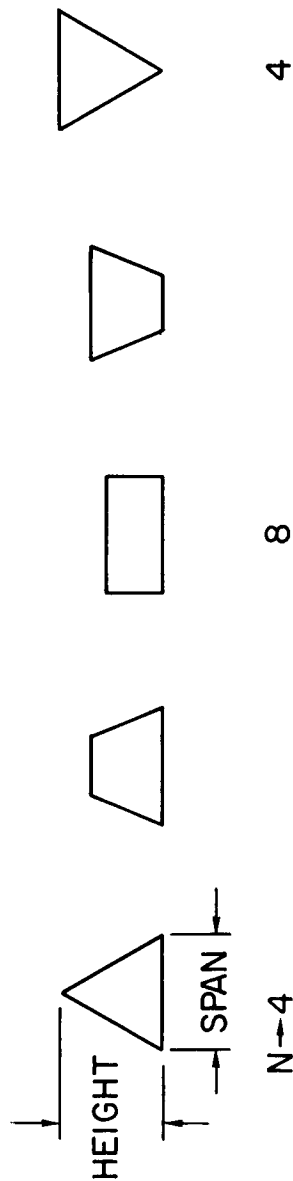
LENGTH

VOLUME

PLANFORM AREA

LONGITUDINAL DISTR. OF CROSS-SECTIONAL AREA

SPAN



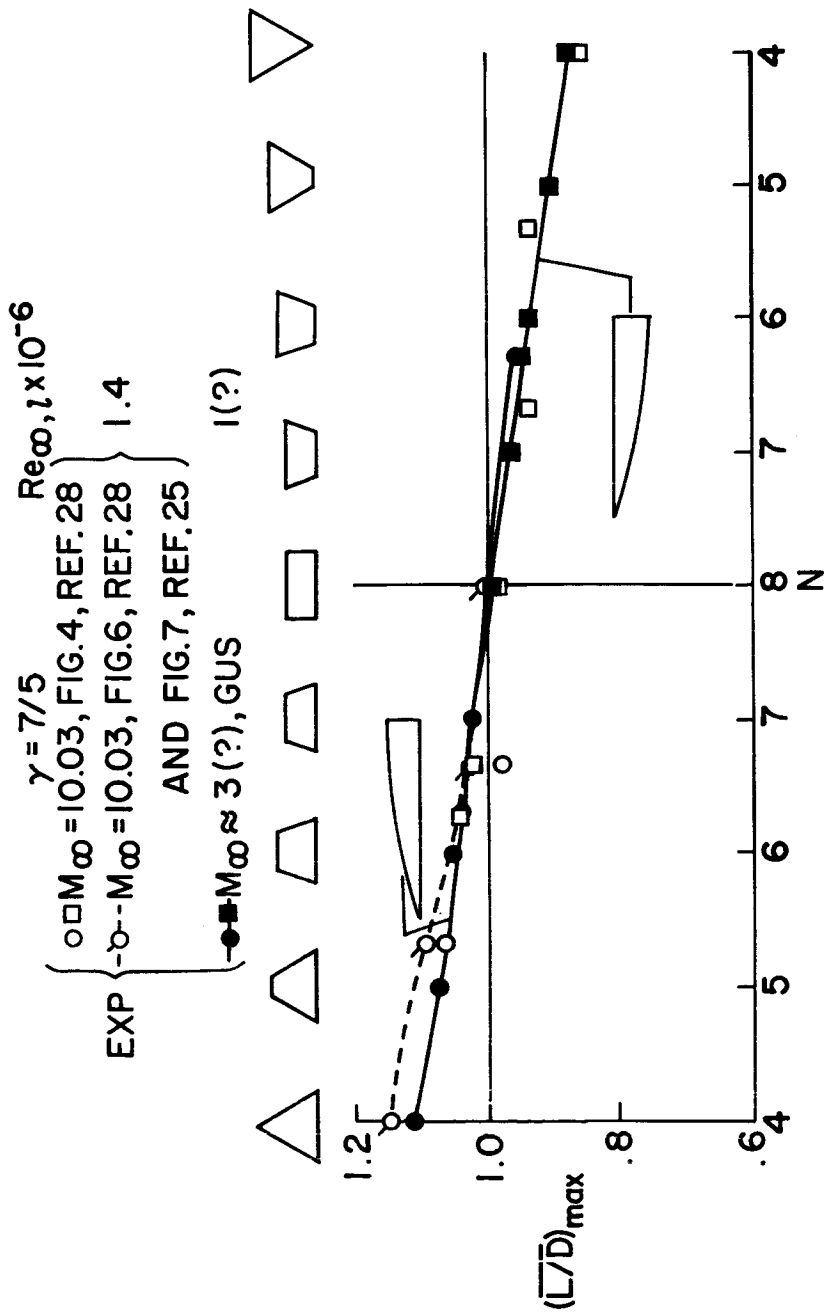
$$N = \pi \left( \frac{\text{SPAN}}{\text{HEIGHT}} \right)$$

REFERENCE HALF-BODY; SEMICIRCULAR CROSS SECTION;  $N = 2\pi$

GUS DATA: OGIVE;  $F = 3.5$

SPENCER AND OTHER DATA: ERD BODY (L-AND-V CONSTRAINT);  
 $F = 3.54$

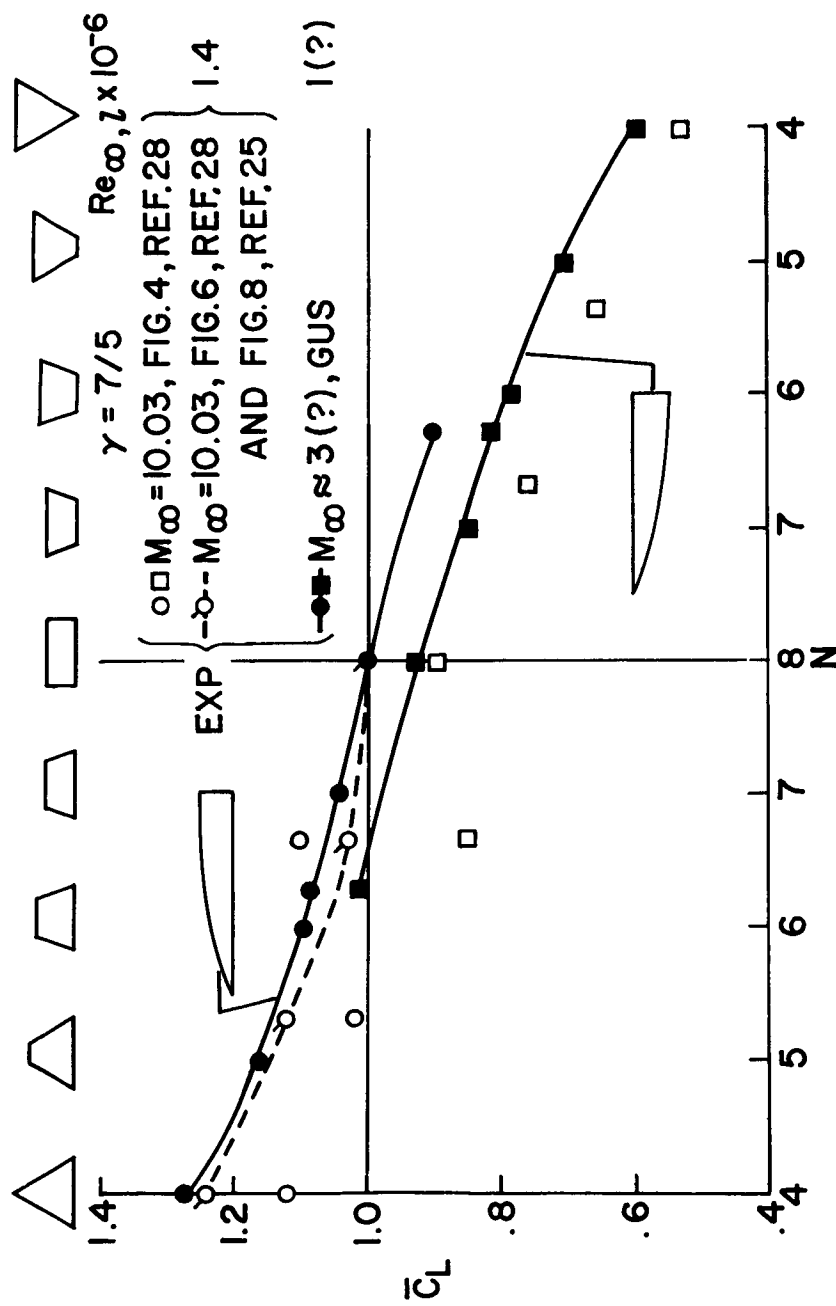
Figure 23.- Trapezoidal body family.



(a) Effect of span-height ratio and camber upon  $(\overline{L/D})_{\max}$ .

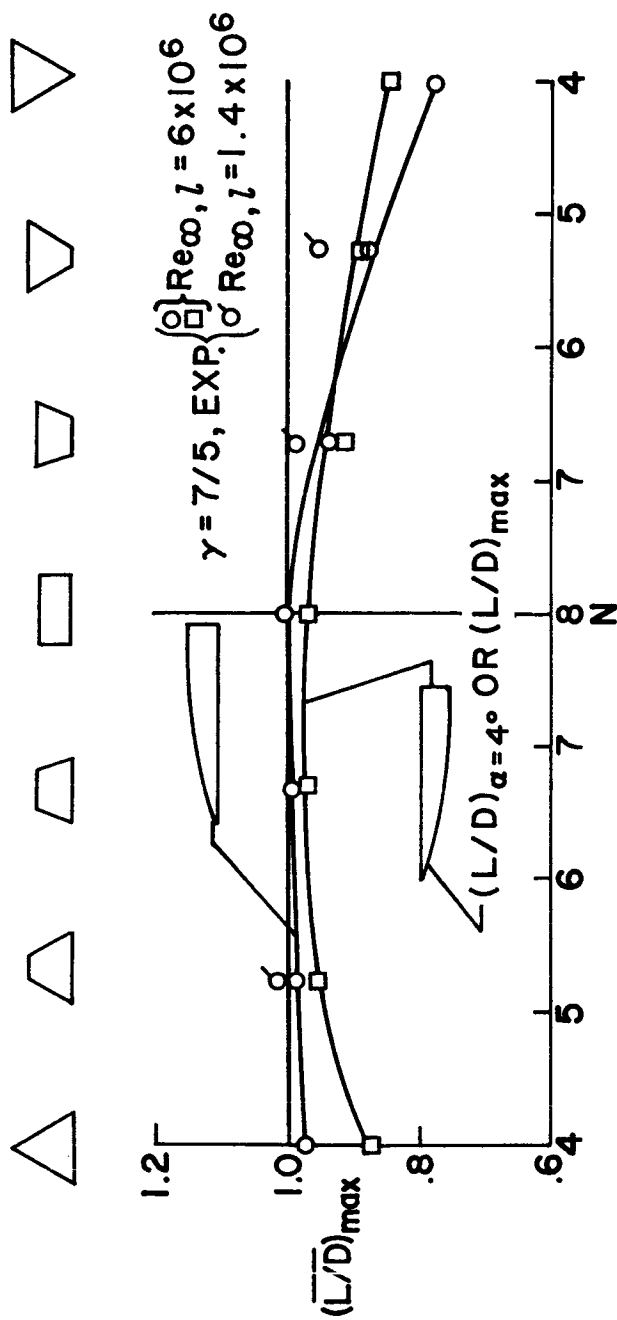
Figure 24.- Trapezoidal family. Comparison of Spencer's data and GUS data.



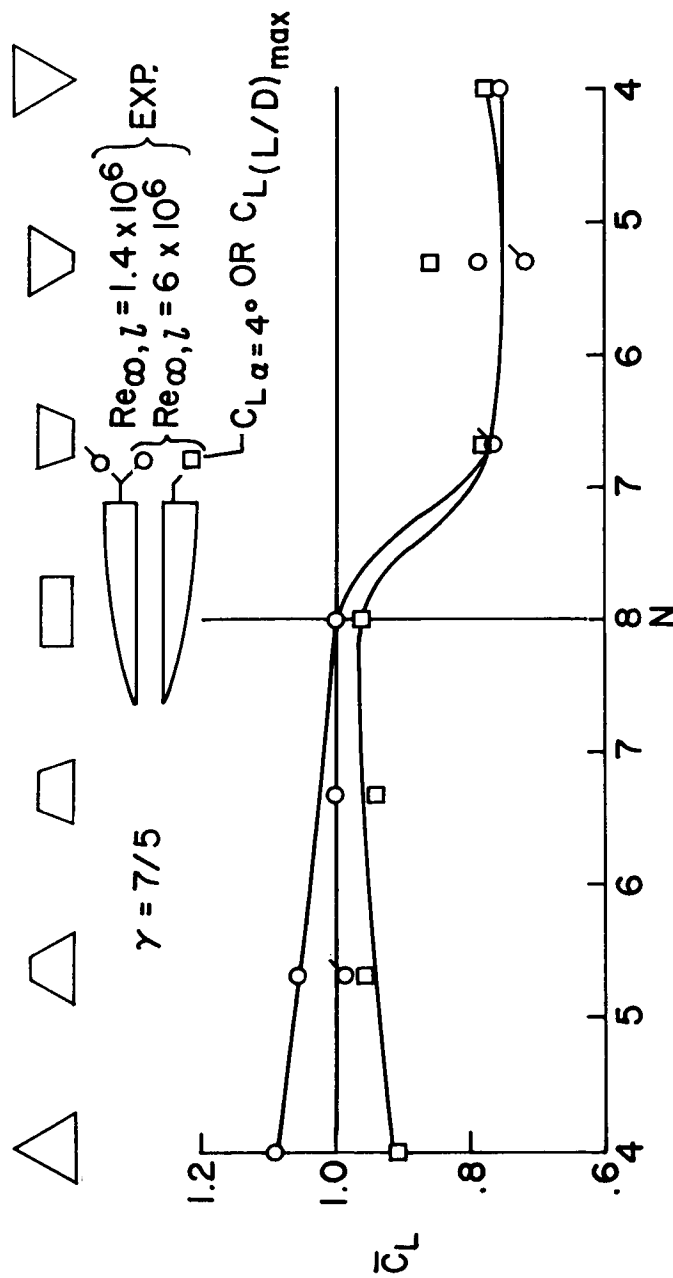


(b) Effect of span-height ratio and camber upon  $\bar{C}_L$ .

Figure 24.- Concluded.

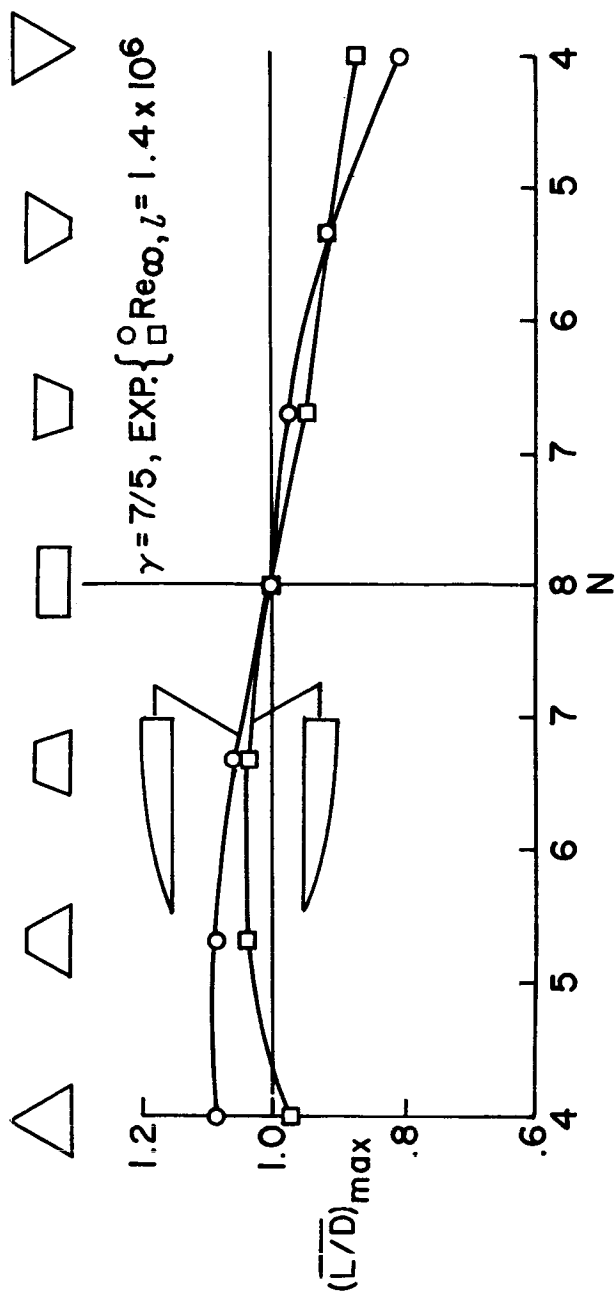


(a) Effect of span-height ratio and camber upon  $(L/D)_{\max}$ .  
 Figure 25.- Trapezoidal family. Experimental data at  $M_\infty = 6.0$ .



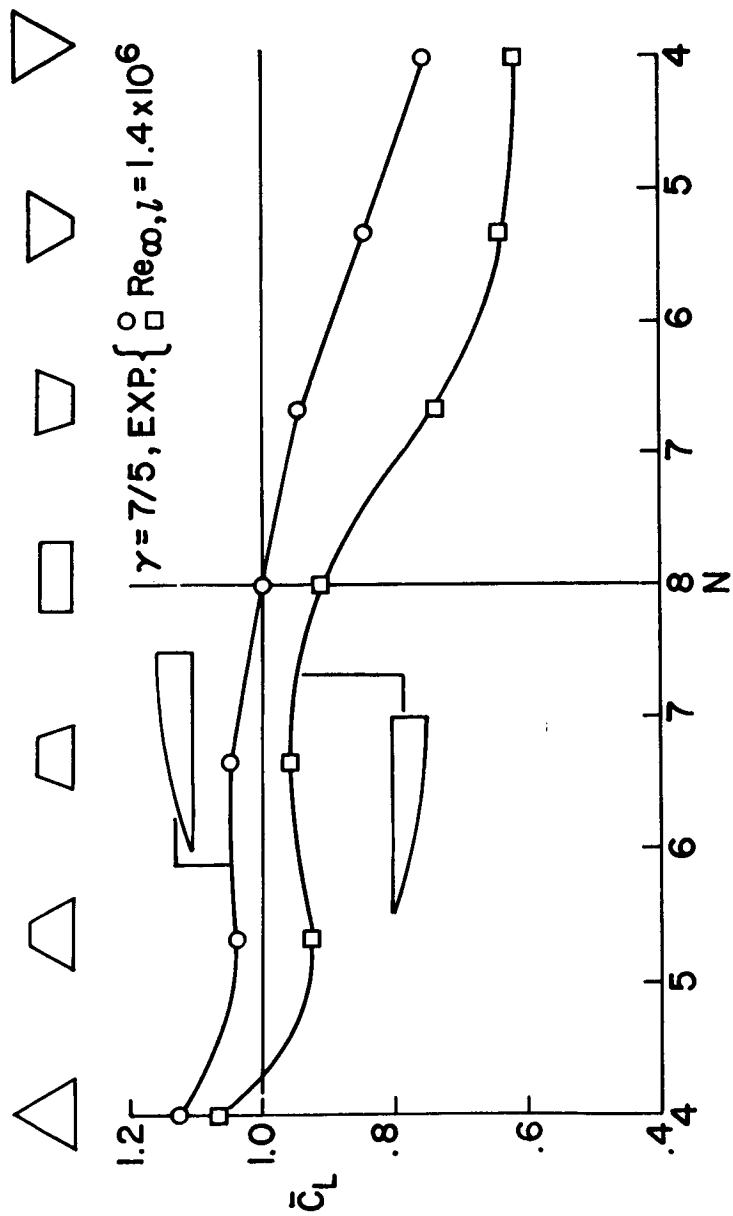
(b) Effect of span-height ratio and camber upon  $\bar{C}_L$ .

Figure 25.- Concluded.



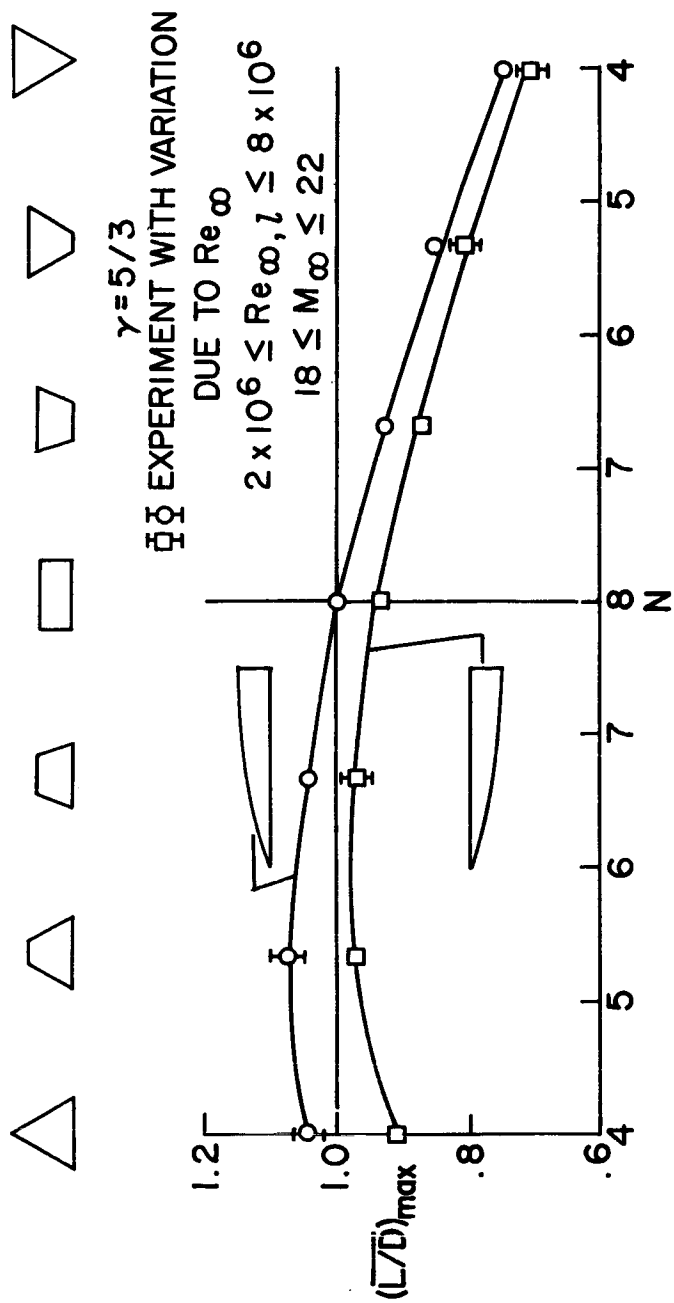
(a) Effect of span-height ratio and camber on  $(\overline{L/D})_{\max}$ .

Figure 26.- Trapezoidal family. Experimental data at  $M_\infty = 10.4$ .



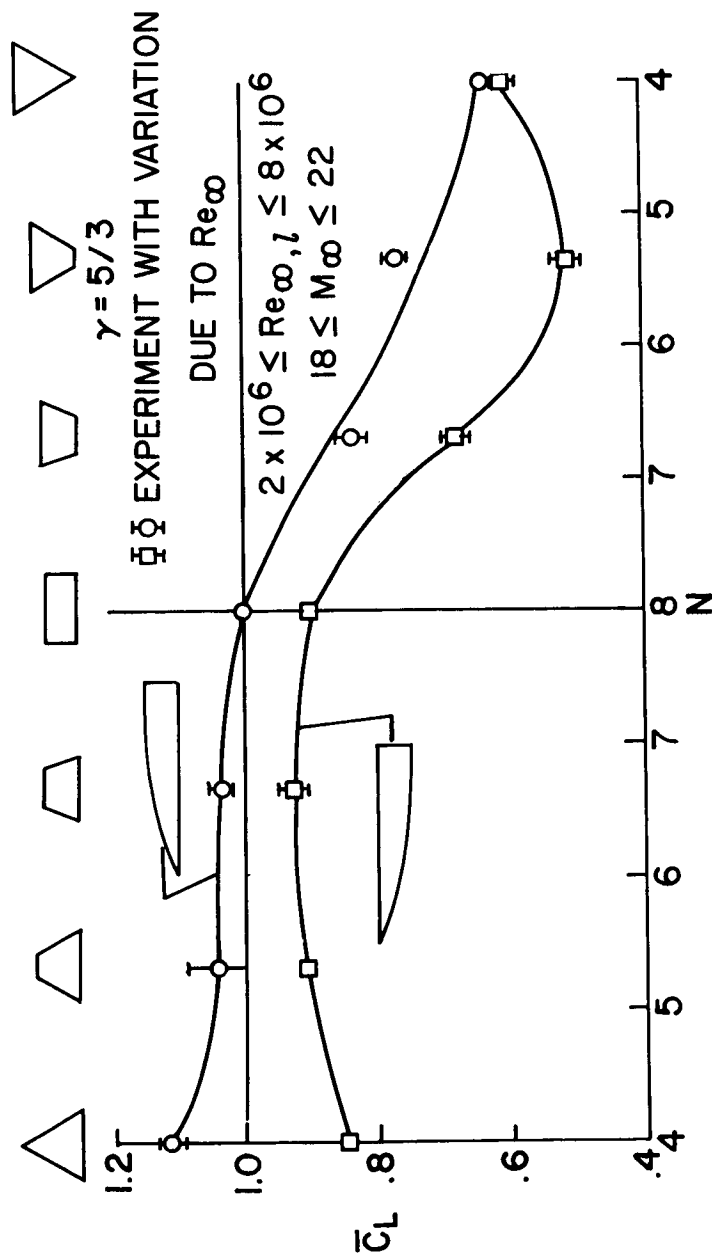
(b) Effect of span-height ratio and camber on  $\bar{C}_L$ .

Figure 26.- Concluded.



(a) Effect of span-height ratio and camber upon  $(L/D)_{max}$ .

Figure 27.- Trapezoidal family. Experimental data at  $M_\infty \approx 20$ .



(b) Effect of span-height ratio and camber upon  $\bar{C}_L$ .

Figure 27.- Concluded.

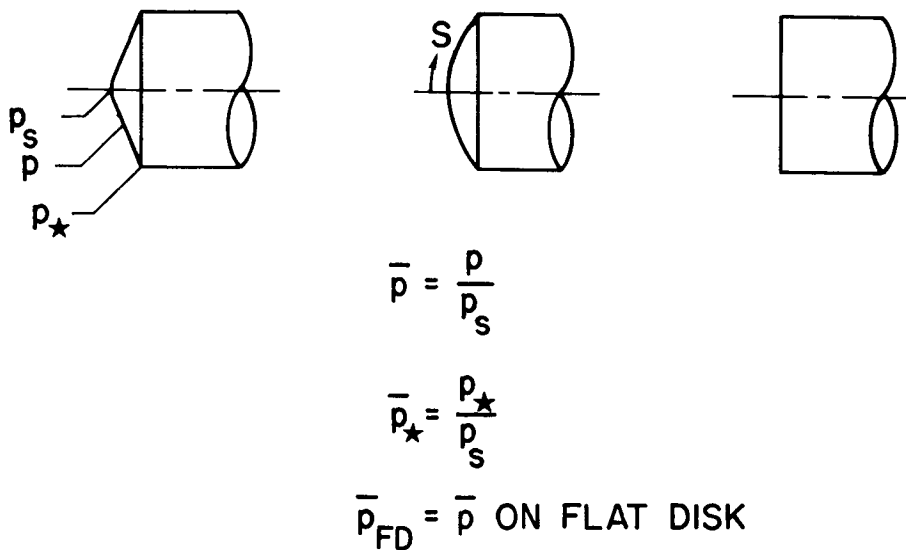
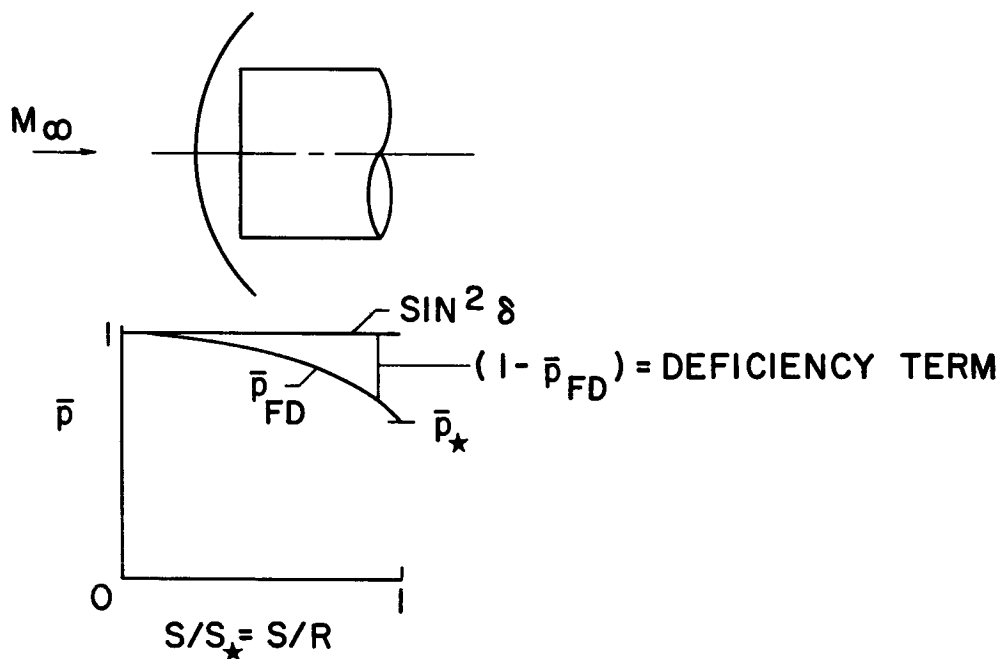


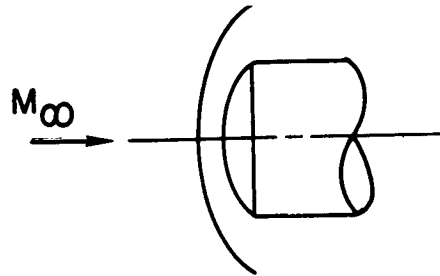
Figure 28.- Illustrative basic blunt shapes and pressure parameters ( $0 \leq S \leq S_\star$ ).



BASIS OF  
APPROXIMATION :  $\bar{p} = \sin^2 \delta - \text{DEFICIENCY}$   
 $\bar{p} = \sin^2 \delta - (1 - \bar{p}_{FD})$

Figure 29.-  $\sin^2$  deficiency for flat disk.





APPROACH: APPLY DEFICIENCY TERM AT CORRESPONDING  $S/S_\star$   
IN PROPORTION TO  $\Delta \bar{p} / \Delta \bar{p}_{\text{MAX}}$

$$\text{WHERE } \begin{cases} \Delta \bar{p} = \bar{p} - \bar{p}_\star = \text{SIN}^2 \delta - \bar{p}_\star \\ \Delta \bar{p}_{\text{MAX}} = \bar{p}_S - \bar{p}_\star = 1 - \bar{p}_\star \end{cases}$$

$$\bar{p} = \text{SIN}^2 \delta - (1 - \bar{p}_{\text{FD}}) \left( \frac{\text{SIN}^2 \delta - \bar{p}_\star}{1 - \bar{p}_\star} \right)$$

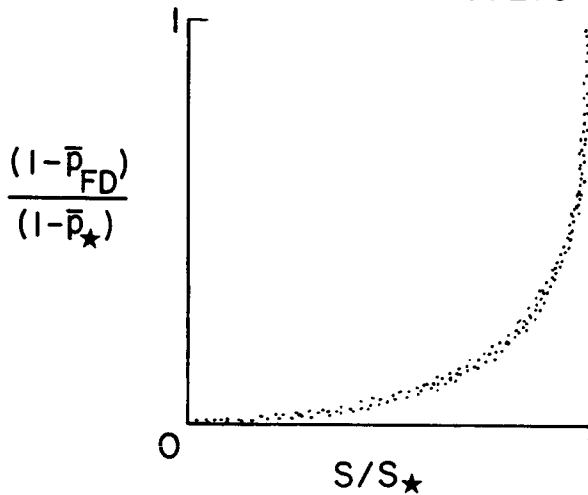
$$\bar{p}_\star = \left( \frac{2}{\gamma + 1} \right)^{\frac{\gamma}{\gamma - 1}}$$

Figure 30.-  $\text{Sin}^2$ -deficiency method for smoothly contoured convex blunt bodies.

NUMERICAL SOLUTION FOR  $\bar{p}_{FD}$ , SEVERAL VALUES OF  $\gamma$

- a) VARIABLE STREAM-TUBE-AREA APPROXIMATION FOR SHOCK SHAPE - (DIRECT METHOD)
- b) DEPARTURE POINT FOR GARABEDIAN-LIEBERSTEIN CALCULATIONS-(INVERSE METHOD)
- c) ITERATIONS

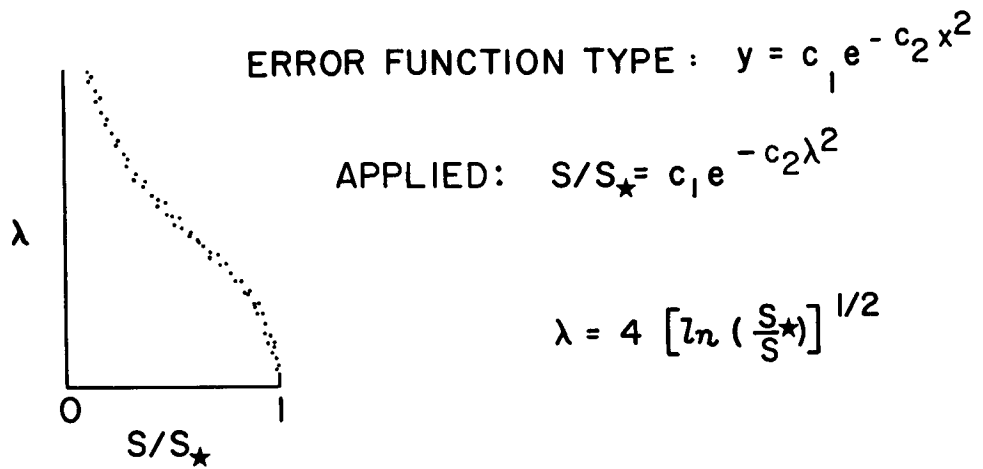
NUMERICAL RESULTS



$$\therefore \text{LET } \frac{(1 - \bar{p}_{FD})}{(1 - \bar{p}_{\star})} = e^{-\lambda}$$

EVALUATE  $\lambda$  vs  $S/S_{\star}$

Figure 31.- Development of solution for  $\bar{p}_{FD}$ .



$$\text{SINCE } \bar{p}_{FD} = 1 - e^{-\lambda} (1 - \bar{p}_*)$$

$$\text{FOR } \gamma = 7/5,$$

$$\bar{p}_{FD} = 1 - 0.472 e^{-\lambda}$$

Figure 32.- The  $\bar{p}_{FD}$  solution via error function.

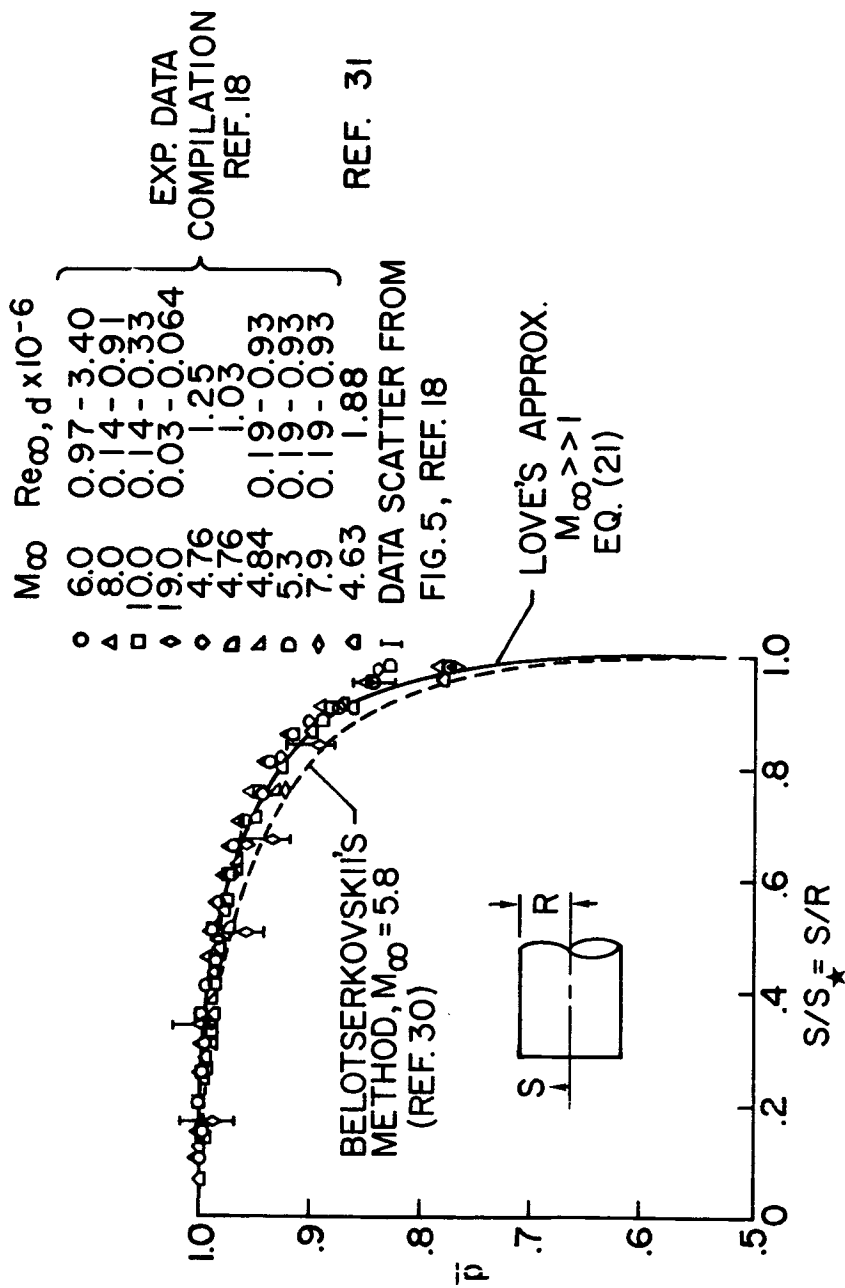


Figure 33.- Pressure distribution over flat disk.

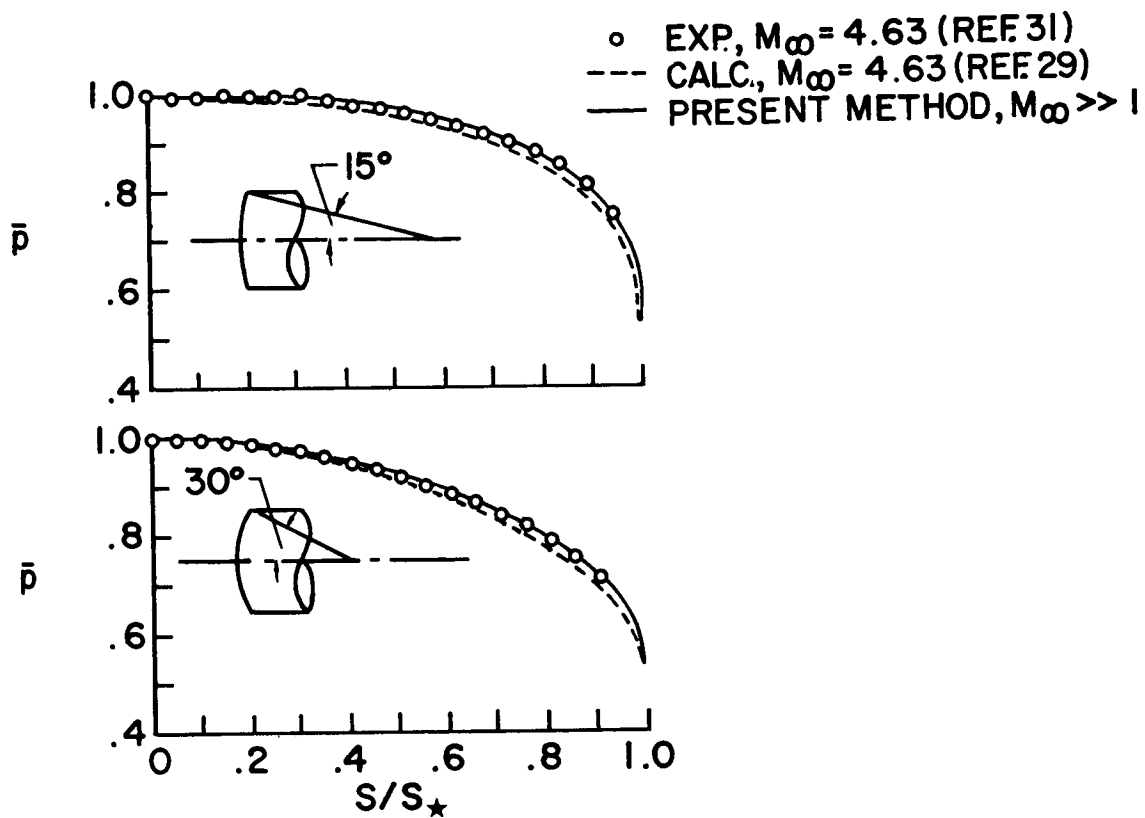
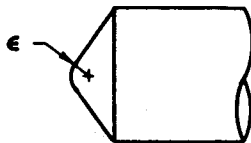
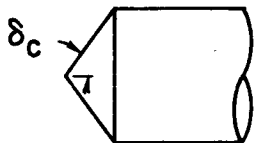


Figure 34.- Pressure distribution over spherical caps.

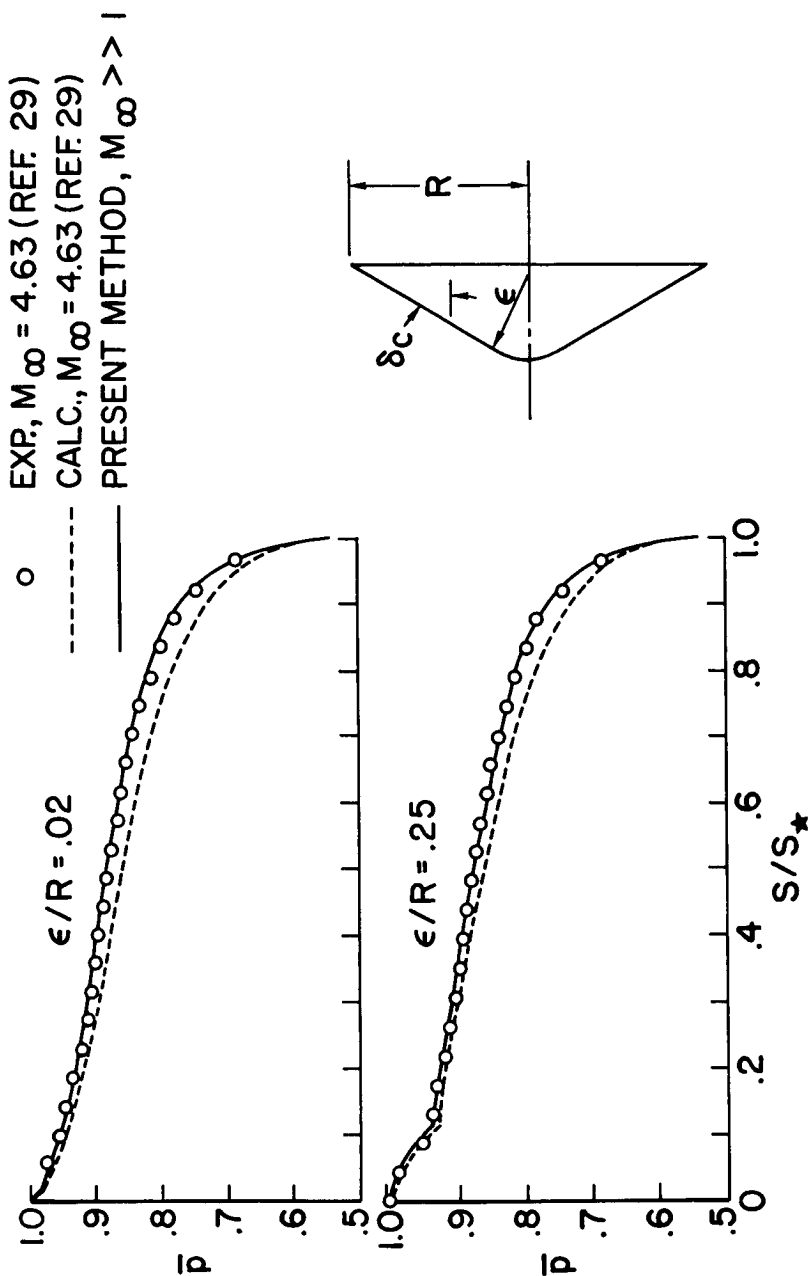


SPHERICAL BLUNTING TANGENT  
TO CONE SURFACE

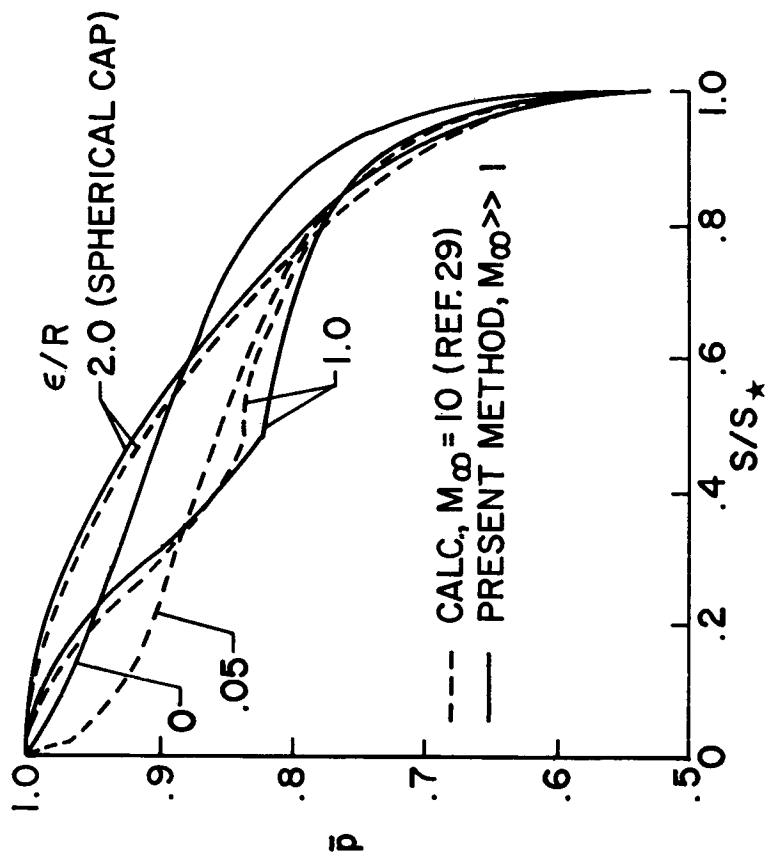
$\epsilon, \epsilon_0$  : NOSE RAD. & MAX. NOSE RAD.

$$\begin{aligned} \bar{p} = & \sin^2 \delta - (1 - \bar{p}_{FD}) \left( \frac{\sin^2 \delta - \bar{p}_\star}{1 - \bar{p}_\star} \right) \\ & + \left( 1 - \frac{\epsilon}{\epsilon_0} \right) \left\{ (1 - \sin^2 \delta)(1 - S/S_\star) + \frac{S/S_\star}{2} \left[ \bar{p}_{FD} - 1 + S/S_\star(1 - \sin^2 \delta) \right. \right. \\ & \left. \left. + (1 - \bar{p}_{FD}) \left( \frac{\sin^2 \delta - \bar{p}_\star}{1 - \bar{p}_\star} \right) \right] \right\} \end{aligned}$$

Figure 35.-  $\sin^2$ -deficiency method for sharp and blunted cones ( $\delta_c > \delta_{c\star}$ ).



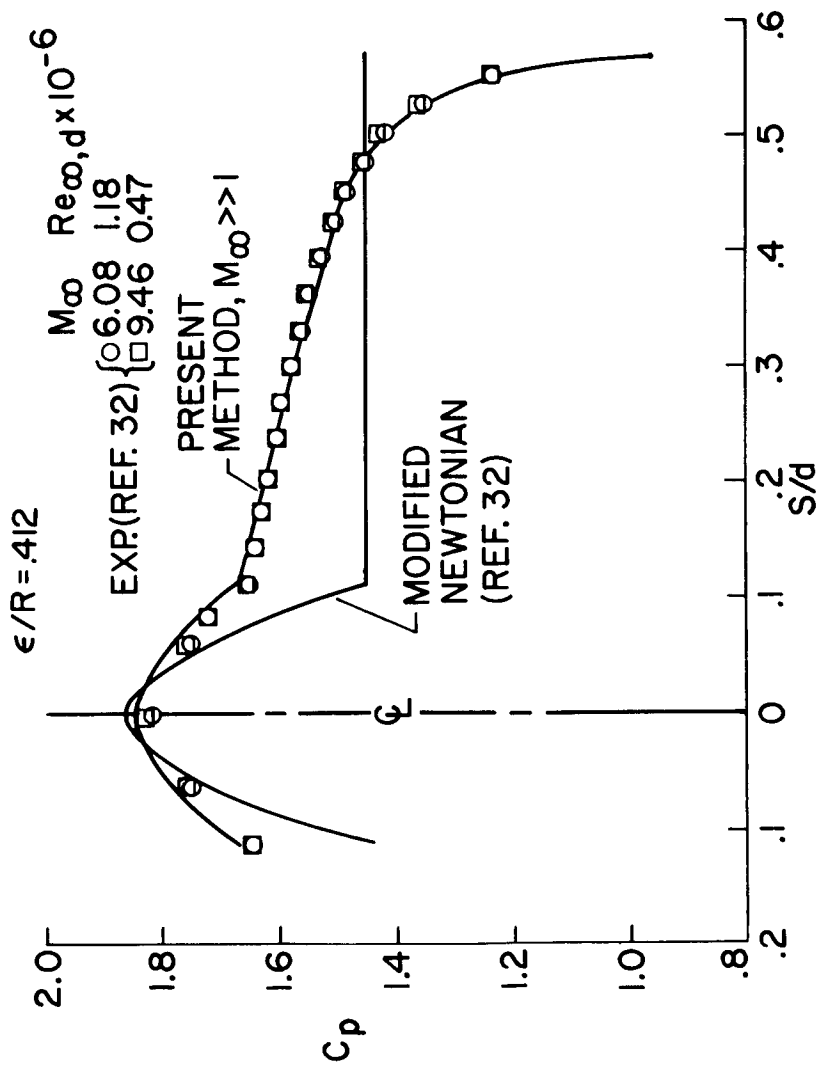
(a) Comparison of predictions with experiment at  $M_\infty = 4.63$ .  
 Figure 36.- Pressure distribution over spherically blunted cones with sonic corners.  
 $\delta_c = 60^\circ$ ;  $\gamma = 7/5$ .



(b) Additional comparisons of predictions.

Figure 36.- Continued.





(c) Comparison of present method and modified Newtonian with experiment.

Figure 36.- Concluded.

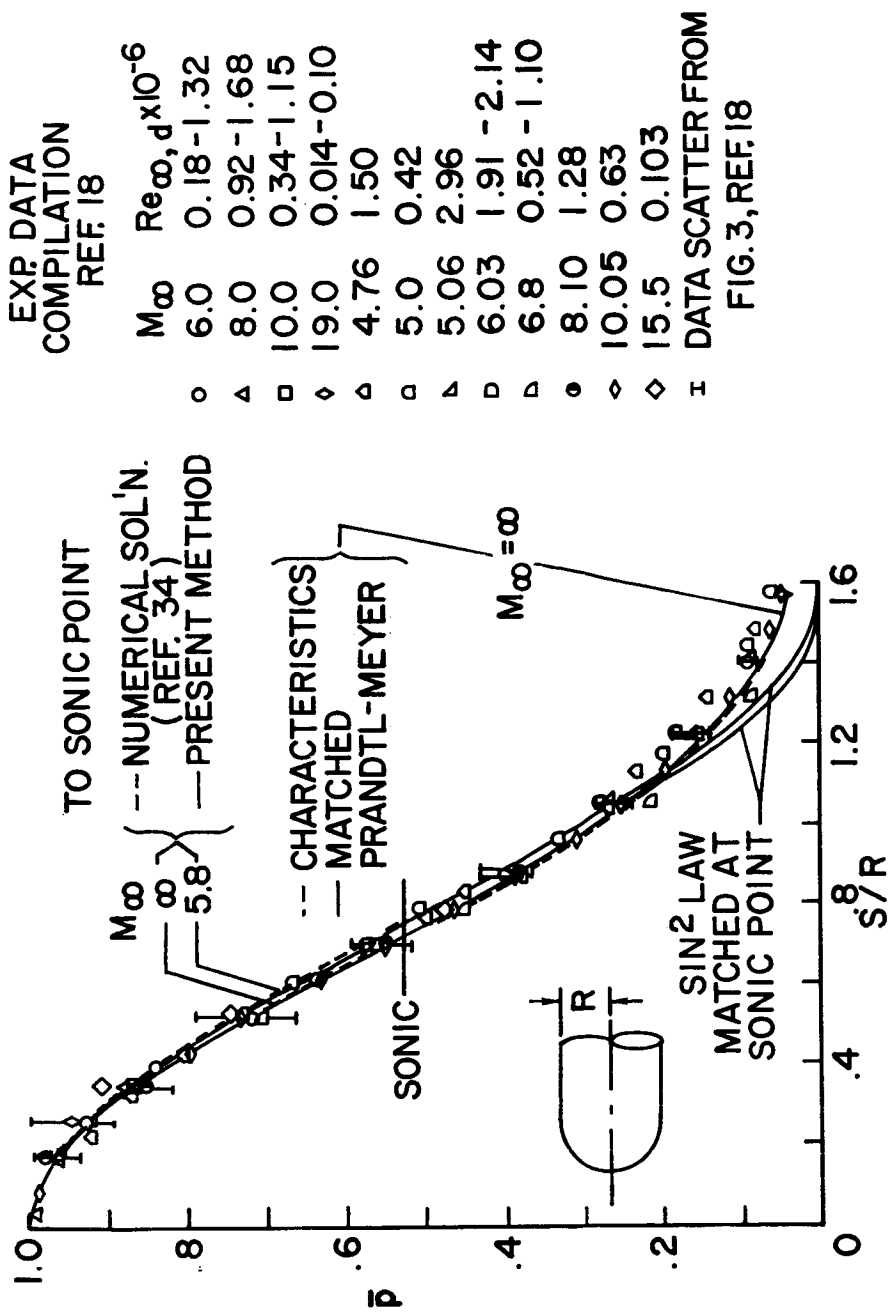


Figure 37.- Pressure distribution on hemisphere.

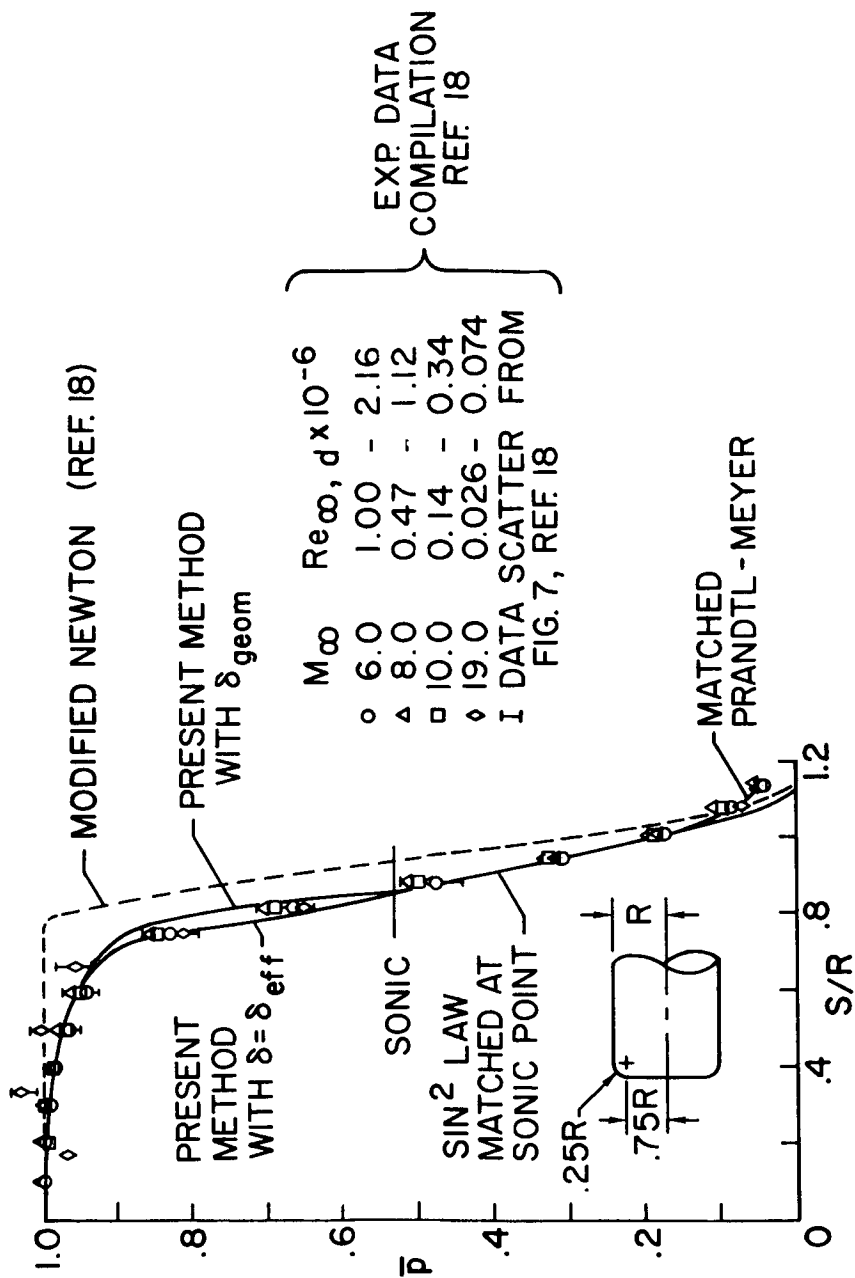


Figure 38.- Pressure distribution on flat-face cylinder with rounded shoulder.

## 4. PROBLEMS OF ATMOSPHERIC ENTRY

By Percy J. Bobbitt  
Langley Research Center

### ABSTRACT

Aerodynamic and heating problems of planetary entry are discussed with particular emphasis on Mars and Venus. Real-gas and atmospheric-composition effects on the drag and radiative and convective heating of entry spacecraft are illustrated. Considerations involved in the selection of an ablation material are reviewed and typical heat protection weights given. Aerodynamic data for blunt cones from a number of different facilities are shown and some of the shortcomings of various test techniques pointed out.

### INTRODUCTION

An engineer who concerns himself with the problems of atmospheric entry, whether he be a specialist or project manager, must, of necessity, become knowledgeable in a whole variety of subjects to be effective. The reason for this is that the various phases of an entry mission and the major systems of an entry vehicle are so interdependent that a change in any one can have a substantial impact on many others. Some of the more important subjects and systems of interest are as follows:

- Space mechanics
- Communications
- Power
- Deboost and spin rockets
- Flight mechanics
- Aerodynamic forces and moments
- Aerodynamic and reaction controls
- Instrumentation
- Atmospheric physics
- High-temperature gas physics
- Radiative and convective heating
- Aerodynamic heat protection systems
- Fluid mechanics (pressure loads)
- Structural mechanics
- Aerodynamic decelerators
- Terminal retro-rockets
- Landing systems

These subjects are listed roughly in the order in which they become important during an entry, starting from space and ending up on the ground. This is not the order, however, in which they are considered in the course of laying out a mission plan or designing an entry vehicle. Since every mission has a different set of constraints and objectives, the relative importance of the various technologies changes. More importantly, when complex interactions exist between various phases of an entry mission, iterations to satisfy all (or most) of the constraints may involve the technologies in a variety of combinations.

The purpose of the present paper is to discuss primarily those topics which are of concern during entry, with particular emphasis on those subjects related to aerodynamics. Some of the interactions and options will be pointed out as they arise; many others will be evident. Even with these restrictions, it is not possible in a paper of this type to discuss all of the selected topics in detail; some will be given only fleeting notice. The choice of which subjects to emphasize has been influenced to a certain extent by a desire to emphasize those aspects in a Mars or Venus entry that differ from an Earth entry owing to such things as atmospheric composition, atmospheric density, and entry velocity differences.

The discussion will be given within the context of two specific space-entry missions which have received substantial attention in the past few years. One is the delivery of a payload to the surface of Mars and the other is the placing of a buoyant probe in the lower atmosphere of Venus. These two missions together provide most of the complications, utilize most of the systems, and involve all of the technology disciplines that can be envisioned in an unmanned entry mission. While these missions may not be flown in the years for which data are given, similar considerations must be made whenever they are seriously undertaken.

## SYMBOLS

$a$	speed of sound, ft/sec (m/sec)
$A$	reference area, usually maximum cross-sectional area, ft <sup>2</sup> (m <sup>2</sup> )
$c_p$	specific heat at constant pressure, ft <sup>2</sup> /sec <sup>2</sup> -°R (joules/kg-°K)
$C_c$	constant in convective heating rate equation (see eq. (1))
$C_r$	constant in radiative heating rate equation (see fig. 27)
$C_D$	drag coefficient, $\frac{\text{Drag force}}{q_\infty}$

$C_A$	axial-force coefficient, $\frac{\text{Axial force}}{q_\infty}$
$C_L$	lift coefficient, $\frac{\text{Lift force}}{q_\infty}$
$C_m$	pitching-moment coefficient, $\frac{\text{Pitching moment}}{q_\infty}$
$C_{D,F}$	forebody drag coefficient, $\frac{\text{Forebody drag force}}{q_\infty}$
$C_N$	normal-force coefficient, $\frac{\text{Normal force}}{q_\infty}$
$D$	diameter, ft (m)
$e$	internal energy per unit mass, $\text{ft}^2/\text{sec}^2$ ( $\text{m}^2/\text{sec}^2$ ) or Napierian base (2.718)
$g$	gravitational constant, $\text{ft}/\text{sec}^2$ ( $\text{cm}/\text{sec}^2$ )
$h$	altitude above surface, ft (km); static enthalpy, $\text{ft}^2/\text{sec}^2$ or Btu/lbm (joules/kg)
$h_T$	terrain height above mean surface, ft (km)
$H_\rho$	density scale height, attitude change required to change density by a factor $e$ , ft (km)
$H_O$	stagnation enthalpy at edge of boundary layer, $\text{ft}^2/\text{sec}^2$ or Btu/lbm (joules/kg)
$H_W$	enthalpy at wall, $\text{ft}^2/\text{sec}^2$ or Btu/lbm (joules/kg)
$k$	conductivity, $\text{lb}/\text{ft}\cdot\text{sec}\cdot^\circ\text{R}$ or $\text{Btu}/\text{ft}\cdot\text{sec}\cdot^\circ\text{R}$ (joules/cm $\cdot\text{sec}\cdot^\circ\text{K}$ )
$K = \frac{C_D A \rho_s}{\beta m \sin \phi_E}$	
$k_\lambda$	absorption coefficient, $\text{ft}^{-1}$ ( $\text{cm}^{-1}$ )
$L$	lift force, lb (kg)
$m$	vehicle mass, slugs (kg)

$m, n$	exponents
$M$	Mach number, $V/a$
$N_c$	shape factor (see eq. (7))
$Nur$	Nusselt number (see eq. (B6))
$p$	pressure, lbf/ft <sup>2</sup> or lbf/in <sup>2</sup> (mb)
$p_o$	reference pressure, $2.09 \times 10^{-3}$ lbf/ft <sup>2</sup> ( $1.013 \times 10^6$ dynes/cm <sup>2</sup> )
$Pr$	Prandtl number, $\frac{\eta_c p}{k}$
$q$	pitching velocity, rad/sec
$\dot{q}_c$	convective heating rate, ft-lbf/ft <sup>2</sup> -sec or Btu/ft <sup>2</sup> -sec
$\dot{q}_r$	radiative heating rate, ft-lbf/ft <sup>2</sup> -sec or Btu/ft <sup>2</sup> -sec
$q_\infty$	free-stream dynamic pressure, $\frac{1}{2}\rho_\infty V_\infty^2$ , lbf/ft <sup>2</sup> (g/cm <sup>2</sup> )
$q_c$	total convective heat input during entry, ft-lbf/ft <sup>2</sup> or Btu/ft <sup>2</sup>
$q_r$	total radiative heat input during entry, ft-lbf/ft <sup>2</sup> or Btu/ft <sup>2</sup>
$Q_r$	total radiative heat input to entire body during entry, Btu (joule)
$Q_c$	total convective heat input to entire body during entry, Btu (joule)
$r$	distance from planet center or radial coordinate, ft (km or cm)
$R$	gas constant, ft <sup>2</sup> /sec <sup>2</sup> -°R (J/kg-°K)
$R_n$	nose radius, ft (cm)
$Re$	Reynolds number (see eq. (B7))
$R_b$	base radius, ft (m)

s	distance measured along body surface, ft (m)
t	time, sec
T	temperature, °R (°K)
T <sub>0</sub>	reference temperature, 492° R (273.2° K)
u	velocity at edge of boundary layer, ft/sec (m/sec) or component of entry vehicle's velocity perpendicular to radius vector from center of planet, ft/sec (km/sec)
v	component of entry vehicle's velocity along radius vector from center of planet, ft/sec (km/sec)
v <sub>w</sub>	wind speed, ft/sec (m/sec)
V <sub>∞</sub>	flight velocity, ft/sec (m/sec)
ΔV	incremental velocity given spacecraft to put it on collision course with planet, ft/sec (m/sec)
x <sub>cp</sub>	longitudinal location of center of pressure measured from base of body
y	distance measured normal to axes of body

$$C_{mq} = \left( \frac{\partial C_m}{\partial \left( \frac{qD}{2V_\infty} \right)} \right)_{\frac{qD}{2V_\infty} \rightarrow 0}$$

$$C_{m\dot{\alpha}} = \left( \frac{\partial C_m}{\partial \left( \frac{\dot{\alpha}D}{2V_\infty} \right)} \right)_{\frac{\dot{\alpha}D}{2V_\infty} \rightarrow 0}$$

$$C_{m\alpha} = \left( \frac{\partial C_m}{\partial \alpha} \right)_{\alpha \rightarrow 0}$$



$$C_{N\alpha} = \left( \frac{\partial C_N}{\partial \alpha} \right)_{\alpha \rightarrow 0}$$

$\alpha$	angle of attack, deg
$\beta$	inverse density scale height, $\frac{1}{H_\rho}$ , 1/ft (1/km)
$\gamma$	ratio of specific heats
$\bar{\gamma}$	ratio of static enthalpy to internal energy, $h/e$
$\Gamma$	adiabatic lapse rate, $dT/dh$ , $^{\circ}\text{R}/\text{ft}$ ( $^{\circ}\text{K}/\text{m}$ )
$\delta$	shock-layer thickness
$\eta$	viscosity, $\text{lbm}/\text{ft}\cdot\text{sec}$ ( $\text{g}/\text{cm}\cdot\text{sec}$ )
$\eta^*$	nondimensional viscosity, $\eta/\eta_0$
$\eta_0$	reference viscosity $1.61 \times 10^{-6} \sqrt{T, ^{\circ}\text{R}}$ , $\text{lbm}/\text{ft}\cdot\text{sec}$ ( $3.2095 \times 10^{-5} \sqrt{T, ^{\circ}\text{K}}$ , $\text{g}/\text{cm}\cdot\text{sec}$ )
$\theta$	angular coordinate, deg
$\theta_c$	cone half-angle, deg
$\lambda$	wavelength, $\text{\AA}$
$\rho$	free-stream density, $\text{slugs}/\text{ft}^3$ ( $\text{g}/\text{cm}^3$ )
$\rho_0$	reference density, $2.51 \times 10^{-3}$ $\text{slugs}/\text{ft}^3$ ( $1.292 \text{ kg}/\text{m}^3$ )
$\phi$	flight-path angle, deg

#### Subscripts:

D	value at parachute deployment
---	-------------------------------

e	value at edge of boundary layer
E	value at entry, 800 000 ft for Mars and 200 km for Venus
L	value just prior to landing
max	maximum value during entry
o	stagnation-point value or reference value
r	value at recovery temperature
s	value at planet surface
T	value at tropopause
w	value at body surface (wall value)
1	value behind shock
$\infty$	value immediately ahead of shock in free stream

A dot over a symbol indicates a time derivative.

#### ABBREVIATIONS

BVS	buoyant Venus station
HARA	high-altitude radar altimeter
MV	Mariner V spacecraft
RTG	radioisotope thermoelectric generator
S/C	spacecraft/capsule
TDLR	terminal descent and landing radar

VM           Voyager Mars

VIV          USSR Venus IV spacecraft

## SPACE MECHANICS, MISSION PROFILES, AND SPACECRAFT

The term "space mechanics" is used here to differentiate the type of analysis used for that part of a mission which takes place in space, where the perturbing forces are gravitational in nature or due to rocket thrusters, from that used for the part which takes place in an atmosphere where aerodynamic effects must also be considered. Space mechanics will be used for many purposes during the course of a Mars or Venus mission (see fig. 1) including the determination of the spacecraft's Earth orbit, interplanetary trajectory, midcourse corrections, planet approach trajectories, planet orbits, and planet fly-by trajectories. Also, space-mechanics must be used in determining the trajectory of the entry capsule from the point where it separates from the parent spacecraft down to where it enters the planet's atmosphere. The approach and fly-by (or orbit) trajectories provide the initial position and velocity of the entry spacecraft at the time of separation. Immediately following separation, the entry spacecraft is given an incremental velocity to put it on a collision course with the planet or, expressed in another way, to put it in its entry corridor. As is seen later, entry from orbit and from the approach trajectory impose different requirements on the entry vehicle design. The choice of entry mode may also have an impact on the mission objectives as well since it can affect the payload weight available and the ability to reach a prescribed surface location. Determining the deboost parameters, that is, position, magnitude, and direction of  $\Delta V$  (the incremental velocity given the entry spacecraft) to satisfy all the mission constraints is a major task in either mode. A good summary of the space-mechanic considerations for a Mars mission is given in references 1 and 2. References 3 to 5 contain similar material but in much greater detail.

Before proceeding with a discussion of some of the entry problems, it may be of interest to look briefly at the kinds of systems and missions which have been considered. Figure 1 gives the various phases of a Mars mission culminating in the entry and landing of a capsule. The mission mode in which the entry spacecraft is separated from its parent spacecraft in orbit (lower right-hand corner of fig. 1) is the one currently being used in Viking-Mars project studies. Other options which have been studied are the release of the entry capsule on the approach trajectory with the parent spacecraft subsequently following the fly-by trajectory or being injected into a Mars orbit. The former is depicted in the upper right-hand corner of figure 1.

A sketch of a proposed Viking-Mars spacecraft configuration mounted in the Titan III-Centaur launch vehicle is given in figure 2. This figure shows the clearance between the spacecraft and shroud required because of structural deflections during

launch, the orbiter, the bioshield enclosing the lander (labeled "Viking lander capsule"), and the air-conditioning connections. The latter are necessary to keep the capsule from overheating on the launch pad owing to the heat emitted by the RTG's (radioisotope thermonuclear generator) located on the lander vehicle. A drawing of the lander situated inside the entry capsule which, in turn, is inside the bioshield is shown in figure 3. Some of the more prominent features of the entry capsule and lander are the deorbit and terminal propulsion systems, the parachute container, the RTG's, the landing legs (in retracted position), and the blunt,  $140^\circ$  conical aeroshell. The entry capsule pictured, not including the biocanister and the deorbit engine, has been estimated to weigh between 1600 and 1700 lbm.

A time sequence of events during entry is depicted in figure 4 starting with the separation of the capsule from the orbiter. This is followed by a retro-rocket firing to put the entry capsule on its proper entry trajectory. It subsequently may be pitched (aligned) to facilitate communication with the orbiter during coast and again just before entry to minimize the angle of attack of the aeroshell. Obviously these maneuvers require an altitude control system on the capsule to maintain a desired orientation in space. For capsules which are spun to maintain orientation, changes in alinement are not usually attempted and compromises in the communications geometry and entry angle of attack may then result. It should be noted here that spin stabilization has most often been considered for entry spacecraft that are separated on the approach trajectory. One of the reasons for this is that an active control system might require a large amount of propellant if the coast time from deboost to entry were on the order of several days.

Entry is defined as commencing at 800 000 feet (244 km) where the velocity, for the orbital case, is in the range of 12 800 to 16 100 ft/sec (3.9 to 4.9 km/sec). For a direct entry, that is, capsule separation on the approach trajectory, the velocity range is 18 000 to 21 000 ft/sec (5.5 to 6.4 km/sec). (These numbers are for a 1973 launch from Earth.) The aeroshell and its heat protective coating of ablation material have the responsibility of reducing these large initial velocities, and hence energies, to values that will permit a safe decelerator deployment. Most of this energy goes into heating the air just ahead of the capsule; some is disposed of in the wake and some is conducted into the ablation shield where it is expended through pyrolysis of the ablation material. If the air is heated to a sufficiently high temperature, as in a high-velocity Venus entry, it will also radiate. Some of the radiant energy will reach the surface of the aeroshell and some will be radiated to space.

Shortly after the maximum heating rate has been incurred, the aeroshell will be subjected to the maximum pressure load (hence maximum deceleration). The magnitude will be dependent upon the entry velocity and flight-path angle, the density scale height of the atmosphere, and the ballistic coefficient  $m/C_D A$  of the entry vehicle.

In the altitude range of 15 000 to 20 000 feet, a parachute is deployed at an expected Mach number of 2.5 or less. A few seconds later, the aeroshell will be released and the payload-parachute combination continued to decelerate until about an altitude of 6000 feet where, in the case of a soft lander, the terminal propulsion engines ignited. With ignition assured, the parachute is released (at about 4000 feet above the terrain) and the terminal guidance and control system takes over to place the capsule 15 to 20 feet (4.57 to 6.1 km) above the surface with a near-zero velocity. The engines are then turned off and the lander drops to the surface.

The hard-lander terminal decelerator system shown in figure 4 is much simpler. The payload, which is encapsulated in a ball of crushup or shock absorbing material, is extracted from the aeroshell at parachute inflation. The parachute remains attached until near the surface at which time the payload is released and the parachute is propelled off to the side.

At the bottom left-hand corner of figure 4, note that the terrain height has been set equal to two values, 0 and 6000 feet (1.83 km). This has been done to signify the fact that in many of the Mars terminal decelerator systems studies the effect of a terrain height 6000 feet (1.83 km) above Mars "sea level" has been studied.

The Venus missions studied are similar to those for Mars in that capsule deployments from both fly-by and orbiting spacecraft have been considered. Fly-by missions include an April 1972 launch and an October 1973 launch, with the latter providing the parent spacecraft an opportunity for a Mercury swing-by. The orbit mission assumes a November 1973 launch. Figure 5 shows schematically the flight profile of the first of these missions starting at booster spacecraft separation. As in the Mars mission, mid-course corrections are applied to put the spacecraft on the desired approach trajectory. After about 121 days into the mission and 2 days from encounter, the capsule is deployed and given a velocity increment in the direction of the planet. It can be seen that the probe will land near the terminator and be in view of both the spacecraft and Earth at entry.

A sketch of a Venus fly-by spacecraft-capsule combination enshrouded by a Titan IIIC payload fairing is given in figure 6. The spacecraft in this case is a 1969 Mariner modified to account for the larger angular inertia of the spacecraft-capsule combination, the sun shadow of the aeroshell, and to act as a communications relay for the capsule during entry. Note that the capsule, like that of Mars, is surrounded by a bio-canister; note also that the capsule is not as blunt as the Mars capsule. The total apex angle of the Venus aeroshell has been chosen to be  $110^\circ$ , whereas that for Mars was  $140^\circ$ .

A closer look at the Venus entry capsule is provided by figure 7. Indicated in this figure are some typical dimensions and weights of the aeroshell, parachute canisters, balloon gondola, inflation module, and subsonic probe. The location of the roll rockets on the afterbody are also shown. These are required to spin up the capsule following

separation from the spacecraft so as to minimize the effects of thrust asymmetric during the firing of the rocket engine (see top right-hand corner of fig. 7) which puts the capsule on the desired entry trajectory. In addition, the spin ( $\approx 2.2$  rad/sec) maintains the attitude (as mentioned earlier) of the capsule during the 2-day coast period so that it will not enter the atmosphere backwards.

Before looking at the mission profile subsequent to entry, it is of interest to make a comparison of the 1972 fly-by mission depicted in figure 5 with the 1973 orbital and 1973 fly-by missions from the standpoint of entry velocity and communications geometry. Figure 8 shows the 1972 fly-by geometry again but from a different viewing angle and also indicates that the entry velocity is 37 400 ft/sec (14 km/sec). The orbital mission shown in the center of figure 8 yields a 32 000-ft/sec (9.76 km/sec) entry velocity, whereas the 1973 fly-by on the right gives 43 500 ft/sec (13.26 km/sec). An alternate, direct-entry option for the 1973 orbital mission is noted as providing a 36 500-ft/sec (11.6 km/sec) entry velocity. The spread in initial energy from the orbit entry to the 1973 swing-by mode is nearly a factor of 2; therefore, substantial differences would be expected in the heating loads and decelerations and, hence, the aeroshell and heat-protection (ablation material and insulation) weights.

Communication differences for the three missions are shown schematically and tabled in figure 9. For the 1973 orbital mission, all communications from the capsule or buoyant station are relayed by the orbiting spacecraft. In the 1972 fly-by mission, communications follow the same format, except when the buoyant station becomes operative, it communicates directly with Earth. The 1973 Venus and Mercury swing-by mission requires all communications to be directly with Earth. Since the entry is made out of sight of the spacecraft, the data obtained during this period must be stored and transmitted to Earth by the buoyant Venus station (BVS). The communications requirements, then, are different for each mission. As a result, the power requirements of the spacecraft, capsule, and BVS would also be expected to be different. Similar communication differences occur for the various possible modes of Mars entry.

Entry into the Venus atmosphere is assumed to start at 656 000 ft (200 km) with a flight-path angle of  $30^\circ \pm 5^\circ$ . Approximately 19 seconds later (see fig. 10), the maximum aerodynamic heating rate will be incurred followed almost immediately by the maximum deceleration. At 70 seconds, the capsule will have been slowed to subsonic speeds and a parachute is deployed to extract the payload. A probe weighing up to 80 or 90 pounds is then dropped to make measurements in the atmosphere all the way to the ground. This probe would measure such things as pressure, temperature, composition, and radiation at selected frequencies. It might even contain a television camera to take pictures of the surface.

When the parachute-payload combination has been slowed to about 30 ft/sec, a balloon is deployed and inflated with hydrogen (see fig. 7) and the parachute released. The balloon will continue to drop until the hydrogen is warmed sufficiently for the balloon to reach an equilibrium state. As it continues to heat up, the balloon will rise and it is likely that some venting will be required for it to stabilize at an altitude of 190 000 ft (58 km). Winds will then carry the balloon over the surface so that scientific measurements can be made at widely scattered points. In the BVS study of reference 4, provision was made for two drop sondes. These sondes are very much simpler than the subsonic probe. They weigh only 5.0 pounds and make pressure, temperature, and water-vapor measurements.

The effect of winds on possible regions of exploration by the BVS for the mission options of 1973 are indicated in figure 11. On the left of this figure, a 1973 fly-by mission is shown in which the entry occurs near the evening terminator. With the spectrum of possible wind speeds and directions assumed, the BVS will reach the dark side in anywhere from 40 to 350 hours. A similar time range exists for the orbital case, although the directions of drift are different. For the Mercury-Venus fly-by, the entry occurs on the dark side and it is not expected that the winds would carry the BVS across the terminator. Type II and Type I notations in figure 11 simply indicate heliocentric transfer angles from Earth to Mars of greater than or less than  $180^\circ$ , respectively. Type II trajectories are used when the initial energy requirements for a Type I trajectory are excessive.

## PHYSICAL PROPERTIES AND ATMOSPHERES OF MARS AND VENUS

Once the entry spacecraft enters the atmosphere, it will begin to slow down and heat up. The rate at which the velocity decreases and the heating rate increases will depend primarily on the atmospheric density and composition, the gravitational constant, and the spacecraft's velocity, flight-path angle and ballistic coefficient  $m/C_D A$ . The spacecraft velocity will, in addition, depend on the rate at which the density increases. There are other dependencies but these are sufficient to indicate the need for accurate physical-property and atmospheric data. Where uncertainties exist in these quantities, they must be accounted for in attempting to satisfy the mission constraints and in the aeroshell design.

Table I gives some of the physical properties and atmospheric data for Mars and Venus. Comparable values for Earth are also included to point up the differences and similarities of the three planets. It is evident from this table that the surface temperature, pressure, and density of Venus are much higher than those of Earth, whereas these same quantities for Mars are much lower. The size and gravitational constant of Venus and Earth, listed in the table, are nearly the same; the values for Mars are much lower.

Mars rotational period however is nearly identical with that of Earth. Recent radar observations of Venus indicate that it also rotates but there is considerable uncertainty as to its precise rate.

Another fact apparent from table I is that there is considerable uncertainty in the surface density and pressure of the Mars and Venus atmospheres. This uncertainty can have a major impact on the terminal decelerator systems, especially for Mars, but very little on the entry heating and pressure loads. It will be shown later that the primary atmospheric quantity affecting the level of entry heating and loads is the density scale height. The uncertainty in its value for Mars (see table I), therefore, causes considerable aggravation.

Some insight into the cause of the uncertainties in the atmospheric data of Venus is provided by figures 12 and 13 (developed by George P. Wood of the Langley Research Center). Figure 12 gives a plot of various temperature measurements and calculations as a function of the distance from the planet's center. At high altitudes, data shown are those from Mariner V; at low altitudes both Mariner V and the USSR's Venus IV probe data are given. In between, that is, from  $r = 6110$  km to  $6190$  km, several discrete data points have been obtained with a resulting uncertainty of about  $100^{\circ}$  K. There is general agreement that the cloud tops are in the  $r$ -range of  $6110$  to  $6120$  km. (Note that if the BVS is in equilibrium flight at  $70^{\circ}$  F ( $300^{\circ}$  K), it will float in the clouds.)

Good agreement seems to exist between the Mariner V and Venus IV data at low altitudes. The major uncertainty then is the location of the surface itself. Venus IV stopped transmitting at roughly  $6080$  km, which was explained at one time as the top of a  $10$ -km mountain or plateau. Accepting this explanation, the surface would be at  $6070$  km, which is still well above the best radar measurement. The differences in surface temperature given in table I are the Venus IV  $10$ -km peak and the radar surface values.

The pressure variations associated with the temperatures of figure 12 are plotted in figure 13. There is an overall consistency of the measurements for pressure; however, the surface value is still uncertain for the same reasons as cited for the surface temperature. The Venus IV  $10$ -km peak surface pressure is  $40$  atmospheres, and the radar surface value is  $100$  atmospheres. Most recent measurements indicate that the radar value is probably the most accurate.

Differences similar to those of Venus also exist in the properties of the Mars atmosphere; however, because of the previously mentioned uncertainties in the density scale height, they are of more concern in the design of an entry capsule. The most credible source of Mars atmospheric data until the recent Mariner VI and VII flights has been the occultation experiment of Mariner IV. Basically, this experiment consists of the measurement of the attenuation of the radio signal as it goes behind and re-emerges from



behind the planet. A summary of the atmospheric quantities computed from immersion and emersion data is given in reference 6 and repeated in table II. It is clear from this table that the overall uncertainty in the surface quantities could be written as follows:

Pressure, mb . . . . .	6.8 ± 2.7
Temperature, °K . . . . .	205 ± 50
Mars density, 10 <sup>-5</sup> g/cm <sup>3</sup> . . . . .	1.67 ± 0.33

This "lumping" together of emersion and immersion data may, however, be an unduly pessimistic interpretation of the accuracy of the data. Several plausible explanations for the difference have been proposed. One centers around the differences in elevation of the areas where immersion and emersion took place, and the other suggests that the mean gravitational equipotential surface may be shaped in such a way as to produce the measured difference. Elevation differences could have been caused by local features and/or by planet ellipticity. Obviously, until more is known about the topography and ellipticity of the planet, mission planners will have to accommodate uncertainties of the magnitude listed.

Some hypothesized atmospheric temperature profiles, based in part on Mariner IV data, are given in figure 14. The curves labeled VM-8 and VM-9 are the lowest and highest density-scale-height atmospheres from a set used in the Voyager program. (A program involving a Saturn launched Mars spacecraft with a 19-foot-diameter entry capsule. This project has been superseded by the Viking project.) The minimum, maximum, and most probable curves are those used in early Viking project studies. The minimum and maximum surface temperatures differ by 100° K, whereas at high altitudes, the differences are in the hundreds of degrees. Corresponding density profiles are plotted in figure 15 and show that down to densities of 10<sup>-10</sup> g/cm<sup>3</sup> the two sets of atmospheres (solid- and dashed-line curves) have about the same density bounds. Tables III and IV give a complete listing of the important variables for the Voyager-Mars and minimum, maximum, and mean atmospheres. Appendix A shows how the atmospheric-quantity profiles are derived starting with the equation of state and the barometric equation.

Another atmospheric property of concern is the wind, including gusts. If a parachute-payload combination is subjected for a long enough time to the wind, it will become entrained. This added velocity component imposes an additional burden on the retropropulsion system of a Mars soft lander for it must cancel out this lateral velocity component to achieve a successful landing. A proposed probability distribution for the near-surface wind speed is shown in figure 16. The most probable wind speed is on the order of 45 miles/hour (20.1 m/sec); the maximum speed is 142 miles/hour (63.6 m/sec). Winds for a Venus buoyant probe are important also since, as noted earlier, they will determine the distances over which the probe will be able to obtain data and whether or not the probe will cross the terminator.

## HIGH-TEMPERATURE GAS PHYSICS

Real-gas effects are sometimes not fully appreciated; therefore, the added emphasis provided by a special section seems warranted. The principal concern here is the departure of the behavior of the gas from that at low temperatures. A better understanding of these phenomena may be obtained by looking at a simplified model of a gas molecule in various states of excitation (see fig. 17). At low temperatures, for example, room temperature, only the translational and rotational modes need to be considered to provide the ideal gas model. However, as the temperature of the gas increases, other internal degrees of freedom come into play. In air at about  $1500^{\circ}\text{K}$ , the vibrations of the molecules become important; at approximately  $3000^{\circ}\text{K}$ , the collisions become so violent that dissociation occurs; and above  $6000^{\circ}\text{K}$ , electronic excitation and ionization (loss of electrons from atoms and molecules) must be considered. (Temperatures for the excitation of various degrees of freedom vary with pressure; hence, the numbers given are typical values.) When the electrons in an atom have sufficient energy to shift orbits, radiation is emitted. The loss of electrons from gas atoms and molecules (ionization) causes free electrons to be distributed in the gas and creates problems in transmitting electronic signals through the hot gas layer surrounding entry vehicles (blackout).

A mathematical model for the gas chemistry starts with an assumption of the composition of the cold gas mixture and the percentage of the total volume or mass of the gas each component occupies. For example, a model for everyday air might be 78-percent nitrogen and 22-percent oxygen by volume. Then with the knowledge of the characteristic energies of each of the processes for each chemical species, the thermodynamic properties such as density, enthalpy, entropy, and the chemical composition for a given temperature and pressure can be calculated.

These real-gas effects must be accounted for in any theoretical prediction of radiative and convective heating rates, surface pressures, and force and moment coefficients for entry bodies. In the case of experimental data for these quantities, care must be taken not to use perfect-gas tunnel results as a substitute for real-gas hypervelocity data without thoroughly examining the validity of such a procedure. For instance, pressure-distribution (hence force and moment) data for slender bodies with flares (or control surface deflections) and blunt aeroshells can be significantly affected by real-gas effects. Few wind-tunnel facilities can simulate real-gas flow conditions and often theory must be relied on in whole, or in part, to predict adequately the performance of hypervelocity flight vehicles. This point will be discussed in more detail in the section entitled "Aerodynamic Forces and Moments."

One indicator of real-gas effects is the ratio of specific heats  $\gamma$ . At low temperatures in air, this ratio is 1.4 but as the temperature increases, it generally decreases.

Figure 18(a) (from ref. 7) shows a plot of an effective ratio of specific heats  $\bar{\gamma}$  for air in thermodynamic and chemical equilibrium defined as the ratio of  $h/e$ , which at low temperatures is exactly  $\gamma$ . Using the normal shock density, pressure, temperature, and static-enthalpy jump conditions for  $M_\infty = 34.66$ , where  $h = 200\,000$  feet (given in ref. 8), the calculation of  $\bar{\gamma}$  behind a normal shock can be demonstrated. The following table gives the shock jump conditions in column 1 and the values behind the shock in column 2:

Shock jump	Quantity behind shock
$\frac{\rho_1}{\rho_\infty} = 15.84$	$\rho_1 = 9.69 \times 10^{-6}$ slugs/ft <sup>3</sup>
$\frac{p_1}{p_\infty} = 1576$	$p_1 = 743$ lbf/ft <sup>2</sup>
$\frac{T_1}{T_\infty} = 44.94$	$T_1 = 20\,200^\circ$ R
$\frac{h_1}{h_\infty} = 241.2$	$h_1 = 6.48 \times 10^8$ ft <sup>2</sup> /sec <sup>2</sup>

By eliminating  $e$  from the two relations

$$p = (\bar{\gamma} - 1)\rho e$$

$$h = \bar{\gamma}e$$

and substituting the preceding values of  $p_1$ ,  $\rho_1$ , and  $h_1$ , a value of  $\bar{\gamma}$  of 1.135 is obtained. From the equation  $h = \bar{\gamma}e$ , with  $\bar{\gamma} = 1.135$ , a value of 675 for the nondimensional energy parameter  $e_1/RT_0$  may be calculated. Higher Mach numbers for the same free-stream quantities (subscript 1 quantities) will result in even higher temperatures, pressures, and densities behind the shock. The relationship between these quantities at high temperatures is illustrated by the plot in figure 18(b).

The speed of sound for the preceding conditions may be determined from figure 19. The ordinate parameter  $a_o^2/RT_0$  will have a value of 1.4 for air at low temperature as may be seen by dividing the equation for  $a_o^2$

$$a_o^2 = \gamma RT_0$$

by  $RT_0$ ; thus

$$\frac{a_o^2}{RT_0} = \gamma = 1.4$$

For  $a^2/RT_0 = 100$ , which is roughly the value obtained by using the values previously computed for  $e_1/RT_0$  and  $\rho_1/\rho_0$ , the speed of sound  $a$  will be  $10/\sqrt{1.4} = 8.46$  times its low-temperature value for  $\gamma = 1.4$ .

The solid-line curves in figures 18 and 19 are curve fits used in reference 7 to compute the flow field about bodies traveling at planetary return velocities. Since the computation of the thermodynamic properties of a gas requires considerable computer time, the use of curve fits is almost mandatory in flow-field calculations. Real-gas effects on the thermodynamic properties of planetary gas mixtures are similar to those shown for air.

Real-gas effects also play an important part in the transport properties of a gas, that is, viscosity  $\eta$ , conductivity  $k$ , and the diffusion coefficient. From a convective-heating standpoint, viscosity and Prandtl number  $\eta c_p/k$  are the most important of the transport-property parameters. This can be seen from the following approximate expression for the axisymmetric stagnation-point heating rate (see ref. 9):

$$\dot{q}_{c,o} = \frac{1}{2(\overline{Pr})^{2/3}} \sqrt{(\rho_e \eta_e)_o} (H_o - H_w) \sqrt{(du_e/ds)_o}$$

where  $\overline{Pr}$  is an average value for the Prandtl number in the boundary layer. As previously indicated, real-gas effects have a substantial influence on the density behind the shock and hence on  $\rho_{e,o}$ ; also,  $(du_e/ds)_o$  is affected but to a lesser extent.

Real-gas effects on  $\eta_{e,o}$  and  $Pr$  for several different gases including air can be shown with the aid of figures 20 to 25 (ref. 10). Figures 20 and 21 give the variations of a viscosity parameter and Prandtl number with temperature for a range of pressures from 0.001 to 10 atmospheres in air. Note in figure 20 that real-gas effects do not noticeably affect the viscosity parameter until a temperature of  $2500^\circ K$  and have only a small influence up to  $4000^\circ K$ . Pressure independent equations of the type used at low speed may then be useful up to this temperature. Real-gas effects are seen to affect the Prandtl number (fig. 21) at a much lower temperature and have an increasing effect as the temperature is increased. Similar observations can be made concerning figures 22 and 23 which give these two properties for  $CO_2$ . Comparisons of the viscosity variations from figures 20 and 22 for a pressure of 0.1 atmosphere along with similar curves for 100-percent  $N_2$  and a mixture of 50-percent  $N_2$  and 50-percent  $CO_2$  are given in figure 24. It is evident from this figure that real-gas effects on viscosity are similar for the various atmospheres considered so that composition is almost a second-order effect. A comparable plot for Prandtl number is given in figure 25. Clearly, composition effects are more important for this quantity. Maximum changes in heating rates due to real-gas and composition effects for the atmospheres (and temperature range) considered here on the order of 20 and 15 percent, respectively.

## CONVECTIVE AND RADIATIVE HEATING

Convective heating, which has already been discussed briefly in connection with the real-gas effects, is due to the viscous nature of the flow adjacent to the surface of a body, that is, in the boundary layer. The flow velocity at the surface is zero and, therefore, has the same temperature as the surface. (This is not true in free molecule or slip flow, but usually in these flow regimes convective heating rates are low and do not influence the design of the heat shield.) Going away from the boundary layer, the temperature and velocity increase. Since heat will be conducted where a temperature gradient exists, the body surface will receive heat from the gas. On entry bodies traveling at high speed, these gradients can become quite large, therefore, the heat transferred to the body is a major concern in entry vehicle design.

Several authors have shown, references 9 and 11 for example, that the stagnation-point convective heating rate can be approximated by equations similar in form to

$$\dot{q}_{c,o} = \frac{C_c \rho^m V_\infty^n}{\sqrt{R_n}} \quad (1)$$

where for laminar flow,  $m = 0.5$ . Values of  $n$  from 3.0 to 3.22 have been proposed along with a range of values for the constant  $C_c$ . In appendix B, an equation for  $\dot{q}_{c,o}$  is derived, following the analysis of reference 12, in which  $n = 3$  and  $C_c = 15.25 \times 10^{-6}$ ; that is

$$\dot{q}_{c,o} = \frac{15.25 \times 10^{-6} \sqrt{\rho_\infty} V_\infty^3}{\sqrt{R_n}} \text{ ft-lbf/ft}^2\text{-sec} \quad (2)$$

While some of the assumptions made to obtain equation (2) are subject to question, it helps to understand why equations in the form of equation (1) are capable of correlating experimental data as well as numerical solutions of the boundary-layer equations. (The objective of the heating analysis of ref. 12 was to obtain the correct form of  $\dot{q}_{c,o}$  and not necessarily the magnitude.) In any case, the important fact about equation (2) is that it shows that the convective heating rate varies roughly with the cube of the velocity, the square root of the density, and inversely with the square root of the nose radius. Consequently, the more blunt a body, the lower will be the convective heating rate in the nose region. This fact was first discovered by H. Julian Allen, one of the authors of reference 12.

Appendix B also shows that when a straight-line trajectory is assumed, the maximum convective heating rate during entry is given by

$$(\dot{q}_{c,o})_{\max} = 15.25 \times 10^{-6} \sqrt{\frac{\beta \sin \phi_E}{3eR_n} \frac{m}{C_{DA}}} V_E^3 \text{ ft-lbf/ft}^2\text{-sec} \quad (3)$$

The maximum rate occurs at an altitude of

$$h = \frac{1}{\beta} \ln 3K \quad (4)$$

and a velocity of

$$V_{\infty} = V_E e^{-1/6} = 0.85V_E \quad (5)$$

Obviously, the maximum heating rate will vary directly as the square root of the ballistic coefficient, the inverse scale height and the entry flight-path angle. If the Mars atmospheres of table III were used, then the VM-8 and VM-2 atmospheres would be expected to yield the maximum heating rate by virtue of their large inverse density scale heights. Note also that the maximum heating rate is proportional to  $V_E^3$ . With Venus entry velocities on the order of two to three times larger than those of a Mars orbit entry, the maximum Venus heating rates will be substantially larger than those of Mars.

The total heat input to the stagnation point during entry is shown in appendix B (also ref. 13) to be

$$q_{c,o} = \frac{15.25 \times 10^{-6} \sqrt{\pi}}{(R_n \beta \sin \phi_E)^{1/2}} \left( \frac{m}{C_{DA}} \right)^{1/2} V_E^2 \text{ ft-lbf/ft}^2 \quad (6)$$

A comparison of this equation with equation (3) shows that the dependence on  $\beta \sin \phi$  of the total heat input is just the inverse of that for the maximum rate. Consequently, steep entry angles and large inverse scale heights which give rise to large heating rates provide low total heat inputs. The Voyager-Mars set of Mars atmospheres, VM-1, VM-3, VM-7, and VM-9, have the same low value of  $\beta$  and yield the same maximum total heat input during entry.

The preceding discussion of Mars and Venus convective heating rates and heat inputs in terms of equations (3) and (6) may seem unwarranted if it is realized that these two equations, though approximate, were derived with an air atmosphere in mind. Some indication of the validity of using air heating-rate expressions for  $\text{CO}_2\text{-N}_2\text{-Ar}$  gas mixtures was given in the previous section, where in figures 24 and 25 the viscosity and Prandtl number for several planetary gas mixtures were compared with those for air. The differences in the calculated values of these quantities were postulated to have a maximum effect on the convective heating rate on the order of 15 percent.

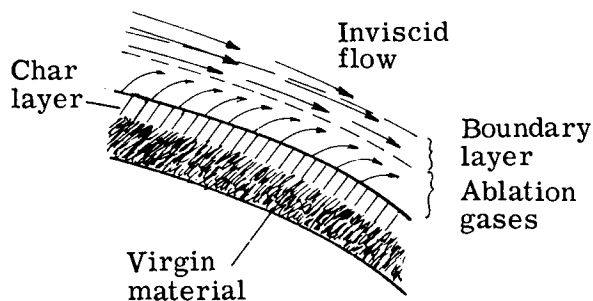
Experimental data on the effect of composition on convective heating have been obtained by a number of investigators. Figure 26 contains two plots from a paper by Horton and Babineaux (ref. 14), one of which compares heating rates for three  $\text{CO}_2\text{-N}_2\text{-Ar}$

gas mixtures with air. Generally, it can be concluded from this data that composition has a small effect on heating rate except for the gas mixture with 65-percent CO<sub>2</sub> and 35-percent Ar and even this effect is greatly reduced for flight velocities below 25 000 ft/sec. The left-hand plot of figure 26 shows the experimental data upon which the air curve in the right-hand plot is based (includes data from ref. 15) along with predictions based on the methods of Fay and Kemp and Hoshizaki (refs. 16 and 17).

The discussion to this point has not considered the interaction of the gases emitted by the ablation material with the boundary layer. The equations and experimental data discussed are for a clean, smooth surface which acts as a heat sink. If the surface is covered with ablation material, the heat absorbed during entry causes the material to pyrolyze and emit gases into the boundary layer. This process has the effect of reducing the heating rate to the surface by a factor, determined in reference 18, of approximately

$$\frac{1}{1 + \text{const} \times V_{\infty}^2 / E_V}$$

The constant in the denominator depends on the type of ablation material and whether the flow is laminar or turbulent. (Values of this constant will range from zero (for very low heating rates) up to about a maximum of 0.4.) The quantity  $E_V$  is the heat energy required to vaporize a unit mass of the ablator. For sufficiently high velocities, the flux of emitted ablation gases will lift the boundary layer off the surface. The flow adjacent to the surface under these conditions is (depicted in the following sketch)



quite different from that for which ordinary boundary-layer solutions are applicable. One attempt at a solution to this problem is given in reference 19. Additional discussion of ablation material behavior is given in the next section.

Stagnation-point convective heating rates are useful in entry studies in which convective heating is the major source of heat input to the surface. With some knowledge of the distribution of convective heating rates around a given shape, a judgement can be made of the relative amount of heat protection material that will be required for different trajectories or entry bodies. However, when both convective and radiative heating are

important contributors to the heat received by the surface, stagnation-point heating rates are no longer sufficient (ref. 13). Since the distribution of heating rate is quite different for radiation and convection, it is necessary to calculate the time variations of the heat inputs to the entire body.

In reference 13 the total laminar convective heating rate for a series of shapes with the same volumes and diameters was calculated by using Lee's similarity solution (ref. 9). It was found that the results could be represented by the following equations

$$\dot{Q}_c = \frac{\pi N_c (D)^{3/2} \sqrt{R_n}}{4} \dot{q}_{c,o} \quad (7a)$$

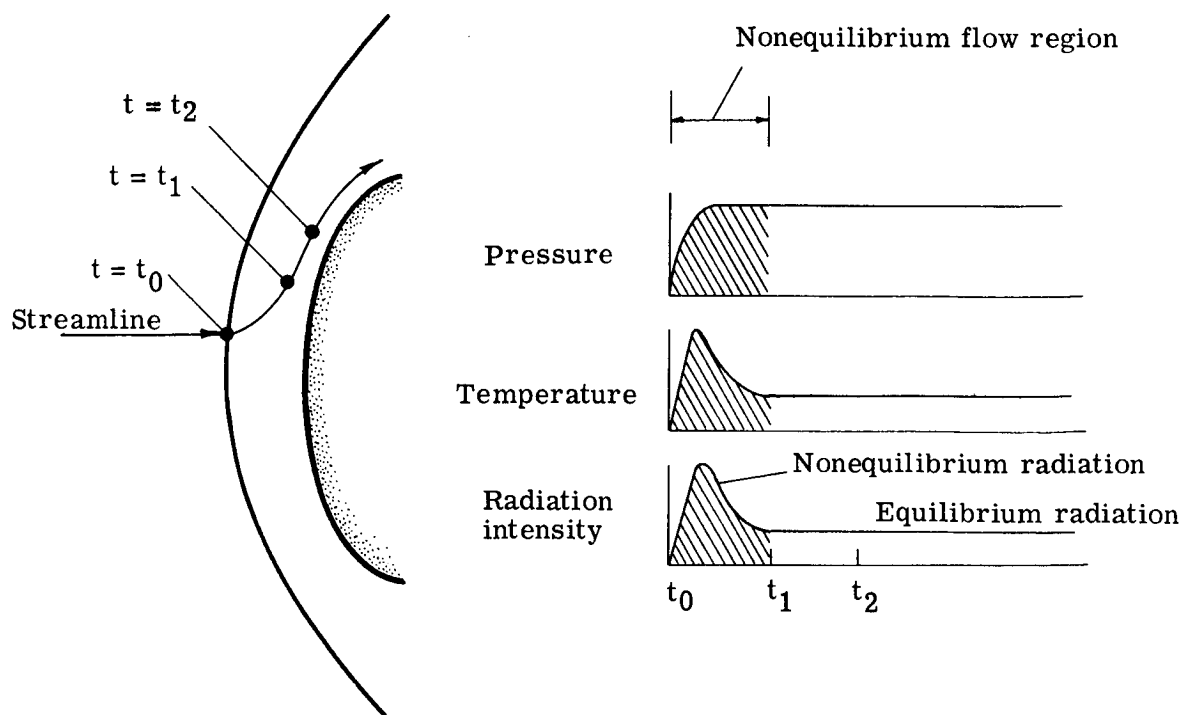
$$\dot{Q}_c = \frac{\pi N_c (D)^{3/2}}{4} (\dot{q}_{c,o})_{R=1} \quad (7b)$$

The symbol  $N_c$  is a shape factor which varied from 1.04 for a  $26.5^\circ$  half-angle blunted cone to 0.96 for an Apollo-like body. With the constraint, then, of equal volume and diameter, shape has only a minor affect on the total (entire body) convective heating rate for a given velocity and altitude. Shape does affect the drag force, however, and bodies with different drag coefficients will be subjected to a different maximum heating rate and total heat input during entry. For more slender bodies than those of reference 13, the integration of heating rates over the surface would no doubt yield values of  $N_c$  larger than those mentioned previously.

Another way the body surface receives heat is by radiation from the hot gases in the shock layer. The air passing through the shock is slowed down and a substantial fraction of the kinetic energy of the flow is converted to heat energy. (It may be recalled in our earlier example, normal-shock calculations, that the temperature behind the shock was  $20\,200^\circ \text{R.}$ ) The internal degrees of freedom will become excited with the translational, rotational, and vibrational degrees of freedom being excited in that order. If the vehicle velocity is large enough, the energy behind the shock will be sufficient to cause the gas to dissociate and ionize. These highly excited molecules and atoms give off radiant energy, a part of which will reach the body.

Immediately after the flow moves across the shock, the pressure and temperature will rise abruptly with the temperature attempting to reach its perfect-gas value. (See following sketch of flow behind shock.) However, the diversion of energy to the excitation of various internal degrees of freedom and to the dissociation and ionization of molecules and atoms causes the temperature to "peak out" and decrease to its equilibrium value. During the time when the temperature changes too rapidly for the various degrees of





freedom and the chemical reactions to reach their equilibrium state, the flow is termed nonequilibrium flow. In the earlier shock calculation, the density behind the shock was too high for the nonequilibrium zone to be significant, hence, the gas was assumed to achieve its equilibrium state immediately upon passing through the shock. As density decreases, the nonequilibrium zone becomes an increasingly larger portion of the shock layer. The condition may be achieved where the entire shock layer is in a nonequilibrium state.

The radiation emitted from the nonequilibrium and equilibrium zones behind the shock is, naturally, termed nonequilibrium and equilibrium radiation. For most entry trajectories where radiative heating is important (i.e., relative to convective), the contribution of nonequilibrium radiation is not a significant factor. Measurements have been made of nonequilibrium radiative intensities (see refs. 20 and 21) for planetary gas mixtures, and though some discrepancies exist, as noted in reference 22, these data indicate that, for the Mars mission considered, it can be neglected. Indeed for Mars entry velocities less than 20 000 ft/sec and entry angles below  $25^\circ$ , even equilibrium radiative heating is negligible. Therefore the remaining discussion will be restricted to equilibrium radiative heating incurred during Earth and Venus entries.

Radiation from the gas in the shock layer and the ability of the gas to absorb radiation is dependent on the temperature and density of the gas and the atmospheric composition. The radiation intensity will depend on wavelength, and the gas will absorb in a wavelength dependent manner as well. The amount of radiant energy that a point on a

body will absorb from an elemental radiating volume of gas in the shock layer will depend on the intensity of radiation, how much radiation is absorbed by the gas between the surface and the volume element, the orientation of the volume element with respect to a surface element, and the absorption characteristics of the surface material. An analysis taking into account all of the known variables in the radiating shock-layer problem has not been attempted; however, methods do exist which account for the major ones.

To begin with, it will be convenient to discuss radiative-heating equations which result from a number of simplifying assumptions so as to achieve some insight into the effects of ballistic coefficient and entry conditions. If it is assumed that the shock layer at the stagnation point is an infinite slab with a thickness equal to the stagnation-point detachment distance, that the temperature is the same everywhere, and that absorption of radiant energy and depletion of shock-layer energy due to radiation can be neglected, then simple power-law correlation equations of the type derived for convective heating rate can be obtained. Perrine in reference 23 has derived the following set for air to cover a velocity range up to hyperbolic

$$(\dot{q}_{r,o})_1 = 1.585 \times 10^4 \left( \frac{\rho}{\rho_s} \right)^{1.78} \left( \frac{V_\infty}{10^4} \right)^{12.5} R_n \text{ ft-lbf/ft}^2\text{-sec} \quad (V > 35\,000 \text{ ft/sec}) \quad (8)$$

$$(\dot{q}_{r,o})_2 = 2.33 \left( \frac{\rho}{\rho_s} \right)^{1.78} \left( \frac{V}{10^4} \right)^{19.5} R_n \text{ ft-lbf/ft}^2\text{-sec} \\ (30\,000 \text{ ft/sec} < V < 35\,000 \text{ ft/sec}) \quad (9)$$

$$(\dot{q}_{r,o})_3 = \frac{(\dot{q}_{r,o})_1}{3} \quad (25\,000 \text{ ft/sec} < V < 30\,000 \text{ ft/sec}) \quad (10)$$

For heating equations that have the form  $\rho^l V_\infty^n$  it may be easily verified that the maximum occurs where  $V_\infty = V_E e^{-l/n}$  so that

$$(V_\infty)_{\dot{q}_r=\max} = V_E e^{-l/n} \quad (11)$$

This assumes that the velocity is given by

$$V_\infty = V_E e^{\frac{-C_D \rho_s A}{2\beta_m \sin \phi_E}} e^{-\beta h} \quad (12)$$

(see appendix C) and the density is approximated by  $\rho = \rho_s e^{-\beta h}$ . Using equation (11) with the exponents of equations (8) and (9) results in

$$(V_{\infty})\dot{q}_{r,o}=\max = 0.867V_E \quad (13)$$

for equations (8) and (10) and

$$(V_{\infty})\dot{q}_{r,o}=\max = 0.912V_E \quad (14)$$

for equation (9). A comparison of equations (13) and (14) with equation (5) shows that the maximum radiative heating rate will occur before that for convection.

Expressions for the maximum heating rate itself are easily obtained from equations (8) to (12). They are

$$(\dot{q}_{r,o})_{1,\max} = 1.585 \times 10^4 \left( \frac{2\beta \sin \phi_E}{e\rho_s} \frac{m}{C_{DA}} \frac{1.78}{12.5} \right)^{1.78} \left( \frac{V_E}{10^4} \right)^{12.5} R_n \quad \text{ft-lbf/ft}^2\text{-sec} \quad (V_E > 40\,000 \text{ ft/sec}) \quad (15)$$

$$(\dot{q}_{r,o})_{2,\max} = 2.33 \left( \frac{2\beta \sin \phi_E}{e\rho_s} \frac{m}{C_{DA}} \frac{1.78}{19.5} \right)^{1.78} \left( \frac{V_E}{10^4} \right)^{19.5} R_n \quad \text{ft-lbf/ft}^2\text{-sec} \quad (33\,000 \text{ ft/sec} < V_E < 40\,000 \text{ ft/sec}) \quad (16)$$

$$(\dot{q}_{r,o})_{3,\max} = \frac{(\dot{q}_r)_{1,\max}}{3} \quad (V_E < 33\,000 \text{ ft/sec}) \quad (17)$$

Note that the range of applicability for equations (15) to (17) is given in terms of  $V_E$ . Clearly, the dependence of the radiative heating rate on the entry conditions, the density scale height, and ballistic coefficient is greatly different from that of the convective heating rate. It should be pointed out that the dependency of  $\rho_s$  indicated in equations (8) to (10) and (15) to (17) is fictitious. The numerical constant in these equations includes a factor  $\rho_s^{1.78}$  where  $\rho_s$  is approximately  $0.0027 \text{ slug/ft}^3$ .

The total radiative heat input to the stagnation point during the entire flight is obtained with the aid of appendix D and is given by

$$(q_r)_1 = \frac{6.54 \times 10^{-2} (\beta \sin \phi_E)^{0.78}}{(\rho_s)^{1.78}} \left( \frac{m}{C_{DA}} \right)^{1.78} \left( \frac{V_E}{10^4} \right)^{11.5} R_n \quad \text{ft-lbf/ft}^2 \quad (V_E > 40\,000 \text{ ft/sec}) \quad (18)$$

$$(q_r)_2 = \frac{4.05 \times 10^{-6} (\beta \sin \phi_E)^{0.78}}{(\rho_s)^{1.78}} \left( \frac{m}{C_{DA}} \right)^{1.78} \left( \frac{V_E}{10^4} \right)^{18.5} \text{ Rn} \quad \text{ft-lbf/ft}^2$$

$$(33\,000 \text{ ft/sec} < V_E < 40\,000 \text{ ft/sec}) \quad (19)$$

$$(q_r)_3 = \frac{(q_r)_1}{3} \quad (V_E < 33\,000 \text{ ft/sec}) \quad (20)$$

Equations (15) to (20) show, in contrast to those for convective heating, that increasing the entry angle causes both the maximum radiative heating rate and heat input to increase.

Curves enabling the determination of the exponents and factors in radiative heating rate equations similar to equations (8) to (10) for mixtures of  $\text{CO}_2$  and  $\text{N}_2$  are given in figure 27. These curves are based on the data of reference 24 and the equation given in the figure is derived on the same basis as equations (8) to (10). The data of reference 24 are for a range of free-stream velocities from roughly 16 000 ft/sec to 26 000 ft/sec and free-stream densities from 0.004 to 0.08 times sea-level density. These data show that, except for high percentages of  $\text{N}_2$ , radiation intensity levels exceed those of air with the difference increasing with velocity. Two more recent papers on the radiative properties of planetary gases are references 25 and 26.

As mentioned previously, the distribution of convective and radiative heating rates around a body are quite different. For example, the convective heat rate on a sphere varies approximately as the  $(\cos \theta)^{3/2}$  while the radiative heating rate for a transparent, adiabatic gas cap varies as  $(\cos \theta)^n$  where  $n$  may be anywhere between 6 and 8 depending on the velocity. In reference 13, the radiative heating rate distributions on the shapes at the top of figure 28 were derived and integrated over the surface to obtain the total-body radiative heating rates. These were then integrated over the entire trajectory along with the total-body convective heating rates given by equation (7). Some typical results are shown at the bottom of figure 28 for  $m/A$  of 1.55, an entry flight path angle of  $10^\circ$ , and entry velocities of 36 000, 40 000, and 44 000 ft/sec.

At the top of figure 28 are the total heat inputs to the stagnation point. It is clear from a comparison of the stagnation point and entire body heat inputs that when radiative heating becomes important, stagnation-point heating rates and heat inputs are no longer accurate indicators of the relative heat load incurred by bodies of different shape. Another fact evident from figure 28 is that as Earth entry velocities increase beyond the 40 000-ft/sec level, the more slender bodies will be subjected to a smaller total, convective plus radiative, heat input. It should be remembered that the curves in this figure are based on the transparent adiabatic shock-layer assumption and any conclusions derived

from it may require modification when these assumptions are removed. In the remaining part of this section additional discussion of this matter will be given.

The preceding discussion of radiative heating has been for a gas which is transparent to radiation and for which no account was made of the radiant energy given up by the gas to radiation. Removal of these assumptions will lead, clearly, to a more exact solution.

For air, nontransparent radiation generally occurs only for wavelengths less than 1200 Å and results from the recombination of  $N^+$  and  $O^+$  ions with electrons and from bound-bound atomic electron transitions. In reference 7, the absorption coefficient for air was approximated by the two-step model shown in figure 29. One step is for the wavelength range from 400 Å to 1130 Å and accounts for the optically thick, or nontransparent, radiation just discussed. The second step is for wavelengths from 1130 Å to infinity and accounts for optically thin, or transparent, radiation from molecular band systems, free-free electron transition, and the photo-ionization of O, as well as the electron recombination of  $N^+$  and  $O^+$  and the bound-bound atomic electron transition for wavelengths greater than 2000 Å. It should be noted that the radiation spectrum for bound-bound transitions of atomic electrons consists of a very thin line with a large absorption coefficient which is bounded by wings with a smaller absorption coefficient. In reference 7, it was assumed that the line centers were self-absorbed so that only the wings of the lines needed to be considered.

Another approximation to the absorption coefficient for a high-temperature gas, which is frequently used, is the gray absorption coefficient. This is a weighted average of the frequency-dependent absorption coefficient which is used for all wavelengths. The gray absorption coefficient model is shown in figure 29 as the dashed line. In general, the gray absorption coefficient is transparent, and hence it does not properly represent the nontransparent phenomenon.

Calculations using the two-step absorption coefficient discussed previously have been made in reference 7 for the flow fields about spheres of various sizes traveling at hyperbolic speeds in the Earth's atmosphere. A time-dependent finite difference method is used to perform the calculation. The radiation which is absorbed at each point in the flow field is dependent upon the radiation which is emitted elsewhere and which passes through the point. In order to estimate this absorbed radiation at each point, the radiating shock layer is approximated by an infinite one-dimensional slab as shown in the left of figure 29. The width of the slab is the same as the local shock-layer thickness and the profiles of the gas properties across the slab are the same as those across the shock layer. This approximation is made because the integration over a one-dimensional slab can be performed numerically with relative ease, whereas the integration over a multi-dimensional shock layer involves a prohibitive amount of work.

In figure 30 results are shown for the flow of radiating air over 3-inch and 5-foot-radius spheres traveling at 50 000 ft/sec at an altitude of 190 000 feet in the Earth's atmosphere. Calculations are made for both adiabatic and nonadiabatic flow. It is seen that the nondimensional surface heat flux distributions for both spheres are essentially the same for both the adiabatic and the nonadiabatic models. This similarity in the nondimensional surface heat distributions exists although the shock layers about the two spheres differ appreciably. For example, it is seen in the left of figure 30 that the enthalpy along the stagnation streamline of the 3-inch sphere is considerably higher than the stagnation streamline enthalpy of the 5-foot sphere near the body surface. This depletion of the enthalpy in the shock layer results because the high-temperature gas is releasing energy by radiation. It should be noted that the adiabatic and the nonadiabatic models are in fair agreement for the stagnation-point heat flux for the 3-inch sphere. However, for the 5-foot sphere the adiabatic model yields a value for the stagnation-point heat flux which is three times higher than the nonadiabatic model.

It is shown in figure 31 that the relative contributions to the normalized surface heat flux of the parts of the spectrum below and above a wavelength of  $1130 \text{ \AA}$  differ for the two spheres although the two normalized distributions are virtually the same. For the 3-inch sphere, the optically thick portion of the spectrum below  $1130 \text{ \AA}$  contributes more than half of the radiation which impinges on the body; whereas for the 5-foot sphere, this portion of the spectrum contributes about 10 percent of the surface radiation. The interpretation is that the shock layer adjacent to the body has been cooled by radiation for the case of the 5-foot body, and this cooled air absorbs much of the optically thick radiation being emitted by the hot air near the shock. Since the air adjacent to the 3-inch sphere has not been cooled, it contributes to the nontransparent radiation which impinges on the surface.

It has been shown in figures 30 and 31 that the nondimensional surface heat flux distribution for a sphere traveling at 50 000 ft/sec and an altitude of 190 000 feet in air is not affected appreciably by the size of the sphere. To examine the possibility that changes in these free-stream conditions could affect the shape of the distribution, calculations were made for a 5-foot sphere traveling at speeds of 50 000, 41 000, and 34 000 ft/sec at altitudes of 220 000, 190 000, and 140 000 feet. The nondimensional surface heat flux distributions for these cases are shown in figure 32. It is seen that the altitude has no appreciable effect on the shape of the distribution and that the vehicle speed has a very pronounced effect. It should be noted that the results shown in this figure are for the nonadiabatic model. A more complete discussion of the radiative properties of air and stagnation-point heating rates are given in reference 27.

An analysis similar to that of reference 7 has been carried out in reference 28 for a gas mixture appropriate to Venus. With the results of this analysis, Norman in reference 29 has calculated the stagnation-point and cone-edge heating rates for a series of

cones with various nose radii and half-angles. Consistent with figure 30, reference 29 indicates a much less rapid increase in radiative heating with increasing bluntness than evidenced in figure 28. Figure 33 illustrates the type of results obtained in reference 27 and shows the effect on radiative and convective heating of increasing nose radii for two values of  $m/C_{DA}$ . Increasing the nose radius from 1 foot to 3 feet causes the maximum radiative heating rates to increase roughly by a factor of three while convective rates are reduced by one third. The total radiative heat input to the stagnation point for the same increase in  $R_n$  is approximately doubled while convective heat inputs are reduced by 40 percent. Since  $m/C_{DA}$  is assumed constant as the nose radius, and hence drag, increases the variation of radiative and convective heating rates and heat inputs for a constant mass entry vehicle cannot be obtained from figure 33. If drag changes were accounted for, then the rate of increase of radiative heating rate and heat input with increasing nose radius would be smaller. Results similar to those depicted in figure 33 for the stagnation point are given for the cone edge and also for various cone half-angles and entry velocities in reference 29.

## AERODYNAMIC HEAT PROTECTION SYSTEMS

The three most practical types of heat shields are: a radiative heat shield, a heat-sink heat shield, and an ablative heat shield. The latter is by far the most common since it has become possible to tailor an ablation shield for a particular maximum heating rate and total heat load. In figure 34 (ref. 30) the capabilities of the various types of heat shields in terms of their ability to withstand heating loads (total heat input) and heating rates are shown. A molybdenum radiative shield can accept very large heat loads but heating rates beyond 40 Btu/ft<sup>2</sup>-sec will cause excessive surface temperatures. Copper is an extremely good heat sink; however, when the heat loads exceed 10 000 Btu/ft<sup>2</sup>, a heat shield of this metal becomes too heavy to be practical. Present-day ablation-material technology is capable of handling efficiently almost any combination of heating rate and heat input including many combinations where metal shields are adequate. An entry from orbit into the Mars atmosphere provides maximum heating rates on the order of 20 to 60 Btu/ft<sup>2</sup>-sec and a maximum heat input on the order of 2000 Btu/ft<sup>2</sup>. While these inputs are within the capabilities of a heat-sink heat shield, aeroshells with ablative coatings are lighter. Heat loads for a Venus entry are in the 4000- to 6000-Btu/ft<sup>2</sup> range, and an ablative heat shield is required.

Many types of ablation materials have been devised; the basic constituents of composite ablative materials are listed in table V. Figure 35 (ref. 30) depicts the manner in which these materials dispose of heat. A ceramic ablation shield is illustrated for comparison on the left of this figure. Aerodynamic heating of the virgin material will cause it to melt and flow as a liquid along the surface. Some of this liquid at the liquid gas

interface may vaporize and be transported away by the airstream. During ablation, heat is dissipated in bringing about the phase change and is also transported away from the surface by convection in the liquid and gas layers. The quartz ablation shield, formerly used on ICBM nose cones behaves in this way.

On the right of figure 35 is illustrated a charring ablation shield. Pyrolysis of the virgin material produces a carbonaceous char which can sustain high surface temperatures. Heat energy is disposed by radiation from the surface, by convective transport, and by pyrolysis within the material. It should be noted that the ability of an ablator's char to withstand viscous shear forces varies widely; often a honeycomb reinforcement is used to improve the shear tolerance of an ablator.

The capability of the ablation material to dispose of heat cannot be defined without reference to the conditions of heating. The enthalpy of the airstream and the type of heating encountered (whether convective or radiative heating) may play an important part in the response of the material and hence in the selection of a material for a particular mission. Clearly a number of factors must be considered to arrive at the optimum combination of resin and filler: first, the amount of heat it can dispose of per pound of material; second, its conduction properties; third, the ability of the char to withstand the viscous shear forces; and fourth, its ability to withstand launch vibration and acceleration loads. For a Mars and Venus mission, additional criteria are the ability to withstand space vacuum, cold soak, and sterilization effects. Materials most efficient in disposing of heat (such as graphite composites) are usually good conductors (see fig. 36); hence, they may require some insulation on the back side to prevent the structure from becoming excessively hot. Low-temperature low-density ablators are much better insulators but substantial material losses over long heating periods may require much thicker ablation shields and cancel out any weight advantage. Most often the heat-shield material selected for a given application is a compromise between several candidates. Note in figure 36 that the composite charring ablators have good insulation qualities up to temperatures of 4000° R.

Table VI gives a list of measured characteristics of a number of ablators and shows again that the heavy ablators with high-energy-disposal and temperature-tolerance ability are also the best conductors.

The ablation-material weight and thickness requirements for Mars and Venus capsules are given in table VII where the materials shown are those whose properties were listed in table VI. It is clear from the weights listed for the Venus direct entry mission that the proper choice of heat-shield ablation material can effect a substantial weight saving. Mars heat-shield requirements are given for a 10.5-foot-diameter aeroshell, whereas the present Viking configuration is 11.5 feet. Reference 31 contains additional information on ablative heat shields for Mars and Venus entry vehicles.



## AERODYNAMIC FORCES AND MOMENTS

Force and moment data are usually divided into two types, static and dynamic, and within these types they are further subdivided according to velocity range. As indicated earlier, there is another distinction required when flight at near-orbital velocities is considered, that is, the distinction between ideal and real-gas data. Few ground-test facilities are available to simulate more than two of the environmental factors such as Mach number, Reynolds number, and real-gas effects at the same time, and theory must be used to "extrapolate" perfect-gas data to real-gas conditions or low Reynolds number data to high Reynolds number conditions. In some cases the uncertainties may not affect the attainment of mission objectives and they can be ignored or gradually eliminated by the analysis of flight data. Most of the time, however, a strenuous effort will be made to obtain the most accurate data possible before committing a vehicle to flight.

Static force and moments are obtainable in most all speed regimes and in a variety of ways. To illustrate the point, static data have been obtained for the  $120^\circ$  cone in the Langley spin tunnel, Langley high-speed 7- by 10-foot tunnel, Ames 2- by 2-foot transonic tunnel, Langley Unitary Plan wind tunnel, JPL 20-inch supersonic and 21-inch hypersonic tunnels, NOL pressurized ballistic and 1000-foot hyperballistic ranges (at subsonic, supersonic, and hypersonic speeds in air), NOL pressurized ballistic range in  $\text{CF}_4$  at hypersonic speeds (to simulate real-gas effects) and flight tests. Some typical wind-tunnel results for a series of cones with half-cone angles from  $40^\circ$  to  $90^\circ$  are plotted in figure 37. Of particular interest is the nonlinear variation of  $C_D$  and  $C_L$  with increasing cone angle. This points up the dangers inherent in using interpolated data without a full understanding of flow phenomena. The flow ahead of cones in the shock layer is supersonic until half-cone angles slightly in excess of  $50^\circ$  are reached whereupon it becomes subsonic and the trend of the drag and lift curves with increasing cone angle changes abruptly.

As noted previously another type of facility in which blunt-body static aerodynamic data has been obtained is the ballistic range. Figure 38 shows some static pitching-moment derivatives  $C_{m_\alpha}$  obtained in the NOL ballistic ranges along with other types of data for the  $120^\circ$  cone (refs. 32 to 34). The point to note here is that when all the data are transferred to the moment center of the ballistic-range models, there is excellent correlation. When the data are plotted for the moment center at the nose, the ballistic-range data are substantially more negative. The reason for this is that the values of  $C_{N_\alpha}$  for very blunt cones measured in the ballistic range are not sufficiently accurate for transferring the pitching moments; as the bodies become more slender, the accuracy improves. In any case, the values of  $C_{m_\alpha}$  for the center-of-gravity location of the model are accurately determined.

It was shown in figure 37 that increasing cone angle produced significant changes in the drag. Another way of increasing bluntness and hence drag is to take a cone and round off its apex. The effect of this blunting on the forebody pressure drag of a  $120^\circ$  cone is shown in figure 39 (from ref. 35). The results shown here are for Mach numbers of 3, 5, and 10 and for a range of nose-radius-to-base-radius ratios which include the pointed cone  $R_n/R_b = 0$  and the spherical cap  $R_n/R_b = 2.0$ . Of particular note here is the rapid increase in drag that occurs as the blunting causes the slopes near the outer edge to become steeper, that is, as  $R_n/R_b \rightarrow 2.0$ .

Some indication of the influence on static stability of spherical blunting can be obtained from figure 40 (ref. 36). The pitching-moment plot at the top of this figure shows that the spherical cap has greater stability than the  $120^\circ$  cone. This is somewhat misleading since the moment center for both bodies is at the base, and for a given payload shape and volume the center of gravity of the cone would be expected to be further ahead of the base than on a spherical cap. Even accounting for differences in practical center-of-gravity locations, it is clear that the stability of the spherical cap will be comparable to the  $120^\circ$  cone. Another point of interest in figure 40 is the large difference in the location of the center of pressure of the two bodies ( $x_{cp}$  measured from base).

Data of the type shown in figure 40 provided some of the impetus for investigating cones with apex angles greater than  $120^\circ$  for a Mars capsule where high drag is essential for the most rarefied atmospheres postulated. Figure 41 shows some of the supersonic data obtained for a  $140^\circ$  cone compared with data for a  $120^\circ$  cone (ref. 37). It can be seen that the  $140^\circ$  cone has roughly 5 percent greater drag and has comparable stability for the realistic moment centers shown on the right of the figure. Additional comparisons are afforded by the drag-coefficient data plotted in figure 42. These results were obtained in the NOL pressurized ballistic range (ref. 34) at high Mach numbers in air and  $CF_4$ . The latter was used since it has a low ratio of specific heats ( $\approx 1.15$ ) similar to that of gases in the shock layer of bodies traveling at entry speeds. Clearly, the data for air are comparable to those previously presented; the data for  $CF_4$  indicate a higher level of drag, particularly for the  $140^\circ$  cone (note value of 1.76 for  $C_D$ ). The reason that the  $140^\circ$  cone appreciates more in drag than the  $120^\circ$  cone when tested at low values of  $\gamma$  is that the flow field behind the shock on the  $140^\circ$  cone remains subsonic to much lower values of  $\gamma$  than that of the  $120^\circ$  cone. It can be seen in figure 43 that the drag of a  $140^\circ$  cone increases for values of  $\gamma$  all the way down to 1.1 after which the flow becomes supersonic. The drag of a  $120^\circ$  cone, on the other hand, will diminish after a value of  $\gamma \approx 1.2$  is reached. With the aid of figures 44 and 45 (ref. 38), this phenomenon can be more easily seen. Figures 44 and 45 depict the shock shape and pressure-distribution calculations for  $120^\circ$  and  $140^\circ$  cones where the ratio of specific heats is 1.17. In figure 44 for the  $120^\circ$  cone, the shock is supersonic-like, that is, straight, and the pressure distribution

is flat as that for supersonic cone flow. Figure 45 on the other hand shows that the  $140^\circ$  cone has a shock shape and pressure distribution typical of blunt-body subsonic shock layers.

Dynamic forces and moments are also obtainable in many facilities using various techniques. In contrast to the measurement of static force and moments, where all techniques yield accurate data (except in the case noted earlier), the measurement of dynamic forces and moments do not yield uniformly accurate data and even accurate data may be difficult to interpret. One of the most common facilities for measuring the dynamic damping derivative is the ballistic range. In a ballistic test, the altitude and time histories are determined by taking shadowgraphs and recording the time that the model passes each station. To determine the damping requires three to four oscillations over the distance where shadowgraphs are being taken. Blunt cones have so much static stability that in order to get the three to four cycles for a solid metal model, the dynamic pressures must be extremely low. When the dynamic pressure is reduced, the damping is also reduced, and it becomes very difficult to measure accurately any angle-of-attack amplitude decay. To circumvent this problem, a heavy metal base extension or other ballasting and construction features are used; this reduces  $C_{m_\alpha}$  and also in some cases the mass inertia ratio, both of which are effective in reducing the frequency. Typical homogeneous, solid, blunt-body values of  $C_{m_q} + C_{m_{\dot{\alpha}}}$  given in figure 46 for the  $120^\circ$  cone indicate the problem that exists when unballasted small models are used. The uncertainty in the measurements shown by the line on either side of the symbol is so large as to render the data useless except as a trend indicator.

Another difficulty with free-flight data (both ballistic range and wind tunnel) is that the damping (or  $C_D$ ,  $C_{m_\alpha}$ ,  $C_{N_\alpha}$ ) is an average over the whole angle-of-attack range through which it oscillates. Unless a large number of tests at various amplitudes are made at the same flight velocity, the variation of these quantities with angle of attack cannot be ascertained. Very often scatter in the free-flight data can be ascribed to variations with angle of attack of the quantity being measured.

Some insight into the angle-of-attack variation of the damping moments can be obtained by using the forced-oscillation technique. This technique measures the damping at discrete angles of attack when the model is oscillated with a small amplitude typically  $1^\circ$  or  $2^\circ$  about the desired angle of attack. This type of testing has two drawbacks: First, a sting is required which alters the flow in the base region; and second, the motion for which the damping is measured is not a good simulation of the actual free-flight motion except for small amplitude motion about the trim angle of attack. Nevertheless, these data do a very effective job of explaining free-flight measurements of large amplitude.

Figure 47 gives a plot of  $C_{m_q} + C_{m_{\dot{\alpha}}}$  for the  $120^\circ$  and  $140^\circ$  cones at Mach numbers of 3 and 5 obtained by the forced-oscillation method in the von Kármán gas dynamics facility 40-inch supersonic tunnel (A) at Arnold Engineering and Development Center (ref. 39). These data indicate that the  $120^\circ$  cone is slightly more stable than the  $140^\circ$  cone and that both yield values larger than Newtonian predictions. A plot of  $C_{m_q} + C_{m_{\dot{\alpha}}}$  for the  $120^\circ$  cone at a Mach number of 5.02 from  $0^\circ$  to  $34^\circ$  angle of attack is given in figure 48. The nonlinearity of the curve shown here points up the value of a forced-oscillation test and at the same time indicates the difficulty of interpreting free-flight data.

### TIME HISTORIES OF HEATING RATES, DYNAMIC PRESSURES, AND DECELERATIONS

In carrying out trade-off or parametric studies for atmospheric-entry capsules, the point-mass equations of motion are usually used to predict the trajectory and the trajectory-dependent quantities such as convective and radiative heating rates, free-stream dynamic pressure, and impact point. It should also be noted that with the analysis of reference 40 it is possible to do parametric studies of the dynamical behavior of the entry vehicle. From this paper a "first cut" evaluation of its dynamic stability as well as the maximum oscillatory frequency and angular acceleration may be obtained. Once the capsule system becomes well defined, the six-degree-of-freedom motion equations may be employed to assess in a more exact fashion the effects of the entry vehicles oscillatory motion on the trajectory and heating.

Results of parametric studies for the Mars and Venus missions described earlier are given in references 3 to 5. Curves illustrating the type of data obtained in these studies are shown in figures 49 and 50. They were calculated by using the point-mass trajectory equations derived in appendix E and a convective heating rate equation similar to equation (2). The radiative heating calculations shown in figure 50 were obtained from reference 29 and based in part on the analysis of reference 28. Figure 49, which shows results for several Mars orbit entries, substantiates the heating trends discussed previously. Increasing  $m/C_D A$ , entry angle, entry velocity, and inverse density scale height  $\beta$  causes the maximum convective heating rates to increase. The total heat input during entry is decreased when entry angle and inverse scale height are increased.

Maximum dynamic pressures are clearly sensitive to entry angle and increase with increasing  $m/C_D A$ . The effect of decreasing entry velocity from 16 000 to 14 000 ft/sec for the VM-8 atmosphere and  $\phi_E = 15^\circ$  results in an anomalous increase in maximum dynamic pressure and deceleration. This is typical of the kind of results obtained for entry angles which are near the skipout boundary.

Table VIII lists the maximum values of the curves shown in figure 49 plus data on several 12 000-ft/sec entries. For  $m/C_D A = 0.3$ , the maximum stagnation-point heating rates vary from 16.8 to 65.5 Btu/ft<sup>2</sup>-sec. Total heat inputs to the stagnation point range from 719 to 2776 Btu/ft<sup>2</sup>. (Note that for nose radii greater than 1.0 foot these values will be reduced by the square root of the nose radius.) Clearly, the heat shield will have to be designed to the large total heat input of the VM-9 atmosphere while the aeroshell structure must be designed to accommodate the large dynamic pressures incurred during entry into the VM-8 atmosphere.

Curves for Venus entries similar to those just discussed for Mars are shown in figure 50 for a 55° half-angle cone (obtained from ref. 29). The ballistic coefficient for these calculations is 0.3 and the entry angle is 40°. Results for three entry velocities typical of the various Venus missions discussed previously are given. It can be seen in figure 50 that the maximum dynamic pressures, decelerations, and heating rates are over an order of magnitude higher than they are for Mars. Also, it is evident that the duration of the dynamic pressure, deceleration pulses, and heating rate is much shorter. This is due primarily to the steeper entry angle, 40° versus 15° or 20°.

Figures 50(c) and 50(d) for a 38 000-ft/sec entry show that both the radiative and convective heating rates are significant. Three separate contributions to the radiative heating rate are plotted, the equilibrium, nonequilibrium, and ultraviolet. At the stagnation point, all three contribute significantly to the total heat input, while at the cone edge the shock layer is not as hot as the stagnation-point region and ultraviolet radiation is no longer a factor. As the entry velocity is increased beyond 38 000 ft/sec, the shock-layer temperatures will increase and ultraviolet radiation can become significant in the cone-edge region.

The abrupt increase in the convective heating rate at 8.5 seconds is due to transition to turbulent flow. Obviously, after transition occurs, the cone-edge heating rates become comparable to those at the stagnation point. Criteria available to determine whether the flow is laminar or turbulent are empirical and unreliable. One procedure is to assume that the flow is turbulent when the local Reynolds number exceeds some arbitrary value, usually on the order of 300 000 to 400 000. Another criterion is based on the local momentum thickness Reynolds number. The latter was used in reference 29 and a value of 250 was assumed. Increasing the cone angle will probably delay transition to a later point in the flight and thus reduce the convective heat input, but this advantage must be weighed against the increase in radiative heating that will also result. Calculations of the stagnation-point and cone-edge heating rates for a range of cone angles and nose radii are given in reference 29.

## CONCLUDING REMARKS

The discussion of problems associated with Mars and Venus entry vehicles has been directed mainly at those aspects related to fluid mechanics and gas dynamics. Elementary considerations involved in the calculation of convective and radiative heating rates and in the selection of a heat-shield material are reviewed. Aerodynamic force and moment data for blunt cones from a number of different facilities are illustrated and some of the shortcomings of various test techniques are pointed out. The importance of considering real-gas and atmospheric-composition effects in the extrapolation of low Mach number (say less than 10) aerodynamic and heating data to high Mach numbers is emphasized. Mathematical derivations have been avoided except where an attempt was made to illustrate the important parameters governing aerodynamic heating and free-stream dynamic pressure. These derivations stem mainly from references 12 and 13.

Time histories of aerodynamic heating, accelerations, and dynamic pressure were given for values of  $m/C_D A$  and entry conditions appropriate to Mars and Venus entries. It was assumed in these calculations that the entry vehicles were nonlifting, had no motion, and did not lose mass (from the ablation shield, for example) during entry. For Venus, the mass loss from the heat shield is large enough for the highest velocity entries that the trajectory prediction could be improved if mass loss were considered. Ablation-material losses during Mars entry are trivial. Motion effects are very much configuration and mission dependent. The detail variation of the aerodynamic forces and moments, the aerodynamic damping, vehicle mass and inertia, entry conditions including initial angle of attack, rotational rate and spin rate, and the properties of the atmosphere itself all affect the entry spacecraft motion and hence its trajectory.

Normally when precise entry-vehicle trajectories and motions are required, computer programs utilizing the six-degree-of-freedom equations of motion are employed (see, for example, ref. 41). Little insight is afforded into the governing parameters, however, by six-degree-of-freedom computations except through a number of runs. Insight is most easily obtained from analyses such as presented in references 40 and 42 to 44. Reference 40 treats the motion of nonspinning entry bodies and references 42 to 44 the spinning case.

As noted previously, the few calculations presented in the present paper were for nonlifting vehicles. Many present-day spacecraft are designed as lifting vehicles so as to minimize accelerations (manned vehicles) or to provide a maneuver capability. For a Mars entry vehicle, lift enables it to reach a prescribed velocity at a higher altitude or a fixed altitude with a lower velocity than is possible with no lift. In addition, a lifting spacecraft permits a higher entry weight than a nonlifting one for fixed terminal conditions. Further information on the advantages and problems of lifting entry may be obtained from references 45 to 47.

One final topic of importance for Mars and Venus entries which, although it relates to aerodynamics, has not been covered in the present paper is decelerators. Much research has been carried out in the past few years to provide a reliable high-drag parachute for the low-density Mars atmosphere. References 48 to 50 discuss results of some of these programs and also some of the decelerator options open to the designer. Parachute technology required for Venus mission of the type described previously is the same as that for low-velocity low-altitude Earth applications. A general state-of-the-art study is given in reference 51.

In conclusion, it should be pointed out that only a general, broad-brush treatment of a few selected technology areas has been attempted. More detailed information can be obtained on most of the subjects in the referenced documents.

## APPENDIX A

### DERIVATION OF ATMOSPHERIC DENSITY AND PRESSURE EQUATIONS

The purpose of this appendix is to show how the pressure, density, temperature, and composition are related through the use of the barometric equation

$$dp = -\rho g dh \quad (A1)$$

and the equation of state

$$p = \rho RT \quad (A2)$$

First differentiate equation (A2) to obtain  $dp$  and substitute it into equation (A1) to arrive at

$$RT d\rho + R\rho dT + \rho T dR = -\rho g dh$$

Dividing by  $\rho RT$ , the basic differential equation is obtained

$$\frac{d\rho}{\rho} + \frac{dT}{T} + \frac{dR}{R} = -\frac{g dh}{RT} \quad (A3)$$

For complicated variations of temperature and composition (variations in  $R$ ) equation (A3) must be integrated numerically; for atmospheres where these quantities are constant or vary in a simple manner closed-form expressions can be derived. For instance, with  $g$ ,  $R$  and  $T$  constant ( $g = g_s$ ,  $T = T_s$ ), equation (A3) can be integrated by inspection to yield

$$\rho = \rho_s e^{-g_s h / RT} \quad (A4)$$

With the definition

$$\frac{RT_s}{g_s} = H\rho = \frac{1}{\beta_s} \quad (A5)$$

equation (A4) becomes

$$\rho = \rho_s e^{-\beta_s h} \quad (A6)$$

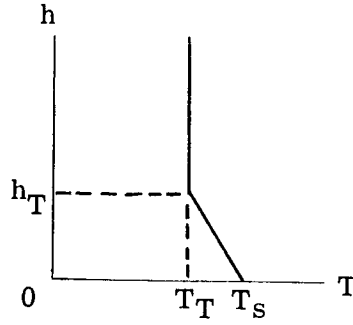
The pressure may now be determined from equations (A6) and (A2) as

$$p = p_s e^{-\beta_s h} \quad (A7)$$

For a temperature profile similar to that of the VM-8 atmosphere, the density and pressure can again be obtained in closed form ( $R$  and  $g$  assumed constant). See following sketch:



# APPENDIX A



With  $T$  now given by

$$\left. \begin{aligned} T &= T_S + \Gamma h & (0 < h \leq h_T) \\ T &= T_T & (h > h_T) \end{aligned} \right\} \quad (A8)$$

equation (A3) can be integrated to obtain

$$\rho = \rho_S \left( 1 + \frac{\Gamma h}{T_S} \right)^{-\frac{g_S}{R\Gamma} - 1} \quad (0 < h < h_T) \quad (A9)$$

Equations (A8) and (A9) are then substituted in equation (A2) to determine the pressure as

$$p = p_S \left( 1 + \frac{\Gamma h}{T_S} \right)^{-\frac{g_S}{R\Gamma}} \quad (0 < h < h_T) \quad (A10)$$

Above the tropopause where  $T = T_T$ , integration of equation (A3) results in

$$\left. \begin{aligned} \rho &= \rho_T e^{-\beta(h-h_T)} \\ \rho &= \rho_T e^{\beta h_T} e^{-\beta h} \end{aligned} \right\} \quad (h > h_T) \quad (A11)$$

Note that  $\rho_T e^{\beta h_T}$  can be thought of as an effective surface density (compare with eq. (A6)). Setting  $h = h_T$  in equation (A9) determines the tropopause density  $\rho_T$  in terms of surface quantities as

$$\rho_T = \rho_S \left( 1 + \frac{\Gamma h_T}{T_S} \right)^{-\frac{g_S}{R\Gamma} - 1} \quad (A12)$$

In equation (A11)  $\beta$  is defined by

$$\beta = \frac{RT_T}{g_S} \quad (A13)$$

As before, substitution of  $\rho$  (eq. (A11)) and  $T$  into equation (A2) yields the pressure

$$p = p_T e^{-\beta(h-h_T)} \quad (h > h_T) \quad (A14)$$

## APPENDIX A

where  $p_T$  is obtained from equation (A10) with  $h = h_T$ . Thus

$$p_T = p_s \left( 1 + \frac{\Gamma h_T}{T_s} \right)^{-\frac{g_s}{R\Gamma}} \quad (\text{A15})$$

One further element of realism may be added to the solution of equation (A3) by allowing for the variations of the gravitational constant. With the same temperature profile as in the preceding sketch and

$$g = g_s \left( \frac{r_s}{r_s + h} \right)^2 \quad (\text{A16})$$

the integration of equation (A3) gives the density as

$$\rho = \frac{\rho_s e^{-\frac{g}{RT_s} \frac{h}{\left(1 - \frac{r_s \Gamma}{T_s}\right) \left(1 + \frac{h}{r_s}\right)}}}{1 + \frac{\Gamma h}{T_s}} \left( \frac{1 + \frac{\Gamma h}{T_s}}{1 + \frac{h}{r_s}} \right)^{-\frac{\Gamma g r_s^2}{RT_s^2 \left(1 - \frac{r_s \Gamma}{T_s}\right)^2}} \quad (0 < h < h_T) \quad (\text{A17})$$

and

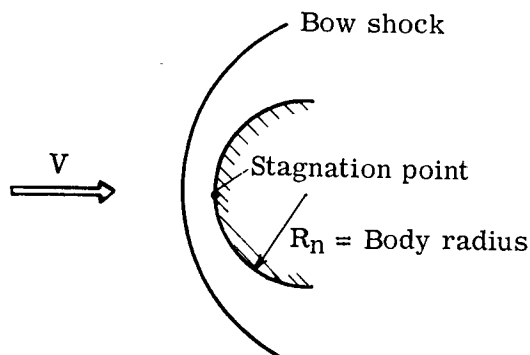
$$\rho = \rho_T e^{-\frac{g_s}{RT_s} \frac{h - h_T}{\left(1 + \frac{h}{r_s}\right) \left(1 + \frac{h_T}{r_s}\right)}} \quad (h > h_T) \quad (\text{A18})$$

Expressions for  $\rho_T$ ,  $p$ , and  $p_T$  are determined as in equations (A12), (A14), and (A15), respectively.

## APPENDIX B

### STAGNATION-POINT CONVECTIVE HEAT TRANSFER

The following derivation of the stagnation-point convective heating rate equation is the same, except for minor modifications and additions, as that given in reference 12. It is repeated here because of the insight it affords into the basic parameters governing convective heating during entry. In addition, since reference 12 may not be readily available to the reader, it provides a measure of completeness. The flow situation appropriate to the present analysis is given in the following sketch:



The convective heating rate can be expressed as

$$\frac{dq_{c,o}}{dt} = \dot{q}_{c,o} = -\frac{Nu_R k_R (T_w - T_R)}{R_n} \quad (B1)$$

where  $Nu_R$  is the Nusselt number, a form of heat-transfer coefficient,  $k_R$  is the conductivity of the gas at the recovery temperature of the gas  $T_R$ , and  $T_w$  is the gas temperature at the wall. The recovery temperature  $T_R$  is given by

$$T_R = T_\infty \left[ 1 + f(Pr) \frac{\gamma - 1}{2} M_\infty^2 \right]$$

and with the approximation  $Pr \approx 1$ ,  $T_R$  becomes (see section entitled "High-Temperature Gas Physics" for discussion of  $Pr$ )

$$T_R = T_\infty \left( 1 + \frac{\gamma - 1}{2} M_\infty^2 \right) \quad (B2)$$

The addition of  $T_w$  to both sides of the negative of equation (B2) yields

$$T_w - T_R = - \left( T_\infty - T_w + \frac{\gamma - 1}{2} M_\infty^2 T_\infty \right) \quad (B3)$$

## APPENDIX B

Noting that for large  $M$

$$T_{\infty} - T_w \ll \frac{\gamma - 1}{2} M_{\infty}^2 T_{\infty}$$

equation (B3) can be reduced to

$$T_w - T_r = -\frac{\gamma - 1}{2} M_{\infty}^2 T_{\infty} \quad (B4)$$

With the substitution of the relationship

$$M_{\infty}^2 T_{\infty} = \frac{V_{\infty}^2}{(\gamma - 1)c_p}$$

into equation (B4), there results

$$T_w - T_r = -\frac{V_{\infty}^2}{2c_p} \quad (B5)$$

According to Sibulkin (ref. 52)  $Nu_r$  is given by

$$Nu_r = 0.934(Re)^{1/2}(Pr)^{2/5} \quad (B6)$$

Again with  $Pr = 1$  and

$$Re = \frac{\rho V_{\infty} R_n}{\eta_r} \quad (B7)$$

equation (B1) becomes

$$\dot{q}_{c,o} = 0.47 \sqrt{\frac{\rho V_{\infty} R_n}{\eta_r}} \frac{V_{\infty}^2 k_r}{R_n c_p} = 0.47 \sqrt{\frac{\rho V_{\infty} \eta_r}{R_n}} V_{\infty}^2 \left( \frac{k_r}{\eta_r c_p} \right) \quad (B8)$$

But

$$\frac{\eta_r c_p}{k_r} = Pr = 1$$

so that

$$\dot{q}_{c,o} = 0.47 \sqrt{\frac{\rho V_{\infty} \eta_r}{R_n}} V_{\infty}^2 \quad (B9)$$

Assuming

$$\eta_r = 2.31 \times 10^{-8} T_r^{1/2} \quad (B10)$$

and making the approximation that  $T_w \ll T_r$ , then using equation (B5) in equation (B8)

$$\eta_r = \frac{2.31 V_{\infty}}{\sqrt{2} \sqrt{c_p}} \times 10^{-8} \quad (B11)$$

## APPENDIX B

Replacing  $\eta_r$  in equation (B9) by equation (B11) results in

$$\dot{q}_{c,o} = 0.47 \sqrt{\frac{\rho V_\infty^2 2.31 \times 10^{-8}}{\sqrt{c_p R_n} \sqrt{2}}} V_\infty^2$$

A low-temperature value of  $c_p$  of 6006 ft<sup>2</sup>/sec<sup>2</sup>-°R is used to arrive at

$$\dot{q}_{c,o} = 6.8 \times 10^{-6} \sqrt{\frac{\rho}{R_n}} V_\infty^3 \text{ ft-lbf/ft}^2\text{-sec} \quad (\text{B12})$$

This equation gives values lower than most stagnation-point heating equations by roughly a factor of 2 owing to the approximations made in the stagnation-point velocity gradient in deriving equation (B1); the fact that the density in equation (B12) is taken as the free-stream value rather than the value at the stagnation point, and the values of  $c_p$  and  $Pr$  used. Nevertheless, the functional form was the prime consideration in reference 12 and more recently derived equations for  $\dot{q}_c$  differ little in form from equation (B12). In the remainder of this section the following equation for  $\dot{q}_{c,o}$ , different from equation (B12) by a constant factor, will be used

$$\dot{q}_{c,o} = 15.25 \times 10^{-6} \sqrt{\frac{\rho}{R_n}} V_\infty^3 \text{ ft-lbf/ft}^2\text{-sec} \quad (\text{B13})$$

Combining the expression for  $V$  derived in appendix C with equation (B13) results in

$$\dot{q}_{c,o} = 15.25 \times 10^{-6} \sqrt{\frac{\rho_s}{R_n}} V_E^3 e^{-\frac{\beta h}{2}} e^{-\frac{3C_D \rho_s A}{2\beta m \sin \phi_E} e^{-\beta h}} \text{ ft-lbf/ft}^2\text{-sec} \quad (\text{B14})$$

The maximum value of heating rate during entry can now be easily obtained as

$$(\dot{q}_{c,o})_{\max} = 15.25 \times 10^{-6} \sqrt{\frac{\rho_s}{3eR_n K}} V_E^3 \left( K = \frac{\rho_s C_D A}{\beta m \sin \phi_E} \right) \text{ ft-lbf/ft}^2\text{-sec} \quad (\text{B15})$$

which occurs at an altitude of

$$h = \frac{1}{\beta} \ln 3K \quad (\text{B16})$$

and a velocity of

$$V = V_E e^{-1/6} = 0.85V_E \quad (\text{B17})$$

Equation (B15) applies only to the case where  $h$  determined by equation (B16) is positive (see ref. 12).

## APPENDIX B

The total heat input to the stagnation point over the entire flight may be obtained by integrating equation (B13) with the aid of the integration given in appendix D (see ref. 13) as

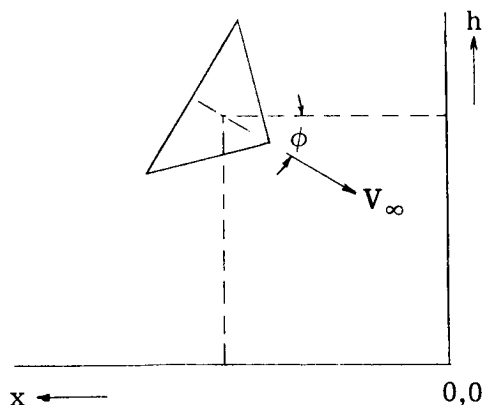
$$q_{c,o} = \frac{15.25 \times 10^{-6} \sqrt{\pi}}{(R_n^\beta \sin \phi_E)^{1/2}} V_E^2 \left( \frac{m}{C_{DA}} \right)^{1/2} \text{ ft-lbf/ft}^2 \quad (\text{B18})$$

## APPENDIX C

### STRAIGHT-LINE-FLIGHT TRAJECTORY EQUATIONS

Closed-form solutions of the point-mass trajectory equations do not exist. Therefore, to obtain the required insight into the effects of ballistic coefficients, entry velocity, and entry flight-path angle on such things as maximum entry heating and loads, some assumptions must be made to affect an analytical solution. One possibility for ballistic (nonlifting) vehicles is to assume the flight-path angle constant. Examination of point-mass trajectories (see appendix E) shows that flight-path angles change very little (except for shallow entry angles) up to peak heating and deceleration so that the aforementioned assumption is not a great handicap. A second assumption which has even less effect on the heating and deceleration calculations is that of neglecting gravity. Using both of these assumptions, Allen and Eggers in reference 12 developed a rather classical analysis for the velocity and deceleration experienced by entry vehicles. It shows in a straightforward manner how these quantities are influenced by the ballistic coefficient, entry vehicle, and atmospheric properties. A part of this analysis will be repeated here with some minor additions.

The balance of forces on the entry vehicle shown in the following sketch:



yields the following two equations

$$\frac{d^2h}{dt^2} = -g + \frac{C_D \rho V_\infty^2 A}{2m} \sin \phi \quad (C1)$$

$$\frac{d^2x}{dt^2} = \frac{C_D \rho V_\infty^2 A}{2m} \cos \phi \quad (C2)$$

where  $x$  is the distance measured parallel to the surface. By considering only the

## APPENDIX C

vertical-flight situation and by assuming that the atmospheric density can be expressed in the form  $\rho = \rho_s e^{-\beta h}$  (see appendix A) over the altitude range of interest, equation (C1) can be written as

$$\frac{d^2 h}{dt^2} = -\frac{dV_\infty}{dt} = -g + \frac{C_D \rho_s V_\infty^2 A}{2m} e^{-\beta h} \quad (C3)$$

Since

$$\frac{dV_\infty}{dt} = \frac{dV_\infty}{dh} \frac{dh}{dt} = -V_\infty \frac{dV_\infty}{dh}$$

equation (C3) can be rewritten to yield

$$V_\infty \frac{dV_\infty}{dh} = -g + \frac{C_D \rho_s A V_\infty^2}{2m} e^{-\beta h} \quad (C4)$$

A new variable  $Z = V_\infty^2$  is now introduced and equation (C4) becomes

$$\frac{dZ}{dh} - \frac{C_D \rho_s A}{m} e^{-\beta h} Z + 2g = 0 \quad (C5)$$

the solution of which is

$$Z = e^{\int \frac{C_D \rho_s A}{m} e^{-\beta h} dh} \left( -2g \int e^{-\int \frac{C_D \rho_s A}{m} e^{-\beta h} dh} dh + \text{const} \right) \quad (C6)$$

or

$$Z = e^{-\frac{C_D \rho_s A}{\beta m} e^{-\beta h}} \left( \frac{2g}{\beta} \int \frac{e^Y dY}{Y} + \text{const} \right)$$

where  $Y$  is defined  $\frac{C_D \rho_s A}{\beta m} e^{-\beta h}$ . Carrying out the previously indicated integration gives

$$Z = e^{-\frac{C_D \rho_s A}{\beta m} e^{-\beta h}} \left[ \frac{2g}{\beta} \left( \log Y + \sum_{n=1}^{\infty} \frac{Y^n}{nn!} \right) + \text{const} \right]$$



# APPENDIX C

If  $Y$  and  $Z$  are replaced by the original variables, the following equation for  $V_\infty^2$  results

$$V_\infty^2 = e^{-\frac{C_D \rho_s A}{\beta m} e^{-\beta h}} \left[ \frac{2g}{\beta} \sum_{n=1}^{\infty} \frac{\left( \frac{C_D \rho_s A}{\beta m} e^{-\beta h} \right)^n}{n n!} - 2gh + \text{const} \right] \quad (C7)$$

The equation for deceleration is obtained by the substitution of equation (C7) in equation (C3)

$$\frac{-\frac{dV_\infty}{dt}}{g} = \frac{C_D \rho_s A}{2mg} e^{-\beta h} e^{-\frac{C_D \rho_s A}{\beta m} e^{-\beta h}} \left[ \frac{2g}{\beta} \sum_{n=1}^{\infty} \frac{\left( \frac{C_D \rho_s A}{\beta m} e^{-\beta h} \right)^n}{n n!} - 2gh + \text{const} \right] - 1 \quad (C8)$$

It may be of interest to note that the integration of equation (C6) could have been written in terms of the  $\overline{\text{Ei}}(x)$  function which is defined and tabulated in reference 53. It has been shown that for the high speed portion of orbital entry  $g$ -terms have a negligible effect; therefore equation (C7) can be written

$$V_\infty^2 = \text{const} e^{-\frac{C_D \rho_s A}{\beta m} e^{-\beta h}}$$

The arbitrary constant is determined by letting  $V_\infty = V_E$  at  $h = h_E$  so that the preceding equation for  $V_\infty^2$  becomes

$$V_\infty^2 = V_E^2 e^{-\frac{C_D \rho_s A}{\beta m} (e^{-\beta h} - e^{-\beta h_E})}$$

With the realization that

$$e^{\frac{C_D \rho_s A}{\beta m} e^{-\beta h_E}} \approx 1$$

the final simplified expression for the velocity and deceleration in vertical flight are seen to be

$$V_\infty = V_E e^{-\frac{C_D \rho_s A}{2\beta m} e^{-\beta h}} \quad (C9)$$

## APPENDIX C

and

$$\frac{-\frac{dV_{\infty}}{dt}}{g} = \frac{C_D \rho_s A V_E^2}{2mg} e^{-\beta h} e^{-\frac{C_D \rho_s A}{\beta m} e^{-\beta h}} \quad (C10)$$

respectively. A more compact form of equations (C9) and (C10) is obtained if

$\frac{C_D \rho_s A}{\beta m} = K$  is defined; that is

$$\frac{V_{\infty}}{V_E} = e^{-\frac{K}{2} e^{-\beta h}} \quad (C11)$$

and

$$\frac{-d\left(\frac{V_{\infty}}{V_E}\right)}{d(\beta V_E t)} = \frac{K}{2} e^{-\beta h} e^{-K e^{-\beta h}} \quad (C12)$$

By considering now the inclined flight-path case, and again by assuming that gravity is negligible, it is seen that equation (C1) becomes

$$\frac{d^2 h}{dt^2} = -\frac{d(V_{\infty} \sin \phi_E)}{dt} = \frac{C_D \rho V_{\infty}^2 A}{2m} \sin \phi_E \quad (C13)$$

or

$$\frac{-dV_{\infty}}{dt} = \frac{C_D \rho V_{\infty}^2 A}{2m} \quad (C14)$$

Equation (C14) may be written with  $h$  as the independent variable as

$$V_{\infty} \sin \phi_E \frac{dV_{\infty}}{dh} = \frac{C_D \rho V_{\infty}^2 A}{2m} e^{-\beta h} \quad (C15)$$

with the use of

$$\frac{dV_{\infty}}{dt} = \frac{dV_{\infty}}{dh} \frac{dh}{dt} = -V_{\infty} \sin \phi_E \frac{dV_{\infty}}{dh}$$

## APPENDIX C

and

$$\rho = \rho_s e^{-\beta h}$$

By rearranging equation (C15) in the following form

$$\frac{dV_\infty}{V_\infty} = \frac{C_D \rho_s A}{2m \sin \phi_E} e^{-\beta h} dh$$

the integration may be readily accomplished to yield a slightly more general expression than equation (C9). Thus

$$V_\infty = V_E e^{\frac{-C_D \rho_s A}{2\beta m \sin \phi_E} e^{-\beta h}} \quad (C16)$$

The counterpart to equation (C10) is

$$-\frac{dV_\infty}{dt} = \frac{C_D \rho_s A V_E^2}{2mg} e^{-\beta h} e^{\frac{-C_D \rho_s A}{\beta m \sin \phi_E} e^{-\beta h}} \quad (C17)$$

Equations similar to equations (C11) and (C12) are obtained if  $K$  is redefined as

$$K = \frac{C_D \rho_s A}{\beta m \sin \phi_E} \quad (C18)$$

and the reduced time as  $\beta V_E t \sin \phi_E$ .

With equations (C16) and (C17), it is possible to determine the velocity or acceleration in terms of altitude. To obtain the relationship between altitude and time and hence velocity and acceleration with time, use is made of

$$\frac{dh}{dt} = -V_\infty \sin \phi_E$$

and equation (C16) to write

$$\frac{dh}{dt} = -V_E \sin \phi_E e^{-\frac{K}{2} e^{-\beta h}}$$

## APPENDIX C

Rearranging the previous equation and multiplying both sides by  $\beta$  results in

$$\int_{\beta h_E}^{\beta h} \frac{-d(\beta h)}{e^{-\frac{K}{2}e^{-\beta h}}} = \int_0^t d(\beta V_E t \sin \phi_E) \quad (C19)$$

If  $\frac{K}{2}e^{-\beta h} = x$  and  $\frac{K}{2}e^{-\beta h_E} = x_E$ , the left-hand side of equation (C18) becomes

$$\int_{x_E}^x \frac{e^x dx}{x} = \int_0^x \frac{e^x dx}{x} - \int_0^{x_E} \frac{e^x dx}{x}$$

and from reference 53 the equation

$$\beta V_E t \sin \phi_E = \overline{\text{Ei}}(x) - \overline{\text{Ei}}(x_E)$$

or

$$\beta V_E t \sin \phi_E = \overline{\text{Ei}}\left(\frac{K}{2}e^{-\beta h}\right) - \overline{\text{Ei}}\left(\frac{K}{2}e^{-\beta h_E}\right) \quad (C20)$$

is obtained. A table of  $\overline{\text{Ei}}(x)$  is given in reference 53 but it is inadequate at low values of the argument which are needed to establish the value of  $\overline{\text{Ei}}\left(\frac{K}{2}e^{-\beta h_E}\right)$ . A plot of this function is given in figure 51.

By taking a derivative of equation (C12) with respect to  $h$  to obtain the maximum deceleration, the condition obtained is

$$Ke^{-\beta h} = 1 \quad (C21)$$

or from equation (C16)

$$V_\infty = V_E e^{-\frac{1}{2}} \quad (C22)$$

at maximum deceleration. The value of the maximum deceleration is

$$\frac{-d(V_\infty/V_E)}{d(\beta V_E t \sin \phi_E)} = \frac{1}{2e} \quad (C23)$$

## APPENDIX C

and it occurs at

$$h = \frac{1}{\beta} \ln K \quad (C24)$$

with  $K$  given by equation (C20).

The free-stream dynamic pressure is defined by

$$q_{\infty} = \frac{1}{2} \rho V_{\infty}^2$$

and maximum pressure loads occur when  $q_{\infty}$  is a maximum. With  $dV_{\infty}/dt$  equal to a constant times  $q_{\infty}$ , the dynamic pressure will be a maximum at the same time as  $dV_{\infty}/dt$ .

## APPENDIX D

### INTEGRATION REQUIRED TO OBTAIN TOTAL HEAT INPUT

In order to obtain  $q_c$  and  $q_r$  from  $\dot{q}_c$  and  $\dot{q}_r$  an integration of the form  $\int_0^{t_s} \rho^m V_\infty^n dt$  must be accomplished. Utilization of equations (3) and (4) enables the integral under consideration to be written as

$$\rho_s^m V_E^n \int_0^{t_s} e^{-\beta h m} e^{-n \frac{K}{2} e^{-\beta h}} dt \quad (D1)$$

Further convenience is offered by changing the variable of integration from  $t$  to  $h$  through use of equation (1). By carrying out this manipulation, expression (D1) becomes

$$-\frac{\rho_s^m V_E^{n-1}}{\sin \phi_E} \int_{h_E}^0 e^{-\beta h m} e^{-(n-1) \frac{K}{2} e^{-\beta h}} dh \quad (D2)$$

If  $(n-1) \frac{K}{2} e^{-\beta h}$  is now set equal to a new variable  $\eta$ , the following simpler form of expression (D2) will result

$$\frac{\rho_s^m (V_E)^{n-1}}{\beta \sin \phi_E \left[ (n-1) \frac{K}{2} \right]^m} \int_{(n-1) \frac{K}{2} e^{-\beta h_E}}^{(n-1) \frac{K}{2}} \eta^{m-1} e^{-\eta} d\eta \quad (D3)$$

The lower limit in expression (D3) for practical values of  $K$  and  $h_E$  is effectively zero; the upper limit however is large enough that the value of the integral between this limit and  $\infty$  is negligible. Expression (D3) may therefore be approximated by

$$\frac{\rho_s^m (V_E)^{n-1}}{\beta \sin \phi_E \left[ (n-1) \frac{K}{2} \right]^m} \int_0^\infty \eta^{m-1} e^{-\eta} d\eta \quad (D4)$$

with negligible error. With the identification of the integral in expression (D4) as the gamma function, the original integral becomes completely defined in terms of prescribed and tabulated quantities; that is

$$\int_0^{t_s} \rho^m V_\infty^n dt \approx \frac{\rho_s^m V_E^{n-1} \Gamma(m)}{\beta \sin \phi \left[ (n-1) \frac{K}{2} \right]^m} \quad (D5)$$

## APPENDIX E

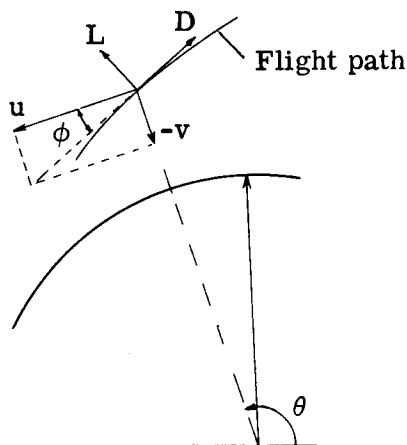
### DERIVATION OF POINT-MASS TRAJECTORY EQUATIONS

The derivation of the point-mass equations of motion given in this section is also found in many books and papers and is only repeated here for those who are new to the field. Also, it enables the interested reader to assess the consequences of the assumptions made in developing the straight-line trajectory equations of appendix C. In this respect, the reader is referred to the analysis of reference 54. This reference contains an approximate method of solution for the point-mass equations and gives computed results which, in some cases, are compared with those obtained by the equations of reference 12 (appendices B and C).

The vector acceleration in terms of the unit vectors  $\vec{e}_r$  and  $\vec{e}_\theta$  is

$$\vec{a} = \vec{e}_r \left( \frac{dv}{dt} - \frac{u^2}{r} \right) + \vec{e}_\theta \left( \frac{du}{dt} + \frac{uv}{r} \right) \quad (\text{E1})$$

where the positive direction of the velocities, forces, and angles are given in the following sketch:



With  $\tan \phi = -\frac{v}{u}$ , the aerodynamic force vector is

$$\vec{f} = (-mg + L \cos \phi + D \sin \phi) \vec{e}_r - (D \cos \phi - L \sin \phi) \vec{e}_\theta \quad (\text{E2})$$

If  $\vec{a}$  is multiplied by  $m$  and equated to  $\vec{f}$ , the two component acceleration equations are obtained as

$$-\frac{d^2h}{dt^2} = -\frac{dv}{dt} = g - \frac{u^2}{r} - \frac{L}{m} \cos \phi - \frac{D}{m} \sin \phi \quad (\text{E3})$$

## APPENDIX E

$$\frac{du}{dt} + \frac{uv}{r} = -\frac{D}{m} \left( \cos \phi - \frac{L}{D} \sin \phi \right) \quad (\text{E4})$$

In the interest of simplicity the lift term will be dropped for now. From the definition of  $C_D$

$$D = \frac{1}{2} \rho V_\infty^2 C_D A \quad (\text{E5})$$

and from equations (E3) and (E4)

$$-\frac{dv}{dt} = g - \frac{u^2}{r} - \frac{1}{2} \rho V_\infty^2 \frac{C_D A}{m} \sin \phi \quad (\text{E6})$$

and

$$-\frac{du}{dt} = \frac{uv}{r} + \frac{1}{2} \rho V_\infty^2 \frac{C_D A}{m} \cos \phi \quad (\text{E7})$$

(Note that  $V_\infty^2 = u^2 + v^2$ .) Replacing  $\sin \phi$  by  $-\frac{v}{V_\infty}$  and  $\cos \phi$  by  $\frac{u}{V_\infty}$  in equations (E6) and (E7) results in

$$-\frac{dv}{dt} = g - \frac{u^2}{r} + \frac{1}{2} \rho v V_\infty \frac{C_D A}{m} \quad (\text{E8})$$

and

$$-\frac{du}{dt} = \frac{uv}{r} + \frac{1}{2} \rho u V_\infty \frac{C_D A}{m} \quad (\text{E9})$$

respectively. Now equation (E8) is multiplied by  $v$  and equation (E9) by  $u$ ; then the two results are added to give

$$-V_\infty \frac{dV_\infty}{dt} = -g V_\infty \sin \phi + \frac{1}{2} \rho V_\infty^3 \frac{C_D A}{m} \quad (\text{E10})$$

or

$$\frac{dV_\infty}{dt} = g \sin \phi - \frac{1}{2} \rho V_\infty^2 \frac{C_D A}{m} \quad (\text{E11})$$

Differentiating the equation defining  $\tan \phi$ , that is

$$\tan \phi = -\frac{v}{u} \quad (\text{E12})$$

results in

$$\sec^2 \phi \frac{d\phi}{dt} = -\frac{1}{u} \frac{dv}{dt} + \frac{v}{u^2} \frac{du}{dt} \quad (\text{E13})$$



## APPENDIX E

Now  $\sec^2 \phi = \frac{u^2 + v^2}{u^2}$  and  $\frac{dv}{dt}$  and  $\frac{du}{dt}$  are given by equations (E8) and (E9) so that equation (E13) can be rewritten as

$$\frac{u^2 + v^2}{u} \frac{d\phi}{dt} = g - \frac{u^2}{r} - \frac{v^2}{r} \quad (\text{E14})$$

and finally

$$\frac{d\phi}{dt} = \frac{g \cos \phi}{V_\infty} - \frac{V_\infty \cos \phi}{r} + \left( \frac{1}{2} \rho V_\infty^2 \frac{C_{LA}}{m} \right) \quad (\text{E15})$$

Note that the term  $\frac{1}{2} \rho V_\infty^2 \frac{C_{LA}}{m}$  giving the lift contribution has been added. Equations (E11) and (E15) along with

$$\frac{dr}{dt} = -V_\infty \sin \phi \quad (\text{E16})$$

comprise the point-mass equations of motion.

## REFERENCES

1. Marquet, D. W.: Launch Period, Targeting and Error Analysis for Mars Direct and Orbital Missions. Space Projections From the Rocky Mountain Region, Vol. 1, Amer. Astronaut. Soc., 1968.
2. Praguski, W. J.; and Marquet, D.: Deorbit Maneuver and Targeting Strategy for Unmanned Mars Landers. Proceedings Fifth Space Congress, Vol. 1, Canaveral Council Tech. Soc., 1968, pp. 6.3-1 - 6.3-34.
3. Anon.: Soft Lander. Part I. Mars Soft Lander Capsule Study (Entry From Orbit) - Summary. Rep. G346 (Contract No. NAS 1-7977), McDonnell Douglas Astronautics Co., Sept. 1968. (Available as NASA CR-66665-1.)
4. Zeiner, Hugh N.; and Marquet, Donald W.: Study of Direct Versus Orbital Entry for Mars Missions. Vol. III: Appendix A - Launch Vehicle Performance and Flight Mechanics. Contract No. NAS 1-7976, Martin Marietta Corp., Aug. 1968. (Available as NASA CR-66661.)
5. Baxter, John F.; Frank, Ronald E.; Froistad, John N.; and Cody, Gene R.: Buoyant Venus Station Mission Feasibility Study for 1972 and 1973 Launch Opportunities. Vol. I - Mission Summary Definition and Comparison. Contract NAS 1-7590, Martin Marietta Corp., Jan. 1969. (Available as NASA CR-66725-1.)
6. Sloan, R. K.: Mariner Mars 1964 Project Report: Scientific Experiments. Tech. Rep. 32-883 (Contract No. NAS 7-100), Jet Propulsion Lab., California Inst. Technol., July 15, 1968. (Available as NASA CR-95876.)
7. Barnwell, Richard W.: Inviscid Radiating Shock Layers About Spheres Traveling at Hyperbolic Speeds in Air. NASA TR R-311, 1969.
8. Marrone, Paul V.: Normal Shock Waves in Air: Equilibrium Composition and Flow Parameters for Velocities From 26,000 to 50,000 ft/sec. Cal Rep. No. AG-1729-A-2 (Contract No. NASr-119), Cornell Aeronaut. Lab., Inc., Aug. 1962.
9. Lees, Lester: Laminar Heat Transfer Over Blunt-Nosed Bodies at Hypersonic Flight Speeds. Jet Propulsion, vol. 26, no. 4, Apr. 1956, pp. 259-269, 274.
10. Lee, Jerry S.; and Bobbitt, Percy J.: Transport Properties at High Temperatures of  $\text{CO}_2\text{-N}_2\text{-O}_2\text{-Ar}$  Gas Mixtures for Planetary Entry Applications. NASA TN D-5476, 1969.
11. Romig, Mary F.: Stagnation Point Heat Transfer for Hypersonic Flow. Jet Propulsion, vol. 26, no. 12, Dec. 1956, pp. 1098-1101.

12. Allen, H. Julian; and Eggers, A. J., Jr.: A Study of the Motion and Aerodynamic Heating of Ballistic Missiles Entering the Earth's Atmosphere at High Supersonic Speeds. NACA Rep. 1381, 1958. (Supersedes NACA TN 4047.)
13. Bobbitt, Percy J.: Effects of Shape on Total Radiative and Convective Heat Inputs at Hyperbolic Entry Speeds, Vol. 13 of Advances in Astronautical Sciences, Eric Burgess, ed., Western Periodicals Co., c.1963, pp. 290-319.
14. Horton, T. E.; and Babineaux, T. L.: Experimental Assessment of the Effect of Large Amounts of Argon in a Planetary Atmosphere on Stagnation-Point Convective Heating. AIAA Pap. No. 66-29, Jan. 1966.
15. Rose, P. H.; and Stankevics, J. O.: Stagnation-Point Heat-Transfer Measurements in Partially Ionized Air. AIAA J., vol. 1, no. 12, Dec. 1963, pp. 2752-2763.
16. Fay, James A.; and Kemp, Nelson H.: Theory of Stagnation-Point Heat Transfer in a Partially Ionized Diatomic Gas. AIAA J., vol. 1, no. 12, Dec. 1963, pp. 2741-2751.
17. Hoshizaki, H.: Heat Transfer in Planetary Atmospheres at Super-Satellite Speeds. ARS J., vol. 32, no. 10, Oct. 1962, pp. 1544-1552.
18. Adams, Mac C.: Recent Advances in Ablation. ARS J., vol. 29, no. 9, Sept. 1959, pp. 625-632.
19. Olstad, W. B.: Nongray Radiating Flow About Smooth Symmetric Bodies With Large Blowing. AIAA Pap. No. 69-637, June 1969.
20. Arnold, James O.; Reis, Victor H.; and Woodward, Henry T.: Studies of Shock-Layer Radiation of Bodies Entering Planetary Atmospheres. AIAA J., vol. 3, no. 11, Nov. 1965, pp. 2019-2025.
21. Thomas, G. M.; and Menard, W. A.: Experimental Measurements of Nonequilibrium and Equilibrium Radiation From Planetary Atmospheres. AIAA J., vol. 4, no. 2, Feb. 1966, pp. 227-237.
22. Bunting, Jackie O.: Experimental Investigation of the Nonequilibrium Radiation Emitted by Mars-Like Gas Mixtures. NASA CR-1740, 1970.
23. Perrine, C.: Estimation of Maximum Heating Rates and Total Heat Load During Supercircular Re-Entry. MLV TN-10, Martin Co., Aug. 1960.
24. James, Carlton S.: Radiative and Convective Stagnation-Point Heating in Carbon Dioxide - Nitrogen Mixtures. Atmospheric Entry and Gas Thermodynamics, NASA TM X-50119, 1963, pp. 25-34.

25. Wolf, Fred; and Spiegel, Joseph M.: Status of Basic Shock Layer Radiation Information for Inner-Planet Atmospheric Entry. AIAA Pap. No. 66-421, June 1966.
26. Menard, W. A.; Thomas, G. M.; and Helliwell, T. M.: Experimental and Theoretical Study of Molecular, Continuum, and Line Radiation From Planetary Atmospheres. AIAA Pap. No. 67-323, Apr. 1967.
27. Olstad, Walter B.: Blunt-Body Stagnation-Region Flow With Nongray Radiation Heat Transfer - A Singular Perturbation Solution. NASA TR R-295, 1968.
28. Deacon, H. J., Jr.; and Rumpel, W. F.: Radiation Heating Characteristics of Venus Entry. [Preprint] 68-8-6, Amer. Astronaut. Soc., July 1968.
29. Norman, Herbert C.; and Hart, Paul M.: Mission Influence on the Aerothermodynamic Environment for a Venus Entry Vehicle. [Preprint] 68-4-6, Amer. Astronaut. Soc., July 1968.
30. Roberts, Leonard: Ablation Materials for Atmospheric Entry. Proceedings of the NASA-University Conference on the Science and Technology of Space Exploration, Vol. 2, NASA SP-11, 1962, pp. 461-468. (Also available as NASA SP-27.)
31. Strauss, Eric L.; and Sparhawk, H. Edwin, Jr.: Ablative Heat Shields for Planetary Entry Vehicles. [Preprint] 68-8-5, Amer. Astronaut. Soc., July 1968.
32. Bendura, Richard J.: Low Subsonic Static and Dynamic Stability Characteristics of Two Blunt 120° Cone Configurations. NASA TN D-3853, 1967.
33. Campbell, James F.; and Howell, Dorothy T.: Supersonic Aerodynamics of Large-Angle Cones. NASA TN D-4719, 1968.
34. Krumins, Maigonis V.: Drag and Stability of Various Mars Entry Configurations. IAF Paper RE 138, Oct. 1968.
35. South, Jerry C., Jr.: Calculation of Axisymmetric Supersonic Flow Past Blunt Bodies With Sonic Corners, Including a Program Description and Listing. NASA TN D-4563, 1968.
36. Nichols, James O.; and Nierengarten, Edward A.: Aerodynamic Characteristics of Blunt Bodies. Tech. Rep. No. 32-677 (Contract NAS 7-100), Jet Propulsion Lab., California Inst. Technol., Nov. 19, 1964.
37. Walker, Billy; and Weaver, Robert W.: Static Aerodynamic Characteristics of Blunted Cones in the Mach-Number Range From 2.2 to 9.5. Tech. Rep. 32-1213. (Contract No. NAS 7-100), Jet Propulsion Lab., California Inst. Technol., Dec. 1, 1967.

38. Cohen, Gerald A.; Foster, Richard M.; and Dowty, James R.: Synthesis of Optimum Structural Designs for Conical and Tension Shell Mars Entry Capsules. NASA CR-1365, 1969.
39. Uselton, B. L.: Damping-in-Pitch Derivatives for 60- and 70-Deg Blunted Cones at Mach Numbers 3 Through 5. AEDC-TR-69-119, U.S. Air Force, June 1969.
40. Allen, H. Julian: Motion of a Ballistic Missile Angularly Misaligned With the Flight Path Upon Entering the Atmosphere and Its Effect Upon Aerodynamic Heating, Aerodynamic Loads, and Miss Distance. NACA TN-4048, 1957. (Supersedes NACA RM A56F15.)
41. Lovelace, Uriel M.; Hoffman, Sherwood; and Mayhue, Robert J.: Analysis of the Trajectory and Large-Amplitude Motions of a Scout Vehicle During Fourth-Stage Reentry Flight. NASA TN D-2309, 1964.
42. Powell, Rex B.; and Smith, Robert L.: Dynamics of Spinning Reentry Bodies. AIAA Pap. No. 64-470, June-July 1964.
43. Tobak, Murray; and Peterson, Victor L.: Angle-of-Attack Convergence of Spinning Bodies Entering Planetary Atmospheres at Large Inclinations to the Flight Path. NASA TR R-210, 1964.
44. Prislin, Robert H.; and Jaffe, Peter: Entry Dynamics of a Spinning Vehicle. Tech. Mem. 33-398 (Contract NAS 7-100), Jet Propulsion Lab., California Inst. Technol., Aug. 15, 1968.
45. Allen, H. Julian: Gas Dynamics Problems of Space Vehicles. Proceedings of the NASA-University Conference on the Science and Technology of Space Exploration, Vol. 2, NASA SP-11, 1962, pp. 251-267. (Also available as NASA SP-24.)
46. McLellan, Charles H.; and Pritchard, E. Brian: Use of Lift To Increase Payload of Unmanned Martian Landers. J. Spacecraft Rockets, vol. 3, no. 9, Sept. 1966, pp. 1421-1425.
47. Pritchard, E. Brian; and Harrison, Edwin F.: Lifting Entry ( $L/D \leq 0.2$ ) for Unmanned Viking Class Mars Landers. NASA TN D-5828, 1970.
48. Guy, L. D.: Structural and Decelerator Design Options for Mars Entry. J. Spacecraft Rockets, vol. 6, no. 1, Jan. 1969, pp. 44-49.
49. Gillis, C. L.: Deployable Aerodynamic Decelerators for Space Missions. J. Spacecraft Rockets, vol. 6, no. 8, Aug. 1969, pp. 885-890.
50. Murrow, Harold N.; and McFall, John C., Jr.: Some Test Results From the NASA Planetary Entry Parachute Program. J. Spacecraft Rockets, vol. 6, no. 5, May 1969, pp. 621-623.

51. Alexander, William C.; and Lau, Richard A.: State-of-the-Art Study for High-Speed Deceleration and Stabilization Devices. GER-12616 (Contract NASW-1288), Goodyear Aerosp. Corp., Sept. 10, 1966. (Available as NASA CR-66141.)
52. Sibulkin, M.: Heat Transfer Near the Forward Stagnation Point of a Body of Revolution. J. Aeronaut. Sci., vol. 19, no. 8, Aug. 1952, pp. 570-571.
53. Jahnke, Eugene; and Emde, Fritz: Tables of Functions. Fourth ed., Dover Publ., Inc., c.1945.
54. Chapman, Dean R.: An Approximate Analytical Method for Studying Entry Into Planetary Atmospheres. NASA TR R-11, 1959. (Supersedes NACA TN 4276.)

TABLE I.- PHYSICAL PROPERTIES AND ATMOSPHERIC DATA OF EARTH, MARS, AND VENUS

	$p_s$ , lbf/ft <sup>2</sup>	$\rho_s \times 10^5$ , slugs/ft <sup>3</sup>	$T_s$ , °R	$H_{\rho,T}$ , ft	Composition by volume, percent	Mean value of $r_s$ , ft	$g_s$ , ft/sec <sup>2</sup>	Rotational period
Earth	2116	238	519	23 500	79 N <sub>2</sub> , 21 O <sub>2</sub> , 1 Ar	$20.89 \times 10^6$	32.1	23 <sup>h</sup> 56 <sup>m</sup> 4.09 <sup>s</sup>
Mars	10 to 40	1.32 to 7.44	360 to 495	16 470 to 46 500	100 CO <sub>2</sub> 20 CO <sub>2</sub> , 80 N <sub>2</sub> 68 CO <sub>2</sub> , 32 Ar	10.91	12.3 ± 0.5	24 <sup>h</sup> 37 <sup>m</sup> 22.668 <sup>s</sup>
Venus	$85 \times 10^3$ to $211 \times 10^3$	6685 to 14 100	1115 to 1322	17 100	CO <sub>2</sub> > 95	20.01	28.6	(a)

<sup>a</sup>Precise rate uncertain.TABLE II.- COMPARISON OF ATMOSPHERIC QUANTITIES COMPUTED FROM  
MARS OCCULTATION IMMERSION AND EMERSION DATA

[From ref. 6]

Parameter	Immersion	Emersion
Scale height near surface, km . . . . .	9.0 ± 1	12.0 ± 1
Surface number density, 10 <sup>17</sup> moles/cm <sup>3</sup> :		
100% CO <sub>2</sub> . . . . .	1.9 ± 0.1	2.25 ± 0.15
80% CO <sub>2</sub> , 20% Ar . . . . .	2.1 ± 0.1	2.45 ± 0.15
Surface mass density, 10 <sup>-5</sup> g/cm <sup>3</sup> :		
100% CO <sub>2</sub> . . . . .	1.43 ± 0.1	1.65 ± 0.15
80% CO <sub>2</sub> , 20% Ar . . . . .	1.55 ± 0.1	1.85 ± 0.15
Surface temperature, °K:		
100% CO <sub>2</sub> . . . . .	180 ± 20	240 ± 20
80% CO <sub>2</sub> , 20% Ar . . . . .	175 ± 20	235 ± 20
Surface pressure, mb:		
100% CO <sub>2</sub> . . . . .	4.9 ± 0.8	7.6 ± 1.3
80% CO <sub>2</sub> , 20% Ar . . . . .	5.2 ± 0.8	8.2 ± 1.3

TABLE III.- VOYAGER-MARS ENGINEERING MODEL ATMOSPHERES AND PLANETARY PHYSICAL CONSTANTS

Property	Unit	VM-7	VM-8	VM-1	VM-2	VM-3	VM-4	VM-9	VM-10
Surface pressure, $p_s$ . . . . .	mb (lb/ft <sup>2</sup> )	5.0 (10.4)	5.0 (10.4)	7.0 (14.6)	7.0 (14.6)	10.0 (20.9)	10.0 (20.9)	20 (41.7)	20 (41.7)
Surface density, $\rho_s$ . . . . .	(g/cm <sup>3</sup> )10 <sup>5</sup> ((slugs/ft <sup>3</sup> )10 <sup>5</sup> )	0.68 (1.32)	1.32 (2.56)	0.955 (1.85)	1.85 (3.59)	1.365 (2.65)	2.57 (4.98)	2.73 (5.30)	3.83 (7.44)
Density at 15 000-ft altitude, $\rho_{15\ 000}$ . . . . .	(g/cm <sup>3</sup> )10 <sup>5</sup> ((slugs/ft <sup>3</sup> )10 <sup>5</sup> )	0.57 (1.11)	0.93 (1.8)	0.80 (1.55)	1.3 (2.53)	1.15 (2.23)	1.85 (3.59)	2.29 (4.43)	3.01 (5.84)
Density at tropopause, $\rho_T$ . . . . .	(g/cm <sup>3</sup> )10 <sup>5</sup> ((slugs/ft <sup>3</sup> )10 <sup>5</sup> )	0.295 (0.573)	0.205 (0.397)	0.413 (0.803)	0.286 (0.556)	0.593 (1.15)	0.524 (1.016)	1.20 (2.32)	0.75 (1.53)
Surface temperature, $T_s$ . . . . .	°K (°R)	275 (495)	200 (360)	275 (495)	200 (360)	275 (495)	200 (360)	275 (495)	200 (360)
Stratospheric temperature, $T_s$ . . . . .	°K (°R)	200 (360)	100 (180)	200 (360)	100 (180)	200 (360)	100 (180)	200 (360)	100 (180)
Temperature at 15 000-ft altitude, $T_{15\ 000}$ . . . . .	°K (°R)	257.3 (463.1)	175.5 (316.0)	257.3 (463.1)	175.5 (316.0)	257.3 (463.1)	173.4 (312.1)	142.8 (463.05)	135.05 (324.3)
Speed of sound at 15 000-ft altitude, $a_{15\ 000}$ . . . . .	ft/sec (km/sec)	1009.0 (0.3075)	699.0 (0.213)	1009.0 (0.3075)	699.0 (0.213)	1009.0 (0.3075)	720.8 (0.2197)	1008.0 (0.3072)	843.74 (0.2572)
Composition:									
CO <sub>2</sub> (by mass) . . . . .		28.2	100.0	28.2	100.0	28.2	70.0	28.2	13.0
CO <sub>2</sub> (by volume) . . . . .		20.0	100.0	20.0	100.0	20.0	68.0	20.0	9.5
N <sub>2</sub> (by mass) . . . . .		71.8	0.0	71.8	0.0	71.8	0.0	71.8	62.0
N <sub>2</sub> (by volume) . . . . .		80.0	0.0	82.0	0.0	80.0	0.0	80.0	70.5
Ar (by mass) . . . . .		0.0	0.0	0.0	0.0	0.0	30.0	0.0	25.0
Ar (by volume) . . . . .		0.0	0.0	0.0	0.0	0.0	32.0	0.0	20.0
Molecular weight, $M$ . . . . .	mole <sup>-1</sup>	31.2	44.0	31.2	44.0	31.2	42.7	31.2	31.9
Specific heat of mixture, $c_p$ . . . . .	cal/g °C	0.230	0.166	0.230	0.166	0.230	0.153	0.230	0.207
Specific heat ratio, $\gamma$ . . . . .		1.38	1.37	1.38	1.37	1.38	1.43	1.38	1.41
Adiabatic lapse rates . . . . .	°K/km (°R/1000 ft)	-3.88 (-2.13)	-5.39 (-2.96)	-3.88 (-2.13)	-5.39 (-2.96)	-3.88 (-2.13)	-5.85 (-3.21)	-3.88 (-2.13)	-4.33 (-2.38)
Tropopause altitude, $h_T$ . . . . .	km (1000 ft)	19.3 (63.3)	18.6 (61.0)	19.3 (63.3)	18.6 (61.0)	19.3 (63.3)	17.1 (56.1)	19.3 (63.3)	23.1 (75.8)
Pressure scale height, $H_p$ . . . . .	km (1000 ft)	14.18 (46.520)	5.02 (16.480)	14.18 (46.520)	5.02 (16.480)	14.18 (46.520)	5.18 (16.980)	14.18 (46.520)	6.70 (22.68)
Inverse scale height, $\beta$ . . . . .	km <sup>-1</sup> (ft <sup>-1</sup> × 10 <sup>5</sup> )	0.0705 (2.15)	0.199 (6.07)	0.0705 (2.15)	0.199 (6.07)	0.0705 (2.15)	0.193 (5.89)	0.0705 (2.15)	0.145 (4.41)
Continuous surface wind speed, $V_w$ . . . . .	ft/sec	220.0	220.0	186.0	186.0	155.5	155.5	110.0	110.0
Peak surface wind speed, $V_{w,max}$ . . . . .	ft/sec	556.0	556.0	470.0	470.0	390.0	390.0	278.0	278.0
Design vertical wind gradient, $dV/dh$ . . . . .	ft/sec/1000 ft	-2.0	-2.0	-2.0	-2.0	-2.0	-2.0	2	2
Effective height of atmosphere . . . . .	1000 ft (km)	621 (189.3)	252 (76.8)	636 (193.85)	258 (78.64)	653 (199.03)	269 (81.99)	777.4 (237.0)	392.6 (119.7)



TABLE IV.- SUMMARY OF ATMOSPHERIC CONDITIONS NEAR  
MEAN SURFACE FOR FIVE MODEL ATMOSPHERES

Parameter	Minimum $\rho_s$	Minimum $H_{\rho,s}$	Most probable	Maximum $\rho_s$	Maximum $H_{\rho,s}$
Surface pressure, mb . . . . .	4	4	6	10	10
Surface temperature, °K . . . . .	280	180	230	180	280
Abundance of CO <sub>2</sub> , m-atm . . . . .	55	55	72	100	100
Composition by mass, percent:					
CO <sub>2</sub> . . . . .	100	100	88	73	73
Ar . . . . .	0	0	12	27	27
Composition by volume, percent:					
CO <sub>2</sub> . . . . .	100	100	87	71.1	71.1
Ar . . . . .	0	0	13	28.9	28.9
Molecular mass, kg/(kg mole) . .	44	44	43.5	42.8	42.8
Acceleration due to gravity, m/sec <sup>2</sup> . . . . .	3.72	3.72	3.72	3.72	3.72
Equatorial radius, km . . . . .	3393	3393	3393	3393	3393
Universal gas constant, J/°K-(kg mole) . . . . .	8314	8314	8314	8314	8314

TABLE V.- CONSTITUENTS OF COMPOSITE ABLATIVE MATERIALS

Base resin	Fibrous fillers	Low-density fillers	Subliming fillers	Fine-particle fillers
Phenolic	Glass	Phenolic microballoons	Nylon	Colloidal silica
Epoxy	Asbestos	Glass microspheres	Ammonium chloride	Carbon black
Silicone	Silica	Silica microspheres		Carbide powder
Teflon	Carbon	Cork		
Polyphenylene	Graphite	Gas-filled interstices (foam)		
Polybenzimidazole	Pluton			
	Nylon			
	Magnesia			
	Zirconia			

TABLE VI.- PROPERTIES OF TYPICAL ABLATORS

Ablator	Density, lbm/ft <sup>3</sup>	Fraction volatilized	Char density, lbm/ft <sup>3</sup>	Thermal conductivity, Btu-in./hr-ft <sup>2</sup> -°F	Tensile strength, lbf/in <sup>2</sup>	Elongation at 70° F, percent
Superlight:						
SLA-561	14	0.44	8	0.36	60	2.50
SLA-220	16	.28	11	.55	83	5.90
Low-density charring:						
ESA-3560	31	.65	11	.67	100	12.00
ESA-5500	58	.54	26	1.60	135	36.00
Subliming:						
Teflon	131	1.00	---	1.70	2000	150.00
Porous teflon	32	1.00	---	.42	49	11.00
Reinforced:						
Silica phenolic	109	.17	91	3.60	4000	.41
Carbon phenolic	90	.18	74	7.10	6500	.29

TABLE VII.- PLANETARY ENTRY HEAT-SHIELD REQUIREMENTS

Entry-vehicle configuration				Heat-shield requirements				
Cone half-angle, deg	Base diameter, ft	Entry weight, lbm	Ballistic coefficient, slug/ft <sup>2</sup>	Material	Thickness, in.	Unit weight, lbm/ft <sup>2</sup>	Total weight, lbm	Weight fraction
Venus direct entry								
55	8.5	850	0.34	ESA-5500	0.53	2.56	240	0.28
55	8.5	850	.34	ESA-5500M	.24	1.16	140	.16
55	8.5	850	.34	Carbon phenolic	.55	4.35	350	.41
Venus orbit entry								
55	8.5	850	0.34	ESA-5500M	0.22	1.06	133	0.156
Mars direct entry								
70	10.5	1600	0.35	SLA-561	0.53	0.65	57	0.04
Mars orbit entry								
70	10.5	1600	0.35	SLA-561	0.43	0.53	46	0.03

TABLE VIII.- CALCULATED MAXIMUM DYNAMIC PRESSURES, DECELERATIONS, STAGNATION-POINT HEATING RATES, AND HEAT INPUTS FOR MARS ENTRIES

Atmosphere	$\phi_E$ , deg	$V_E$ , ft	$\frac{m}{C_D A}$ , slug/ft <sup>2</sup>	Dynamic pressure, lbf/ft <sup>2</sup>	$\frac{dV_\infty}{dt}$ , ft/sec <sup>2</sup>	$\dot{q}_{c,o}$ , Btu/ft <sup>2</sup> -sec (a)	$q_c$ , Btu/ft <sup>2</sup> (a)
VM-8	20	16 000	0.4	280.0	688	75.6	1601
VM-8	20	16 000	.3	223.0	731	65.5	1373
VM-8	15	16 000	.3	84.3	276	41.0	2116
VM-9	15	16 000	.3	50.3	160	31.1	2776
VM-8	15	14 000	.3	114.0	376	36.5	1304
VM-8	20	12 000	.3	163.0	532	33.7	719
VM-9	15	12 000	.3	45.9	145	16.8	1368

<sup>a</sup>Based on  $R_n = 1.0$  ft.

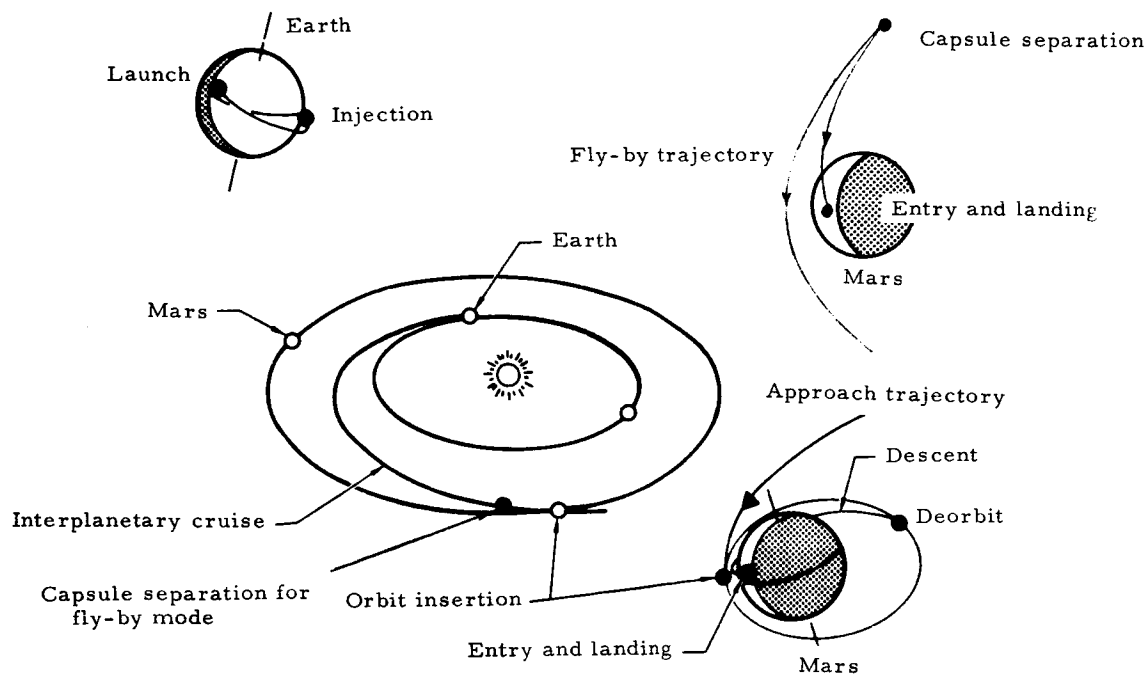


Figure 1.- Typical Mars mission profiles.

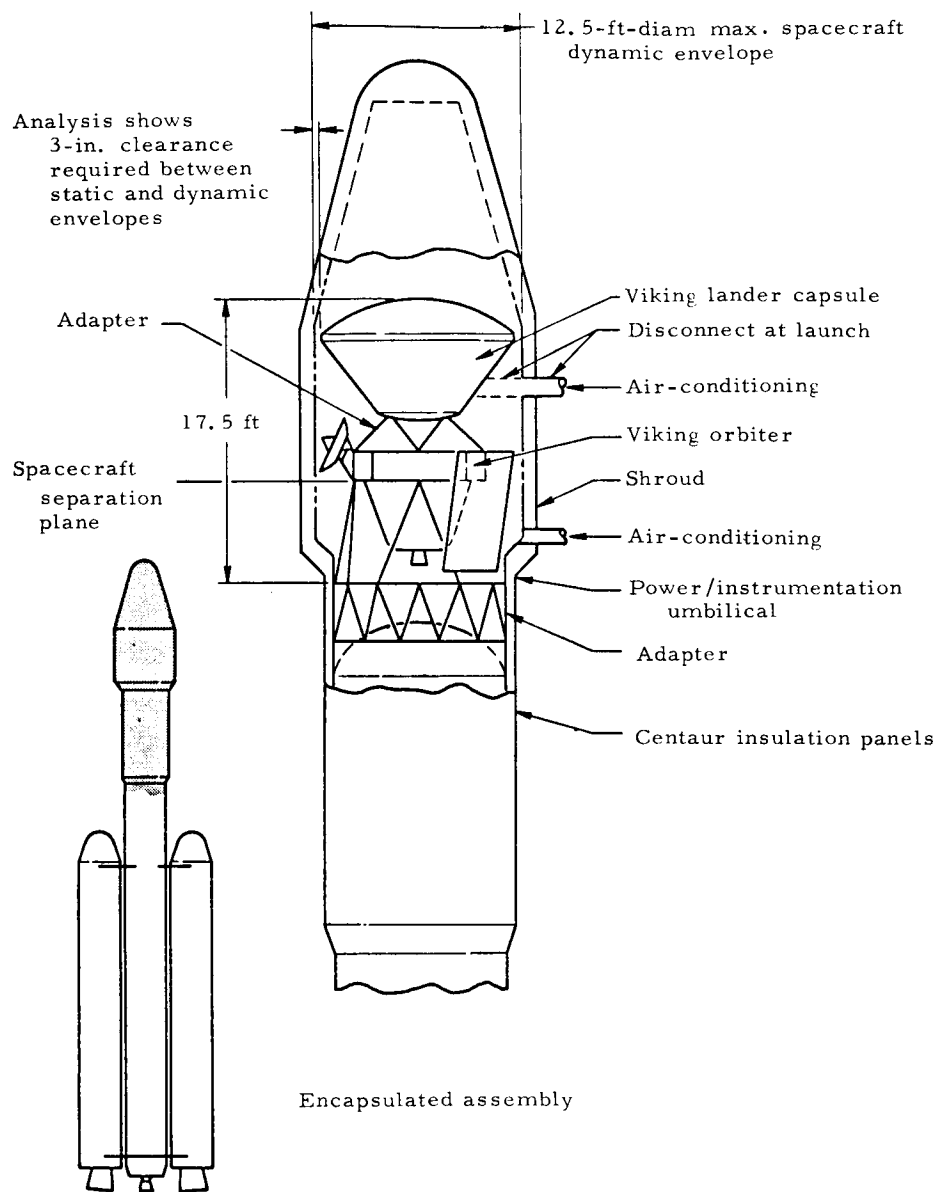


Figure 2.- Viking-Mars spacecraft mounted in Titan III-Centaur launch vehicle.

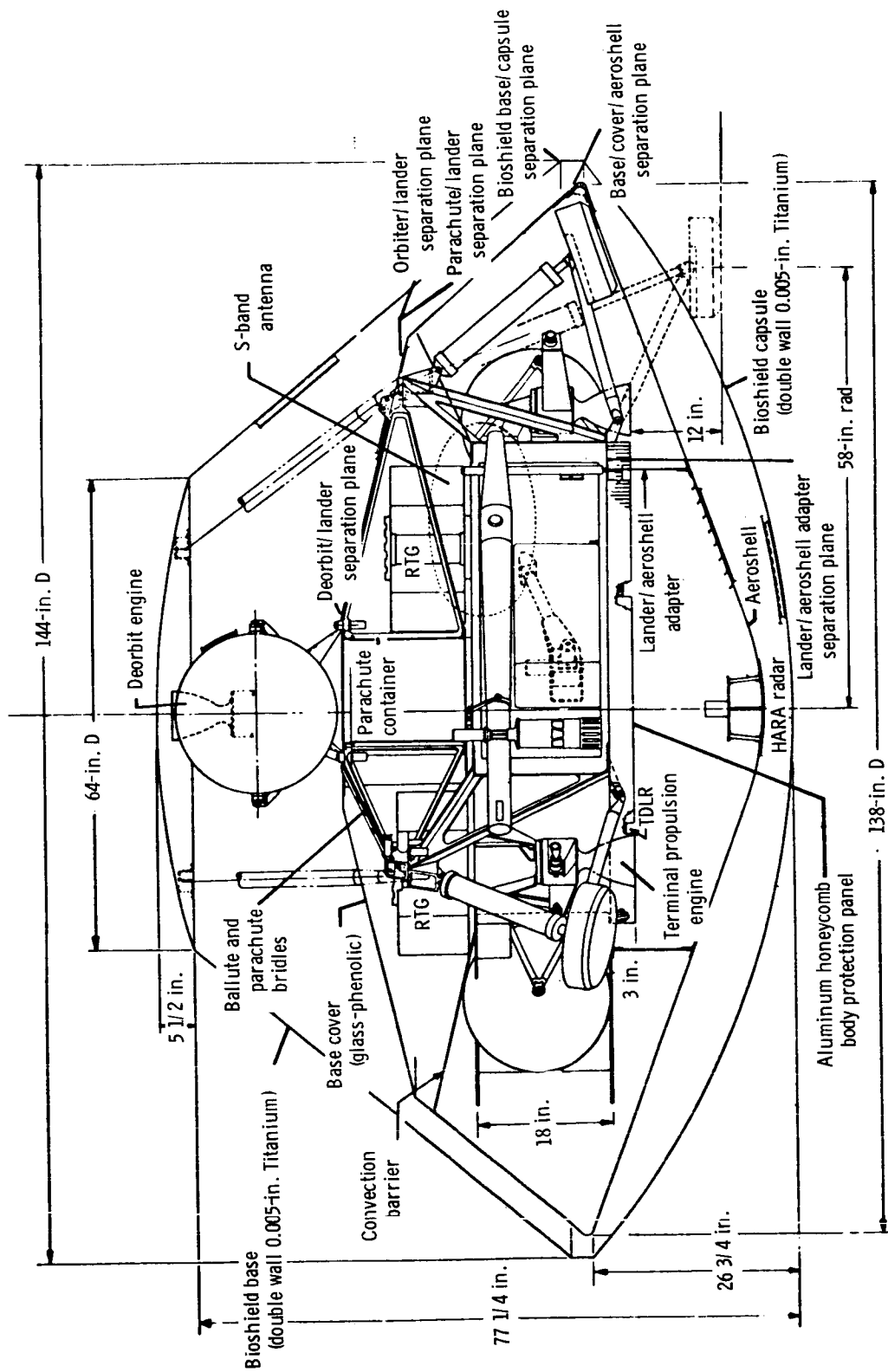


Figure 3.- A proposed Viking-Mars lander capsule.

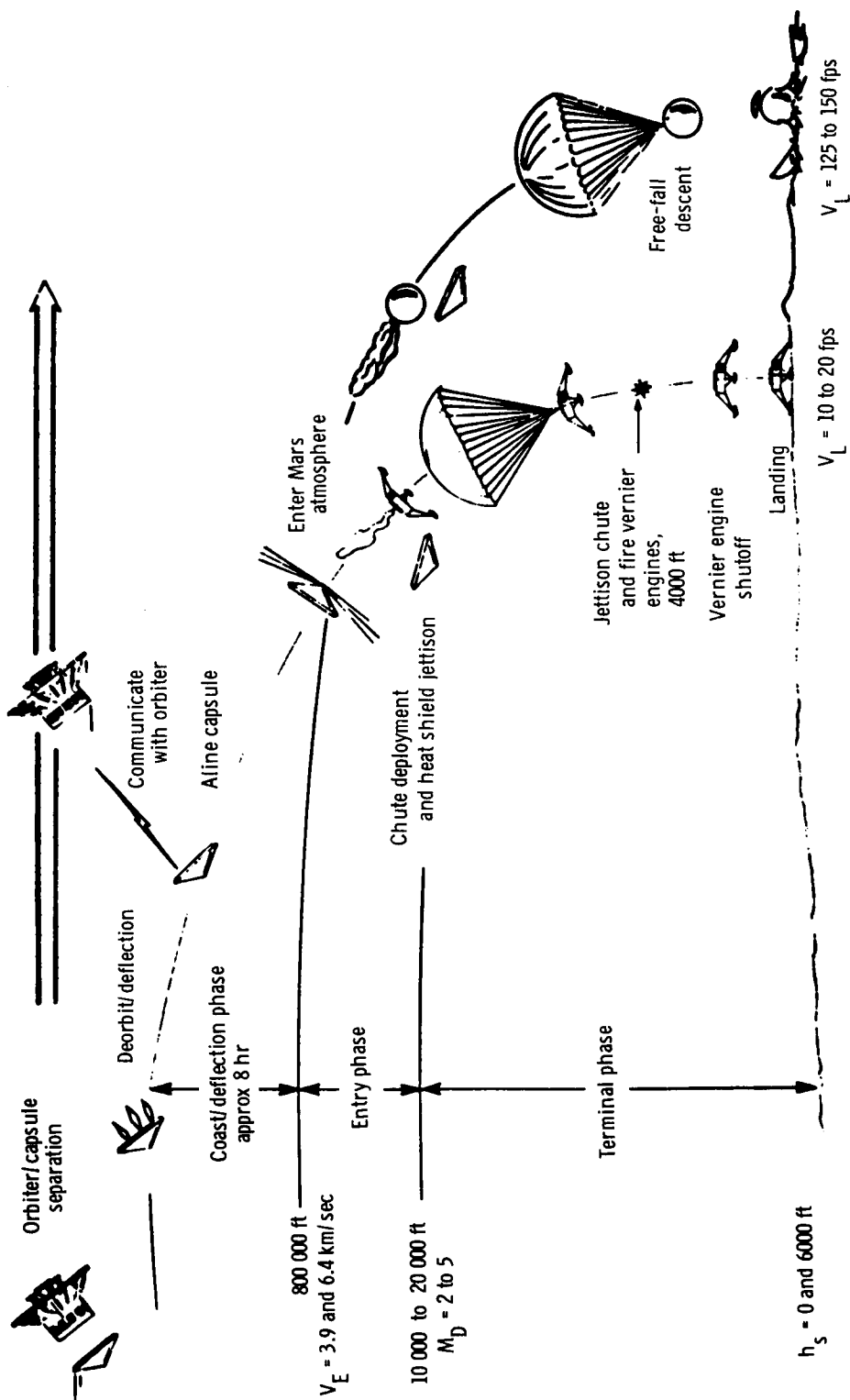


Figure 4.- Descent profile for a Mars landing.

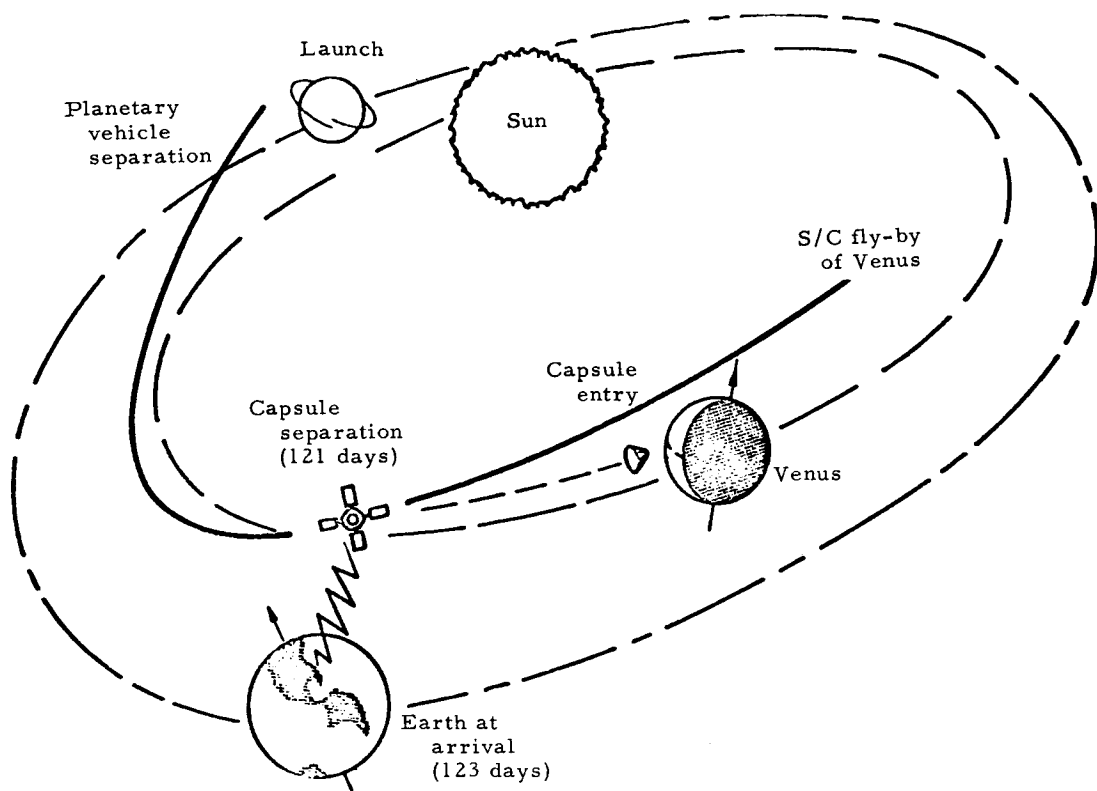


Figure 5.- 1972 fly-by mission profile for BVS.

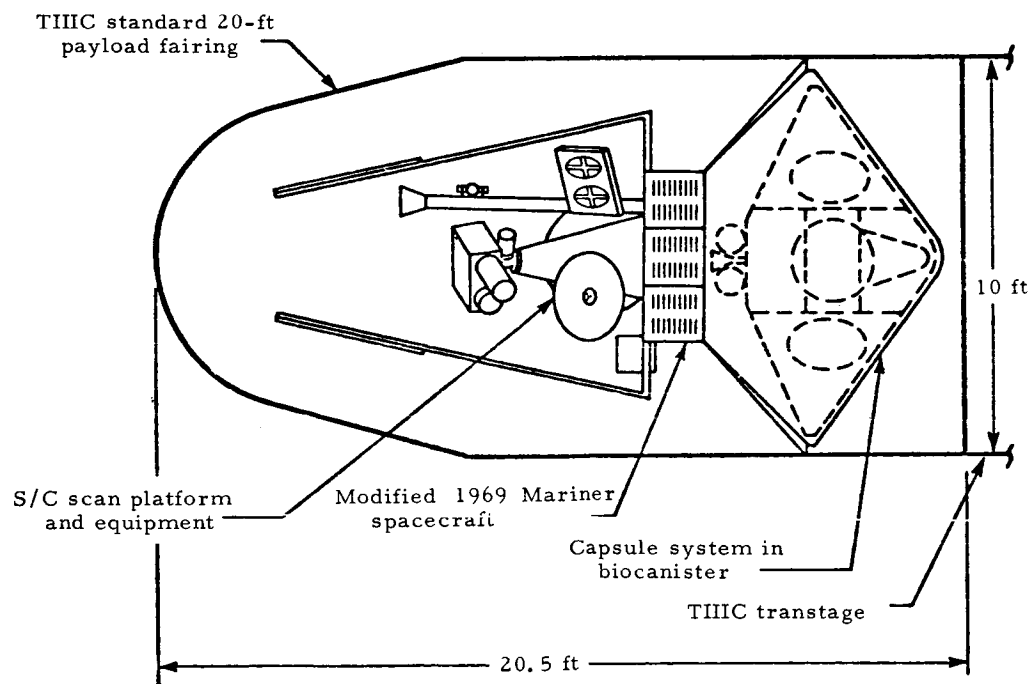


Figure 6.- Venus planetary vehicle on Titan IIIC.



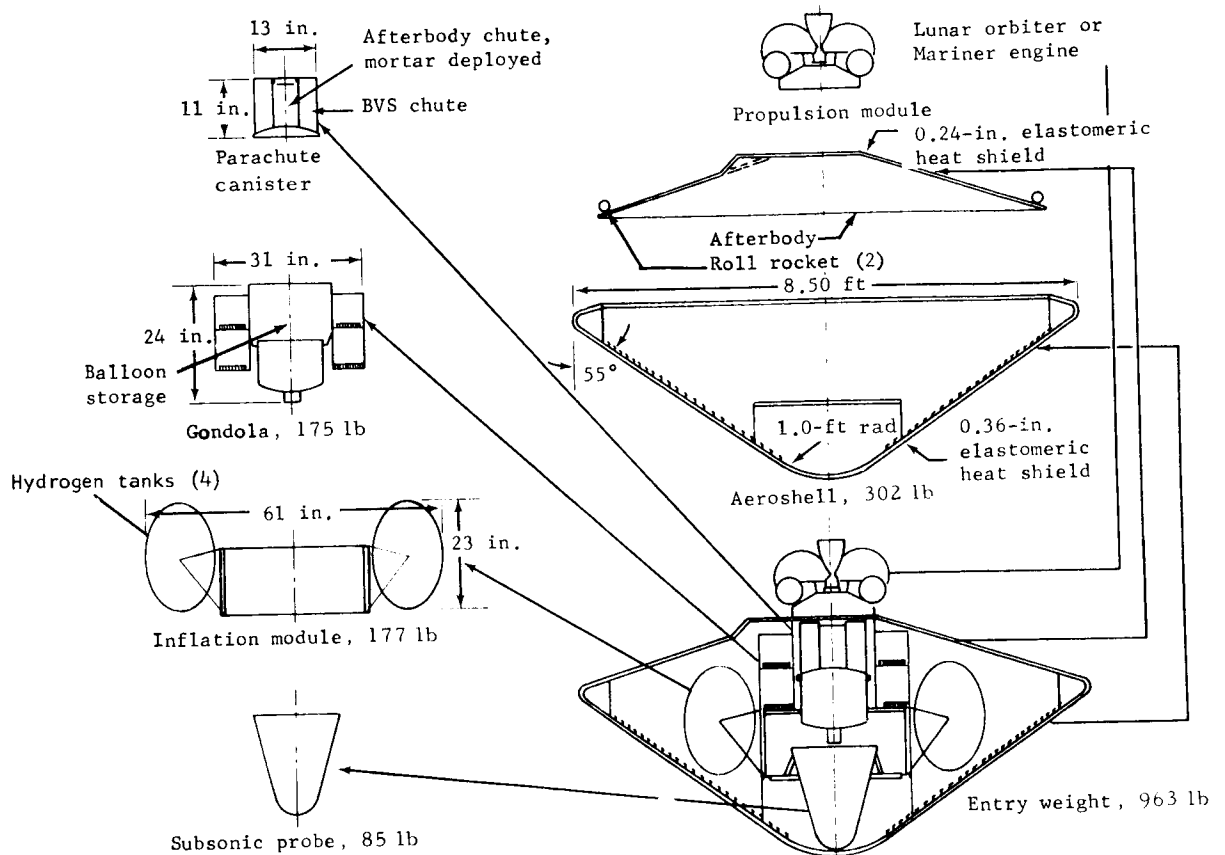
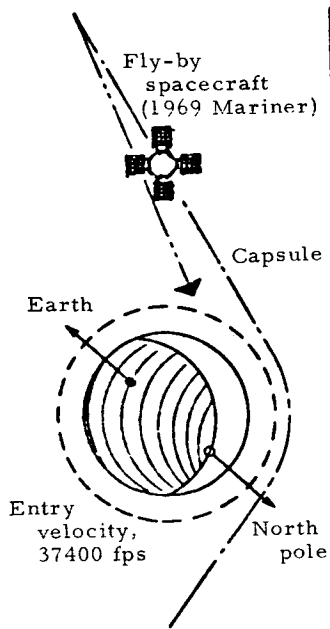


Figure 7.- Systems of Venus entry capsule.

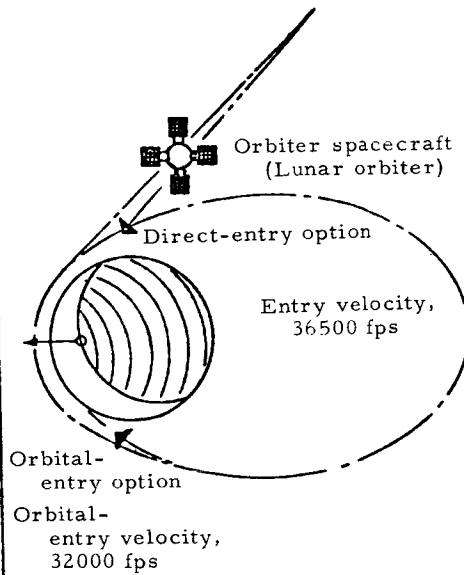
1972 Fly-by mission:

Titan IIIC booster;  
Direct communication link



1973 Orbital mission:

Titan IIIC booster;  
Relay communication link



1973 Venus/Mercury mission:

Titan IIIC  
Direct communication link;  
Options for mission-  
retro capsule before entry,  
propulsion maneuver of  
spacecraft at Venus,  
all-ballistic flight

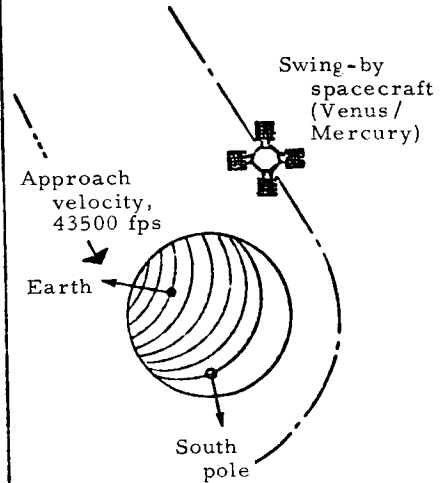
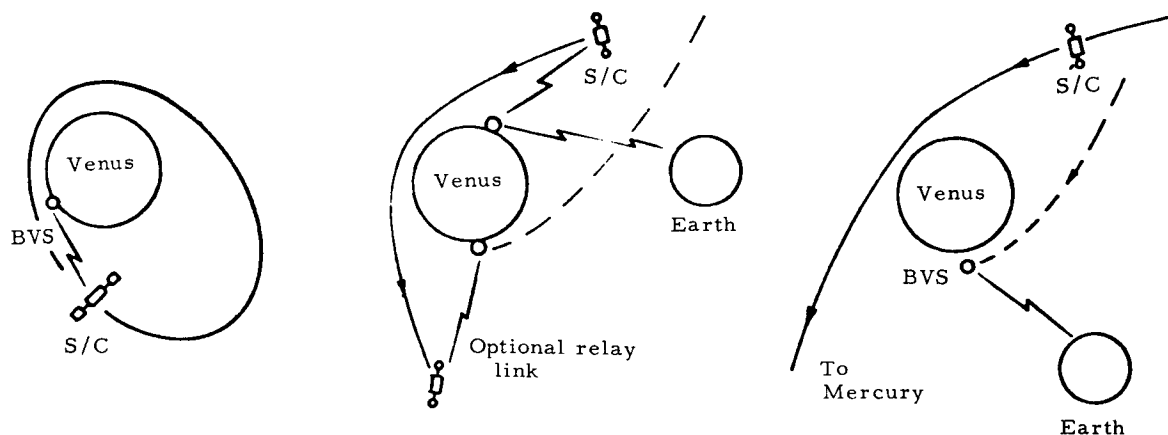


Figure 8.- Venus mission options.



Mission phases	Communications		
	Orbital	Fly-by	Venus/Mercury
Separation and $\Delta V$	Capsule to S/C	-----	Store data
Entry/deploy	BVS to S/C	BVS to S/C	BVS to Earth
Subsonic probe to surface	Probe to S/C	Probe to S/C	Probe to Earth
BVS in flotation	BVS to S/C S/C to BVS	BVS to Earth Earth to BVS	BVS to Earth Earth to BVS

Figure 9.- Communication modes for three Venus missions.

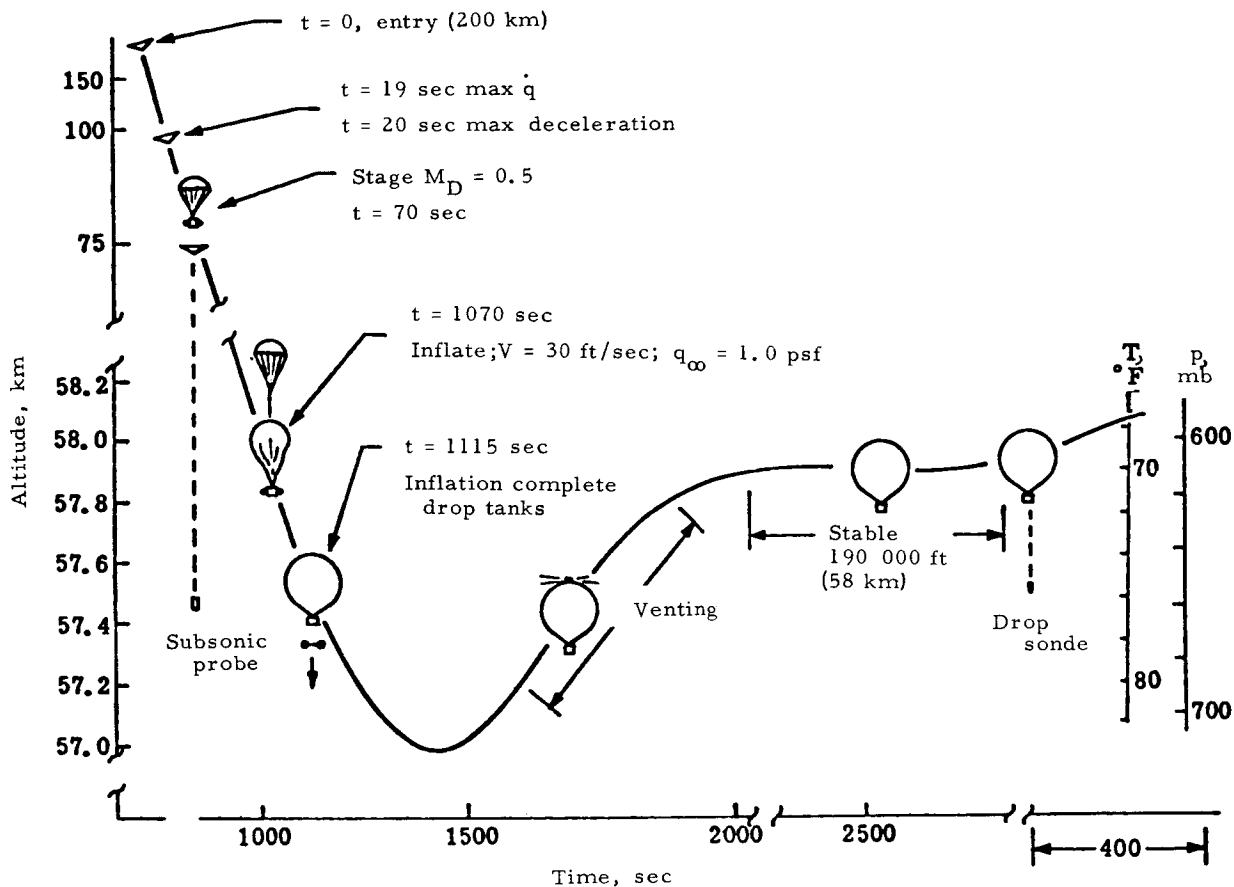


Figure 10.- Entry and deployment sequence for Venus entry capsule and BVS.

1973 Fly-by - type II

1973 Orbital - type II

1973 Mercury - Venus fly-by - type I

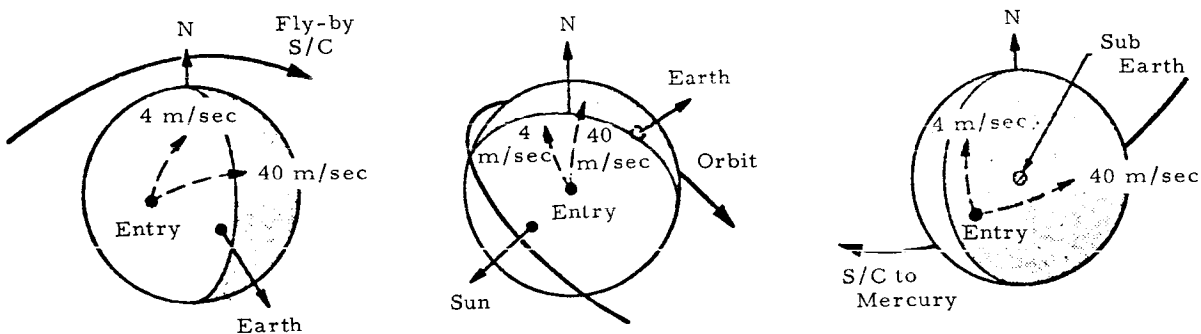


Figure 11.- Effect of winds on three 1973 mission options.

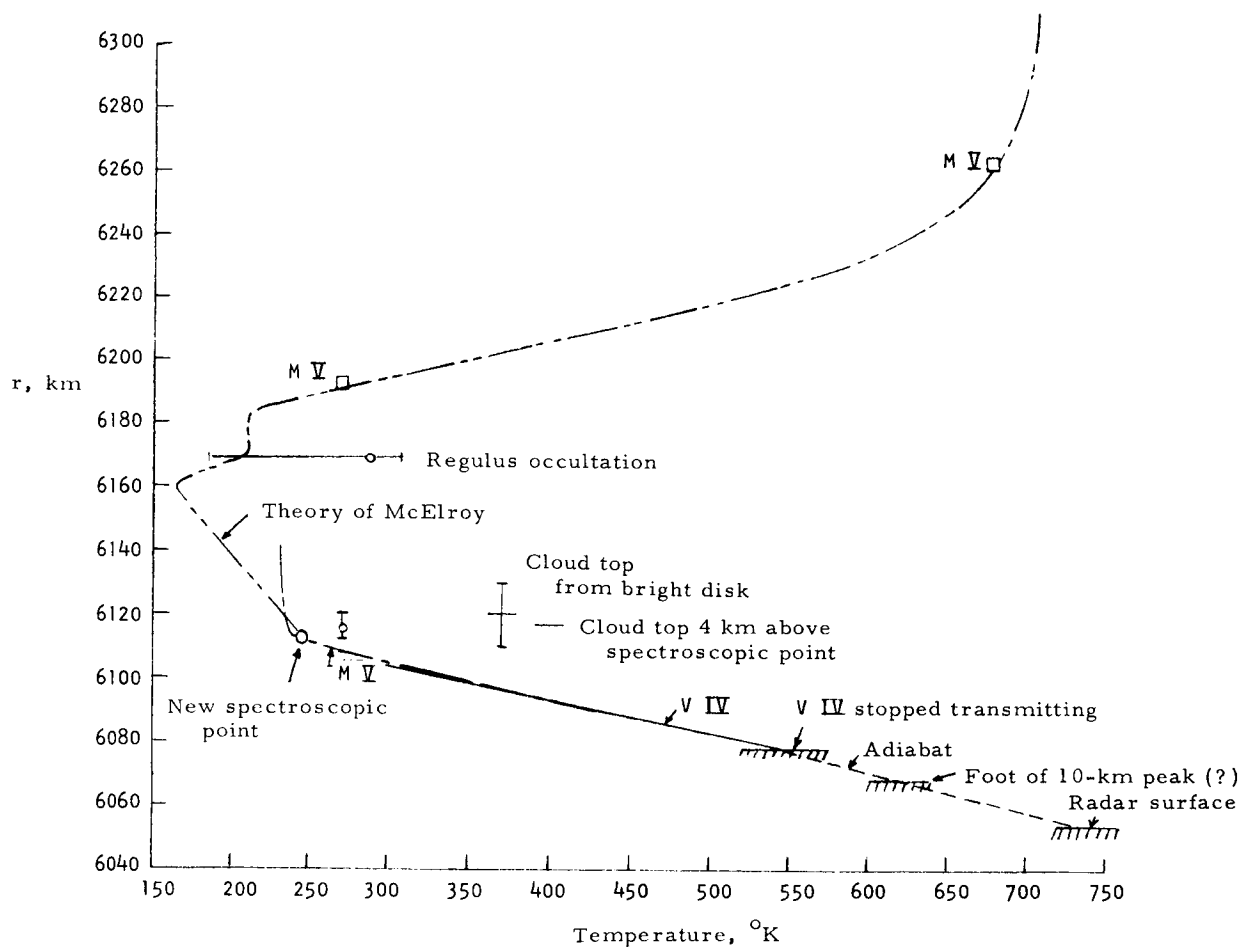


Figure 12.- Variation of temperature with altitude for atmosphere of Venus.

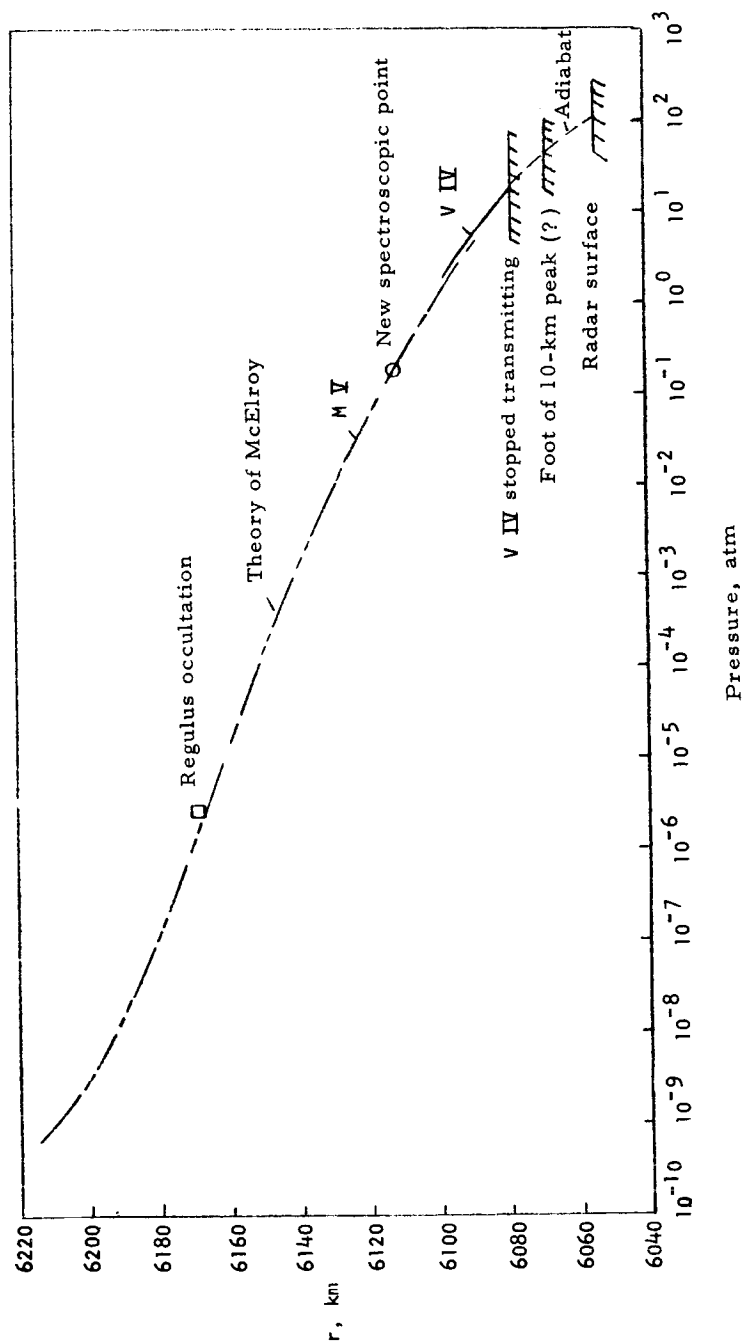


Figure 13.- Variation of pressure with altitude for atmosphere of Venus.

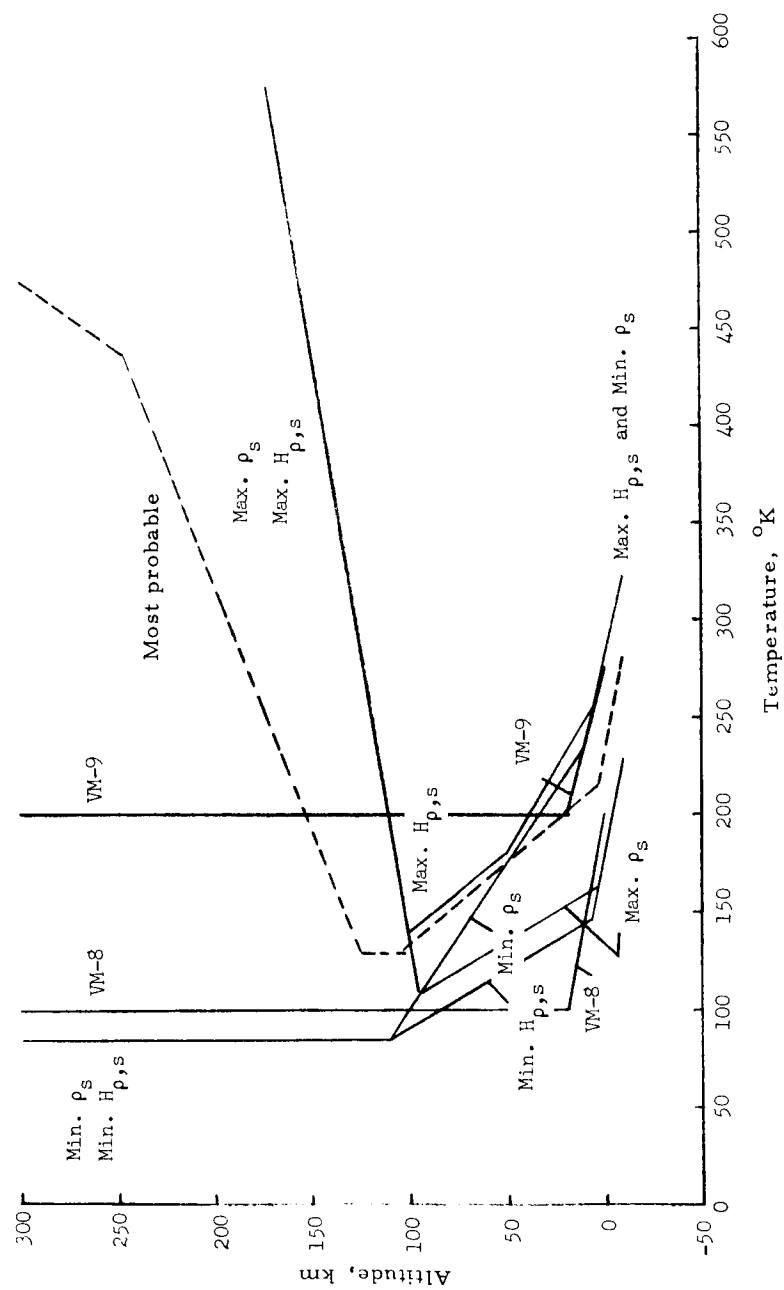


Figure 14.- Temperature profiles for Mars atmospheres.

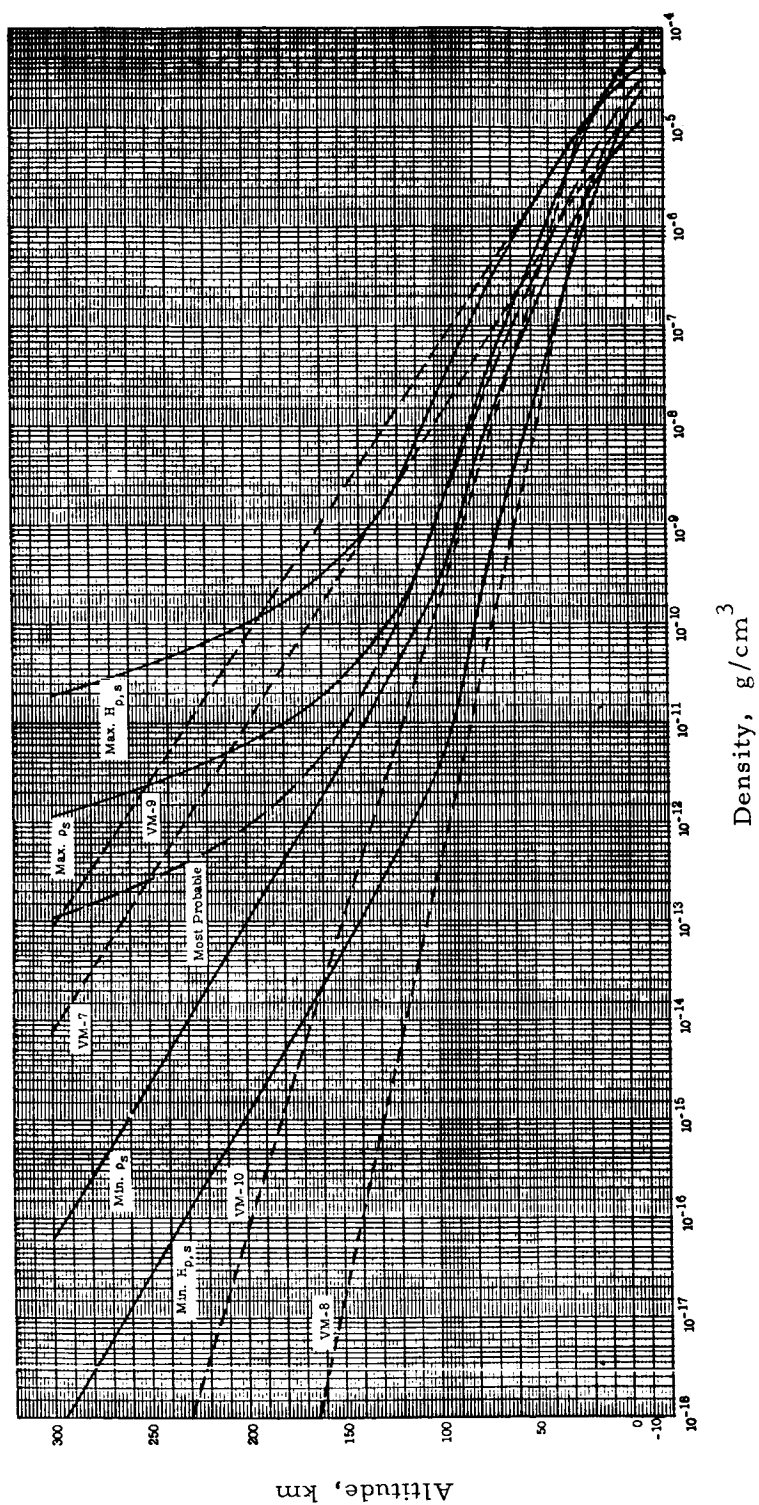


Figure 15.- Comparison of density profiles of five model and four VM atmospheres.



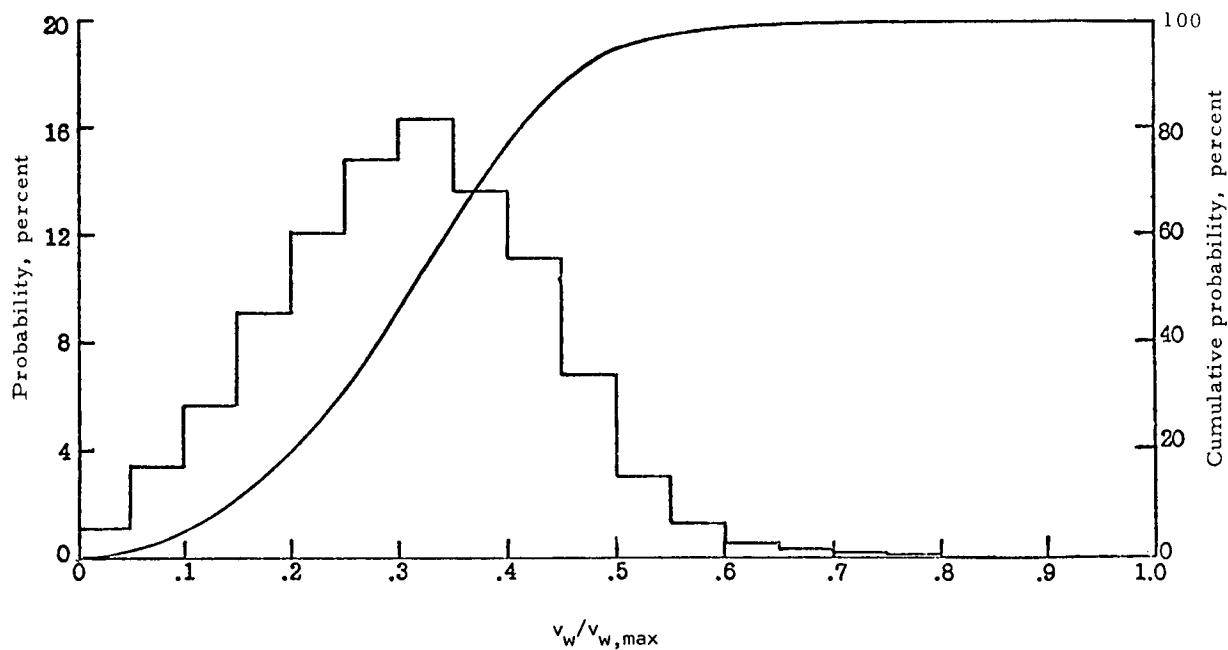


Figure 16.- Probability distribution of near-surface wind speed on Mars between  $\pm 28^\circ$  latitude near vernal equinox in northern hemisphere.  $v_{w,max} = 63.6$  m/sec.

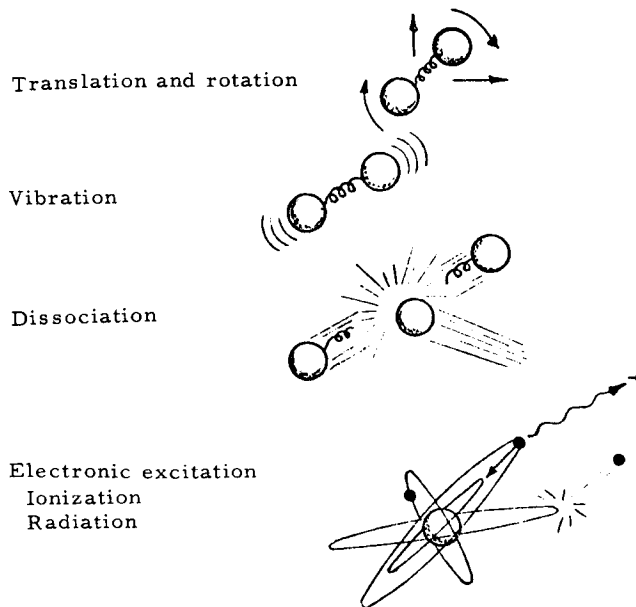
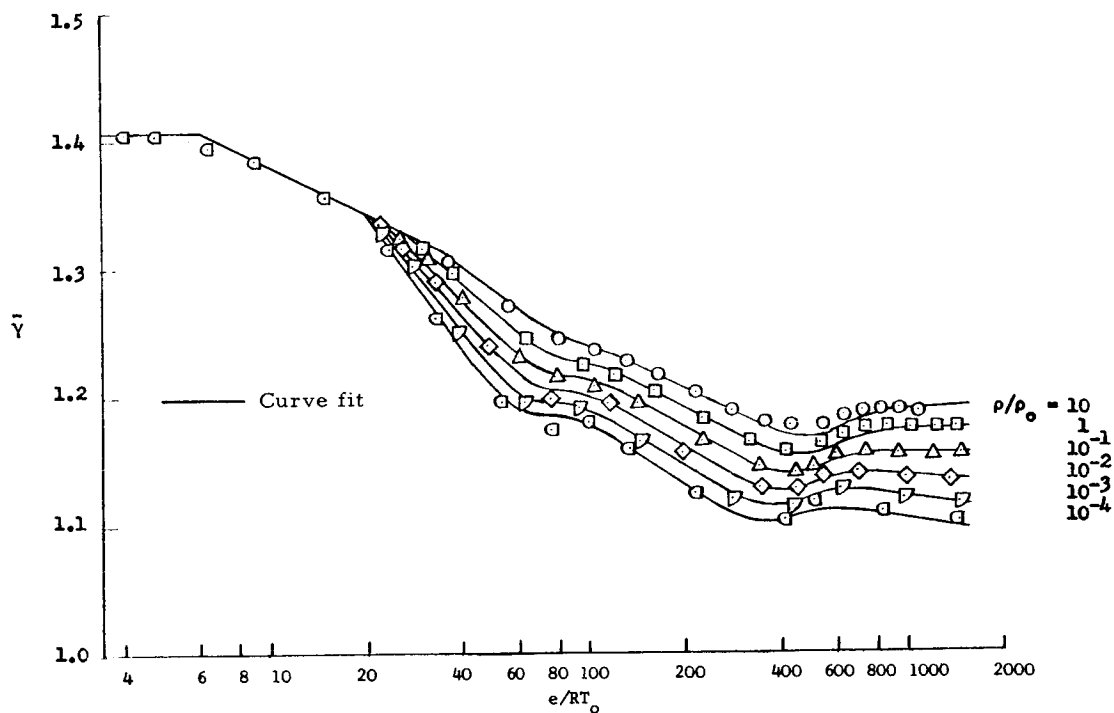
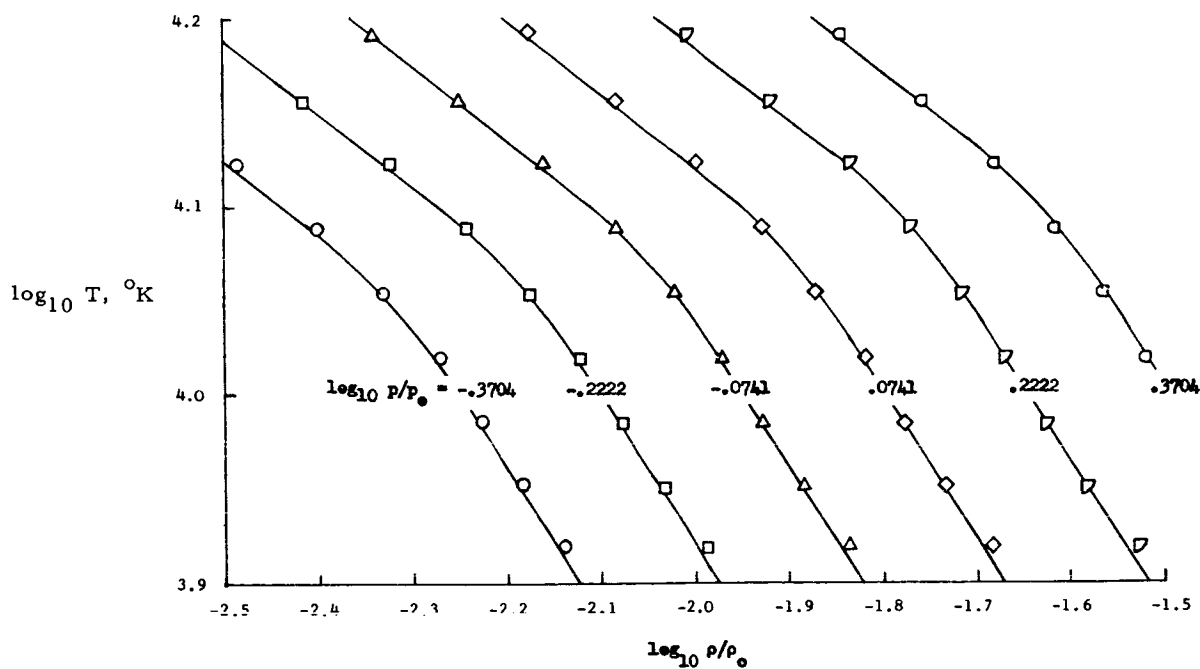


Figure 17.- Degrees of freedom of gas molecules and atoms.



(a) Ratio of enthalpy to internal energy for equilibrium air.



(b) Thermal equation of state for equilibrium air.

Figure 18.- Equilibrium thermodynamic properties for air (obtained from ref. 7).

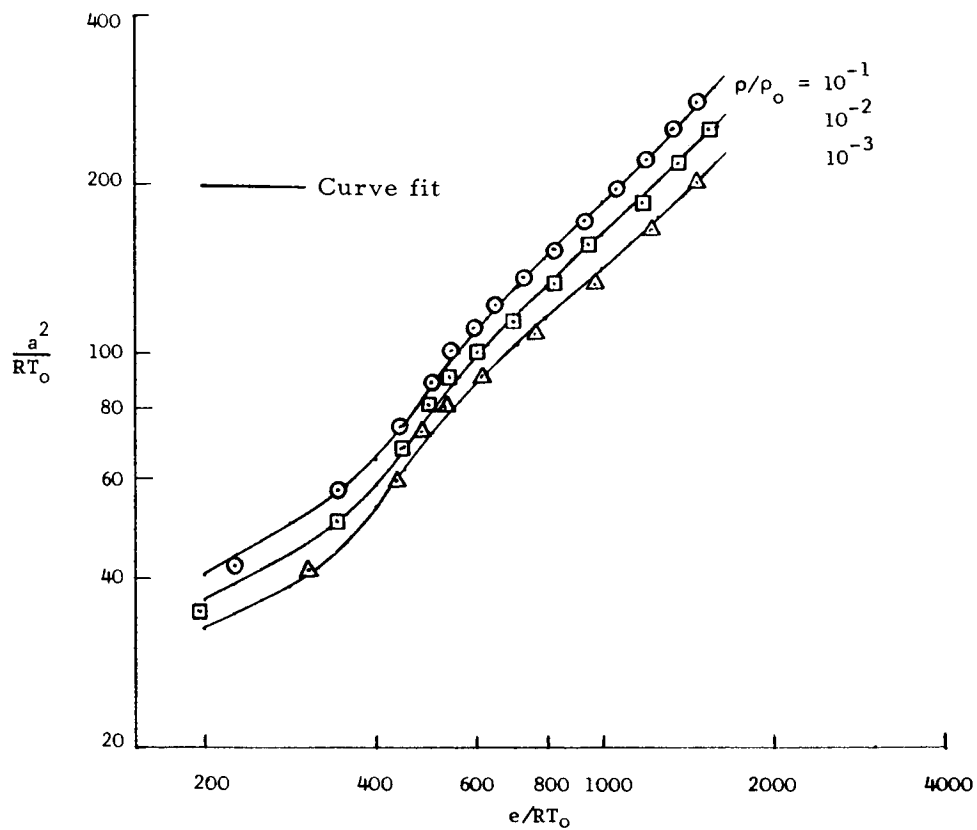


Figure 19.- Variation of speed of sound with internal energy for equilibrium air (obtained from ref. 7).

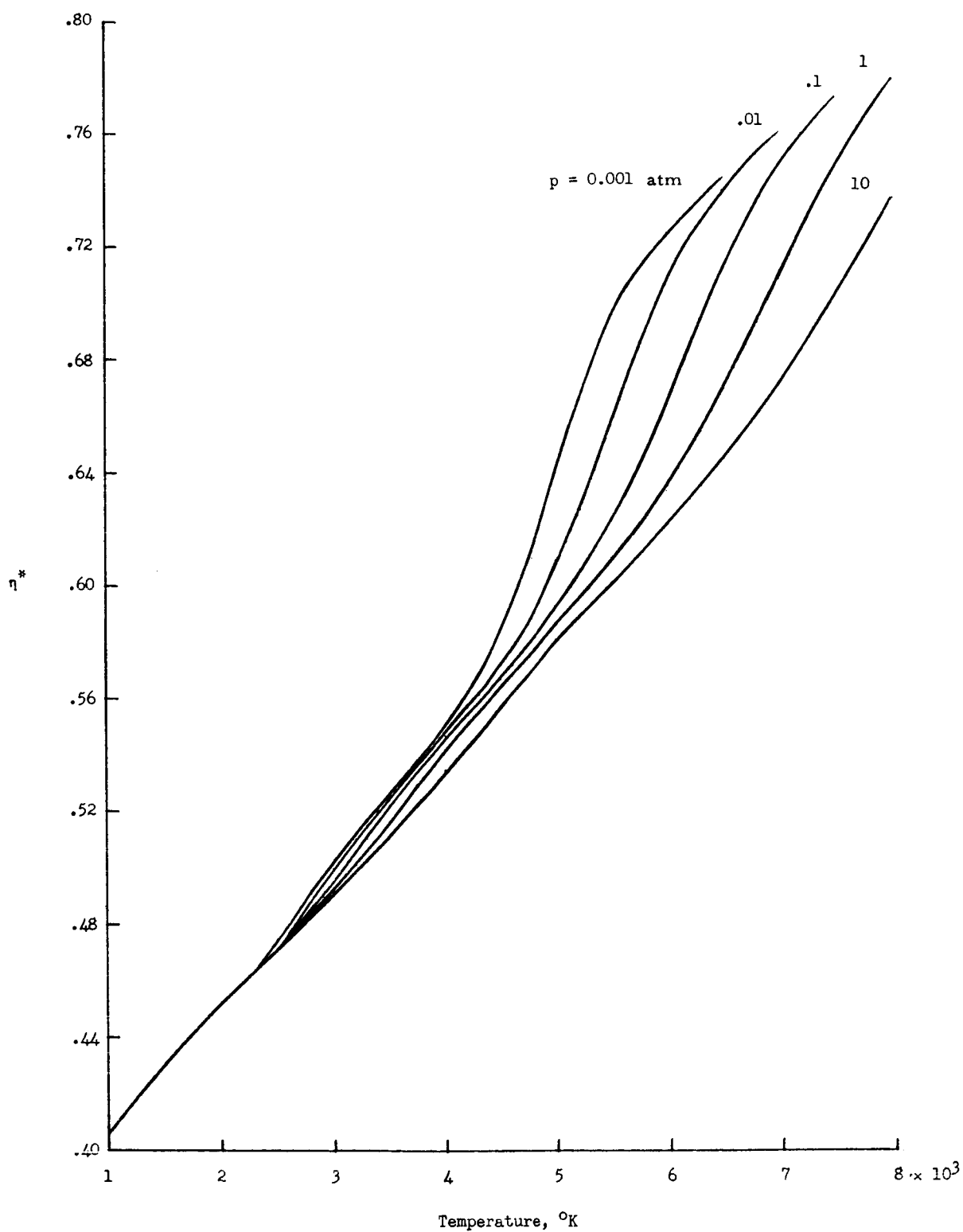


Figure 20.- Variation of viscosity of air with temperature for range of pressures.

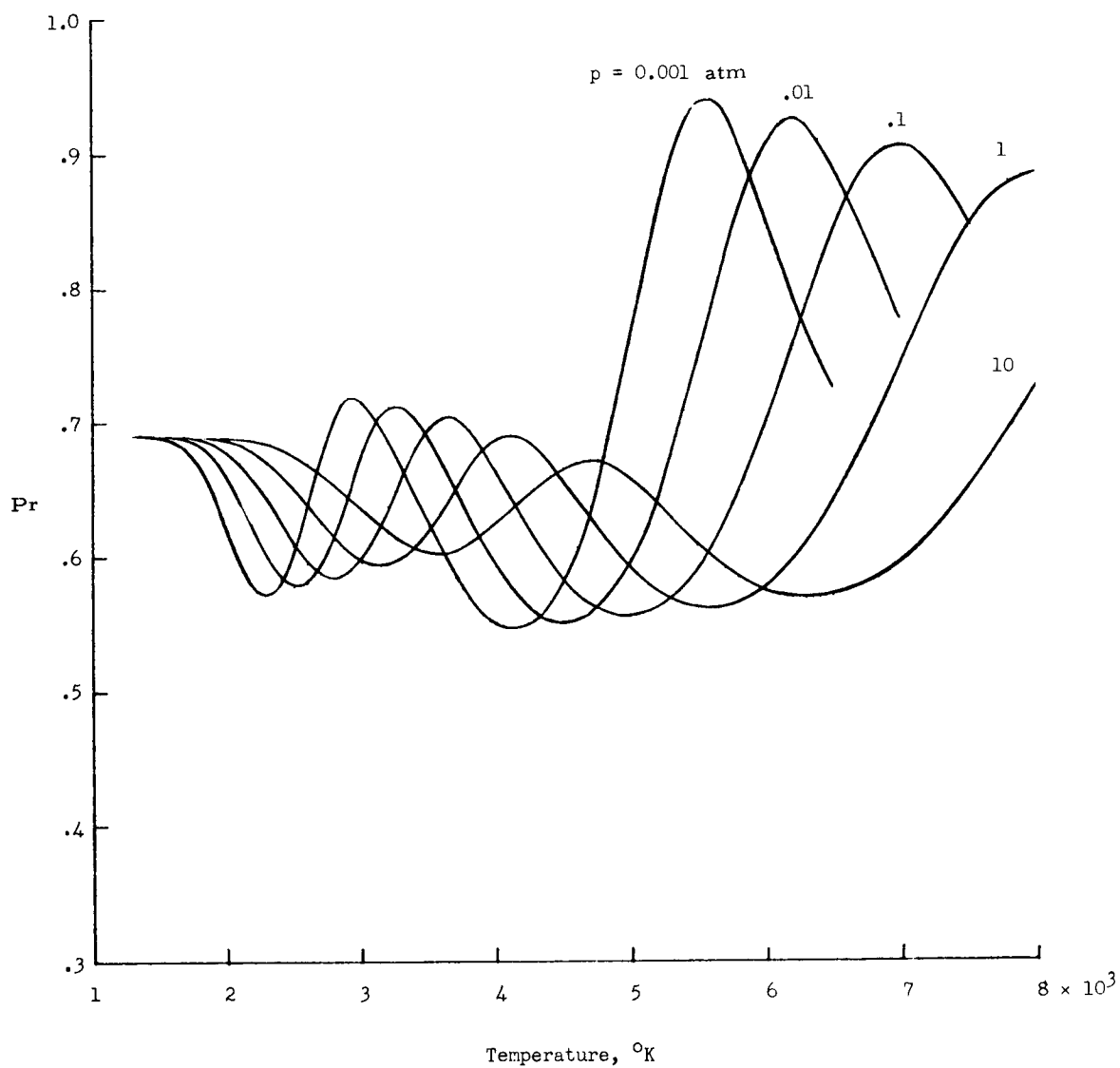


Figure 21.- Variation of Prandtl number of air with temperature for range of pressures.

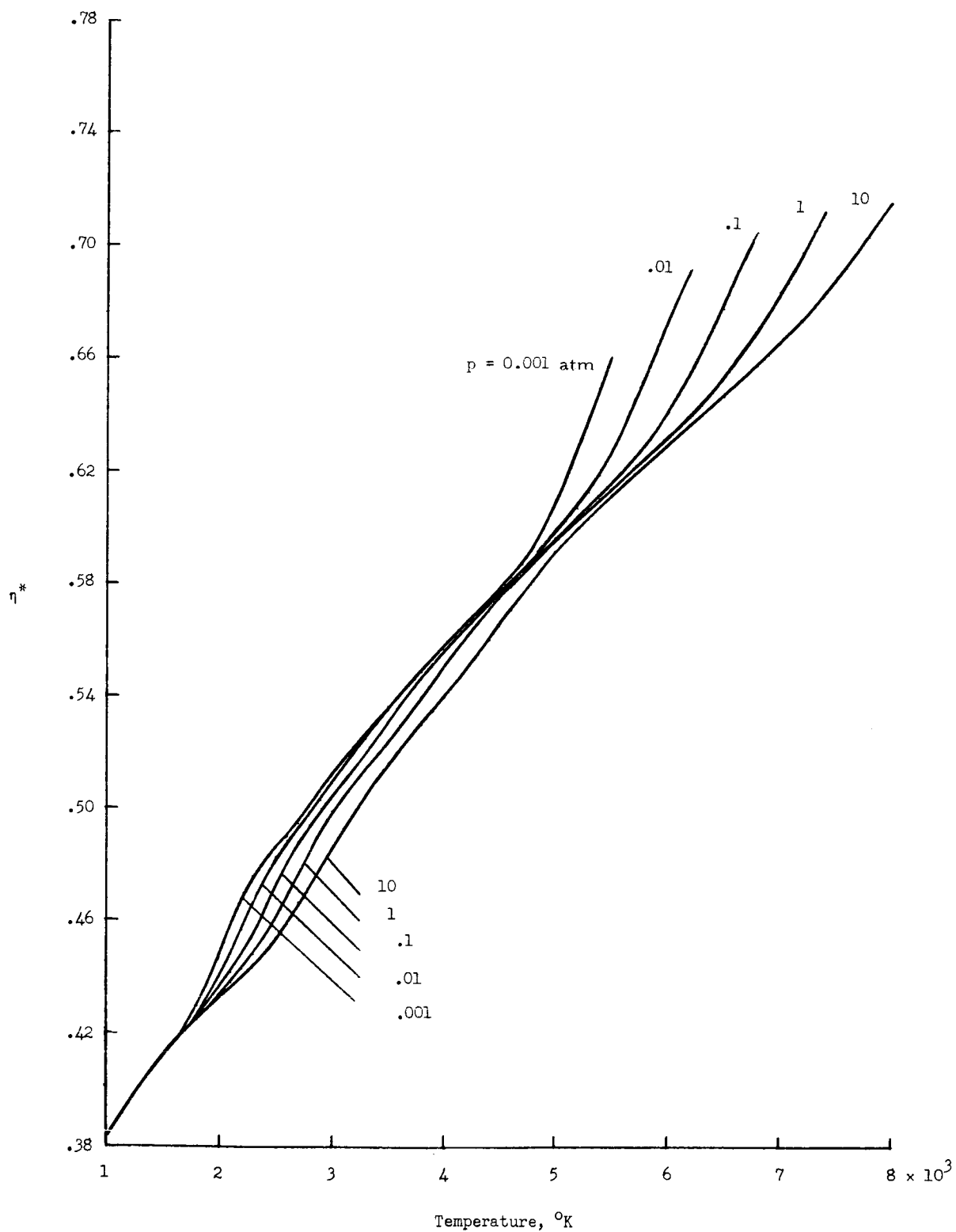


Figure 22.- Variation of viscosity of  $\text{CO}_2$  with temperature for range of pressures.

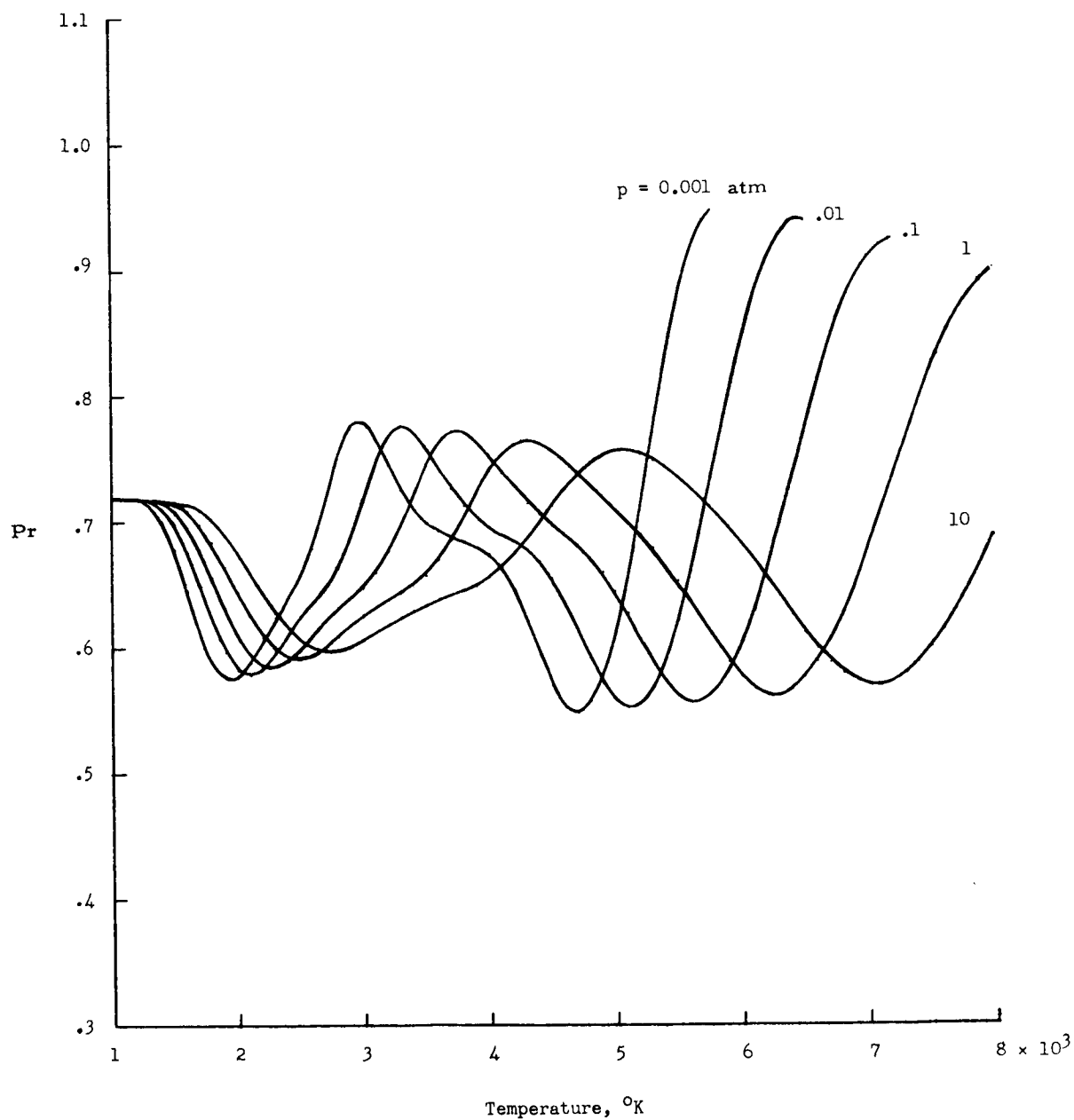


Figure 23.- Variation of Prandtl number of  $\text{CO}_2$  with temperature for range of pressures.

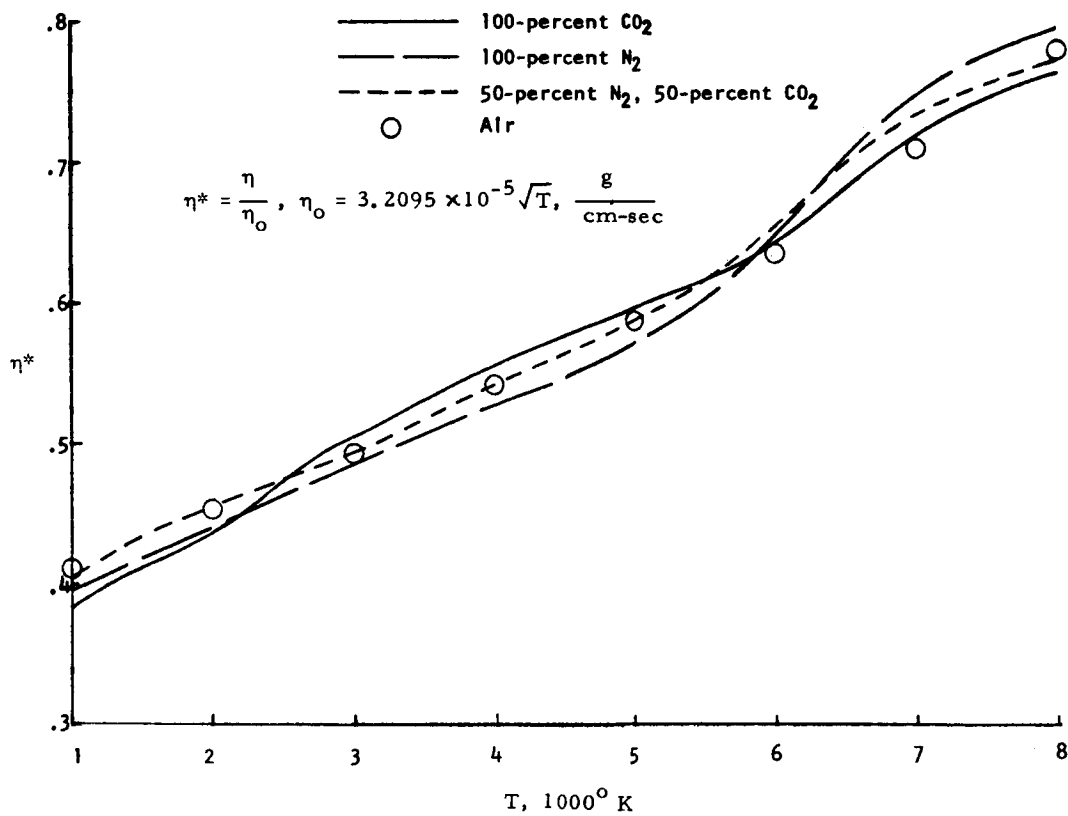


Figure 24.- Comparison of viscosities of CO<sub>2</sub> and N<sub>2</sub> mixtures with air.  
p = 0.1 atm.



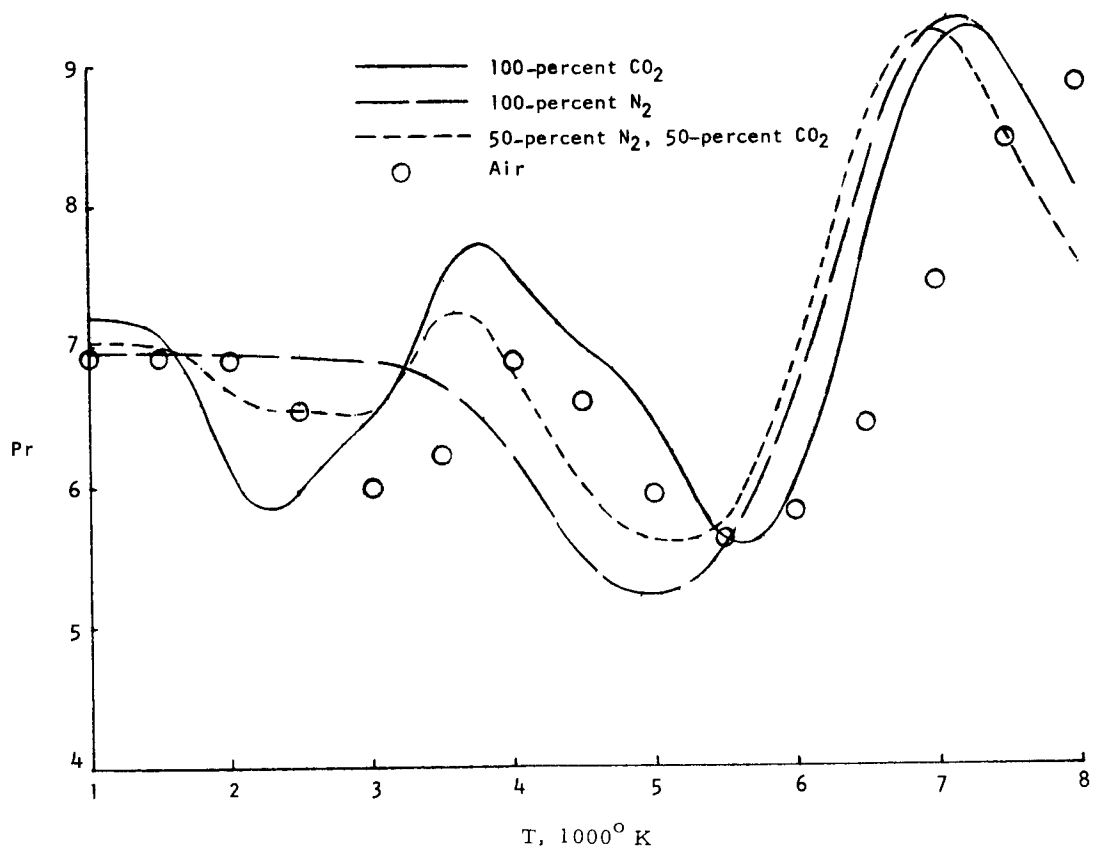
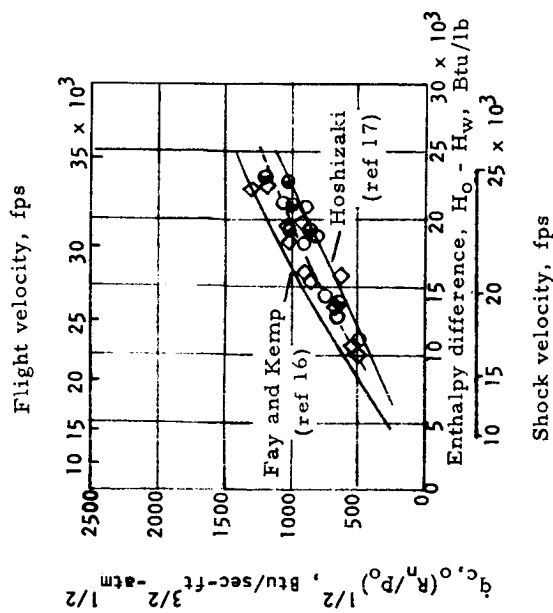


Figure 25.- Comparison of Prandtl numbers of CO<sub>2</sub> and N<sub>2</sub> mixtures with air.  
p = 0.1 atm.

Stagnation-point heat transfer in air

- Curve fit for present air data
- ◇ 0.25 mm with 1-in. -D model
  - 1.0 mm (ref 15)
  - 0.25 mm (ref 15)



Stagnation-point heat transfer for various atmospheres

- Curve for present air data
- Curve for present 9% CO<sub>2</sub>-90% N<sub>2</sub>-1% Ar
  - - - Curve for present 30% CO<sub>2</sub>-40% N<sub>2</sub>-30% Ar after radiation correction
  - - - Curve for present 65% CO<sub>2</sub>-35% Ar after radiation correction

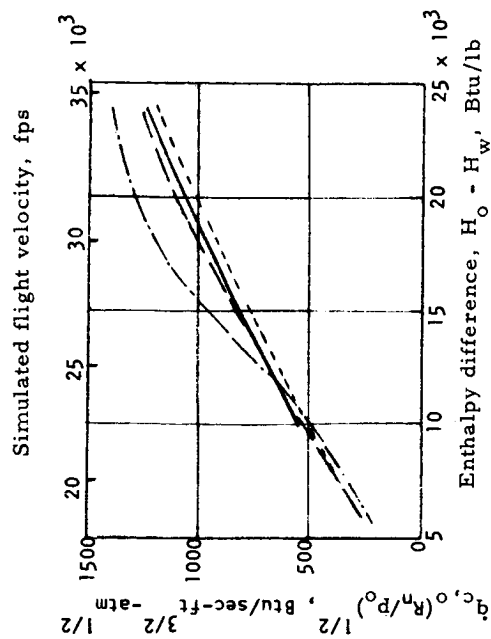


Figure 26.- Effect of composition on stagnation-point convective heating rates.

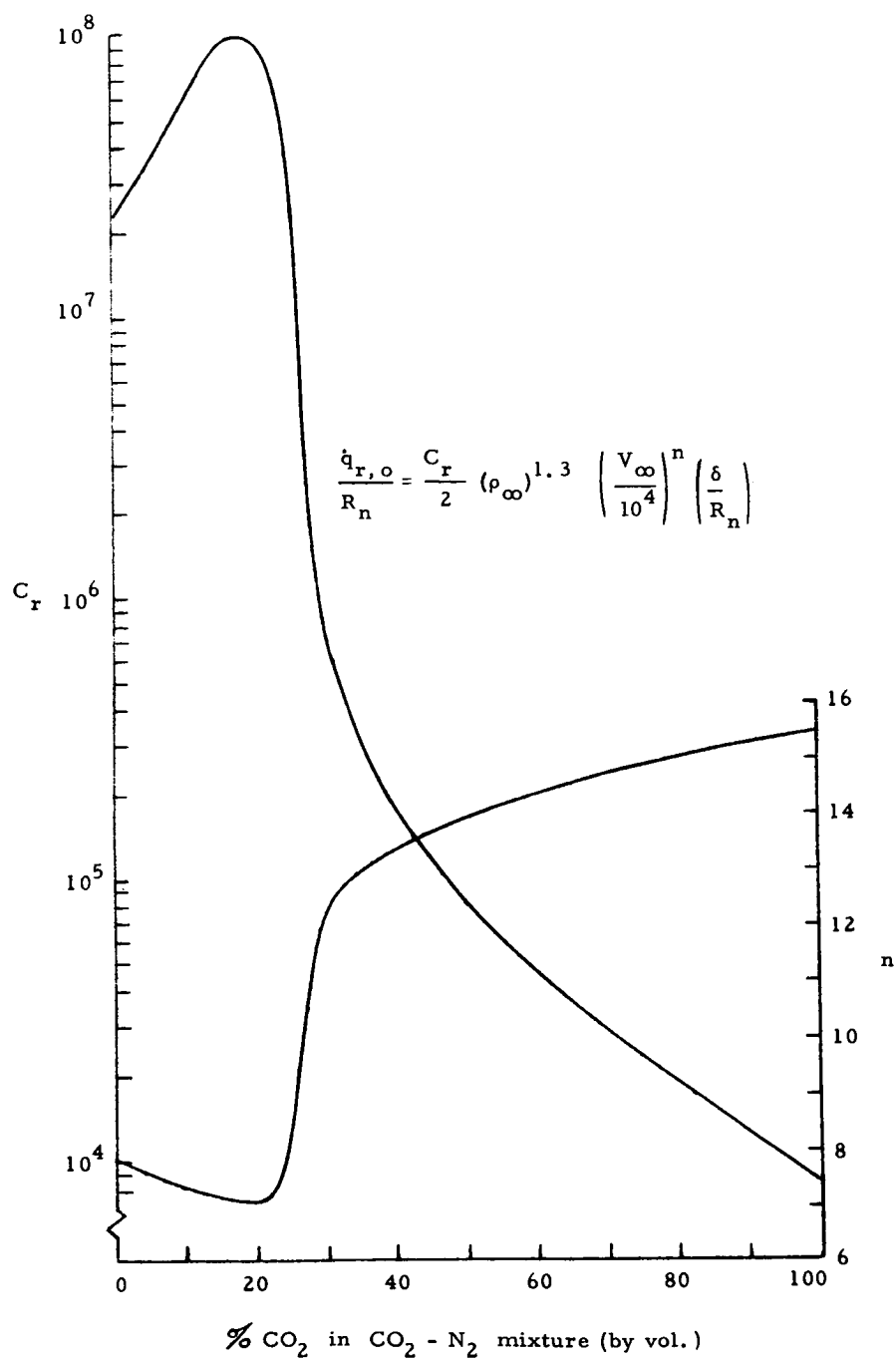


Figure 27.- Correlation equation constants for radiation intensity.

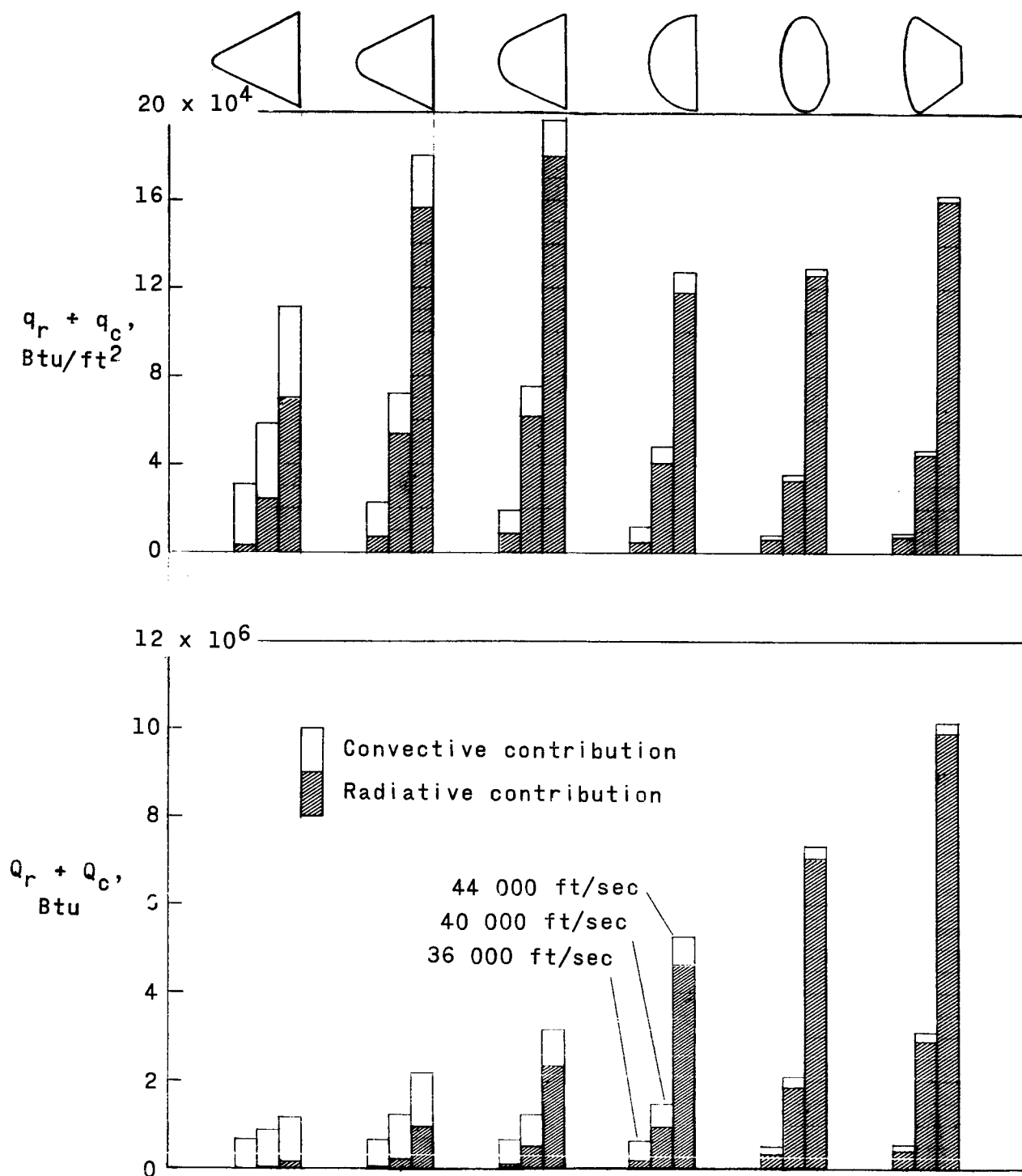
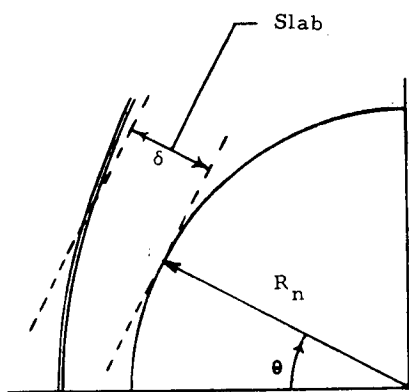
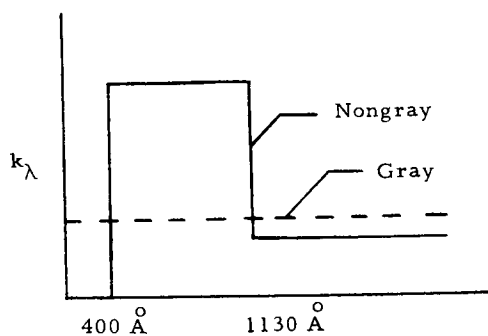


Figure 28.- Bar graph plots (ref. 13) showing relative contribution of radiative and convective heating to stagnation-point and entire-body heat inputs for  $m/A = 1.55$ ,  $\phi_E = 10^\circ$ , and three entry velocities. The maximum diameter of all bodies is 11 feet.



Slab approximation

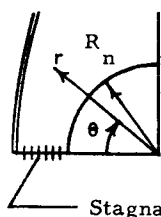
$400 \text{ \AA} \leq \lambda \leq 1130 \text{ \AA}$   
 $\text{N}^+$  and  $\text{O}^+$  electron recombination  
 Wings of atomic lines  
 $1130 \text{ \AA} \leq \lambda \leq \infty$   
 Molecular band systems  
 Free-free electron transitions  
 Photoionization of O  
 $\text{N}^+$  and  $\text{O}^+$  electron recombination  
 Wings of atomic lines for  $\lambda < 2000 \text{ \AA}$   
 Atomic lines for  $\lambda > 2000 \text{ \AA}$



Wavelength,  $\lambda$

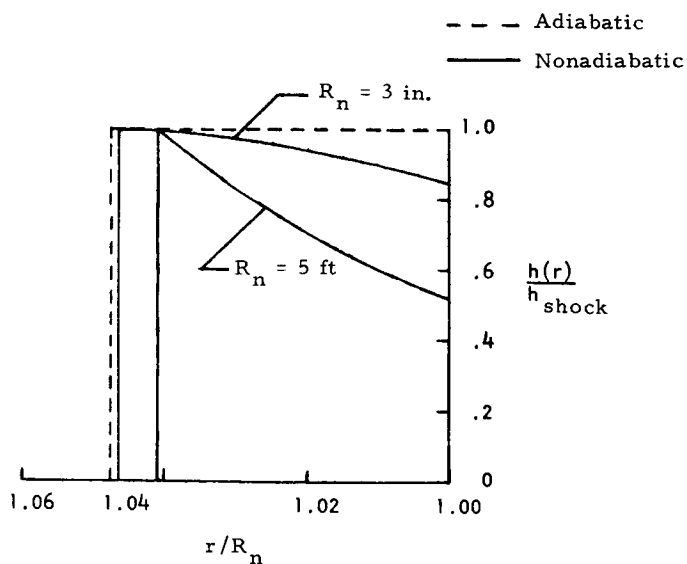
Absorption coefficient model

Figure 29.- Two-step absorption coefficient model and shock-layer slab approximations.

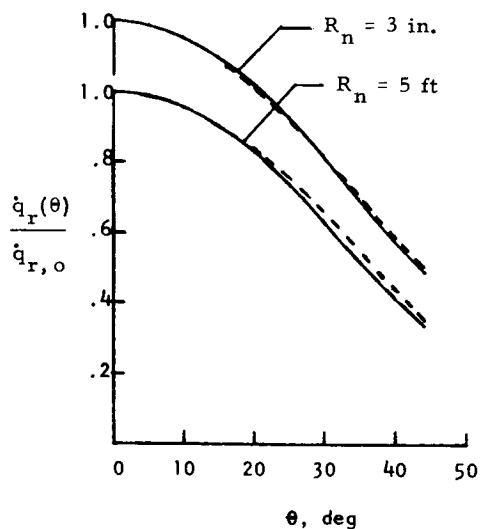


Radius	3 in.	5 ft
Adiabatic	2060	19760
Nonadiabatic	1806	7530

Stagnation-point heat flux, Btu/ft<sup>2</sup> sec

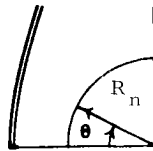


Stagnation streamline enthalpy distribution



Surface heat flux distributions

Figure 30.- Effect of sphere size on nongray heat-transfer rate distribution.  
 $V_\infty = 50\,000$  ft/sec;  $h = 190\,000$  ft.



— Total  
 - - -  $400 \text{ Å} \leq \lambda \leq 1130 \text{ Å}$   
 — — —  $1130 \text{ Å} \leq \lambda < \infty$

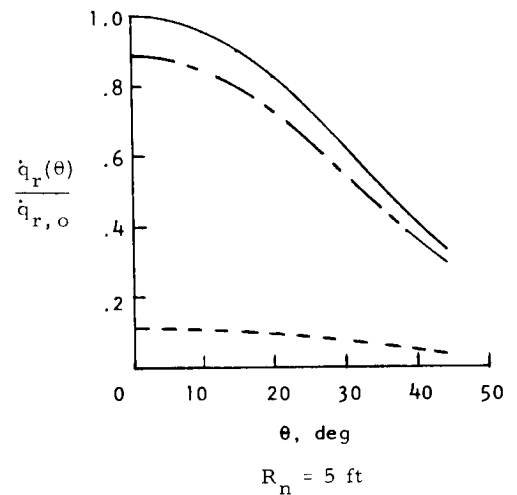
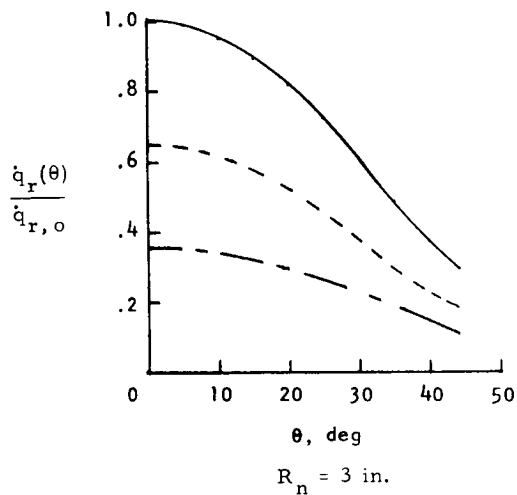
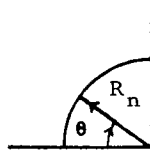
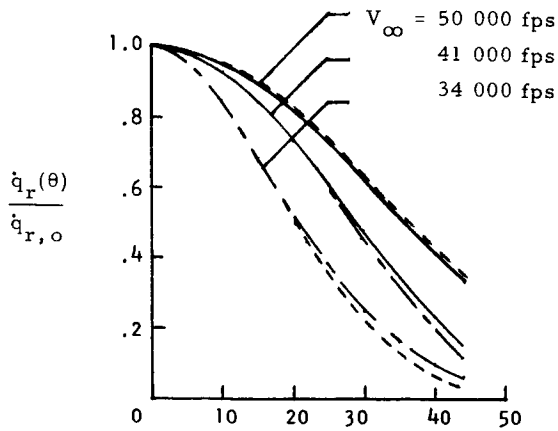


Figure 31.- Spectral breakdown of nongray radiative heating-rate distribution for 3-inch- and 5-foot-radius spheres.  $V_\infty = 50\,000 \text{ ft/sec}$ ;  $h = 190\,000 \text{ feet}$ .



—————  $h = 220\,000\text{ ft}$   
 - - - - -  $190\,000\text{ ft}$   
 — — — —  $140\,000\text{ ft}$



Surface heat flux distributions

Altitude, h, ft	Velocity $V_\infty$ , fps		
	34 000	41 000	50 000
220 000	---	562	2114
190 000	243	---	7530
140 000	2760	25 740	---

Stagnation-point heat flux,  
Btu/ft<sup>2</sup>-sec

Figure 32.- Effect of velocity and altitude on nongray radiative heating-rate distribution on a sphere.



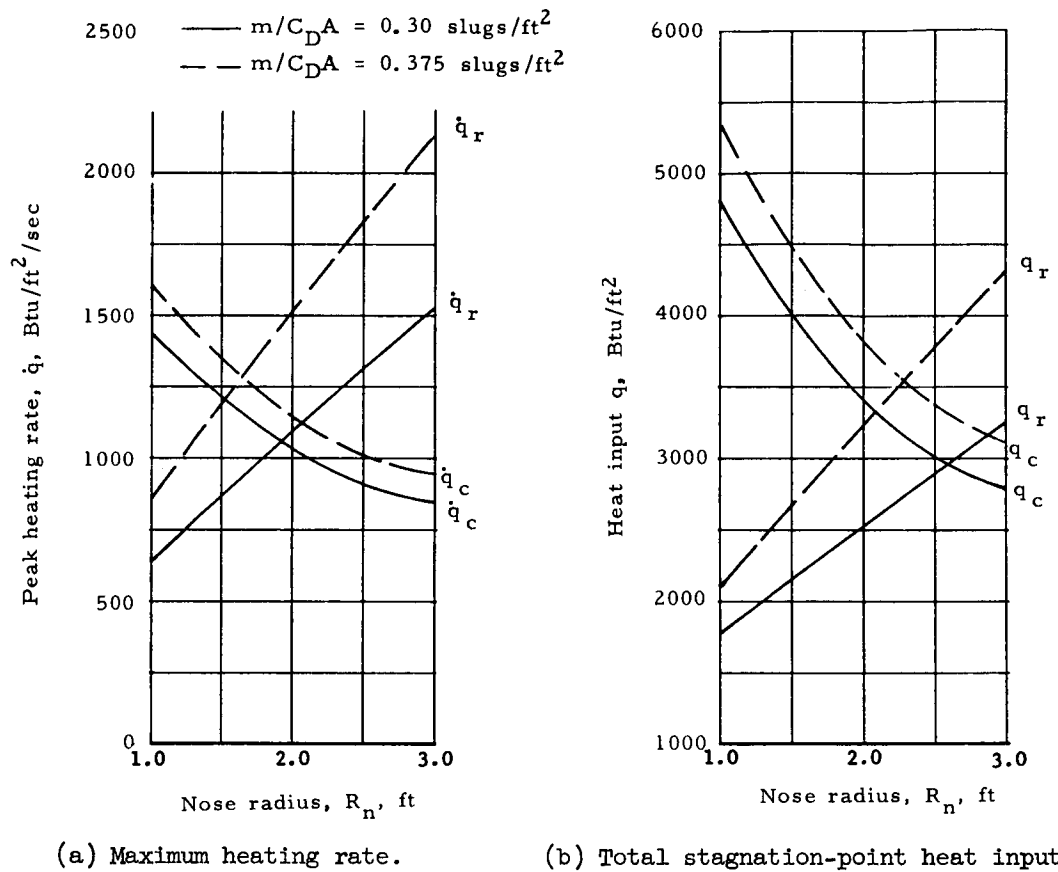


Figure 33.- Configuration influence on aerodynamic heating rates and heat inputs at stagnation point (ref. 29).  $V_E = 38\,000 \text{ ft/sec}$ ;  $\phi_E = 40^\circ$ .

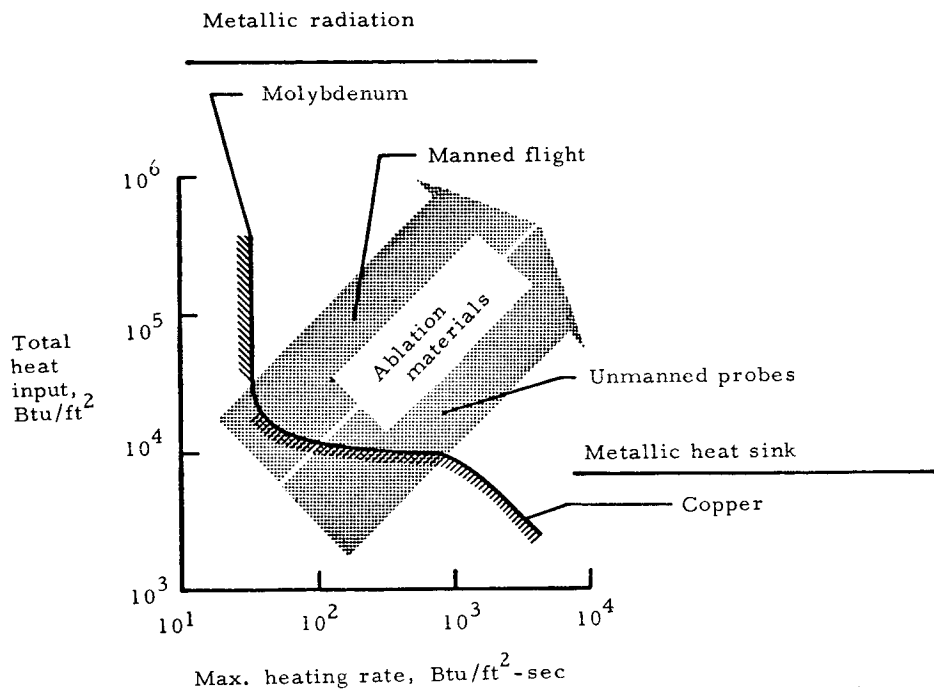


Figure 34.- Entry-vehicle heating environment and materials capability (ref. 30).

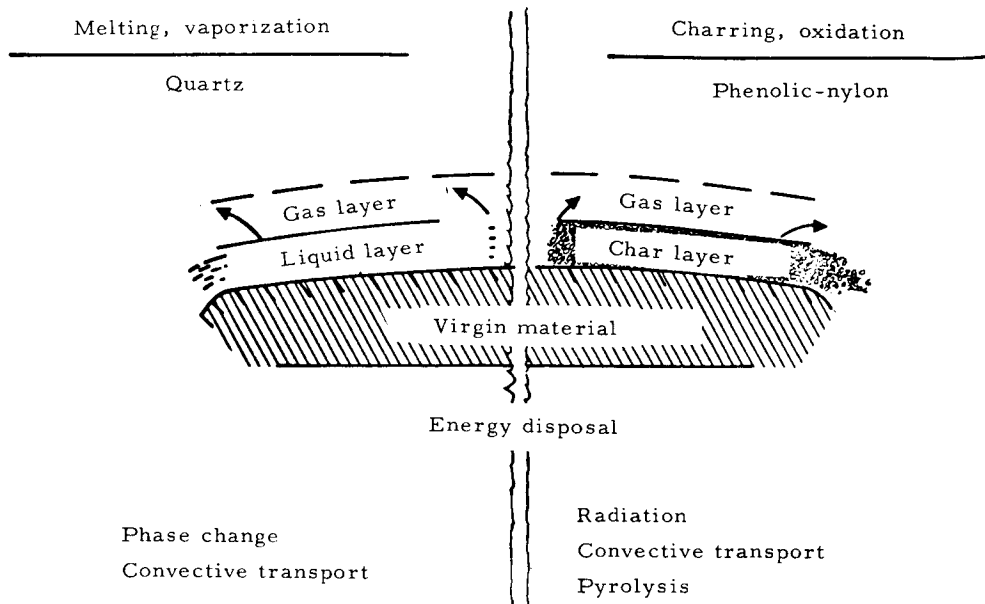


Figure 35.- Energy disposal for two ablation concepts (ref. 30).

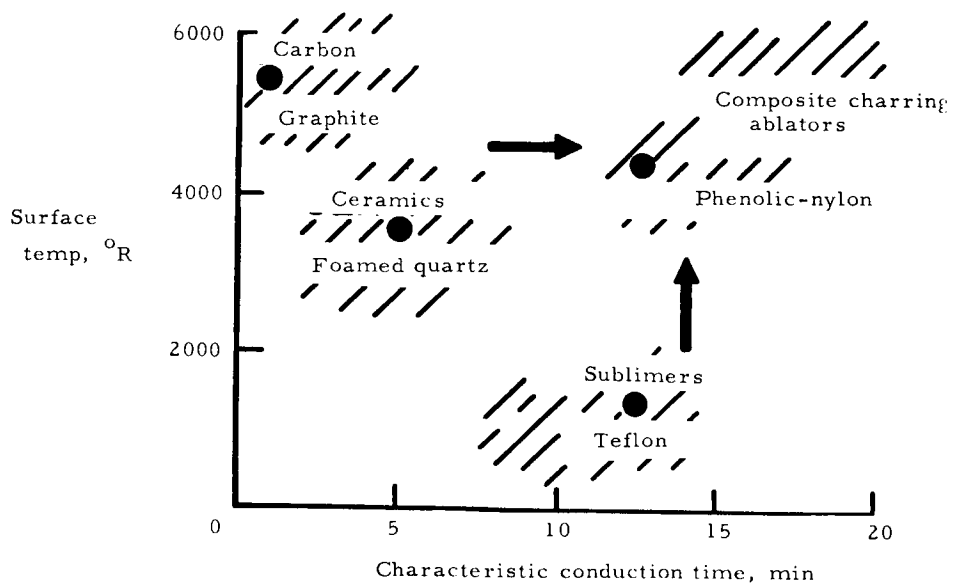
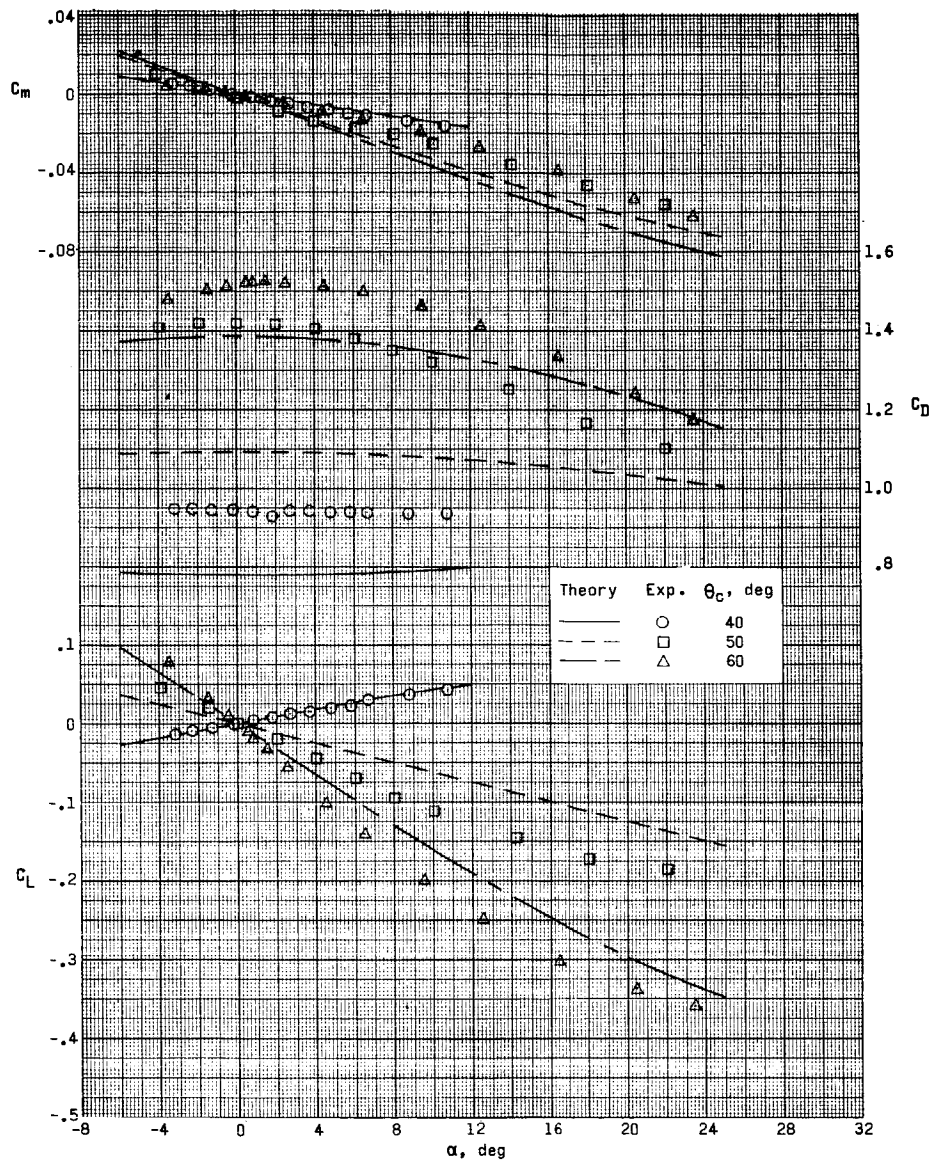
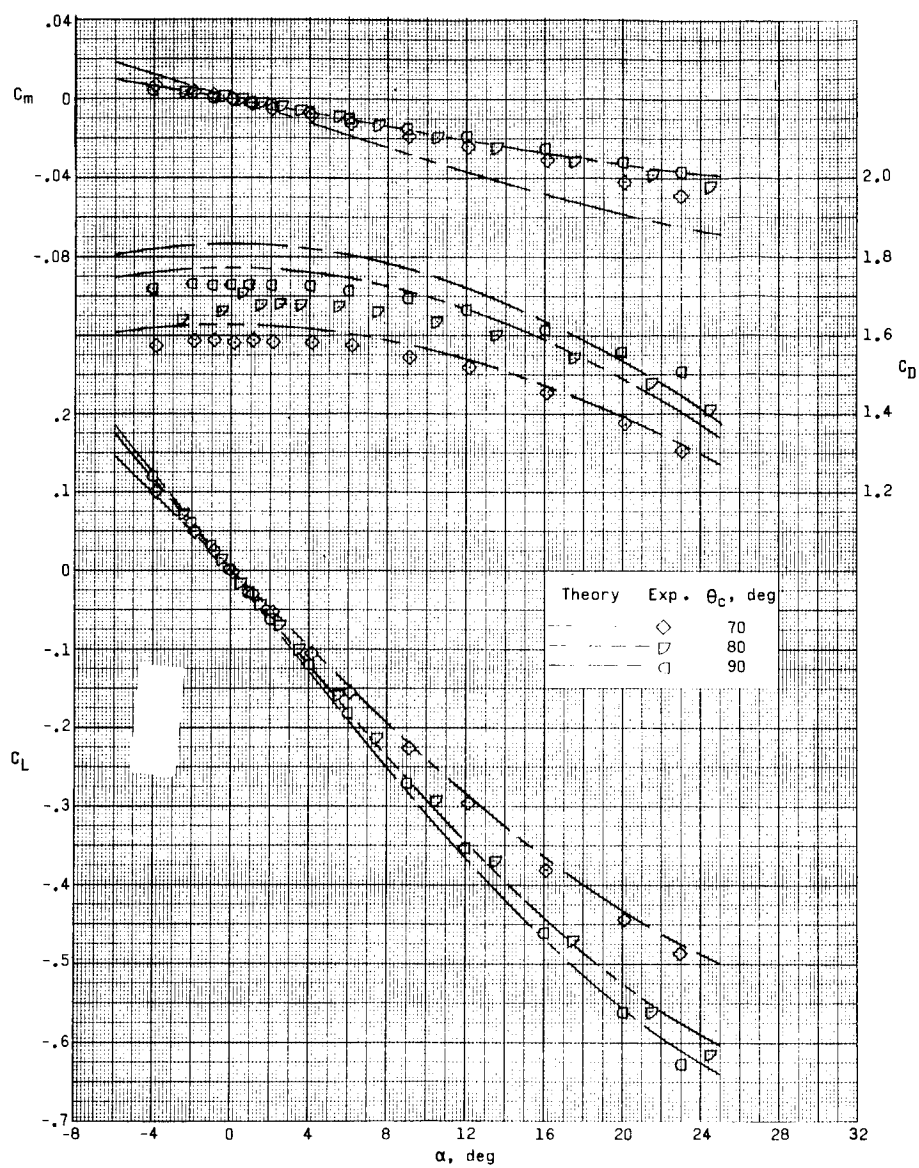


Figure 36.- Insulation capabilities of various ablation materials (ref. 30).



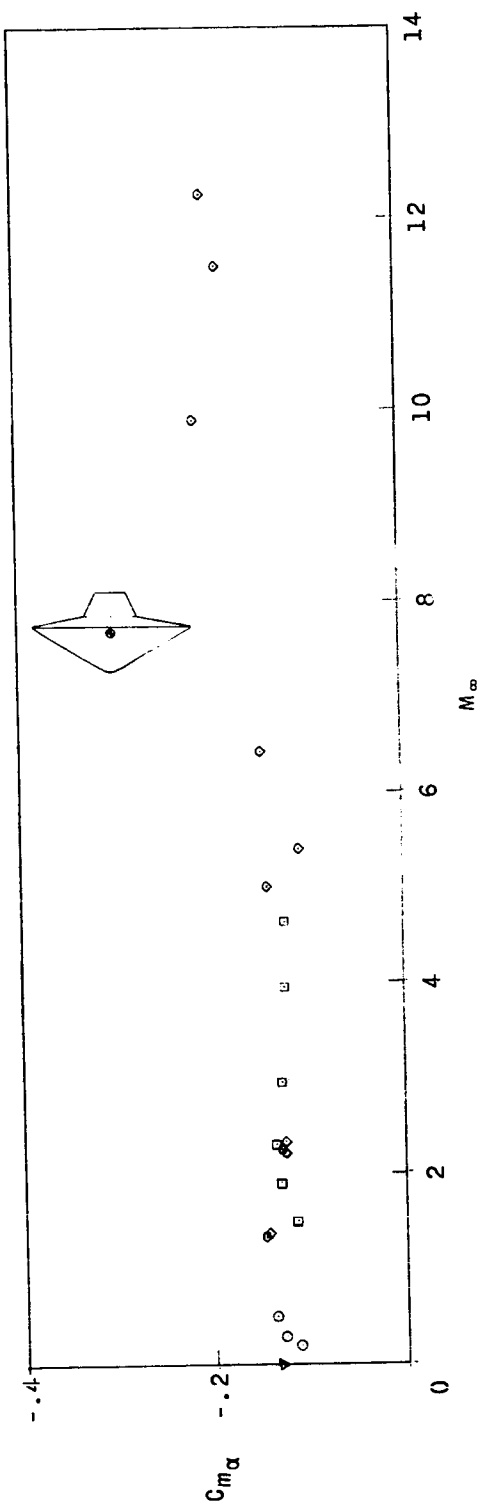
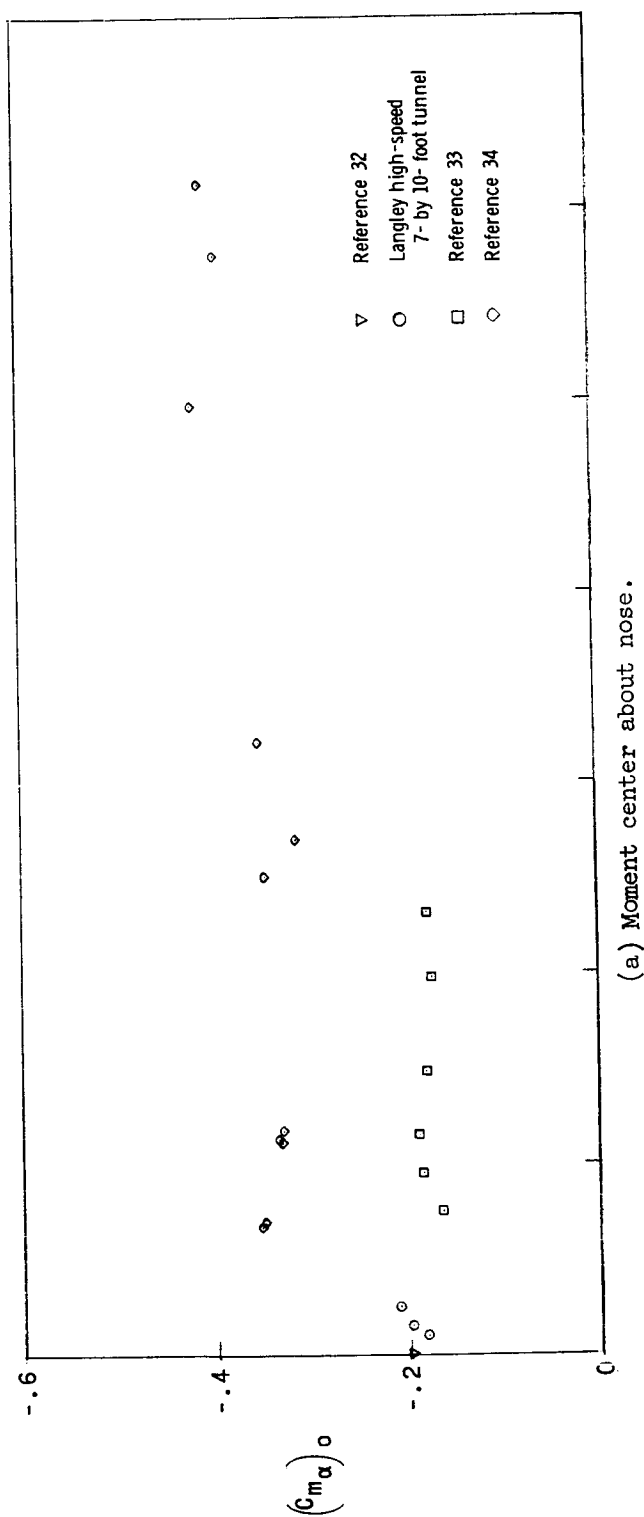
(a) 40°, 50°, and 60° cones.

Figure 37.- Static aerodynamic coefficients for blunt pointed cones at Mach number of 4.63 (ref. 33).



(b) 70°, 80°, and 90° cones.

Figure 37.- Concluded.



(b) Moment center at NOL model center-of-gravity location (0.8-inch model).

Figure 38.- Comparison of ballistic range and wind-tunnel pitching-moment coefficients.

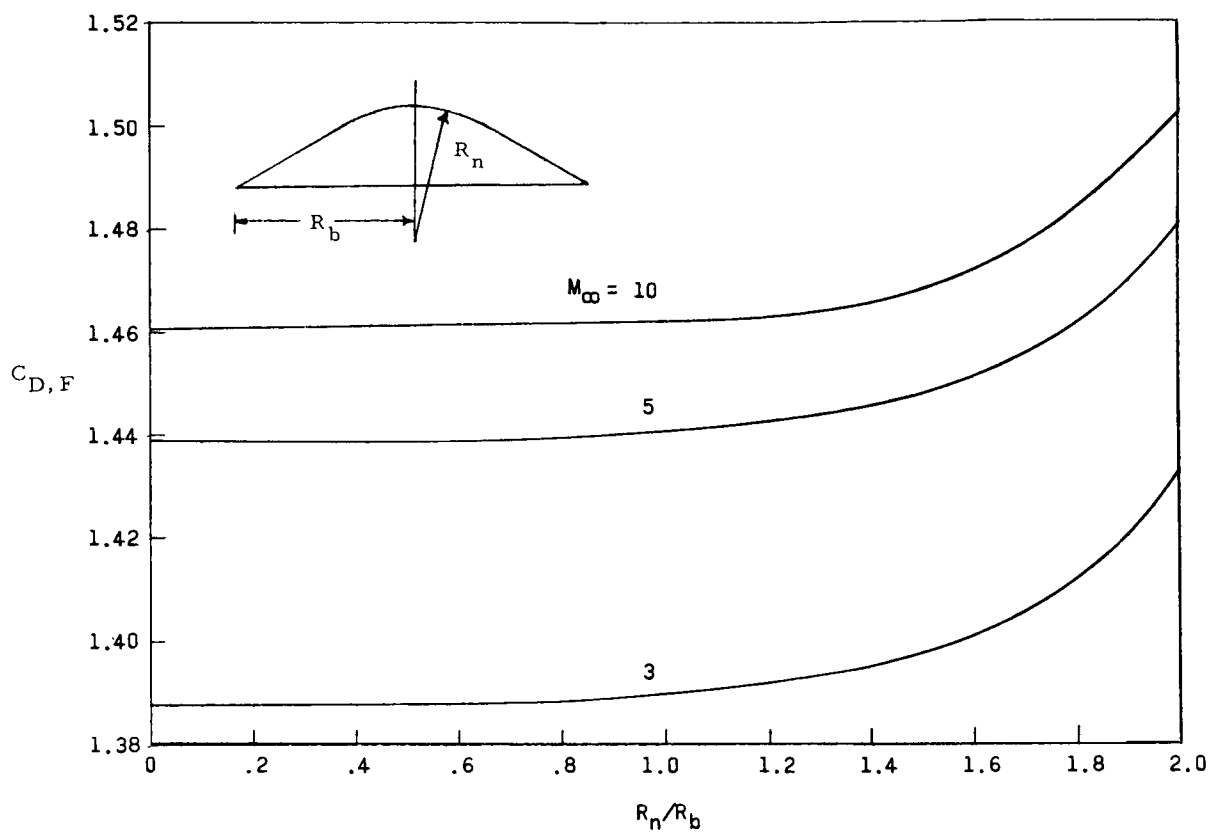


Figure 39.- Drag-coefficient dependence on bluntness ratio for 60° spherically blunted cone (ref. 35).  $\gamma = 1.4$ .

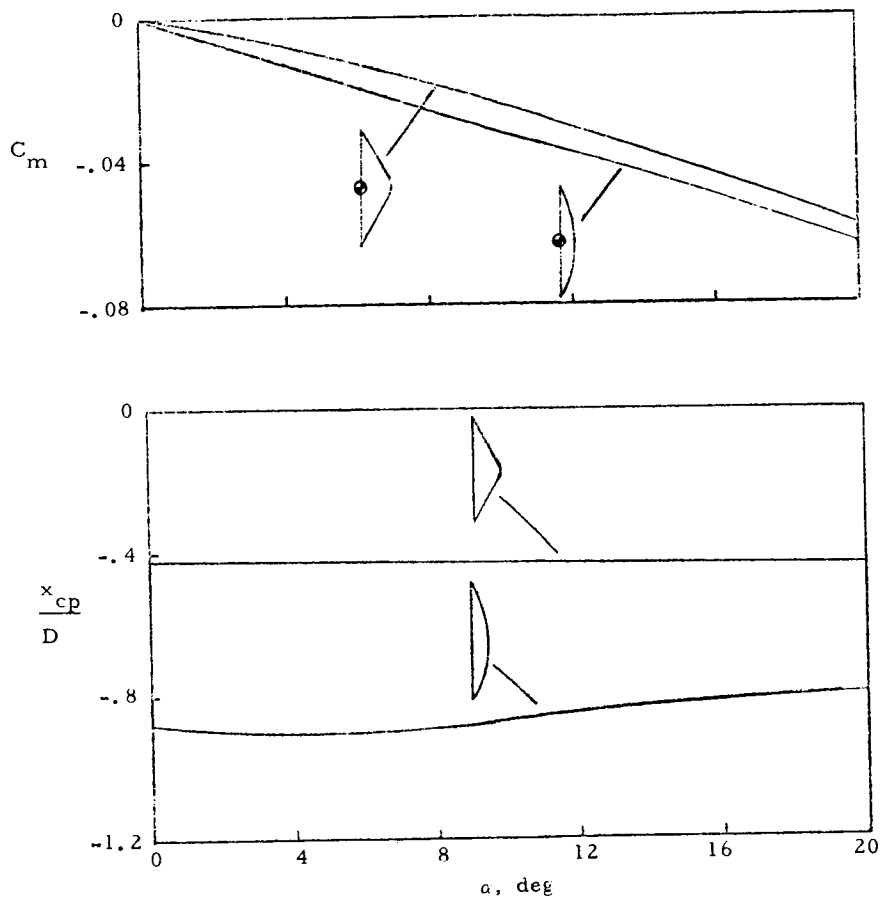


Figure 40.- Variation of pitching moment and center of pressure with angle of attack for spherical cap and 120° cone at a Mach number of 9.02 (ref. 36).  
 $x_{cp}/D$  measured from base of body.



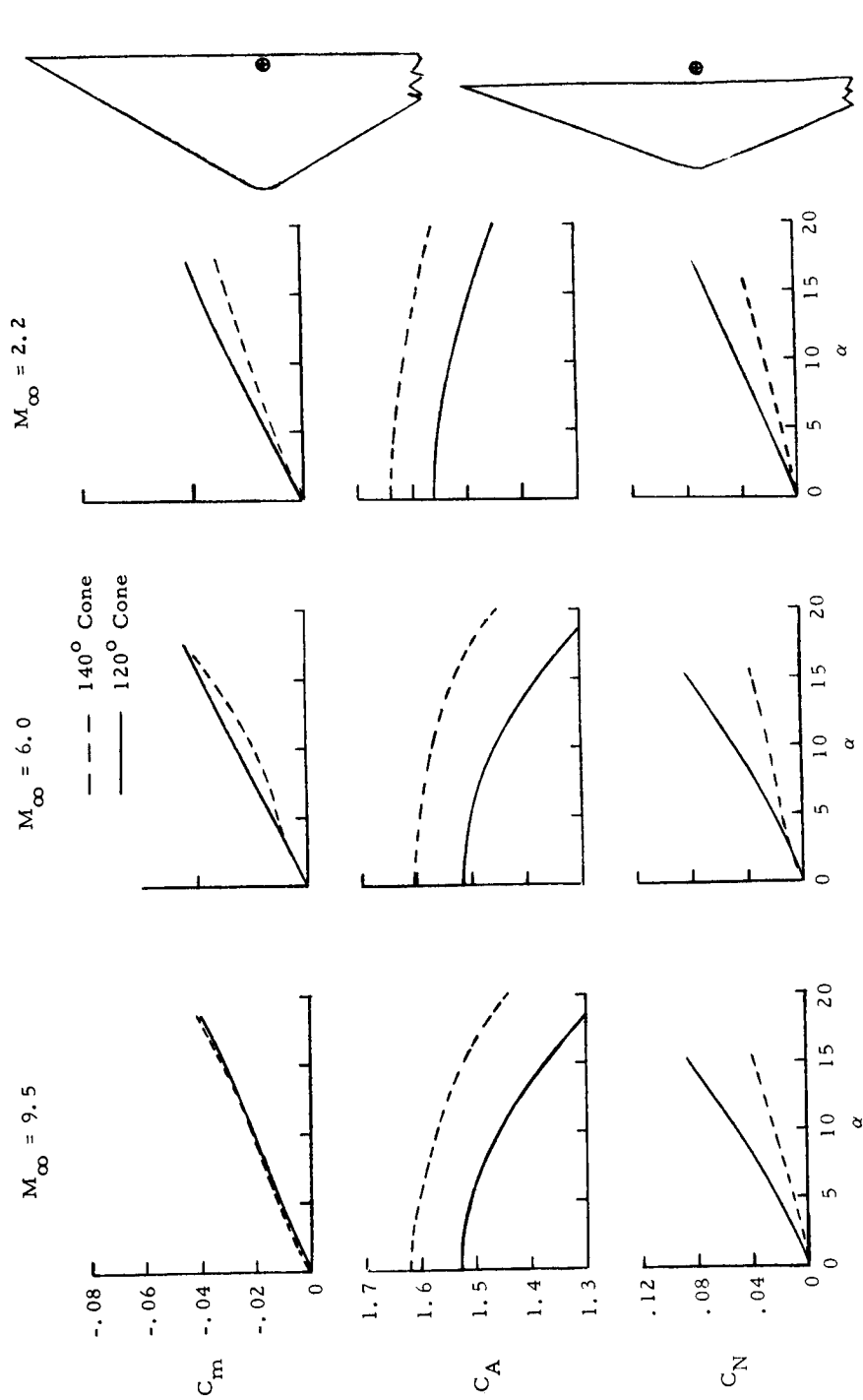


Figure 41.- Supersonic aerodynamic coefficients for 120° and 140° cones at three Mach numbers (ref. 37).

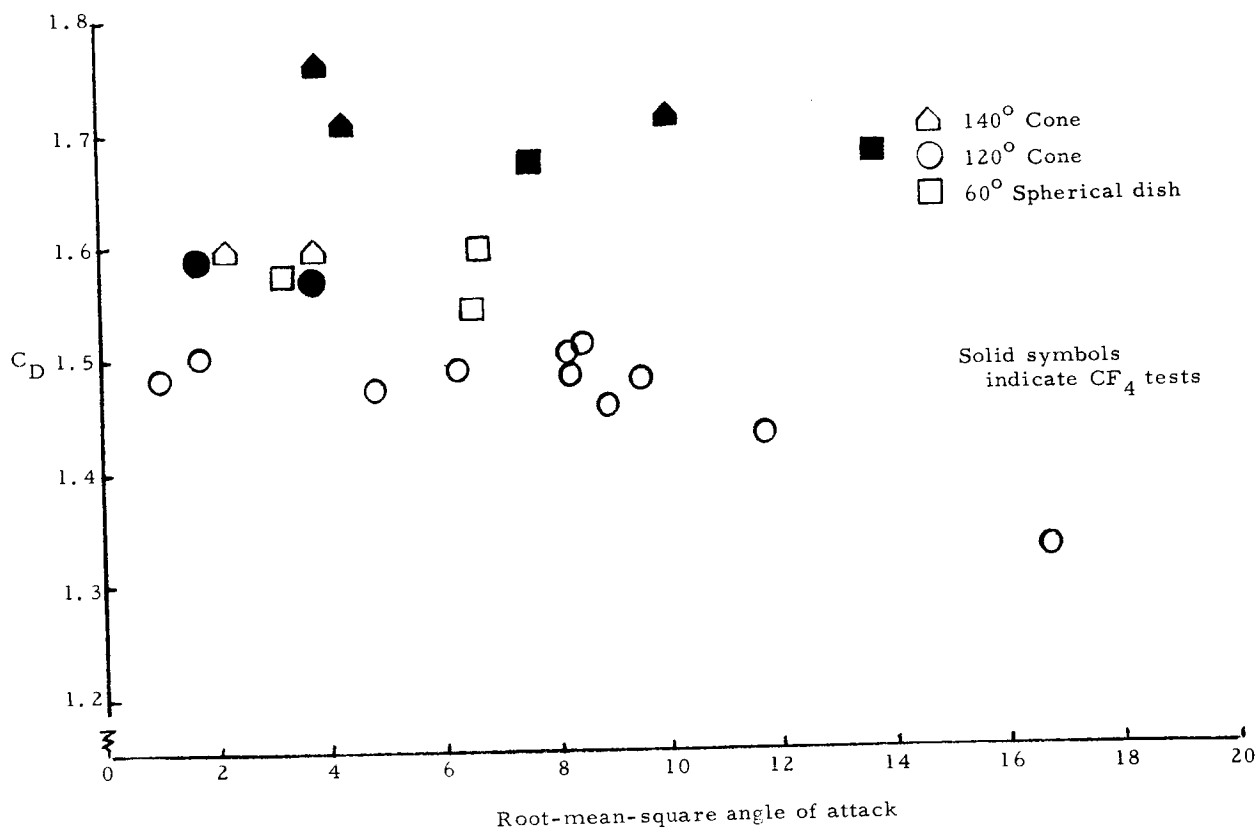


Figure 42.- Density-ratio effect on drag coefficient from ballistic-range tests (ref. 34).

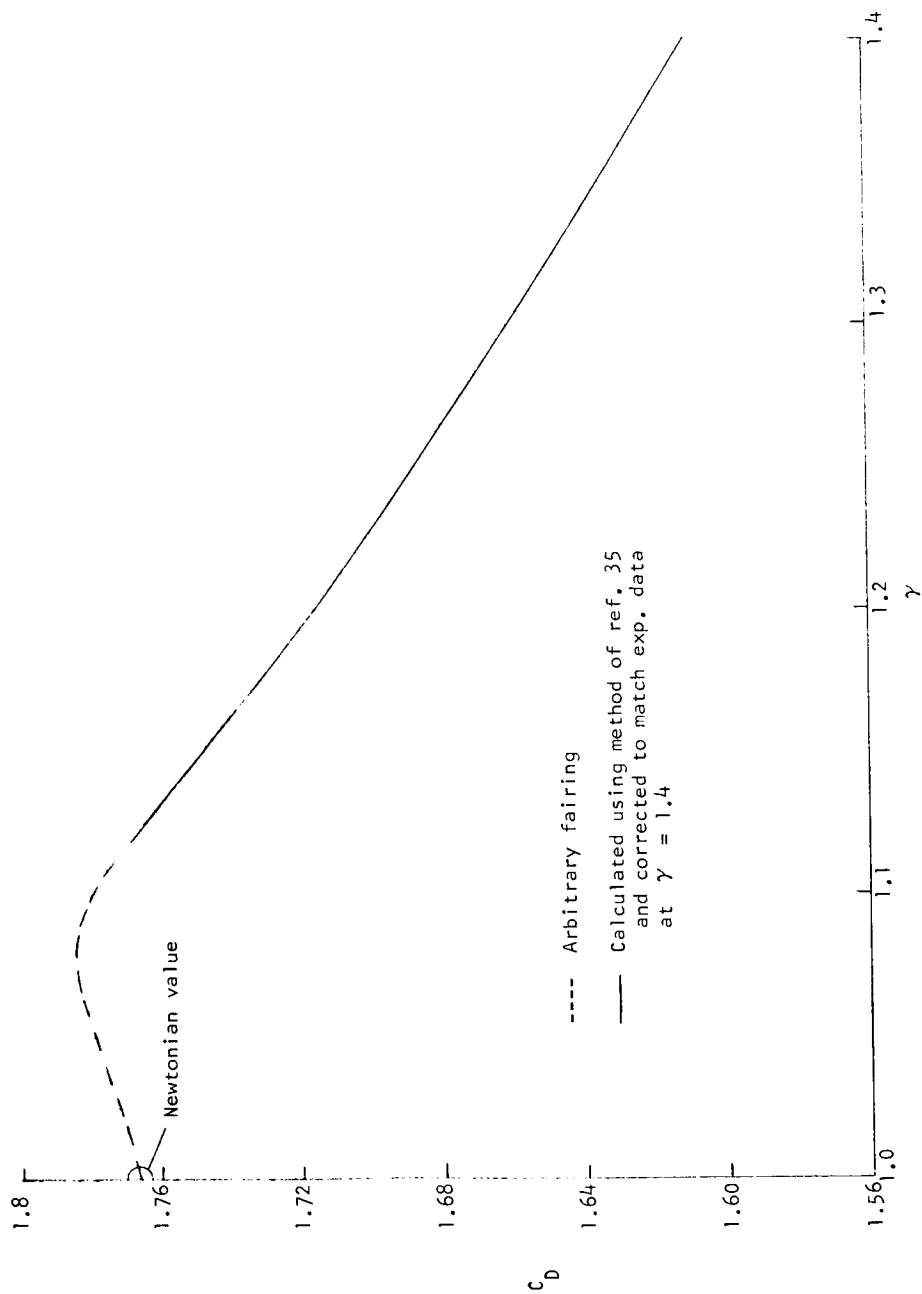


Figure 43.- Effect of ratio of specific heats on drag coefficient of 140° cone.

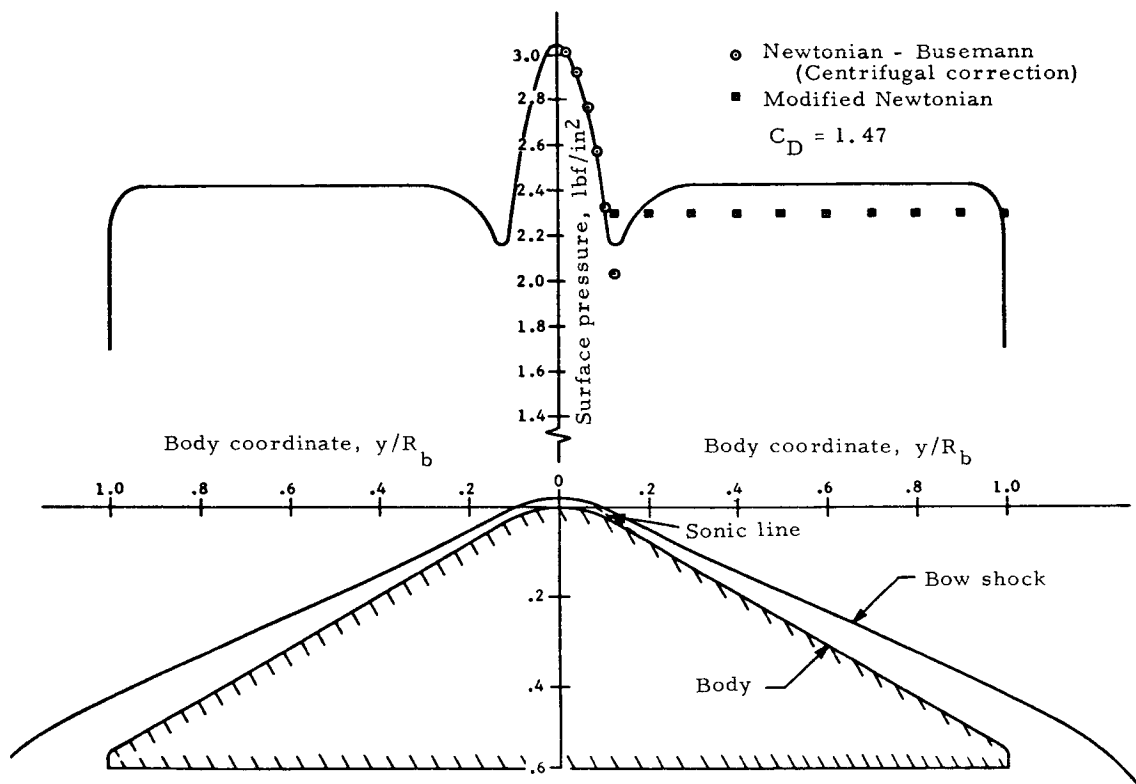


Figure 44.- Body pressure distribution and bow shock position for 120° cone (from ref. 38).  $R_n/R_b = 0.25$ ;  $\gamma = 1.17$ ; VM-8 atmosphere;  $V_\infty = 11\,000\text{ ft/sec}$ ;  $h = 61\,000\text{ ft}$ .

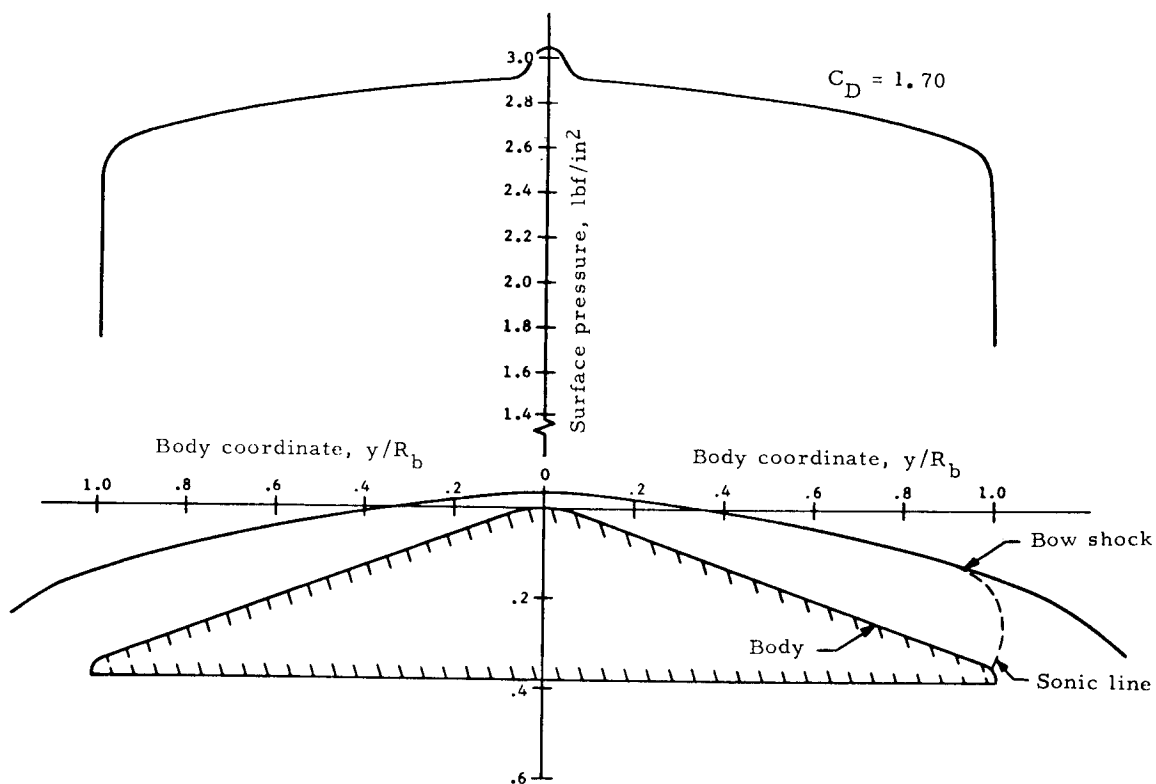


Figure 45.- Body pressure distribution and bow shock position for 140° cone (from ref. 38).  $R_n/R_b = 0.25$ ;  $\gamma = 1.17$ ; VM-8 atmosphere;  $V_\infty = 11\ 000$  ft/sec;  $h = 61\ 000$  ft.

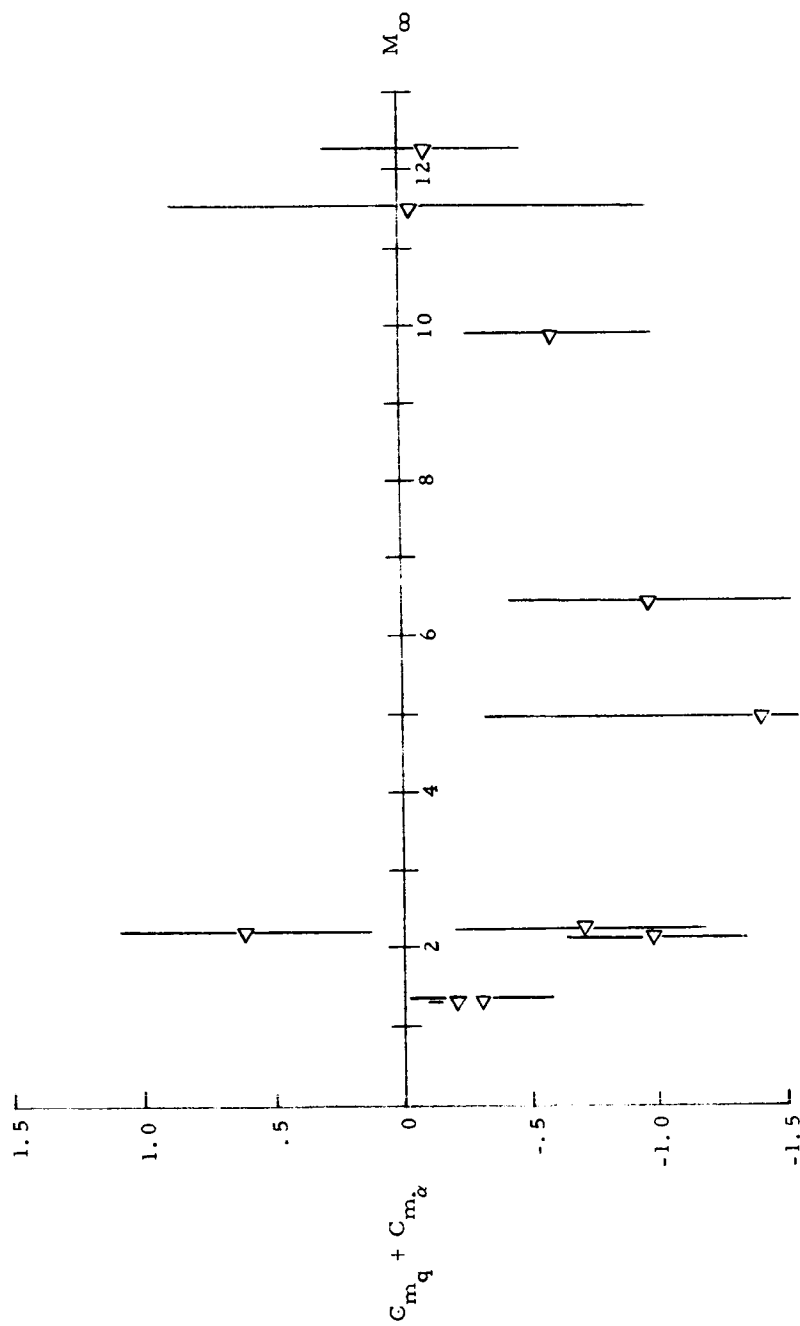


Figure 46.- Variation of damping coefficient  $C_{mq} + C_{ma}$  for solid L200 cone model as obtained in NOL ballistic range.

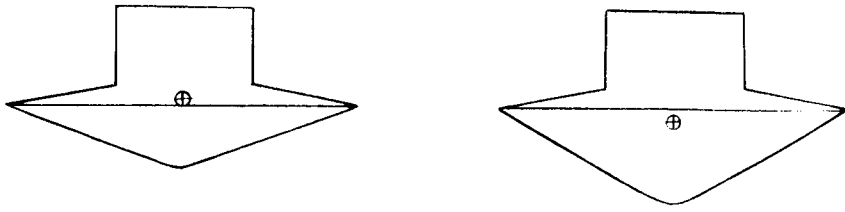
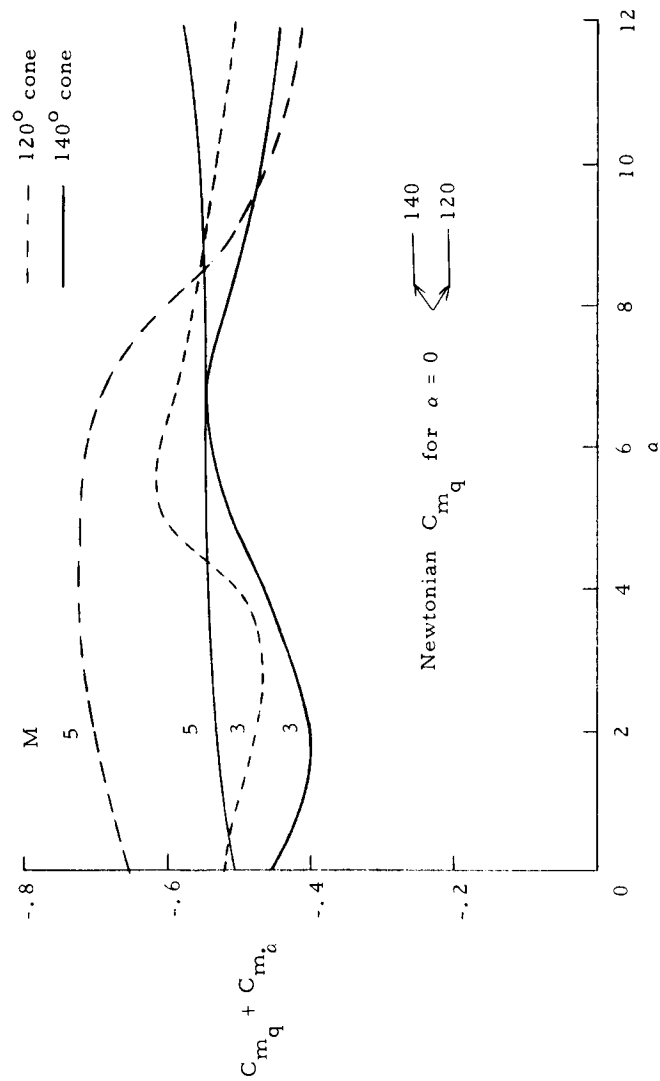


Figure 47.- Damping in pitch for 120° and 140° cones at Mach numbers of 3 and 5. Forced-oscillation tests (ref. 39).

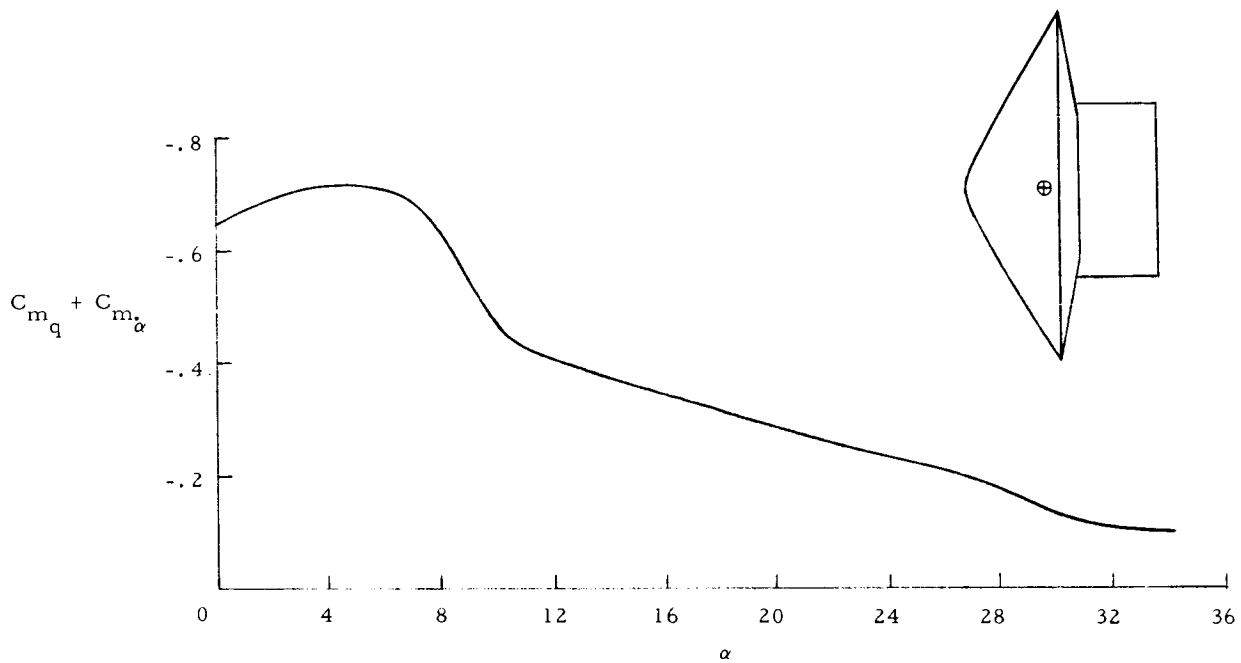
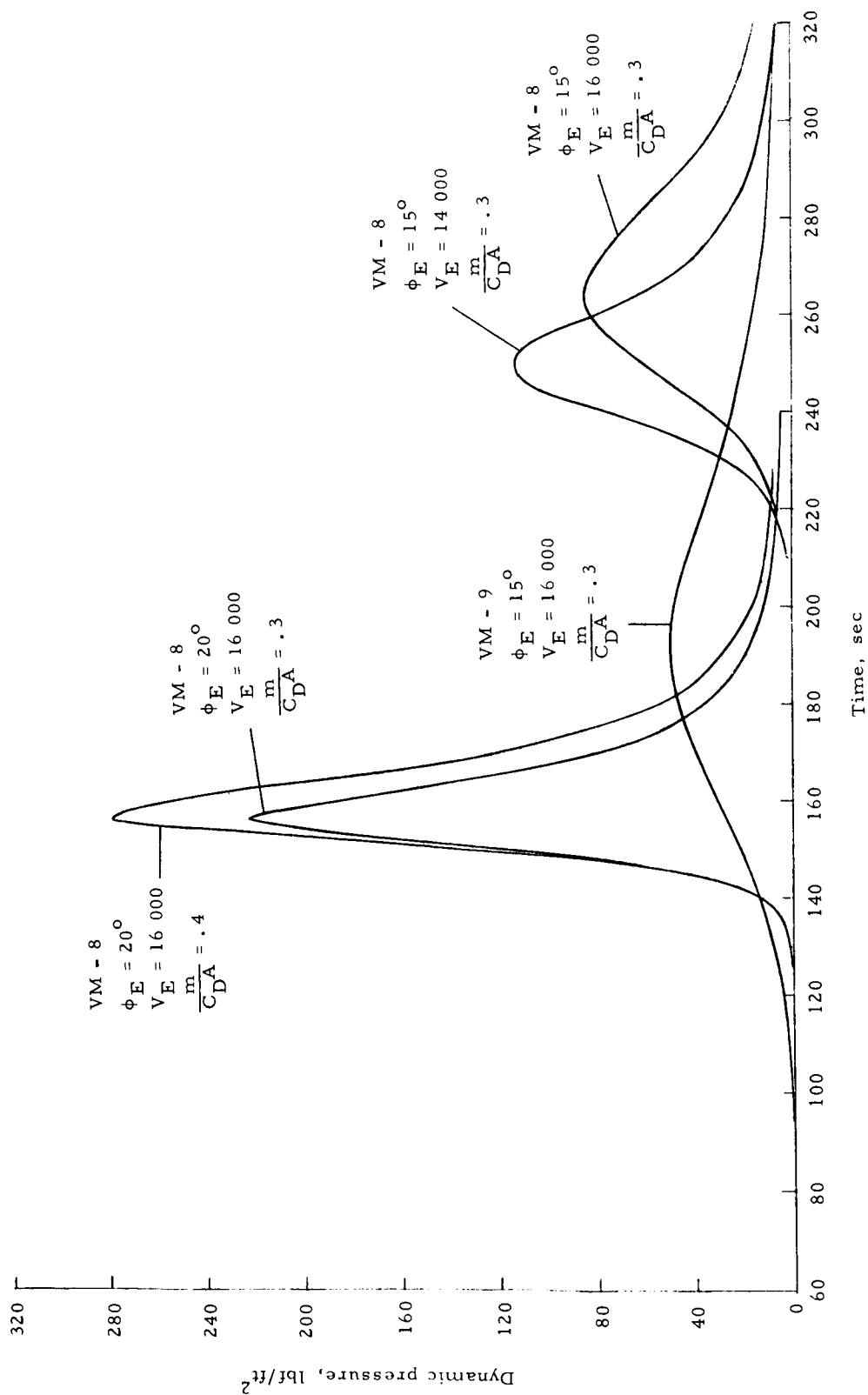


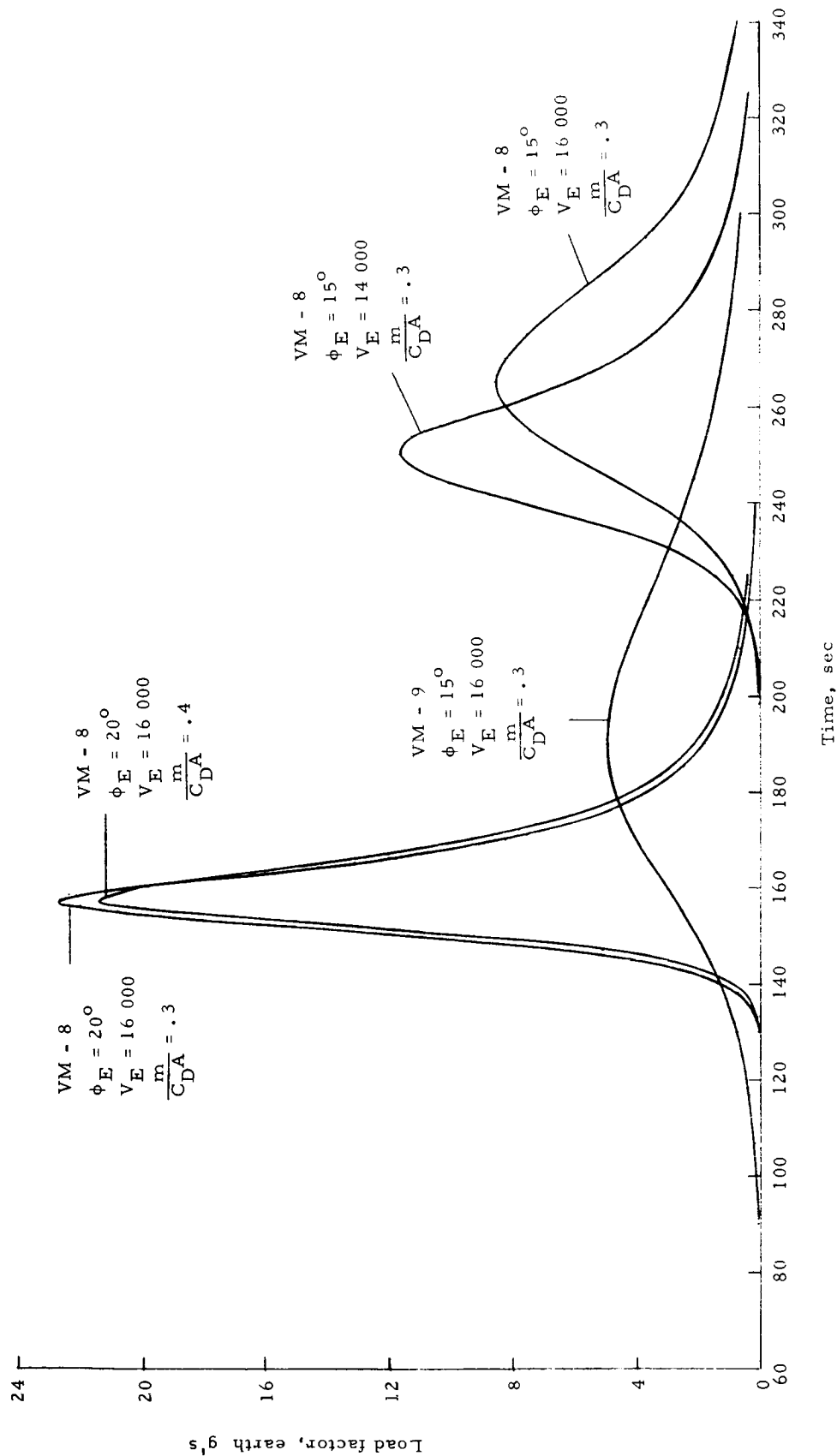
Figure 48.- Damping in pitch for 120° cone at Mach number of 5.02.  
Forced-oscillation tests (ref. 39).





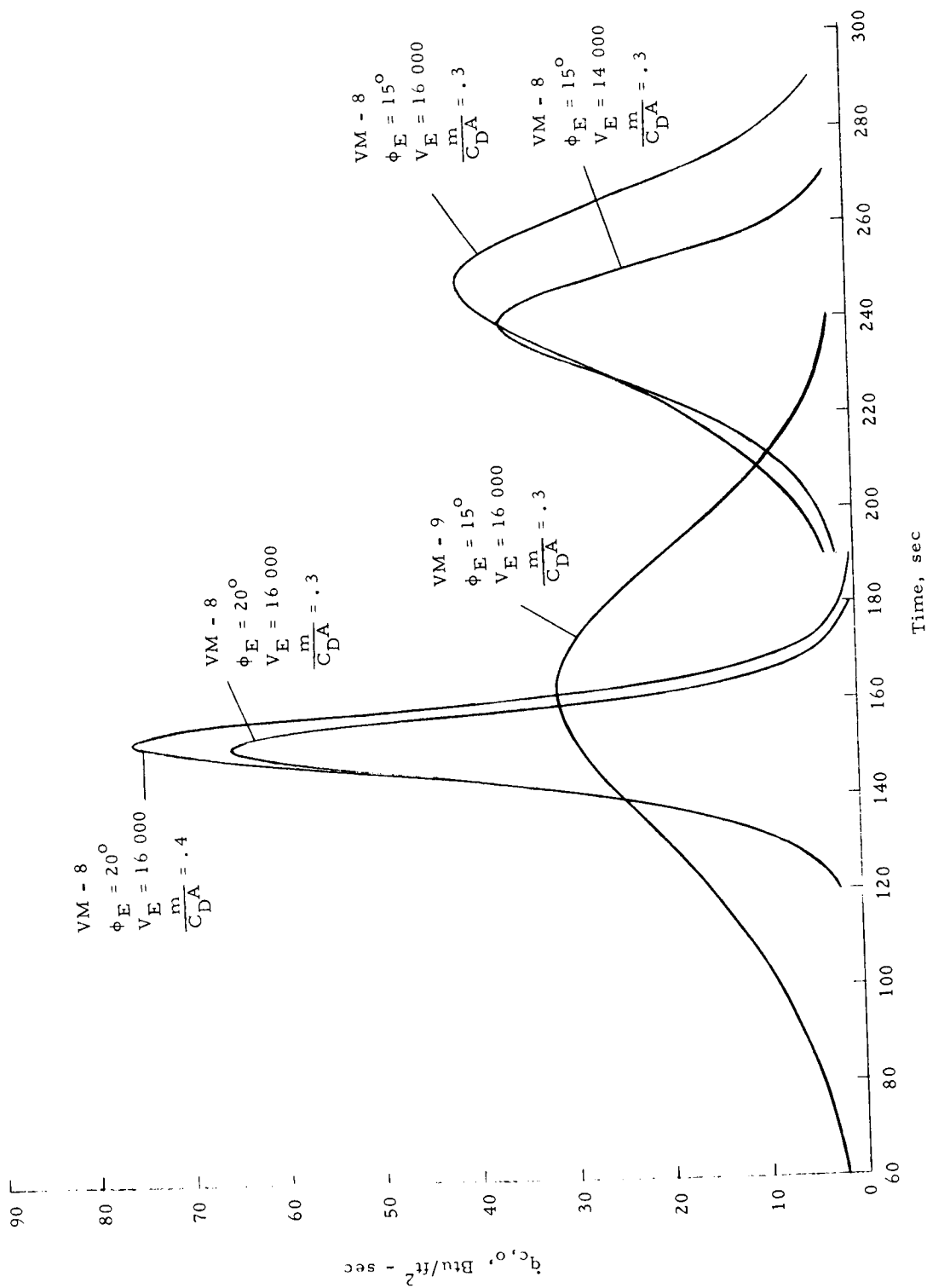
(a) Dynamic-pressure time histories.

Figure 49.- Typical dynamic pressure, acceleration, and heating-rate time histories for Mars entry.



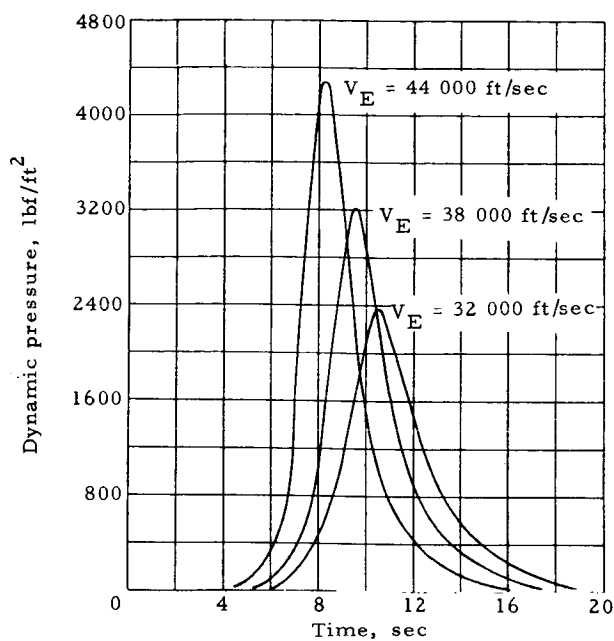
(b) Deceleration-load time histories.

Figure 49.- Continued.

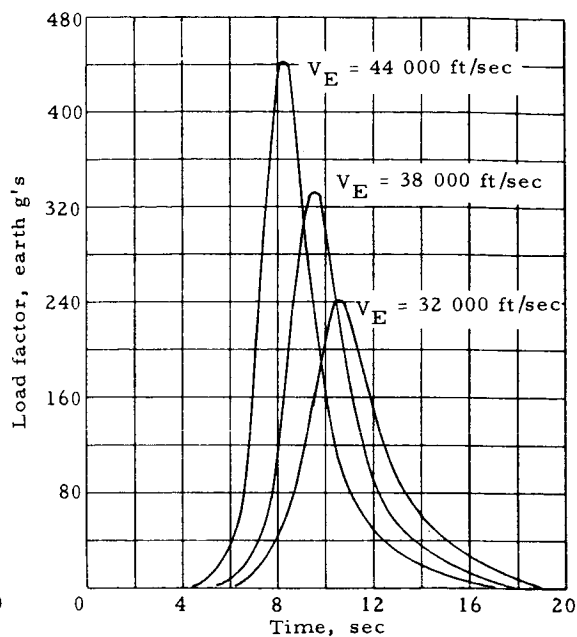


(c) Stagnation-point heating rates.

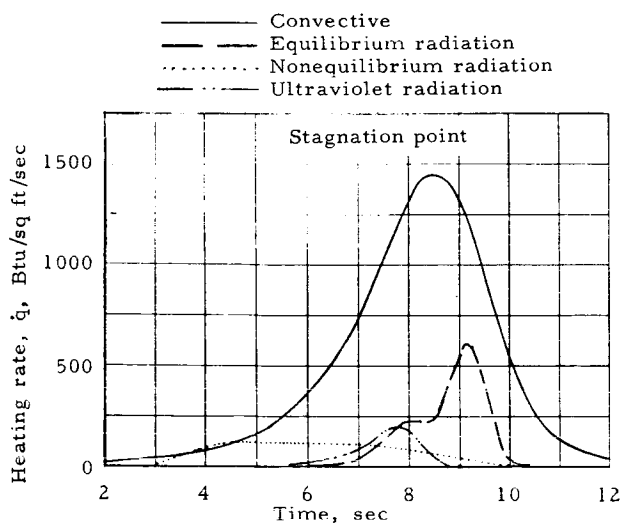
Figure 49.- Concluded.



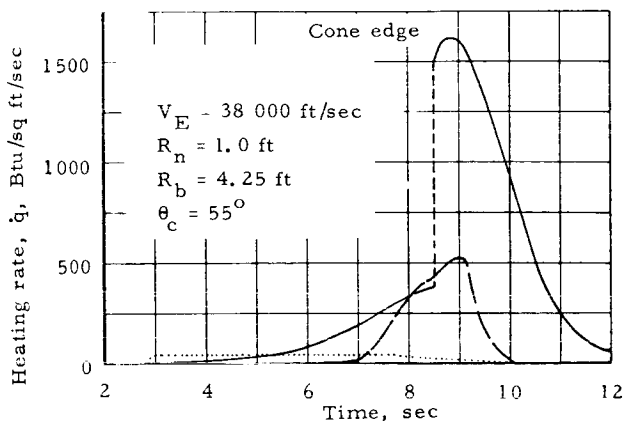
(a) Dynamic-pressure time histories.



(b) Acceleration-load time histories.



(c) Stagnation-point heating rates.



(d) Cone-edge heating rates.

Figure 50.- Typical dynamic pressure, acceleration, and heating-rate time histories for Venus entry (ref. 29).  $\frac{m}{C_D A} = 0.3$ ;  $\phi_E = 40^\circ$ .

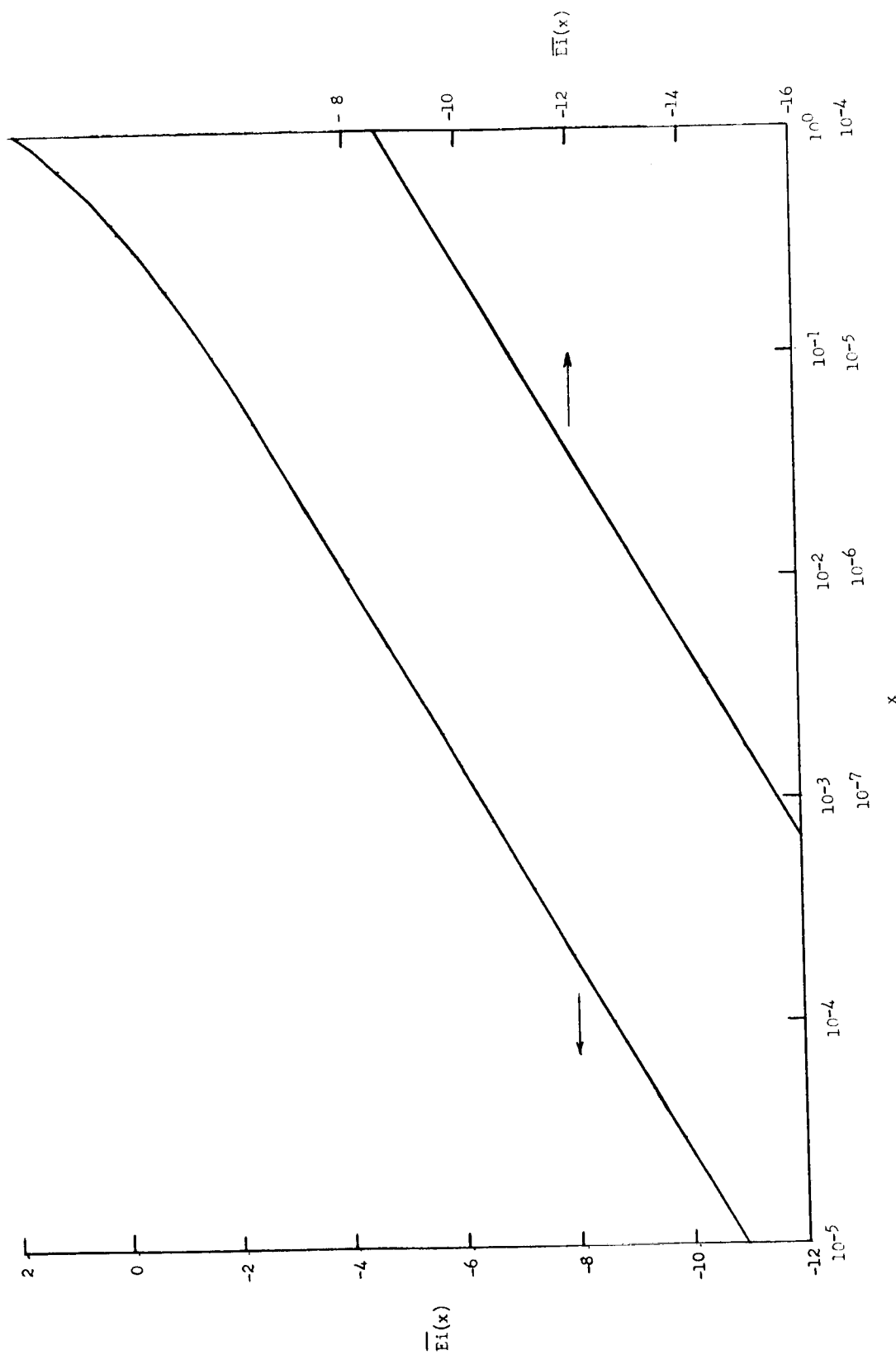


Figure 51.- Variation of function  $Ei(x)$  with  $x$ .

## 5. FLUTTER AND UNSTEADY-LIFT THEORY

By E. Carson Yates, Jr.  
Langley Research Center

### ABSTRACT

Since this is the first of several papers in aeroelasticity and unsteady-flow phenomena, a brief introduction to the aeroelastic problems of aircraft is given. Emphasis in this lecture is on the flutter of lifting surfaces, and the most commonly used technique for the theoretical determination of flutter stability boundaries is shown. Classical theoretical methods are presented for evaluating the required oscillatory aerodynamic forces in subsonic, supersonic, and hypersonic speed ranges. Some comparisons of theoretical and experimental results are included. Rigorous mathematical developments are not emphasized because the objective of this lecture is to present basic ideas, concepts, and methods and to promote an understanding and appreciation of principles and techniques.

### PREFATORY REMARKS

This paper is the first of several on topics in aeroelasticity and unsteady-flow phenomena. First this general subject is introduced, and some of the more important aeroelastic phenomena, including flutter, are defined so that the explicit subject matter on flutter and unsteady aerodynamics may be presented and viewed in proper context.

A course in aeroelasticity obviously cannot be taught in three or four lectures, nor flutter and unsteady lift theory in one. Therefore, no attempt is made to develop the material either chronologically or completely; instead, some applications of current technology are presented with emphasis on theory rather than experiment, although some comparisons between theoretical and experimental data are shown. Rigorous mathematical developments are not emphasized because the objective is to present basic ideas, concepts, and methods and to promote an understanding and appreciation of principles and techniques. An extensive bibliography is provided.

An outline of the topics presented in this paper follows:

#### INTRODUCTION TO AEROELASTICITY

Definition of Aeroelasticity

Three-Ring Diagram

Aeroelastic Problems in Relation to Flight Envelope

## FLUTTER THEORY

Two-Dimensional Theory

Three-Dimensional Theory

## THEORETICAL PREDICTION OF OSCILLATORY AERODYNAMIC LOADS

Basic Assumptions and Governing Equations

Two-Dimensional Flow

Three-Dimensional Flow

Simple strip theory

Modified strip analysis

Subsonic kernel function

Supersonic influence-coefficient method

Piston theory

## COMPARISONS OF ANALYTICAL AND EXPERIMENTAL RESULTS

## CONCLUDING REMARKS

## INTRODUCTION TO AEROELASTICITY

### Definition of Aeroelasticity

Aeroelasticity is the study of aeronautical problems which involve interactions of aerodynamics (steady or unsteady) and structures (flexibility and sometimes mass properties).

Aeroelastic problems are indicated in reference 1 to be aggravated by:

(a) Low stiffness due to:

- (1) Thin lifting surfaces
- (2) Slender fuselages
- (3) High-strength materials
- (4) Efficient structures
- (5) High temperatures

(b) A wide range of operating conditions that include:

- (1) Dynamic pressure
- (2) Mach number
- (3) Altitude
- (4) Weight
- (5) Configuration

### Three-Ring Diagram

The three-ring diagram (fig. 1) represents diagrammatically aerodynamic forces, mass forces, and elastic forces. (See also fig. 1-1 of ref. 2.) These types of forces in themselves constitute separate problem areas, for example, steady-state aerodynamics, classical mechanics, and elasticity, respectively. Other problem areas involve interactions of two or more of these types of forces: for example, dynamic stability of "rigid" aircraft involves a consideration of aerodynamic forces and mass forces. Mechanical vibrations involve inertia forces and elastic forces; whereas static aeroelastic problems such as steady-state loads on elastic aircraft, control effectiveness, and divergence involve elastic and aerodynamic forces. The center area of the three-ring diagram indicates a region in which all three types of forces are important. This region, referred to as "dynamic aeroelasticity," encompasses such problems as flutter, buffet, and dynamic response to disturbances such as atmospheric turbulence.

Implications for flutter investigation. - Because of the complex interactions of three different kinds of time-dependent forces, theoretical work may become rather involved. In addition, models for experimental work must have correct mass and stiffness distributions as well as correct shape and must be tested under conditions dynamically similar to full-scale conditions.

Static aeroelasticity (not time dependent). - Static aeroelasticity involves steady-state aerodynamics. Mass forces (for example, weight) may or may not be significant. Static aeroelasticity includes effects of structural flexibility on the following:

(1) The aerodynamic load distribution which includes:

(a) Loads imposed on structure that dictate structural design.

(b) Aerodynamic coefficients that determine:

Performance (especially at off-design conditions)

Static stability (affected by lift-curve slope, aerodynamic center, center of pressure). An example of aeroelastic influence on stability occurs when lifting air loads cause the tips of a swept wing to bend upward.

The wing surface continues to deform until the elastic restoring forces of the structure balance the external aerodynamic forces plus the internal mass forces. This deformation tends to unload the tips, reduce lift, shift the center of pressure forward and can significantly affect the aerodynamic, control, and stability characteristics.

(2) Control effectiveness and reversal

(3) Divergence - an instability (corresponding to flutter at zero frequency) involving a monotonically increasing deflection of the structure caused by aerodynamic



load building up more rapidly than the elastic restoring forces. Static aeroelasticity is covered more fully in paper no. 6 by John E. Lamar.

Dynamic aeroelasticity (time dependent). - Dynamic aeroelasticity involves unsteady aerodynamics and includes flutter, buffet, and dynamic response.

Flutter:

Flutter is a self-excited oscillation in which the motion gives rise to aerodynamic forces which sustain the oscillation - a structural instability that is frequently destructive. The motion is both cause and effect. In the motion, energy is extracted from the airstream. Flutter is the oscillatory counterpart of divergence.

Flutter may involve a single lifting surface, a single control surface, or the entire aircraft.

Types of flutter include:

- (1) Bending-torsion flutter of beam-like lifting surfaces
- (2) Flutter of plate-like lifting surfaces
- (3) Control-surface flutter
  - (a) Single degree of freedom (control rotation only)
  - (b) Coupled with parent-surface motion
- (4) Panel flutter (may cause sudden destruction of panel or eventual fatigue failure)
- (5) Propeller-whirl flutter
- (6) Stall flutter

This lecture is concerned only with flutter types (1) and (2).

Flutter investigation either of components or of a complete aircraft involves theoretical and/or experimental determination of:

- (1) The neutral stability boundary (flight conditions for incipient flutter)
- (2) The flutter mode and frequency
- (3) The subcritical (below-flutter-speed) response to:
  - (a) Oscillatory or impulsive excitation
  - (b) Random excitation

Flutter alleviation must be considered if flutter margins (separation between flutter boundary and operating envelope) are inadequate. The following are some of the methods that may be employed to increase margins, but each involves a potential penalty on the overall efficiency of the aircraft:

Method	Penalty
Increase structural stiffness by:	
Beefing up structure . . . . .	Increased weight
Increasing airfoil thickness . . . . .	Increased wave drag
Increasing box-beam size . . . . .	More local stiffening required, less room for high-lift devices
Reduce flight dynamic pressure . . . . .	Reduced mission economy
Change shape, e.g., plan form . . . . .	Reduced performance
Change mass distribution . . . . .	Loss of structural efficiency, aggravated balance problems

#### Buffet:

Buffet is response (in terms of pressure fluctuations, accelerations, stresses, etc.) to the fluctuating (periodic or random) aerodynamic forces caused by separation of flow from the aircraft surface. Structural flexibility may or may not be significant. Buffet may be caused by:

- (a) Flow separation due to adverse pressure gradients
- (b) Wake from a more forward portion of the vehicle
- (c) Shock-boundary-layer interaction

Buffet is most likely to occur at high angles of attack, for example, at high altitude or high load factor. Buffet may be alleviated by minimizing regions of flow separation (a requirement for drag reduction anyway). Buffet is not readily amenable to analytical study.

#### Dynamic response:

Included in dynamic responses are responses to both random and transient excitations.

In aircraft response to gusts and turbulence, structural flexibility may or may not be significant. Response affects structural loads, ride qualities. Distinction is made between gust response (caused by disturbances in the atmosphere), buffet (caused by disturbances generated by the aircraft itself), and flutter (an aeroelastic instability). Moreover, flutter instabilities must be well removed from the flight envelope, and buffet may be minimized by cleaning up flow separation, but the aircraft must be designed to withstand gust loads.

Two types of gust loads are studied:

- (1) Discrete gusts for which transient responses are examined by a time-history method and maximum-response conditions are identified.

(2) Continuous turbulence is considered as a random process and is treated by statistical methods. Determine the root-mean-square response and the number of loading cycles. These procedures require knowledge of the statistical properties of the atmospheric turbulence, for example, gust intensity as a function of gust wave length or frequency, as well as the frequency-response characteristics (transfer function) of the aircraft, for example, variation with gust frequency of the response to a sinusoidal input gust. Gust loads are covered more fully in paper no. 7 by Kermit G. Pratt.

Other types of dynamic response not explicitly treated in this lecture include:

- (1) Control deflection – transient response
- (2) Engine failure or inlet unstart – transient response
- (3) Forces transmitted to the airframe through the landing gear. Such forces include those caused by landing impact (transient) and runway or taxiway roughness (random). (Aerodynamic forces may be significant.)

Effects of flexibility on dynamic stability:

Structural flexibility can affect frequency and damping characteristics (lateral, longitudinal). Aerodynamics may usually be treated as steady or quasi-steady.

#### Aeroelastic Problems in Relation to Flight Envelope

A few of the more important aeroelastic problem areas are illustrated in figure 2. (See also ref. 1.) The curve, which is a function of altitude and Mach number, illustrates the design dive flight condition for a high-performance airplane such as a supersonic transport. The flight region is above this dive boundary. Flutter of lifting surfaces (and divergence for surfaces with low sweep angle), panel flutter, gust response, and buffet are most likely to be critical near transonic speeds. Aeroelastic effects on stability and control may be greatest at the high supersonic Mach numbers or wherever dynamic pressure is greatest, although problems may also be encountered elsewhere. For a satisfactory aircraft design, these instabilities, excessive loads, and other undesirable conditions must fall a sufficient distance below or above the flight region. The area of ground loads is shown at the low end of the Mach number scale.

Importance of aeroelastic problems: Aeroelastic phenomena frequently produce critical design loads for high performance aircraft.

Typical flutter boundaries are shown in more detail in figure 3. Increasing the leading-edge sweep  $\Lambda_{LE}$  of the wing is shown to improve the flutter margin, that is, to move the flutter boundary away from the flight envelope. Figure 3 shows that flutter may also be a problem in the higher supersonic range where the flutter boundary may again approach the flight envelope.

In review, several types of aeroelastic problems, both static and dynamic, have been enumerated, and comments have been made upon the interactions of aerodynamic, inertia, and elastic forces that are involved in these phenomena. Several types of flutter have been indicated, and attention is now directed to the flutter of lifting surfaces, for which the equations of motion are developed in the next section.

## FLUTTER THEORY

In flutter theory, attention is directed toward establishing the neutral stability boundary between converging and diverging oscillations, that is, conditions are sought under which oscillation of the lifting surface continues at constant amplitude (harmonic motion). Note that the counterpart in static aeroelasticity is divergence (flutter at zero frequency).

### Two-Dimensional Theory

Equations of motion. - Consider a two-dimensional wing (fig. 4) to be supported at a point called the elastic axis (e.a.) by a translation spring with spring constant  $k_h$  (deflected by displacement  $h$ ) and by a torsion spring with the constant  $k_\alpha$  (deflected by displacement  $\alpha$ ). The origin of the streamwise coordinate  $x$  is at the midchord point 0, and the airfoil center of gravity (c.g.) is a distance  $x_{\alpha b}$  behind the elastic axis which in turn is the distance  $ab$  behind the midchord. Positive directions are indicated in the figure. A complete list of letter symbols used in this lecture is given as appendix A.

Summing forces in the  $h$ -direction leads to

$$m\ddot{h} + S_\alpha \ddot{\alpha} + g_h k_h \frac{\dot{h}}{|\dot{h}|} h + k_h h = -L(\dot{h}, \ddot{h}, \alpha, \dot{\alpha}, \ddot{\alpha}) \quad (1)$$

Summing moments in the  $\alpha$ -direction leads to

$$I_\alpha \ddot{\alpha} + S_\alpha \ddot{h} + g_\alpha k_\alpha \frac{\dot{\alpha}}{|\dot{\alpha}|} \alpha + k_\alpha \alpha = M_\alpha(\dot{h}, \ddot{h}, \alpha, \dot{\alpha}, \ddot{\alpha}) \quad (2)$$

where

- $h$  translational displacement of wing at elastic axis (positive downward)
- $m$  mass of wing per unit span
- $S_\alpha$  static unbalance of wing, first moment of wing section mass about the neutral or elastic axis (positive for center of gravity aft of elastic axis),  $mbx_\alpha$

$\alpha$	torsional displacement of wing about elastic axis (positive leading edge up)
$a$	nondimensional distance from midcord to elastic axis (positive rearward), fraction of semichord $b$
$g_h$	structural damping coefficient for plunging motion
$k_h$	spring constant for plunging motion, $m\omega_h^2$
$I_\alpha$	mass moment of inertia of unit span of wing about elastic axis, $mb^2r_\alpha^2$
$g_\alpha$	structural damping coefficient for pitching motion
$k_\alpha$	spring constant for pitching motion, $I_\alpha\omega_\alpha^2$
$L$	oscillatory lift per unit span (positive upward)
$M_\alpha$	oscillatory moment per unit span about elastic axis (positive leading edge up)
$b$	wing semichord
$x_\alpha$	nondimensional distance from elastic axis to section center of gravity (positive rearward), fraction of semichord $b$
$r_\alpha$	nondimensional radius of gyration of wing section about elastic axis
$\omega_h$	circular natural frequency of wing in plunging motion (uncoupled)
$\omega_\alpha$	circular natural frequency of wing in pitching motion (uncoupled)

A dot over a symbol indicates differentiation with respect to time.

The terms  $g_h k_h \frac{\dot{h}}{|\dot{h}|} h$  and  $g_\alpha k_\alpha \frac{\dot{\alpha}}{|\dot{\alpha}|} \alpha$  in equations (1) and (2), respectively, represent structural damping forces which are proportional to displacement but in phase with velocity. This type of relationship is a more representative (though empirical) description of energy dissipation in solid structure than is the more familiar viscous damping (forces proportional to velocity). If viscous damping forces are present, however, they may be represented by adding the terms  $C_h \dot{h}$  and  $C_\alpha \dot{\alpha}$  to the left sides of equations (1) and (2), respectively, where

$C_h$  viscous damping coefficient for plunging motion

$C_\alpha$  viscous damping coefficient for pitching motion

The following assumptions are made:

(1) Perturbations from free-stream conditions are small. This assumption implies thin airfoil and small camber and angle of attack.

(2) No camber deformation occurs.

(3) Motion is harmonic and of small amplitude.

Thus, both structure and flow may be represented by linearized theory.

For harmonic motion

$$\left. \begin{aligned} h &= h_0 e^{i\omega t} \\ \alpha &= \alpha_0 e^{i\omega t} \end{aligned} \right\} \quad (3)$$

where

$h_0, \alpha_0$  complex amplitudes

$\omega$  circular frequency of oscillation

$t$  time

Also,

$$\dot{h} = i\omega h \quad (4)$$

$$\ddot{h} = -\omega^2 h \quad (5)$$

$$\dot{\alpha} = i\omega \alpha \quad (6)$$

$$\ddot{\alpha} = -\omega^2 \alpha \quad (7)$$

Then the lift force  $L$  and the pitching moment  $M_\alpha$  for harmonic (constant-amplitude) oscillation may be expressed in the forms

$$\begin{aligned} L &= L(h, \alpha) \\ &= \pi \rho b^3 \omega^2 \left\{ l_h \frac{h}{b} + \left[ l_\alpha - \left( \frac{1}{2} + a \right) l_h \right] \alpha \right\} \end{aligned} \quad (8)$$

and

$$M_{\alpha} = M_{\alpha}(h, \alpha) \\ = \pi \rho b^4 \omega^2 \left\{ \left[ m_h - \left( \frac{1}{2} + a \right) l_h \right] \frac{h}{b} + \left[ m_{\alpha} - \left( \frac{1}{2} + a \right) (l_{\alpha} + m_h) + \left( \frac{1}{2} + a \right)^2 l_h \right] \alpha \right\} \quad (9)$$

where

$\rho$	fluid density
$l_h$	lift factor associated with plunging motion
$l_{\alpha}$	lift factor associated with pitching about quarter chord ( $a = -1/2$ )
$m_h$	pitching-moment factor (about quarter chord) associated with plunging motion
$m_{\alpha}$	pitching-moment factor (about quarter chord) associated with pitching about quarter chord

The derivation of equations (8) and (9) is given in the appendix of reference 3. Explicit expressions for  $L$  and  $M_{\alpha}$  are subsequently presented herein (section entitled "Theoretical Prediction of Oscillatory Aerodynamic Loads").

Equations (8) and (9) may also be written

$$L = 2\pi q k^2 b \left( l_h' \frac{h}{b} + l_{\alpha}' \alpha \right) \quad (10)$$

$$M_{\alpha} = 2\pi q k^2 b^2 \left( m_h' \frac{h}{b} + l_{\alpha}' \alpha \right) \quad (11)$$

where flow may be subsonic or supersonic, and

$q$	dynamic pressure, $\frac{\rho}{2} V^2$
$V$	speed
$k$	reduced frequency, $\frac{b\omega}{V}$
$l_h' \equiv l_h$	lift factor associated with plunging motion
$l_{\alpha}'$	lift factor associated with pitching about elastic axis

$m_h'$  pitching-moment factor (about elastic axis) associated with plunging motion

$m_{\alpha}'$  pitching-moment factor (about elastic axis) associated with pitching about elastic axis

Note that  $l_h, l_{\alpha}, m_h, m_{\alpha}$  are complex quantities which are functions of reduced frequency  $k$  and Mach number  $M$ . Substituting equations (10) and (11) into equations (1) and (2) leads to

$$\left\{ \mu \left[ 1 - \frac{\omega_h^2}{\omega_{\alpha}^2} \frac{\omega_{\alpha}^2}{\omega^2} (1 + ig_h) \right] - l_h' \right\} \frac{h}{b} + (\mu x_{\alpha} - l_{\alpha}') \alpha = 0 \quad (12)$$

and

$$(\mu x_{\alpha} + m_h') \frac{h}{b} + \left\{ \mu r_{\alpha}^2 \left[ 1 - \frac{\omega_{\alpha}^2}{\omega^2} (1 + ig_{\alpha}) \right] + m_{\alpha}' \right\} \alpha = 0 \quad (13)$$

where  $\mu$  is mass-density ratio,  $\frac{m}{\pi \rho b^2}$ .

Flutter determinant.— Nontrivial solution of equations (12) and (13) exists if and only if the determinant of coefficients vanishes. Thus, the flutter determinant is

$$\begin{vmatrix} \mu \left[ 1 - \frac{\omega_h^2}{\omega_{\alpha}^2} \frac{\omega_{\alpha}^2}{\omega^2} (1 + ig_h) \right] - l_h' & \mu x_{\alpha} - l_{\alpha}' \\ \mu x_{\alpha} + m_h' & \mu r_{\alpha}^2 \left[ 1 - \frac{\omega_{\alpha}^2}{\omega^2} (1 + ig_{\alpha}) \right] + m_{\alpha}' \end{vmatrix} = 0 \quad (14)$$

In the solution of equation (14) for the neutral-stability (incipient-flutter) condition, Mach number  $M$  is usually held constant, and reduced frequency  $k = \frac{b\omega}{V}$  is treated as an input parameter (independent variable) because the aerodynamic parameters  $l_h', l_{\alpha}', m_h', m_{\alpha}'$  are usually rather involved functions of  $k$  and  $M$ . Since the flutter determinant contains complex quantities, direct solution of equation (14) will in general yield complex values of  $\omega$ . This complication is avoided by introducing the variable

$$\Omega = X + iY = \frac{\omega_{\alpha}^2}{\omega^2} (1 + ig)$$



as the dependent variable (eigenvalue) in place of  $\omega_\alpha^2/\omega^2$  so that  $\omega$  can be treated as real and  $g$  represents additional (fictitious) structural damping required to produce constant-amplitude oscillation. Then, the equation

$$\begin{vmatrix} \mu \left[ 1 - \frac{\omega_h^2}{\omega_\alpha^2} (1 + i g_h) \right] \Omega - l_h' & \mu x_\alpha - l_\alpha' \\ \mu x_\alpha + m_h' & \mu r_\alpha^2 \left[ 1 - (1 + i g_\alpha) \Omega \right] + m_\alpha' \end{vmatrix} = 0 \quad (14a)$$

can be solved for  $\Omega$  and hence

$$\left. \begin{aligned} \frac{V}{b\omega_\alpha} &= \frac{1}{k\sqrt{X}} \\ \frac{\omega}{\omega_\alpha} &= \frac{1}{\sqrt{X}} \\ g &= \frac{Y}{X} \end{aligned} \right\} \quad (15)$$

and the neutral stability point corresponds to  $g = 0$ .

Solution procedure.- The procedure for solution is as follows:

- (1) Find the quantities in equation (15) by solving equation (14a) for several values of  $k$ .
- (2) Plot  $g$  as a function of  $V/b\omega_\alpha$  and  $g$  as a function of  $\omega/\omega_\alpha$  (fig. 5).
- (3) Read flutter conditions at  $g = 0$ .

### Three-Dimensional Theory

Formulation of flutter equations.- The flutter equations for three-dimensional lifting surfaces are conveniently obtained from Lagrange's equations of motion. Lagrange's equations may be written in the form

$$\frac{d}{dt} \left( \frac{\partial T}{\partial \dot{q}_i} \right) - \frac{\partial T}{\partial q_i} + \frac{\partial U}{\partial q_i} + \frac{\partial D}{\partial \dot{q}_i} = Q_i \quad (i = 1(1)n) \quad (16)$$

where

$T$             kinetic energy

$U$             potential energy (strain energy of the elastic system)

D	dissipation function (damping)
$Q_i$	generalized force for ith degree of freedom (aerodynamic)
$q_i$	ith generalized coordinate
n	number of modes

Assume that the oscillatory (small) deflection  $Z(x,y,t)$  of the wing (with coordinate system as shown in fig. 6) can be represented by a linear combination of  $n$  chosen mode shapes  $Z_i(x,y)$ . Thus,

$$Z(x,y,t) = \sum_{i=1}^n Z_i(x,y) Z_{0,i} e^{i\omega t} = \sum_{i=1}^n Z_i(x,y) q_i(t) \quad (17)$$

where

x	streamwise coordinate	} undeflected wing lies in x,y plane
y	spanwise coordinate	

$Z(x,y,t)$  deflection shape of oscillating wing (displacement normal to x,y plane)

$Z_i(x,y)$  normalized deflection shape of ith mode (may be coupled or uncoupled vibration mode)

$Z_{0,i}$  complex amplitude for ith mode

The normalization of the mode shapes  $Z_i(x,y)$  is accomplished by dividing the modal deflection at each point  $(x,y)$  by the deflection at some reference point on the wing.

The kinetic energy of the vibrating wing may be written

$$T = \frac{1}{2} \iint_S m(x,y) [\dot{Z}(x,y,t)]^2 dx dy \quad (18)$$

or, with equation (17),

$$T = \frac{1}{2} \sum_{i=1}^n \sum_{j=1}^n \dot{q}_i \dot{q}_j \iint_S m Z_i Z_j dx dy \quad (19)$$

where  $m(x,y)$  is mass of wing per unit area. The integration indicated in equations (18) and (19) extends over the entire lifting surface  $S$ . If the  $Z_i$  are taken to be the normal modes of vibration of the wing in a vacuum, the modes are orthogonal and so

$$\iint_S m Z_i Z_j \, dx \, dy = M_i \delta_{ij} \quad (20)$$

where

$M_i$  generalized mass for  $i$ th mode

$\delta_{ij}$  Kronecker delta

and

$$T = \frac{1}{2} \sum_{i=1}^n M_i \dot{q}_i^2 \quad (21)$$

If convergence of the series representation in equation (17) is to be assured, the modal functions  $Z_i(x,y)$  should be elements of a complete set. The normal modes constitute such a set.

Potential energy  $U$  can be found from  $T$  by considering the undamped free oscillation of the wing in a vacuum. For this type of motion equation (16) reduces to

$$\frac{d}{dt} \left( \frac{\partial T}{\partial \dot{q}_i} \right) + \frac{\partial U}{\partial q_i} = 0 \quad (i = 1(1)n) \quad (22)$$

and, with equation (21),

$$\frac{\partial U}{\partial q_i} = -M_i \ddot{q}_i = \omega_i^2 M_i q_i \quad (23)$$

where  $\omega_i$  is the frequency of  $i$ th normal mode. Then,

$$U = \frac{1}{2} \sum_{i=1}^n \omega_i^2 M_i q_i^2 \quad (24)$$

is a manifestation of Rayleigh substitution (frequency squared times generalized mass equals generalized stiffness). (See, for example, equation (7.29) of reference 3.) Alternatively, the potential energy (strain energy) can be formulated directly in terms of stiffness as is illustrated in appendix B.

The dissipation function for structural damping is

$$D = \frac{1}{2} \sum_{i=1}^n M_i g_i \frac{\omega_i^2}{\omega} \dot{q}_i^2 \quad (25)$$

where  $g_i$  is the structural damping coefficient for the  $i$ th mode.

Substituting equations (21), (24), and (25) into equation (16) and assuming harmonic motion leads to

$$\left[ \frac{\omega_i^2}{\omega^2} (1 + i g_i) - 1 \right] \omega^2 M_i q_i = Q_i \quad (i = 1(1)n) \quad (26)$$

Generalized forces  $Q_i$  are obtained from the expression for virtual work  $\delta W$ :

$$\delta W(t) = \iint_S \delta Z(x, y, t) \Delta p(x, y, t) dx dy = \sum_{i=1}^n Q_i(t) \delta q_i \quad (27)$$

where  $\Delta p(x, y, t)$  is the lifting pressure at point  $x, y$  on the lifting surface  $S$  at time  $t$ .

The integration again extends over the entire lifting surface  $S$ . Now from equation (17),

$$\delta Z(x, y, t) = \sum_{i=1}^n Z_i(x, y) \delta q_i(t) \quad (28)$$

Substitute equation (28) into equation (27) and note that the  $q_i$  are independent variables. Then,

$$Q_i(t) = \iint_S \Delta p(x, y, t) Z_i(x, y) dx dy \quad (29)$$

Assuming motion of very small amplitude permits  $\Delta p$  to be expressed as the sum of the contributions from each mode:

$$\Delta p = \sum_{j=1}^n \Delta p_j(x, y, \omega, M) \frac{q_j}{b_0} \quad (30)$$

where  $\Delta p_j(x, y, \omega, M)$  is the lifting pressure at point  $(x, y)$  on the wing caused by motion of the wing in the  $j$ th mode, and  $b_0$  is the nondimensionalizing reference length introduced so that  $\Delta p_j$  will have same units as  $\Delta p$ . The reference length  $b_0$  is often taken to be wing-root semichord, or sometimes the semispan. Then,

$$Q_i = \sum_{j=1}^n \frac{q_j}{b_0} \iint_S \Delta p_j Z_i \, dx \, dy \quad (31)$$

Nondimensionalize by letting

$$\left. \begin{aligned} x &= b_0 x_1 \\ y &= l y_1 \end{aligned} \right\} \quad (32)$$

where  $l$  is the semispan. Then,

$$Q_i = \frac{\rho V^2}{2} \sum_{j=1}^n A_{ij} q_j \quad (33)$$

where

$$A_{ij} = \iint_S \frac{\Delta p_j}{q} Z_i \, dx_1 \, dy_1 = A_{ij}(k, M) \quad \begin{pmatrix} i = 1(1)n \\ j = 1(1)n \end{pmatrix} \quad (34)$$

The generalized aerodynamic force  $A_{ij}$  is a function of wing plan-form shape, mode shapes, frequency, and Mach number. The dynamic pressure  $q$  is  $\frac{\rho V^2}{2}$ .

Then, the equations of motion (26) can be written

$$\sum_{j=1}^n \left\{ A_{ij} + \left[ 1 - \frac{\omega_j^2}{\omega_r^2} (1 + i g_j) \right] \Omega_r \frac{k_0^2 M_j}{\frac{\rho l b_0^2}{2}} \delta_{ij} \right\} q_j = 0 \quad (i = 1(1)n) \quad (35)$$

where

$\omega_r$  reference frequency (arbitrary constant)

$k_0$  reduced frequency (input parameter),  $\frac{b_0 \omega}{V}$

$\Omega_r$  dependent variable (eigenvalue),  $\frac{\omega_r^2}{\omega^2} (1 + i g) = X + i Y$

As in equation (14a), the fictitious factor  $(1 + i g)$  is again introduced in order to avoid the complication of dealing with complex frequencies; and again the neutral-stability (flutter) condition is associated with  $g = 0$ . Also

$$\left. \begin{aligned} \frac{V}{b_0 \omega_r} &= \frac{1}{k_0 \sqrt{X}} \\ \frac{\omega}{\omega_r} &= \frac{1}{\sqrt{X}} \\ g &= \frac{Y}{X} \end{aligned} \right\} \quad (36)$$

Compare with equations (15).

Solution of the flutter equations.— Equations (35) are homogeneous in the  $n$  generalized coordinates, so that these equations have a nontrivial solution if and only if the determinant of coefficients vanishes. Thus,

$$\left| A_{ij} + \left[ 1 - \frac{\omega_j^2}{\omega_r^2} (1 + ig_j) \Omega_r \right] \frac{k_0^2 M_j}{\frac{\rho l b_0^2}{2}} \delta_{ij} \right| = 0 \quad (i, j = 1(1)n) \quad (37)$$

This equation is the flutter determinant for three-dimensional lifting surfaces corresponding to equation (14a) for two-dimensional wings.

Note that equation (14a) contains off-diagonal mass terms  $\mu x_{\alpha}$  which represent the static unbalance of the two-dimensional wing about the elastic axis. Equation (37) would contain corresponding terms only if the vibration modes chosen to describe the motion of the three-dimensional wing (eq. (17)) were nonorthogonal. (See eq. (20).)

Also note that in comparison with equation (14a), equation (37) has been multiplied through by  $k_0^2$  so that the generalized aerodynamic forces  $A_{ij}$  will remain finite at low  $k_0$ .

Note finally that aerodynamics enters into the flutter equations (35) and the flutter determinant (37) only through the generalized aerodynamic forces  $A_{ij}$  is given in equation (34) and appears in the form of lifting-pressure distributions  $\frac{\Delta p_j(x_1, y_1, k_0, M)}{q}$ .

For a particular wing, set of mode shapes, and Mach number, solution of equation (37) is similar to that described for equation (14), except that figure 5 will now contain  $n$  curves instead of 2, and these  $n$  curves may indicate more than one flutter point.

If desired, the mode of motion at flutter may be found by substituting the values of  $k_0$  and  $\Omega_r$  (at flutter) back into equation (35) to obtain the  $q_j$  (complex eigenvector) and finally by using equation (17) to find  $Z(x, y, t)$  (also complex).

In summary the equations of flutter motion have been formulated for both two-dimensional and three-dimensional wings, the latter on the basis of energy considerations employing Lagrange's equations. A procedure for solving these equations to find the flutter-stability boundary has been described. As yet, no method has been given for evaluating the aerodynamic forces involved in the flutter motion. Several theoretical methods for doing so are now presented.

## THEORETICAL PREDICTION OF OSCILLATORY AERODYNAMIC LOADS

Aerodynamic loads associated with a harmonic (constant-amplitude) oscillation are required in analyses of flutter and of subcritical frequency-response characteristics as used in gust studies. Oscillatory aerodynamic theories apply equally to both types of problems since the two problems differ aerodynamically only with regard to the prescribed downwash distribution over the wing. For flutter, the free stream is considered steady, and the downwash at any point on the wing is only that associated with the harmonic motion of the wing itself at that point. For gust studies, the wing may also be allowed to deflect harmonically, but an additional oscillatory downwash must be included to represent waves (sinusoidal gusts) in the free stream.

### Basic Assumptions and Governing Equations

Assumptions. - The usual assumptions made in the development of aerodynamic loads and the results of making them are:

- (1) Conservation laws lead to the equations of motion.
- (2) Inviscid, irrotational fluid flow leads to concepts of potential flow:
  - a. Velocity potential
  - b. Acceleration or pressure potential
- (3) Small perturbations permit linearization of the flow equations and use of superposition procedures.
- (4) Boundary conditions specify no flow through the wing surface and no flow separation. If the trailing edge is subsonic, these boundary conditions lead to the Kutta condition.

Governing equations. - These assumptions lead to the linearized wave equation

$$c^2 \nabla^2 \phi = \frac{\partial^2 \phi}{\partial t^2} \quad (38)$$

governing propagation of small disturbances from a disturbance source at the origin of coordinates  $x, y, z$  through a fluid initially at rest. In equation (38),  $c$  is the speed of sound in the undisturbed fluid and  $\phi$  is the potential function.

More detailed derivation of equation (38) and discussion of the application of the wave equation to lifting surface theories are given in appendix C. To apply (38) to a disturbance source moving in the  $-x$  direction with speed  $V$ , transform to moving coordinates. Let

$$\left. \begin{aligned} x' &= x + Vt \\ y' &= y \\ z' &= z \\ t' &= t \end{aligned} \right\} \quad (39)$$

Then equation (38) becomes

$$\frac{\partial^2 \phi}{\partial x'^2} + \frac{\partial^2 \phi}{\partial y'^2} + \frac{\partial^2 \phi}{\partial z'^2} = \frac{1}{c^2} \left( \frac{\partial}{\partial t} + V \frac{\partial}{\partial x'} \right)^2 \phi \quad (40)$$

where  $\phi$  may be the velocity potential so that the velocity vector  $\vec{u} = \nabla \phi$ . Equation (40) also governs acceleration potential  $\psi$  which is related to  $\phi$  by

$$\psi = \frac{D\phi}{Dt} = \frac{\partial \phi}{\partial t} + V \frac{\partial \phi}{\partial x} = -\frac{p}{\rho} = \frac{\Delta p}{2\rho} \quad (41)$$

(See appendix A of ref. 4.) Equation (40) applies to subsonic or supersonic speeds.

Boundary conditions are:

- (1) No flow-through wing surface, no flow separation.
- (2) Perturbations vanish at infinity.

(See also Assumptions preceding equation (38).)

#### Two-Dimensional Flow

Assumptions include those preceding equations (3) and (38) and following equation (41). Assume also incompressible flow as in reference 5 and in the appendix of reference 3. (See ref. 6 for subsonic compressible flow and ref. 7 for supersonic flow.)

Equation (40) then reduces to Laplace's equation

$$\frac{\partial^2 \phi}{\partial x^2} + \frac{\partial^2 \phi}{\partial z^2} = 0 \quad (42)$$



Solve by superposition of elementary solutions, for example, source of strength  $\Delta H$  for which the velocity potential is

$$\phi_s = \frac{\Delta H}{2\pi} \log_e \sqrt{x^2 + z^2} = \frac{\Delta H}{4\pi} \log_e (x^2 + z^2) \quad (43)$$

and vortex of strength  $\Delta \Gamma$  for which the velocity potential is

$$\phi_v = \frac{\Delta \Gamma}{2\pi} \tan^{-1} \frac{z}{x} \quad (44)$$

Noncirculatory loading terms.- Even in the absence of a free-stream velocity, an oscillating wing experiences aerodynamic forces associated with the up-and-down pumping action of the wing. These forces are related to the familiar virtual-mass effect experienced, for example, by an accelerating cylinder. Consider plunging motion represented by a distribution of sources to simulate the advancing side of the wing and a distribution of sinks to simulate the receding side. Seek first the velocity potential associated with single elements of each distribution as illustrated on the left side of figure 7.

The velocity potential for the single source and sink elements is conveniently obtained by mapping the airfoil into a circle by means of the Joukowski transformation.

The Joukowski transformation

$$2W = \zeta + \frac{1}{\zeta} \quad (45)$$

transforms the airfoil in the  $W$ -plane into a unit circle in the  $\zeta$ -plane (fig. 7). Flow does not penetrate the wing surface, so the wing surface in the  $W$ -plane, and hence the circle in the  $\zeta$ -plane, are streamlines of the flow. A source and a sink of equal strength located on the circle as shown preserve the circle as a streamline of the flow. Hence, transforming back to the  $W$ -plane preserves the airfoil as a streamline. Source strength is proportional to  $h$ . From equation (43), the velocity potential for a source of strength  $2\Delta H$  at  $(\xi_1, \eta_1)$  and a sink of equal strength at  $(\xi_1, -\eta_1)$  is (in  $\zeta$ -plane):

$$\phi = \frac{\Delta H}{2\pi} \log_e \frac{(\xi - \xi_1)^2 + (\eta - \eta_1)^2}{(\xi - \xi_1)^2 + (\eta + \eta_1)^2}$$

Source (and sink) strength  $2\Delta H$ , rather than just  $\Delta H$ , is used because only half of the source flow is evident outside the airfoil (or circle in  $\zeta$ -plane), the other half being "lost" inside the contour.

Transforming to the W-plane, letting  $\Delta H = \dot{h} dx$ , and integrating (summing sources) over the chord leads to

$$\phi(\dot{h}) = \dot{h} \sqrt{1 - x^2} \quad (46)$$

which is the velocity potential for the airfoil in plunging motion. Similarly for angular (pitching) motion

$$\left. \begin{aligned} \phi(\alpha) &= V \alpha \sqrt{1 - x^2} \\ \phi(\dot{\alpha}) &= \dot{\alpha} \left( \frac{x}{2} - a \right) \sqrt{1 - x^2} \end{aligned} \right\} \quad (47)$$

Note that  $\phi(\dot{h})$  and  $\phi(\dot{\alpha})$  do not depend on the existence of a free stream  $V$ . The pressures associated with equations (46) and (47) are called "noncirculatory" and are found from Bernoulli's equation:

$$\Delta p = 2\rho \left( \frac{\partial \phi}{\partial t} + V \frac{\partial \phi}{\partial x} \right) = \text{Lifting pressure} \quad (48)$$

Substituting equations (46) and (47) into equation (48) and integrating from leading edge to trailing edge gives the total noncirculatory contribution to lift:

$$L_N = \pi\rho(\ddot{h} + V\dot{\alpha} - a\ddot{\alpha}) \quad (49)$$

Circulatory loading terms.— Pressures associated with "bound" vorticity in the wing and "free" vorticity in the wake are called "circulatory." If the Kutta condition at trailing edge is to be satisfied, changes in angle of attack must be accomplished by vortices shed into the wake. Kelvin's circulation theorem requires that these vortices be accompanied by equal and opposite bound vortices "shed" inside the wing. The circle in the  $\zeta$ -plane and hence the airfoil in W-plane are preserved as streamlines if these bound vortices are located at points that are the reflections (reciprocals) of the free-vortex points (fig. 8). The velocity potential for a vortex of strength  $-\Delta\Gamma$  at  $(\xi_0, 0)$  and its image of equal and opposite strength at  $(1/\xi_0, 0)$  is (in  $\zeta$ -plane)

$$\phi = \frac{\Delta\Gamma}{2\pi} \left( \tan^{-1} \frac{\eta}{\xi - \xi_0} - \tan^{-1} \frac{\eta}{\xi - \frac{1}{\xi_0}} \right) \quad (50)$$

Now as the wing oscillates in a free stream of speed  $V$ , vorticity of harmonically varying strength continuously sheds into the wake. So transform to W-plane and let

$$\Delta\Gamma = U_0 e^{i\omega(t-t_0)} dx_0 = U_0 e^{ik\frac{V}{b}(t-t_0)} dx_0 = U_1 dx_0 \quad (51)$$

to represent vorticity of a strength that varies harmonically with time (or with distance downstream since the free vortices are assumed to move downstream with free-stream velocity). This vortex picture and the associated aerodynamic forces to be calculated for it are related to the single shed vortex and associated load build-up (Wagner function) resulting from a step change in angle of attack or from an impulsive start. The Wagner function will be discussed more explicitly in paper no. 7 by Kermit G. Pratt.

Observing that  $t \rightarrow \infty$  for steady-state oscillation, and integrating equation (50) from  $x_0 = 1$  to  $x_0 = \infty$  defines  $\phi(\Gamma)$ , the velocity potential due to vorticity. The strength  $U_0$  of the vorticity (and hence of  $\phi(\Gamma)$ ) is found from the Kutta condition which may be stated as

$$\left. \frac{\partial}{\partial x} \left[ \phi(\Gamma) + \phi(\dot{h}) + \phi(\alpha) + \phi(\dot{\alpha}) \right] \right|_{x=1} = \text{Finite value} \quad (52)$$

The Kutta condition in effect relates vortex strength (and hence lift) to the downwash at the three-quarter chord.<sup>1</sup> But it is not necessary to find  $U_0$  explicitly. Substituting equations (46), (47), (50), and (51) into equation (52) leads to

$$\frac{1}{2\pi} \int_1^\infty \sqrt{\frac{x_0+1}{x_0-1}} U_1 dx_0 = \dot{h} + V\alpha + \left(\frac{1}{2} - a\right)\dot{\alpha} = Q \quad (53)$$

which is equal to the downwash at  $x = \frac{1}{2}$  (the three-quarter chord).

---

<sup>1</sup>The relation between lift and downwash at the three-quarter chord is easily illustrated for a thin two-dimensional wing in steady incompressible flow. For such a wing, the lift  $L$  may be expressed in terms of a bound vortex of strength  $\Gamma$  located at the quarter chord. Thus,  $L = \rho V \Gamma = 2\pi\alpha\left(\frac{\rho}{2}V^2\right)(2b)$  or  $\Gamma = 2\pi\alpha bV$ . Now a vortex of strength  $\Gamma$  induces a velocity (e.g., downwash) of magnitude  $w = \frac{\Gamma}{2\pi r}$  so that

$$\Gamma = 2\pi r w = 2\pi r V \alpha$$

where  $r$  is the distance from the vortex. These two expressions for  $\Gamma$ , can be equated to determine a distance  $r$ , which is the distance from the bound vortex (quarter chord) to the point at which the vortex-induced downwash is the same as the physical downwash  $w = V\alpha$  on the wing. Thus,  $r = b$  which is a distance of one-half chord from the vortex, or the three-quarter-chord point. Conversely, then, if the downwash at three-quarter chord is known, the lift may be found from

$$L = 2\pi \frac{w_{3c/4}}{V} \left(\frac{\rho}{2}V^2\right)(2b)$$

Substituting equations (50) (transformed to W-plane) and (51) into equation (48) and integrating from  $x = -1$  (leading edge) to  $x = 1$  (trailing edge) gives the total circulatory contribution to the lift  $L_C$  and with equation (53)

$$L_C = \rho V \int_1^\infty \frac{x_0}{\sqrt{x_0^2 - 1}} U_1 dx_0 = 2\pi\rho VQ \frac{\int_1^\infty \frac{x_0}{\sqrt{x_0^2 - 1}} U_1 dx_0}{\int_1^\infty \frac{x_0 + 1}{\sqrt{x_0^2 - 1}} U_1 dx_0} = 2\pi\rho VQC \quad (54)$$

where

$$C = C(k) = F + iG = \frac{\int_1^\infty \frac{x_0}{\sqrt{x_0^2 - 1}} e^{-ikx_0} dx_0}{\int_1^\infty \frac{x_0 + 1}{\sqrt{x_0^2 - 1}} e^{-ikx_0} dx_0} \quad (55)$$

or in terms of Bessel functions,

$$C(k) = \frac{-J_1 + iY_1}{-(J_1 + Y_0) + i(Y_1 - J_0)} \quad (56)$$

(See fig. 9.) The complex factor  $C$ , called the "Theodorsen circulation function" (ref. 5), modifies both the magnitude and the phase angle of both  $L$  and  $M_\alpha$ .

**Combined loading.**— Combining equations (54) and (49) gives total lift on a harmonically oscillating two-dimensional wing in incompressible flow, and with corresponding expressions for pitching moment about the elastic axis, the following expressions are obtained (in dimensional form with chord =  $2b$ ):

$$L = \pi\rho b^2(\ddot{h} + V\dot{\alpha} - b\alpha\ddot{\alpha}) + 2\pi\rho VbC \left[ \dot{h} + V\alpha + b\left(\frac{1}{2} - a\right)\dot{\alpha} \right] \quad (57)$$

and

$$\begin{aligned} M_\alpha = & -\pi\rho b^3 \left[ -a\ddot{h} + \left(\frac{1}{2} - a\right)V\dot{\alpha} + \left(\frac{1}{8} + a^2\right)b\ddot{\alpha} \right] \\ & + 2\pi\rho Vb^2 \left(\frac{1}{2} + a\right)C \left[ \dot{h} + V\alpha + b\left(\frac{1}{2} - a\right)\dot{\alpha} \right] \end{aligned} \quad (58)$$

The original development of these expressions in reference 5 provides for the inclusion of a trailing-edge control surface also. Two-dimensional subsonic compressible flow is discussed in references 6 and 8, and supersonic flow is examined in references 7 and 8.

### Three-Dimensional Flow

Simple strip theory (subsonic or supersonic).— The strip-theory concept originated as a means of applying two-dimensional aerodynamic theory to wings of finite span. In this regard it has largely been superseded by development of the more rigorous lifting-surface theories for three-dimensional wings. Nevertheless, approximate methods such as strip theory remain useful for heuristic purposes and for practical applications where their simplicity, flexibility, and economy are advantageous.

Applications to unswept wings:

In applications to unswept wings:

(1) The motion of each strip (fig. 10) is taken to be that associated with the three-dimensional wing.

(2) Uncoupled vibration modes are frequently used (that is, bending along and torsion about an elastic axis).

(3) Camber modes may be incorporated if necessary.

(4) Natural (coupled) modes may be used if they are decomposed into bending, torsional, and possibly camber components.

Aerodynamic forces on each strip are taken to be those associated with a two-dimensional wing undergoing the same motion as the particular section of the three-dimensional wing. This approach implies that aerodynamic interactions between strips are ignored. This simplification, of course, is not a very good representation of the three-dimensional loading near the tip, but it may be acceptable if the aspect ratio is not too small.

The motion and forces for each strip are then given by equations (1), (2), (10), and (11), except that now wing properties, deflections, and loads are functions of  $y$ . For example,

$$h = h(y) = \sum_{i=1}^m h_i f_{h,i}(y) e^{i\omega t} \quad (59)$$

and

$$\alpha = \alpha(y) = \sum_{j=1}^n \alpha_j f_{\alpha,j}(y) e^{i\omega t} \quad (60)$$

where  $\underline{h}_i$  and  $\underline{\alpha}_j$  are complex amplitude functions (which define the eigenvectors in the flutter problem), and  $f_{h,i}$  and  $f_{\alpha,j}$  are uncoupled vibration mode shapes. (Compare with equation (17).)

Then for application of Lagrange's equations (16), the kinetic energy becomes

$$T = -\omega^2 e^{i\omega t} \left[ \frac{1}{2} \sum_{i=1}^m \underline{h}_i^2 \int_0^l m f_{h,i}^2 dy + \sum_{i=1}^m \sum_{j=1}^n \underline{h}_i \underline{\alpha}_j \int_0^l S_{\alpha} f_{h,i} f_{\alpha,j} dy + \frac{1}{2} \sum_{j=1}^n \underline{\alpha}_j^2 \int_0^l I_{\alpha} f_{\alpha,j}^2 dy \right] \quad (61)$$

Note that the cross-product (off-diagonal) generalized masses are not all zero. Compare with equations (18) to (21).

The potential energy is

$$U = \frac{1}{2} e^{i\omega t} \left[ \sum_{i=1}^m \omega_{h,i}^2 \underline{h}_i^2 \int_0^l m f_{h,i}^2 dy + \sum_{j=1}^n \omega_{\alpha,j}^2 \underline{\alpha}_j^2 \int_0^l I_{\alpha} f_{\alpha,j}^2 dy \right] \quad (62)$$

where

$\omega_{h,i}$  frequency of  $i$ th uncoupled bending mode

$\omega_{\alpha,j}$  frequency of  $j$ th uncoupled torsion mode

See appendix B for alternative derivation of potential energy (strain energy) directly in terms of stiffness.

Damping and aerodynamic loads (both nonconservative forces) may be incorporated into the generalized forces:

$$Q_{h,i} = \int_0^l \left( -L - i m \omega_{h,i}^2 g_{h,i} f_{h,i} \underline{h}_i \right) f_{h,i} dy \quad (63)$$

$$Q_{\alpha,j} = \int_0^l \left( M_{\alpha} - i I_{\alpha} \omega_{\alpha,j}^2 g_{\alpha,j} f_{\alpha,j} \underline{\alpha}_j \right) f_{\alpha,j} dy \quad (64)$$

where  $L$  and  $M_{\alpha}$  are given by equations (8) and (9) or (10) and (11) with  $h$  and  $\alpha$  represented by equations (59) and (60).

Solution for the flutter condition proceeds as before, except the flutter determinant is now of order  $m + n$ , and figure 5 contains  $m + n$  curves.

## Application to swept wings:

For swept wings strip-theory concepts may be applied to streamwise strips (identified herein as type A) or strips perpendicular to the swept elastic axis (identified as type B) as illustrated in figure 11. (See ref. 9.)

The advantage of the type A concept is that root and tip geometry are accurately represented. The disadvantage is that inclusion of camber mode is probably required.

The converse applies to the type B concept.

In applying the type B concept, the aerodynamic loads are considered to be defined by the component of free-stream velocity  $V_n$  perpendicular to the elastic axis (fig. 11). The component parallel to the elastic axis is considered to contribute only to the downwash on the strip, which for calculation purposes is evaluated at the three-quarter-chord point of the strip as indicated previously.

Modified strip analysis.— The modified strip analysis (refs. 10 to 14) is similar to the type B concept previously given with aerodynamic expressions of the type given for two-dimensional incompressible flow in equations (57) and (58), but with the following modifications:

- (1) Arbitrary section lift-curve slope  $c_{l_{\alpha,n}} = c_{l_{\alpha,n}}(y)$  used instead of  $2\pi$ .
- (2) Arbitrary section aerodynamic center  $a_{c,n} = a_{c,n}(y)$  used instead of the quarter chord.
- (3) The circulation function  $C = C(k)$  in equations (57) and (58) is modified on the basis of two-dimensional compressible-flow theory to account approximately for effects of compressibility on the magnitudes and phase angles of the section lift and moment vectors. (See refs. 10 and 13.)

The resulting expressions for section lift  $L$  and pitching moment about the elastic axis  $M_\alpha$  are (see eqs. (4) to (6) of ref. 13):

$$L = \pi \rho b^2 \left[ \ddot{h} + V_n \dot{\alpha} + V_n \dot{\sigma} \tan \Lambda_{ea} - ba(\ddot{\alpha} + V_n \dot{\tau} \tan \Lambda_{ea}) \right] + c_{l_{\alpha,n}} \rho V_n b C Q$$

$$\begin{aligned} M_\alpha = & -\pi \rho b^4 \left( \frac{1}{8} + a^2 \right) (\ddot{\alpha} + V_n \dot{\tau} \tan \Lambda_{ea}) + \pi \rho b^2 V_n (\dot{h} + V_n \dot{\sigma} \tan \Lambda_{ea}) \\ & + \pi \rho b^3 a (\ddot{h} + V_n \dot{\sigma} \tan \Lambda_{ea}) + \pi \rho b^2 V_n^2 (\alpha - ab\tau \tan \Lambda_{ea}) \\ & - 2\pi \rho V_n b^2 \left[ \frac{1}{2} - (a - a_{c,n}) \frac{c_{l_{\alpha,n}}}{2\pi} C \right] Q \end{aligned}$$

where the downwash  $Q$  is given by

$$Q = \dot{h} + V_n \alpha + V_n \sigma \tan \Lambda_{ea} + b \left( \frac{c_{l\alpha,n}}{2\pi} + a_{c,n} - a \right) (\dot{\alpha} + V_n \tau \tan \Lambda_{ea})$$

and

$V_n = V \cos \Lambda_{ea}$  component of freestream velocity normal to elastic axis

$\Lambda_{ea}$  sweepback angle of elastic axis

$\sigma$  local bending slope of elastic axis

$\tau$  local rate of change of twist along elastic axis

The spanwise distributions of the steady-flow aerodynamic parameters  $c_{l\alpha,n}(y)$  and  $a_{c,n}(y)$  to be used in these equations are those distributions that are pertinent to the particular planform and Mach number being studied. Such distributions may be obtained from any suitable steady-flow theory or from pressure-distribution measurements in flight or in a wind tunnel. Thus, the important effects of three-dimensional compressible flow are represented in the modified strip analysis even though the mathematical structure of the method stems from the theory of two-dimensional incompressible nonsteady flow as given in reference 5.

Synthesis of the modified-strip-analysis method may be illustrated in terms of the section lift force on an unswept wing:

(1) For three-dimensional, compressible, steady flow,

$$L = c_{l\alpha,n} \alpha \frac{\rho}{2} V^2 (2b) = c_{l\alpha,n} \rho V b Q$$

In steady flow the downwash  $Q$  is given by  $Q = V\alpha$ .

(2) For two-dimensional, incompressible, oscillatory flow (method of ref. 5),

$$L = 2\pi\rho V b Q C + \text{Noncirculatory terms}$$

where  $C = C(k) = F_I + iG_I$ . Subscript  $I$  indicates incompressible flow, and downwash  $Q$  is associated with the oscillatory motion. (See eq. (53).)

(3) For three-dimensional, compressible, oscillatory flow (modified strip analysis, ref. 13),

$$L = c_{l\alpha,n} \rho V b Q C + \text{Noncirculatory terms}$$



where

$$C = C(k, M) = \sqrt{\frac{F_C^2 + G_C^2}{F_I^2 + G_I^2}} (F_I + iG_I) \approx \frac{F_C}{F_I} (F_I + iG_I)$$

and subscript C indicates compressible flow.

Features of the modified strip analysis are:

(1) The method uses distributions of aerodynamic parameters from linear or non-linear theories or from measured loads for the undeformed wing in steady flow (subsonic to hypersonic).

(2) Circulation functions for two-dimensional incompressible flow are modified in magnitude only to account for compressibility.

(3) Automatic selection of reduced frequency by a computing program is practical because the computing time required for each  $k$  value is extremely small in comparison with requirements of the more elaborate aerodynamic theories.

Limitations of the modified strip analysis are:

(1) Application of this or any strip theory to wings of low aspect ratio is questionable.

(2) For compressible flow, the modified strip analysis is of questionable validity at high reduced frequencies because of feature (2).

(3) The method is not applicable when the component of free-stream Mach number normal to the leading edge is near 1.0 ("sonic leading edge").

Subsonic kernel function. - The subsonic kernel function method (refs. 4, 15 and 16, and appendix C herein) is based on the linearized potential-flow theory for lifting surfaces. (See eq. (40).) The acceleration potential (eq. (41)) is used to avoid having to extend surface integration over the wake. Acceleration-potential (or pressure) discontinuities exist only across the lifting surface, whereas velocity-potential discontinuities exist across the lifting surface and the wake vortex sheet.

Downwash-pressure integral equation and kernel function:

An elementary solution of equation (40) is

$$\psi_s = \frac{H}{4\pi R'} e^{i\omega \left[ t + \frac{M}{c\beta^2} (x - \xi) - \frac{R'}{c\beta^2} \right]} \quad (65)$$

where

$H$  source strength

c speed of sound in undisturbed flow

M Mach number of undisturbed flow

$$\beta = \sqrt{1 - M^2}$$

$$R' = \sqrt{(x - \xi)^2 + \beta^2(y - \eta)^2 + \beta^2 z^2}$$

Equation (65) represents the acceleration potential at point  $(x, y, z)$  due to a harmonically pulsating pressure source at point  $(\xi, \eta, 0)$ . (See coordinates in fig. 6.) The corresponding solution for a doublet with axis in the  $z$ -direction is

$$\psi_d = \frac{\partial}{\partial z} \psi_s \quad (66)$$

Note that these solutions are singular at the location of the source or doublet.

The distribution of (unknown) lifting pressure on a wing may be represented by a distribution of pressure (acceleration-potential) doublets over the plan form. Then, solution for the pressure (doublet-strength) distribution may be obtained by requiring that the downwash induced on the wing by the doublets be the same as that associated with the prescribed deformation or motion of the wing.

Now, the downwash on the lifting surface  $S$  (fig. 6) is

$$w(x, y, 0, t) = \left. \frac{\partial \phi}{\partial z} \right|_{z=0} = \left( \frac{\partial}{\partial t} + V \frac{\partial}{\partial x} \right) Z(x, y, t) = \left( i\omega + V \frac{\partial}{\partial x} \right) \sum_{i=1}^n Z_i(x, y) q_i(t) \quad (67)$$

from equation (17). To find  $\phi$  (and hence  $w$ ) due to the superposition of pressure doublets requires that  $\phi$  be found in terms of  $\psi$ . From equation (41),

$$V \frac{d\phi}{dx} + i\omega\phi = \psi \quad (68)$$

This first-order ordinary differential equation has the solution

$$\phi(x, y, z) = \frac{1}{V} e^{\frac{-i\omega x}{V}} \int_{-\infty}^x \psi(\lambda, y, z) e^{\frac{i\omega \lambda}{V}} d\lambda \quad (69)$$

since both  $\phi$  and  $\psi$  vanish at  $x = -\infty$ . Note that  $e^{i\omega t}$  may be removed from both sides of (68) and (69). With equations (65) to (67), equation (69) gives the downwash at

$(x, y, z)$  due to a unit-strength pressure doublet (unit  $p/\rho$ , see eq. (41)) at  $(\xi, \eta, 0)$ :

$$\frac{\partial \phi}{\partial z} = \frac{H}{4\pi V} \frac{\partial^2}{\partial z^2} e^{\frac{-i\omega(x-\xi)}{V}} \int_{-\infty}^{x-\xi} (\lambda^2 + r^2)^{-1/2} e^{\frac{i\omega}{V\beta^2}(\lambda - M\sqrt{\lambda^2 + r^2})} d\lambda \quad (70)$$

where  $r = \beta \sqrt{(y - \eta)^2 + z^2}$ .

By superposition the downwash at  $(x, y, 0)$  due to all the doublets over the plan form is, for unit amplitude of the  $i$ th vibration mode,

$$w_i(x, y, 0) = V \frac{\partial Z_i}{\partial x} + i\omega Z_i = \frac{1}{4\pi} \oint_S \frac{\Delta p_i(\xi, \eta)}{\rho V} K(x-\xi, y-\eta, k, M) d\xi d\eta \quad (71)$$

where the kernel function is

$$K = \lim_{z \rightarrow 0} \frac{\partial^2}{\partial z^2} e^{\frac{-i\omega(x-\xi)}{V}} \int_{-\infty}^{x-\xi} (\lambda^2 + r^2)^{-1/2} e^{\frac{i\omega}{V\beta^2}(\lambda - M\sqrt{\lambda^2 + r^2})} d\lambda \quad (72)$$

Compare equation (72) with equation (70). The symbol  $\Delta p_i(\xi, \eta)$  is the lifting pressure at point  $(\xi, \eta)$  on the wing due to deflection (or motion) of wing in the  $i$ th vibration mode.

Divide all lengths by the reference length  $b_0$  to nondimensionalize. Then equation (71) may be written

$$\frac{w_i}{V} = \frac{\partial Z_i}{\partial x} + ikZ_i = \frac{1}{8\pi} \oint_S \frac{\Delta p_i}{q} K d\xi d\eta \quad (73)$$

and equation (72) may be expressed as

$$K = \lim_{z \rightarrow 0} e^{-ik(x-\xi)} \frac{\partial^2}{\partial z^2} \int_{u_1}^{\infty} (1 + u^2)^{-1/2} e^{-ik_1 u} du \quad (74)$$

where

$$k_1 = k \frac{r}{\beta}$$

$$u_1 = \frac{MR' - (x - \xi)}{\beta r}$$

Equation (71) or (73) establishes the relation between downwash distribution over a wing and the pressure distribution over the wing. The integral on the right side of either equation (71) or (73) may be evaluated to determine the downwash distribution (and hence the

shape of mean camber surface) required to produce a prescribed steady or oscillatory pressure distribution, or the relation may be solved as an integral equation to determine the pressure distribution generated by a prescribed steady or oscillatory downwash distribution. The latter is the usual situation in oscillatory-flow problems such as flutter and gust response, and hence equation (71) or (73) is usually referred to as the "downwash-pressure integral equation."

Since the potential for the doublet building block is singular at the doublet location, the kernel function has singularities at  $x = \xi, y = \eta$  of the form

$$-\frac{f_1(\theta)}{\epsilon^2}; \quad \frac{ik}{\epsilon}; \quad -\frac{k^2}{2} \left[ f_2(\theta) + \log_e \epsilon \right]$$

where

$$\left. \begin{aligned} f_1(\theta) &= \frac{\beta^2}{1 - \sin \theta} \\ f_2(\theta) &= \log_e \frac{k(1 - \sin \theta)}{2(1 - M)} \end{aligned} \right\} \quad (75)$$

and

$$\left. \begin{aligned} x - \xi &= \epsilon \sin \theta \\ \beta(y - \eta) &= \epsilon \cos \theta \end{aligned} \right\} \quad (76)$$

and therefore

$$\epsilon = \sqrt{(x - \xi)^2 + \beta^2(y - \eta)^2} = R' \Big|_{z=0}$$

(Note that only the first of the three singularities listed remains in steady flow ( $k = 0$ ).) For integration over  $S$ , equation (73) is divided into parts in order to treat the singularities accurately in the integration.

Solution of downwash-pressure integral equation (73) – pressure-mode functions:

For solution of equation (73), assume that the lifting pressure at any point on the wing can be represented by a linear combination of chosen pressure modes

$$\frac{\Delta p_1(\xi, \eta)}{q} = \sum_{m=0}^M \sum_{n=0}^N a_{nm} i \sqrt{\frac{1 - \xi}{1 + \xi}} \sqrt{1 - \eta^2} f_n(\xi) g_m(\eta) \frac{b_0}{b(\eta)} \quad (77)$$

where

$b(\eta)$  local semichord at spanwise station  $\eta$

$b_0 = b(0)$  root semichord

$f_n(\xi)$  nth chordwise pressure mode

$g_m(\eta)$  mth spanwise pressure mode

Also,

$$\left. \begin{aligned} \xi &= \frac{\xi' - \xi_m'}{b(\eta)} \\ \eta &= \frac{\eta'}{l} \end{aligned} \right\} \quad (78)$$

where

$\xi_m = \xi_m(\eta)$  chordwise location of mean-chord line at spanwise station  $\eta$

$l$  semispan

$a_{nm}^i$  arbitrary constant (may be complex) coefficients to be determined by solution of equation (73).

Primes denote dimensional coordinates.

The factors  $\sqrt{\frac{1-\xi}{1+\xi}}$  and  $\sqrt{1-\eta^2}$  are included to satisfy the boundary conditions on lifting pressure at leading edge ( $\xi = -1$ ), trailing edge ( $\xi = +1$ ), and tips ( $\eta = \pm 1$ ), regardless of the values of the  $a_{nm}^i$ . Thus, solving equation (73) for an unknown pressure distribution means solving for the values (complex for  $k > 0$ ) of the associated  $a_{nm}^i$  coefficients. (See eq. (77).)

Equations (78) map the plan form into a square ( $-1 \leq \xi \leq 1$ ,  $-1 \leq \eta \leq 1$ ).

For convergence of the series representation in equation (77), both  $f_n(\xi)$  and  $g_m(\eta)$  must be elements of a complete set of functions.

The  $f_n(\xi)$  are preferably polynomials orthogonal with respect to  $\sqrt{\frac{1-\xi}{1+\xi}}$  over the chord. Thus,

$$f_n(\xi) = \frac{\sin \left[ \left( n + \frac{1}{2} \right) \cos^{-1} \xi \right]}{\sin \left( \frac{1}{2} \cos^{-1} \xi \right)} \quad (79)$$

Old method (for example, ref. 15):

$$\left. \begin{aligned} f_0(\xi) &= \cot \frac{\theta}{2} \\ f_n(\xi) &= \frac{4}{2^{2n}} \sin n\theta \end{aligned} \right\} \quad (n \geq 1) \quad (80)$$

This is Birnbaum-Glauert series.

The  $g_m(\eta)$  are preferably polynomials orthogonal with respect to  $\sqrt{1 - \eta^2}$  over the span. Thus,  $g_m(\eta) = U_m(\eta)$  are Chebyshev polynomials of the second kind.

Old method (for example, ref. 15):

$$g_m(\eta) = \eta^m \quad (81)$$

Solution of downwash-pressure integral equation (73) – collocation procedure:

With equation (77), equation (73) can be written

$$\frac{w_i(x, y)}{V} = \frac{\partial Z_i}{\partial x} + ikZ_i = \frac{1}{8\pi} \sum_{m=0}^M \sum_{n=0}^N a_{nm}^i F_{nm}^i(x, y) \quad (82)$$

where

$$F_{nm}^i(x, y) = \oint_{-1}^1 \int_{-1}^1 \sqrt{\frac{1-\xi}{1+\xi}} \sqrt{1-\eta^2} f_n(\xi) g_m(\eta) K(x-\xi, y-\eta, k, M) \frac{b(\eta)}{b_0} d\xi d\eta \quad (83)$$

In this process of going from equation (73) to equation (82), by means of the pressure approximation of equation (77), an infinite number of unknowns (that is, the lifting pressure at every point on the wing surface) has been in effect replaced by a finite number of unknowns (that is, the  $(M+1)(N+1)$  coefficients  $a_{nm}^i$ ). All quantities in equation (83) are known, so that the  $F_{nm}^i(x, y)$  may be evaluated and substituted into equation (82) which may then be inverted to find the  $a_{nm}^i$  if the downwash is specified at a number of points at least equal to the number of unknown  $a_{nm}^i$  values. This manipulation is the collocation procedure in which it is required that the downwash induced by the pressure distribution over the wing coincide with the prescribed downwash at a finite number of discrete points on the wing called "collocation points" or "control points."

Evaluation of  $F_{nm}^i(x,y)$  from equation (83) – method of integration:

For evaluation of  $F_{nm}^i(x,y)$  from equation (83), chordwise and spanwise integrations are each broken up into four parts (fig. 12) because of singularities and discontinuities in the kernel. (See also refs. 15 and 17.) Gaussian integrations are used in each region.

Elements of kernel-function analysis include:

- (1) Suitable expression for kernel function and its evaluation
- (2) Choice of pressure-mode functions
- (3) Choice of location for control points
- (4) Methods of integration
- (5) Number of pressure modes
- (6) Number of control points
- (7) Number of integration stations

} convergence

The advantages of the analysis are:

(1) The method applies to lifting surfaces of arbitrary plan form, although difficulties may be encountered if the aspect ratio is high.

(2) The method applies for arbitrary vibration modes (coupled or uncoupled) that are continuous through the first derivative. In particular, camber deformations require no special attention.

A limitation of this approach is that it does not give consistently reliable results for Mach numbers near 1.0, nor for low mass ratios (ref. 14).

Alternate method of solving the downwash-pressure integral equation:

An alternate method for solving the downwash-pressure integral equation utilizes superposition of discrete singularities rather than continuous distribution (ref. 18).

The procedure is as follows:

- (1) Divide the wing into a number of area elements or "boxes."
- (2) Consider a line of acceleration-potential doublets to be located at the quarter chord of each box.
- (3) Solve for doublet strengths (and hence pressure) by collocating downwash at the three-quarter chord of each box.

Discrete-element methods in application to steady-state aerodynamics are discussed more fully in the next paper by John E. Lamar (paper no. 6).

Supersonic influence-coefficient method. – The supersonic aerodynamic-influence-coefficient method (refs. 19 to 22) is based on linearized potential-flow theory for lifting surfaces. (See eq. (40).) Velocity potential is used rather than acceleration potential

because flow aft of trailing-edge Mach cone does not affect flow over wing, and hence integrations over the entire wake downstream to infinity need not be performed.

Equation (40) can be written in hyperbolic form for  $M > 1$ .

$$\beta^2 \phi_{XX} - \phi_{YY} - \phi_{ZZ} = \frac{-1}{c^2} (i2\omega V \phi_X - \omega^2 \phi) \quad (84)$$

where harmonic motion has been assumed, and  $\beta = \sqrt{M^2 - 1}$ .

$\phi(x, y, z, \omega, M)$  = Perturbation velocity potential

Letting

$$x = X, \quad y = \beta Y, \quad z = \beta Z, \quad t = T \quad (85)$$

transforms equation (84) to an equivalent problem at  $M = \sqrt{2}$ . Thus equation (84) becomes

$$\phi_{XX} - \phi_{YY} - \phi_{ZZ} = \frac{-1}{\beta^2 c^2} (i2\omega V \phi_X - \omega^2 \phi) \quad (86)$$

The lifting pressure from equation (41) is

$$\Delta p = \frac{1}{2} \rho V^2 \left( -\frac{2}{V} \Delta \phi_X - i \frac{2\omega}{V^2} \Delta \phi \right) \quad (87)$$

where  $\Delta \phi$  is potential difference between upper and lower wing surface. An elementary solution of equation (86) is a pulsating source at  $(\xi, \eta, \zeta)$  for which the velocity potential is

$$\phi_s(x, y, z) = -\frac{H}{\pi R} \exp \left[ \frac{-i\omega V}{\beta^2 c^2} (x - \xi) \right] \cos \frac{\omega R}{\beta^2 c} \quad (88)$$

where

$$R = \sqrt{(x - \xi)^2 + (y - \eta)^2 + (z - \zeta)^2}$$

and the source strength is  $H = H(\xi, \eta, \zeta)$

The condition of flow tangency at the wing surface requires that

$$H(\xi, \eta, 0) = w(\xi, \eta, 0) \quad (89)$$



and downwash  $w$  is prescribed. Then by superposition, the total perturbation velocity potential at a point  $(x, y)$  on the wing is

$$\phi(x, y) = \frac{-1}{\pi\beta} \iint_A H(\xi, \eta) R^{-1} \exp \left[ \frac{-i\omega M^2}{\beta^2 V} (x - \xi) \right] \cos \frac{\omega M R}{\beta^2 V} d\xi d\eta \quad (90)$$

Note that the downwash (and hence  $\phi$ ) may differ for upper and lower surfaces of wing. Thus, nonzero wing thickness may be incorporated. The area of integration  $A$  is the surface of the wing intercepted by the Mach forecone from the point  $(x, y)$ . Note that equation (90) is an integral, not an integral equation as in the subsonic kernel-function method.

The method of evaluating equation (90) is as follows:

- (1) Cover the wing with a grid of boxes, preferably rectangles with diagonals parallel to the Mach lines (called "Mach boxes"). (See fig. 13.)
- (2) Assume that the source strength over each box is constant and equal to the value at the box center. Then, for a planar wing ( $z \approx \zeta \approx 0$ ), equation (90) is replaced by

$$\phi(x_i, y_j) = \frac{b}{\beta} \sum_A H(\xi_m, \eta_n) \phi_{ijmn}(x_i - \xi_m, y_j - \eta_n, k, M) \quad (91)$$

where

$b$  streamwise length of boxes

$\phi_{ijmn}$  velocity-potential influence coefficient (VPIC) and is the potential induced at  $(x_i, y_j)$  by unit-strength source box with center  $(\xi_m, \eta_n)$

and

$$\phi_{ijmn} = \frac{-1}{\pi} \iint_{A_{mn}} R_1^{-1} \exp \left[ -i \frac{b\omega}{V} \frac{M^2}{\beta^2} (x_i - \xi_m) \right] \cos \left( \frac{b\omega}{V} \frac{M}{\beta^2} R_1 \right) d\xi d\eta \quad (92)$$

where

$$R_1 = \sqrt{(x_i - \xi_m)^2 + (y_j - \eta_n)^2}$$

and integration extends only over the box with center at  $(\xi_m, \eta_n)$ .

Problems encountered with the Mach box method are:

- (1) Convergence of solution with increasing number of boxes.
- (2) Treatment of "jagged" leading and trailing edges as represented by the Mach boxes.
- (3) Treatment of highly swept wings at low supersonic Mach numbers.

A method analogous to the Mach box method has been formulated for the transonic range (specifically  $M = 1.0$ ) (refs. 23 to 27). This method, employing square boxes, is also based on potential-flow theory which can be linearized even in the transonic range if the frequency of oscillation is high enough. (There is no counterpart in steady-flow!) It appears, however, that a less restricted approach (for example, ref. 28) must be developed before consistent accuracy can be expected in this speed range.

Piston theory.— Piston theory (refs. 29 and 30) is not a potential-flow method.

As Mach number increases toward the hypersonic range, the Mach forecone narrows, and lateral influences on the pressure at a point on the wing diminish. Further, shock waves and Mach waves approach parallel to the wing surface. Since the predominant changes through shock waves occur along a perpendicular to the wave front with little change parallel to the wave, upstream influences diminish.

Thus, pressure at a point  $(x,y)$  becomes predominantly dependant on flow conditions in the immediate vicinity of  $(x,y)$ ; that is,  $p(x,y)$  becomes approximately a point function and hence can be described by a one-dimensional theory. Thus,  $p(x,y)$  can be considered as the result of a piston moving perpendicular to the wing surface with velocity  $w(x,y,t)$ , the prescribed downwash at wing point  $(x,y)$ .

The piston (one-dimensional) equation for isentropic flow is

$$\frac{p}{p_{\infty}} = \left[ 1 + \frac{\gamma - 1}{2} \left( \frac{w}{c_{\infty}} \right)^2 \right]^{\frac{2\gamma}{\gamma - 1}} \quad (93)$$

where  $\gamma$  is the ratio of specific heats.

By binomial expansion

$$\begin{aligned} \frac{p}{p_{\infty}} &= 1 + \gamma \left( \frac{w}{c_{\infty}} \right)^2 + \frac{\gamma(\gamma + 1)}{4} \left( \frac{w}{c_{\infty}} \right)^4 + \frac{\gamma(\gamma + 1)}{12} \left( \frac{w}{c_{\infty}} \right)^6 + \dots \\ &= 1 + \gamma M^2 \left( \frac{w}{V} \right)^2 + \frac{\gamma(\gamma + 1)}{4} M^4 \left( \frac{w}{V} \right)^4 + \frac{\gamma(\gamma + 1)}{12} M^6 \left( \frac{w}{V} \right)^6 + \dots \end{aligned} \quad (94)$$

Note that upper and lower surfaces may be treated separately, so that wing thickness can be accounted for and in general must be accounted for to obtain accuracy at the higher supersonic Mach numbers.

Limitations on the applicability of piston theory are:

- (1)  $M\delta < 1.0$ , and either  $M^2 \gg 1.0$ ,  $kM^2 \gg 1.0$ , or  $k^2M^2 \gg 1.0$ , where  $\delta$  is inclination of airfoil surface relative to free-stream direction.
- (2) The theory does not account for any affect of plan form (e.g., wing tips) on the pressure distribution.

In review, the assumptions leading to the potential-flow equation and its linearization in both subsonic and supersonic flow have been stated. The equation itself, with pertinent boundary conditions has been presented, and solutions of the equation to find pressures on an oscillating wing have been indicated through a building-block approach employing elementary solutions and superposition. Expressions pertinent to two-dimensional incompressible flow, strip-theory adaptations for three-dimensional wings, and three-dimensional lifting-surface theory for subsonic and supersonic flow have been presented. In addition, a nonpotential-flow method based on piston-pressure concepts has been given for the higher supersonic range. The next section shows applications of these theories to some flutter problems, including comparisons with experimental data, and illustrates some of the features of wing flutter boundaries.

## COMPARISONS OF ANALYTICAL AND EXPERIMENTAL RESULTS

Some comparisons of theoretical and experimental flutter data are presented in figures 14 to 24. Figure 14 includes also an indication of the range of applicability of the theoretical methods previously discussed for a typical swept wing.

Figure 15 shows calculated spanwise distributions of steady-flow section lift-curve slope and section aerodynamic center for four rectangular wings as required for use in the modified strip analysis. (See ref. 14.) Figure 16 shows the flutter-speed index  $\frac{V}{b\omega_\alpha\sqrt{\mu}}$  for one of these wings over a wide range of mass ratio, extending from the aircraft range down almost to the range pertinent to hydrofoils. The variation with mass ratio shown is typical for most wings. Figure 17 shows the corresponding flutter frequencies.

Figures 18 (from ref. 13) and 19 (from ref. 11) illustrate the effect of Mach number on the flutter speed of a swept wing of aspect ratio  $A = 4.0$ , taper ratio  $\lambda = 0.6$ , and quarter-chord sweep angle  $\Lambda_{c/4} = 45^\circ$ . The variations with Mach number shown are quite typical for most wings of reasonably conventional plan form. The spanwise distributions of  $c_{l_{\alpha,n}}$  and  $a_{c,n}$  used in the modified strip analysis were obtained from steady-state lifting-surface theory, from lifting-line theory, and from wind-tunnel measurements of pressure distributions. The agreement between calculations and

experiments for data obtained in the air and in Freon-12 shows that the wide differences in flutter-speed index  $\frac{V}{b_0 \omega_\alpha \sqrt{\mu}}$  obtained in these two media are attributable to wide differences in mass ratio ( $\mu$  as low as 10 in Freon-12 and as high as 260 in air). Note that flutter speeds in figure 19 are nondimensionalized with a calculated reference flutter speed  $V_R$  instead of with the more usual quantity  $b_0 \omega_\alpha \sqrt{\mu}$ .

Figures 20 and 21 (from ref. 13) show further comparisons between modified strip analysis, kernel functions, and experiment. In addition, the abrupt increase in both flutter speed and frequency, which occurred experimentally at Mach number near 1.07, indicates a sudden change in flutter mode. The possibility of such a sudden change is also predicted by the modified strip analysis which, at somewhat higher Mach number, yields two flutter solutions at very nearly the same speed but different frequencies.

Figure 22 shows flutter speeds in the supersonic range as calculated by the Mach box method and by quasi-steady second-order theory which is essentially the same as piston theory at high Mach numbers.

Figure 23 (from ref. 13) presents flutter speeds into the hypersonic range as obtained from the modified strip analysis employing steady-flow aerodynamic parameters obtained from shock-expansion theory and by quasi-steady second-order theory, which is again representative of piston theory at these high Mach numbers.

Figure 24 shows a typical flutter boundary as a function of the two independent variables, Mach number  $M$  and mass ratio  $\mu$ . (See ref. 12.) As illustrated, the variation of flutter boundary with  $\mu$  typically becomes steeper as Mach number increases in the supersonic range. Also, the track traced across this surface by flutter data obtained in a particular wind tunnel (yielding point  $F_t$  for example) may not coincide with the track corresponding to standard atmosphere (including point  $F_a$  for example). Hence, careful interpretation of the tunnel data may be required.

## CONCLUDING REMARKS

Some topics in aeroelasticity have been reviewed with emphasis on flutter and unsteady-lift theory. Simplified methods have been included for heuristic purposes, and the elements of some routinely used aerodynamic theories for subsonic to hypersonic speeds have also been covered.

A wide range of problems are currently under investigation but are not yet in a satisfactory state. These include:

- (1) Convergence of kernel-function and finite-summation (influence coefficient) procedures

- (2) Lifting surfaces at high reduced frequencies (needed for both flutter and gust-analysis frequency-response functions)
- (3) Transonic aerodynamics, especially accounting for variations in local Mach number over the lifting surface
- (4) Lifting surfaces with controls, especially partial-span controls
- (5) Interference problems
  - (a) Coplanar surfaces (wing-tail or wing-canard)
  - (b) Nonplanar surfaces (T-tails, V-tails, etc.)
  - (c) Wing-fuselage and wing-nacelle interactions
  - (d) Wind-tunnel wall effects, including resonance conditions
- (6) Nonlinear aerodynamics
  - (a) Second-order potential flow
  - (b) Lifting surfaces with free-vortex flow, e.g., leading-edge separation vortices and fuselage-separation vortices

## APPENDIX A

### SYMBOLS

$A$	portion of wing plan form intercepted by Mach forecone from point $(x,y)$ ; also, wing aspect ratio
$A_{ij}$	generalized aerodynamic force (see eq. (34))
$A_{mn}$	area of box with center at $(\xi_m, \eta_n)$ (see eq. (92))
$a$	nondimensional distance from midchord to elastic axis (positive rearward), fraction of semichord $b$
$a_{c,n}$	nondimensional distance from midchord to local aerodynamic center (for steady flow) measured perpendicular to elastic axis, positive rearward, fraction of semichord $b$
$a_{nm}^i$	coefficient of pressure-mode function $f_n(\xi)g_m(\eta)$ in the pressure expansion associated with motion of the lifting surface in the $i$ th vibration mode (see eq. (77))
$b$	semichord of two-dimensional wing; also, streamwise length of boxes super- imposed on wing planform (see eq. (91))
$b(\eta)$	local streamwise semichord of three-dimensional wing at spanwise station $\eta$ (see eq. (77))
$b_0$	wing-root semichord, $b(0)$ (see eq. (77))
$C = C(k)$	circulation function (eq. (55)), $F + iG$
$C_h$	viscous damping coefficient for plunging motion
$C_\alpha$	viscous damping coefficient for pitching motion
$c$	speed of sound in undisturbed fluid
$c_{l_{\alpha,n}}$	local lift-curve slope for a section perpendicular to elastic axis in steady flow

D	dissipation function (damping)
F	real part of complex circulation function $C$ (see eq. (55))
$F_{nm}^i$	function defined in equation (83)
$f_1(\theta), f_2(\theta)$	functions defined in equations (75)
$f_{h,i}(y)$	mode shape of $i$ th uncoupled bending mode (see eq. (59))
$f_n(\xi)$	$n$ th chordwise pressure-mode function (see eq. (77))
$f_{\alpha,j}(y)$	mode shape of $j$ th uncoupled torsion mode (see eq. (60))
G	imaginary part of complex circulation function $C$ (see eq. (55))
g	structural damping coefficient
$g_h$	structural damping coefficient for plunging motion (see eq. (1))
$g_{h,i}$	structural damping coefficient associated with motion in $i$ th uncoupled bending mode (see eq. (63))
$g_m(\eta)$	$m$ th spanwise pressure-mode function (see eq. (77))
$g_\alpha$	structural damping coefficient for pitching motion (see eq. (2))
$g_{\alpha,j}$	structural damping coefficient associated with motion in $j$ th uncoupled torsion mode (see eq. (64))
H	source strength (see eq. (65), (88))
$\Delta H$	strength of source element (see eq. (43))
h	translational displacement of wing at elastic axis (positive downward)
$h_0$	complex amplitude of plunging (translation) motion (see eq. (3))
$\underline{h}_i$	complex amplitude of $i$ th uncoupled bending mode (see eq. (59))

$I_\alpha$	mass moment of inertia of unit span of wing about elastic axis, $mb^2r_\alpha^2$
$i$	$\sqrt{-1}$
$J_0, J_1$	Bessel functions of first kind (see eq. (56))
$K$	kernel function of the downwash-pressure integral equation (see eqs. (71) to (74))
$k$	reduced frequency, $\frac{b\omega}{V}$
$k_0$	reduced frequency based on root semichord, $\frac{b_0\omega}{V}$
$k_1 = k \frac{r}{\beta}$	
$k_h$	spring constant for plunging motion, $m\omega_h^2$
$k_\alpha$	spring constant for pitching motion, $I_\alpha\omega_\alpha^2$
$L$	oscillatory lift per unit span (positive upward)
$L_C$	circulatory contribution to lift (see eq. (54))
$L_N$	noncirculatory contribution to lift (see eq. (49))
$l$	wing semispan
$l_h \equiv l_h'$	lift factor associated with plunging motion (see eqs. (8) and (10))
$l_\alpha$	lift factor associated with pitching about quarter chord ( $a = -1/2$ ) (see eq. (8))
$l_\alpha'$	lift factor associated with pitching motion (see eq. (10))
$M$	free-stream Mach number
$M_i$	generalized mass for $i$ th vibration mode (see eqs. (20) and (21))



$M_\alpha$	oscillatory moment per unit span about elastic axis (positive leading edge up)
$m, m(y)$	mass of wing per unit span (see eqs. (1), (61), (62))
$m(x, y)$	mass of wing per unit area (see eqs. (19), (20))
$m_h$	pitching-moment factor (about quarter chord) associated with plunging motion (see eq. (9))
$m_h'$	pitching-moment factor (about elastic axis) associated with plunging motion (see eq. (11))
$m_\alpha$	pitching-moment factor (about quarter chord) associated with pitching about quarter chord (see eq. (9))
$m_\alpha'$	pitching-moment factor (about elastic axis) associated with pitching about elastic axis (see eq. (11))
$n$	number of vibration modes (see eq. (16))
$p$	local pressure (see eq. (41))
$\Delta p$	local lifting pressure on wing (see eqs. (27), (29), (30))
$\Delta p_j$	local lifting pressure on wing associated with motion of wing in $j$ th vibration mode (see eqs. (30), (34))
$Q$	effective downwash for oscillating wing (see eqs. (53), (54))
$Q_{h,i}$	generalized force for $i$ th bending mode (see eq. (63))
$Q_i$	generalized force for $i$ th degree of freedom (see eq. (16))
$Q_{\alpha,j}$	generalized force for $j$ th torsion mode (see eq. (64))
$q$	free-stream dynamic pressure, $\frac{\rho V^2}{2}$

$q_i$                  $i$ th generalized coordinate

$\delta q_i$               virtual displacement in  $i$ th generalized coordinate

$$R = \sqrt{(x - \xi)^2 + (y - \eta)^2 + (z - \zeta)^2}$$

$$R' = \sqrt{(x - \xi)^2 + \beta^2(y - \eta)^2 + \beta^2 z^2}$$

$$R_1 = \sqrt{(x_i - \xi_m)^2 + (y_j - \eta_n)^2}$$

$$r = \beta \sqrt{(y - \eta)^2 + z^2}$$

$r_\alpha$                 nondimensional radius of gyration of wing section about elastic axis

$S$                    lifting-surface plan form

$S_\alpha$                static unbalance of wing (first moment of wing section mass about the neutral or elastic axis) positive for center of gravity aft of elastic axis,  $mbx_\alpha$

$T$                    kinetic energy (see eqs. (16), (18))

$t, t'$                time

$t_0$                   reference (initial) time (see eq. (51))

$U$                    potential energy (strain energy of the elastic system)

$U_0, U_1$            strength of vorticity (see eqs. (51), (53))

$U_m$                 Chebyshev polynomial of second kind

$\vec{u}$                    velocity vector

$$u_1 = \frac{MR' - (x - \xi)}{\beta r}$$

$V$	free-stream speed
$V_n$	component of free-stream velocity normal to elastic axis, $V \cos \Lambda_{ea}$
$V_R$	calculated reference flutter speed obtained from modified-strip-analysis method by using aerodynamic parameters for two-dimensional incompressible flow
$W = x + iz$	complex plane containing airfoil (see eq. (45) and fig 7)
$\delta W$	virtual work (see eq. (27))
$w$	local downwash at lifting surface (see eq. (67))
$w_i$	local downwash at lifting surface associated with motion in the $i$ th vibration mode (see eq. (71), (73), (82))
$X$	real part of eigenvalue $\Omega$
$x, y, z$	rectangular Cartesian coordinates (see fig. 6)
$x', y', z'$	transformed coordinates (see eq. (39))
$x_0$	particular value of $x$
$x_1, y_1$	nondimensional coordinates (see eqs. (32))
$x_\alpha$	nondimensional distance from elastic axis to section center of gravity (positive rearward), fraction of semichord $b$
$Y$	imaginary part of eigenvalue $\Omega$
$Y_0, Y_1$	Bessel functions of second kind (see eq. (56))
$Z(x, y, t)$	deflection shape of oscillating wing (displacement normal to $x, y$ plane)
$Z_i(x, y)$	normalized deflection shape of $i$ th mode (may be coupled or uncoupled vibration mode)

$Z_{0,i}$	complex amplitude for $i$ th mode
$\delta Z$	virtual displacement in deflection shape of oscillating wing (see eqs. (27), (28))
$\alpha$	torsional displacement of wing about elastic axis (positive leading edge up)
$\alpha_0$	complex amplitude of pitching motion (see eq. (3))
$\underline{\alpha}_j$	complex amplitude of $j$ th uncoupled torsion mode (see eq. (60))
$\beta = \sqrt{ 1 - M^2 }$	
$\Delta\Gamma$	strength of vortex element (see eq. (44))
$\gamma$	ratio of specific heat at constant pressure to specific heat at constant volume (see eqs. (93), (94))
$\delta$	inclination of airfoil surface relative to free-stream direction
$\delta_{ij}$	Kronecker delta
$\epsilon = R' \Big _{z=0} = \sqrt{(x - \xi)^2 + \beta^2(y - \eta)^2}$	
$\zeta = \xi + i\eta$	complex plane containing circle into which airfoil is mapped (see eq. (45) and fig. 7)
$\theta$	angle variable defined in equations (76)
$\Lambda$	sweepback angle
$\lambda$	taper ratio
$\mu$	mass ratio
$\xi, \eta, \zeta$	rectangular Cartesian coordinates (see fig. 6)
$\xi_0$	particular value of $\xi$

$\xi_m(\eta)$	chordwise location of mean-chord line at spanwise station $\eta$
$\rho$	fluid density
$\sigma$	local bending slope of elastic axis, $\frac{dh}{d\eta}$
$\tau$	local rate of change of twist along elastic axis, $\frac{d\alpha}{d\eta}$
$\phi$	velocity potential
$\Delta\phi$	local potential difference between upper and lower wing surface (see eq. (87))
$\phi_{ijmn}$	velocity-potential influence coefficient (VPIC), that is, the potential induced at $(x_i, y_j)$ by unit-strength source box with center at $(\xi_m, \eta_n)$
$\psi$	acceleration potential (see eq. (41))
$\Omega = X + iY = \left(\frac{\omega_\alpha}{\omega}\right)^2 (1 + ig)$ (see eq. (14))	
$\Omega_r = \left(\frac{\omega_r}{\omega}\right)^2 (1 + ig)$ (see eq. (35))	
$\omega$	circular frequency of oscillation
$\omega_h$	circular natural frequency of wing in plunging motion (uncoupled)
$\omega_{h,i}$	frequency of $i$ th uncoupled bending mode
$\omega_i$	frequency of $i$ th natural mode
$\omega_r$	reference frequency (arbitrary constant)
$\omega_\alpha$	circular natural frequency of wing in pitching motion (uncoupled)
$\omega_{\alpha,j}$	frequency of $j$ th uncoupled torsion mode

**Subscripts:**

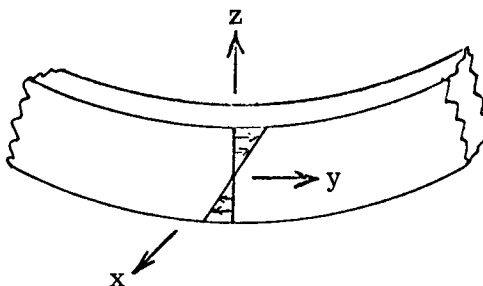
<b>C</b>	<b>compressible flow</b>
<b>c/4</b>	<b>quarter chord</b>
<b>d</b>	<b>doublet</b>
<b>ea</b>	<b>elastic axis</b>
<b>I</b>	<b>incompressible flow</b>
<b>i,j</b>	<b>ith or jth mode of vibration (e.g., eqs. (59), (60)) or generalized coordinate (e.g., eqs. (16), (19)) or box center (e.g., eqs. (91), (92))</b>
<b>s</b>	<b>source</b>
<b>v</b>	<b>vortex</b>
<b><math>\infty</math></b>	<b>infinity or free-stream conditions</b>

**Dot over a quantity indicates differentiation with respect to time.**

## APPENDIX B

### POTENTIAL ENERGY OF A BEAM IN BENDING AND IN TORSION (ALTERNATIVE TO EQUATIONS (24) AND (62))

The potential energy consists of the strain energy stored in the wing beam, that is, the work done in deforming the wing. Consider bending first:



Both stresses  $\sigma_y$  and elongations  $\epsilon_y$  have this profile since by Hooke's law for the assumed pure bending (pure compression and pure tension stresses only),

$$\sigma_y = E\epsilon_y \quad (B1)$$

where  $E$  is Young's modulus.

Then the work done at a section  $y = \text{Constant}$  and over a unit area of the beam parallel to  $x, z$  directions is  $\int \sigma_y d\epsilon_y$  analogous to work done on a linear spring. Now

$$\int \sigma_y d\epsilon_y = \int \frac{\sigma_y}{E} d\sigma_y = \frac{\sigma_y^2}{2E} \quad (B2)$$

Then over the cross section of the beam the work done is, since  $\sigma_y$  is independent of  $x$ ,

$$\int_{-u/2}^{u/2} \int_{-w/2}^{w/2} \frac{\sigma_y^2}{2E} dz dx = \int_{-w/2}^{w/2} \frac{\sigma_y^2}{2E} u dz \quad (B3)$$

where

$u$  width of beam in  $x$ -direction

$w$  depth of beam in  $z$ -direction

Now,

$$\sigma_y = \frac{Mz}{I_x} = \frac{z}{I_x} \left( EI_x \frac{\partial^2 h}{\partial y^2} \right) \quad (B4)$$

The work done over the cross section is, therefore,

$$\int_{-w/2}^{w/2} \frac{u}{2E} E^2 z^2 \left( \frac{\partial^2 h}{\partial y^2} \right)^2 dz = \frac{uE}{2} \left( \frac{\partial^2 h}{\partial y^2} \right)^2 \left[ \frac{z^3}{3} \right]_{-w/2}^{w/2} = \frac{uE}{2} \left( \frac{\partial^2 h}{\partial y^2} \right)^2 \frac{w^3}{12} \quad (B5)$$

but  $\frac{1}{12} uw^3 = I_x$  = Moment of inertia of the cross sectional area about the x-axis through the neutral point.

So the work done over the cross section is

$$\frac{1}{2} EI_x \left( \frac{\partial^2 h}{\partial y^2} \right)^2$$

Then the potential energy over the entire beam is

$$U_{\text{bending}} = \int_0^l \frac{1}{2} EI_x \left( \frac{\partial^2 h}{\partial y^2} \right)^2 dy = \frac{1}{2} h^2 \int_0^l EI \left( \frac{d^2 f_h}{dy^2} \right)^2 dy e^{i\omega t} \quad (B6)$$

Similarly for torsion, the work at a given cross section and for unit area of cross section is  $\int s_s d\gamma$  but by Hooke's law,

$$\gamma = \frac{s_s}{G} \quad (B7)$$

where  $\gamma$  is the shearing strain,  $s_s$  the shear stress, and  $G$  the shear modulus.

Then,

$$\int s_s d\gamma = \int \frac{s_s}{G} ds_s = \frac{s_s^2}{2G} \quad (B8)$$

and

$$s_s = Gr \frac{d\theta}{dy} \quad (B9)$$

where  $r$  is the radial distance from neutral axis, and  $\theta$  is the torsional displacement angle. So over the entire cross section, the work done in deflecting the beam is



$$\int \frac{s_s^2}{2G} dA = \int \frac{G^2 r^2}{2G} \left( \frac{d\theta}{dy} \right)^2 dA = \frac{G}{2} \left( \frac{d\theta}{dy} \right)^2 \int r^2 dA = \frac{GI_p}{2} \left( \frac{d\theta}{dy} \right)^2 \quad (B10)$$

where  $I_p$  is the polar moment of inertia of the section for a circular shaft, or, in general,  $GI_p$  becomes  $GJ$  ("torsional rigidity").

Then over the whole length of the wing the potential energy is

$$U_{\text{torsion}} = \int_0^l \frac{1}{2} GJ \left( \frac{d\theta}{dy} \right)^2 dy = \frac{1}{2} \theta^2 \int_0^l GJ \left( \frac{df_\theta}{dy} \right)^2 dy \quad (B11)$$

For bending and torsional motion of a beam, the potential energy (strain energy) given by the sum of equations (B6) and (B11) corresponds to the potential energy in equations (24) and (62), where  $\underline{h}$  and  $\underline{\theta}$  are the same as the generalized coordinates  $q_i$ .

## APPENDIX C

### AERODYNAMIC INFLUENCE COEFFICIENTS AND THE KERNEL FUNCTION METHOD FOR DETERMINING LOADS ON AN OSCILLATING, FLEXIBLE WING

Aerodynamic influence coefficients.- Before the lifting-surface methods of flutter calculation are discussed, a review of the concept of aerodynamic influence coefficients will be instructive. Consider the surface of an oscillating or nonoscillating wing to be subdivided into a number of small segments or "boxes," as illustrated in figure 25. Then, the downwash  $w$  at any point  $(x,y)$  on the wing surface can be considered to be the sum of the incremental downwashes  $\Delta w$  at  $(x,y)$  induced by the loads on each of the boxes:

$$w(x,y) = \sum_i \Delta w_i(x,y) \quad (C1)$$

where  $\Delta w_i(x,y)$  is the downwash at  $(x,y)$  caused by the load on box  $i$ . This relation may also be written as

$$w(x,y) = \sum_i L_i K_i(x,y) \quad (C2)$$

where  $K_i(x,y)$  is the downwash at  $(x,y)$  caused by a unit load on box  $i$  and is called the aerodynamic influence coefficient.  $L_i$  is the load on box  $i$ . Or again

$$w(x,y) = \sum_i \Delta p_i K_i(x,y) \Delta A_i \quad (C3)$$

where  $\Delta p_i$  is the pressure on box  $i$ , and  $\Delta A_i$  is the area of box  $i$ . The aerodynamic influence coefficient  $K_i(x,y)$  will obviously depend on the stream Mach number  $M$  and on the frequency of oscillation  $\omega$ , as well as on the longitudinal distance  $x - \xi$  and lateral distance  $y - \eta$  between  $(x,y)$  and box  $i$  (fig. 25).

The downwash-kernel-function integral equation.- The summation equation (C3), if taken to the limit as  $\Delta A_i \rightarrow 0$ , becomes an integral equation

$$\frac{w(x,y)}{V} = \iint_S \Delta p(\xi,\eta) K \left[ \frac{\omega}{V}(x - \xi), \frac{\omega}{V}(y - \eta), M \right] d\xi d\eta \quad (C4)$$

where  $\Delta p(\xi,\eta)$  is the magnitude of the lifting pressure at point  $(\xi,\eta)$  and

$K \left[ \frac{\omega}{V}(x - \xi), \frac{\omega}{V}(y - \eta), M \right]$  is the kernel function which represents the downwash induced at

at point  $(x, y)$  by a unit lift at point  $(\xi, \eta)$  oscillating with frequency  $\omega$  in a flow of Mach number  $M$  and speed  $V$ . The area of integration  $S$  is, for subsonic speeds, the entire wing area and, for supersonic speeds, the wing area lying within the forward Mach cone from  $(x, y)$ .

By virtue of the boundary condition that no fluid flows through the wing surface and that no flow separation occurs, the summation (or integral) at a point on the wing of the downwash due to all lift elements on the wing surface must equal the downwash due to the geometrical motion of the wing. In an analysis employing chosen modes, the geometrical motion is specified by the mode shapes so that for a given frequency  $\omega$  (or reduced frequency  $k$ ), the  $w(x, y)$  is known. Thus, if expressions can be obtained for the kernel  $K\left[\frac{\omega}{V}(x - \xi), \frac{\omega}{V}(y - \eta), M\right]$ , the only remaining unknown in equation (C4) is the load intensity  $\Delta p(\xi, \eta)$  which we are seeking.

If attention is confined to small perturbations in an inviscid fluid, the governing equation for the propagation of disturbances will be the wave equation.

Derivation of wave equation. - Euler's equation of motion may be written as

$$\frac{D\bar{u}}{Dt} = \frac{-1}{\rho} \nabla p + \bar{F}$$

or

$$\frac{\partial \bar{u}}{\partial t} + \bar{u} \cdot \nabla \bar{u} = \frac{-1}{\rho} \nabla p + \bar{F} \quad (C5)$$

where  $\frac{D}{Dt}$  denotes the substantial derivative,  $\bar{u}$  is the fluid velocity vector,  $\rho$  is the local fluid density,  $p$  is the local fluid pressure,  $t$  is time, and  $\bar{F}$  is the body force vector (force per unit mass). If the body forces arise from a conservative force field (for example, gravity) then  $\bar{F}$  may be expressed as the gradient of a scalar potential  $U$

$$\bar{F} = -\nabla U \quad (C6)$$

Further, if a unique relation exists between  $p$  and  $\rho$  (for example, as in adiabatic flow), then  $p = p(\rho)$ , and a function  $P$  may be defined so that

$$dP = \frac{dp}{\rho} = \frac{dp}{d\rho} \frac{d\rho}{\rho} \quad (C7)$$

then

$$\frac{\partial P}{\partial \mathbf{x}} = \frac{\partial P}{\partial p} \frac{\partial p}{\partial \mathbf{x}} = \frac{1}{\rho} \frac{\partial p}{\partial \mathbf{x}}$$

or

$$\nabla P = \frac{1}{\rho} \nabla p \quad (\text{C8})$$

Substituting equations (C6) and (C8) into equation (C5) and using the vector identity

$$\bar{\mathbf{u}} \cdot \nabla \bar{\mathbf{u}} \equiv \nabla \left( \frac{u^2}{2} \right) - \bar{\mathbf{u}} \times (\nabla \times \bar{\mathbf{u}}) \quad (\text{C9})$$

yields

$$\frac{\partial \bar{\mathbf{u}}}{\partial t} + \nabla \left( \frac{u^2}{2} \right) - \bar{\mathbf{u}} \times (\nabla \times \bar{\mathbf{u}}) = -\nabla P - \nabla U$$

or

$$\nabla \left( P + U + \frac{u^2}{2} \right) = \bar{\mathbf{u}} \times (\nabla \times \bar{\mathbf{u}}) - \frac{\partial \bar{\mathbf{u}}}{\partial t} \quad (\text{C10})$$

which is Bernoulli's equation for the flow of an inviscid fluid. Now, make the following assumptions:

- (1) No force field exists.
- (2) The fluid is initially at rest.
- (3) All disturbances are of infinitesimal amplitude.
- (4) Thermodynamic equilibrium exists.

By virtue of assumption (1),  $\nabla U = 0$ . By virtue of assumption (2), and Kelvin's circulation theorem, the propagation of disturbances is irrotational so that  $\nabla \times \bar{\mathbf{u}} = 0$ . By virtue of assumption (3), second and higher powers of the fluid velocity may be neglected, so that  $\nabla \frac{u^2}{2} \approx 0$ . Assumption (4) is already contained in Bernoulli's equation in the form of the unique relation  $p = p(\rho)$ . With these assumptions Bernoulli's equation reduces to

$$\nabla P + \frac{\partial \bar{\mathbf{u}}}{\partial t} = 0 \quad (\text{C11})$$

Since the flow is irrotational, a velocity potential  $\phi$  may be introduced such that

$$\bar{\mathbf{u}} = \nabla \phi \quad (\text{C12})$$

Thus,

$$\nabla P + \frac{\partial}{\partial t} \nabla \phi = 0$$

or

$$\nabla \left( P + \frac{\partial \phi}{\partial t} \right) = 0$$

or

$$P + \frac{\partial \phi}{\partial t} = \text{Const.} = P_{\infty} \quad (\text{C13})$$

Since disturbances of small amplitude are assumed, the function  $p = p(\rho)$  may be expressed as  $p = p(\rho_{\infty} + \Delta\rho)$  where  $\rho_{\infty}$  is the density of the undisturbed fluid. Expanding this relation in a Taylor series gives

$$p = p(\rho) = p(\rho_{\infty} + \Delta\rho) = p(\rho_{\infty}) + \left[ \frac{dp}{d\rho} \right]_{\rho_{\infty}} \Delta\rho + \dots$$

so that, for small disturbances,

$$\frac{dp}{d\rho} \approx \left[ \frac{dp}{d\rho} \right]_{\rho_{\infty}} \quad (\text{C14})$$

Then, equation (C7) may be integrated to give

$$P - P_{\infty} = \int_{P_{\infty}}^P dP = \int_{P_{\infty}}^P \frac{dp}{\rho} = \int_{\rho_{\infty}}^{\rho} \frac{dp}{d\rho} \frac{d\rho}{\rho} = \left[ \frac{dp}{d\rho} \right]_{\rho_{\infty}} \int_{\rho_{\infty}}^{\rho} \frac{d\rho}{\rho} = \left[ \frac{dp}{d\rho} \right]_{\rho_{\infty}} \log_e \frac{\rho}{\rho_{\infty}} \quad (\text{C15})$$

and since

$$\left[ \frac{dp}{d\rho} \right]_{\rho_{\infty}} = c^2$$

where  $c$  = Speed of sound in the undisturbed fluid, the result is

$$P - P_{\infty} = c^2 \log_e \frac{\rho}{\rho_{\infty}} \quad (\text{C16})$$

Taking the substantial derivative of equation (C16) gives

$$\frac{DP}{Dt} = c^2 \frac{D}{Dt} \log_e \frac{\rho}{\rho_\infty} = \frac{c^2}{\rho} \frac{D\rho}{Dt} \quad (C17)$$

The continuity equation is

$$\frac{\partial \rho}{\partial t} + \nabla \cdot (\rho \bar{\mathbf{u}}) = 0$$

or

$$\frac{\partial \rho}{\partial t} + \rho \nabla \cdot \bar{\mathbf{u}} + \mathbf{u} \cdot \nabla \rho = 0$$

or

$$-\frac{1}{\rho} \frac{D\rho}{Dt} = \nabla \cdot \bar{\mathbf{u}} \quad (C18)$$

so from equations (C17) and (C18), there results

$$\frac{DP}{Dt} = -c^2 \nabla \cdot \bar{\mathbf{u}} = -c^2 \nabla^2 \phi \quad (C19)$$

Also, from equation (C13),

$$\frac{DP}{Dt} + \frac{D}{Dt} \frac{\partial \phi}{\partial t} = 0$$

or

$$\begin{aligned} \frac{DP}{Dt} &= -\frac{\partial^2 \phi}{\partial t^2} - \bar{\mathbf{u}} \cdot \nabla \frac{\partial \phi}{\partial t} \\ &= -\frac{\partial^2 \phi}{\partial t^2} - \bar{\mathbf{u}} \cdot \frac{\partial \bar{\mathbf{u}}}{\partial t} \\ &= -\frac{\partial^2 \phi}{\partial t^2} \end{aligned} \quad (C20)$$

since second and higher powers of the velocity are neglected. Thus, from equations (C19) and (C20) the linearized wave equation (see, for example, ref. 31) is obtained:

$$c^2 \nabla^2 \phi = \frac{\partial^2 \phi}{\partial t^2} \quad (C21)$$

which is the same as equation (38) in the text.

Equation (C21) is the governing equation for the propagation of small disturbances from a disturbance source at the origin of coordinates  $x, y, z$  through a fluid initially at rest. For this equation to be applied to disturbances originating from a disturbance source moving with speed  $V$  in the  $-x$  direction (e.g., a small lifting element), equation (C21) must be expressed in terms of moving coordinates  $x', y', z'$  so that

$$\left. \begin{aligned} x' &= x + Vt \\ y' &= y \\ z' &= z \\ t' &= t \end{aligned} \right\} \quad (C22)$$

This transformation leads to

$$\frac{\partial^2 \phi}{\partial x'^2} + \frac{\partial^2 \phi}{\partial y'^2} + \frac{\partial^2 \phi}{\partial z'^2} = \frac{1}{c^2} \left( \frac{\partial}{\partial t} + V \frac{\partial}{\partial x} \right)^2 \phi \quad (C23)$$

This transformed wave equation governs propagation of small disturbances from a moving body. It should be noted that in equation (C23) the function  $\phi$  may be either a velocity potential or an acceleration potential. The boundary conditions used in connection with equation (C23) for most aerodynamic problems are:

- (1) There is no flow through the surface of the body (wing) and no flow separation from the wing. For the oscillating wing, this condition is contained in equation (C4).
- (2) Uniform flow exists at infinity.

Expressions for the kernel function.— The function  $K$  which is required for the solution (inversion) of equation (C4) represents an expression for the downwash field induced by an element of lift which is pulsating at the reduced frequency  $k$ . In classical aerodynamics such an element of lift can be represented by a doublet. Now the potential function for a simple pulsating doublet satisfies the wave equation (C23), and hence is admissible in the solution of our problem equation (C4). Further, since equation (C23) is a linear differential equation, a superposition of doublet potentials is also a solution. Therefore, our summation or integration procedure indicated by equations (C3) and (C4) is permissible.

For subsonic free-stream conditions, the kernel function associated with a pulsating doublet of unit strength is derived in reference 4 in the form

$$K = \lim_{z \rightarrow 0} \frac{\partial^2}{\partial z^2} \exp \frac{-i\omega(x - \xi)}{V} \int_{-\infty}^{x-\xi} \frac{\exp \left[ \frac{i\omega}{V\beta^2} \left( \lambda - M\sqrt{\lambda^2 + \beta^2(y - \eta)^2 + \beta^2 z^2} \right) \right] d\lambda}{\sqrt{\lambda^2 + \beta^2(y - \eta)^2 + \beta^2 z^2}} \quad (C24)$$

where  $\omega$  is the frequency of the pulsation, and  $\beta = \sqrt{1 - M^2}$ .

For supersonic free-stream condition, the function  $K$  is derived in reference 32 in the form

$$K = \frac{2}{V} \lim_{z \rightarrow 0} \exp \frac{-i\omega(x - \xi)}{V} \int_{\beta\sqrt{(y-\eta)^2 + z^2}}^{x-\xi} \exp \frac{-i\omega\lambda}{V\beta^2} \frac{\partial^2}{\partial z^2} \left[ \frac{U \left( \lambda - \beta\sqrt{(y - \eta)^2 + z^2} \right) \cos \frac{M\omega}{V\beta^2} \sqrt{\lambda^2 - \beta^2(y - \eta)^2 - \beta^2 z^2}}{\sqrt{\lambda^2 - \beta^2(y - \eta)^2 - \beta^2 z^2}} \right] d\lambda \quad (C25)$$

where  $U$  is the unit function. It can be seen that these expressions contain singularities which require careful treatment in the numerical solution of equation (C4).

Solution of the downwash-kernel-function integral equation.— One method that has been used at subsonic speeds for the numerical inversion of the equation (C4) is given in reference 33. In this procedure the unknown distribution of lifting pressure  $\Delta p_n(\xi, \eta)$  over the wing, associated with the  $n$ th mode of motion, is assumed to be represented by a doubly infinite series

$$\Delta p_n(\xi, \eta) = \frac{8\rho V^2}{2b(\eta)} \sqrt{s^2 - \eta^2} \left[ \cot \frac{\theta}{2} (a_{00}^n + a_{01}^n \eta + a_{02}^n \eta^2 + \dots) \right. \\ \left. + \sin \theta (a_{10}^n + a_{11}^n \eta + a_{12}^n \eta^2 + \dots) + \sin 2\theta (a_{20}^n + a_{21}^n \eta + a_{22}^n \eta^2 + \dots) + \dots \right] \quad (C26)$$

where  $\rho$  is fluid density,  $b(\eta)$  is local semichord,  $s$  is semispan, and  $\theta$  is a chordwise coordinate such that

$$\xi = f_{ml}(\eta) - b(\eta) \cos \theta$$

where  $f_{ml}(\eta)$  is the equation of the midchord line. The form of the series equation (C26) automatically satisfies boundary conditions on the lifting pressure at leading edge, trailing edge, and wing tip regardless of the values of the unknown coefficients  $a_{rs}^n$ .



The downwash  $w(x,y)$  is determined by the chosen mode shapes and by the frequency:

$$\begin{aligned} w(x,y,t) &= \left( \frac{\partial}{\partial t} + V \frac{\partial}{\partial x} \right) \left[ Z_1(x,y) + Z_2(x,y) + \dots + Z_q(x,y) \right] e^{i\omega t} \\ &= \left[ w_1(x,y) + w_2(x,y) + \dots + w_q(x,y) \right] e^{i\omega t} \end{aligned} \quad (C27)$$

where  $Z_n(x,y)$  is the mode shape of the  $n$ th mode, and  $w_n(x,y)$  is the downwash magnitude for the  $n$ th mode at frequency  $\omega$ .

The procedure followed in the solution for the load distribution is as follows:

(1) Choose the reduced frequency value  $k$  for which the aerodynamic load is to be calculated.

(2) Choose the mode-shape function  $Z_n(x,y)$  and obtain the downwash  $w_n(x,y)$  at a set of chosen "control" points  $(x,y)$  over the wing surface.

(3) Truncate the doubly infinite series equation (C26) so that it contains the same number of unknown coefficients  $a_{rs}^n$  as there are control points.

(4) For each control point in turn, substitute the appropriate  $w_n(x,y)$  into the left side of equation (C4). Substitute expression (C24) and equation (C26) together with the control point coordinate  $(x,y)$  into the right side of the equation (C4). Performing the indicated integration numerically yields an equation which contains the unknown coefficients  $a_{rs}^n$ . Repeating this procedure for each control point leads to a set of simultaneous equations which can be solved for the loading coefficients  $a_{rs}^n$  for the  $n$ th mode at the chosen frequency  $k$  and Mach number  $M$ . The aerodynamic loading has then been determined in the form of equation (C26) and can be used in that form in flutter calculations.

## REFERENCES

1. Boswinkle, Robert W., Jr.; and Yates, E. Carson, Jr.: Aeroelastic Considerations. Proceedings of NASA Conference on Supersonic-Transport Feasibility Studies and Supporting Research. September 17-19, 1963, NASA TM X-905, 1963, pp. 365-380.
2. Bisplinghoff, Raymond L.; Ashley, Holt; and Halfman, Robert L.: Aeroelasticity. Addison-Wesley Pub. Co., Inc., c.1955.
3. Scanlan, Robert H.; and Rosenbaum, Robert: Introduction to the Study of Aircraft Vibration and Flutter. MacMillan Co., 1951. (Also Dover Publications, Inc., 1968.)
4. Watkins, Charles E.; Runyan, Harry L.; and Woolston, Donald S.: On the Kernel Function of the Integral Equation Relating the Lift and Downwash Distributions of Oscillating Finite Wings in Subsonic Flow. NACA Rep. 1234, 1955. (Supersedes NACA TN 3131.)
5. Theodorsen, Theodore: General Theory of Aerodynamic Instability and the Mechanism of Flutter. NACA Rep. 496, 1935.
6. Possio, Camillo: L'Azione aerodinamica sul profilo oscillante in un fluido compressibile a velocita iposonora. L'Aerotecnica, vol. XVIII, fasc. 4, Apr. 1938, pp. 441-458. (Available as British Air Ministry Translation No. 830.)
7. Garrick, I. E.; and Rubinow, S. I.: Flutter and Oscillating Air-Force Calculations for an Airfoil in a Two-Dimensional Supersonic Flow. NACA Rep. 846, 1946.
8. Jordan, P. F.: Aerodynamic Flutter Coefficients for Subsonic, Sonic, and Supersonic Flow (Linear Two-Dimensional Theory). R. & M. No. 2932, British A.R.C., 1957.
9. Barmby, J. G.; Cunningham, H. J.; and Garrick, I. E.: Study of Effects of Sweep on the Flutter of Cantilever Wings. NACA Rep. 1014, 1951.
10. Yates, E. Carson, Jr.: Calculation of Flutter Characteristics for Finite-Span Swept or Unswept Wings at Subsonic and Supersonic Speeds by a Modified Strip Analysis. NACA RM L57L10, 1958.
11. Yates, E. Carson, Jr.: Use of Experimental Steady-Flow Aerodynamic Parameters in the Calculation of Flutter Characteristics for Finite Span Swept or Unswept Wings at Subsonic, Transonic, and Supersonic Speeds. NASA TM X-183, 1960.
12. Yates, E. Carson, Jr.: Subsonic and Supersonic Flutter Analysis of a Highly Tapered Swept Wing Planform Including Effects of Density Variation and Finite Wing Thickness and Comparison With Experiments. NASA TN D-4230, 1967. (Supersedes NASA TM X-764, 1963.)

13. Yates, E. Carson, Jr.: Modified-Strip-Analysis Method for Predicting Wing Flutter at Subsonic to Hypersonic Speeds. *J. Aircraft*, vol. 3, no. 1, Jan.-Feb. 1966, pp. 25-29.
14. Yates, E. Carson, Jr.: Flutter Prediction at Low Mass-Density Ratios with Application to the Finite-Span Noncavitating Hydrofoil. AIAA Paper No. 68-472, Apr.-May, 1968.
15. Watkins, Charles E.; Woolston, Donald S.; and Cunningham, Herbert J.: A Systematic Kernel Function Procedure for Determining Aerodynamic Forces on Oscillating or Steady Finite Wings at Subsonic Speeds. NASA TR R-48, 1959.
16. Richardson, J. R.: A Method for Calculating the Lifting Forces on Wings (Unsteady Subsonic and Supersonic Lifting-Surface Theory). R. & M. No. 3157, British A.R.C., 1955.
17. Darovsky, L.; and Dat, R.: Determination des Forces Aerodynamiques Instationnaires Tridimensionnelles. AGARD Rep. 512, June 1965.
18. Albano, Edward; and Rodden, William P.: A Doublet-Lattice Method for Calculating Lift Distributions on Oscillating Surfaces in Subsonic Flows. AIAA J., vol 7, no. 2, Feb. 1969, pp. 279-285.
19. Pines, Samuel; Dugundji, John; and Neuringer, Joseph: Aerodynamic Flutter Derivatives for a Flexible Wing with Supersonic and Subsonic Edges. *J. Aeronaut. Sci.*, vol. 22, no. 10, Oct. 1955, pp. 693-700.
20. Zartarian, Garabed; and Hsu, Pao-Tan: Theoretical Studies on the Prediction of Unsteady Supersonic Airloads on Elastic Wings - Part I. Investigations on the Use of Oscillatory Supersonic Aerodynamic Influence Coefficients. WADC Tech. Rep. 56-97, Part I, DDC Doc. No. AD 110 591, U.S. Air Force, Dec. 1955.
21. Zartarian, G.: Theoretical Studies on the Prediction of Unsteady Supersonic Airloads on Elastic Wings - Part 2. Rules for Application of Oscillatory Supersonic Aerodynamic Influence Coefficients. WADC Tech. Rep. 56-97, Pt. II, DDC Doc. No. AD 110 592, U.S. Air Force, Feb. 1956.
22. Moore, M. T.; and Andrew, L. V.: Unsteady Aerodynamics for Advanced Configuration. Pt. IV - Application of the Supersonic Mach Box Method to Intersecting Planar Lifting Surfaces. FDL-TDR-64-152, Pt. IV, U.S. Air Force, May 1965.
23. Landahl, Marten T.: Theoretical Studies of Unsteady Transonic Flow. Part. I: Linearization of the Equations of Motion. FFA Rep. 77, Aero. Res. Inst. of Sweden (Stockholm), 1958.

24. Landahl, Marten T.: Unsteady Transonic Flow. Pergamon Press, Inc., 1961.
25. Rodemich, E. R.; and Andrew, L. V.: Unsteady Aerodynamics for Advanced Configurations. Pt. II – A Transonic Box Method for Planar Lifting Surfaces. USAF Rep. FDL-TDR-64-152, Part II, U.S. Air Force, May 1965.
26. Olsen, J. J.: Demonstration of a Transonic Box Method for Unsteady Aerodynamics of Planar Wings. AFFDL-TR-66-121, U.S. Air Force, Oct. 1966. (Available from DDC as AD 647 369.)
27. Stenton, T. E.; and Andrew, L. V.: Transonic Unsteady Aerodynamics for Planar Wings with Trailing Edge Control Surfaces. AFFDL-TR-67-180, U.S. Air Force, Aug. 1968.
28. Andrew, L. V.; and Stenton, T. E.: Unsteady Aerodynamic Forces on a Thin Wing Oscillating in Transonic Flow. AIAA Paper No. 67-16, Jan. 1967.
29. Lighthill, M. J.: Oscillating Airfoils at High Mach Number. J. Aeronaut. Sci., vol 20, no. 6, June 1953, pp. 402-406.
30. Ashley, Holt; and Zartarian, Garabed: Piston Theory – A New Aerodynamic Tool for the Aeroelastician. J. Aeronaut. Sci., vol. 23, no. 12, Dec. 1956, pp. 1109-1118.
31. Watkins, Charles E.; and Berman, Julian H.: On the Kernel Function of the Integral Equation Relating Lift and Downwash Distributions of Oscillating Wings in Supersonic Flow. NACA Rep. 1257, 1956. (Supersedes NACA TN 3438.)
32. Bisplinghoff, Raymond L.; and Ashley, Holt: Principles of Aeroelasticity. John Wiley & Sons, Inc. c.1962.
33. Runyan, Harry L.; and Woolston, Donald S.: Method for Calculating the Aerodynamic Loading on an Oscillating Finite Wing in Subsonic and Sonic Flow. NACA Rep. 1322, 1957. (Supersedes NACA TN 3694.)

## BIBLIOGRAPHY

### General

- Scanlan, Robert H.; and Rosenbaum, Robert: Introduction to the Study of Aircraft Vibration and Flutter. Dover Publications, Inc., c.1968.
- Bisplinghoff, Raymond L.; Ashley, Holt; and Halfman, Robert L.: Aeroelasticity. Addison-Wesley Pub. Co., Inc., c.1955.
- Fung, Y. C.: An Introduction to the Theory of Aeroelasticity. GALCIT Aeronautical Series. John Wiley & Sons, Inc., c.1955.
- Bisplinghoff, Raymond L.; and Ashley, Holt: Principles of Aeroelasticity. John Wiley & Sons, Inc., c.1962.
- Jones, W. P., ed.: Manual on Aeroelasticity. Vol. II – Aerodynamic Aspects. AGARD.
- Miles, John W.: Linearization of the Equations of Non-Steady Flow in a Compressible Fluid. J. Math. Phys., vol. XXXIII, no. 2, July 1954, p. 135.
- Garrick, I. E., ed.: Aerodynamic Flutter. Vol. V of AIAA Selected Reprint Series, Mar. 1969.
- Rodden, William P.; and Revell, James D.: The Status of Unsteady Aerodynamic Influence Coefficients. S.M.F. Fund Pap. No.-FF-33, Inst. Aerosp. Sci., Jan. 1962.
- Boswinkle, Robert W., Jr.; and Yates, E. Carson, Jr.: Aeroelastic Considerations. Proceedings of NASA Conference on Supersonic-Transport Feasibility Studies and Supporting Research. Spetember 17-19, 1963, NASA TM X-905, 1963, pp. 365-380.
- Ashley, Holt; Windnall, Sheila; and Landahl, Marten T.: New Directions in Lifting Surface Theory. AIAA J., vol. 3, no. 1, Jan. 1965, pp. 3-16.
- Laschka, B.: Über Ergebnisse der Experimentellen und Theoretischen Forschung auf dem Gebiet der Instationären Luftkräfte. DLR Mitt. 65-12, 1965.
- Landahl, Mårten T.; and Stark, Valter J. E.: Numerical Lifting-Surface Theory – Problems and Progress. AIAA J., vol. 6, no. 11, Nov. 1968, pp. 2049-2060.

### Two-Dimensional Theory

- Theodorsen, Theodore: General Theory of Aerodynamic Instability and the Mechanism of Flutter. NACA Rep. 496, 1935.
- Possio, Camillo: L'Azione aerodinamica sul profilo oscillante in un fluido compressibile a velocità iposonora. L'Aerotecnica, vol XVIII, fasc. 4, Apr. 1938, pp. 441-458. (Available as British Air Ministry Translation No. 830.)

Garrick, I. E.; and Rubinow, S. I.: Flutter and Oscillating Air-Force Calculations for an Airfoil in a Two-Dimensional Supersonic Flow. NACA Rep. 846, 1946.

Jordon, P. F.: Aerodynamic Flutter Coefficients for Subsonic, Sonic and Supersonic Flow (Linear Two-Dimensional Theory). R. & M. No. 2932, British A.R.C., 1957.

#### Strip Methods

Barmby, J. G.; Cunningham, H. J.; and Garrick, I. E.: Study of Effects of Sweep on the Flutter of Cantilever Wings. NACA Rep. 1014, 1951.

Yates, E. Carson, Jr.: Calculation of Flutter Characteristics for Finite-Span Swept or Unswept Wings at Subsonic and Supersonic Speeds by a Modified Strip Analysis. NACA RM L57L10, 1958.

Yates, E. Carson, Jr.: Use of Experimental Steady-Flow Aerodynamic Parameters in the Calculation of Flutter Characteristics for Finite-Span Swept or Unswept Wings at Subsonic, Transonic, and Supersonic Speeds. NASA TM X-183, 1960.

Yates, E. Carson, Jr.: Subsonic and Supersonic Flutter Analysis of a Highly Tapered Swept-Wing Planform, Including Effects of Density Variation and Finite Wing Thickness, and Comparison With Experiments. NASA TN D-4230, 1967. (Supersedes NASA TM X-764, 1963.)

Yates, E. Carson, Jr.: Modified-Strip-Analysis Method for Predicting Wing Flutter at Subsonic to Hypersonic Speeds. J. Aircraft, vol. 3, no. 1, Jan.-Feb. 1966, pp. 25-29.

Yates, E. Carson, Jr.: Flutter Prediction at Low Mass-Density Ratios With Application to the Finite-Span Noncavitating Hydrofoil. AIAA Pap. No. 68-472, Apr.-May 1968.

#### Subsonic Lifting-Surface Theory

Watkins, Charles E.; Runyan, Harry L.; and Woolston, Donald S.: On the Kernel Function of the Integral Equation Relating the Lift and Downwash Distributions of Oscillating Finite Wings in Subsonic Flow. NACA Rep. 1234, 1955. (Supersedes NACA TN 3131.)

Hsu, Pao-Tan: Some Recent Developments in the Flutter Analysis of Low-Aspect-Ratio Wings. Proc. Nat. Specialists Meeting on Dynamics and Aeroelasticity (Fort Worth, Texas), Inst. Aero. Sci., Nov. 1958.

Runyan, Harry L.; and Woolston, Donald S.: Method for Calculating the Aerodynamic Loading on an Oscillating Finite Wing in Subsonic and Sonic Flow. NACA Rep. 1322, 1957. (Supersedes NACA TN 3694.)

- Watkins, Charles E.; Woolston, Donald S.; and Cunningham, Herbert J.: A Systematic Kernel Function Procedure for Determining Aerodynamic Forces on Oscillating or Steady Finite Wings at Subsonic Speeds. NASA TR R-48, 1959.
- Richardson, J. R.: A Method for Calculating the Lifting Forces on Wings (Unsteady Subsonic and Supersonic Lifting-Surface Theory). R. & M. No. 3157, Brit. A.R.C, 1955.
- Stark, Valter J. E.: A Method for Solving the Subsonic Problem of the Oscillating Finite Wing With the Aid of High-Speed Digital Computers. SAAB TN 41, Saab Aircraft Co. (Linköping, Sweden), Dec. 16, 1968.
- Laschka, Boris: Zur Theorie der harmonisch schwingenden tragenden Fläche bei Unterschallanströmung. Z. Flugwissenschaften, Jahrg. 11, Heft 7, July 1963, pp. 265-292.
- Laschka, Von Boris: Das Potential und das Geschwindigkeitsfeld der harmonisch schwingenden tragenden Fläche bei Unterschallströmung. Z. Angew. Math. Mech., Band 43, Heft 7/8, 1963, pp. 325-333.
- Laschka, B.: Die Druck-, Auftriebs-, und Momentenverteilungen an einem harmonisch schwingenden Pfeilflügel kleiner Streckung im niedrigen Unterschallbereich Vergleich zwischen Theorie und Messung. Proceedings of the 4th Congress of the International Council of the Aeronautical Sciences, Robert R. Dexter, ed., Spartan Books, Inc., 1965, pp. 295-313.
- Davies, D. E.: Calculation of Unsteady Generalized Airforces on a Thin Wing Oscillating Harmonically in Subsonic Flow. R. & M. No. 3409, Brit. A.R.C., 1965.
- Darovsky, L.; and Dat, R.: Determination des Forces Aerodynamiques Instationnaires Tridimensionnelles. AGARD Rep. 512, June 1965.
- Wookcock, David L.: On the Accuracy of Collocation Solutions of the Integral Equation of Linearised Subsonic Flow Past an Oscillating Aerofoil. Proceedings of International Symposium on Analogue and Digital Techniques Applied to Aeronautics, Presses Académiques Européennes (Brussels), 1964, pp. 173-202.
- Rowe, William S.: Collocation Method for Calculating the Aerodynamic Pressure Distributions on a Lifting Surface Oscillating in Subsonic Compressible Flow. AIAA Symposium on Structural Dynamics and Aeroelasticity, Aug.-Sept. 1965, pp. 31-45.
- Dat, Roland; Leclerc, Jacques; and Akamatsu, Yoshio: Optimisation de L'emploi de la Théorie de la Surface Portante en Aéroélasticité Subsonique. La Rech. Aérospatiale, no. 113, July-Aug. 1966, pp. 37-52.

- Kurzin, V. B.: Aerodynamic Interference of Airfoils in a Subsonic Unsteady Flow. Fluid Dyn., vol 1, no. 1, 1966, pp. 81-83. (English translation of article from Izv. Akad. Nauk SSSR, Mekh, Zhidk. Gaza, vol. 1, no. 1, pp. 117-120, 1966.)
- Richardson, J. R.: The Application of the Multhopp-Garner Theory to the Calculation of Control Surface Derivatives. T. O. Rep. No. 135, Fairey Aviat. Co., Ltd. (Hayes, England), Sept. 1954.
- Landahl, M.: Pressure-Loading Functions for Oscillating Wings With Control Surfaces. AIAA J., vol. 6, no. 2, Feb. 1968, pp. 345-348.
- Ashley, Holt: Subsonic Oscillatory or Steady Airloads on Wings With Control Surfaces and Other Discontinuities. AFOSR-68-0419, U.S. Air Force, Dec. 1967.
- Davies, D. E.: Generalized Aerodynamic Forces on a T-Tail Oscillating Harmonically in Subsonic Flow. R. & M. No. 3422, Brit. A.R.C., 1966.
- Stark, Valter J. E.: Aerodynamic Forces on a Combination of a Wing and a Fin Oscillating in Subsonic Flow. SAAB TN 54, Saab Aircraft Co. (Linköping, Sweden), Feb. 1964.
- Vivian, H. T.; and Andrew, L. V.: Unsteady Aerodynamics for Advanced Configurations. Pt. I - Application of the Subsonic Kernel Function to Nonplanar Lifting Surfaces. FDL-TDR-64-152, Pt. I, U.S. Air Force, May 1965.
- Yates, E. Carson, Jr.: A Kernel-Function Formulation for Nonplanar Lifting Surfaces Oscillating in Subsonic Flow. AIAA J., vol. 4, no. 8, Aug. 1966, pp. 1486-1488.
- Landahl, M. T.: Kernel Function for Nonplanar Oscillating Surfaces in a Subsonic Flow. AIAA J., vol. 5, no. 5, May 1967, pp. 1045-1046.

#### Subsonic Discrete-Element Methods

- Hedman, Sven G.: Vortex Lattice Method for Calculation of Quasi Steady State Loadings on Thin Elastic Wings in Subsonic Flow. FAA Rep. 105, Aeronaut. Res. Inst. Swed., 1965.
- Albano, Edward; and Rodden, William P.: A Doublet-Lattice Method for Calculating Lift Distributions on Oscillating Surfaces in Subsonic Flows. AIAA J., vol. 7, no. 2, Feb. 1969, pp. 279-285.

#### Transonic (or Sonic) Lifting-Surface Theory

- Runyan, Harry L.; and Woolston, Donald S.: Method for Calculating the Aerodynamic Loading on an Oscillating Finite Wing in Subsonic and Sonic Flow. NACA Rep. 1322, 1957. (Supersedes NACA TN 3694.)



- Watkins, Charles E.; Runyan, Harry L.; and Woolston, Donald S.: On the Kernel Function of the Integral Equation Relating the Lift and Downwash Distributions of Oscillating Finite Wings in Subsonic Flow. NACA Rep. 1234, 1955. (Supersedes NACA TN 3131.)
- Landahl, Mårten T.: Theoretical Studies of Unsteady Transonic Flow – Part I. Linearization of the Equations of Motion. FFA Rep. 77, Aero. Res. Inst. of Sweden (Stockholm), 1958.
- Landahl, Mårten T.: Unsteady Transonic Flow. Pergamon Press, Inc., 1961.
- Rodemich, E. R.; and Andrew, L. V.: Unsteady Aerodynamics for Advanced Configurations. Pt. II – A Transonic Box Method for Planar Lifting Surfaces. FDL-TDR-64-152, Pt. II, U.S. Air Force, May 1965.
- Olsen, J. J.: Demonstration of a Transonic Box Method for Unsteady Aerodynamics of Planar Wings. AFFDL-TR-66-121, U.S. Air Force, Oct. 1966. (Available from DDC as AD 647 369.)
- Stenton, T. E.; and Andrew, L. V.: Transonic Unsteady Aerodynamics for Planar Wings With Trailing Edge Control Surfaces. AFFDL-TR-67-180, U.S. Air Force, Aug. 1968.
- Andrew, L. V.; and Stenton, T. E.: Unsteady Aerodynamic Forces on a Thin Wing Oscillating in Transonic Flow. AIAA Pap. No. 67-16, Jan. 1967.

#### Supersonic Lifting-Surface Theory

- Miles, John W.: The Potential Theory of Unsteady Supersonic Flow. Cambridge Univ. Press, 1959.
- Watkins, Charles E.; and Berman, Julian H.: On the Kernel Function of the Integral Equation Relating Lift and Downwash Distributions of Oscillating Wings in Supersonic Flow. NACA Rep. 1257, 1956. (Supersedes NACA TN 3438.)
- Pines, Samuel; Dugundji, John; and Neuringer, Joseph: Aerodynamic Flutter Derivatives for a Flexible Wing With Supersonic and Subsonic Edges. J. Aeronaut. Sci., vol. 22, no. 10, Oct. 1955, pp. 693-700.
- Zartarian, Garabed; and Hsu, Pao-Tan: Theoretical Studies on the Prediction of Unsteady Supersonic Airloads on Elastic Wings – Part I. Investigations on the Use of Oscillatory Supersonic Aerodynamic Influence Coefficients. WADC Tech. Rep. 56-97, Pt. I, DDC Doc. No. AD 110 591, U.S. Air Force, Dec. 1955.

- Zartarian, Garabed: Theoretical Studies on the Prediction of Unsteady Supersonic Airloads on Elastic Wings – Part 2. Rules for Application of Oscillatory Supersonic Aerodynamic Influence Coefficients. WADC Tech. Rep. 56-97, pt. II, DDC Doc. No. AD 110 592, U.S. Air Force, Feb. 1956.
- Richardson, J. R.: A Method for Calculating the Lifting Forces on Wings (Unsteady Subsonic and Supersonic Lifting-Surface Theory). R. & M. No. 3157, Brit. A.R.C., 1955.
- Donato, Vincent W.; and Huhn, Charles R., Jr.: Supersonic Unsteady Aerodynamics for Wings with Trailing Edge Control Surfaces and Folded Tips. USAF AFFDL-TR-68-30, Aug. 1968.
- Curtis, Alan R.; and Lingard, Robert W., Jr.: Unsteady Aerodynamic Distributions for Harmonically Deforming Wings in Supersonic Flow. AIAA Pap. No. 68-74, Jan. 1968.
- Moore, M. T.; and Andrew, L. V.: Unsteady Aerodynamics for Advanced Configurations. Pt. IV – Application of the Supersonic Mach Box Method to Intersecting Planar Lifting Surfaces. FDL-TDR-64-152, Pt. IV, U.S. Air Force, May 1965.
- Kacprzynski, J. J.; Ashley, H.; and Sankaranarayanan, R.: On the Calculation of Unsteady Nonlinear Three-Dimensional Supersonic Flow Past Wings. Trans. ASME, Ser. D: J. Basic Eng., vol. 90, no. 4, Dec. 1968, pp. 581-595.

#### Piston Theory

- Lighthill, M. J.: Oscillating Airfoils at High Mach Number. J. Aeronaut. Sci. vol. 20, no. 6, June 1953, pp. 402-406.
- Ashley, Holt; and Zartarian, Garabed: Piston Theory – A New Aerodynamic Tool for the Aeroelastician. J. Aeronaut. Sci., vol. 23, no. 12, Dec. 1956, pp. 1109-1118.
- Chawla, Jagannath P.: Aeroelastic Instability at High Mach Number. J. Aeronaut. Sci., vol. 25, no. 4, Apr. 1958, pp. 246-258.
- Morgan, Homer G.; Huckel, Vera; and Runyan, Harry L.: Procedure for Calculating Flutter at High Supersonic Speed Including Camber Deflections, and Comparison With Experimental Results. NACA TN 4335, 1958.
- Morgan, Homer G.; Runyan, Harry L.; and Huckel, Vera: Theoretical Considerations of Flutter at High Mach Numbers. J. Aeronaut. Sci., vol. 25, no. 4, June 1958, pp. 371-381.

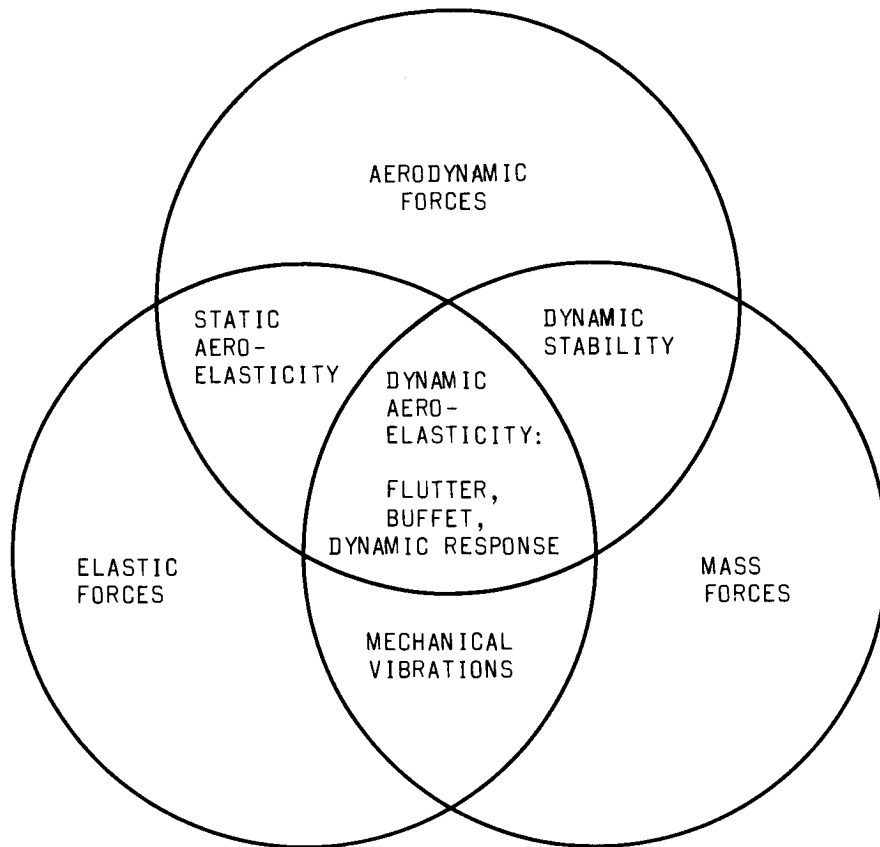


Figure 1.- Three-ring diagram.

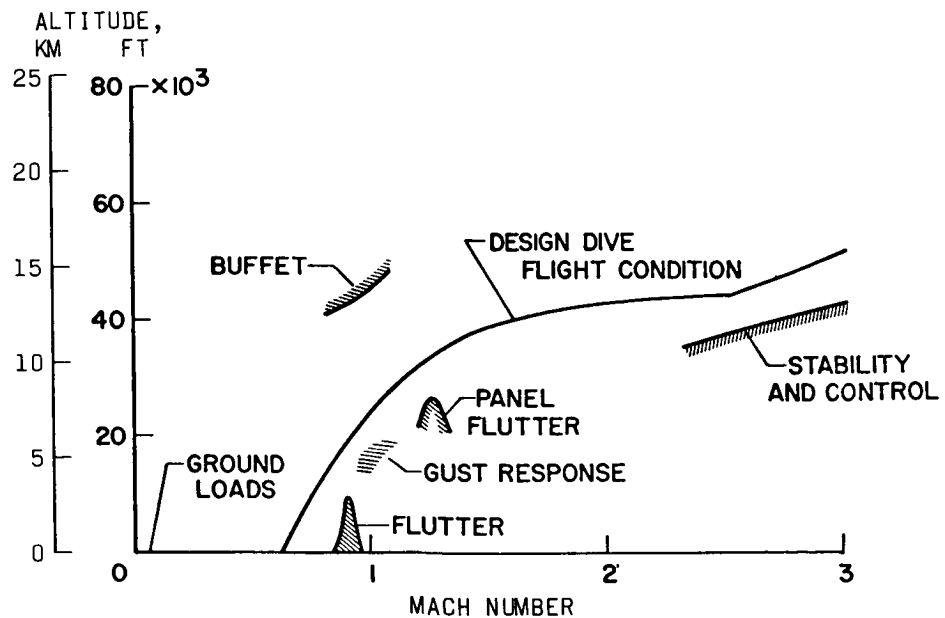


Figure 2.- Aeroelastic problem areas.

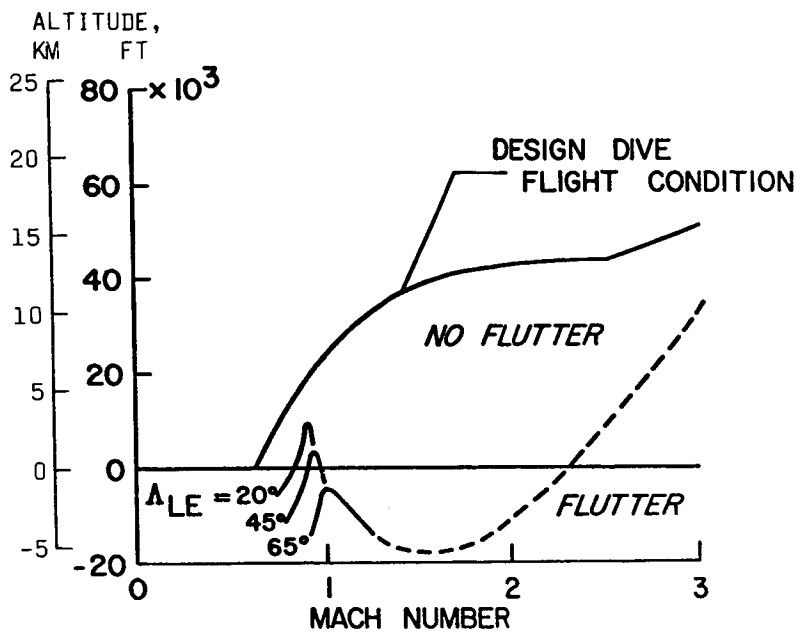


Figure 3.- Flutter boundary.

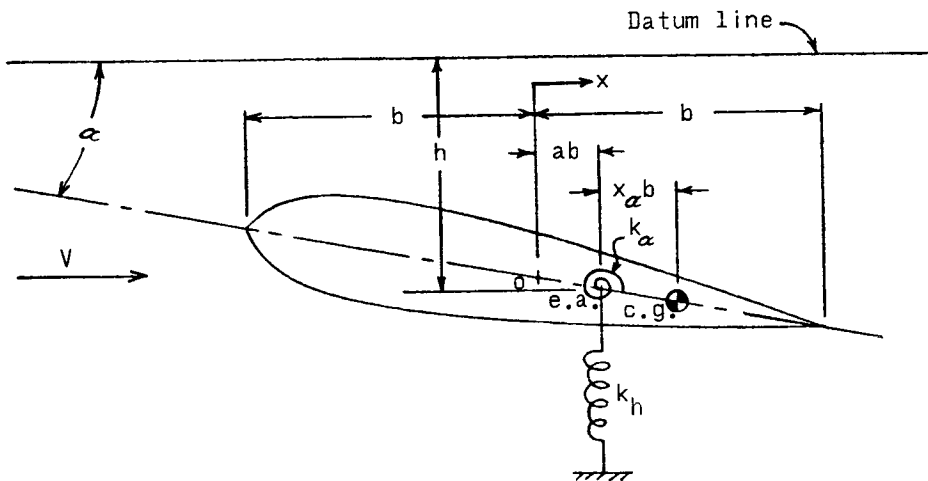


Figure 4.- Two-dimensional airfoil.

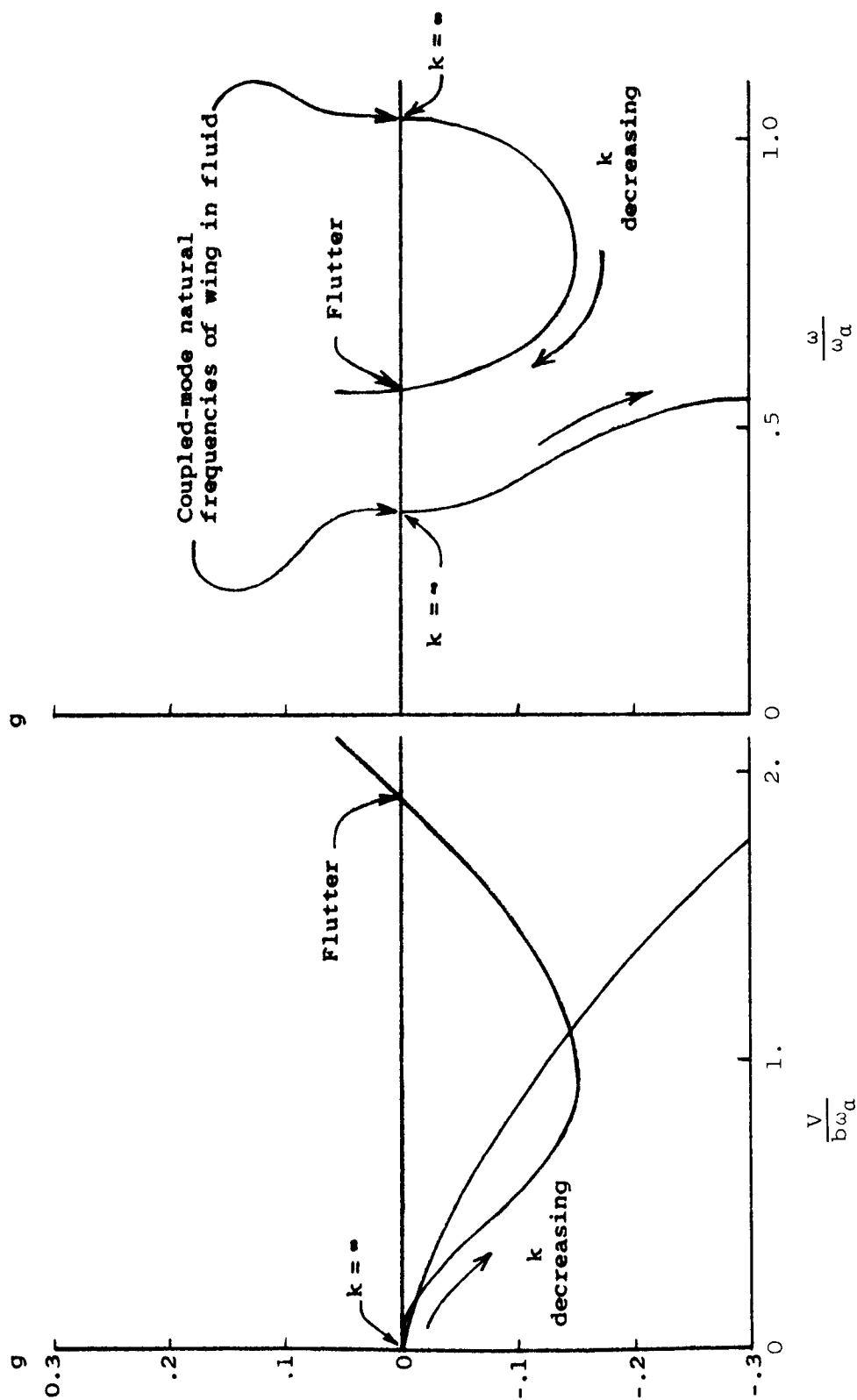


Figure 5.- Determination of flutter point.

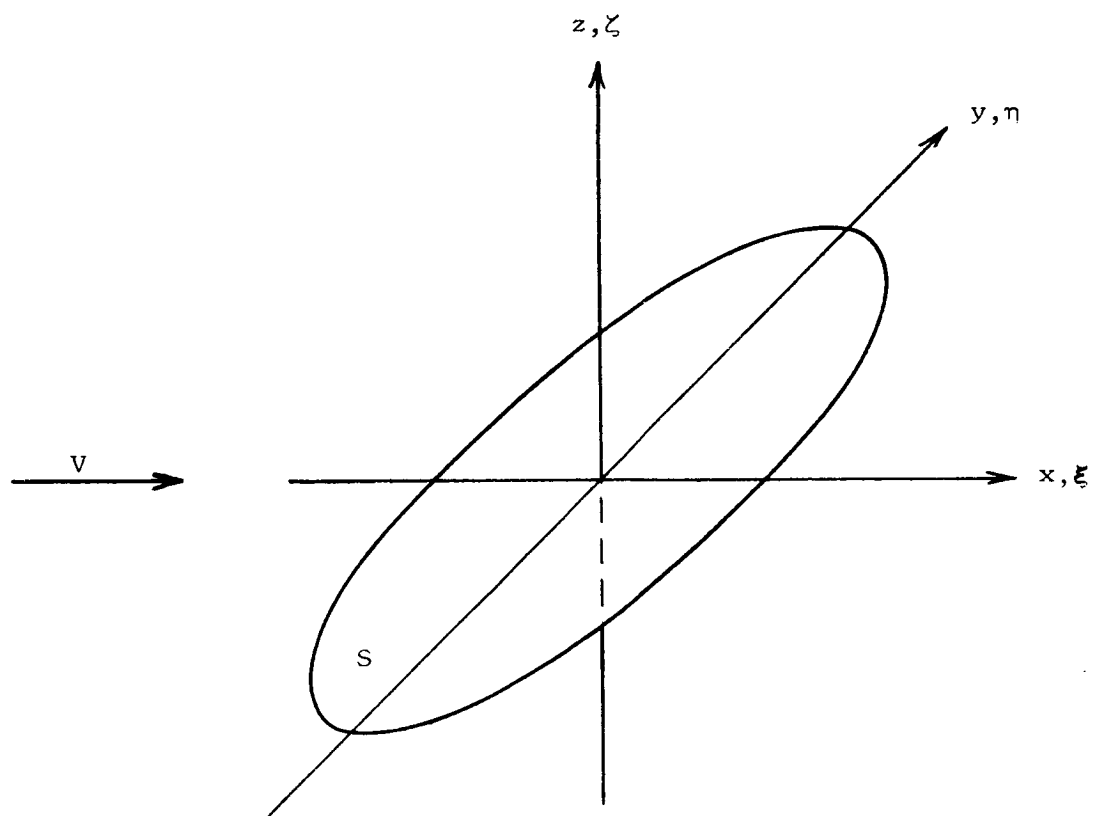


Figure 6.- Wing and coordinates.

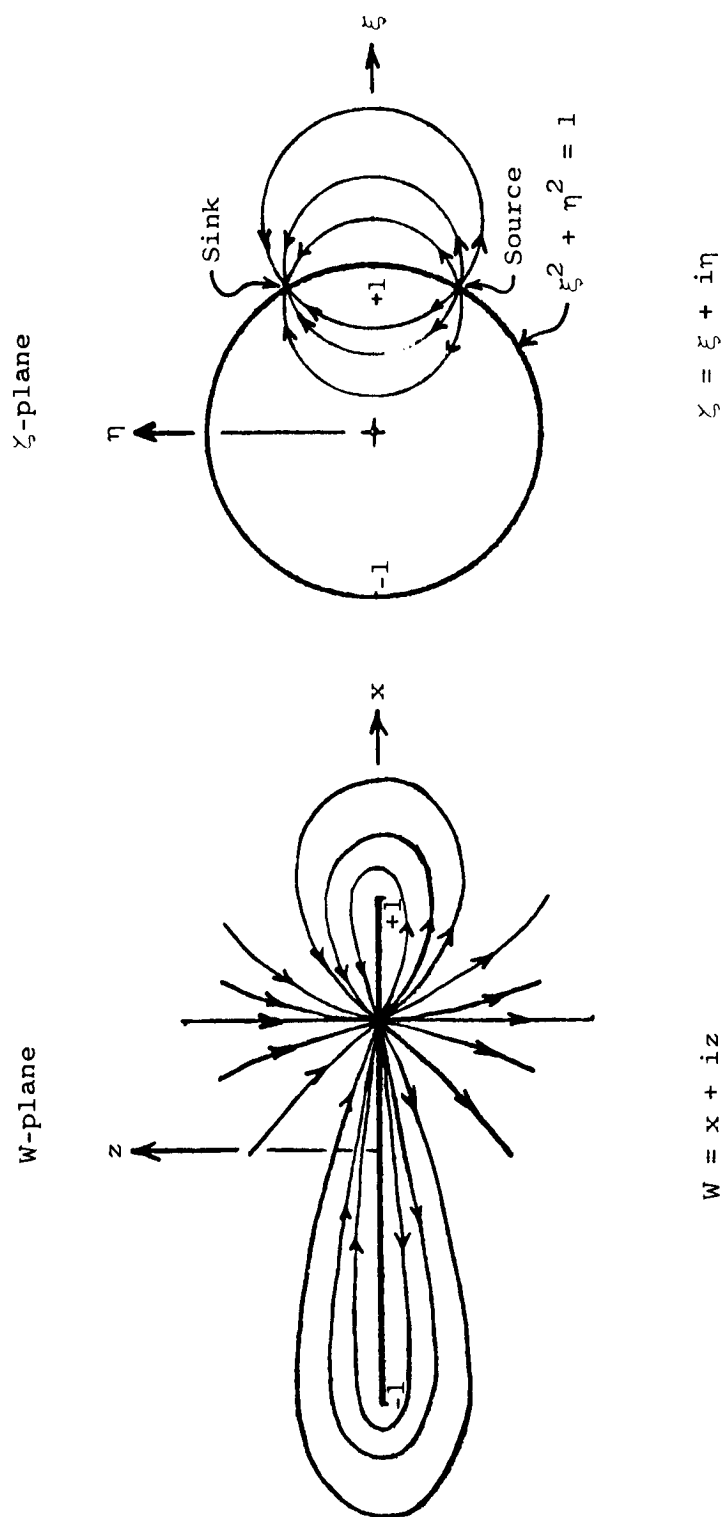


Figure 7.- Representation of airfoil motion by sources and sinks.

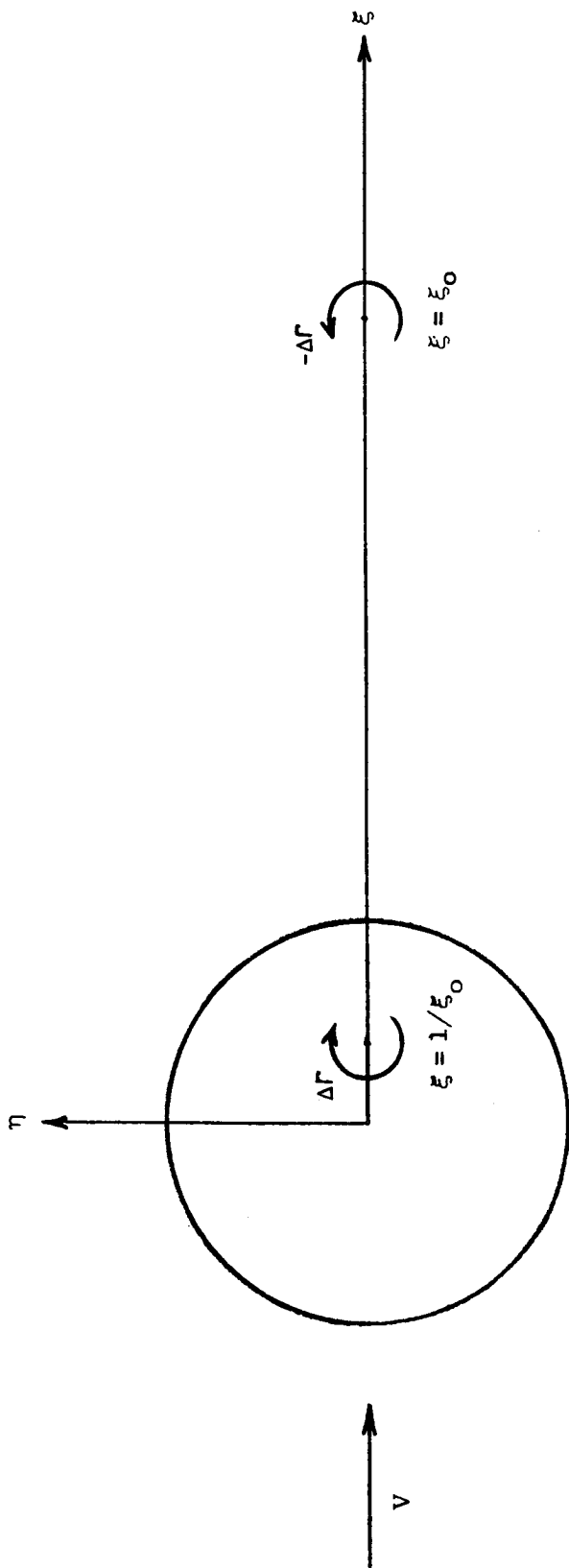


Figure 8.- Shed vortex and image in  $\xi$ -plane.

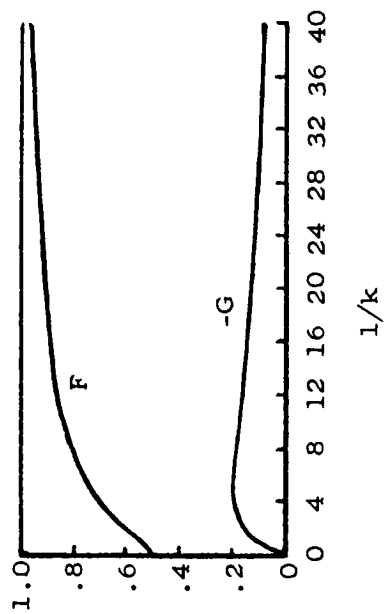


Figure 9.- Real and imaginary components of circulation function  $C(k) = F + iG$ .



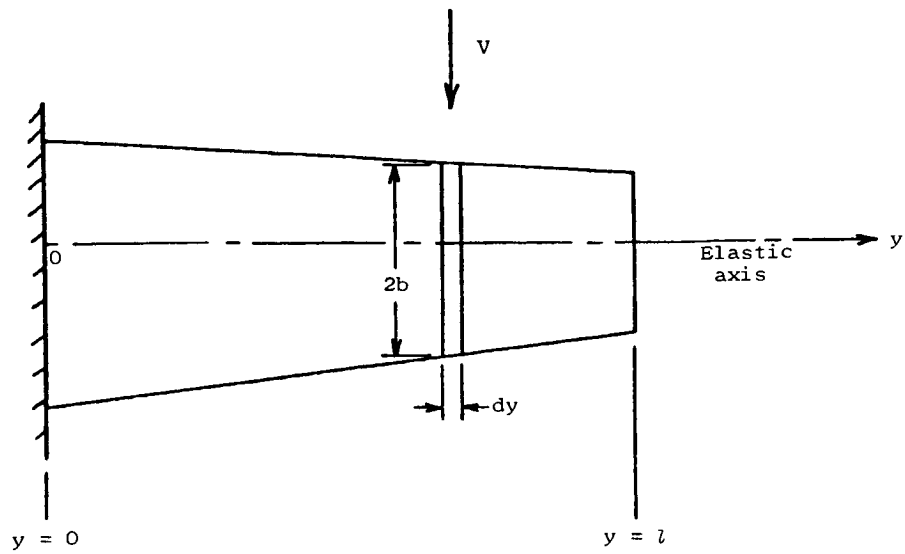


Figure 10.- Strip analysis of three-dimensional wing.

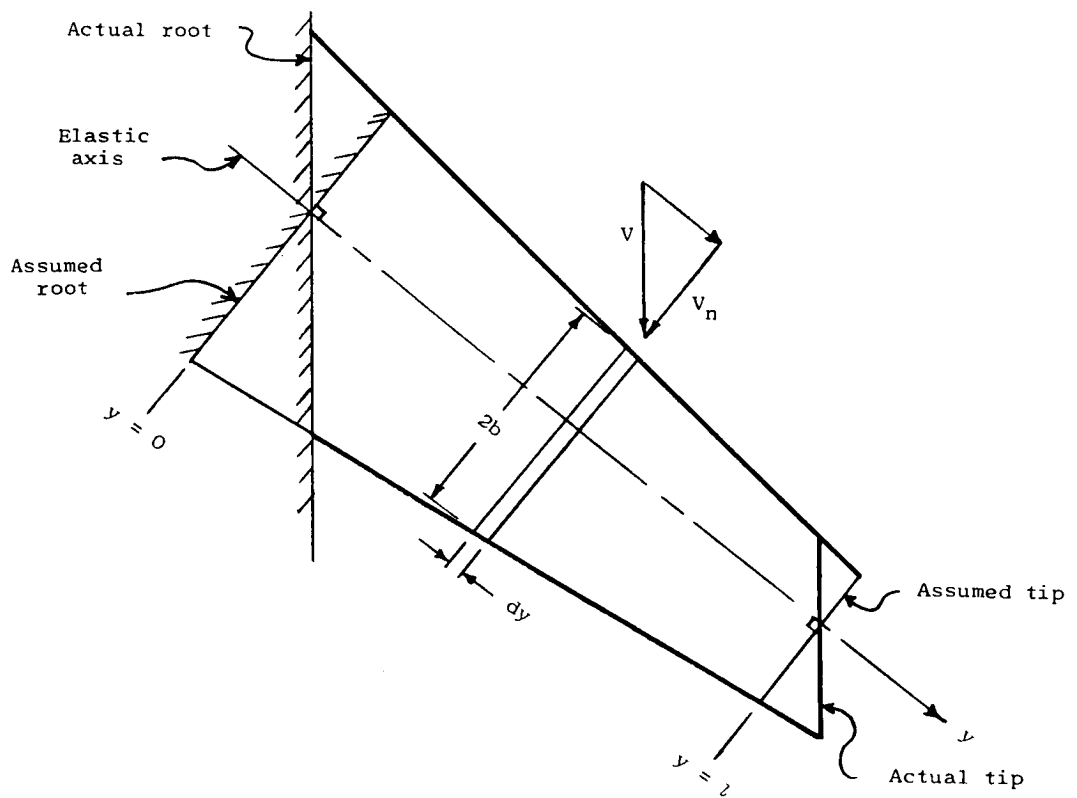
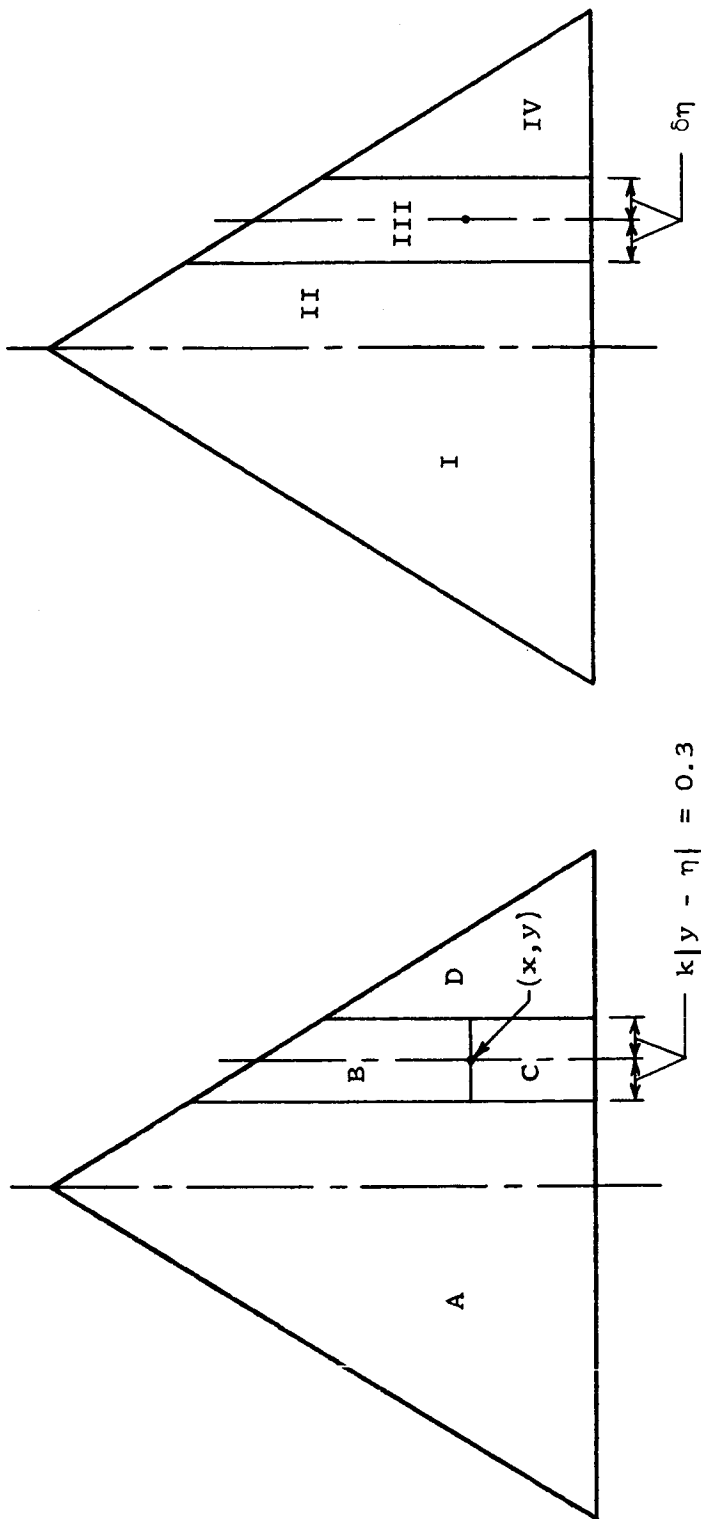


Figure 11.- Type B strip analysis of swept wing.



$$\varphi_n^i(x, y, \eta) = \int_{-1}^1 \sqrt{\frac{1-\xi}{1+\xi}} f_n(\xi) K(x-\xi, y-\eta, k, M) d\xi \quad F_{nm}^i(x, y) = \int_{-1}^1 \sqrt{1-\eta^2} g_m(\eta) \frac{b(\eta)}{b_0} \varphi_n^i(x, y, \eta) d\eta$$

Chordwise integration

Spanwise integration

Figure 12.- Method of integration (refs. 15, 17).

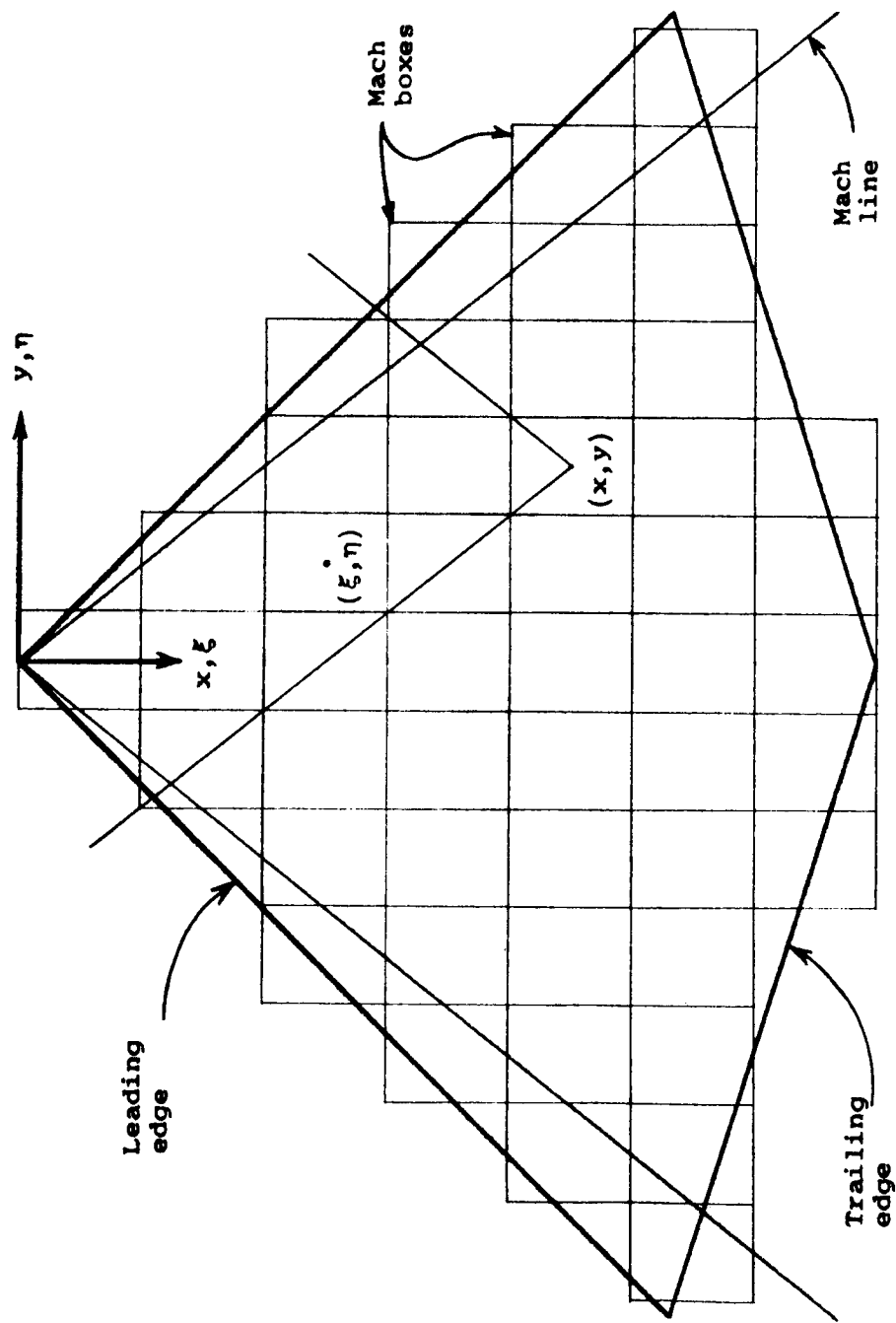


Figure 13.- Mach-box approximation of lifting surface.

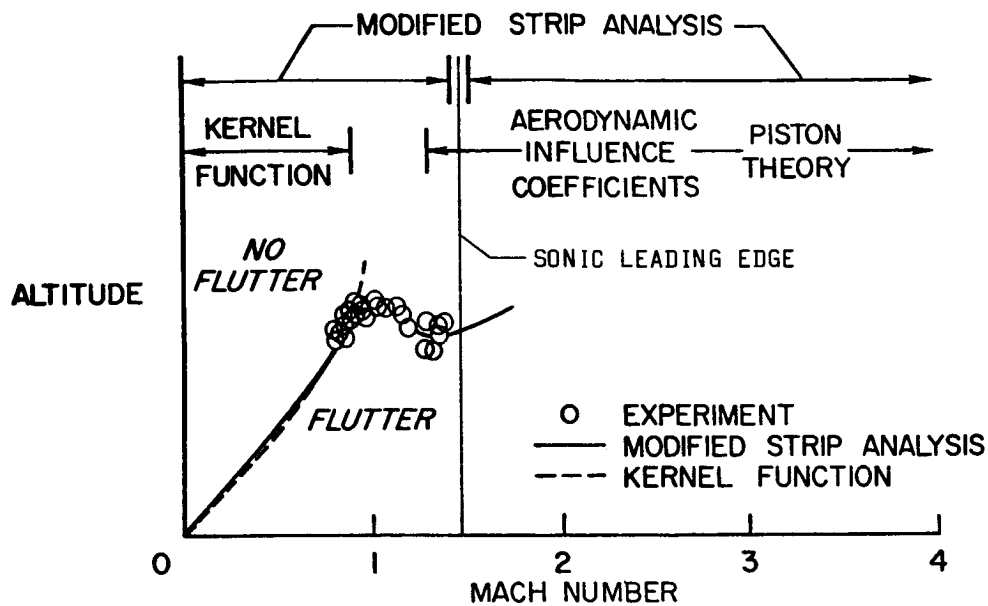


Figure 14.- Comparison of flutter analysis and experiment for swept wing (ref. 1).

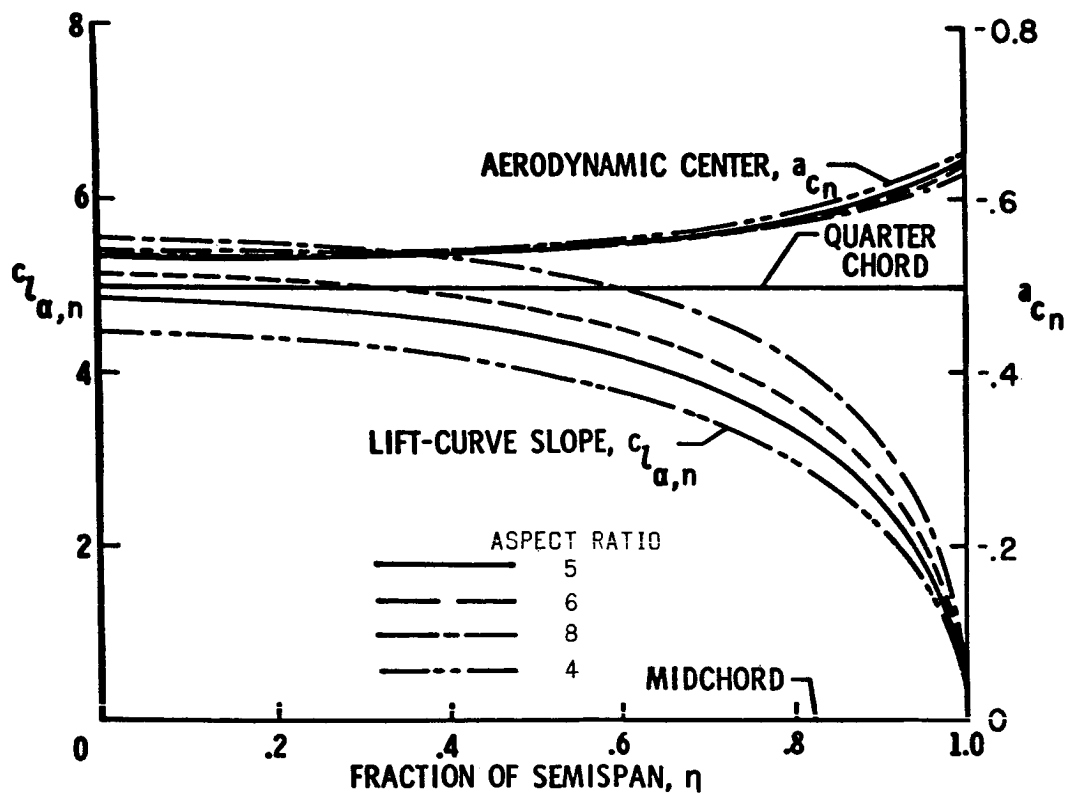


Figure 15.- Aerodynamic parameters for rectangular wings at  $M = 0$  (ref. 14).

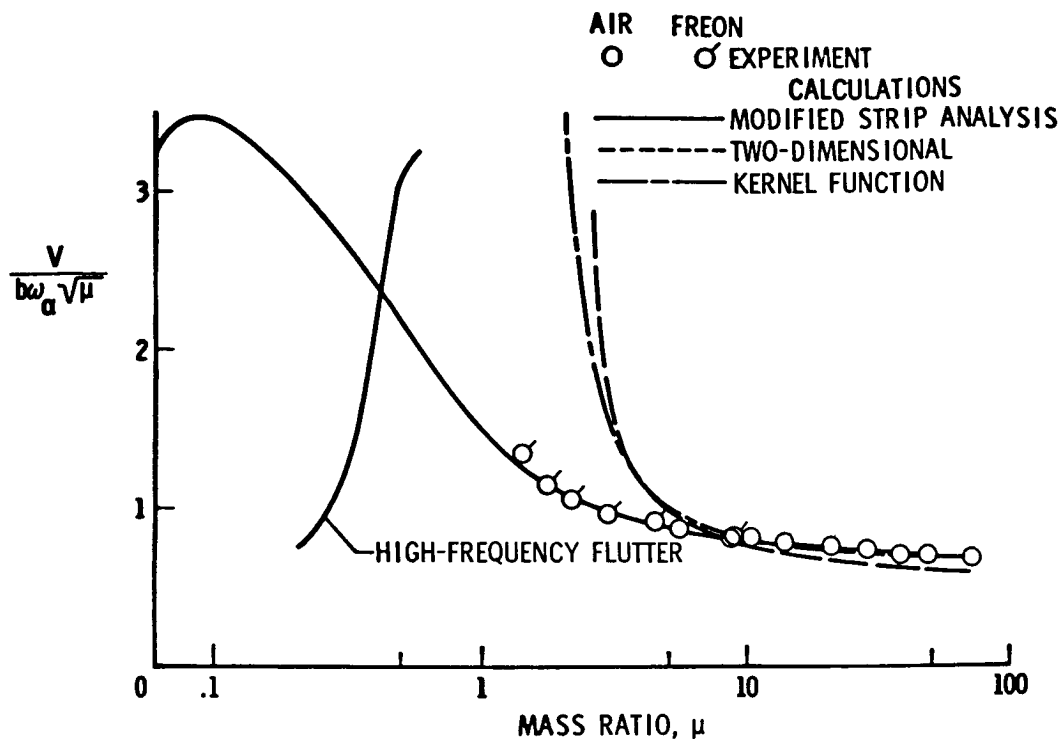


Figure 16.- Flutter-speed index for rectangular wing of aspect ratio 8 at  $M \approx 0$  (ref. 14).

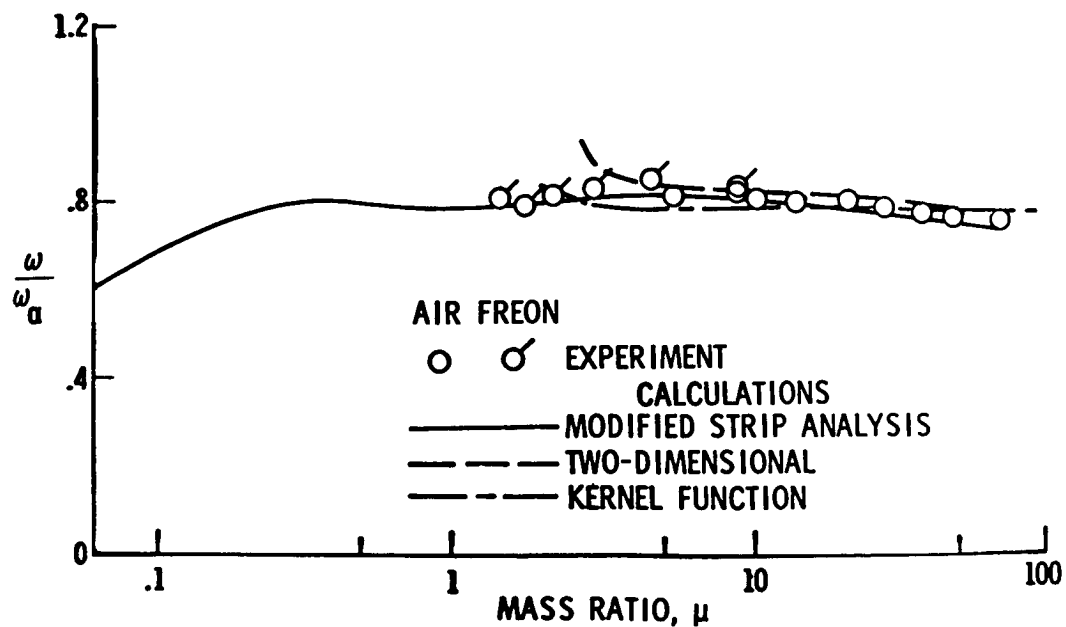


Figure 17.- Flutter-frequency ratio for rectangular wing of aspect ratio 8 at  $M \approx 0$  (ref. 14).

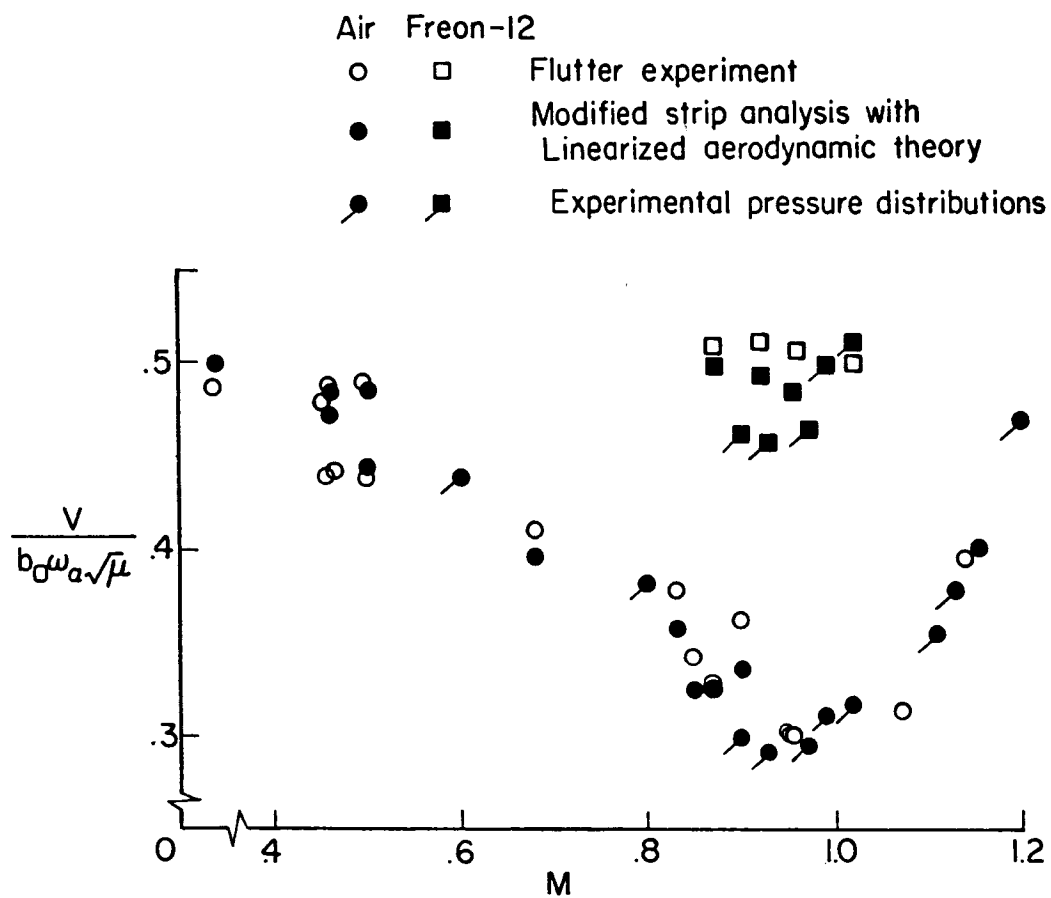


Figure 18.- Flutter of swept wing in air and in Freon-12.  
 $\Lambda_c/4 = 45^\circ$ ,  $\lambda = 0.6$ ,  $A = 4.0$  (ref. 13).

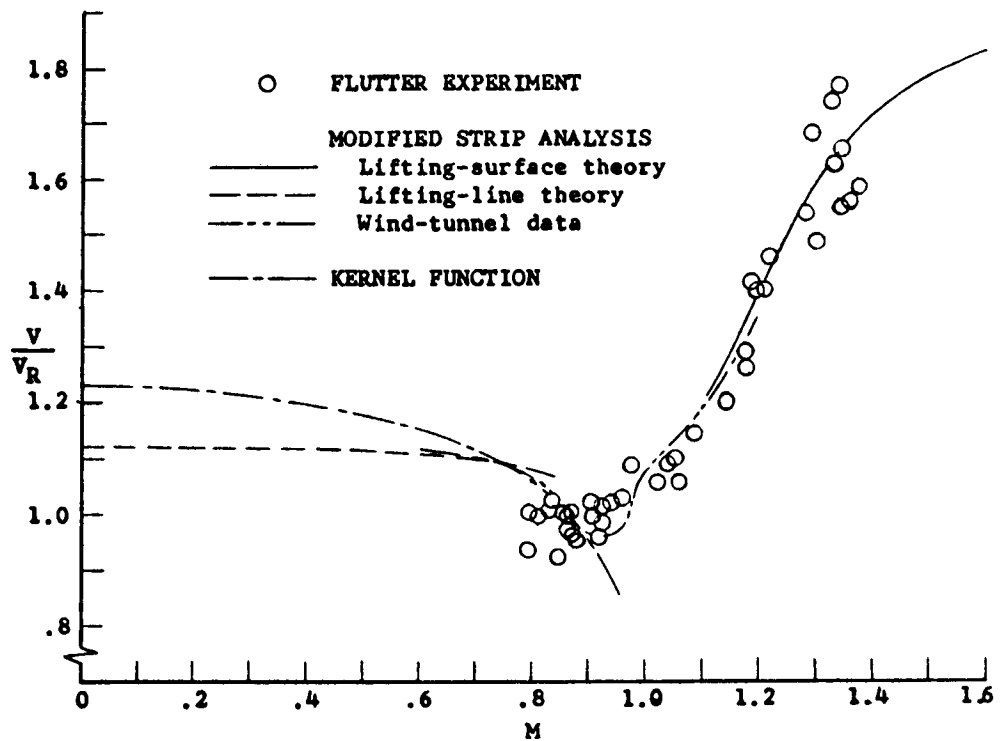


Figure 19.- Flutter of homogeneous swept wing.  
 $\Lambda_c/4 = 45^\circ$ ,  $\lambda = 0.6$ ,  $A = 4.0$  (ref. 11).

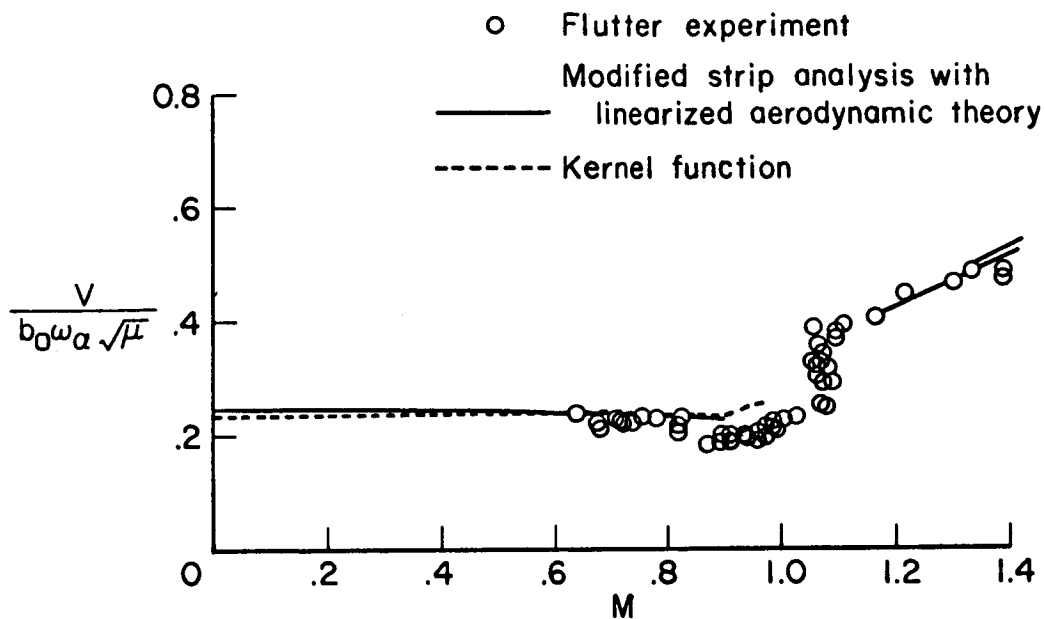


Figure 20.- Flutter of highly tapered swept wing.  
 $\Lambda_c/4 = 45^\circ$ ,  $\lambda = 0.2$ ,  $A = 4.0$  (ref. 13).

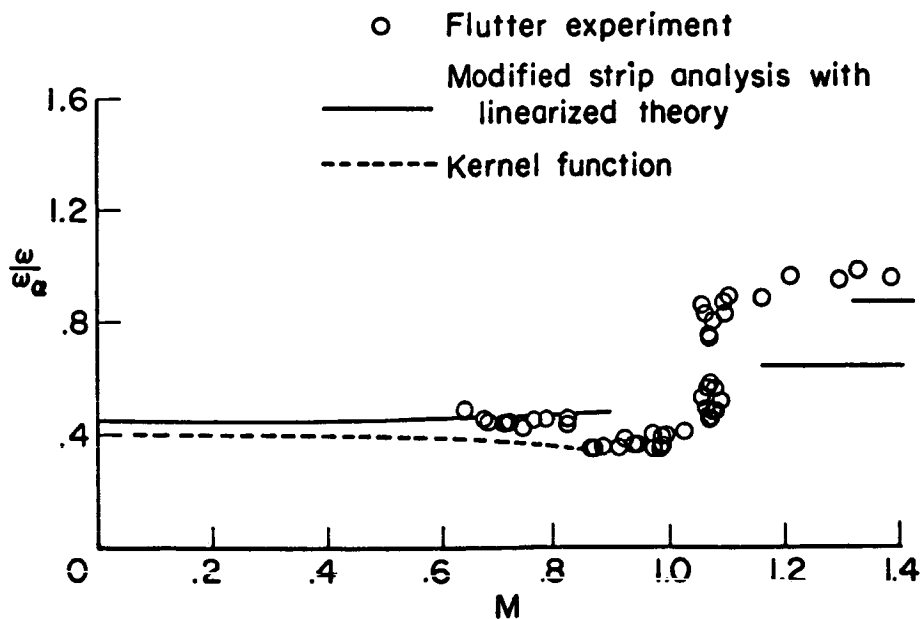


Figure 21.- Flutter frequency of highly tapered swept wing.  
 $\Lambda_c/4 = 45^\circ$ ,  $\lambda = 0.2$ ,  $A = 4.0$  (ref. 13).



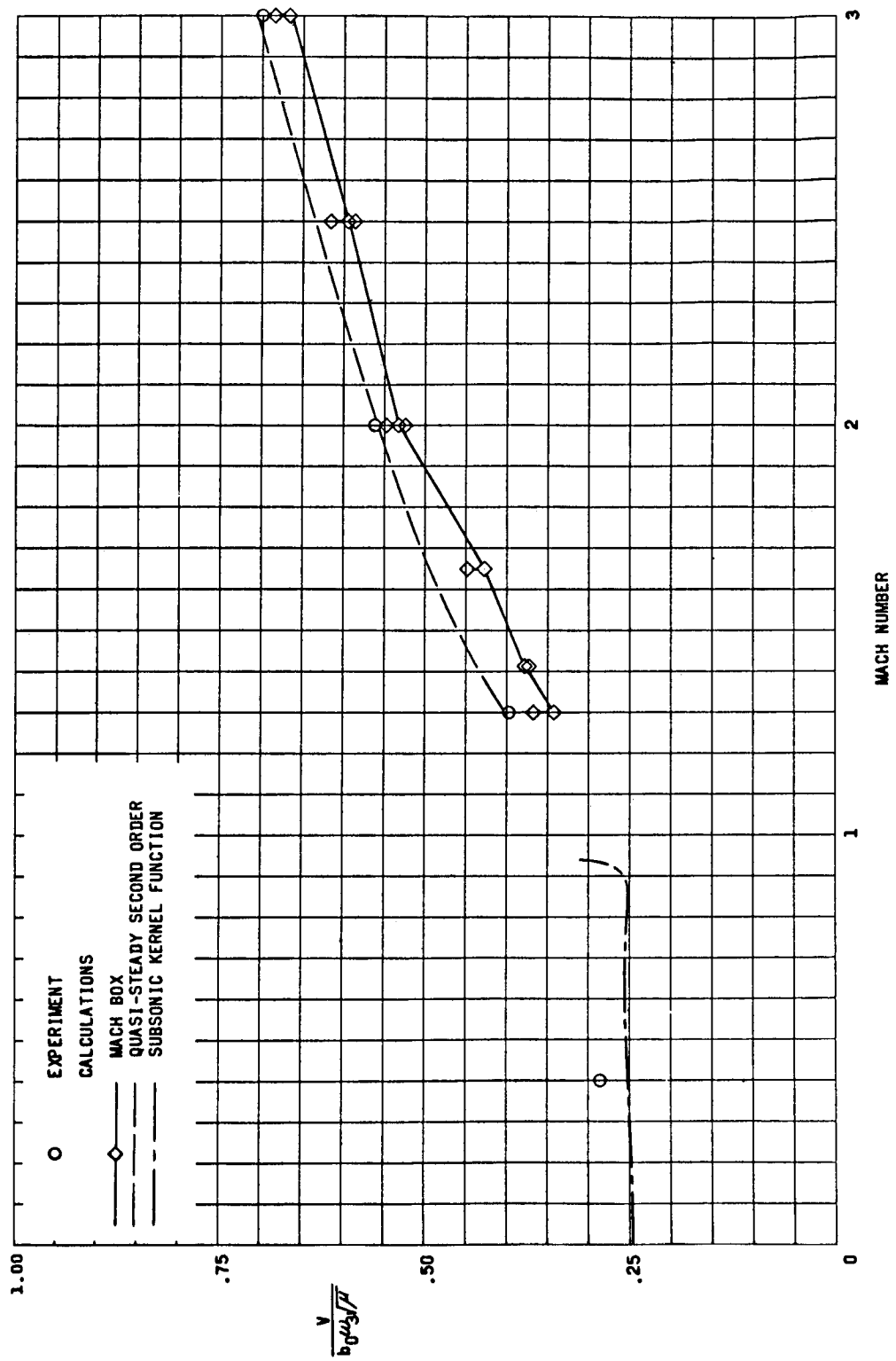


Figure 22.- Flutter-speed index for cantilevered 45° delta wing.

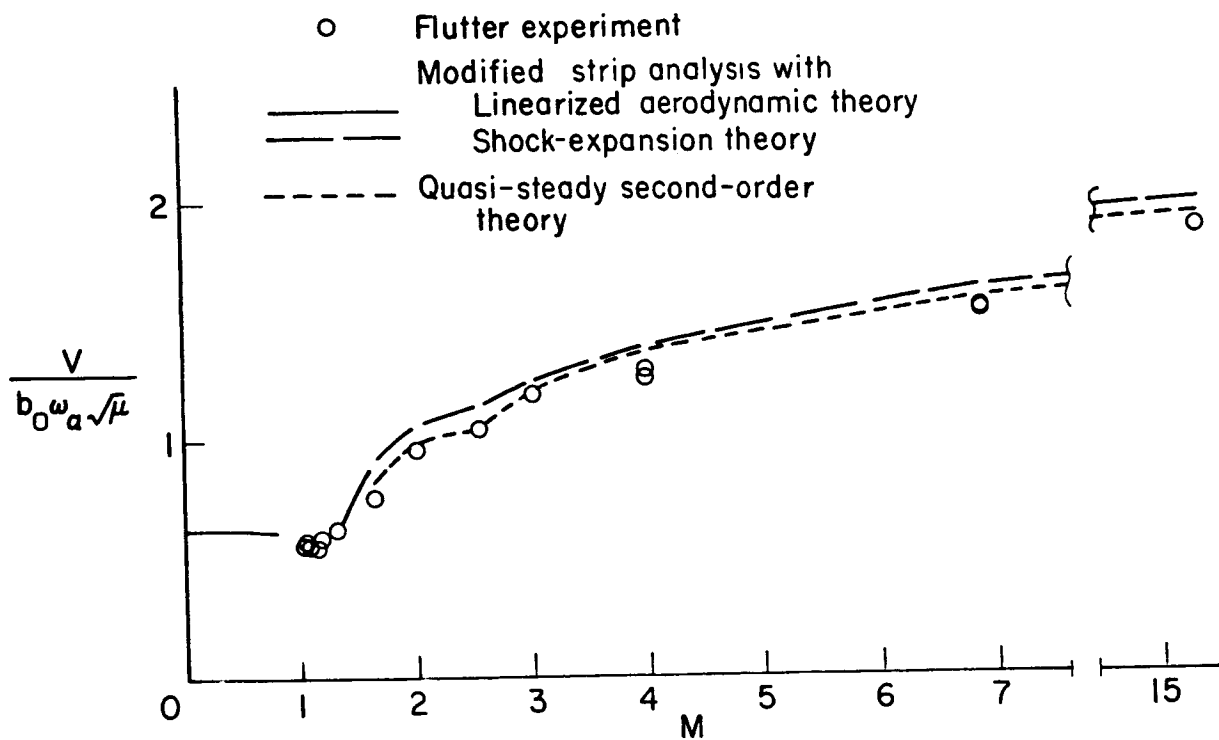


Figure 23.- Flutter of rectangular wing.  $\Lambda_c/4 = 0$ ,  $\lambda = 1.0$ ,  $A = 2.0$  (ref. 13).

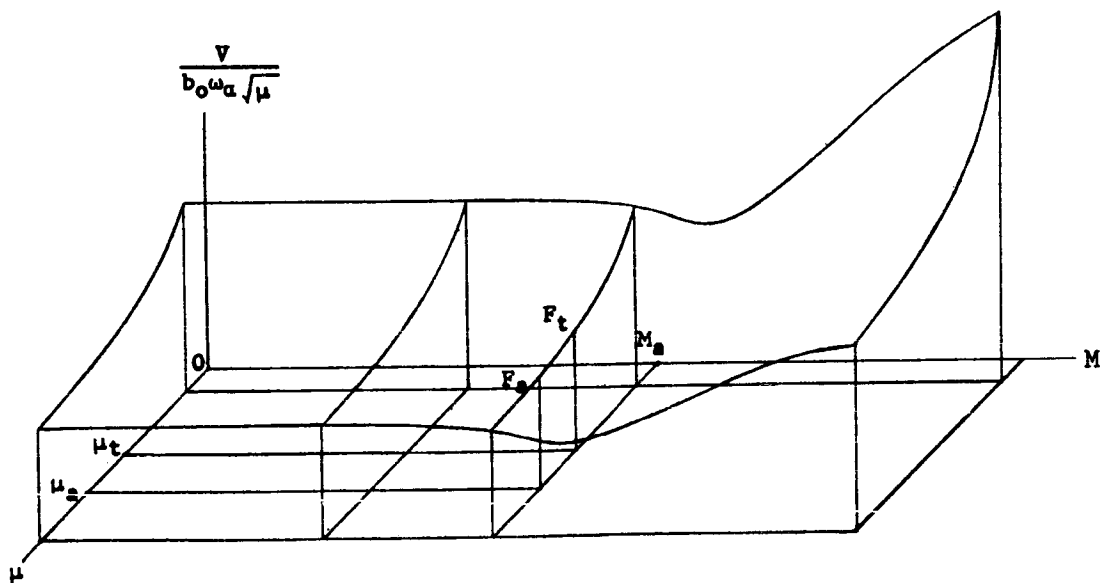


Figure 24.- Typical flutter-speed surface (ref. 12).

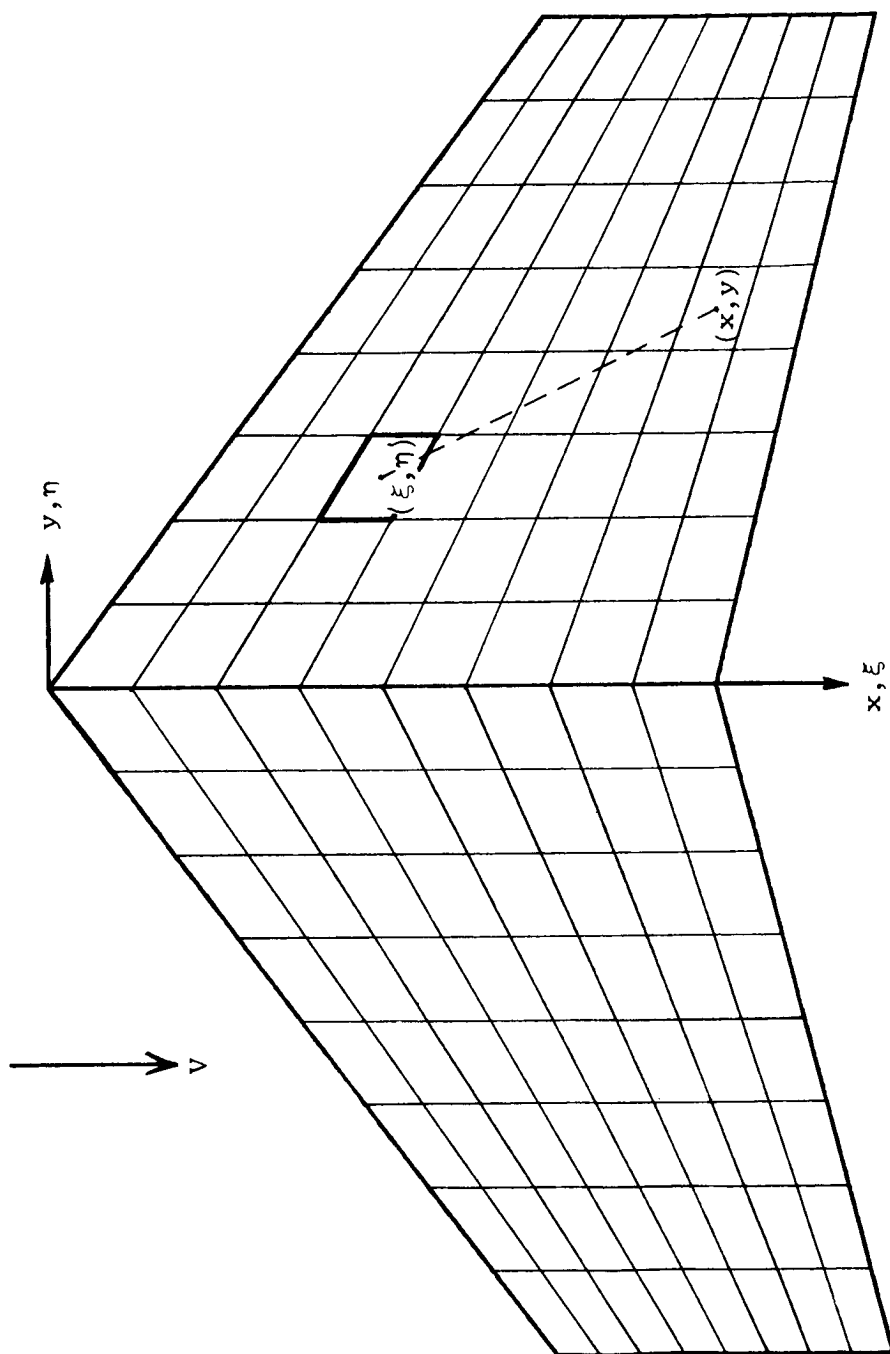


Figure 25.- Subdivision of the lifting surface.

## 6. EFFECTS OF AEROELASTICITY ON STATIC AERODYNAMIC DERIVATIVES

By John E. Lamar  
Langley Research Center

### ABSTRACT

The effects of aeroelasticity on some static longitudinal derivatives are considered in this report as typical problems which the aeroelastician is called upon to solve. Different solution techniques are presented and from these techniques; one, the "force-slope method" (called herein), is selected by which the effects of static aeroelasticity may be computed. In order to use the "force-slope method," the aerodynamic (only subsonic speeds are considered) and structural influence coefficient matrices must first be determined. These methods are developed in some detail, after which solutions for a typical configuration are given.

### INTRODUCTION

The study of static aeroelasticity can be thought of as being divided into at least four parts. In the first part, some of the static aeroelastic problems that engineers are expected to solve are examined and examples are given. In part II, some different prediction methods used to solve the problems outlined earlier are discussed. One of the prediction methods developed is called the "force-slope method" and this method is currently being used at the NASA Langley Research Center. This method, as will be shown, needs an aerodynamic and a structural set of input information. Therefore, in part III, two different methods for predicting subsonic aerodynamics are developed and the accuracy is assessed. (The force-slope method is not limited to subsonic aerodynamics but at this time the supersonic aerodynamic methods at the Langley Research Center have not become operationally compatible with the rest of the force-slope-method solution.) Lastly, part IV presents some derivation of three typical structural analyses employed on airplane configurations and assesses their applicability.

### SYMBOLS

#### English Letters

$a_{n,2m}$	unknown coefficients of surface pressure modes
A	aspect ratio

$$A_{ij} = \sum_n \sum_m (a_{n,2m})_j (b_{n,2m})_i$$

$b$  wing span

$b_o$  wing root semichord

$$b_{n,2m} = \int_{-1}^1 \sqrt{1-\eta^2} \int_0^\pi h_i(\theta, \eta) l_n(\theta) \eta^{2m} \sin \theta \, d\eta \, d\theta$$

$c$  local chord

$c(\eta)$  local half chord

$\bar{c}$  mean geometric chord

$c_l$  section lift coefficient

$c_{m\alpha}$  section pitching-moment-coefficient curve slope about local leading edge

$c_{n\alpha}$  slope of sectional normal-force coefficient

$C_A$  aerodynamic force coefficient

$C_{D,i}$  induced drag coefficient (stagger theorem)

$C_{D,ii}$  induced drag coefficient (thrust concepts)

$C_{L\alpha}$  lift-curve slope

$C_L$  lift coefficient

$$C_{L\delta_e} = \frac{\partial C_L}{\partial \delta_e}$$

$C_{L_i}$  lift coefficient developed by  $i$ th mode

$C_m$  pitching-moment coefficient about  $\bar{c}/4$

$$C_{m,ac\delta_e} = \frac{\partial C_{m,ac}}{\partial \delta_e}$$

$C_N$  normal-force coefficient

$C_T$	thrust coefficient
$C^{\theta\theta}$	flexibility influence coefficient of coiled spring
$d$	perpendicular distance from loading point of wing representable by a slender beam to the elastic axis
$d(\eta)$	x-location of local midchord at $\eta$
$\bar{e}$	chordwise distance between aerodynamic center and elastic axis
$e$	$\bar{e} \cos(\alpha_r + \Delta\alpha) \doteq \bar{e}$ for small angles
$EI$	structural stiffness associated with bending
$F, F_\Sigma$	total flexibilized force
$F_{w,\nu}(x,y;\xi,y_\nu,s_\nu)$	influence function used in vortex-lattice method
$F'_{w,\nu} = (F_{w,\nu})_{\text{left}} + (F_{w,\nu})_{\text{right}}$	
$GJ$	structural stiffness associated with torsion
$h_i(\theta,\eta)$	$i$ th mode shape
$k$	fractional change in either the twist angle or load distribution between consecutive iteration cycles
$l_n(\theta)$	chordwise pressure modes; i.e., $l_0(\theta) = \frac{\cos \theta}{2}$ , $l_1 = \sin \theta$ , etc.
$L$	lift force; Lagrangian
$m$	number of spanwise stations, tip to tip
$m(x,y)$	mass distribution
$M$	moment; Mach number
$M_i$	generalized mass, $\iint_S h_i^2(x,y)m(x,y)dx dy$

$n$	normal direction
$n'_z$	lift/weight
$N$	number of vibration modes; number of chordwise points in Multhopp scheme
$p$	pressure
$q$	dynamic pressure
$q_0(\eta)$	coefficient of $\cot \frac{\theta}{2}$ pressure loading mode
$q_j(\eta)$	coefficient of $\sin j\theta$ pressure loading mode
$q_i, q_j$	ith, jth generalized coordinate
$\bar{q}_j$	cyclic amplitude of jth generalized coordinate
$Q_i$	generalized force
$Q_i^G$	generalized aerodynamic force due to gust, $\iint_S h_i(x,y) \left( \frac{\Delta p^G}{w_G/U} \right) dx dy$
$Q_{ij}^M$	generalized aerodynamic force of the ith wing mode, $\iint_S h_i(x,y) \left( \frac{\partial \Delta p^M}{\partial q_j} \right) dx dy$
$r = \sqrt{(x - \xi)^2 + (y - \eta)^2 + (z - \zeta)^2}$	
$R, R_\Sigma$	total rigid load
$s$	ratio of wing semispan to root semichord; one-half vortex-lattice panel width
$S$	wing area
$S_{ij}$	element in structural slope matrix: slope at $i$ due to a unit load at $j$
$t$	time
$T$	torque
$u$	perturbation velocity component in x-direction

$u_i \Rightarrow$  velocity components in  $x, y, z$  directions ( $U \pm u, v, w$ )

$U$  free-stream velocity; potential energy in a system

$\bar{U}$  strain energy

$v$  perturbation velocity component in  $y$ -direction

$V$  volume

$w$  vertical displacement; also perturbation velocity component in  $z$ -direction

$\bar{w}$  amplitude of cyclic displacement

$W$  weight

$x_i \Rightarrow$  displacement components in  $x, y, z$  directions ( $x, y, z$ )

$x, y, z$  rectangular Cartesian coordinates

$x_0, y_0$  coordinates of elastic axis intersection with fuselage

$x'$  dummy variable in  $x$ -direction

#### Greek Letters

$\alpha$  angle of attack

$\alpha_i$  induced angle of attack

$\alpha_r$  rigid-wing angle of attack

$\gamma, \gamma(\xi), \gamma(\xi, \eta)$  local distributed circulation

$\Gamma, \Gamma(\eta)$  circulation developed over a given chordwise segment,  $\Gamma = - \int_{\xi_0}^{\xi_1} \gamma \, d\xi$

$$\Gamma'_n = \frac{\Gamma_n}{4\pi U}$$

$\delta_e$  elevator deflection angle



$\xi, \eta, \zeta$	a set of distances along the X,Y,Z axes, denote influence or loading-point location
$\Delta C_{L_{n_z}}$	increment in lift coefficient due to a unit load factor
$\Delta p, \Delta p(\vartheta, \eta), \Delta p(\xi, \eta)$	lifting pressure
$\Delta F_\Sigma$	sum of all the forces resulting from flexibility
$\Delta \alpha$	change in angle of attack due to flexibility
$\Delta \alpha_i$	ith incremental twist angle distribution due to flexibility
$\Delta L_{Fi}$	ith incremental twist load distribution due to flexibility
$\theta$	chordwise variable; streamwise slope of mean camber line due to structural flexibility – referenced to rigid wing or airfoil
$\vartheta$	chordwise variable
$\Lambda$	sweep angle (either leading edge or elastic axis), degrees
$\phi_j(y)$	unknown set of polynomial coefficients of the lateral (vertical) displacement of a plate
$\rho$	density of air
$\omega_i$	frequency associated with ith mode shape
$\omega$	circular frequency
$\Omega$	acceleration potential
$\frac{\partial \Delta p^M}{\partial q_j}$	pressure distribution associated with the jth vibration mode
$\bar{\mu}, \bar{\lambda}$	coordinates perpendicular to and along the elastic axis (see fig. 19)

$\bar{\theta}$  slope of mean camber surface in an arbitrary direction due to a (system of) force(s) (see fig. 19)

$\bar{\Omega}$  energy gained in the system by having an external force act upon it

#### Subscripts

ac aerodynamic center

av average

B bending

cp center of pressure

ea elastic axis

F total or combination of rigid and flexible

f flexible results only

G gust

i particular control point; also range index

j particular loading point; also range index

l lower surface

LE leading edge

n particular spanwise value; particular value

R having to do with rigid loadings

r reversal

ref reference

T torsion

TE trailing edge

u	upper surface
wb	wing-body combination
$\nu$	particular vortex-lattice panel
$\infty$	free stream

#### Mathematical

$\nabla^2$	Laplacian operator
$\Delta$	change in
$[ \ ]$	square matrix
$[ \ ]$	diagonal matrix
$\{ \}$	column matrix

#### Matrices

$[A]$	aerodynamic influence coefficient matrix, slope/unit lifting pressure
$[\bar{A}]$	aerodynamic influence coefficient matrix, slope/(unit circulation/free-stream velocity)
$[B]$	area matrix over which the lifting pressure acts
$[\bar{B}]$	kind of area matrix (2 times grid area/grid chord), in units of length
$\{F\}$	total force acting over each grid element, Rigid + Loadings due to flexibility
$[F'_{w,n}]$	aerodynamic influence coefficient matrix, slope/(unit circulation/free-stream velocity)
$[L]$	aerodynamic influence coefficient matrix used in reference 11, slope/unit multiplier of chordwise pressure function

$\{R\}$	rigid loading on each grid element, force
$[S]$	structural-slope matrix, slope/force
$\left\{\frac{w}{U}\right\}$	boundary-condition matrix, local slopes
$\left\{\frac{\Delta w}{U}\right\}$	matrix of changes in downwash due to flexibility
$\{\Delta C_p\}$	lifting pressure coefficients
$\{\Delta F\}$	loadings due to flexibility on each grid element, force
$\{\theta\}$	local structural slope

## I – STATIC AEROELASTIC PROBLEMS

The static aeroelastic problems to be discussed are:

(1) Torsional divergence – Torsional divergence occurs at a flight condition where the air loadings on the elastic wing produce an infinite twist angle. This condition is given in terms of dynamic pressure or airspeed.

(2) Aileron reversal – Aileron reversal is defined as the flight condition at which the aileron becomes ineffective. It is given in terms of a reversal dynamic pressure.

(3) Aerodynamic-center movement and control power – Flexibility affects the pressure loading distribution and consequently the pitching moment and static margin. The designer must know the extent of the changes in static margin in order to determine whether (1) the airplane can be trimmed and (2) whether enough control power is available to meet the required response criteria.

(4) Flexible lift-curve slope – The problem of flexibility relates to the change in  $C_{L\alpha}$  at a given Mach number with variable dynamic pressure  $q$ .

(5) Effect of load factor – The load factor, of course, is related to the effect of inertia and longitudinal maneuvers on the aerodynamic characteristics.

(6) Jig shape and cruise shape – The problem of jig shape is related to how an airplane on the ground must be built so that when it is at its cruise point it has the correct aerodynamic shape. This must be done while keeping in mind that when the airplane is being built, it is supported by the jig so that in essence it is in a zero-gravity environment.

## Torsional Divergence

Two-dimensional wing (or a section on a three-dimensional wing).- If the airfoil shown in figure 1 is used with  $\delta_e = 0$ , an analysis can be developed for the prediction of dynamic pressure required for torsional divergence in the manner of reference 1.

Allowing the rigid airfoil which is attached to a linear coiled spring to develop an air load at the same angle of attack causes the airfoil to change angle of attack by an amount  $\Delta\alpha$ . Let

$$\Delta\alpha = \theta \quad (1)$$

Then, the restoring torque developed by the linear spring is just

$$\Delta M_{ea} = \frac{\theta}{C_{\theta\theta}} = \frac{\Delta\alpha}{C_{\theta\theta}} \neq f_1(q) \quad (2)$$

This relationship is in contrast with the additional moment produced by the increase in angle of attack of

$$\Delta M_{ac} = c_{l_\alpha} \Delta\alpha q c_e = f_2(q) \quad (3)$$

where, by definition, the aerodynamic center is that point on the airfoil that does not experience a change in the pitching moment with a change in the angle of attack. Consequently, the change in pitching moment comes solely from the lift acting at a distance from the point where the moments are to be summed. That is, the lift acts at a distance  $e$  from the elastic axis.

Now, if a plot is made of the amount of restoring moment available due to an increase in angle of attack per increase in angle of attack  $\left(\frac{1}{C_{\theta\theta}}\right)$  as a function of  $q$ , a straight line of zero slope is obtained, since  $\Delta M_{ea} \neq \Delta M_{ea}(q)$  as shown in figure 2. However, the incremental moment resulting from the additional lift produced is seen to be a function of  $q$ .

The  $q$  at which the two curves cross is the divergent dynamic pressure  $q_D$ . After or above this  $q$ , the restoring moment of the wing structure is not sufficient to counteract the lift induced torsions and the wing will therefore twist off. Another way of looking for the divergent dynamic pressure is that given by rewriting equation (2):

$$\theta = C_{\theta\theta} T$$

and defining the total aerodynamic torque as

$$T = (C_{L_e} + C_{m,ac}) q S \quad (4)$$

where  $S$  is the area over which the section characteristics are to be valid. Now, since

$$C_L = C_{L_\alpha}(\alpha_R + \theta) \quad (5)$$

the solution for  $\theta$  can be obtained as follows:

$$\theta = C^{\theta\theta} [C_{L\alpha}(\alpha_R + \theta)e + C_{m,ac}c] qS \quad (6)$$

and

$$\theta(1 - C^{\theta\theta} C_{L\alpha} qSe) = C^{\theta\theta} (C_{L\alpha} \alpha_R e + C_{m,ac} c) qS \quad (7)$$

Therefore,

$$\theta = \frac{C^{\theta\theta} (C_{L\alpha} \alpha_R e + C_{m,ac} c) qS}{1 - C^{\theta\theta} C_{L\alpha} qSe} \quad (8)$$

Now, a value of  $q$  is sought such that an infinite twist angle is produced. Thus, if the denominator of equation (8) is set equal to zero;

$$1 - C^{\theta\theta} C_{L\alpha} qSe = 0 \quad (9)$$

Then, solving for  $q$  gives

$$(q)_{\theta=\infty} = q_D = \frac{1}{C^{\theta\theta} C_{L\alpha} Se} \quad (10)$$

Note that  $q_D = f(C_{L\alpha})$ .

**Three-dimensional wing.-** Torsional divergence for a three-dimensional wing can be found from the force-slope method discussed in a subsequent section either by (1) solving for the  $q$  required to give an infinite twist angle (or pressure) or (2) plotting the ratio of  $C_{L\alpha}$  of the flexible wing to that of the rigid wing as presented in figure 3. The planform shown in this figure has a torsional divergence  $q$  at about 2345 lb/ft<sup>2</sup> (112 278.6 N/m<sup>2</sup>) at  $M = 0.9$ .

**Aileron reversal.-** The load changes produced on the elastically supported rigid wing of figure 1 by an aileron deflection of  $\delta_e$  lead to the following equations (ref. 1):

$$C_L = C_{L\alpha} \theta + C_{L\delta_e} \delta_e \quad (11)$$

$$C_{m,ac} = C_{m,ac\delta_e} \delta_e \quad (12)$$

Following the same line of reasoning used in the second approach for torsional divergence results in

$$\theta = C^{\theta\theta} T = C^{\theta\theta} qS \left[ e(C_{L\alpha} \theta + C_{L\delta_e} \delta_e) + c C_{m,ac\delta_e} \delta_e \right] \quad (13)$$

and

$$\frac{\theta}{\delta_e} = \frac{C^{\theta\theta}_{qS}(eC_{L\delta_e} + cC_{m,ac\delta_e})}{1 - C^{\theta\theta}_{qS}eC_{L\alpha}} = \frac{eC_{L\delta_e} + cC_{m,ac\delta_e}}{\frac{1}{C^{\theta\theta}_{qS}} - eC_{L\alpha}} \quad (14)$$

Substituting equation (14) into equation (11) yields

$$C_L = \left( C_{L\alpha} \frac{\theta}{\delta_e} + C_{L\delta_e} \right) \delta_e = \left[ \frac{C_{L\alpha}(eC_{L\delta_e} + cC_{m,ac\delta_e}) + C_{L\delta_e} \left( \frac{1}{C^{\theta\theta}_{qS}} - eC_{L\alpha} \right)}{\frac{1}{C^{\theta\theta}_{qS}} - eC_{L\alpha}} \right] \delta_e \quad (15)$$

The aileron becomes completely ineffective when  $C_L = 0$ . Thus, setting  $C_L = 0$  gives a solution for the  $q$  at which aileron reversal occurs:

$$C_{L\alpha}(eC_{L\delta_e} + cC_{m,ac\delta_e}) + C_{L\delta_e} \left( \frac{1}{C^{\theta\theta}_{qS}} - eC_{L\alpha} \right) = 0 \quad (16)$$

or

$$C_{L\alpha} cC_{m,ac\delta_e} = - \frac{C_{L\delta_e}}{C^{\theta\theta}_{qS}} \quad (17)$$

Then,

$$q_r = \frac{-C_{L\delta_e}}{C^{\theta\theta}_{qS} C_{L\alpha} C_{m,ac\delta_e} cS} \quad (18)$$

Aerodynamic-center movement and control power.- An example of the fact that the airplane aerodynamic center  $\Delta x_{ac}$  is dependent on flexibility can be seen in figure 4 for several different structural representations when the airplane is at  $M = 0.9$ . The effect of structural representation shown in this figure is discussed in a subsequent section. The design engineer must know whether enough control power, which comes primarily from the horizontal tail, is available to handle any changes in the stability level brought about because of flexibility.

Flexible lift-curve slope.- An example of the fact that the lift-curve slope is also dependent on flexibility can be seen in figure 5 for an airplane wing at  $M = 0.9$ . Again the effect that the structural representation has on the variation of  $(C_{L\alpha})_F / (C_{L\alpha})_R$  is discussed in a subsequent section.

Effect of load factor.- From figure 6 the effect of including the weight at a load factor  $n'_z$  of 1 can be seen to provide what is called an "inertial relief" on the center of

pressure movement due to flexibility for this wing at  $M = 0.9$ . The reason for this effect is that since the weight acts (for small angles of attack) in a direction opposite to that of the lift, its effects on the structure are qualitatively in the opposite sense as the lift induced deflections and slope change.

Jig shape and cruise shape.- Now the last listed static aeroelastic problem is considered; that of going from the zero-gravity airplane shape in the jig to the desired cruise shape where it is to be acted upon by both air and gravity forces. Figure 7 plots the airfoil coordinates  $z/c$  and  $x/c$  at the spacewise station  $2y/b = 0.6925$  and is an extreme example of the changes in shape that a lightly loaded variable-sweep transport can undergo due to the air and gravity forces. (See ref. 2.) It can be seen in this example that the wing experiences both a change in its camber shape and twist angle at the section shown; whereas the tail undergoes primarily a change in the twist angle. Knowledge of the correct jig shape is particularly important for this configuration since the wing and tail were to be held together coplanarly in the cruise shape by a vee-shaped shear tie.

Some static aeroelastic problems and procedures for finding two-dimensional solutions of them have been examined in this section. Solutions valid for three-dimensional wings are taken up in the next section.

## II - METHODS FOR PREDICTING AEROELASTIC EFFECTS

In this part of this report some particular methods of predicting the effects of aeroelasticity are examined. The first method is that of iteration and is one which might first be considered in an effort to relate the aerodynamic loadings to the structural displacement or slope changes. The second method is the reference-surface method, which is a kind of similarity relationship and not too well known. Its main ideas are mentioned in this section so as to acquaint the reader with yet another method that one airplane company has used in determining the aeroelastic effects. Next the modal approach, which is in wide usage among people solving the flutter problem, will be adapted to solving the static problem. The last method is called the force-slope method and is one that is in use at the Langley Research Center in predicting aeroelastic effects.

### Iteration Method

From reference 3, the iteration scheme is described as follows: "If an initial (rigid)\* load is applied to a lifting surface, the structure deforms causing an incremental change in the angle of attack, i.e., a twist angle. The twist angle produces an incremental change in lift, i.e., a twist load. The twist load in turn causes another incremental angle of attack change, which produces another incremental twist load. This procedure continues

---

\*Rigid Load means airload resulting from rigid wing.



until equilibrium is reached. The total twist angle is then the sum of all the incremental twist angles, and the total lift is the initial (rigid) lift plus the sum of the incremental twist loads." Slender beam analysis was used in this reference and no chordwise bending (camber) was considered.

The iteration procedure mathematically, according to reference 3, looks like

$$\begin{array}{ccccccc} L_R/q & & \Delta L_{F1}/q^2 & & \Delta L_{F2}/q^3 & & \Delta L_{Fn}/q^{n+1} \\ & \searrow & \nearrow & \searrow & \nearrow & \searrow & \nearrow \\ & \Delta\alpha_1/q & & \Delta\alpha_2/q^2 & & \Delta\alpha_n/q^n & \end{array} \quad (19)$$

because lift over  $q$  rather than lift itself is the quantity applied to the structure in reference 3.

Summing the above terms leads to

$$\frac{L_{total}}{q} = \frac{L_R}{q} + q \frac{\Delta L_{F1}}{q^2} + q^2 \frac{\Delta L_{F2}}{q^3} + \dots + q^n \frac{\Delta L_{Fn}}{q^{n+1}} \quad (20)$$

$$\frac{\Delta\alpha_{total}}{q} = \frac{\Delta\alpha_1}{q} + q \frac{\Delta\alpha_2}{q^2} + \frac{q^2 \Delta\alpha_3}{q^3} + \dots + q^{n-1} \frac{\Delta\alpha_n}{q^n} \quad (21)$$

Because successive iteration can run into excessive time and cost, the sums of the series based upon knowledge of only a few terms were sought. A good approximation for the  $(n+1)$  term of the series is given by

$$\frac{\Delta L_{Fn}}{q^{n+1}} = \frac{k}{q} \frac{\Delta L_{Fn-1}}{q^n} \quad (22)$$

where  $k/q$  is dependent on the ability of the airplane structure to resist twisting, and its determination is discussed in a subsequent section.

Reference 3 further states that: "The validity of this relation lies in the assumption that successive twist load distributions (and therefore successive twist angle distributions) are of similar shape, an assumption which has been proved reasonable."

Hence

$$\frac{L_{total}}{q} = \frac{L_R}{q} + q \frac{\Delta L_{F1}}{q^2} + q^2 \left(\frac{k}{q}\right) \left(\frac{\Delta L_{F1}}{q^2}\right) + q^3 \left(\frac{k}{q}\right) \left(\frac{k}{q}\right) \left(\frac{\Delta L_{F1}}{q^2}\right) + q^4 \left(\frac{k}{q}\right) \left(\frac{k}{q}\right) \left(\frac{k}{q}\right) \left(\frac{\Delta L_{F1}}{q^2}\right) + \dots \quad (23)$$

$$\frac{L_{total}}{q} = \frac{L_R}{q} + \frac{\Delta L_{F1}}{q^2} \left[ q + q^2 \left(\frac{k}{q}\right) + q^3 \left(\frac{k}{q}\right)^2 + q^4 \left(\frac{k}{q}\right)^3 + \dots \right] \quad (24)$$

But,

$$\frac{q}{1 - \frac{k}{q} q} = q + \frac{k}{q} q^2 + \left(\frac{k}{q}\right)^2 q^3 + \left(\frac{k}{q}\right)^3 q^4 + \dots \quad (25)$$

Hence,

$$\frac{L_{total}}{q} = \frac{L_R}{q} + \frac{\Delta L_{F1}}{q^2} \left( \frac{q}{1 - \frac{k}{q} q} \right) \quad (26)$$

Similarly,

$$\frac{\Delta \alpha_{total}}{q} = \frac{\Delta \alpha_1}{q} \left( \frac{1}{1 - \frac{k}{q} q} \right) \quad (27)$$

Thus, only two iterations are needed to find convergence or the sum of the series, since  $k/q$  can be found from two trials. Recognizing that  $L_{total} = L_F$  yields

$$\frac{L_F/q}{L_R/q} = 1 + \underbrace{\frac{\Delta L_{F1}/q^2}{L_R/q}}_{\text{1st cycle}} \underbrace{\left( \frac{q}{1 - \frac{k}{q} q} \right)}_{\text{Convergence}} \quad (28)$$

Net flexible loss

This relationship is shown graphically in figure 8. Thus the change in the lift or lift coefficient due to flexibility has been determined.

From reference 3, it is noted that: "Similar expressions may be readily developed for flexible-to-rigid ratios of rolling moment and pitching moment."

#### Reference Surface Method

The reference surface method, a kind of similarity relationship, is also defined in reference 3, where it is based on the iteration method and the measured flexible-to-rigid aerodynamic ratios of a known wing. These ratios are adjusted to account for the differences in geometry, stiffness, and design load requirement between the known wing and the wing being designed. The adjustments are made by computing an effective  $k/q$  for each wing which even accounts for some torsional effects and then correcting the "net flexible loss" by the following procedure:

Equation (28) can be written as

$$\left( 1 - \frac{L_F}{L_R} \right) = - \left( \frac{\Delta L_{F1}/q}{L_R} \right) q \left( \frac{1}{1 - \frac{k}{q} q} \right) \quad (29)$$

From reference 3, the parameter  $k/q$  is shown to be related to the ability of the structure to resist a twist load and  $\frac{\Delta L_F 1/q}{L_R}$  to the ability of the structure to resist the rigid load. In cases where the rigid load distribution is very similar to that of the twist load,  $\frac{\Delta L_F 1/q}{L_R}$  and  $k/q$  will approach each other numerically. In the more general case, they will be very different. Hence, an "effective" stiffness is determined not only by actual stiffness but also by the distribution of the applied load. Thus,

$$\frac{\left(1 - \frac{L_F}{L_R}\right)_{\text{new}}}{\left(1 - \frac{L_F}{L_R}\right)_{\text{old}}} = \frac{\left(\frac{k}{q}\right)_{\text{new}} \left(\frac{1}{1 - \frac{k}{q}}\right)_{\text{new}}}{\left(\frac{k}{q}\right)_{\text{old}} \left(\frac{1}{1 - \frac{k}{q}}\right)_{\text{old}}} \quad (30)$$

and so  $\left(\frac{L_F}{L_R}\right)_{\text{new}}$  may be found. Reference 3 gives details for computing  $(k/q)$  by equations and graphs.

#### Modal Approach

Following the approach presented by Dr. E. Carson Yates in paper number 5 which involves Lagrange's equation and also the approach of reference 4 permits equations of motion to be written for the case of a wing which has no damping, as follows:

$$M_i \ddot{q}_i + \omega_i^2 M_i q_i = Q_i = Q_i^M + Q_i^G = \sum_{j=1}^N Q_{ij}^M q_j + Q_i^G \quad (31)$$

where these symbols are defined in the symbol list. Now, employing the concepts of reference 5 yields

$$Q_{ij}^M = 8\pi q b_0 s^2 A_{ij} \quad (32)$$

where

$$A_{ij} = \sum_n \sum_m (a_{n,2m})_j (b_{n,2m})_i \quad (33)$$

The  $b_{n,2m}$  can be calculated for each vibration mode from the definition:

$$b_{n,2m} = \int_{-1}^1 \sqrt{1-\eta^2} \int_0^\pi h_i(\theta, \eta) l_n(\theta) \eta^{2m} \sin \theta \, d\theta \, d\eta \quad (34)$$

The  $a_{n,2m}$  terms are calculated for each mode in the subsonic kernel-function program described in reference 5, where orthogonal vibration modes are actually used in the analysis. In the preceding report by Dr. Yates, the unknown deformed shape of the wing is assumed to be made up of a linear combination of the vibration modes. The vibration modes are used here in the static case only because they constitute a complete set of deformation shapes and hence they can accurately fit any resultant deformation shape. Their use here does not relate to dynamics problems. It is convenient for analysis purposes to let

$$Q_i^G = Q_{i(N+1)}^M \quad (35)$$

and

$$\frac{w_G}{U} = q_{N+1} \quad (36)$$

For steady flight the gust is just equal to  $\alpha$ , and is taken for convenience to be at 1 radian. Hence, combining equations (31) and (32) gives:

$$\left. \begin{aligned} (-8\pi q b_o s^2 A_{11} + \omega_1^2 M_1) \bar{q}_1 + (-8\pi q b_o s^2 A_{12}) \bar{q}_2 - \dots &= 8\pi q b_o s^2 A_{1(N+1)} \frac{\bar{w}_G}{U} \\ (-8\pi q b_o s^2 A_{21}) \bar{q}_1 + (\omega_2^2 M_2 - 8\pi q b_o s^2 A_{22}) \bar{q}_2 - \dots &= 8\pi q b_o s^2 A_{2(N+1)} \frac{\bar{w}_G}{U} \\ \vdots &\vdots \\ \vdots &\vdots \\ \vdots &\vdots \end{aligned} \right\} \quad (37)$$

where

$$q_i = \bar{q}_i e^{i\omega t} \quad (38)$$

and  $\omega$  is the frequency of gust input (0 for this case). Solving this linear set of equations for  $\bar{q}_i$  indicates how much of each mode's results belong in the final answer. That is, for example:

$$C_L = C_{L1} \bar{q}_1 + C_{L2} \bar{q}_2 + \dots + C_{L\alpha} \frac{\bar{w}_G}{U} \quad (39)$$

and so, if  $\bar{w}_G/U$  is set equal to 1

$$C_{L\alpha, F} = C_{L\alpha 1} \bar{q}_1 + C_{L\alpha 2} \bar{q}_2 + \dots + C_{L\alpha} \quad (40)$$

The other aerodynamic characteristics of interest can be calculated in a similar manner. A similar method has already been developed and appears in reference 6. This approach can be characterized by asking the question: How much of the lifting pressure generated

by the wing in each of its basic modes of vibration plus that of the rigid wing in a uniform flow field is required to bring the flexible wing into equilibrium?

### Force-Slope Method

The force-slope method is a closed-form solution for predicting the aeroelastic effects. However, whether the solution simply employs matrix-inversion concepts (as will be developed) or must be handled in an interpolative sense (as in least-squares method) depends on the relationship between the aerodynamic and structural paneling methods. If they are the same then a simple matrix inversion may be used, otherwise an interpolative process must be used.

The force-slope method can be developed in the following manner (which follows basically the method of ref. 7) by making use of four basic aerodynamic and structural relationships expressed in matrix form:

(1) Downwash-pressure:

$$\left\{ \frac{w}{U} \right\}_{\text{total}} = [A] \{ \Delta C_p \}_{\text{total}} \quad (41)$$

This matrix may be broken up into a rigid and a flexible part, which becomes

$$\left\{ \frac{w}{U} \right\}_R + \left\{ \frac{\Delta w}{U} \right\}_f = [A] \{ \Delta C_p \}_R + [A] \{ \Delta C_p \}_f \quad (42)$$

(2) Slope-force:

$$\left\{ \frac{\Delta w}{U} \right\}_f = \{ \theta \} = [S] \{ F \} \quad (43)$$

(3) Total force – rigid and flexible:

$$\{ F \} = \{ R \} + \{ \Delta F \} \quad (44)$$

(4) Force-pressure:

$$\{ F \} = q [B] \{ \Delta C_p \}_{\text{total}} = q [B] \{ \Delta C_p \}_R + q [B] \{ \Delta C_p \}_f \quad (45)$$

Hence, substituting a part of equation (42) into equation (43) gives:

$$[A] \{ \Delta C_p \}_f = [S] \{ F \} \quad (46)$$

and substituting equations (44) and (45) into equation (46) yields

$$[A] \{ \Delta C_p \}_f = [S] \left[ \{ R \} + q [B] \{ \Delta C_p \}_f \right] \quad (47)$$

Solving for  $\{\Delta C_p\}_f$  leads to

$$\{\Delta C_p\}_f = \left[ [A] - q[S][B] \right]^{-1} [S]\{R\} \quad (48)$$

As mentioned under the study of torsional divergence, for three-dimensional wings a solution for the dynamic pressure can be obtained for which infinite flexible pressure loadings would result. A study of equation (48) indicates that this condition will occur for

$$\left| [A] - q[S][B] \right| = 0 \quad (49)$$

and so the  $q_D$  can be found by solving for the smallest positive root of the resulting polynomial.

Once the  $\{\Delta C_p\}_f$  is solved for, a solution for  $\{F\}$  can be found as:

$$\{F\} = \{R\} + q[B]\{\Delta C_p\}_f \quad (50)$$

and then summing up the results yields

$$F_\Sigma = \sum \{F\} = R_\Sigma + \Delta F_\Sigma = \sum \{R\} + \sum \{\Delta F\} \quad (51)$$

Hence the flexible-to-rigid ratios can be formed by dividing by  $R_\Sigma$ . This operation leads to

$$\frac{F_\Sigma}{R_\Sigma} = 1 + \frac{\Delta F_\Sigma}{R_\Sigma} \quad (52)$$

It should be noted that the  $\{R\}$  can be either a distributed air loading or a weight loading, providing the two types have signs consistent with their directions.

Now, the use to which the just-determined flexible-to-rigid ratios for both lift and pitching moment may be put are examined. As an example, the equations are developed for the change in center-of-pressure location due to flexibility for a load factor  $n'_z$  of 1.

$$(C_L)_F = (C_{L\alpha,wb})_F^\alpha + \Delta C_{L_{n'_z}} \quad (53)$$

where  $\Delta C_{L_{n'_z}}$  is the increment in lift coefficient due to a unit load factor  $n'_z$

$$(C_L)_F = (C_{L\alpha,wb})_R \left( \frac{F}{R} \right)^\alpha + \left( \frac{-W}{qS} \right) \left( \frac{\Delta F}{R} \right) C_{L_{n'_z,wb}} \quad (54)$$

In steady 1g straight and level flight, then  $n'_z = 1$ ,  $L_F = W$ ; hence,

$$(C_L)_F = \frac{W}{qS} = (C_{L\alpha,wb})_R \left(\frac{F}{R}\right)_{C_{L\alpha,wb}}^{(\alpha)_{n'_Z=1}} + \left(\frac{-W}{qS}\right) \left(\frac{\Delta F}{R}\right)_{C_{L_{n'_Z},wb}} \quad (55)$$

or

$$\frac{W}{qS} \left(1 + \frac{\Delta F}{R}\right)_{C_{L_{n'_Z},wb}} = \frac{W}{qS} \left(\frac{F}{R}\right)_{C_{L_{n'_Z},wb}} = (C_{L\alpha,wb})_R \left(\frac{F}{R}\right)_{C_{L\alpha,wb}}^{(\alpha)_{n'_Z=1}} \quad (56)$$

Thus,

$$(\alpha)_{n'_Z=1} = \frac{\frac{W}{qS} \left(\frac{F}{R}\right)_{C_{L_{n'_Z},wb}}}{(C_{L\alpha,wb})_R \left(\frac{F}{R}\right)_{C_{L\alpha,wb}}} \quad (57)$$

$$\frac{\Delta x_{cp}}{\bar{c}} = \left(\frac{\partial C_m}{\partial C_L}\right)_R - \left[ \frac{\left(\frac{\partial C_m}{\partial C_L}\right)_R (C_{L\alpha,wb})_R \left(\frac{F}{R}\right)_{C_{m\alpha,wb}}^{(\alpha)_{n'_Z=1}}}{W/qS} + \frac{\frac{W}{qS} \left(\frac{\Delta x'_{wb}}{\bar{c}}\right) \left(\frac{\Delta F}{R}\right)_{C_{m_{n'_Z}}}}{W/qS} \right] \quad (58)$$

Substituting for  $(\alpha)_{n'_Z=1}$  from equation (57) gives

$$\frac{\Delta x_{cp}}{\bar{c}} = \left(\frac{\partial C_m}{\partial C_L}\right)_R - \left[ \left(\frac{\partial C_m}{\partial C_L}\right)_R \left(\frac{F}{R}\right)_{C_{m\alpha,wb}} \frac{\frac{W}{qS} \left(\frac{F}{R}\right)_{C_{L_{n'_Z},wb}}}{\left(\frac{F}{R}\right)_{C_{L\alpha,wb}} \left(\frac{W}{qS}\right)} + \left(\frac{\Delta x'_{wb}}{\bar{c}}\right) \left(\frac{\Delta F}{R}\right)_{C_{m_{n'_Z}}} \right] \quad (59)$$

Hence,

$$\frac{\Delta x_{cp}}{\bar{c}} = \left(\frac{\partial C_m}{\partial C_L}\right)_R - \left(\frac{\partial C_m}{\partial C_L}\right)_R \left(\frac{F}{R}\right)_{C_{m\alpha,wb}} \frac{\left(\frac{F}{R}\right)_{C_{L_{n'_Z},wb}}}{\left(\frac{F}{R}\right)_{C_{L\alpha,wb}}} - \left(\frac{\Delta x'_{wb}}{\bar{c}}\right) \left(-1 + \frac{F}{R}\right)_{C_{m_{n'_Z}}} \quad (60)$$

where

$\frac{\Delta x'_{wb}}{\bar{c}}$  distance from the center of gravity to moment reference point nondimensionalized on  $\bar{c}$

For  $\frac{\Delta x_{cp}}{\bar{c}} > 0$ , the center of pressure of the flexible wing is behind that of the rigid wing since positive stability is represented by a negative value of  $\partial C_m / \partial C_L$ . Contrarywise for  $\frac{\Delta x_{cp}}{\bar{c}} < 0$ .

The Boeing Company in reference 8 has extended the force-slope method to large flexible transports. Other companies use the force-slope method in support of their static aeroelastic prediction efforts.

## SUMMARY REMARKS ON PART II

In part II several methods for predicting the effects of aeroelasticity have been examined and are summarized as follows:

(1) The iteration method is simplest of those using computer techniques, and is easiest to understand; however, it can be inefficient (slow to converge) if the dynamic pressure specified is near the divergence dynamic pressure.

(2) The reference-surface method can be used to get a quick idea of the effects of the flexibility on a wing without having to know a great amount of detail about its structure or weight.

(3) In the modal approach, answers can be accurate if enough vibration modes are used or enough points in structural analysis are taken to define the mode shapes adequately. In order to determine if enough have been used a convergency check on  $C_{L_{\alpha},F}$  is often employed. Also concerning this method there may be the problems of (1) not having modal data available and (2) everytime the mass distribution changes so does the generalized mass. However, this solution does yield continuous pressure loadings.

(4) The force-slope approach leads to closed-form solutions, easy to program, and is the method chosen to be used for the solutions in this lecture.

Methods for developing the  $[A]$  and  $[S]$  matrices used in the force-slope approach are presented in the following sections.

## III - THEORETICAL SUBSONIC AERODYNAMIC METHODS

Two methods are developed for predicting the surface load distributions at subsonic speeds for a given downwash distribution. The first is the kernel-function method and the second is the vortex-lattice method.

### Kernel-Function Method

The development of the kernel-function method is based on a potential function, linearized Euler equations, and the continuity equation. They are used together with Poisson's equation, the procedure which is outlined in reference 9 and is presented here in detail.



Potential function.- The acceleration potential to be used is that which will produce a pressure field and is defined by

$$\Omega = \frac{p_{\infty} - p}{\rho} \quad (61)$$

Euler equation.- The equations of motion for steady, inviscid flow can be written in index notation, where repetition of a suffix indicates summation over that suffix, as

$$u_j \frac{\partial u_i}{\partial x_j} = - \frac{1}{\rho} \frac{\partial p}{\partial x_i} \quad (i, j = 1, 2, 3) \quad (62)$$

where

$$u_k \Rightarrow (U \pm u, v, w) \quad (63)$$

and  $x_1 = x$ ,  $x_2 = y$ ,  $x_3 = z$ . Linearizing (i.e., neglecting products and squares of perturbation velocities and their derivatives) allows the equations of motion to be written as

$$U \frac{\partial u_i}{\partial x} = - \frac{1}{\rho} \frac{\partial p}{\partial x_i} \quad (64)$$

Differentiating with respect to  $x_i$  leads to

$$U \frac{\partial}{\partial x_i} \left( \frac{\partial u_i}{\partial x} \right) = - \frac{1}{\rho} \frac{\partial^2 p}{\partial x_i \partial x_i} = - \frac{1}{\rho} \nabla^2 p \quad (65)$$

Continuity equation.- The equation of continuity for incompressible flow in index notation is

$$\frac{\partial u_i}{\partial x_i} = 0 \quad (66)$$

Here, the order of partial differentiation may be interchanged to yield

$$\frac{\partial}{\partial x_i} \left( \frac{\partial u_i}{\partial x} \right) = \frac{\partial}{\partial x} \left( \frac{\partial u_i}{\partial x_i} \right) \quad (67)$$

Consequently, making use of equations (61) and (67) in equation (65) yields

$$\nabla^2 \Omega = 0 \quad (68)$$

Hence for incompressible flow the acceleration potential satisfies Laplace's equation. It is known in general that the potential  $\Omega$  can be defined at any point by making use of Poisson's equation:

$$\Omega(x, y, z) = \iiint_V \left( \frac{1}{r} \frac{1}{4\pi} \nabla^2 \Omega \right) dV + \frac{1}{4\pi} \iint_{S_u, S_l, S_{wake}} \left[ - \frac{1}{r} \frac{\partial \Omega}{\partial n} + \Omega \frac{\partial}{\partial n} \left( \frac{1}{r} \right) \right] dS \quad (69)$$

With  $\nabla^2 \Omega = 0$  and no pressure jump existing across the wake,

$$\Omega(x,y,z) = \frac{1}{4\pi} \iint_{S_u, S_l} \left[ -\frac{1}{r} \frac{\partial \Omega}{\partial n} + \Omega \frac{\partial}{\partial n} \left( \frac{1}{r} \right) \right] dS \quad (70)$$

The normal  $n$  in this case is  $z$ , where  $z$  is in the same direction as  $n$  on the upper surface and in the opposite direction on the lower surface. Hence

$$\Omega(x,y,z) = \frac{1}{4\pi} \iint_{S_u} \left[ -\frac{1}{r} \frac{\partial \Omega_u}{\partial z} + \Omega_u \frac{\partial}{\partial z} \left( \frac{1}{r} \right) \right] dS + \frac{1}{4\pi} \iint_{S_l} \left[ -\frac{1}{r} \frac{\partial \Omega_l}{\partial (-z)} + \Omega_l \frac{\partial}{\partial (-z)} \left( \frac{1}{r} \right) \right] dS \quad (71)$$

Now since both  $S_u$  and  $S_l$  have the same projected area and use the same limits and since  $\partial \Omega / \partial z$  is related to the downwash  $w$ , which is continuous across the pressure sheet representing the wing, by equations (61) and (64)

$$U \frac{\partial w}{\partial x} = \frac{\partial \Omega}{\partial z} \quad (72)$$

and equation (71) can be written

$$\Omega(x,y,z) = \frac{1}{4\pi} \iint_S \left[ -\frac{1}{r} \left( -U \frac{\partial w}{\partial x} + U \frac{\partial w}{\partial x} \right) \right] dS + \frac{1}{4\pi} \iint_S - \left[ (-\Omega_u + \Omega_l) \frac{\partial}{\partial z} \left( \frac{1}{r} \right) \right] dS \quad (73)$$

Now, with

$$\Omega_u = \frac{p_\infty - p_u}{\rho} \quad (74a)$$

and

$$\Omega_l = \frac{p_\infty - p_l}{\rho} \quad (74b)$$

then

$$\Omega_u - \Omega_l = \frac{p_l - p_u}{\rho} = \frac{\Delta p}{\rho} \quad (75)$$

With

$$r = \sqrt{(x - \xi)^2 + (y - \eta)^2 + (z - \zeta)^2} \quad (76)$$

and the wing midsurface restricted to  $\zeta = 0$ , then

$$\frac{\partial}{\partial z} \left( \frac{1}{r} \right) = \frac{-z}{\left[ (x - \xi)^2 + (y - \eta)^2 + z^2 \right]^{3/2}} \quad (77)$$

so that

$$\Omega(x,y,z) = -\frac{1}{4\pi} \iint_S \frac{\Delta p}{\rho} \frac{z}{r^3} dS \quad (78)$$

The perturbation downwash is required to vanish at  $x = -\infty$  so that uniform free-stream velocity is the only velocity which exists there. As noted previously (eq. (72)),

$$U \frac{\partial w}{\partial x} = \frac{\partial \Omega}{\partial z}$$

so that

$$w(x, y, z) = \frac{1}{U} \int_{-\infty}^x \frac{\partial \Omega}{\partial z} dx' \quad (79)$$

Hence, combining equations (78) and (79) yields

$$w(x, y, z) = \frac{1}{U} \int_{-\infty}^x \frac{\partial}{\partial z} \left( -\frac{1}{4\pi} \right) \iint_S \frac{\Delta p}{\rho} \frac{z}{r^3} dS dx' \quad (80)$$

Now  $w(x, y, z)$  is the downwash of a field point. If the field points are required to lie on the wing midsurface, just as the pressure field is required to lie on the midsurface of the wing, then equation (80) becomes

$$\frac{w(x, y, 0)}{U} = -\frac{1}{8\pi} \int_{-\infty}^x \lim_{z \rightarrow 0} \frac{\partial}{\partial z} \iint_S \frac{\Delta p}{q} \frac{z}{r^3} d\xi d\eta dx' \quad (81)$$

where  $\frac{w(x, y, 0)}{U}$  is merely the boundary condition and is equal to

$$\frac{w(x, y, 0)}{U} = \left( \frac{\partial z}{\partial x} \right) \quad (82)$$

Performing the indicated operations in equation (81) leads to

$$\frac{w(x, y, 0)}{U} = \frac{1}{8\pi} \iint_S \frac{\Delta p(\xi, \eta)}{q} \frac{1}{(y - \eta)^2} \left[ 1 + \frac{x - \xi}{\sqrt{(x - \xi)^2 + (y - \eta)^2}} \right] d\xi d\eta \quad (83)$$

This equation represents the zero frequency limit of the equation previously given by Dr. Yates as equation (73). The term  $\frac{1}{(y - \eta)^2} \left[ 1 + \frac{x - \xi}{\sqrt{(x - \xi)^2 + (y - \eta)^2}} \right]$  is called the

steady-state kernel function and represents the downwash at point  $(x, y, 0)$  produced by a pressure dipole of unit strength lying at the point  $(\xi, \eta, 0)$ . This term is the zero-frequency limit at zero Mach number of Dr. Yates' equation (74). Equation (83) could be derived from pressure dipole considerations almost directly.

Solution technique.— Some authors (refs. 5, 9, 10, and 11) choose to replace the unknown surface pressures by a chordwise set of pressure mode shapes with unknown coefficients at each spanwise station (which is to be an integrating station in the spanwise quadrature formula). It can be expressed as

$$\frac{\Delta p(\vartheta, \eta)}{q} = \frac{q_o(\eta)}{qc(\eta)} \cot \frac{\vartheta}{2} + \sum_{j=1}^{N-1} \frac{q_j(\eta)}{qc(\eta)} \sin j\vartheta \quad (84)$$

where

$$\xi = -c(\eta) \cos \vartheta + d(\eta) \quad (85)$$

These pressure terms are integrated chordwise at each spanwise integrating station for each pressure mode. A singularity occurs when the influence of each pressure mode is sought at the same spanwise station at which the downwash is specified. There are expansion and finite-part approaches which allow an answer to be determined. A set of simultaneous linear equations are formed from as many control points as  $(q_j(\eta_n)/q)$  terms which in matrix notation are of the form

$$\left\{ -\frac{4w(x, y, 0)}{U} \right\} = [L] \left\{ \frac{q_j(\eta_n)}{q} \right\} \quad (86)$$

The  $\frac{q_j(\eta_n)}{q}$  are solved by matrix inversion and hence the surface pressure and wing aerodynamic characteristics can be found.

### Discrete Loading Representation

#### (Vortex Lattice)

Determination of influence coefficients.— Another method that can be used to solve for the pressure loadings in equation (83) employs a vortex-lattice representation. In this method the pressure is assumed constant over a small area of the wing and the wing loading is therefore not a smoothly varying function but a set of discrete loadings which resemble a bar graph in two directions. The solution is formulated as follows.

Assume that  $\frac{\Delta p(\xi, \eta)}{q}$  is constant over a small spanwise distance  $(2s_\nu)$  from say  $y_\nu - s_\nu$  to  $y_\nu + s_\nu$  at a given value of  $(\xi/c)$  where  $y_\nu$  is selected as the spanwise coordinate at which the pressure difference is to be determined.

It is also known that

$$\frac{\Delta p(\xi, \eta)}{q} = -\frac{2\gamma(\xi, \eta)}{U} \quad (87)$$

where  $\gamma$  is the local distributed circulation, and

$$\Gamma = -\int_{\xi_0}^{\xi_1} \gamma d\xi \quad (88)$$

where  $\Gamma$  is the circulation strength accumulated over a given chordwise segment, say from  $\xi_0$  to  $\xi_1$ .

Now differentiating equation (83) with respect to  $\xi$  and making use of equation (87) gives

$$\frac{1}{c} \left[ \frac{\partial w(x, y, 0)/U}{\partial (\xi/c)} \right] = \frac{1}{8\pi} \sum_{\nu=1}^{\nu_{\max}} \int_{y_{\nu}-s_{\nu}}^{y_{\nu}+s_{\nu}} \left[ -\frac{2}{U} \gamma_{\nu}(\xi, \eta) \right] \frac{1}{(y-\eta)^2} \left[ 1 + \frac{(x - \xi \frac{c}{c})}{\sqrt{(x - \xi \frac{c}{c})^2 + (y - \eta)^2}} \right] d\eta \quad (89)$$

Now if  $\gamma(\xi, \eta)$  is assumed to be constant from  $y_{\nu} - s_{\nu}$  to  $y_{\nu} + s_{\nu}$  for a given  $\xi/c$ , then

$$\frac{1}{c} \left[ \frac{\partial w(x, y, 0)/U}{\partial (\xi/c)} \right] = \sum_{\nu=1}^{\nu_{\max}} \frac{1}{8\pi} \left[ -\frac{2\gamma(\xi, \eta)}{U} \right] \int_{y_{\nu}-s_{\nu}}^{y_{\nu}+s_{\nu}} \frac{1}{(y-\eta)^2} \left[ 1 + \frac{(x - \xi \frac{c}{c})}{\sqrt{(x - \xi \frac{c}{c})^2 + (y - \eta)^2}} \right] d\eta \quad (90)$$

Integrating equation (90) with respect to  $\eta$  (as Crigler did in ref. 12) yields three terms which can be identified as the contributions to downwash of the two trailing legs and the bound portion of a horseshoe vortex having a lateral spacing of  $2s_{\nu}$  and located at  $(\xi/c)$  and  $y_{\nu}$  where  $\xi_0 < \xi < \xi_1$ . This relation is called the influence function and is denoted by  $F_{W,\nu}$  indicating that this is the downwash produced by the  $\nu$ th rectangular horseshoe vortex in the  $x$ - $y$  plane at a particular value of  $\xi/c$ . The parameter  $F_{W,\nu}$  is a function of  $x, y; \xi, y_{\nu}, s_{\nu}$ , as given in the following equation:

$$F_{W,\nu}(x, y; \xi, y_{\nu}, s_{\nu}) = - \frac{1}{(x - \xi)} \left( \frac{(y - y_{\nu}) + s_{\nu}}{\left\{ (x - \xi)^2 + [(y - y_{\nu}) + s_{\nu}]^2 \right\}^{1/2}} - \frac{(y - y_{\nu}) - s_{\nu}}{\left\{ (x - \xi)^2 + [(y - y_{\nu}) - s_{\nu}]^2 \right\}^{1/2}} \right) \quad \left. \begin{array}{l} \text{Bound-} \\ \text{vortex} \\ \text{effect} \end{array} \right\}$$

$$- \frac{1}{[(y - y_{\nu}) - s_{\nu}]} \left( 1 - \frac{(x - \xi)}{\left\{ (x - \xi)^2 + [(y - y_{\nu}) - s_{\nu}]^2 \right\}^{1/2}} \right) \quad \left. \begin{array}{l} \text{Trailing-} \\ \text{leg} \\ \text{effects} \end{array} \right\} + \frac{1}{[(y - y_{\nu}) + s_{\nu}]} \left( 1 - \frac{(x - \xi)}{\left\{ (x - \xi)^2 + [(y - y_{\nu}) + s_{\nu}]^2 \right\}^{1/2}} \right) \quad (91)$$

If this result is compared with that of Glauert in reference 13 (pp. 158-159), the expressions are found to be different because the positive  $x$  directions are opposite. The coordinate system used herein is shown in figure 9.

Solution technique.- Integrating now the results of equations (90) and (91) in the chordwise direction yields

$$\frac{w(x,y,0)}{U} = \int_{x_{LE}}^{x_{TE}} \left( -\frac{2}{8\pi} \right) \sum_{\nu=1}^{\nu_{\max}} \frac{\gamma_{\nu}(\xi)}{U} F_{w,\nu} d\xi \quad (92)$$

However, before this equation is integrated in small chordwise increments, it should be noted that over a small range of  $\xi$  the function  $F_{w,\nu}$  will not vary too much so that an effective value of  $F_{w,\nu}$  can be associated with a range of  $\xi$  and according to equation (88), also with a range of  $\Gamma$ . Hence

$$\frac{w(x,y,0)}{U} = \frac{1}{4\pi U} \sum_{n=1}^{n_{\max}} \Gamma_n F_{w,n} = \sum_{n=1}^{n_{\max}} \Gamma'_n F_{w,n} \quad (93)$$

where

$$\Gamma'_n = \frac{\Gamma_n}{4\pi U}$$

If the span loading is symmetrical, only half of the horseshoe vortex strengths but still all of the influence functions need be considered, so that

$$\frac{w(x,y,0)}{U} = \sum_{n=1}^{n_{\max}/2} \Gamma'_n F'_{w,n} \quad (94)$$

where

$$F'_{w,n} = (F_{w,n})_{\text{right}} + (F_{w,-n})_{\text{left}}$$

Taking as many boundary points (fig. 10) as unknown circulation strengths yields a set of simultaneous linear equations which are, as before, solved by matrix inversion

$$\{\Gamma'_n\} = [F'_{w,n}]^{-1} \left\{ \frac{w}{U} \right\} \quad (95)$$

Knowing the circulation strengths allows the aerodynamic characteristics to be found. (See refs. 14 and 15 for other vortex-lattice-representation developments.)

## Determination of "Best" Aeronautical Results for the Theoretical Methods

An analytical method that provides a numerical solution from information at only a few places or that uses integration procedures which can be carried out over a range of grid sizes must have either preferred places for information to be supplied or a preferred grid size for a particular wing. This section describes four methods which may be used to determine when the "best" answers are to be expected for a numerical solution to the subsonic lifting-surface problem. The four methods to be used herein are:

(1) The "downwash-fit" method uses the results of the numerical solution to compute the downwash all along the chord, including the control points; these computations are then compared with the original downwash as specified in the problem statement.

(2) The "correct leading-edge-thrust" method is one in which the thrust computed by the far-field theory is compared with the thrust developed in the near field by making use of the section pressure loadings.

(3) The "converged-aerodynamic-center" method consists in examining the aerodynamic-center variation with different sets of either stations or grid sizes to determine where convergence takes place.

(4) The "converged  $C_{L\alpha}$ " method examines the lift-curve-slope variation with different sets of either stations or grid sizes to determine where convergence takes place.

Downwash-fit method.- In figure 11 can be seen the relationship between the chord-wise pressure loading, the downwash, and the mean camber line required for both typical two-dimensional (2-D) and three-dimensional (3-D) results. At the top of figure 11 are the results for a two-dimensional flat plate at angle of attack, in the middle are those of a two-dimensional cambered wing at  $\alpha = 0$  and at the bottom are those for a flat three-dimensional wing at angle of attack. The three-dimensional-wing results show that the wing has pressure loadings made up of both flat-plate results and induced-camber loadings.

The downwash-fit test is illustrated in the second plot at the bottom of figure 11. It can be seen that the original downwash (solid line) is constant along the chord (corresponding to a wing at angle of attack) whereas two numerical solutions result in downwash distributions which oscillate about the original curve. The short-dash-line results might come from a least-squares solution; whereas the line with crossmarks might result from an even determined solution such as the modified Multhopp (ref. 11).

Correct leading-edge-thrust method.- The Munk stagger theorem leads to

$$C_{D,i} = A \int_{-1}^1 \gamma \alpha_i d\eta \quad (96)$$

In addition, resolving the aerodynamic force (fig. 12) into components and assuming small angles of attack gives

$$C_{D,ii} = C_L^{\alpha} - C_T \quad (97)$$

These two results should be the same if the distributed thrust is correctly predicted. Since the induced drag or thrust is the most sensitive of the aerodynamic characteristics, a comparison of these two results is a good check on the chordwise loading distribution. The modified Multhopp method has used this procedure to determine the validity of its answers. A typical pattern of stations where information is to be supplied for the modified Multhopp method is shown for a general wing in figure 13 for  $m = 7$  and  $N = 3$ . Induced drag results obtained by using many different patterns for an  $A = 7$  rectangular wing are shown in figure 14. From figure 14 it can be seen that for  $N = 2$ ,  $m = 13$  and for  $N = 4$ ,  $m = 39$  (filled symbols) the two induced drag results are the same. Hence either pattern should give equally good results. However, the figure does show that for increasing the number of chordwise stations at a given number of spanwise stations the results do not approach those of the filled symbol, instead they move farther away. Thus, care must be used in selecting the number and location of control points so that a proper balance or proportion is achieved over the planform.

Converged-aerodynamic-center method.- At the top of figure 15 the variation of the aerodynamic center for the  $A = 7$  rectangular wing is shown for different patterns for both the modified Multhopp and the vortex-lattice methods. It can be seen that the patterns which gave good induced drag agreement (filled symbols) lie on what appears to be the converged-aerodynamic-center results. Note that the result from the vortex-lattice scheme showed no variation with number of spanwise panels and is slightly aft of the converged modified Multhopp results.

Converged- $C_{L_{\alpha}}$  method.- At the bottom of figure 15 the variation of the lift-curve slope for the  $A = 7$  rectangular wing is shown for different patterns for both the modified Multhopp and vortex-lattice methods. Here, too, it can be seen that the patterns which gave good induced drag agreement (filled symbols) lie on the converged-lift-curve-slope results. Note that the vortex-lattice results are sensitive to the number of spanwise panels and its lift-curve slope tends to converge to a slightly higher value than the modified Multhopp results.

#### Comparison of Analytical Methods With Each Other and Experiment

After methods have been employed to indicate when best agreement of results can be expected from the numerical solutions, the "best" answers that can be obtained from different methods will be compared with each other and with experiment to determine which numerical solution to select in developing the  $[A]$  matrix. The following aerodynamic characteristics of several wings are selected for use in the comparison process:



- (1) Lifting pressures
- (2) Span loadings
- (3) Overall lift coefficient
- (4) Aerodynamic center
- (5) Section lift-curve and moment-curve slopes and some of the preceding aerodynamic characteristics as a function of sweepback.

Lifting pressures.- Comparisons are presented in figure 16 of lifting-pressure coefficient on a modified delta wing as obtained by using the modified Multhopp, vortex-lattice, and subsonic kernel-function solutions and in figure 17(a) on a variable-sweep wing by using the modified Multhopp method and experiment. In figure 16 the subsonic kernel function (wing alone) and the vortex lattice (both wing alone and with fuselage and tail) agreed well over most of the span except near the tip where the subsonic kernel-function results indicated that a negative lift was generated. The Multhopp results agreed well over the rear 50 percent of the chord but disagreed over the forward portion of the chord. The effect of fuselage and tail on the vortex-lattice results reduced the lifting pressure everywhere by a small to moderate amount.

Figure 17(b) shows that the modified Multhopp does predict well the experimental lifting-pressure distribution across the wing.

Span loading.- In figure 17(a) theoretical span loadings from the vortex-lattice and modified Multhopp methods are compared with experiment and the modified Multhopp methods seem to give slightly better agreement with experiment than the vortex-lattice method.

Overall lift coefficient and aerodynamic center.- In figure 17(a) it can be seen that whereas there is no appreciable difference between the two theoretical  $C_L$  results that the vortex-lattice aerodynamic-center result is closer to experiment than that of the modified Multhopp.

Section lift-curve and moment-curve slope.- In figure 17(c) the modified Multhopp method is seen to predict reasonably well the section lift-curve and moment-curve slopes found experimentally.

Aerodynamic characteristics as a function of sweepback.- Figure 18 shows a comparison between the modified Multhopp and vortex-lattice methods and experimental values of  $C_{L_\alpha}$  and aerodynamic center at different sweep angles. Whereas, there is no appreciable difference in  $C_{L_\alpha}$  prediction given by either method, both are about 10 percent higher than experiment. However, for the aerodynamic center we see that the vortex-lattice method gives better agreement with experiment than does the modified Multhopp method.

### Summary Comments on Part III

The Multhopp method has been shown to give generally good agreement with experimental section data and yet to result in an aerodynamic-center location not in as good agreement with experiment as that found from the vortex-lattice method. The vortex-lattice method tended to give good agreement with the subsonic kernel-function method except near the wing tip where the kernel-function results appeared incorrect.

Both the subsonic kernel-function and vortex-lattice methods can be used to predict the aerodynamic characteristics of arbitrary as well as multiple lifting surfaces. The subsonic kernel function gives continuous pressure distributions, whereas the vortex-lattice representation gives rise to discrete (bar-graph type) loadings or average pressures. In addition, the subsonic kernel function handles the edge conditions exactly, whereas the vortex-lattice method handles them only approximately.

Nevertheless, the lattice method does generally give good results both locally and overall. So, in light of the previous discussion and personal experience, it was decided to use the vortex-lattice method to determine the aerodynamic influence coefficient. Before this determination was possible, however, it was necessary to know the relationship between  $\{\Gamma'_n\}$ ,  $\{\Delta C_p\}$ ,  $[F'_{w,n}]$  and  $[A]$  if the concepts previously developed were to be used. This analysis is made in the following manner:

Since

$$\frac{\Delta p(\xi, \eta)}{q} = \Delta C_p = -\frac{2\gamma(\xi, \eta)}{U} \quad (87)$$

and

$$\Gamma = -\int_{\xi_0}^{\xi_1} \gamma(\xi) d\xi \quad (88)$$

or

$$\Gamma_n = -c \int_{\frac{\xi_{n-1}}{c}}^{\frac{\xi_n}{c}} \gamma(\xi) d\left(\frac{\xi}{c}\right) = -c\gamma_{av}\left(\xi_n, y\right) \Delta\left(\frac{\xi}{c}\right) \quad (98)$$

and

$$\Delta C_p(x_n, \eta)_{av} = \frac{2}{c} \frac{\Gamma_n}{\Delta(\xi/c)} \left( \frac{\Gamma_n}{U} \right) \quad (99)$$

and from equations (41) and (95)

$$\left\{ \frac{w(x, y, 0)}{U} \right\} = [A] \{\Delta C_p\} = [F'_{w,n}] \left\{ \frac{\Gamma_n}{4\pi U} \right\} \quad (100)$$

If the  $\{\Delta C_p\}$  are taken to be average values rather than to be mode shapes, then an equivalence results:

$$[A] \left\{ \frac{2}{c \Delta(\xi/c)} \frac{\Gamma_n}{U} \right\} = [F'_{w,n}] \left\{ \frac{\Gamma_n}{4\pi U} \right\} \quad (101)$$

Hence

$$[A] \left\{ \frac{2}{c \Delta(\xi/c)} \right\} = [\bar{A}] = \frac{1}{4\pi} [F'_{w,n}] \quad (102)$$

The actual evaluation can be done, therefore, in terms of  $[F'_{w,n}]$ , or this matrix can become our new  $[A]$  matrix. It is used by rewriting equation (48) as

$$\{\Delta \Gamma\}_F = \left[ \frac{1}{4\pi} [F'_{w,n}] - q[S][\bar{B}] \right]^{-1} [S] \{R\} \quad (103)$$

#### IV - STRUCTURAL ANALYSES

Some of the structural analyses currently employed to develop structural influence-coefficient matrices are slender-beam, plate (and shell), and finite-element methods. Each of these methods has its applicability both to configuration shape and to the time at which it is employed in the design cycle. The slender-beam analysis is usually applied at the preliminary design stage to wings which have a beamlike structure. The plate method is used for wings which do not have an elastic axis that is essentially or piecewise straight, but have instead sets of node lines associated with each fundamental mode due to both bending and torsional loadings. This method is applied to delta and delta-like wings of low aspect ratio in the preliminary design cycle. The finite-element method is most often used in the final design cycle and incorporates the stiffness effects of the individual pieces such as cover plates, ribs, webs, and so forth.

##### Slender-Beam Method

From figure 19 it can be seen that a unit upward force applied at some point  $(\xi_j, \eta_j)$  on a wing with an elastic axis is resolvable into a unit upward force perpendicular to and a coupled force along the elastic axis. Each of these forces produces a streamwise change in the slope at point  $(x_i, y_i)$ . The slope change which occurs at point  $(x_i, y_i)$  due to the upward bending of the elastic axis is represented by a vector perpendicular to the elastic axis and can be determined from the basic differential equation of a beam, namely,

$$\frac{d\theta_B(x,y)}{d\bar{\lambda}} = \frac{M}{EI} \quad (104)$$

by integrating along the elastic axis. Multiplying this result by  $\sin \Lambda_{ea}$  yields the streamwise slope component which is what we need.

The slope change at point  $(x_i, y_i)$  which results from the couple (or torque) is represented by a vector parallel to the elastic axis and can be determined from a basic differential equation, namely,

$$\frac{d\theta_T(x, y)}{d\bar{\lambda}} = \frac{T}{GJ} \quad (105)$$

by integrating along the elastic axis. Multiplying this result by  $\cos \Lambda_{ea}$  yields the streamwise slope component which is that needed. Putting this together leads to:

For loading point ahead of the elastic axis:

$$S_{ij} = S(x_i, y_i; \xi_j, \eta_j) = \left\{ \begin{array}{ll} -\int_0^{\bar{\lambda}_y} \left( \frac{\sin \Lambda_{ea}(\bar{\lambda}_\eta - \bar{\lambda})}{EI} - \frac{\cos \Lambda_{ea} d}{GJ} \right) d\bar{\lambda} & (|\bar{\lambda}_y| \leq |\bar{\lambda}_\eta|) \\ -\int_0^{\bar{\lambda}_\eta} \left( \frac{\sin \Lambda_{ea}(\bar{\lambda}_\eta - \bar{\lambda})}{EI} - \frac{\cos \Lambda_{ea} d}{GJ} \right) d\bar{\lambda} & (|\bar{\lambda}_y| > |\bar{\lambda}_\eta|) \end{array} \right\} \quad (106a)$$

For loading point behind the elastic axis:

$$S_{ij} = S(x_i, y_i; \xi_j, \eta_j) = \left\{ \begin{array}{ll} -\int_0^{\bar{\lambda}_y} \left( \frac{\sin \Lambda_{ea}(\bar{\lambda}_\eta - \bar{\lambda})}{EI} + \frac{\cos \Lambda_{ea} d}{GJ} \right) d\bar{\lambda} & (|\bar{\lambda}_y| \leq |\bar{\lambda}_\eta|) \\ -\int_0^{\bar{\lambda}_\eta} \left( \frac{\sin \Lambda_{ea}(\bar{\lambda}_\eta - \bar{\lambda})}{EI} + \frac{\cos \Lambda_{ea} d}{GJ} \right) d\bar{\lambda} & (|\bar{\lambda}_y| > |\bar{\lambda}_\eta|) \end{array} \right\} \quad (106b)$$

where

$$\bar{\lambda}_y = \sin \Lambda_{ea}(x_0 - x_i) + \cos \Lambda_{ea}(y_0 - y_i) \quad (107)$$

$$\bar{\lambda}_\eta = \sin \Lambda_{ea}(x_0 - \xi_j) + \cos \Lambda_{ea}(y_0 - \eta_j) \quad (108)$$

$$d = \sqrt{(\xi_j - \xi_1)^2 + (\eta_j - \eta_1)^2} \quad (109)$$

$$\xi_1 = x_0 - \bar{\lambda}_\eta \sin \Lambda_{ea} \quad (110)$$

$$\eta_1 = y_0 - \bar{\lambda}_\eta \cos \Lambda_{ea} \quad (111)$$

and  $x_0, y_0$  is defined in figure 19. A positive slope change is a positive angle-of-attack change. (See ref. 1, pp. 43 to 49 for a similar development.)

## Plate Methods

The structural slope matrix for wings which behave like plates can be solved for by several different procedures. Two of these procedures are (1) finding the mode shape and frequencies and using them in conjunction with a generalized force which results from a unit load and finding the sum of the mode shapes at each slope point and (2) using the principle of minimum potential energy in the manner of Rayleigh-Ritz. (See ref. 1, p. 50.)

Mode-shape procedure.- In the mode-shape procedure, the mode shape and frequencies of the plate-like structure must first be determined. One method for determining these is given in reference 16 where it begins with Lagrange's equation for the undamped, unforced system as given below:

$$\frac{d}{dt} \left( \frac{\partial L}{\partial \dot{\hat{q}}_k} \right) - \frac{\partial L}{\partial \hat{q}_k} = 0 \quad (112)$$

where

$$L = T \text{ (kinetic energy)} - \bar{U} \text{ (strain energy)} \quad (113)$$

and  $\hat{q}_k$  are generalized coordinates. Let the generalized coordinates  $\hat{q}_k$  be replaced by discrete vertical displacements  $z_i$  of the plate from the reference surface and the differentiation by a finite-difference scheme and the surface integrations for  $T$  and  $\bar{U}$  be performed by the trapezoidal rule. This procedure leads to:

$$[m_i] \{\ddot{z}_i\} + [K] \{z_i\} = 0 \quad (114)$$

where  $[m_i]$  is the mass matrix and  $[K]$  is a stiffness matrix. For

$$z_i = \bar{z}_i e^{i\omega_i t} \quad (115)$$

there results

$$[K] \{\bar{z}_i\} + [m_i] (\bar{z}_i) (-\omega_i^2) = 0 \quad (116)$$

Then, solving

$$[K] - \omega_i^2 [m_i] \{\bar{z}_i\} = 0 \quad (117)$$

yields the eigenvectors (mode shapes)  $\bar{z}_i$  and the eigenvalues (frequencies)  $\omega_i^2$ .

Any arbitrary deflection shape can be approximated by the linear combination of a complete set of orthogonal functions with appropriate coefficients. The mode shapes are such an orthogonal set of functions. (See description of solution to modal approach previously presented in Dr. Yates' report as an example of this procedure.) However, although a complete set may not always be obtained when a modal analysis is performed, enough mode shapes are usually determined for the present analysis. Proceed by writing

$$\{z\} = \sum_j q_j \{\bar{z}_j\} \quad (118)$$

where

$$q_j = q_j(t) = \bar{q}_j e^{i\omega_j t} \quad (119)$$

Use of equation (31) is also needed with the generalized force retained, thusly,

$$M_j \ddot{q}_j(t) + \omega_j^2 M_j q_j(t) = Q_j(t) \quad (120)$$

For the case of no acceleration (steady motion), then,

$$q_j(t) = \frac{Q_j}{\omega_j^2 M_j} \quad (121)$$

If  $Q_j$  is considered to be the generalized force based on a unit concentrated load placed at, say, the  $k$ th loading point, then the set of  $q_j(t)$  which are associated with that loading point in each of the  $j$  modes can be found. Repeating this procedure for each loading point allows the deflections at each slope point due to a unit load at each of the loading points to be found by making use of equation (118). After the deflections are determined, then, by differentiating chordwise (using finite difference techniques), the structural slope matrix  $[S]$  can be formed.

An example of this procedure is given in reference 1 (pp. 94-95) for a beam whose mode shapes and frequencies are known.

Rayleigh-Ritz method.- A Rayleigh-Ritz approach may be used in conjunction with the principle of minimum potential energy in the following way:

First, define the Rayleigh-Ritz approach as being based upon the assumption that the unknown displacement shape (surface deflections) can be approximated by chosen deflection-mode functions, each of which satisfies the physical boundary conditions. The coefficients of the deflection-mode functions become the unknowns of the problem. (See preceding discussion.) For present purposes, the deflection-mode functions are chosen to be a power series in the  $x$ -direction with the coefficients being functions of the  $y$ -direction.

$$z = \sum_{j=0}^N \phi_j(y) x^j \quad (122)$$

Second, determine the total system potential energy by combining the strain energy in the plate due to internal deformations with the energy gained from a unit concentrated load acting at a loading point. If each of these functions is recognized to be a surface integral, write the foregoing relations as, simply,

$$U = \bar{U} + \bar{\Omega} \quad (123)$$

Third, employing the principle that the potential energy should be a minimum with respect to each  $\phi_j(y)$  in order that the plate may be in equilibrium yields

$$\frac{\partial U}{\partial \phi_j(y)} = 0 \quad (124)$$

This operation can be applied for each  $\phi_j(y)$  and from this result,  $N$  simultaneous equations can be formed, and a solution for the  $\phi_j(y)$  terms can be made.

Fourth, equation (118) can be used to determine the deflections, and differentiating gives the slope at each slope point due to a unit concentrated load at the loading point.

Fifth, moving the unit concentrated load to every loading point over the wing and repeating the second, third, and fourth steps yields the structural slope matrix  $[S]$ .

Chordwise deflection shapes constrained to be either linear or parabolic as well as one shape which was developed from using all of the structural mode shapes available can be seen in figure 20. Solutions for plates having linear and parabolic chordwise deflection shapes are given in references 17 and 18. The effect of constraining the chord shape to a simple functional form is to introduce artificial stiffness into the system which can lead to poor results. This is shown later.

#### Finite-Element Method

The determination of  $[S]$  for a built-up structure can be handled in a manner like that described in the Rayleigh-Ritz method except that instead of only the strain energy for a plate being used, the strain energies for cover plates, spars, ribs, etc., are also included. (See fig. 21 for a sketch of a built-up wing structure.) Solutions for  $\phi_j(y)$  are given in reference 19 for linear and parabolic chordwise camber deflection shapes.

#### Example

Applying plate theory to the wing shown in figure 22 and allowing the chordwise deflection shapes to take on the three forms described previously permits determination of three different structural slope matrices. When each of these three representatives are used in the force-slope method with the same aerodynamic influence coefficient matrix, the pressure-coefficient results (fig. 22), the flexible-to-rigid  $C_{L\alpha}$  results (fig. 5), and the movement of the aerodynamic center on the flexible wing (fig. 4) can be determined. These data show how the artificial stiffening, mentioned earlier, leads to a loss of accuracy in the results obtained, and gives answers which appear to be at least quantitatively as initially expected.

### Summary Remarks on Part IV

Three methods of analysis, slender beam, plate, and finite element, have been outlined and some details given concerning their use in developing a structural slope matrix. Plate theory has been applied to a sample wing and the effects on accuracy in the form of constraining the chordwise deflection shape have been shown.



## REFERENCES

1. Bisplinghoff, Raymond L.; Ashley, Holt; and Halfman, Robert L.: *Aeroelasticity*. Addison-Wesley Pub. Co., Inc., c.1955.
2. Roskam, J.: *Comments, Interpretation and Application of a Method for Predicting Aerodynamic Characteristics of Large Flexible Airplanes. Aeroelastic Effects From a Flight Mechanics Standpoint*, AGARD CP No. 46, Apr. 1969, pp. 13-1 - 13-18.
3. Landrum, L. L.; and Lawrence, R. E.: *Extension of Aeroelastic Reference Surface Method*. NA-67-193, N. Amer. Aviat., Inc., June 28, 1967.
4. Murrow, Harold N.; Pratt, Kermit G.; and Drischler, Joseph A.: *An Application of a Numerical Technique to Lifting-Surface Theory for Calculation of Unsteady Aerodynamic Forces Due to Continuous Sinusoidal Gusts on Several Wing Planforms at Subsonic Speeds*. NASA TN D-1501, 1963.
5. Watkins, Charles E.; Woolston, Donald S.; and Cunningham, Herbert J.: *A Systematic Kernel Function Procedure for Determining Aerodynamic Forces on Oscillating or Steady Finite Wings at Subsonic Speeds*. NASA TR R-48, 1959.
6. Wykes, John H.; and Lawrence, Robert E.: *Aerothermoelasticity: Its Impact on Stability and Control of Winged Aerospace Vehicles*. J. Aircraft, vol. 2, no. 6, Nov.-Dec. 1965, pp. 517-526.
7. Durgin, F. H.; and Bartlett, C. J.: *A Measurement of the Static Aeroelastic Deformation and Loading of a Wing in Supersonic Flow*. ASD-TDR-63-366, U.S. Air Force, Sept. 1963. (Available from DDC as AD 422 262.)
8. Boeing Co.: *An Analysis of Methods for Predicting the Stability Characteristics of an Elastic Airplane. Appendix A - Equations of Motion and Stability Criteria*. NASA CR-73274, 1968.
9. Van Spiegel, E.; and Wouters, J. G.: *Modification of Multhopp's Lifting Surface Theory With a View to Automatic Computation*. NLR-TN W.2, Nat. Lucht- Ruimtevaartlab. (Amsterdam), June 1962.
10. Multhopp, H.: *Methods for Calculating the Lift Distribution of Wings (Subsonic Lifting-Surface Theory)*. R. & M. No. 2884, Brit. A.R.C., Jan. 1950.
11. Lamar, John E.: *A Modified Multhopp Approach for Predicting Lifting Pressures and Camber Shape for Composite Planforms in Subsonic Flow*. NASA TN D-4427, 1968.

12. Crigler, John L.: Comparison of Calculated and Experimental Load Distributions on Thin Wings at High Subsonic and Sonic Speeds. NACA TN 3941, 1957.
13. Glauert, H.: The Elements of Aerofoil and Airscrew Theory. Second ed., Cambridge Univ. Press, 1947.
14. Falkner, V. M.: The Solution of Lifting-Plane Problems by Vortex-Lattice Theory. R. & M. No. 2591, Brit. A.R.C., 1953.
15. Hedman, Sven G.: Vortex Lattice Method for Calculation of Quasi Steady State Loadings on Thin Elastic Wings in Subsonic Flow. FFA Rep. 105, Aeronaut. Res. Inst. Swed., 1966.
16. Walton, William C., Jr.: Applications of a General Finite-Difference Method for Calculating Bending Deformations of Solid Plates. NASA TN D-536, 1960.
17. Reissner, Eric; and Stein, Manuel: Torsion and Transverse Bending of Cantilever Plates. NACA TN 2369, 1951.
18. Stein, Manuel; Anderson, J. Edward; and Hedgepeth, John M.: Deflection and Stress Analysis of Thin Solid Wings of Arbitrary Plan Form With Particular Reference to Delta Wings. NACA Rep. 1131, 1953. (Supersedes NACA TN 2621.)
19. Stein, Manuel; and Sanders, J. Lyell, Jr.: A Method for Deflection Analysis of Thin Low-Aspect-Ratio Wings. NACA TN 3640, 1956.

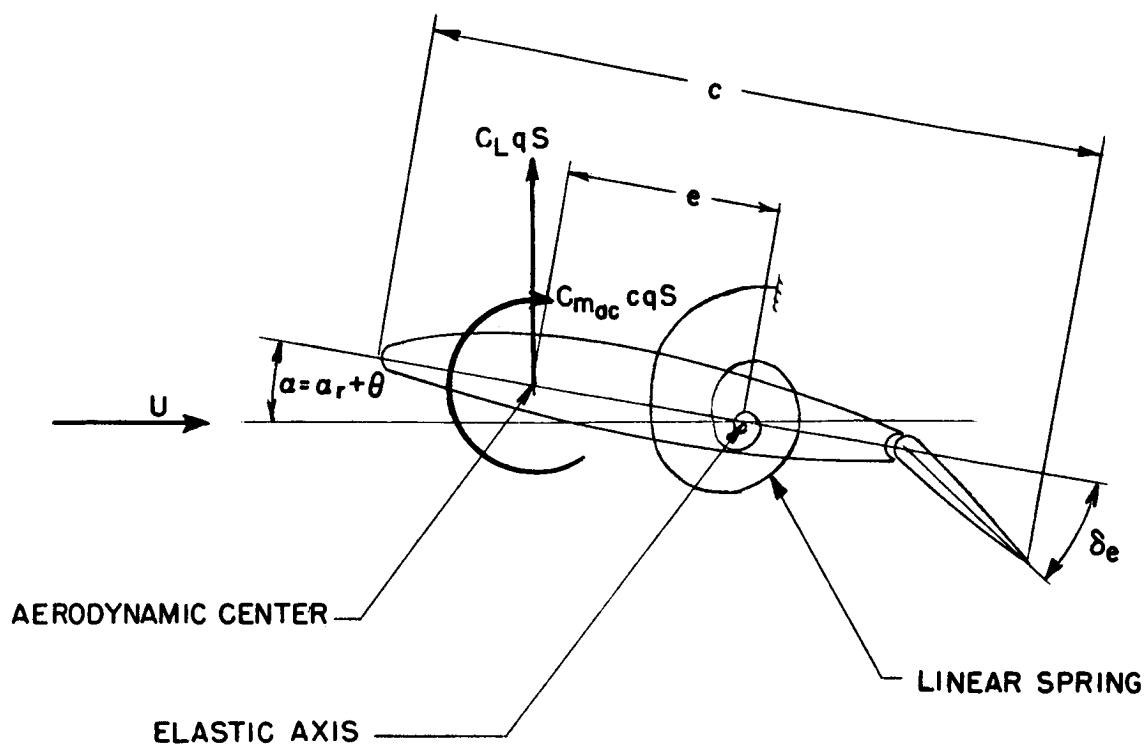


Figure 1.- Rigid airfoil supported elastically.

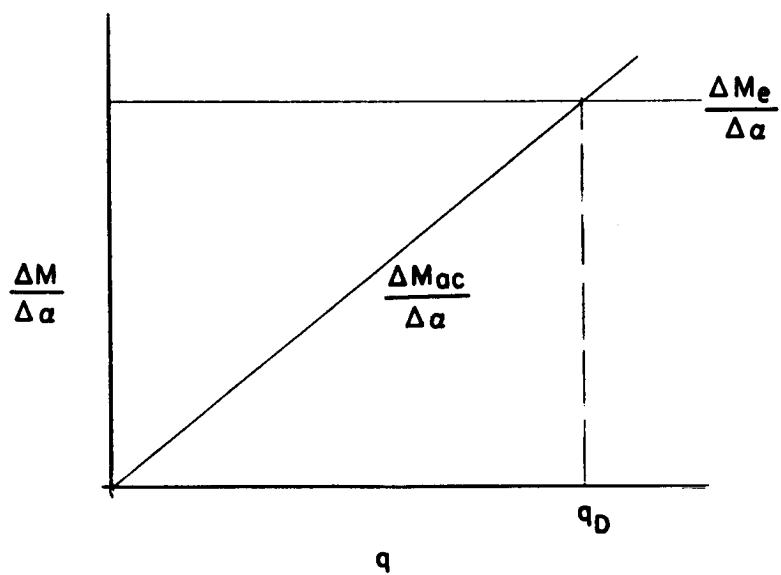


Figure 2.- Graphical solution for the torsional divergence dynamic pressure.

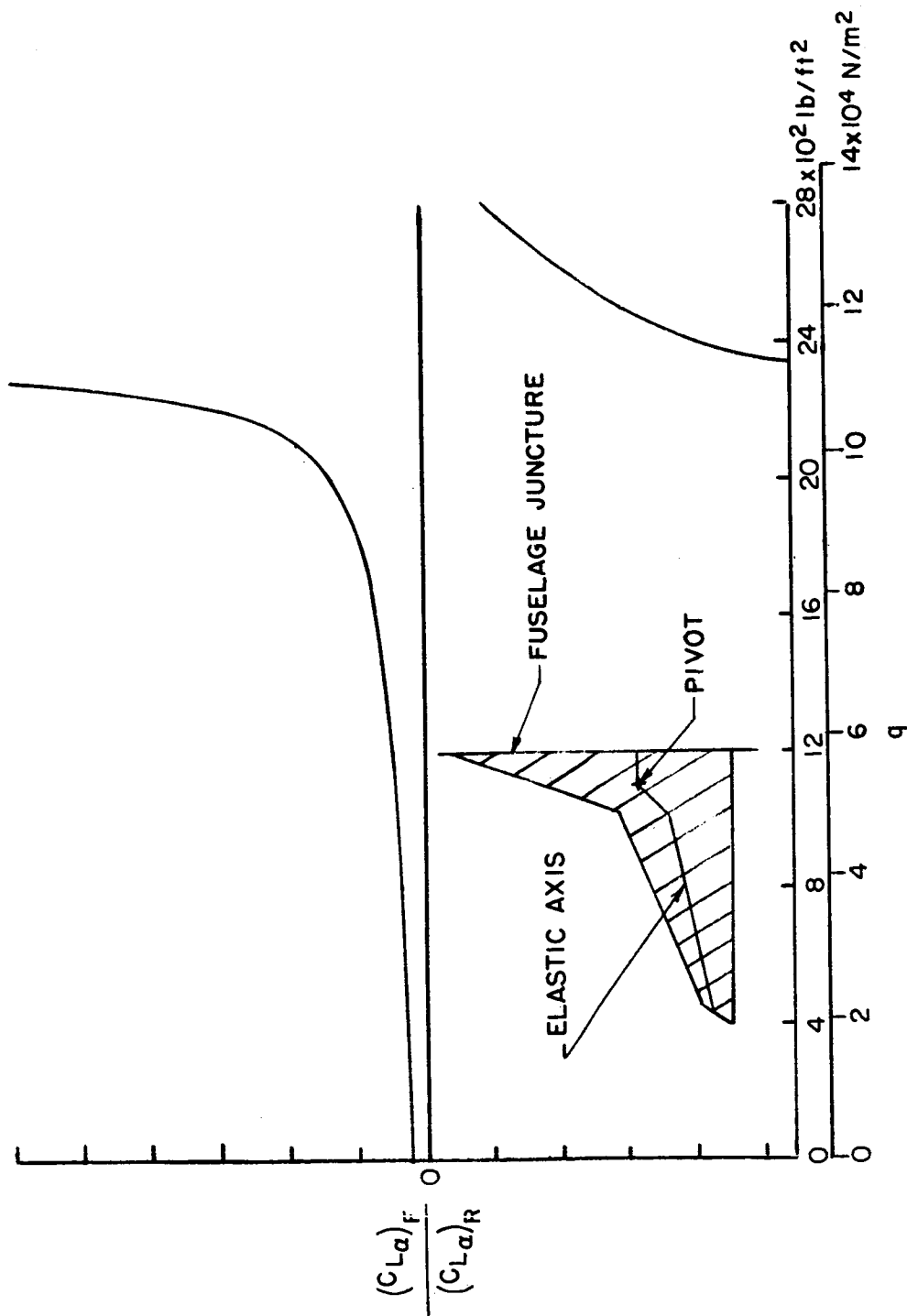


Figure 3.- Torsional divergence.  $M = 0.9$ .

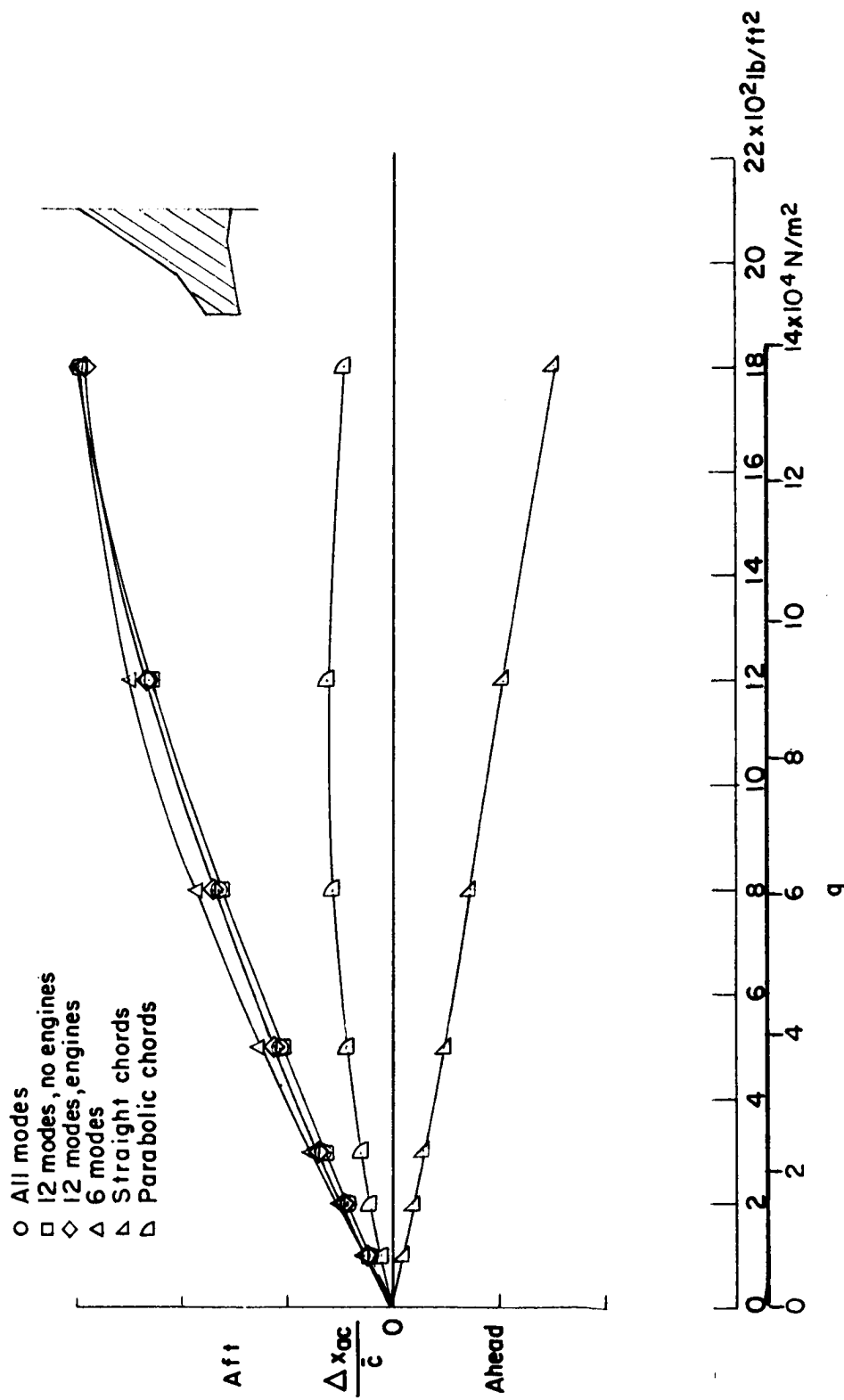


Figure 4.- Effect of structural representation and altitude on flexible aerodynamic-center location.  
Massless,  $M = 0.9$ .

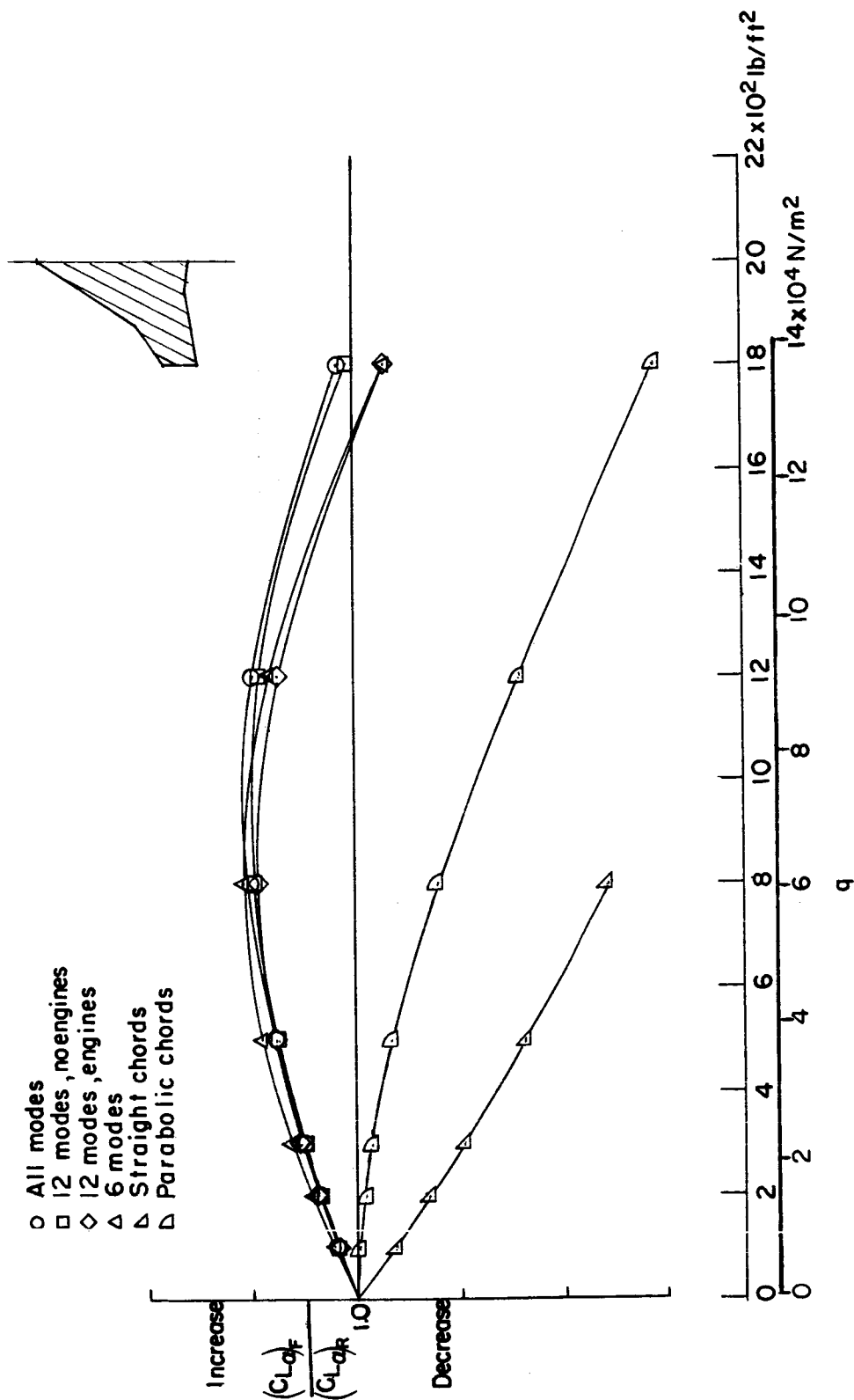


Figure 5.- Effect of structural representation and altitude on flexible lift-curve slope. Massless,  $M = 0.9$ .

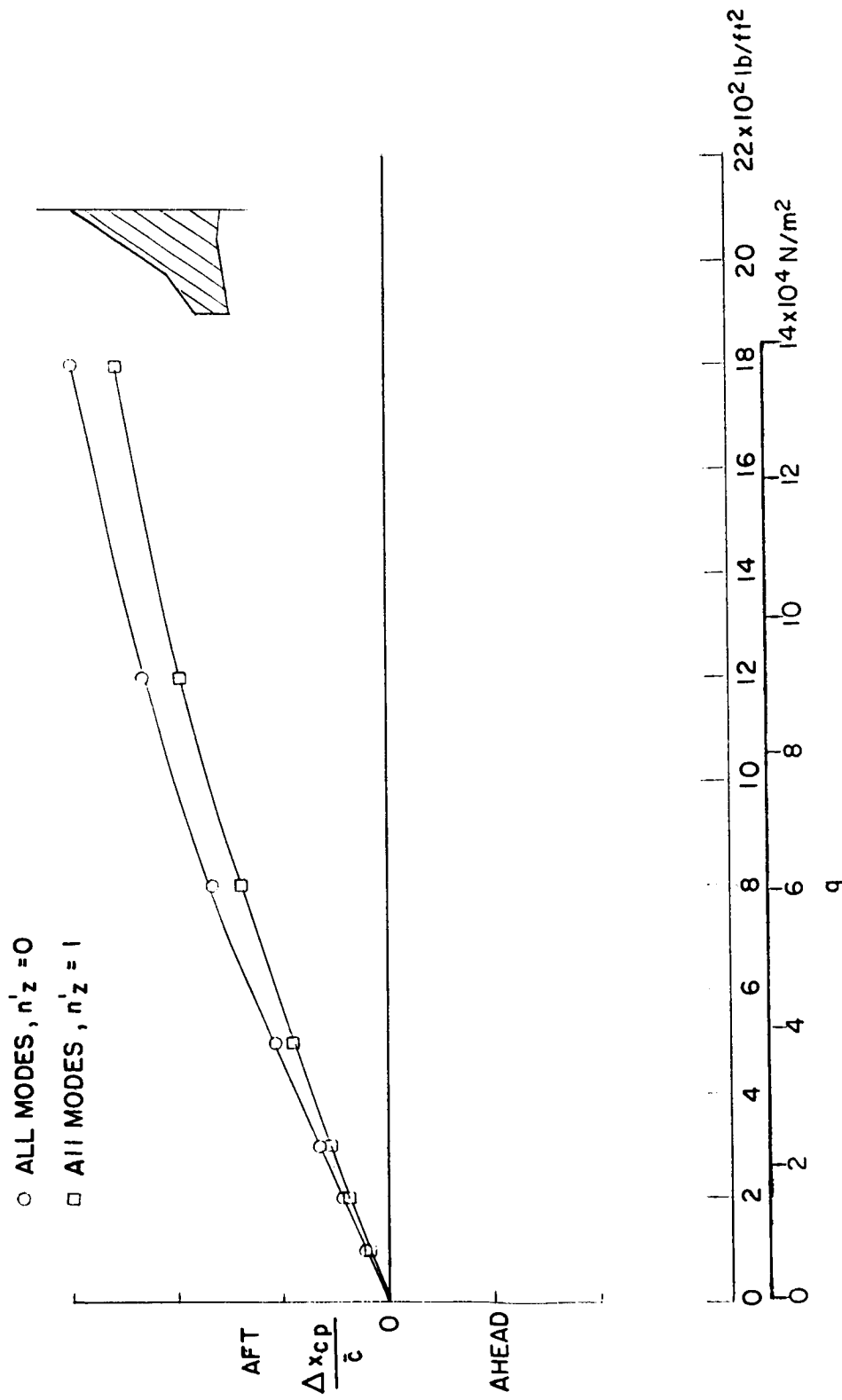


Figure 6.- Effect of load factor on the flexible center of pressure movement.  $M = 0.9$ .

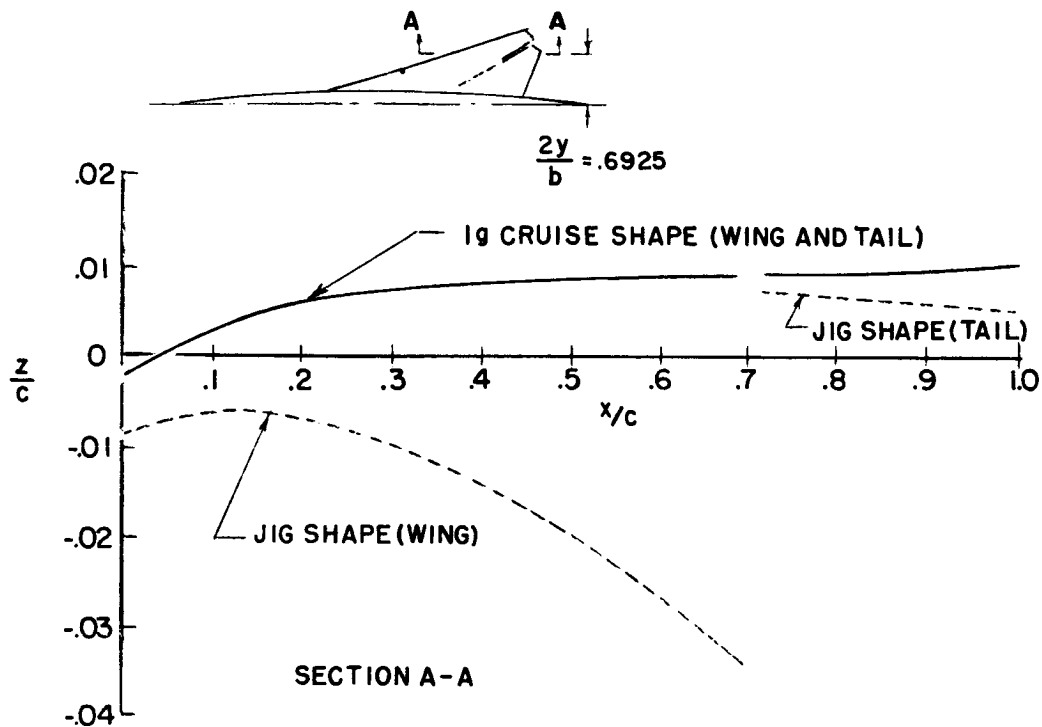


Figure 7.- Jig shape and cruise shape.

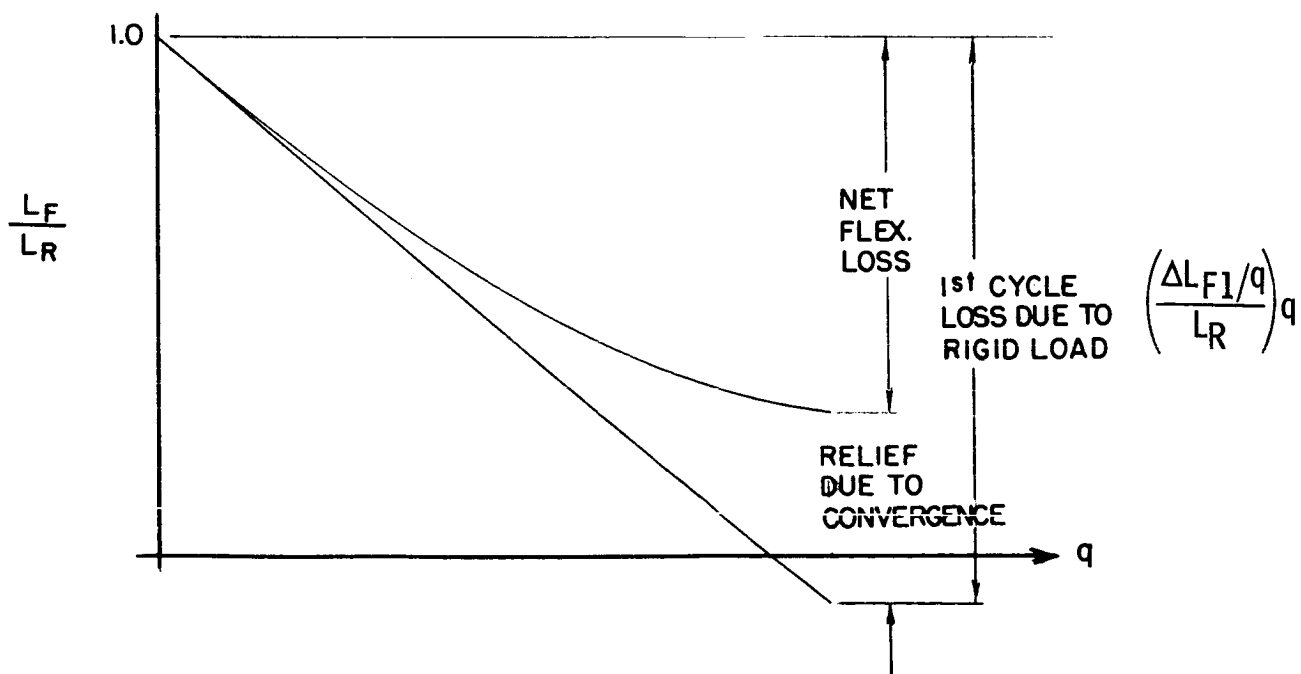
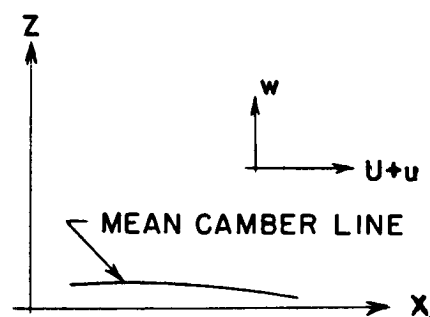
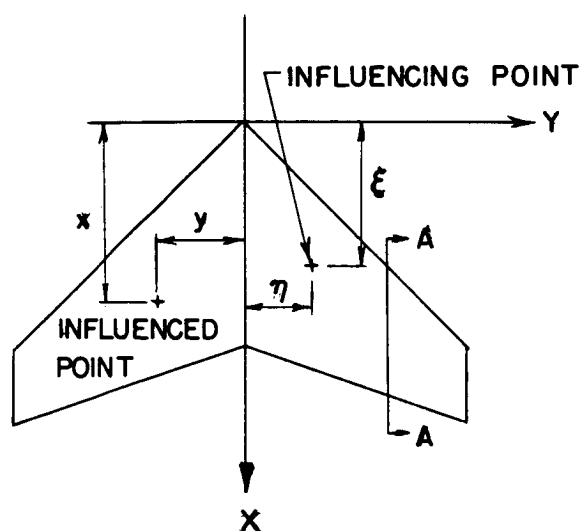


Figure 8.- Moderation of flexible-lift loss due to convergence.

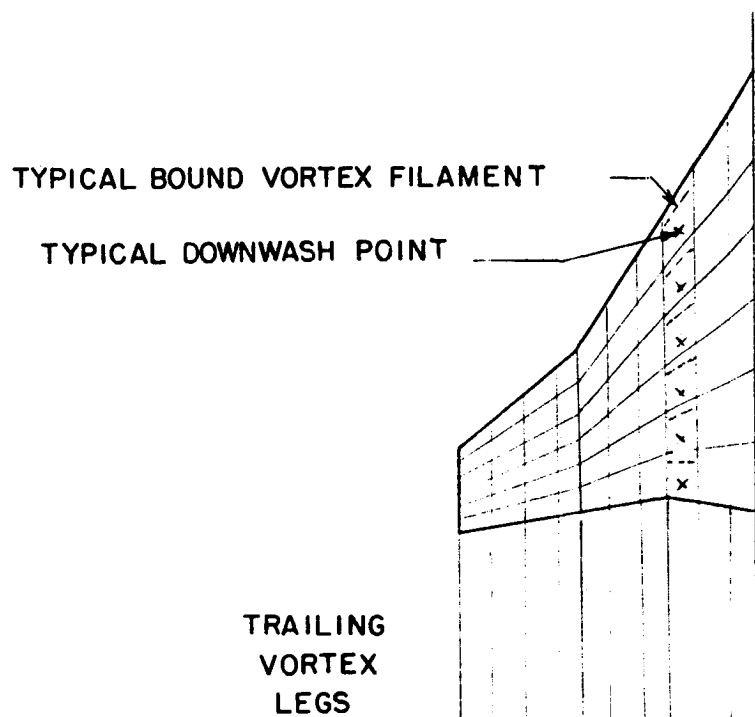




SECTION A-A

WING MEAN CAMBER LINE APPROXIMATED BY PROJECTING THE SURFACE SLOPES TO CORRESPONDING POINTS IN THE X-Y PLANE.

Figure 9.- Coordinate system.



SIX CHORDWISE  
STATIONS ILLUSTRATED,  
EQUALLY SPACED  
ALONG THE LOCAL  
CHORD. THE LOAD POINT  
IS AT THE PANEL  $c/4$   
AND THE DOWNWASH POINT  
IS AT THE PANEL  $3c/4$   
POINT.

Figure 10.- Paneling on a wing.

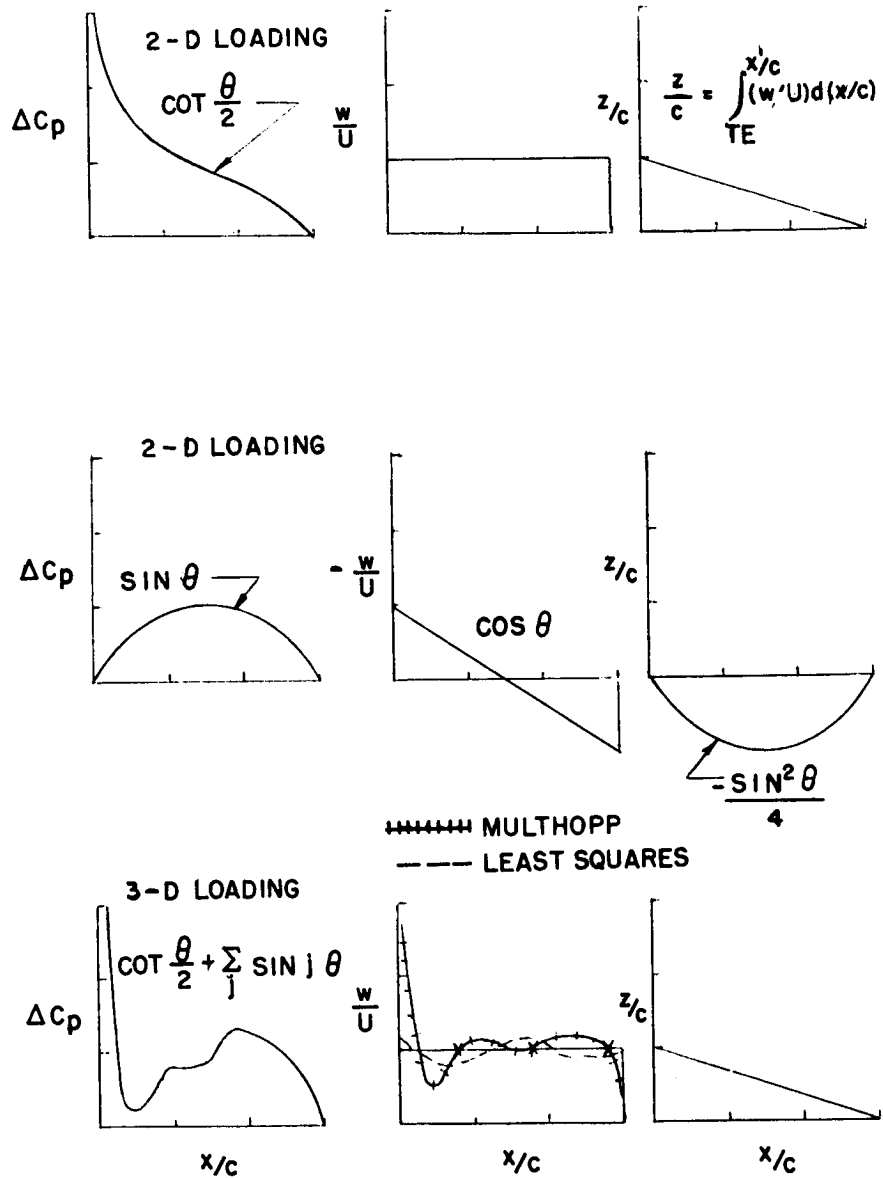


Figure 11.- Downwash fit method.

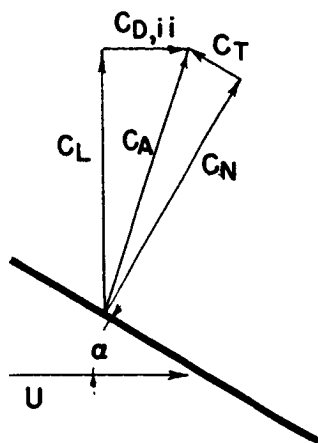


Figure 12.- Resolution of aerodynamic-force coefficient into components.

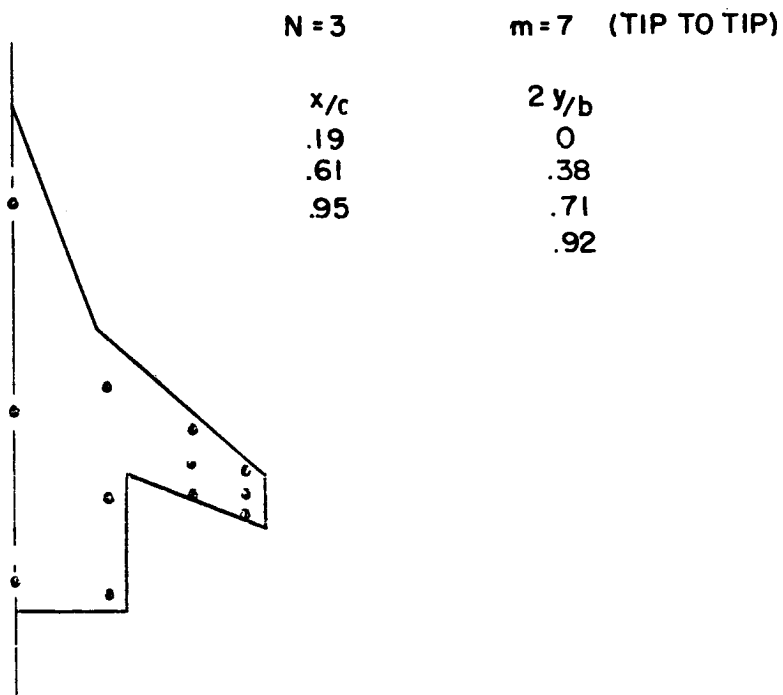


Figure 13.- Typical control point pattern with Multhopp method.

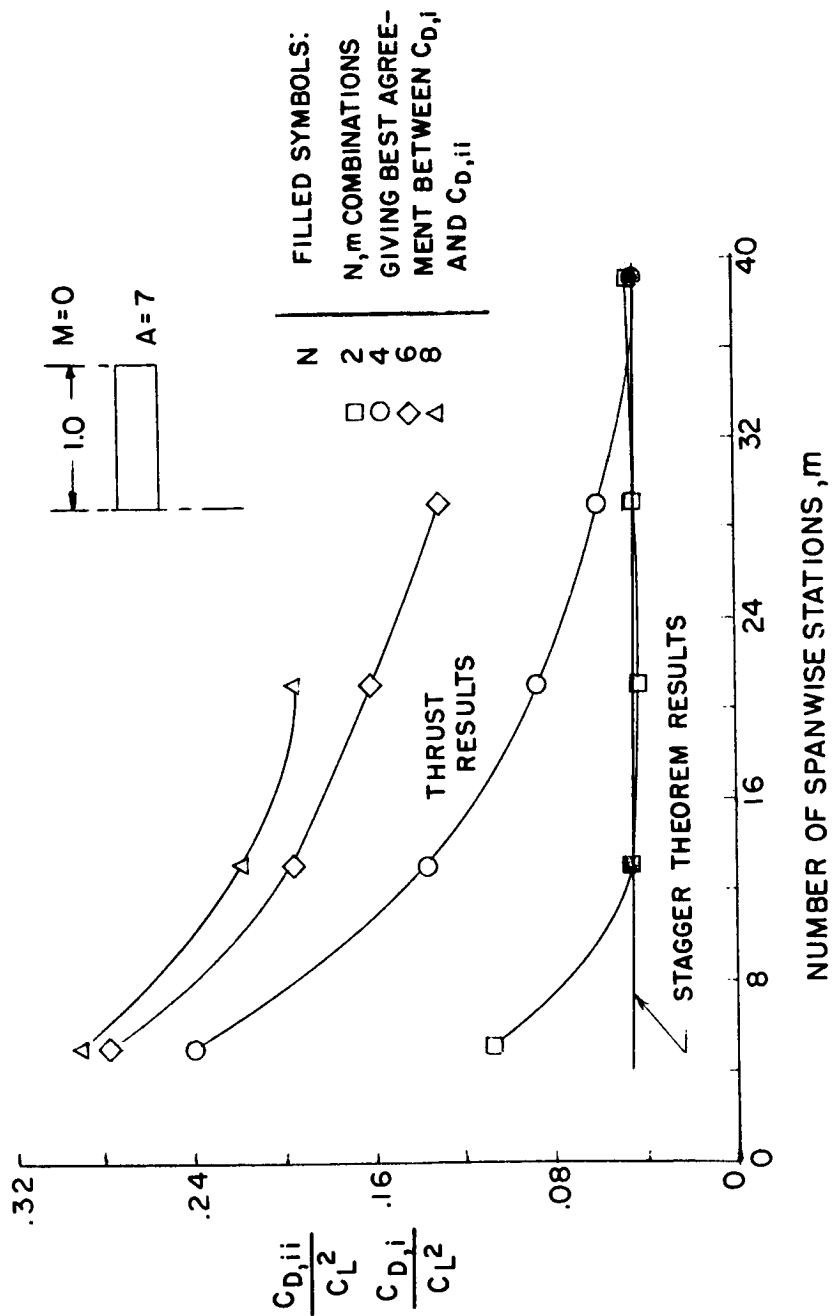


Figure 14.- Effect of number of chordwise and spanwise stations on induced drag.

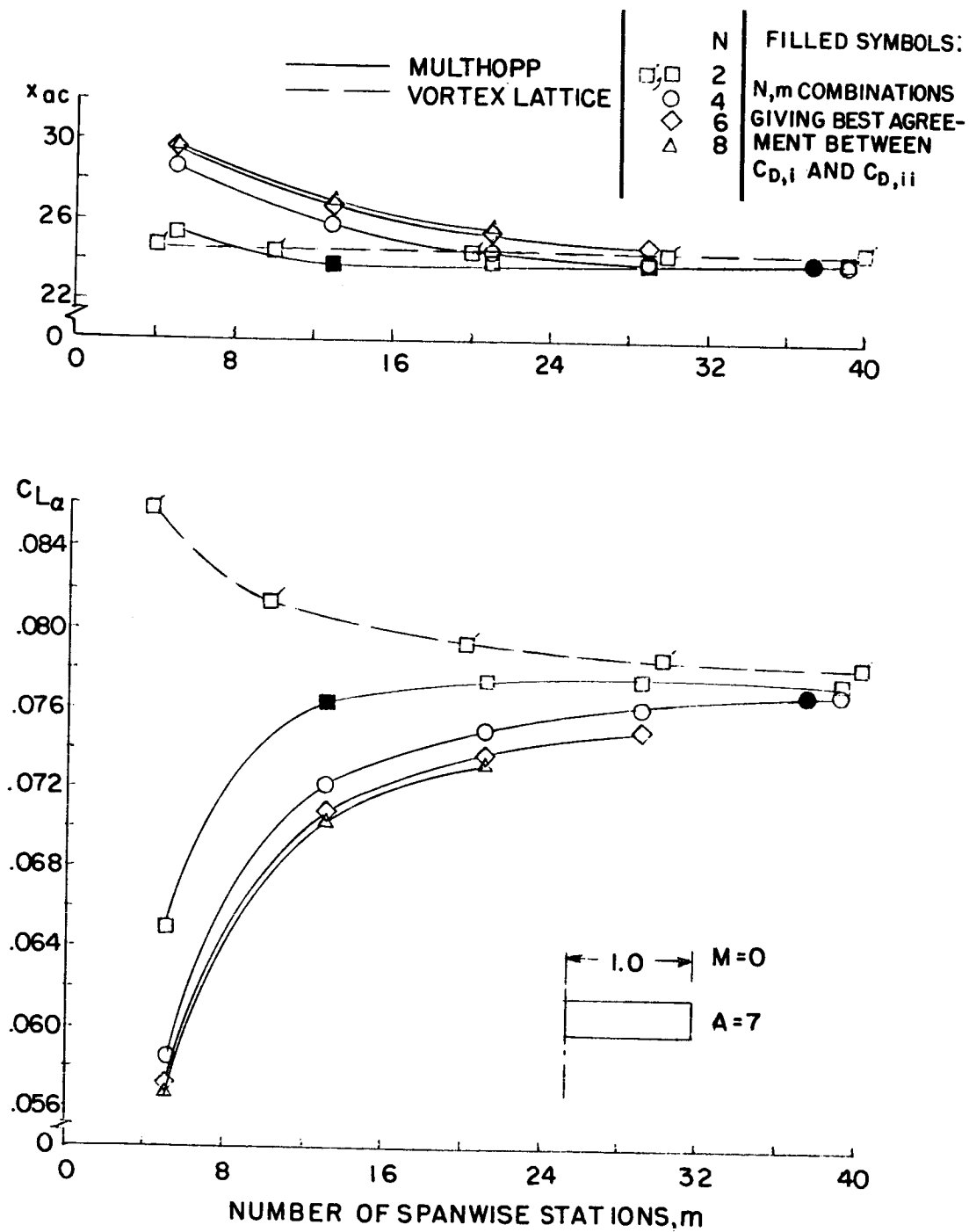
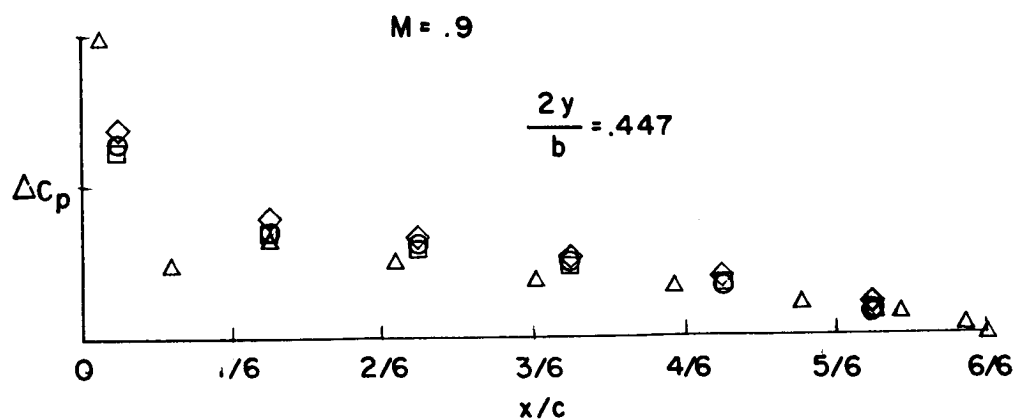


Figure 15.- Effect of  $N$  and  $m$  on aerodynamic characteristics.



- SUBSONIC KERNEL APPROACH
- VORTEX LATTICE - WITH FUS/TAIL
- ◇ VORTEX LATTICE - WING ALONE
- △ MUTHOPP - WING ALONE

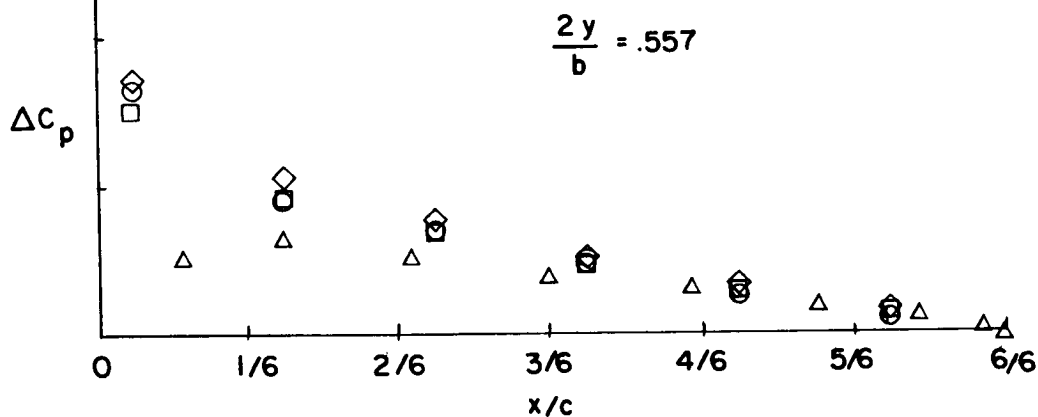


Figure 16.- Lifting pressures predicted by different subsonic theoretical methods.

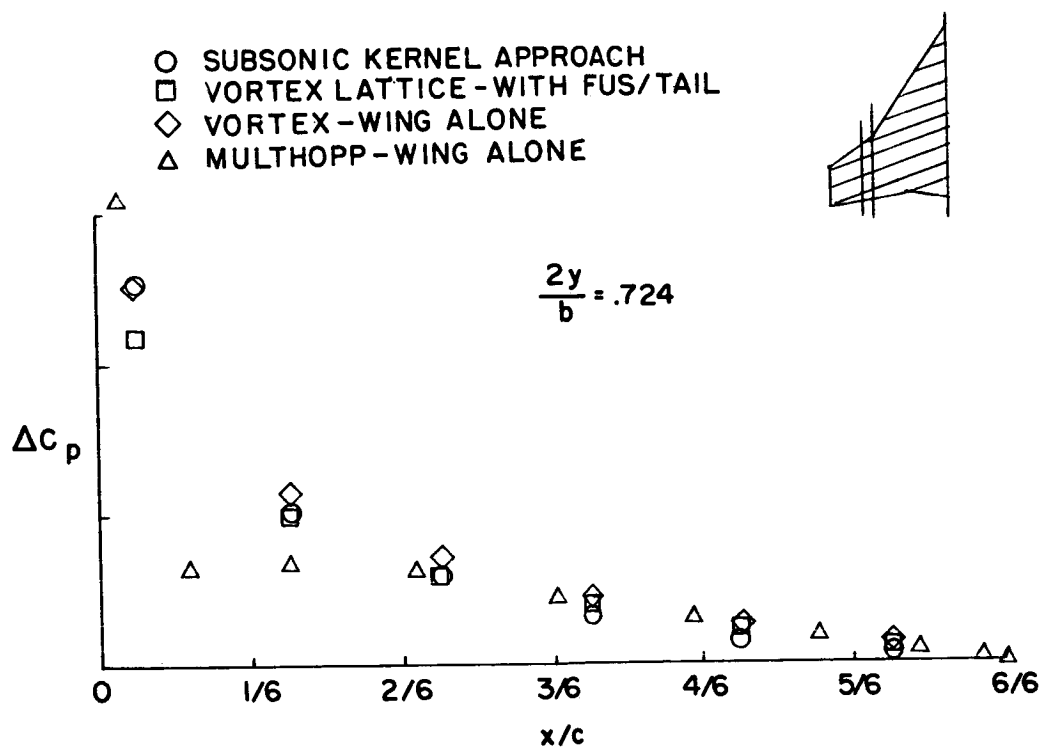
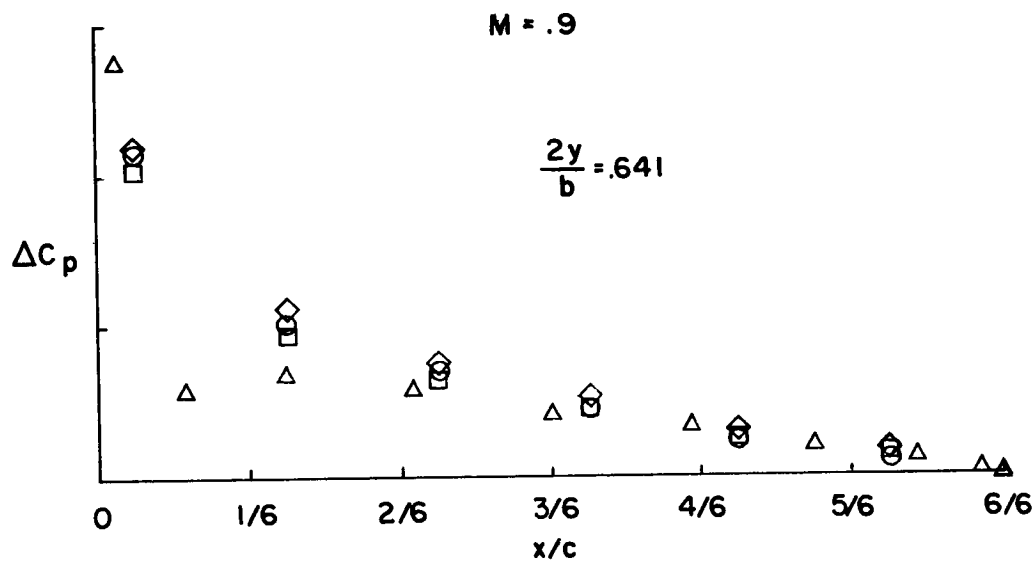


Figure 16.- Continued.



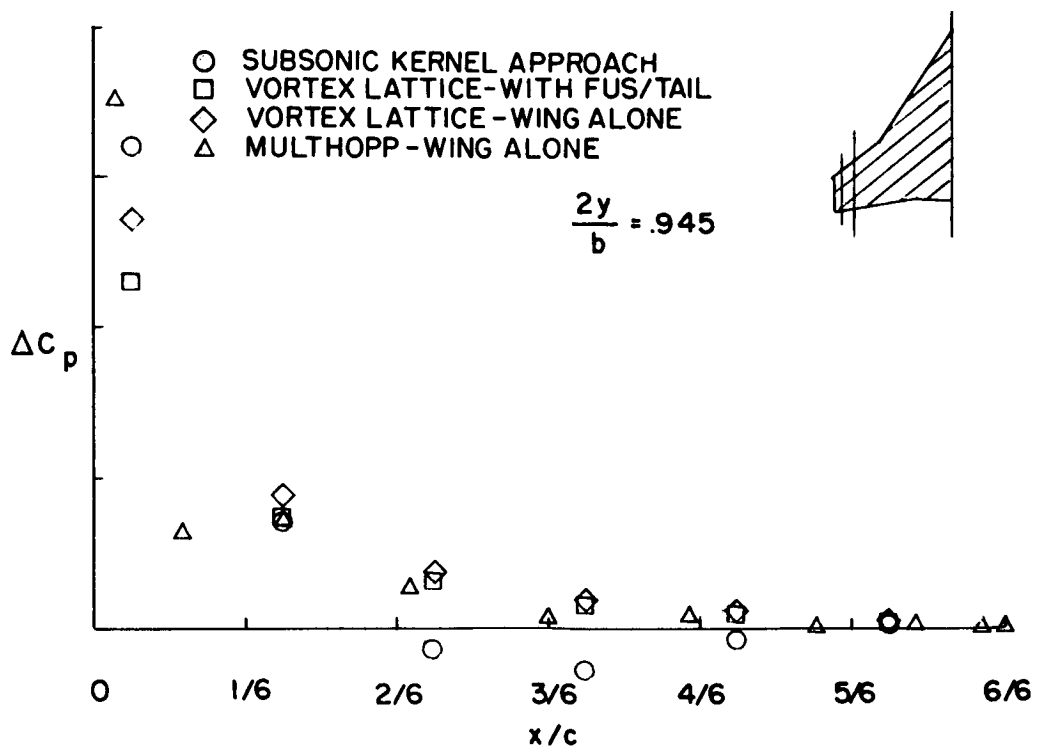
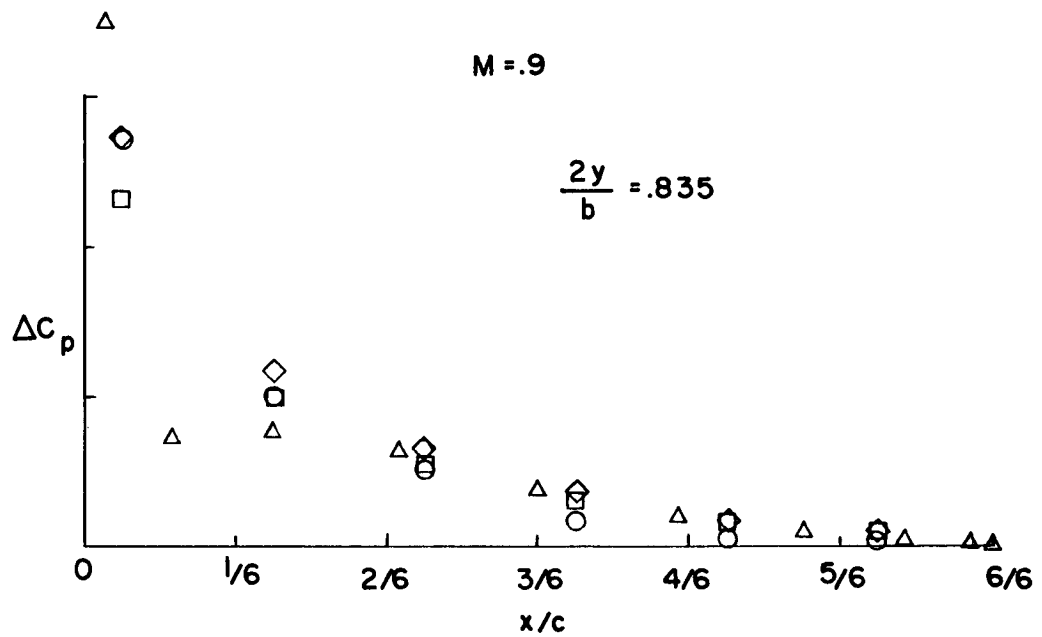
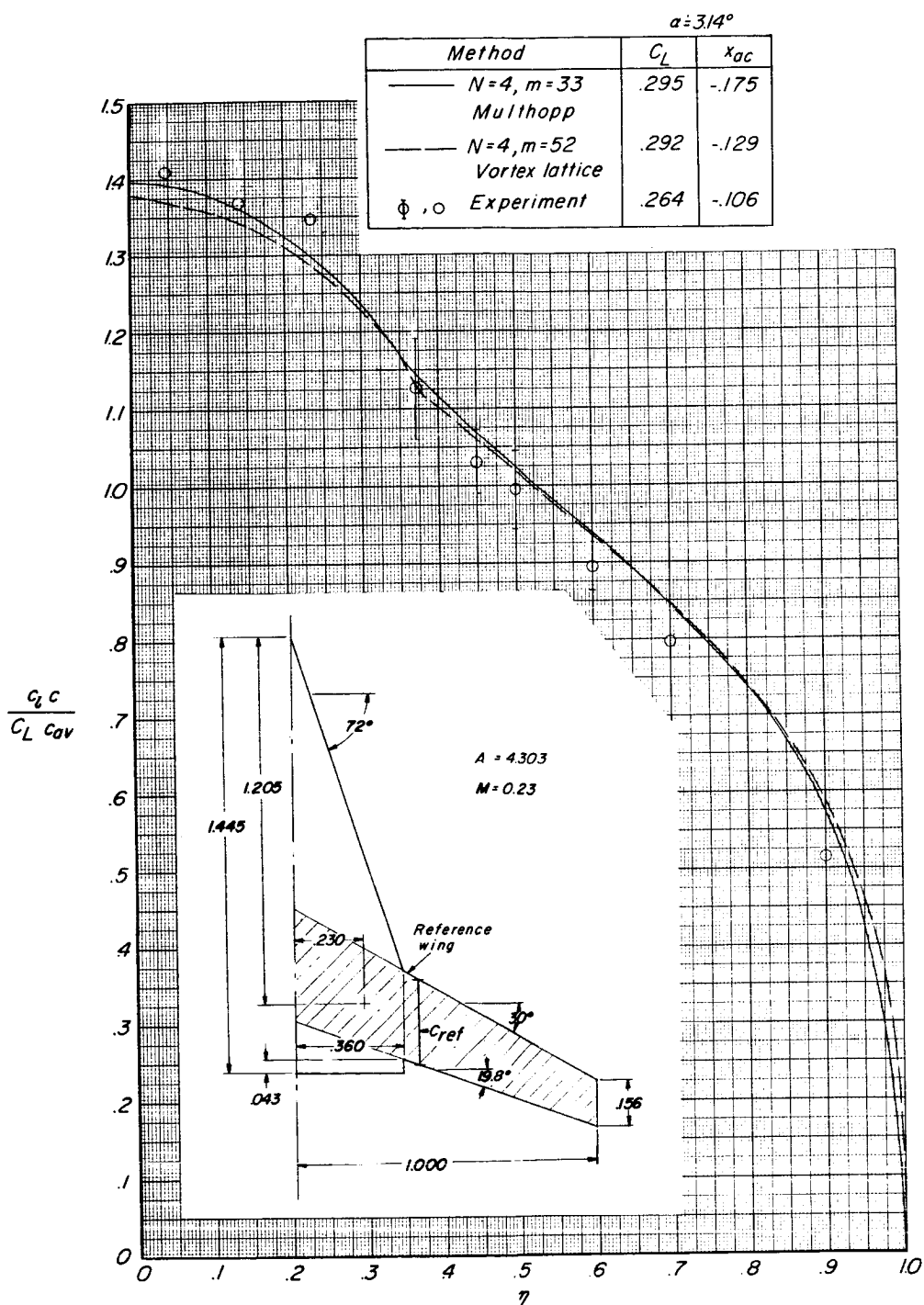
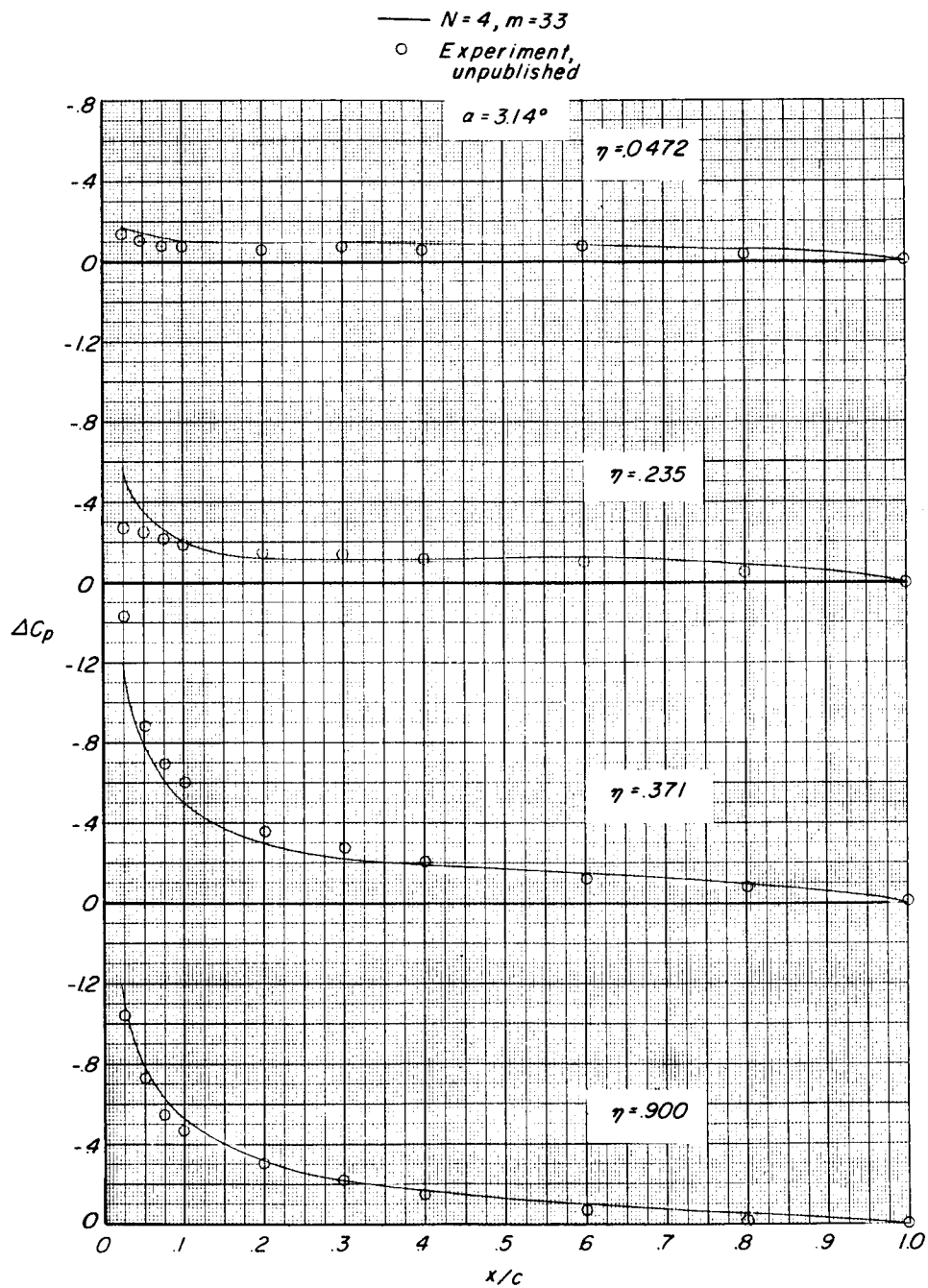


Figure 16.- Concluded.



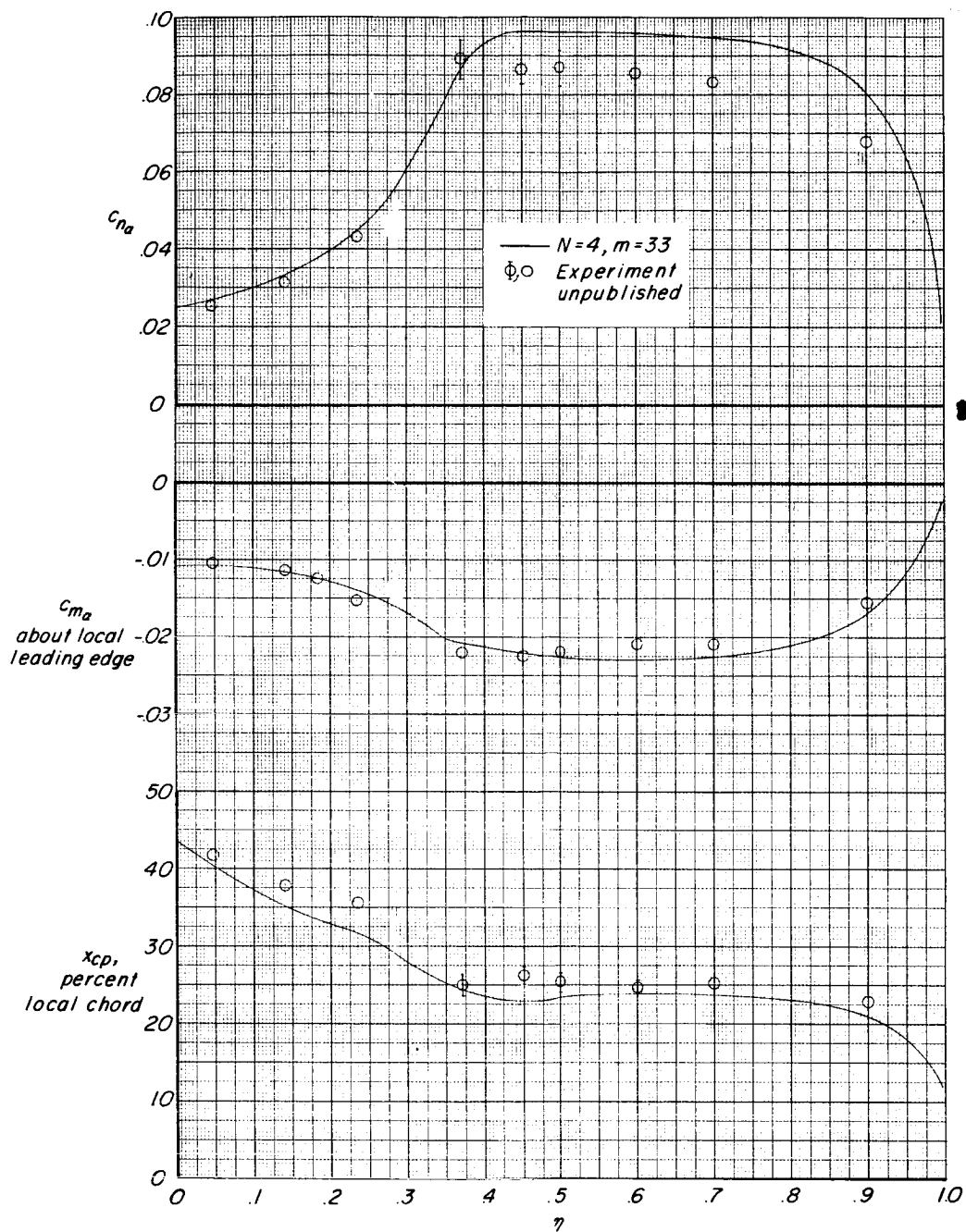
(a) Spanwise loading.

Figure 17.- Loading and moment distributions predicted by the modified Multhopp method and compared with experiment for a variable sweep planform of  $A = 4.303$  at  $M = 0.23$ .



(b) Local chordwise loadings.

Figure 17.- Continued.



(c) Local slope of the normal-force and pitching-moment coefficients and centers of pressure.

Figure 17.- Concluded.

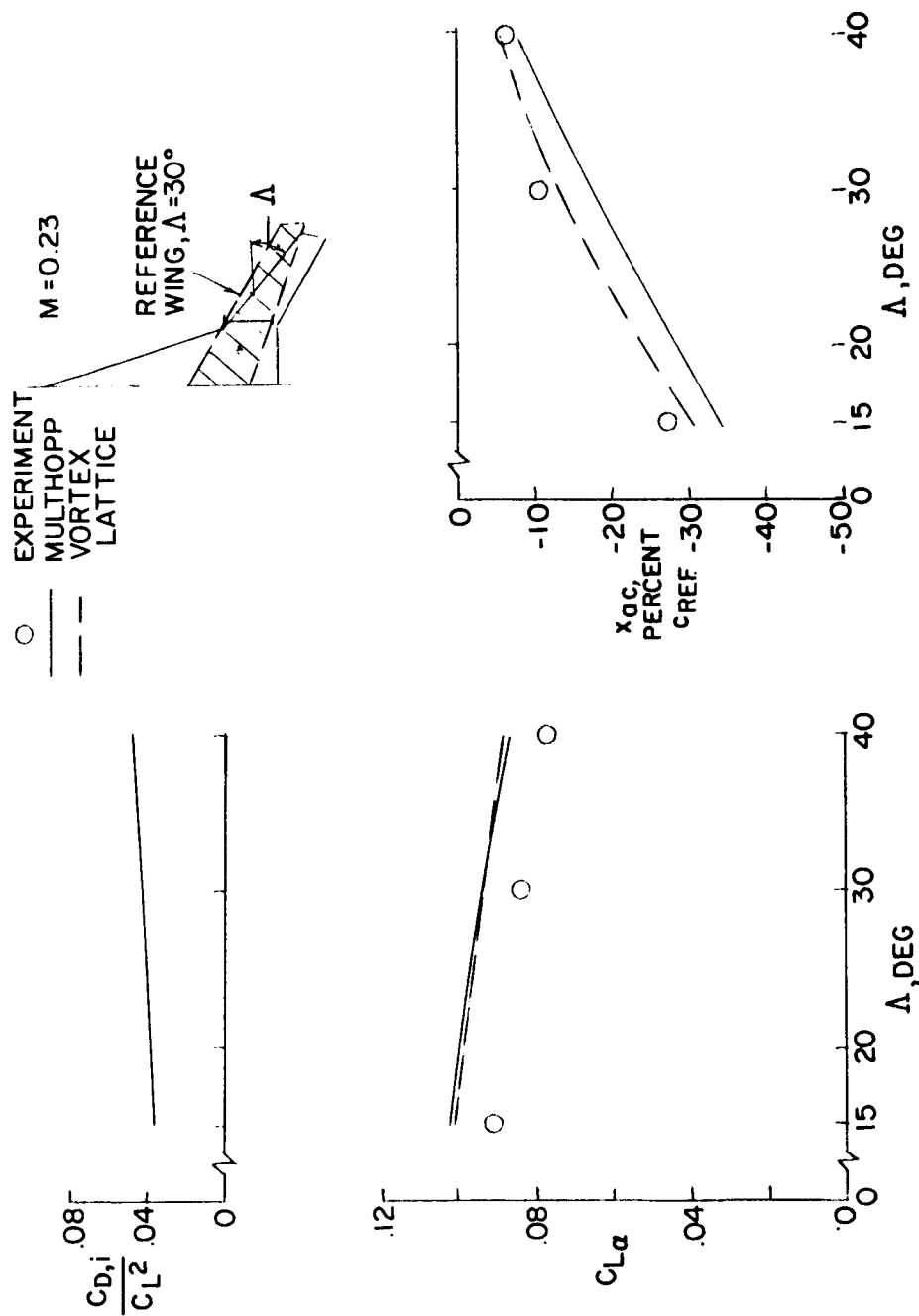


Figure 18.- Effect of increasing leading-edge outboard sweep on aerodynamic characteristics.

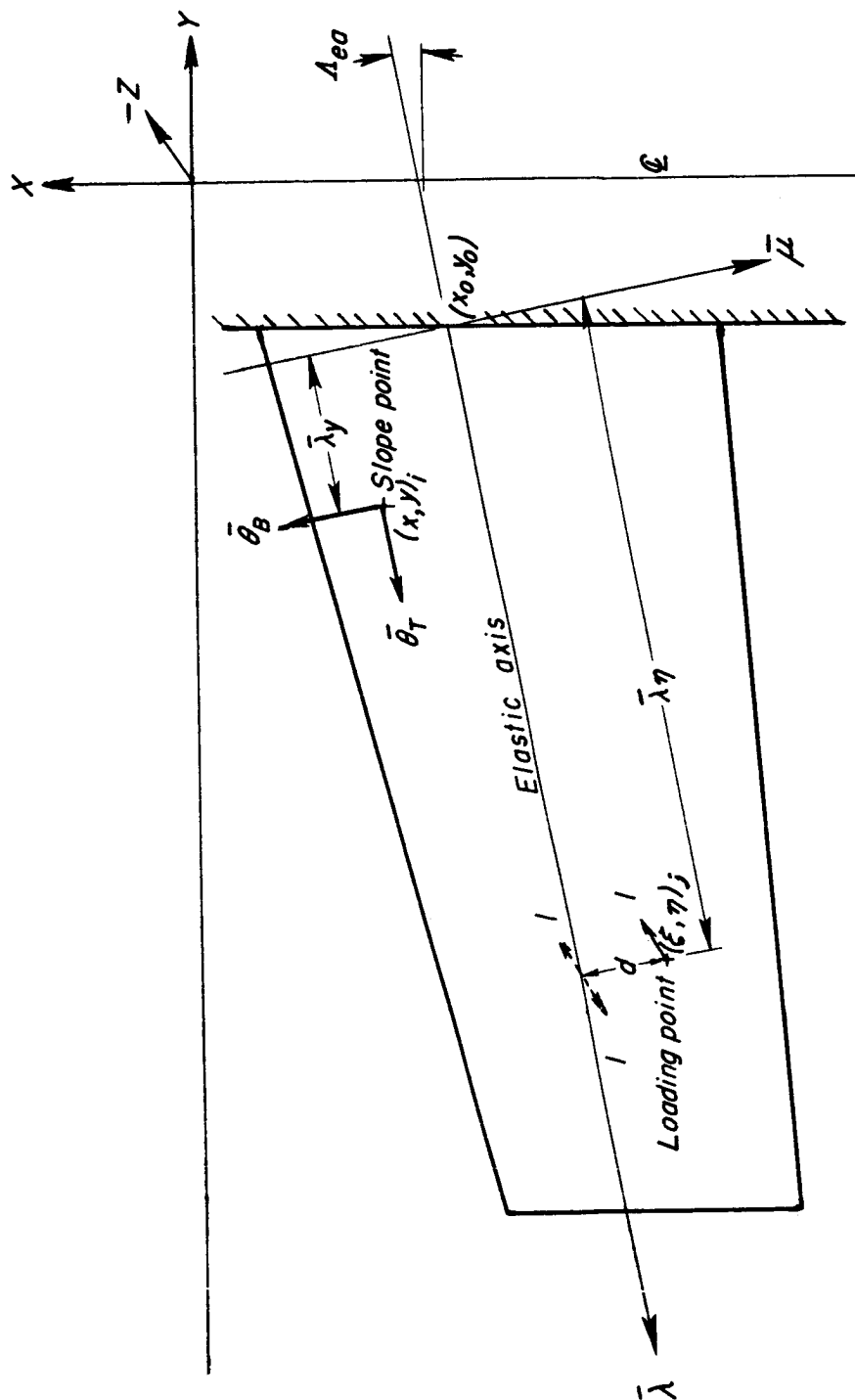
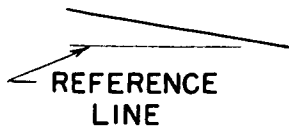
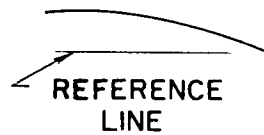


Figure 19.- Slender-beam coordinate system.

STRAIGHT CHORD  
(TWIST ONLY)



PARABOLIC CHORD  
(TWIST AND PRESCRIBED CAMBER MODE)



ALL MODES (FULLY FLEXIBLE)

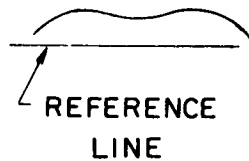


Figure 20.- Chordwise results from structural constraints.

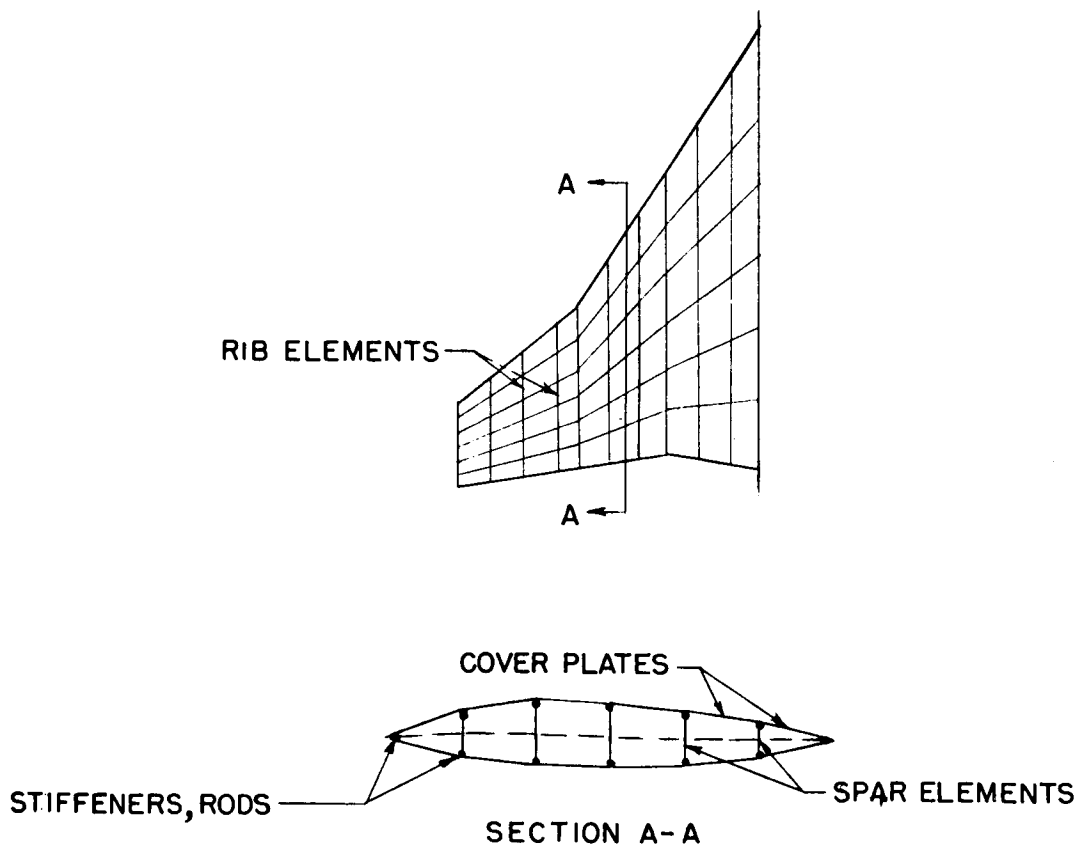


Figure 21.- Finite element representation.

$$M = .9$$

$$q = 1200 \text{ LB/FT}^2 (57456 \text{ N/m}^2)$$

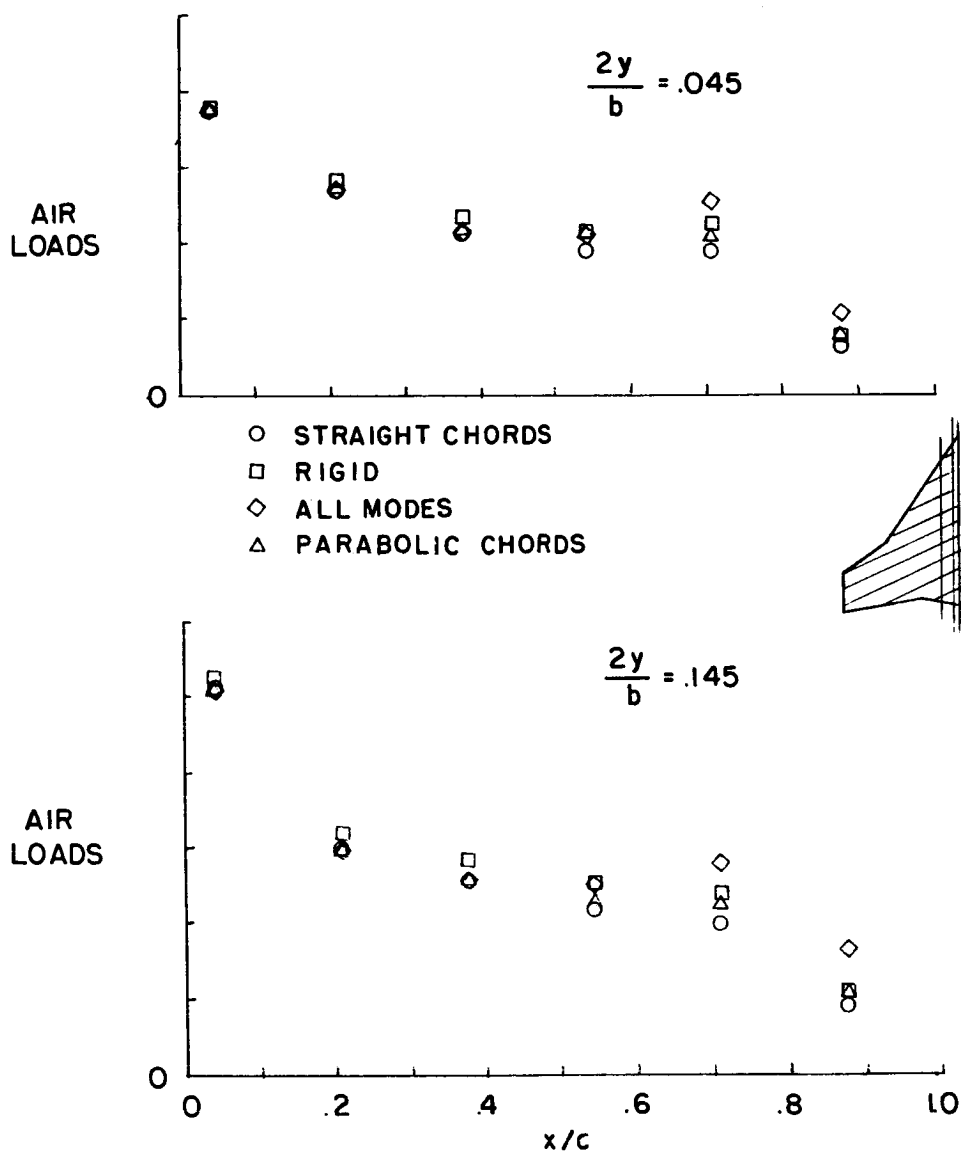


Figure 22.- Effect of structural representation on air loads developed over each grid element.



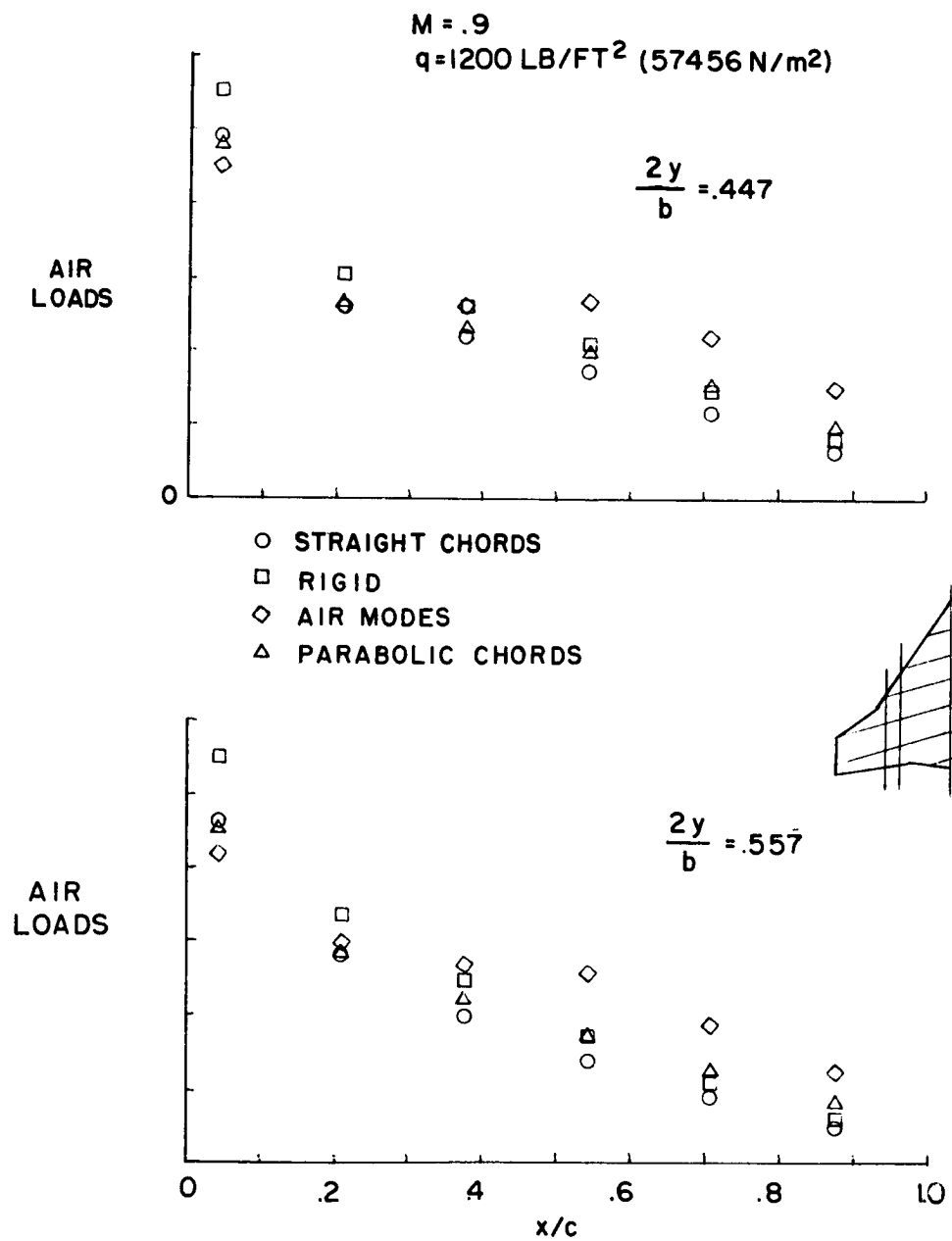


Figure 22.- Continued.

$$M = .9$$

$$q = 1200 \text{ LB/FT}^2 (57456 \text{ N/m}^2)$$

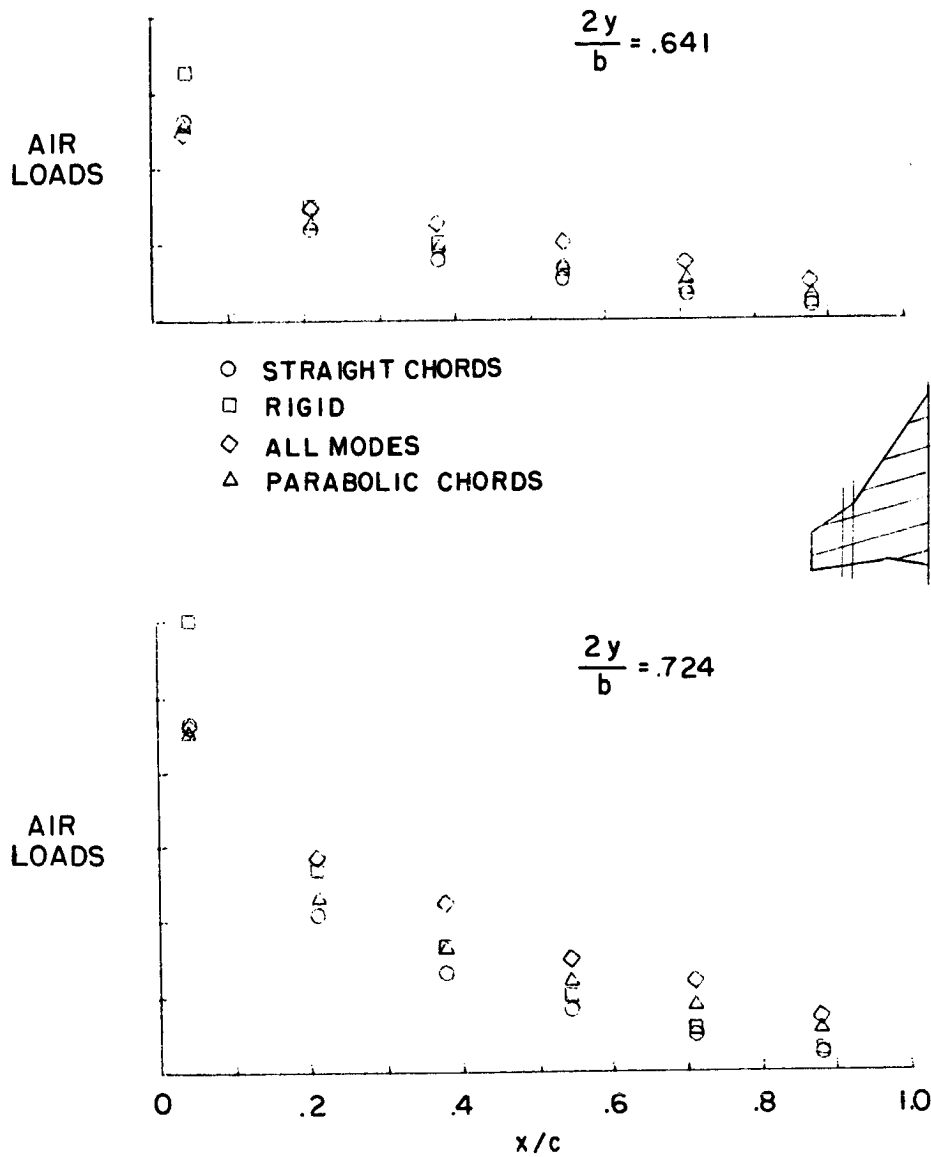


Figure 22.- Continued.

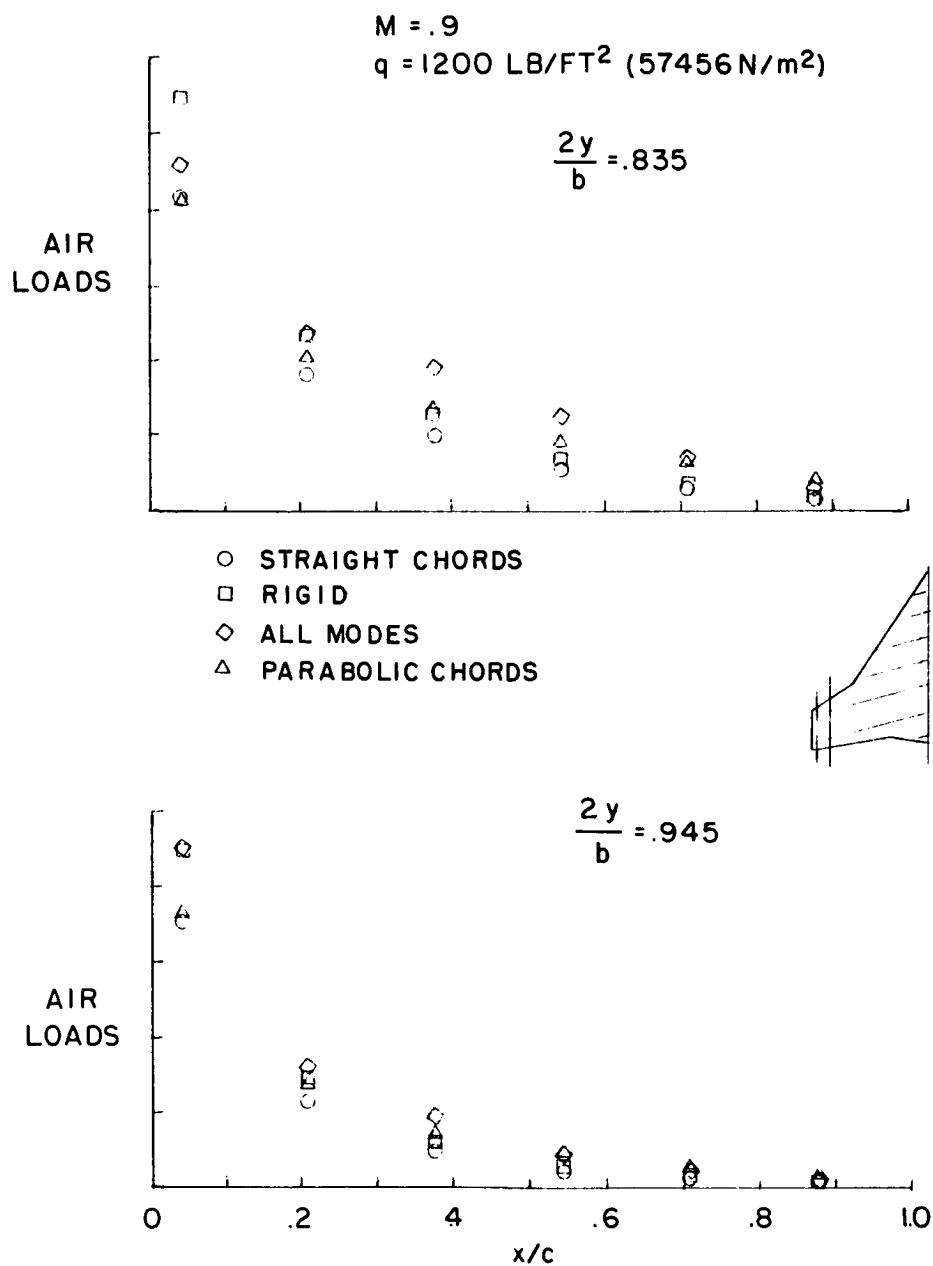


Figure 22.- Concluded.

## 7. RESPONSE OF FLEXIBLE AIRPLANES TO ATMOSPHERIC TURBULENCE

By Kermit G. Pratt  
Langley Research Center

### ABSTRACT

Current random-process-theory methods for the estimation of the theoretical average frequency of exceeding peak responses (particularly loads) of various levels are described, and calculated results are compared with results from flight measurements. Contents include (1) the statistical characteristics of the airplane responses and of the turbulence velocities, (2) the relationship of these characteristics in terms of power spectral density (PSD) functions and frequency responses to a sinusoidal gust field of various wavelengths, (3) the relation of PSD functions to random time functions and to statistical parameters, (4) methods of calculating frequency responses and aerodynamic forces due to gusts, and (5) the synthesis of the responses experienced during routine flight operations.

### INTRODUCTION

From the first days of aviation, airplane pilots and passengers have been jostled and shaken, and the airplane structures have been loaded by frequent disturbances during flight. Early airplane travelers spoke of "bumps" caused by "air pockets," but people with technical backgrounds were aware that the disturbances felt were varying accelerations of the airplane in response to the turbulent motion of the atmosphere.

Turbulence is caused principally by wind shears and by convective action as in cumulus clouds and thunderstorms. The turbulent air moves with varying speeds and directions; the velocity fluctuations that noticeably disturb an airplane are called gusts. In fact, gusts and turbulence are often used synonymously.

The fundamental link between the airplane disturbances or responses and the turbulence velocities is the change in angle of attack (or sideslip) induced by the turbulence velocity in conjunction with the forward speed of the airplane. This relationship is indicated in figure 1 in which an airplane, which is shown flying from right to left, encounters a portion of turbulence with a vertical velocity component labeled  $w_g$ . The vector diagram describes the angle of attack on the lifting surface  $\alpha_g$ , which results from the combination of  $w_g$  and the flight velocity  $V$ . This angle of attack, of course, produces an aerodynamic force, called a gust force, which in turn causes the airplane to accelerate. Concurrently, there is an angle of attack due to the disturbed motion of the airplane, and

consequently another aerodynamic force exists that modifies the airplane acceleration. These relations will be examined in much more detail subsequently.

The airplane responses to turbulence generally adversely affect the airworthiness of the airplane and have been considered in design throughout almost the entire history of aviation. The evolution of the airplane with regard to increased speed, size, weight, and improved structural efficiency with attendant increase in flexibility has aggravated the adverse effects and at the same time has increased the complexity of design procedures.

## SYMBOLS

$A_{\overline{M}}, A_n$	gust sensitivity factor for bending moment and load factor, respectively
$A_z$	gust sensitivity factor for any response quantity $z$ , $\sigma_z / \sigma_{wg}$
$a_n$	normal acceleration
$B, C$	constants
$d$	distance of flight
$d_i$	distance of flight in turbulence of intensity $\sigma_i$ ( $i = I, II, III$ )
$d_0$	distance of flight in smooth air
$d_T$	total distance of flight
$d_1$	flight distance in nonstorm conditions
$d_2$	flight distance in storm conditions
$EI$	structural stiffness
$e$	base of natural system of logarithms, 2.71828
$F$	force
$f$	frequency (1 cycle per second = 1 hertz)
$F(t), f(t)$	random time functions

$f(t + \tau)$	random time function displaced by time lag
$\mathcal{F} \mathcal{I}\{\}$	Fourier transform
$G_Z(t)$	response to step gust
$G_Z(t - \tau)$	response to step gust displaced by time lag
$g$	acceleration of gravity, 32.2 ft/sec <sup>2</sup> (9.81 m/sec <sup>2</sup> )
$H(f), H(\omega)$	frequency response functions, with accompanying subscript denoting specific type of response
$h$	pressure altitude
$h_Z(\ )$	response to impulse gust $\left( \text{for example, } h_Z(t) = \frac{dG_Z(t)}{dt} \right)$
$I$	aerodynamic influence function
$i, j$	mode designations
$K$	kernel function in integral equation
$k'$	wave number or reduced frequency, $\omega L/V$
$L$	scale of turbulence; lift force
$L_g$	lift due to gust velocity
$L_\infty$	steady-state lift
$M$	Mach number
$\overline{M}$	bending moment
$M_{ii}$	generalized mass of $i$ th mode
$M_{ij}$	generalized mass of $i$ th and $j$ th modes

$m$	mass per unit area; mean value; particular "box" in Mach box method
$N$	average frequency of exceeding response peak of a given level
$N(z)$	average frequency of exceeding response peak of level $z$
$N_0$	average frequency of crossing zero level with positive slope
$N_T(z)$	$N(z)$ for total design mission
$n$	load factor; number of modes; number of "boxes" into which the wing is divided in Mach box method
$P_1$	probability of experiencing "nonstorm" turbulence
$P_2$	probability of experiencing "storm" turbulence
$p$	pressure on lifting surface
$p_g$	$p$ due to gust field
$p_i, p_j$	$p$ due to motion in $i$ th mode and $j$ th mode, respectively
$\bar{p}, \bar{p}_g, \bar{p}_i, \bar{p}_j$	amplitude of sinusoidal variation in $p$ , $p_g$ , $p_i$ , and $p_j$ , respectively
$p(z)$	probability density of quantity $z$
$p(\sigma), p(\sigma_i)$	continuous and discrete probability densities, respectively
$Q_{ig}$	generalized aerodynamic force on mode $i$ due to gust
$Q_{ij}$	generalized aerodynamic force on mode $i$ due to motion in mode $j$
$q$	dynamic pressure, $\frac{\rho}{2} V^2$
$R(\tau)$	autocorrelation function
$R_{w_g}(\tau), R_z(\tau)$	autocorrelation function of $w_g$ and $z$ , respectively

$S$	area of airplane in XY-plane
$T$	upper limit of time integration
$t$	time
$u_g, v_g, w_g$	turbulence velocity components in direction of flight, in spanwise direction, and in vertical direction, respectively
$V$	flight velocity; airspeed
$V_e$	equivalent airspeed, $V\sqrt{\rho/\rho_0}$
$V_{\min}$	stalling speed
$W$	airplane weight
$\bar{w}_g$	amplitude of sinusoidal variation in gust downwash $w_g$
$w_j$	downwash due to motion in jth mode
$X, Y$	airplane axes
$x$	distance from airplane reference point in fore and aft direction
$\tilde{x}$	distance of airplane reference point from earth-fixed reference point in direction of flight
$\hat{x}$	distance of point on airplane from earth-fixed reference point in direction of flight
$y$	distance along surface span
$\bar{y}$	wing semispan station, measured in fractions of a semispan
$z$	response quantity; vertical distance from undisturbed flight path
$z_i, z_j$	generalized coordinate for ith mode and jth mode, respectively



$\bar{z}_i$	$z_i$ for sinusoidal gust velocity
$\alpha$	angle of attack
$\alpha_g$	$\alpha$ due to vertical gust velocity only
$\zeta$	ratio of damping to critical damping
$\zeta_I, \zeta_{II}$	first-mode damping ratio for conditions I and II, respectively, in figure 24
$\lambda$	gust wavelength
$\xi, \eta$	dummy variables
$\xi_i(x,y), \xi_j(x,y)$	shape of $i$ th mode of motion and $j$ th mode of motion, respectively
$\rho$	mass density of air
$\rho_0$	value of $\rho$ at sea level
$\sigma$	root-mean-square (rms) value
$\sigma_{c,1}$	rms intensity of composite nonstorm turbulence velocity
$\sigma_{c,2}$	rms intensity of composite storm turbulence velocity
$\sigma_f$	rms value of function $f(t)$
$\sigma_T$	total rms value
$\sigma_{u_g}, \sigma_{v_g}, \sigma_{w_g}, \sigma_z$	rms value of $u_g$ , $v_g$ , $w_g$ , and response $z$ , respectively
$\sigma_1$	truncated rms value of turbulence velocity obtained from power spectrum of measured turbulence ( $\sigma_{1,u_g}$ , $\sigma_{1,v_g}$ , and $\sigma_{1,w_g}$ are truncated rms values for longitudinal, lateral, and vertical components, respectively)
$\tau$	time lag in autocorrelation function

$\Phi(f), \tilde{\Phi}(\omega)$	power spectral density function (power spectrum) for argument $f$ and $\omega$ , respectively, with accompanying subscript indicating specific type of spectrum
$\tilde{\Phi}(k')$	power spectrum for argument $k'$
$\hat{\Phi}(\Omega)$	power spectrum for argument $\Omega$
$\phi(\omega)$	Fourier transform of $R(\tau)$
$\phi_{w_g}(\omega)$	Fourier transform of $R_{w_g}(\tau)$
$\phi_z(\omega)$	Fourier transform of $R_z(\tau)$
$\Omega$	spatial circular frequency, $\omega/V$
$\omega$	circular frequency
$\omega_i$	natural circular frequency of $i$ th vibration mode
$\omega_n$	natural circular frequency

## ADVERSE RESPONSES

Some current problems associated with turbulence responses are discussed in this section.

### Loads and Stresses

Single extreme load.— A single extreme load may lead to failure of some vital part of the airframe structure. It is often critical for airplanes having a low design maneuver load factor such as airline transports. For these airplanes, the wing structure often must be designed for response to the vertical turbulence velocity component. The vertical tail structure is often designed for response to the lateral turbulence velocity. Critical load conditions are associated with high turbulence intensities. The material herein is concerned almost exclusively with this particular adverse response.

Fatigue damage.— Cracking of structural elements is a cumulative effect of all stress variations — small variations as well as large. No rational approach to damage prediction exists. Control is based largely on empirical procedures and inspection. Research toward a better understanding of the problem is continuing.

## Motions and Deformations

Loss of control and upsets.- A number of accidents and near-accidents believed to have been caused by very high intensity turbulence have been experienced. In some cases the airplane dived into the ground; in others, the structure may have been overloaded by the maneuver resulting from an attempt to recover.

Excessive motion.- Large angular or rectilinear displacements are detrimental to precision flying operations such as aerial photography, refueling, and landing.

Physiological effects on pilots and passengers.- Loss of human performance effectiveness due to excessive shaking and vibration may contribute to loss of control; the pilot may be unable to read instruments or move precisely. Effects of motion on the passengers range from minor problems such as spilled coffee to major injuries such as serious contusions and broken bones if seat belts are not used.

### SUBJECT AREAS INVOLVED IN TURBULENCE RESPONSE ANALYSIS

Because of the many problems associated with airplane responses to turbulence, there is a considerable interest in methods of predicting the responses and of designing for their effects. A description of some of these methods is the purpose of the present paper. Emphasis herein is placed on the description of the most modern methods of estimating the responses to turbulence experienced by an airplane of a given type during its entire period of operation. Such information is required to establish the airworthiness of any particular airplane design.

Turbulence response analysis is especially interesting because of the variety of subjects that must be considered in the methods of analysis and synthesis that are applied. The primary subject areas are the following:

- (1) Dynamics of flexible bodies
- (2) Aerodynamics of unsteady flow
- (3) Stability and automatic control
- (4) Loads
- (5) Structures
- (6) Statistics
- (7) Random-process theory
- (8) Turbulence theory
- (9) Fatigue of materials

(10) Flight operations and missions

(11) Flight testing and instrumentation

(12) Mathematical techniques (Laplace and Fourier transforms; numerical methods)

With a few exceptions each of these subjects is a major discipline in itself. The structural-dynamics specialist working on turbulence response problems need not be an expert in each of these disciplines, but he must know how to combine pertinent information from each of them and he must have contacts with authorities in these subject areas in order to obtain this information.

For the purpose of following the material in this paper, it is helpful to have some knowledge of the dynamics of flexible bodies (Lagrange's equation), aerodynamics of unsteady flow, structures, statistics, and mathematical techniques including Laplace and Fourier transforms. Knowledge of the remaining subjects is not a prerequisite.

Random-process theory is a fundamental part of the determination of turbulence response and is a large subject in itself. The elements of random-process theory are described herein. However, the presentation covers only the bare essentials and could lead to an oversimplified impression. The reader is urged, therefore, to study the appropriate reference literature in order to pursue the subject further.

The theory of turbulence is also a large field of study. Little more than a mention of its existence and a presentation of results that are essential to the present subject is included herein.

## CHARACTERISTICS OF AIRPLANE RESPONSES TO TURBULENCE

In describing an analytical framework which relates the airplane responses (such as acceleration, stress, and attitude angle) to the atmospheric turbulence, the characteristics of the airplane responses are examined first. The particular response to be considered is the normal or vertical acceleration at the airplane center of gravity. This response is chosen as an example because for many airplanes that are relatively stiff, the load or stress in the structure is essentially proportional to the normal acceleration at the center of gravity. Relatively stiff means that the frequency of the lowest natural vibration mode of the structure is more than five times the frequency of the short-period longitudinal stability mode.

Some characteristics of acceleration at the airplane center of gravity for a representative routine airline flight are shown in figure 2. This figure illustrates a record from a VGH recorder; a VGH recorder provides measurements of equivalent airspeed  $V_e$ , pressure altitude  $h$ , and normal acceleration  $a_n$  in gravitational units  $g$  (all as time functions or time histories). The total record is many hours long and covers many

flights. The particular flight shown is of about 30 minutes duration. The main thing to concentrate on in this figure is the acceleration response  $a_n$  and, in particular, those sections labeled gust acceleration. These disturbances arise from flight in turbulence, and the principal characteristic to be noted is that the gust accelerations are intermittent and vary in intensity.

A portion of a gust-acceleration time history is shown in greater detail in figure 3. This record includes the wing-root bending strain as well as the normal acceleration at the center of gravity (c.g.) and was taken from special flight-test instrumentation rather than from the VGH recorder with its relatively cramped time scale. The total record time shown is only 15 seconds.

### Statistical Description

The point of figure 3 is that the acceleration and the strain are both random functions of time. The particular variation in the future is not known or predictable. Because it is random, it must be described in terms of statistical parameters such as the mean value, the root-mean-square value, and the probability-density distribution.

Because the adverse response being considered is the single extreme load, still another statistical parameter is important – the average number of times per flight hour or nautical mile that a peak acceleration response is exceeded. As suggested by the random time history in figure 3, one would expect a higher frequency of exceeding peaks of lower levels than peaks of higher levels. This expectation is indicated quantitatively in figure 4.

The definition of a response peak is indicated by the trace sketched as an inset in figure 4. The log scale on the ordinate of the main plot is the average frequency per flight n. mi. of exceeding normal-acceleration peaks having values indicated by the linear scale on the abscissa. Incremental acceleration means variation from a level flight response of  $1g$ . The data are for a fleet of two-engine turboprop airplanes, were read from a number of VGH records, and represent several thousand hours of flight. According to this plot the airplane will fly an average of 5000 n. mi. between peaks of  $1g$  and an average of a half million n. mi. between peaks of  $2.0g$ .

### Risk

The presentation in figure 4 contains the important implication that there may not be any practical upper limit of load that may be experienced. Of course, common sense says that infinite load levels are not expected, but the word practical means that an element of risk in setting design load levels must be considered. The concept of accepting a definite risk of failure is an unsettling idea to some people. However, these same

people accept a certain risk of disaster every time they get up in the morning but they do not acknowledge it.

In this case the risk is faced by choosing a level that is equal to or lower than those from other sources. A risk level is chosen that results in a mean time between critical occurrences that is somewhat greater than the planned life of the vehicle; in other words, the airplane would be expected to be retired from service for obsolescence in less time than the mean failure period. The risk can be reduced further by utilizing methods of avoiding turbulence by radar detection of storms and by dispatching flights around them.

### Critical Loads

Whether or not the structure must be designed for the loads due to turbulence depends on the type of airplane – that is, the service it is to provide. For example, a military fighter or interceptor airplane must make abrupt maneuvers in its missions and consequently may be designed to withstand as great a load factor as its human pilot can tolerate, say 6 or 8. The maneuver load factor is usually very high in comparison with the load due to turbulence at a reasonably low risk level. The turbulence or gust loading is then noncritical in this case. This relationship is indicated in figure 5, which is a V-n diagram; that is, load factor  $n$  is indicated by the ordinate and airspeed  $V$ , by the abscissa. The lowest speed or stalling speed is denoted  $V_{min}$ . The curved portion is load limited by stall. The top line is the maneuver load level set by the airplane usage. This level may be as high as 6 or 8 for a highly maneuverable airplane. Loads due to turbulence at an acceptably low risk level would fall below the maneuver load maximum level and therefore would not be critical.

On the other hand, the maneuver load factor for transport airplanes, because they need not maneuver abruptly (in fact, passengers would object to it), is much lower than for acrobatic-type airplanes; a typical maneuver load factor for transport airplanes is 2.5. For many of these transport airplanes the load due to turbulence at an acceptable risk level is greater than the maneuver load factor; the airplane is called "gust critical" and extra material must be added to the structure to withstand the gust loads.

Some oversimplification was made in presenting the V-n diagram. It is precisely appropriate only for an airplane that is essentially rigid – that is, whose structure is characterized by weakly excited, moderately to well damped elastic modes having frequencies of at least five to 10 times the frequency of the short-period mode. Examples of rigid airplanes include most small general-aviation planes and small jet-propelled transports. For these airplanes the structural stresses are essentially proportional to the normal acceleration at the center of gravity, and thus acceleration at the center of gravity is a suitable index of load.

However, larger airplanes usually have readily excited, poorly damped elastic modes, some with natural frequencies near the frequency of the short-period mode. For these airplanes the dynamic deformations of the elastic modes create a dynamic stress increment that results in increased loads. The stress responses of these airplanes must be considered for a number of locations on the structure. The choice and number of these locations is largely determined by the designer's experience.

Of course, when an airplane design is on the drawing board, initially, it is not known whether gust loads are critical, so engineering studies have to be made to determine the response characteristics. This determination amounts to predicting or synthesizing the exceedance curve shown in figure 4. A description of the development of a method of synthesis is the ultimate objective of the present study.

## CHARACTERISTICS OF TURBULENCE

The source of the responses – atmospheric turbulence – is described in this section. Some sample time histories of the vertical component of turbulence velocity measured by an instrumented airplane for several different atmospheric conditions are shown in figure 6. The sample time period is a little less than 2 minutes.

As might be expected from the response characteristics, the time histories of turbulence velocities are random functions. It is obvious that intensity in terms of root-mean-square value  $\sigma$  is subject to large variations. It is also obvious that some wild variations in vertical velocity are encountered in a thunderstorm, as indicated by a maximum positive value of over 160 ft/sec (48.8 m/sec) and a maximum negative value of more than -100 ft/sec (-30.5 m/sec). It should be noted, however, that this variation takes place over a period of some 20 seconds. The airplane has considerable time to adjust to the velocity variation, and consequently the accompanying variations in acceleration, though not shown, are relatively low compared with those of the turbulence velocity.

As can be inferred from the characteristics of acceleration response, turbulence over whole flights is intermittent and variable in intensity and, in general, must be described in terms of the probability density of intensity. Additional statistical quantities describing the characteristics of relatively short samples of turbulence (say, from 15 to 50 n. mi. in length) are significant in the calculation of airplane responses to turbulence. These quantities are indicated in figure 7 and are discussed next.

### Statistical Properties of Short Samples of Turbulence Velocities

Stationarity.– The property of stationarity is illustrated in the upper left part of figure 7. If the time averages of a sample random time function for a component of

turbulence experienced by an airplane are independent of the starting time of the sample, the sample is regarded as stationary. In the example of stationarity in figure 7, the root-mean-square value of the sample starting at time  $t_1$  and ending at  $t_2$  is equal to that starting at  $t_2$  and ending at  $t_3$  and also equal to that for the total sample from  $t_1$  to  $t_3$ .

Homogeneity.- Another statistical property (not illustrated) is homogeneity, which is manifested as the invariance of the time average of any function of a turbulence velocity component as measured during flight in any direction.

Isotropy.- The property of isotropy is indicated in the upper right part of figure 7. In flight through turbulence, isotropy is indicated by the time average of any function of the velocity components (or their derivatives) being independent of the orientation of the reference axes. The example given in figure 7 is the equality of the root-mean-square values of the three orthogonal velocity components  $\sigma_{w_g}$ ,  $\sigma_{v_g}$ , and  $\sigma_{u_g}$ .

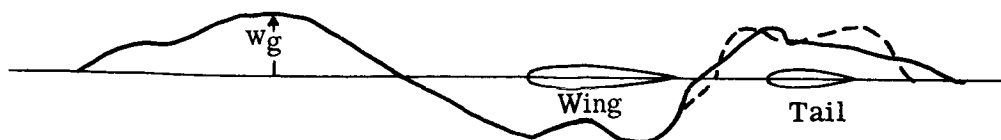
Probability density.- The probability density for turbulence velocity components has been found empirically to be nearly Gaussian or normal, as shown by the familiar bell-shaped curve at the lower left in figure 7.

Ergodicity.- Finally, the turbulence is considered to be an ergodic process; that is, time and ensemble averages are taken to be equal. The concept of ensemble averages is basic in statistical analysis, and an ensemble is illustrated in figure 8 by a series of time-function samples of a stationary random process. The ensemble average is taken at a particular instant of time, say  $t_1$ , over an infinite or at least a very large number of members of the ensemble. In order to apply statistical theory to a single time function, it is necessary to invoke the property of ergodicity; that is, the time average is equal to the ensemble average. Ergodicity is possible only if the process is stationary in time.

### Space and Time Variation

The samples of turbulence velocity have been shown as time functions. The airplane, of course, is traversing space during flight and so, in general, turbulence must be regarded as varying with space at a given instant and varying with time at a given spatial location.

The significance of these variations is indicated in the following sketch, in which the variation of the vertical component of turbulence along the direction of flight at the center line of the airplane is considered:





As far as the airplane is concerned, the variation of turbulence with time is only important during the time that it takes the airplane to travel its own length. If the pattern of turbulence were to change appreciably during this time, then, for example, the tail would experience a somewhat different turbulence velocity than the wing as indicated by the solid and dashed lines above the tail, and this time effect would have to be accounted for.

The time increment for most airplanes, however, is on the order of a fraction of a second, and measurements indicate that the turbulence pattern does not change appreciably in that time. As a result, the turbulence velocity pattern is assumed to be frozen in space, a concept known as Taylor's hypothesis. On this basis, time as used in the time histories is related to distance by the speed of the airplane. However, Taylor's hypothesis should be used with care for gust responses of V/STOL airplanes, particularly in the near-hovering mode because the significant time increment may then be large enough for appreciable time changes in the turbulence to occur.

Turbulence in short samples has been found to be essentially homogeneous, and therefore with respect to the axes of an airplane in level flight, the turbulence velocities would be expected to vary along the span of the airplane as well as along the direction of flight. A model of such a turbulence field for the vertical component is illustrated in figure 9 by the sketch of a two-dimensional gust field. This artist's concept is somewhat misleading for two reasons: (1) the variation along the X-axis appears to be much more rapid than that along the Y-axis and (2) the size of the airplane in comparison with the wavelengths of the turbulence is much too large.

Actually, for all but the very largest airplanes, the variation of the turbulence over the span of the airplane is relatively small, and the simpler model illustrated in figure 9 by the upper sketch for a one-dimensional gust field appears to be adequate for most response calculations. Currently at Langley and elsewhere, research is being conducted on the effects of the two-dimensional model on large airplanes at low altitudes. However, for the remainder of this presentation, the turbulence field will be considered as the one-dimensional model.

## INPUT-OUTPUT RELATION

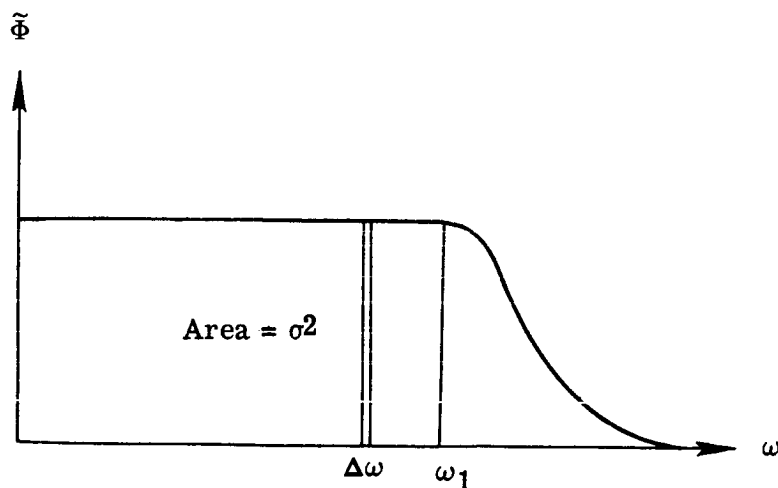
### Random-Process Theory

Some of the statistical properties of the turbulence and of the airplane response have been described. The subject to be considered next is how to relate them. This relation obviously must involve the dynamic characteristics of the airplane. Efforts to obtain a practicable general relation solely on the basis of random time functions have not been successful. As in the treatment of many other problems, it has proven to be more expeditious to transform the problem into the frequency domain by Fourier

transformations. On this basis a powerful method for determining the properties of the responses of systems to random disturbances was originated by Norbert Wiener and contributed to by S. O. Rice, John W. Tukey, and others (see bibliography of ref. 1). This method is known as random-process theory. Investigators who initially applied random-process theory to the response of airplanes to turbulence include Gerhardt C. Clementson, H. W. Liepmann, and Harry Press. Reports on these and later applications are also listed in the extensive bibliography of reference 1.

In its present state of development, random-process theory provides a relatively simple relation between the statistics for the responses of a linear system and those for the short samples of turbulence that have been previously described in terms of stationarity, homogeneity, isotropy, normality (Gaussian probability), ergodicity, and the one-dimensional turbulence field. (This relation is not sufficient to describe the airplane responses for extended flights in turbulence of intermittent occurrence and variable intensity. However, a method of utilizing the relation for this purpose is described in a subsequent section.) An outstanding feature of random-process theory is that a statistical description of the response to turbulence velocities can be deduced without actually considering the random time function.

Power spectrum.- A basic concept in random-process theory is a function of frequency  $\tilde{\Phi}(\omega)$  that contains all the statistical information describing a Gaussian process, including, for example,  $N$  (the average frequency of exceeding a response peak of a given level). The function  $\tilde{\Phi}(\omega)$  is called a power spectral density function or, in short, a power spectrum. The nature of a power spectrum is indicated by the example in the following sketch:



This power spectrum of simple shape is an approximate white-noise or constant-amplitude spectrum that arises, for example, from the discrete electron flow in a vacuum

tube. White noise refers to the equal contributions from all frequency increments  $\Delta\omega$  (at least up to  $\omega_1$ ) to the mean-square value which is equal to the area under the curve. In mathematical notation

$$\sigma^2 = \int_0^{\infty} \tilde{\Phi}(\omega) d\omega \quad (1)$$

This equation illustrates the relation of the power spectrum to one statistical quantity, the mean-square value. The spectrum, therefore, might more appropriately be called a mean-square spectrum. The term power spectrum is indicative of the subject from which it evolved – namely, electrical-circuit theory.

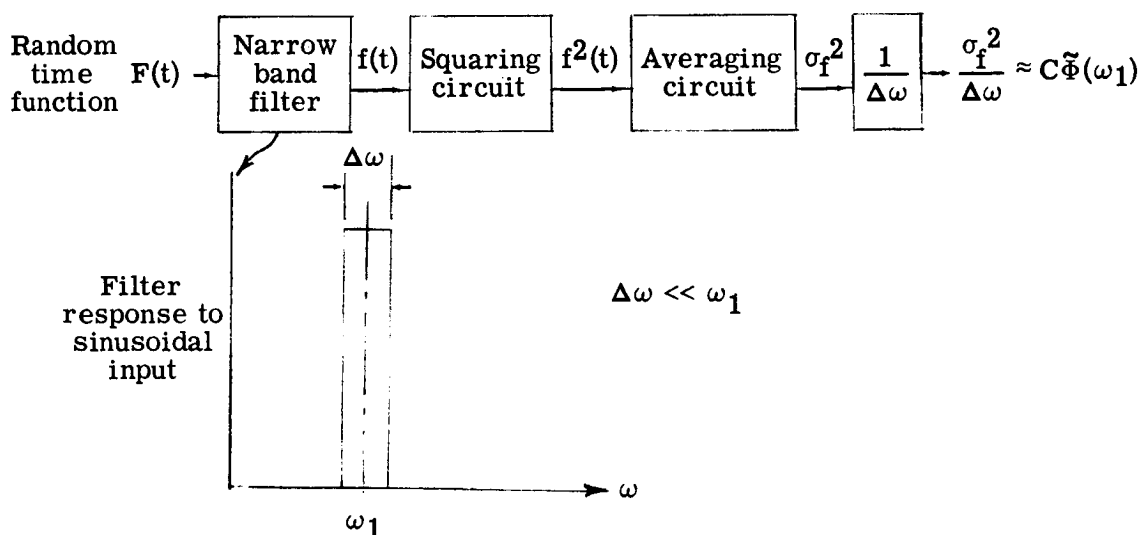
Equation (1) also indicates that the power spectrum is a density function with respect to frequency; that is, the units are quantity-squared per unit frequency. Therefore, if the frequency argument and its units are changed, then the spectrum is functionally changed; for example,

$$\Phi(f) = 2\pi\tilde{\Phi}(\omega) \quad (2)$$

so if  $\tilde{\Phi}(\omega) = \frac{B}{C + \omega^2}$ , then

$$\Phi(f) = \frac{2\pi B}{C + (2\pi f)^2}$$

A further indication of the nature of a power spectrum can be obtained from the following block diagram of an analog circuit:



The output of the block diagram is proportional to the value of the power spectrum at frequency  $\omega_1$ . Variation of the filter frequency  $\omega_1$  over a range from zero to very high frequencies would then result in a function of frequency proportional to the power spectrum.

Relation of output to input in random-process theory.- The power spectrum for a random response  $z$  (that is,  $\tilde{\Phi}_z(\omega)$ ) can be expressed as the product of a power spectrum for an input disturbance (that is,  $\tilde{\Phi}_I(\omega)$ ) and the square of the amplitude of the response  $z$  to a unit sinusoidal input disturbance  $I$  (that is,  $|H_z(\omega)|^2$ ) over a range of frequencies from zero to large values for which there is an appreciable response. In equation form

$$\tilde{\Phi}_z(\omega) = \tilde{\Phi}_I(\omega) |H_z(\omega)|^2 \quad (3)$$

The response  $H_z(\omega)$  is commonly known as the frequency response function and the concept is familiar to those interested in the fidelity of amplifiers in a high-quality sound reproduction system. For those not familiar with this concept, an example of a frequency response function from the subject of mechanical vibrations is presented in figure 10;  $|H_z(\omega)|$  is the amplitude of the oscillatory displacement of a mass-spring-dashpot one-degree-of-freedom system due to a unit sinusoidal applied force.

A graphical illustration of the input-output relation for random disturbance is shown in figure 11. On the left is a power spectrum of a random input force - a low-pass white-noise spectrum. This input power spectrum is multiplied by the square of the modulus of the mechanical-system frequency response, and the result is the output power spectrum on the right. The output power spectrum in this example looks like the system frequency response (modulus squared) because the input spectrum is essentially constant over the frequency range of significant response.

Relation of power spectrum to statistical parameters.- It has been stated previously herein that the integral of the power spectrum is equal to the mean-square value. Other statistical parameters can be determined from the power spectrum of a Gaussian process. One which has already been indicated as particularly pertinent to the single-extreme-load condition is the average frequency of exceeding a response peak of a given level. The average frequency of exceeding a response peak of level  $z$  (in terms of the power spectrum of  $z$ ) is

$$N(z) = N_{0,z} e^{-\frac{z^2}{2\sigma_z^2}} \quad (4)$$

where

$$N_{0,z} = \frac{1}{2\pi} \left[ \frac{\int_0^\infty \omega^2 \tilde{\Phi}_z(\omega) d\omega}{\sigma_z^2} \right]^{1/2} \quad (5)$$

and

$$\sigma_z^2 = \int_0^\infty \tilde{\Phi}_z(\omega) d\omega \quad (6)$$

Note that  $N_0$  is the average frequency of crossing the zero level with positive slope and is proportional to the radius of gyration of the power spectrum about the axis  $\omega = 0$ . The expression for  $N(z)$  is an exact description of the average frequency of crossing a level  $z$ , and for values of  $z$  greater than about  $2\sigma_z$ , the expression is a useful approximation of the average frequency of exceeding response peaks of level  $z$ . The equations for  $N(z)$  and  $N_0$  were derived by S. O. Rice in reference 2. This derivation is somewhat involved and therefore is not presented herein.

#### Relation of Power Spectrum to Random Time Function

The relation of the power spectrum to the random time function is described in figure 12. The power spectrum is proportional to the Fourier transform of a statistical average called an autocorrelation function. The autocorrelation function  $R(\tau)$  in turn is determined from the random time function, as indicated by the sketch and the equations in figure 12;  $R(\tau)$  is the average of the product of the time function  $f(t)$  and the time function displaced by a time lag  $f(t + \tau)$ . One of the important features of the autocorrelation function is that the value for zero lag is the mean-square value. Other properties of the autocorrelation function can be observed from the example given in figure 13. This function is symmetrical with respect to  $\tau = 0$  and decays in amplitude with increasing values of  $|\tau|$ , as indicated in the upper sketch. The particular function shown is similar to the form  $\sin \omega T / \omega T$ . The associated power spectrum obtained by the Fourier transformation is shown in the lower sketch. In general, it too is symmetrical (about the axis  $\omega = 0$ ).

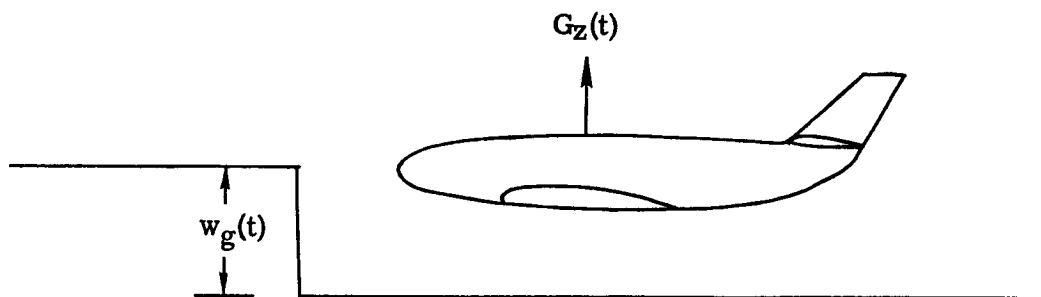
#### Derivation of Power Spectral Input-Output Relation

The input-output relation has been simply stated. In this section derivations are presented for the relation, starting with the random variation of a component of turbulence velocity with time  $w_g(t)$ .

In the example to follow and in other material to be presented subsequently, consideration is given to the responses to the vertical component of turbulence. However,

responses to the other components, particularly the lateral component, should be considered. Generally, the procedures developed for the vertical turbulence component are applicable to the other components.

The following derivation is based on a fundamental assumption that the airplane is a linear system; that is, the responses are directly proportional to the turbulence velocity. This assumption has been found to be valid for many airplane problems. The linearity of the system permits a response  $z(t)$  to a random variation of turbulence or gust velocity  $w_g(t)$  to be expressed by the superposition of the responses to step gusts  $G_z(t)$ . The step gust  $w_g(t)$  and response  $G_z(t)$  are indicated in the sketch below:



The response  $z(t)$  to a random variation of gust velocity with time  $w_g(t)$  is described by the superposition integral

$$z(t) = \int_0^{\infty} G_z(t - \tau) \frac{dw_g(t)}{d\tau} d\tau \quad (7)$$

It is more convenient to express this integral in terms of the derivative of  $G_z(t)$ ; that is,

$$h_z(t) = \frac{dG_z(t)}{dt} \quad (8)$$

which is the response to an impulse gust. Then

$$z(t) = \int_0^{\infty} h_z(t - \tau) w_g(\tau) d\tau \quad (9)$$

or alternately

$$z(t) = \int_0^{\infty} w_g(t - \tau) h_z(\tau) d\tau \quad (10)$$

The autocorrelation function  $R_Z(\tau)$  is defined as

$$R_Z(\tau) = \lim_{T \rightarrow \infty} \frac{1}{T} \int_0^T z(t)z(t + \tau)dt \quad (11)$$

where, in terms of the superposition integral,

$$z(t)z(t + \tau) = \int_0^\infty \int_0^\infty h_Z(\xi)h_Z(\eta)w_g(t - \xi)w_g(t + \tau - \eta)d\xi d\eta \quad (12)$$

Then

$$R_Z(\tau) = \int_0^\infty \int_0^\infty h_Z(\xi)h_Z(\eta)R_{w_g}(\tau + \xi - \eta)d\xi d\eta \quad (13)$$

where  $R_{w_g}$  is the autocorrelation function of  $w_g$ .

The Fourier transform of this equation yields

$$\phi_Z(\omega) = H_Z(\omega)H_Z^*(\omega)\phi_{w_g}(\omega) = |H_Z(\omega)|^2 \phi_{w_g}(\omega) \quad (14)$$

where  $H_Z^*(\omega)$  is the complex conjugate of  $H_Z(\omega)$  and where

$$\phi_{w_g}(\omega) = \int_{-\infty}^\infty R_{w_g}(\tau)e^{-i\omega\tau}d\tau \quad (15)$$

and

$$H_Z(\omega) = \int_{-\infty}^\infty h_Z(t)e^{-i\omega t}dt \quad (16)$$

In terms of the autocorrelation function of response  $z$

$$\phi_Z(\omega) = \int_{-\infty}^\infty R_Z(\tau)e^{-i\omega\tau}d\tau \quad (17)$$

The quantity  $H_Z(\omega)$  is the frequency response of airplane response  $z$  to a vertical-gust velocity field that is sinusoidal in the direction of flight and uniform in the spanwise direction. This gust field is illustrated in figure 14 together with the relation between frequency  $f$  and wavelength  $\lambda$ .

The Fourier transforms in the preceding equations ( $\phi_{w_g}(\omega)$  and  $\phi_z(\omega)$ ) must be multiplied by a suitable constant in order to be defined as power spectra so that their integrals will be equal to mean-square values. The constant is determined from the inverse relations between  $R(\tau)$  and  $\phi(\omega)$ ; that is,

$$R(\tau) = \frac{1}{2\pi} \int_{-\infty}^{\infty} \phi(\omega) e^{i\omega\tau} d\omega \quad (18)$$

However,

$$\phi(\omega) = \phi(-\omega)$$

so

$$R(\tau) = \frac{1}{\pi} \int_0^{\infty} \phi(\omega) e^{i\omega\tau} d\omega \quad (19)$$

but

$$R(0) = \sigma^2 \equiv \int_0^{\infty} \tilde{\Phi}(\omega) d\omega \quad (20)$$

where  $\tilde{\Phi}(\omega)$  is the power spectrum. Combining the last two equations for the condition  $\tau = 0$  yields

$$\frac{1}{\pi} \phi(\omega) = \tilde{\Phi}(\omega) \quad (21)$$

The input-output power spectral relation is then

$$\tilde{\Phi}_z(\omega) = |H_z(\omega)|^2 \tilde{\Phi}_{w_g}(\omega) \quad (22)$$

It should be noted that no phase information is involved.

Attention is turned next to the individual terms in the input-output relation and to analytical expressions for them.

## ANALYTICAL EXPRESSIONS FOR TERMS IN INPUT-OUTPUT RELATION

### Power Spectra of Atmospheric Turbulence

An analytical expression for a generalized power spectrum of turbulence has been developed from the theory of isotropic turbulence. As indicated previously, this theory is a major discipline in itself. All that can be done herein is to call attention to some important contributors to the development of the theory and to briefly state some of the basic concepts. Some important contributors include Osborne Reynolds, G. I. Taylor,



A. N. Kolmogoroff, W. Heisenberg, Theodore von Kármán, L. Howarth, G. K. Batchelor, and Hugh L. Dryden (see ref. 3). Some of the basic concepts are as follows:

- (1) Definition of correlation tensors for random velocity components in three dimensions
- (2) Combination with Navier-Stokes equations
- (3) Definition of time averages
- (4) Solution of equations for very small and very large values of Reynolds number
- (5) Dryden and von Kármán power spectra

A particular result of the theoretical work that is important to the subject problem is the generalized power spectrum for transverse components of turbulence, developed by von Kármán. The analytical expression is given at the top center of figure 15 in non-dimensional form, involving frequency in the form of a dimensionless wave number  $k'$ . The wave number is defined in figure 15 by an equation, in which the quantity  $L$  is the so-called scale of turbulence in units of distance.

The characteristics of the spectrum are revealed by the log-log plot on the left side of figure 15. It is to be noted that the spectrum approaches a constant value at low values of wave number  $k'$  and approaches an asymptotic slope of  $-5/3$  at the higher values of  $k'$ . Thus most of the power in the spectrum is contributed by the lower frequencies.

In actual application, values of the scale of turbulence  $L$  for the atmosphere must be considered explicitly. The effects of variations in  $L$  are illustrated by the log-log plot on the right side of figure 15. It is to be noted that the mean-square values of the several curves are all unity and that the value of  $L$  determines the "roll-off" frequency between the flat and sloping regions of the spectrum. Thus an increasing value of  $L$  reduces the magnitude of the power for frequencies above the roll-off value and increases the magnitude at the very low frequencies.

### Airplane Frequency Responses

The next term to be considered in the input-output relation is the frequency response function. This quantity is of great importance because it embodies all the dynamic characteristics of the airplane. Although the procedure for the calculation of the frequency responses is applicable to the response to any turbulence component, the symbology used in this section is for a response to the vertical component as an example. Thus the input gust field is a sinusoidal variation of the vertical component  $w_g$ . The modal method of calculating the airplane frequency responses to a one-dimensional sinusoidal gust field is described, and the example considered is response in the classical longitudinal mode of motion.

Mathematical model.- The motions and deformations of the airplane are described by a finite number of rigid-body and elastic modes. The normal displacement is expressed as

$$z(x,y,t) = \sum_{i=1}^n \xi_i(x,y)z_i(t) \quad (23)$$

where  $z_i$  represents generalized coordinates and  $\xi_i$  represents mode shapes including rigid-body modes (e.g.,  $i = 1,2,3$  are modes in which there is freedom in fore and aft displacement, in plunge (normal displacement), and in pitch, respectively;  $i = 4,5, \dots n$  are elastic modes).

Equations of motion.- The relations between the motions and the forces are often most conveniently derived by the method of Lagrange, which, of course, is based on kinetic and potential energies and on virtual work from nonconservative forces. The motion of the airplane is expressed as small perturbations of the mode displacements and velocities from an equilibrium flight condition such as steady level flight. The forces and motions are then linearly related as indicated by the equation

$$M_{ij}\ddot{z}_i + \omega_i^2 M_{ii}z_i + Q_{ij} = Q_{ig} \quad (i = 1,2,3, \dots n; j = 1,2,3, \dots n) \quad (24)$$

where  $\ddot{z}_i = \frac{d^2 z_i}{dt^2}$ . There results an array of equations, one equation for each mode. With the exception of the terms on the right side, the equations of motion and the generalized forces are the same as those used in dynamic stability and flutter analysis. However, a different number of modes may be used than in a gust-response calculation.

Generalized forces.- The coefficients in equation (24) are defined next.

**Inertia:** The generalized mass  $M_{ij}$  is defined by the equation

$$M_{ij} = \int_S \xi_i(x,y)\xi_j(x,y)dm \quad (25)$$

where  $m$  is mass per unit area and  $S$  is the area of the airplane in the  $XY$ -plane. Often the elastic modes chosen are the natural modes of the airplane, in which case the inertia terms are simplified by orthogonality between the modes. Then  $M_{ij} = 0$  if  $i \neq j$ , leaving only the generalized masses for each mode.

**Stiffness:** The generalized stiffness is designated  $M_{ii}\omega_i^2$ , where  $\omega_i$  is the natural circular frequency of the  $i$ th mode.

**Aerodynamic force:** The generalized aerodynamic force for the  $i$ th mode due to motion in the  $j$ th mode is designated  $Q_{ij}$ . The generalized aerodynamic gust force for

the  $i$ th mode is designated  $Q_{ig}$ . These two forces are defined by the equations

$$Q_{ij} = \iint \xi_i(x,y) p_j(x,y,t) dx dy \quad (26)$$

where  $p_j$  is pressure due to the  $j$ th mode, and

$$Q_{ig} = \iint \xi_i(x,y) p_g(x,y,t) dx dy \quad (27)$$

where  $p_g$  is pressure due to the gust field.

Pressure distribution. - Pressure distribution is determined from linearized aerodynamic theory for thin planar lifting surfaces. Pressure due to motion in the  $j$ th mode is defined by the equation

$$p_j(x,y,t) = \iint_S I(x-\xi, y-\eta, t, M) w_j(\xi, \eta, t) d\xi d\eta \quad (28)$$

where  $w_j$  is the downwash on the wing surface at a point  $(\xi, \eta)$  and  $I$  is an aerodynamic influence function relating  $p_j$  at a point  $(x, y)$  to  $w_j$  at all other points. The downwash due to the motion and deformation in the  $j$ th mode is expressed in terms of the slope of the lifting surface and its normal velocity as

$$w_j = \left( V \frac{\partial}{\partial x} + \frac{\partial}{\partial t} \right) \xi_j(x, y) z_j(t) \quad (29)$$

Pressure due to gust is defined by the equation

$$p_g(x, y, t) = \iint_S I(x-\xi, y-\eta, t, M) w_g(\xi, \eta, t) d\xi d\eta \quad (30)$$

The downwash due to the gust field  $w_g$  is described in figure 16. The desired quantity is the gust downwash or gust velocity acting at a chordwise station on the surface at  $x$  referred to an airplane reference point, say a point at the apex of the wing;  $\tilde{x}$  is expressed in terms of the distance traveled by the airplane  $Vt$  in the earth-fixed gust field  $w_g = \bar{w}_g e^{i\omega \tilde{x}/V}$ . The gust downwash is then

$$w_g = \bar{w}_g e^{-i\omega x/V} e^{i\omega t} \quad (31)$$

and is illustrated in figure 17. Passage of the lifting surface through the sinusoidal gust velocity field produces an unsteady flow. One of the features is the penetration of the gust field by the wing. There is, consequently, a variation of gust downwash along the chord as indicated in figure 17.

Unsteady flow.— The effect of gust penetration and also of the wake in unsteady flow is illustrated in figure 18. The effect of the flow in the wake is common to both gust disturbances and motion of the lifting surface, as already pointed out in the paper by E. Carson Yates, Jr. In figure 18,  $w_g$  has been approximated by a series of step gusts. A rough indication of the interaction between the flows on the wing and in the wake in a step gust is given for two-dimensional flow in the sketches at the lower left side of the figure. In the top sketch the wing has not yet penetrated the step gust. In the second sketch the forward section is immersed. The clockwise arrow indicates that an incremental increase in circulation has occurred, while the counterclockwise arrow indicates an equal and opposite circulation concurrent with the first arrow. Thus, the two circulations cancel and there is no net lift on the wing. In the third sketch the wing is immersed still further. The counterclockwise arrow on the right represents the countervortex generated in the preceding sketch and remains at the same point in space relative to the gust front. The matching vortex (not shown) remains bound to the wing. The countervortex on the right induces a downwash on the wing that is less than the downwash from the bound vortex, and consequently an increment in lift  $L$  is developed. At the same time, as a result of the additional penetration, another increment in circulation is developed that is canceled by another countervortex. The bottom sketch indicates conditions after the wing has been fully immersed in the gust for some distance. The countervortices remain in the wake where they were shed. There is a circulation about the wing having a strength equal and opposite to the sum of the strengths of the wake vortices as is specified by the Kelvin circulation theorem; that is, the total vorticity is zero. Owing to the distances between the wake vortices and the wing, the downwash from the wake vortices is much less than that from the wing vortices, and the lift is approaching the steady-state value. After the wing is fully immersed, the penetration effect is nearly complete and the remainder of the transient lift buildup is somewhat similar to that accompanying a sudden change in angle of attack (Wagner function). The characteristics of the lift growth due to a step gust (Küssner function) are indicated by the sketch at the lower right in figure 18.

#### Practical Methods for Calculating Gust Forces on Wings of Finite Aspect Ratio

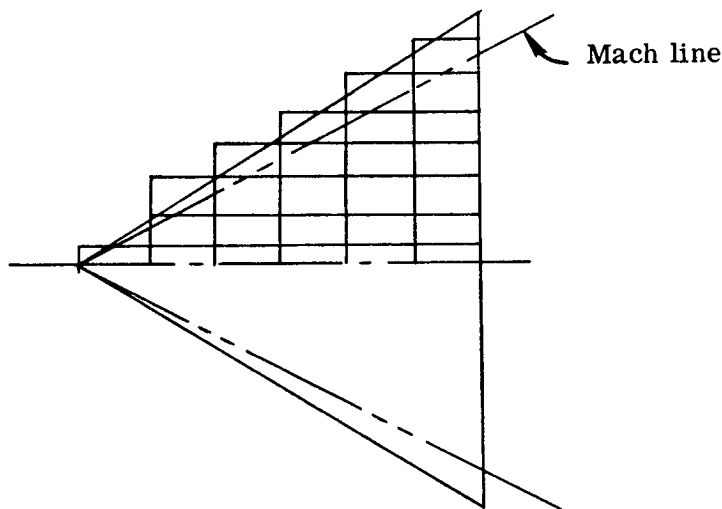
The pressure distribution needed to determine generalized gust forces from equation (27) is obtained from solutions of a lifting-surface equation (e.g., eq. (30), with the use of the gust downwash described by eq. (31)). The formulation and solution of pressure-downwash relations for wing configurations are highly complex. A number of methods have been developed for the various speed ranges. These methods have already been described in considerable detail in the paper by E. Carson Yates, Jr. Two examples are very briefly discussed herein.

For three-dimensional subsonic flow the so-called kernel function method is widely used. The form of the aerodynamic equation differs from that of equation (30); it is an integral equation

$$\overline{w}_g e^{-i\omega x/V} = \frac{V}{8\pi q} \iint_S p_g(\xi, \eta, \omega) K(x-\xi, y-\eta, \omega, M) d\xi d\eta \quad (32)$$

where  $K$  is the kernel function. An inverse solution is obtained by collocation of downwash at a finite number of points on the surface. The unknown pressure is represented by a linear combination of assumed pressure modes having coefficients to be obtained as solutions. Solutions are obtained by numerical methods with a high-speed digital computer.

For supersonic speeds the Mach box method is most frequently used, although the kernel function method can also be employed. As is suggested by the name, in the Mach box method the wing is divided into "boxes" as indicated by the following sketch:



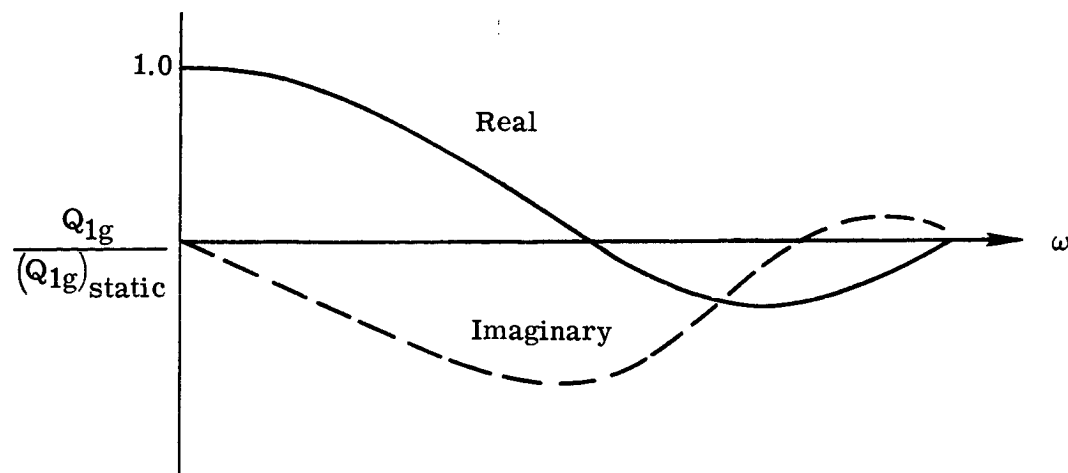
The equation relating the pressure on a box  $m$  at  $(x,y)$  to the gust downwash at all boxes is

$$p_{g,m}(x,y) \approx \sum_n I_{mn} w_{g,n} \Delta S_n \quad (33)$$

where  $I_{mn}$  is an aerodynamic influence matrix and  $\Delta S_n$  is the surface area of box  $n$ . It can be noted that equation (33) is similar in form to equation (30).

For further information on these methods of calculating pressure distributions, the content and references of the paper in the present compilation by E. Carson Yates, Jr., should be reviewed.

After the determination of pressures due to the sinusoidal gust field, the generalized gust forces are obtained from equation (27). A sample gust force is indicated by the following sketch:



The gust forces are, in general, complex numbers; the amplitude approaches zero as the frequency approaches infinity; the amplitude is usually, but not always, a maximum at zero frequency.

#### Operations With Equations of Motion

Stability analyses.- Although stability analyses are not really a part of gust-response calculations, they are mentioned because certainly one desires to avoid calculating the gust response for an unstable airplane. In a trend study in which numerous airplane parameters are changed to determine the effect on gust response, it is not difficult to choose thoughtlessly combinations which may result in an unstable airplane. Incidentally, it is not easy to detect the presence of an instability from an examination of the gust response only.

Solutions for frequency responses of the generalized coordinates.- The direct solution of the equations of motion yields frequency responses of the mode displacements  $\bar{z}_j/\bar{w}_g$ . Some of these responses, such as pitch angle and its derivatives, are of interest in themselves. However, many other responses must be determined from various combinations of the responses of the generalized coordinates.

Frequency responses of selected quantities.- The calculation of responses such as pressures, loads, and accelerations is described in this section. Pressures are obtainable from the equation

$$\frac{\bar{p}}{\bar{w}_g} = \frac{\bar{p}_g}{\bar{w}_g} + \sum \frac{\bar{p}_j}{\bar{w}_g} \quad (34)$$

Values of  $\bar{p}_j/\bar{w}_g$  are obtained from equation (28) with  $\bar{w}_j/\bar{w}_g$  from equation (29) in terms of  $\bar{z}_j/\bar{w}_g$  from the solutions of the equations of motion. The values of  $\bar{p}_g/\bar{w}_g$  are obtained from equations (30) and (31).

Two methods for calculating bending moment (a load response) are widely used. One, called mode displacement, is perhaps the easiest because it requires only the solutions for the generalized coordinates. However, it requires a larger number of modes for a given accuracy than does the alternate method. This method is based on beam theory, and the expression for the bending-moment frequency response function is

$$H_{\bar{M}}(\omega) = \frac{\bar{M}}{\bar{w}_g} = EI \int \frac{\partial^2 \xi_i(x,y)}{\partial x^2} \frac{\bar{z}_i}{\bar{w}_g} \quad (35)$$

The second method is the loads-summation approach. The bending moment is obtained by appropriate integrations of inertial loading from modal accelerations plus the aerodynamic pressures from the modal motion and gust velocity. The loading to be integrated is

$$\int \left[ -m\omega^2 \xi_i(x,y) \frac{\bar{z}_i}{\bar{w}_g} + \frac{\bar{p}_i}{\bar{w}_g} \right] + \frac{\bar{p}_g}{\bar{w}_g} \quad (36)$$

The pressures  $\bar{p}_i/\bar{w}_g$  and  $\bar{p}_g/\bar{w}_g$  are obtained in the same manner as  $\bar{p}_j/\bar{w}_g$  and  $\bar{p}_g/\bar{w}_g$  in equation (34).

## CALCULATED RESULTS

### Frequency Responses

Examples of results obtained from the methods of calculating frequency responses are given in figure 19 for a B-47 jet bomber airplane. The purpose of these results is to indicate how the responses are affected by the various approximations of the airplane motions and deformations. Attention is directed first to the left-hand side of figure 19 where are plotted the frequency-response moduli for normal acceleration at a point on the structure corresponding to the center of gravity of the undeformed airplane (as would be measured by an accelerometer). The one-degree-of-freedom response indicated by the dashed line is the response for the airplane considered rigid and free to plunge only. The addition of rigid-body pitching motion results in the two-degree-of-freedom response indicated by the dashed-dotted line. Note the appearance of a resonant peak at the natural

frequency of the short-period mode. The solid line represents the three-degree-of-freedom response that results from the addition of the first elastic mode, which is predominantly a wing bending deformation. This response is double-humped.

On the right-hand side of figure 19 are plotted wing-root bending moments for the various degrees of freedom. It is obvious that the wing bending mode is the predominant contributor to the bending-moment frequency response and cannot be ignored. These results and a description of the method of calculation are presented in references 1 and 4.

Calculated power spectra and some statistical parameters of the airplane responses are presented next. First, however, the pertinent relations are reviewed. The input-output relation is

$$\Phi_Z(f) = |H_Z(f)|^2 \Phi_{W_g}(f)$$

The mean-square value of response  $z$  is

$$\sigma_Z^2 = \int_0^\infty \Phi_Z(f) df$$

For a Gaussian process the average frequency of exceeding a response peak of level  $z$  is

$$N(z) = N_{0,z} e^{-\frac{z^2}{2\sigma_Z^2}}$$

where

$$N_{0,z} = \frac{1}{2\pi} \left[ \frac{\int_0^\infty f^2 \Phi_Z(f) df}{\sigma_Z^2} \right]^{1/2}$$

For convenience in subsequent applications

$$\frac{\sigma_Z}{\sigma_{W_g}} \equiv A_Z \quad (37)$$

and hence

$$N(z) = N_{0,z} e^{-\frac{z^2}{2A_Z^2 \sigma_{W_g}^2}} \quad (38)$$



## Power Spectra and Statistical Parameters

In figure 20 all terms in the input-output relation and the statistical parameters are shown for the wing-bending-moment response of the airplane for which frequency responses were shown in figure 19.

The von Kármán spectrum in terms of frequency in cps for  $L = 2500$  feet (762 meters), which is a representative turbulence-scale value, is plotted in linear scale on the left side of figure 20. Note the rapidity of the attenuation as the frequency increases.

The square of the modulus of the bending-moment frequency response is plotted in the center. Plotted on the right side is the product of the turbulence spectrum and the square of the modulus of the frequency response; this product is, of course, the response spectrum. It can be seen that the wing bending mode, peaking at about 1.5 cps, is the dominant contributor to the value of  $A_M^2$  and that  $N_0$  is 1.33 cps, which is also indicative of the effect of the bending mode. It can be noted too that the short-period mode is readily identifiable at  $f = 0.5$  cps.

Effects of varying some turbulence and airplane characteristics are shown in figures 21 to 23. The curves from figure 20 are used as reference conditions.

The effect of changing the scale of turbulence from 2500 feet (762 meters) to 500 feet (152 meters) is indicated in figure 21. The level of the turbulence spectrum is increased in the range shown. The frequency response, of course, is not changed. The resulting bending-moment power spectrum is increased in amplitude but not changed in shape. Therefore, the value of  $A_M^2$  has been increased by a factor of 3 and the value of  $N_0$  is essentially unchanged.

The effect of a 50-percent increase in the frequency of the wing bending mode is indicated in figure 22. The input spectrum is not shown; however, it is the same as for the original turbulence-scale value ( $L = 2500$  feet (762 meters)). On the left are shown the moduli of the frequency responses and on the right the corresponding bending-moment power spectra. The amplitude of the bending-mode peak in the power spectrum has been appreciably reduced for the higher natural frequency case (case II) as the result of the attenuation of the turbulence spectrum with increasing frequency. This attenuation has little influence on the value of  $A_M^2$ , however, because the width of the frequency response is proportional to the natural frequency and is therefore larger for the higher frequency mode. The decrease in  $A_M^2$ , consequently, is only about 10 percent. The value of  $N_0$ , however, has increased by about 40 percent as a result of the increase in the natural frequency. (Recall that  $N_0$  is a function of the second moment of the spectrum.)

The effect of increasing the damping ratio (ratio of damping to critical damping) of the wing bending mode by about 40 percent is shown in figure 23. The result, primarily, is the reduction of the magnitude of the resonant peak of the bending-mode frequency response (left side) with an associated reduction in the area under the bending-moment spectrum (right side). The parameter  $A_M^2$  is reduced by about 30 percent and  $N_0$  is reduced by about 5 percent. For low values of the damping ratio of a mode ( $\zeta < 0.1$ ), an increase in damping ratio is effective in reducing the value of  $A_M^2$ .

Thus the procedure for calculating some statistical parameters that describe airplane responses to short patches of atmospheric turbulence has been surveyed. This procedure was based on the application of random-process theory with simplification afforded by particular statistical properties of the turbulence patches and the linearization of the aerodynamics and the airplane dynamic system. The question to be considered next is, can these properties be verified?

## VERIFICATION FROM FLIGHT MEASUREMENTS

### Properties of Short Samples of Turbulence

Isotropy.- Power spectra of atmospheric turbulence in a thunderstorm are presented in figure 24 for the three orthogonal components (vertical,  $w_g$ ; lateral,  $v_g$ ; and longitudinal,  $u_g$ ) together with the respective root-mean-square values. The frequency argument is spatial frequency ( $\Omega = \frac{\omega}{V}$ ) in rad/ft (rad/m). It is to be noted that the values of  $\sigma_1$  are based on an integration from a lower limit of  $\Omega = \Omega_1 = 10^{-3}$  because the spectrum could not be determined accurately at lower frequencies.

The spectra and the truncated root-mean-square (rms) values for the vertical and lateral components are nearly the same. The spectrum and truncated rms value for the longitudinal component are lower than those for the other components. However, this measured difference is not necessarily an indication of nonisotropy because the shape of the theoretical spectrum for the longitudinal component also differs from the shapes for the other components. The theoretical value of  $\sigma_{1,u_g}$  based on the lower limit of integration is indicated in the lower right corner of figure 24. The measured value is not greatly different from the theoretical value, and so isotropy is approximated.

Stationarity.- Spectra and truncated rms values for two halves of a 200-second sample of turbulence in a thunderstorm are shown in figure 25. Ideally the results should be the same. It is apparent that some nonstationarity exists in this sample.

Probability distribution.- Data from a turbulence sample in a thunderstorm were processed to determine the probability of exceeding given levels. The measured data

were then plotted on a chart on which a Gaussian or normal distribution appears as a straight line, as shown in figure 26. The degree of agreement of the measured and normal curves is judged good enough for an assumption of normality, although the data indicate a tendency for the larger values to occur more frequently than for a normal distribution.

Power spectra.- The curves in figure 27 show the results of fitting the von Kármán power spectrum to a spectrum determined from measurements during flight in a thunderstorm by matching the truncated rms values and choosing the value of  $L$  for best fit. The match is fairly good. For this sample the value of  $L$  was 5600 feet (1707 meters); however, similar comparisons with many other measured spectra indicate some variability in the value of  $L$ . A reasonable average appears to be about 2500 feet (762 meters) for altitudes above 2500 feet (762 meters).

Additional power spectra of turbulence for various weather conditions are displayed in figure 28. The rms values are representative of the turbulence intensities associated with the different meteorological conditions. The spectra, although irregular, all are proportional to  $\Omega^{-5/3}$ .

#### Verification of Airplane Frequency Responses

Airplane frequency responses can be determined from power spectra of turbulence and of airplane responses processed from measurements taken during flight. The simplest relationship is the inverse of the input-output relation previously presented; that is,

$$|H_z(f)| = \left[ \Phi_z(f) / \Phi_{wg}(f) \right]^{1/2} \quad (39)$$

Other relations exist in random-process theory that permit phase information to be determined as well.

Frequency responses determined from flight measurements are compared with calculated frequency responses for several airplanes. In some of the figures showing these comparisons, the expression "transfer function" is used synonymously for frequency response function, although strictly speaking it should not be.

Both measured and calculated frequency responses for bending moment at three semispan stations on the wing of a B-47 airplane are shown in figure 29. The ordinate is scaled in units of acceleration per unit gust velocity. This unusual scale was obtained by dividing the bending strain in turbulence by the bending strain per unit acceleration in a slow pull-up maneuver. This procedure was used in lieu of an elaborate calibration of the strain gages on the airplane by application of known forces. The result is a measure

of the dynamic loads in turbulence relative to statically applied loads. While the agreement between calculated and measured results is not close, it is not bad considering the complexity of the problem. (This was, as far as is known, the first time frequency responses were obtained from flight measurements and also the first time they were calculated for an airplane in turbulence for comparison with flight data.)

In figure 30 plots of calculated and measured frequency responses and power spectra for bending moments in the wing of the B-52 airplane are presented. All functions indicate appreciable responses from the first elastic mode below 1 cps and from a higher elastic mode near 2 cps. The calculated values overestimate the response at the lower frequencies and underestimate at the higher frequencies. Another feature, as indicated by the power spectra, is that the contribution of the higher frequency elastic mode to the rms value is appreciably less than that from the first elastic mode.

The sketch in figure 31 depicts the B-58 airplane. Fairly extensive analytical and flight studies of local acceleration responses have been made with this airplane. Some of the results for vertical acceleration components are shown in figures 32 to 34. The particular stations considered are indicated in figure 31; acceleration A428 is at the pilot's station, acceleration A1 is at the nominal center of gravity, and acceleration A11 is at the aft end of the fuselage. The moduli (or magnitudes) of the frequency responses are plotted in figures 32 to 34. The flight speed is subsonic.

In figure 32 fairly good agreement exists between the measured and computed responses at the center of gravity on the basis of two rigid-body and six elastic modes. At the pilot's station (fig. 33) the two sets of responses agree fairly well at the short-period mode near 1 cps; however, at the higher frequencies the calculated response is consistently higher than the response based on the flight test. The results shown in figure 34 for the aft station indicate considerably poorer agreement for modal responses at 4 cps and at higher frequencies.

The statistical parameters  $A_n$  and  $N_0$  are shown in figure 35 as functions of the fuselage station. The values of  $A_n$  from calculations and flight measurements are in very good agreement at the three stations where flight data were obtained. The effect on  $A_n$  of the relatively poorer agreement between calculated and measured frequency responses at the higher frequencies is minimized as a result of the low level of the turbulence spectrum in this frequency range. The agreement between calculated and measured  $N_0$  is not as good as that for  $A_n$ . The second moment of the response spectrum tends to make the effects of differences in the frequency response functions more pronounced.

## APPLICATION TO DESIGN

### Concepts

At the outset of this presentation, the characteristics of airplane responses to turbulence during routine flight operations were described in terms of the statistical parameter  $N(z)$ , the average frequency of exceeding a response peak of level  $z$ , which is significant from the standpoint of the occurrence of single extreme loads. Also, a description was given of the relation of the statistics of response to the statistics of turbulence on the basis of the simplifications permitted by the consideration of short samples of turbulence. The short samples, of course, are not representative of the turbulence experienced in routine flights.

In this section, a description is given of a procedure used to synthesize for design purposes the parameter  $N(z)$  for routine flight by using the results of short samples of turbulence and the measured probability of distribution of turbulence intensity in the atmosphere. In a sense, a full circle will have been completed, in that this paper started with an indication of the need to describe the overall load response experience in terms of  $N(z)$  and it ends with an estimate of  $N(z)$ .

A reminder of events in a routine flight is provided by the VGH record shown in figure 2. As implied by the nature of the acceleration trace  $a_n$ , the turbulence encountered is intermittent and variable in intensity. It is noted that the altitude and airspeed change during the flight. Fuel is consumed and therefore the weight of the airplane changes. The changes in the airplane flight conditions produce changes in the airplane frequency response that must be accounted for in the procedure for synthesizing a statistical description of the responses for an extended flight. Pertinent characteristics that must be considered are summarized in the following listing:

(1) Turbulence characteristics:

- Intermittence
- Variable intensity (nonstationary)
- Variation in scale  $L$

(2) Airplane characteristics:

- Variation in magnitude and distribution of weight
- Airspeed variation
- Altitude variation

The basic approach to applying the relations developed for short samples of turbulence to account for the characteristics of general flight experience just listed includes the following steps:

(1) The total expected turbulence experience is synthesized as a summation of individual patches of turbulence for which random-process methods are valid.

(2) The average frequency of exceeding a given response peak of level  $z$  (that is,  $N(z)$ ) is calculated for each patch.

(3) The value of  $N(z)$  for the total experience is obtained from the summation of the values of  $N(z)$  for the patches, weighted by the probability of occurrence of the patches.

The concept of individual patches is illustrated by the sketch at the top of figure 36. The patch designated  $d_0$  represents distance flown in smooth air, and the other patches represent turbulence having various root-mean-square intensities  $\sigma_i$  ( $i = I, II, III$ ). Probabilities of encountering patches of given intensities are defined by  $d_i/d_T = p(\sigma_i)$ , and the distribution of  $p(\sigma_i)$  with intensity  $\sigma_i$  is illustrated by the sketch at the lower left of this figure. For the limiting case, in which the turbulence is represented by a continuous variation in rms intensity, the probability is expressed as the density function  $p(\sigma)$ , as shown in the lower right sketch.

The corresponding representation of  $N(z)$  in terms of the individual patches is expressed as a summation of contributions from each of the patches based on the relations developed from random-process theory and weighted by the distance flown in each patch. That is, on the basis of equation (38),

$$N(z) = \frac{1}{d} \left[ d_I N_{0,I} e^{-\frac{z^2}{2\sigma_I^2 A_I^2}} + d_{II} N_{0,II} e^{-\frac{z^2}{2\sigma_{II}^2 A_{II}^2}} + \dots \right] \quad (40)$$

For the continuous variation of intensity, the summation becomes the integral involving the probability density  $p(\sigma)$ . That is,

$$N(z) = \int_0^\infty N_0 p(\sigma) e^{-\frac{z^2}{2\sigma^2 A_z^2}} d\sigma \quad (41)$$

From measurements made during many routine flights, the probability density  $p(\sigma)$  has been determined empirically and curve fitting has resulted in the following expression for  $N(z)$  at any given altitude:

$$N(z) = P_1 N_0 e^{-\frac{z}{\sigma_{c,1} A_z}} + P_2 N_0 e^{-\frac{z}{\sigma_{c,2} A_z}} \quad (42)$$

In this equation  $P_1 = \frac{d_1}{d_T}$  and  $P_2 = \frac{d_2}{d_T}$  where  $d_1$  is the flight distance in "nonstorm" conditions,  $d_2$  is the flight distance in "storm" conditions,  $d_T$  is the total flight distance,  $\sigma_{c,1}$  is the rms intensity of composite nonstorm turbulence velocity, and  $\sigma_{c,2}$  is the rms intensity of composite storm turbulence velocity. The designations nonstorm and storm are only very broadly related to meteorological conditions in the sense that generally the intensity  $\sigma_{c,2}$  is larger than  $\sigma_{c,1}$  and the probability  $P_2$  is smaller than  $P_1$ , as might be expected. The function  $N(z)$  was fitted by two exponential terms and the respective designations nonstorm and storm are used primarily for convenience. A graphical illustration of equation (42) is shown in figure 37 in the form of a semilogarithmic plot. From extensive measurements of turbulence, the parameters  $P_1$ ,  $P_2$ ,  $\sigma_{c,1}$ , and  $\sigma_{c,2}$  in equation (42) were established to be functions of altitude as shown in figure 38.

The remaining parameters in equation (42),  $N_0$  and  $A_z$ , also depend on altitude and are affected by airplane weight, airplane speed, and turbulence scale  $L$  as well. The procedure for accounting for the effects on the variations in all these quantities in establishing a design function  $N(z)$  is called "mission analysis."

### Mission Analysis

The initial step in mission analysis is the establishment of a representative flight profile for design purposes. An example is indicated in figure 39 as the variation of altitude  $h$  with flight distance. The associated variations of airspeed  $V$  and airplane weight  $W$  are also shown. The variation of the scale of turbulence  $L$  during the representative flight is also illustrated (fig. 40).

In the next step the total flight distance is divided into a number of stages, and the quantities  $\Phi_{wg}(f)$ ,  $|H_z(f)|^2$ ,  $\Phi_z(f)$ ,  $A_z$ ,  $N_0$ ,  $P_1$ ,  $P_2$ ,  $\sigma_{c,1}$ , and  $\sigma_{c,2}$  are determined for each stage. Examples of the variations of  $A_z$ ,  $N_0$ ,  $P_1$ ,  $P_2$ ,  $\sigma_{c,1}$ , and  $\sigma_{c,2}$  for each stage of flight are shown in figures 40 and 41.

The final step in the mission analysis involves the computation of  $N(z)$  for each stage of flight by use of equation (42) and the summation operation to obtain  $N_T(z)$ , the total  $N(z)$  for the entire flight. This step is illustrated in figure 42. Each semilog plot for an individual stage is of the same form as that illustrated in figure 37. The summation operation is described by the equation at the bottom of figure 42.

The total value  $N_T(z)$  is the basis for establishing the design load for a selected risk level, provided that the flight profile chosen for the mission analysis is truly representative of the type of service in which the airplane is used.

The adequacy of this procedure was investigated by applying the mission-analysis method to the determination of  $N_T(z)$  for the load factor  $n$  of an airplane type that was gust critical and that had been in satisfactory service for a number of years. The results compared with data obtained from flight instruments over a period of about 50 000 flight hours are presented in figure 43. The agreement of measured and calculated results is reasonably good. The calculated values are slightly unconservative at the higher levels, but are considered satisfactory.

The coverage of this subject in a single paper is, of necessity, broad and incomplete. There are a number of related subjects that were not discussed in detail. These subjects include the responses of the lateral modes of motion, cross-spectral relations and two-dimensional turbulence problems, treatment of combined loads, flight measurements of turbulence velocities and airplane responses, methods of processing measured random time functions to obtain power spectra, and statistical error analysis. The reader is referred to the present bibliography and to the extensive bibliography in reference 1 for further information on these subjects.

#### REFERENCES

1. Houbolt, John C.; Steiner, Roy; and Pratt, Kermit G.: Dynamic Response of Airplanes to Atmospheric Turbulence Including Flight Data on Input and Response. NASA TR R-199, 1964.
2. Rice, S. O.: Mathematical Analysis of Random Noise. Bell System Tech. J. Pts. I and II, vol. XXIII, no. 3, July 1944, pp. 282-332. Pts. III and IV, vol. XXIV, no. 1, Jan. 1945, pp. 46-156.
3. Batchelor, G. K.: The Theory of Homogeneous Turbulence. Cambridge Univ. Press, 1959.
4. Bennett, Floyd V.; and Pratt, Kermit G.: Calculated Responses of a Large Sweptwing Airplane to Continuous Turbulence With Flight-Test Comparisons. NASA TR R-69, 1960.

#### BIBLIOGRAPHY

- Bendat, Julius S.; and Piersol, Allan G.: Measurement and Analysis of Random Data. John Wiley & Sons, Inc., c.1966.
- Bisplinghoff, Raymond L.; and Ashley, Holt: Principles of Aeroelasticity. John Wiley & Sons, Inc., c.1962.
- Etkin, Bernard: Dynamics of Flight - Stability and Control. John Wiley & Sons, Inc., c.1959.



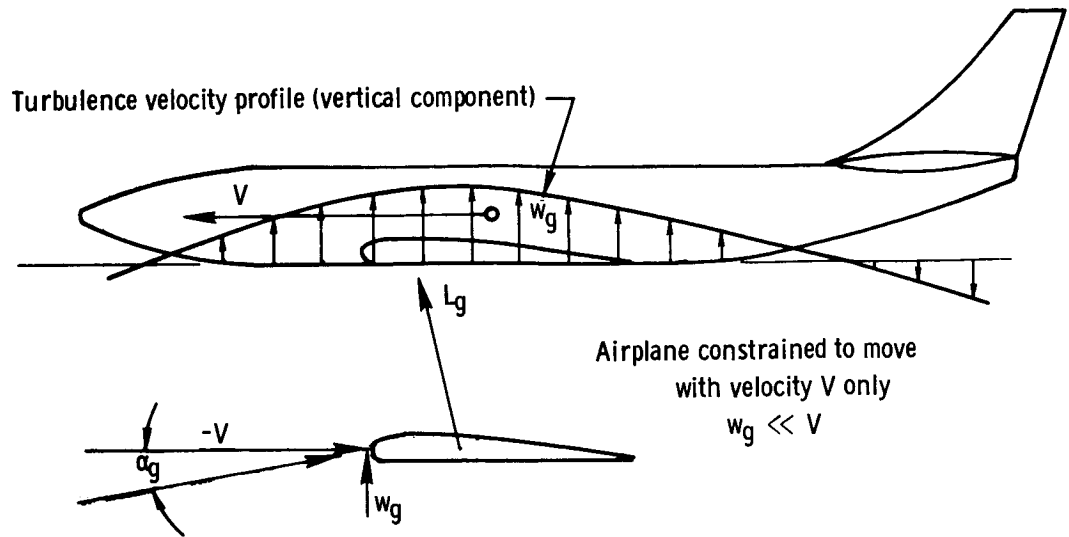


Figure 1.- Diagram showing basic source of turbulence responses.

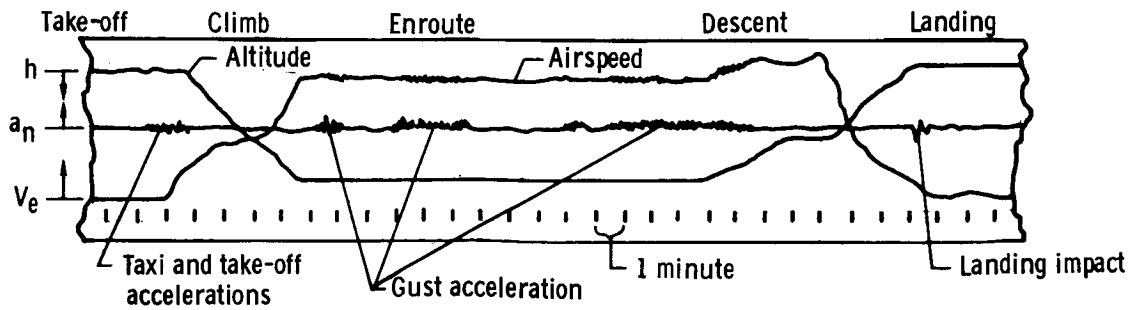


Figure 2.- VGH record of representative routine flight.

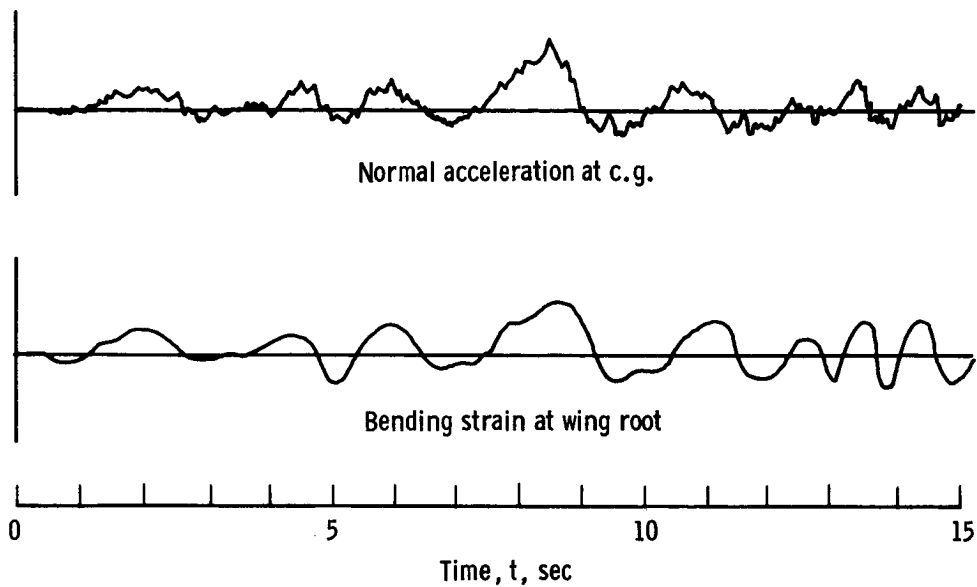


Figure 3.- Sample response time histories.

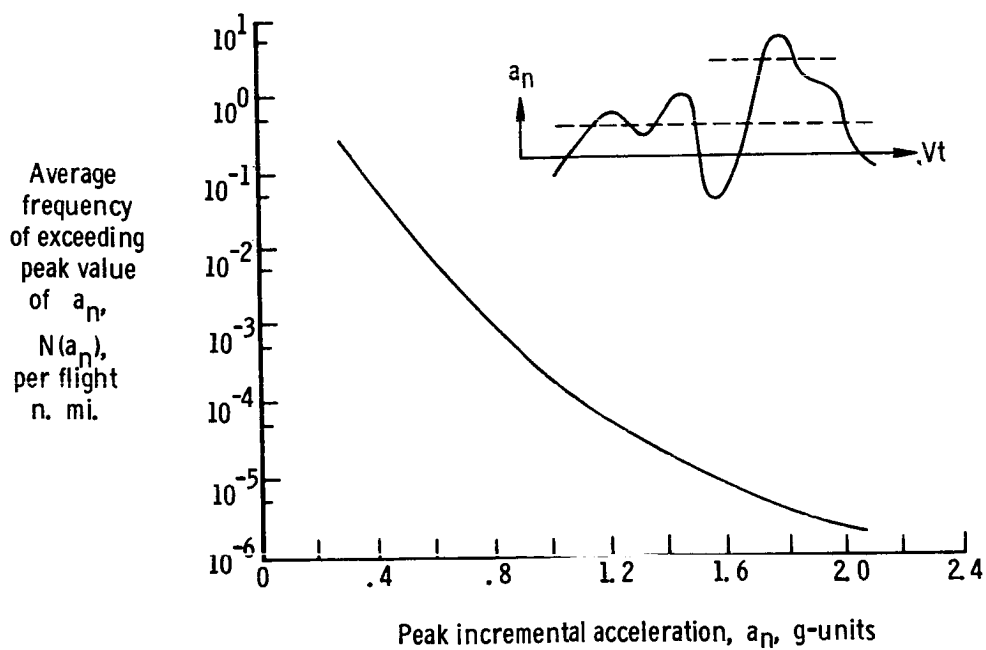


Figure 4.- Turbulence acceleration data for fleet of two-engine turboprop airplanes.

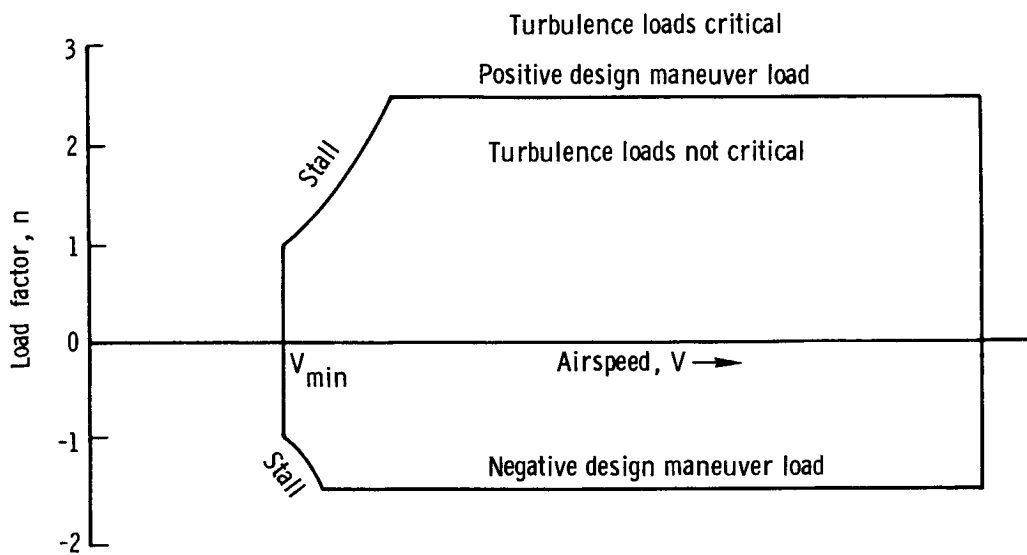


Figure 5.- V-n diagram.

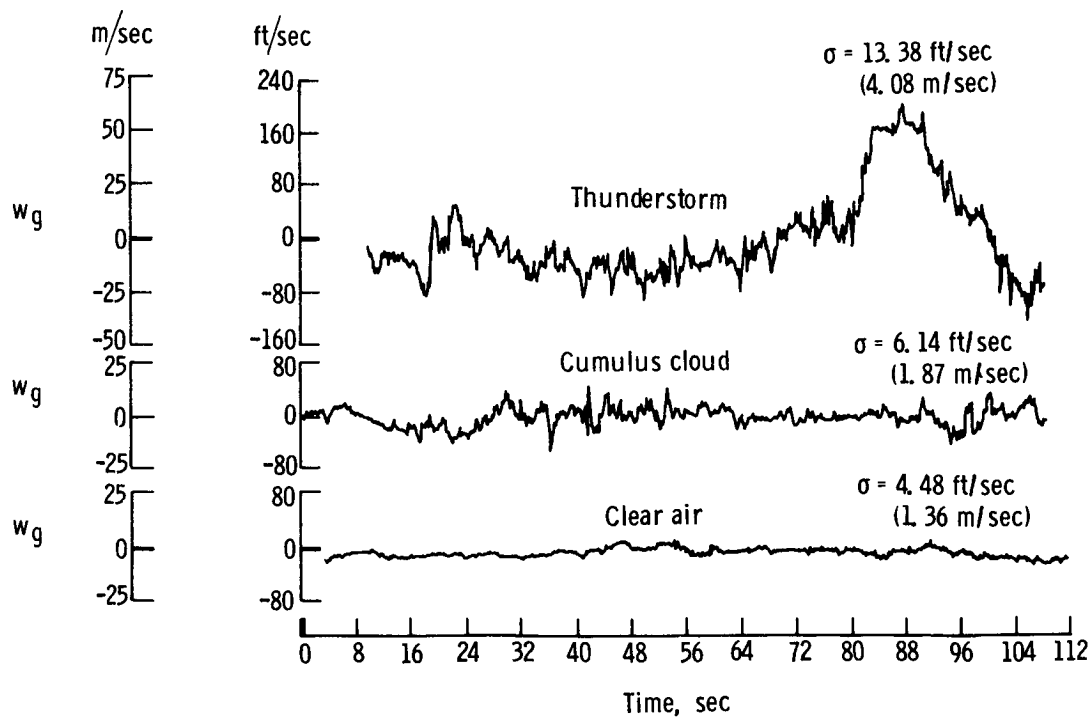


Figure 6.- Sample time histories of vertical component of turbulence velocity.

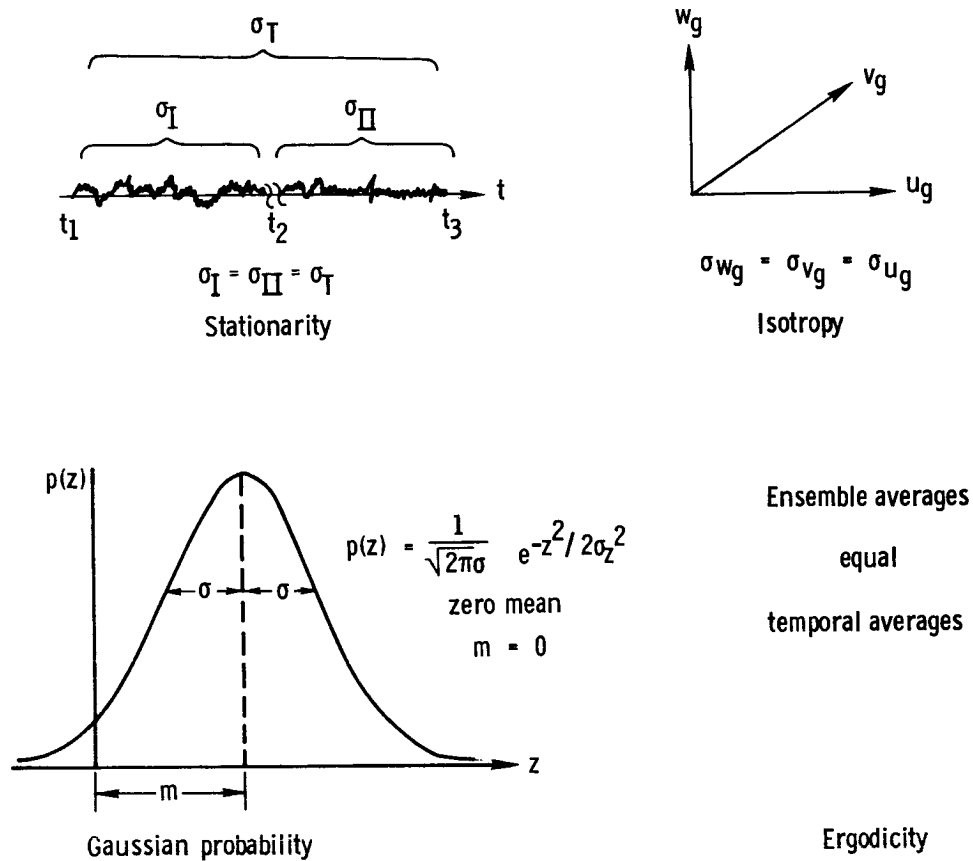


Figure 7.- Statistical properties of short samples of turbulence.

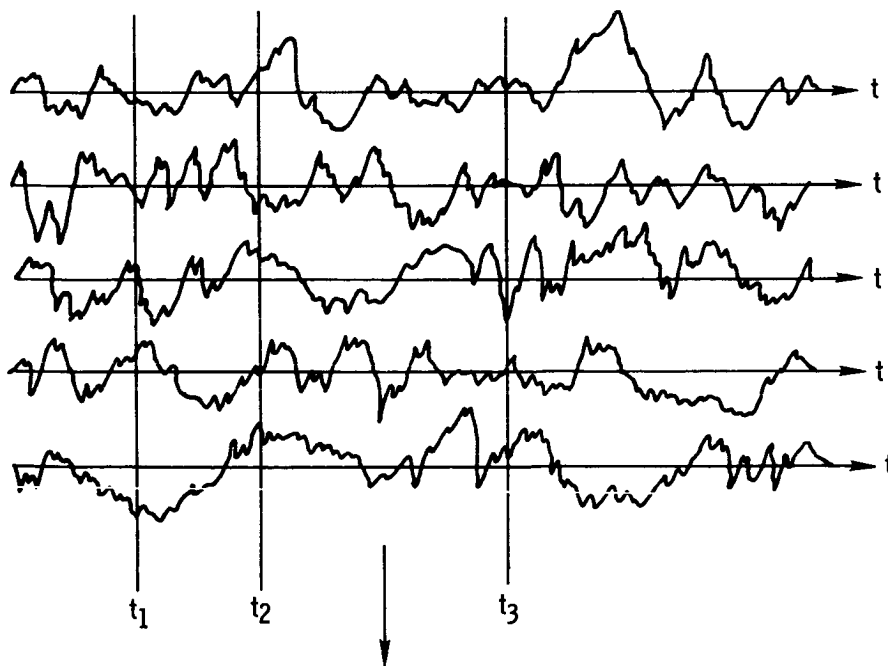


Figure 8.- Ensemble.

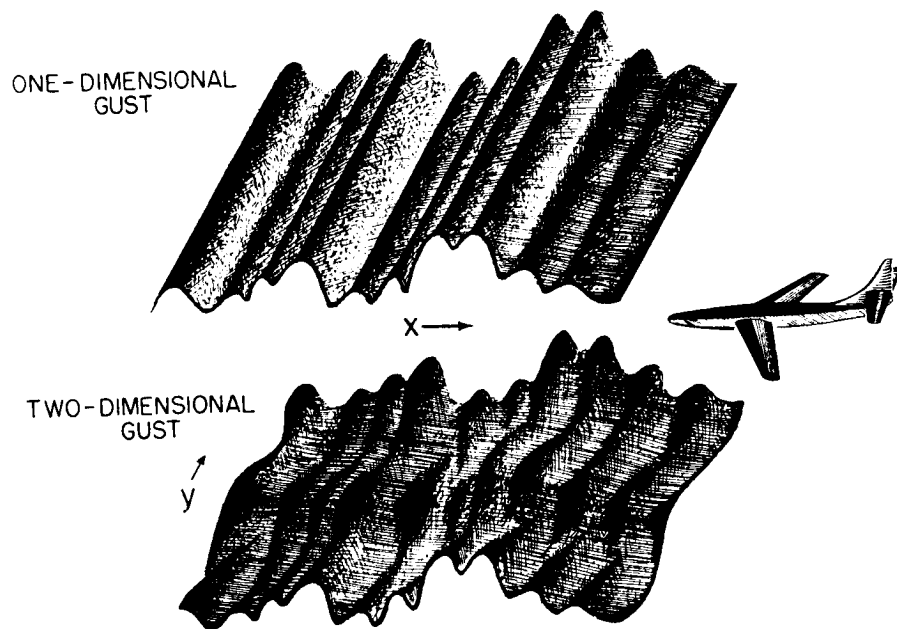


Figure 9.- Models of one- and two-dimensional gusts.

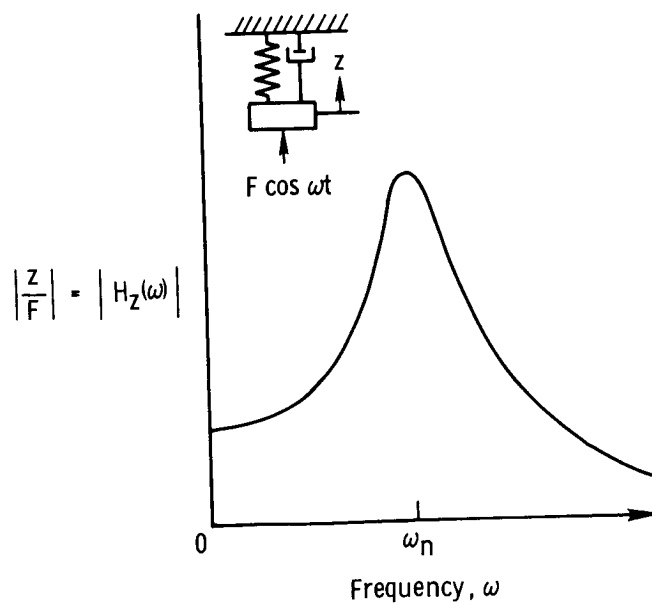
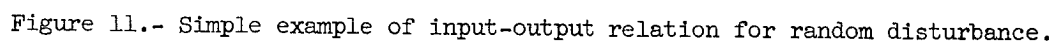


Figure 10.- Example of frequency response function from subject of mechanical vibrations.



**Autocorrelation function**  $R(\tau)$  —

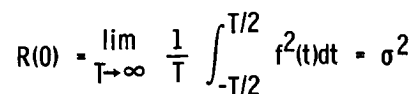


Figure 12.- Relation of power spectrum to random time function.

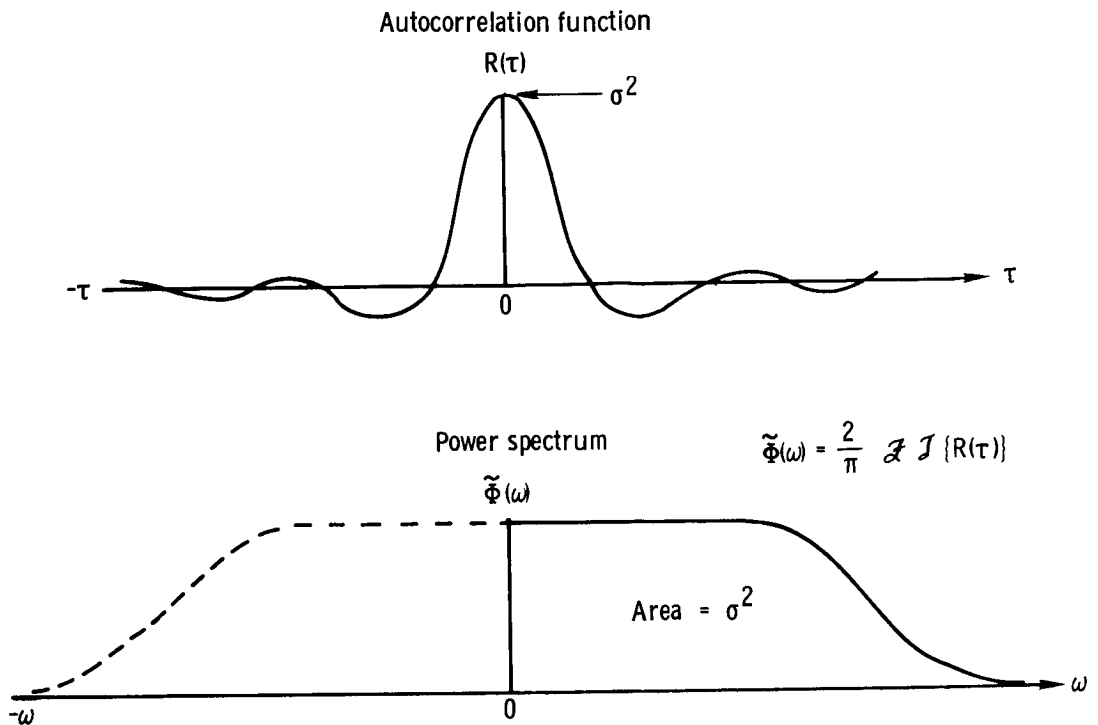


Figure 13.- Example of autocorrelation function and associated power spectrum.

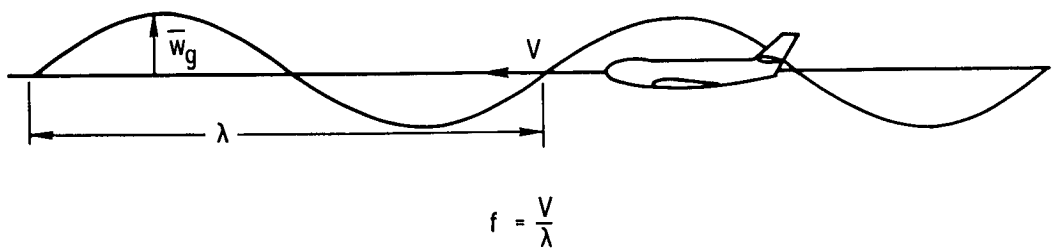


Figure 14.- Frequency relative to one-dimensional gust field.

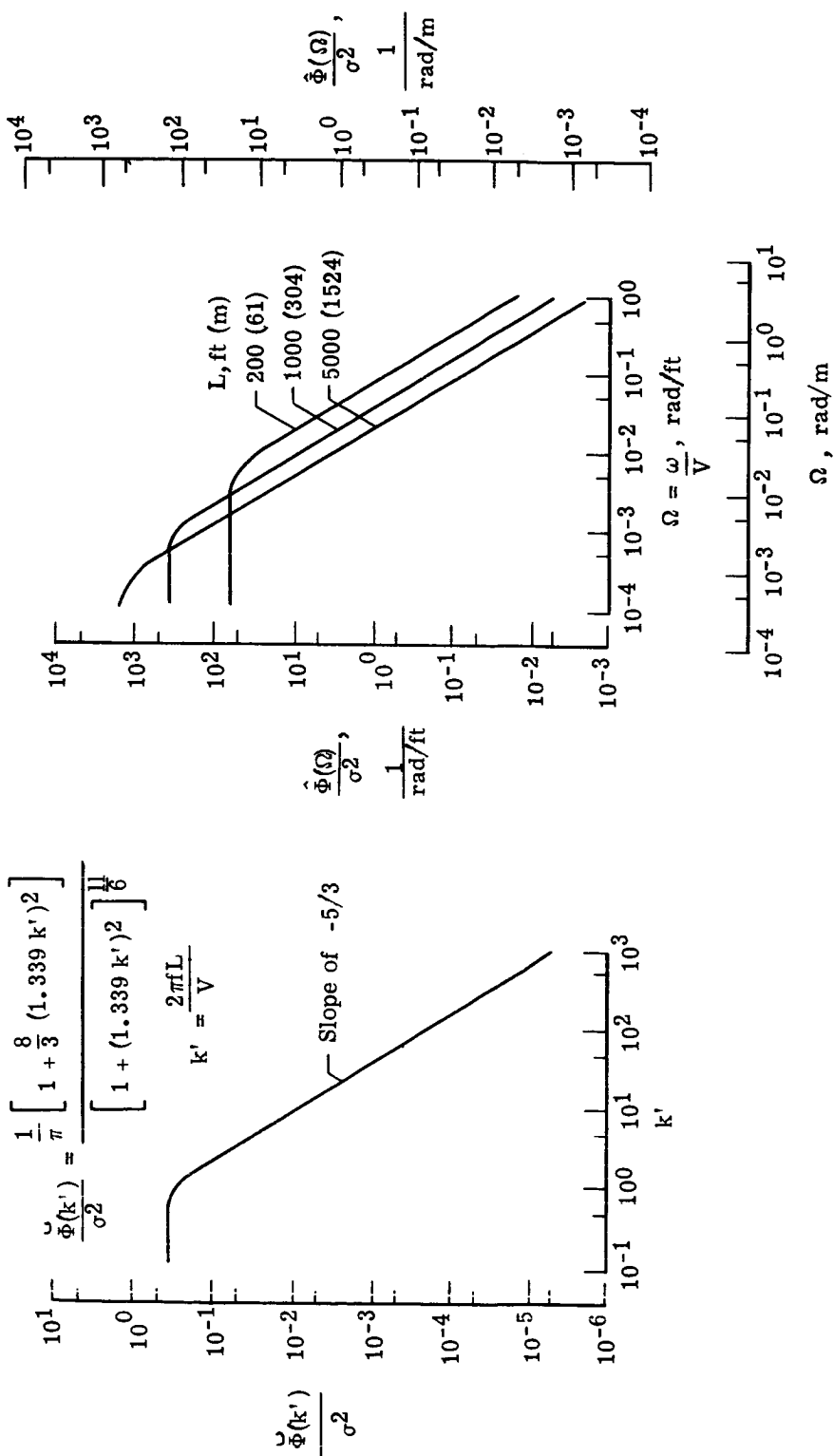


Figure 15.- The von Kármán generalized power spectrum for transverse components of turbulence and the effects of variations in  $L$ .



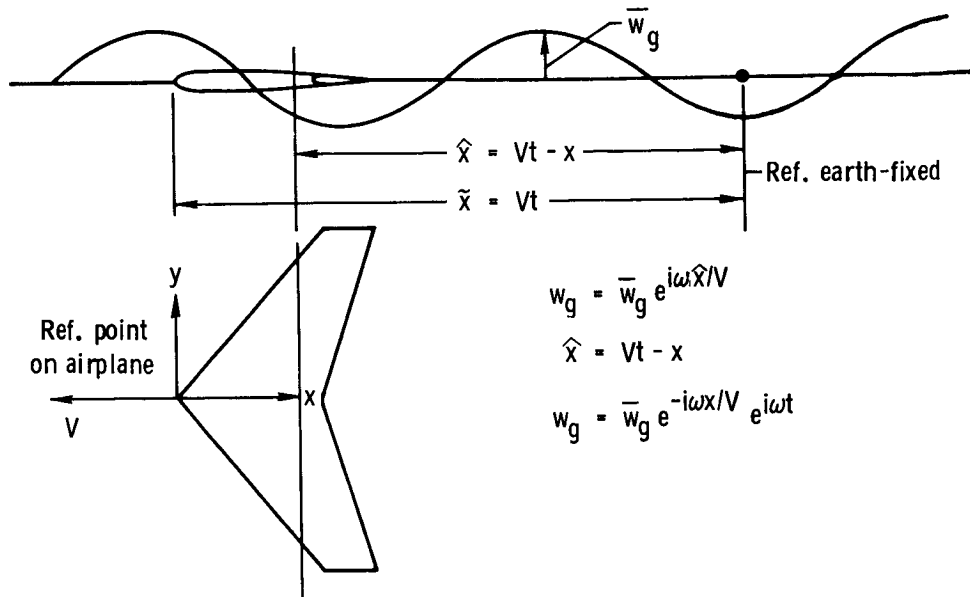


Figure 16.- Gust downwash.

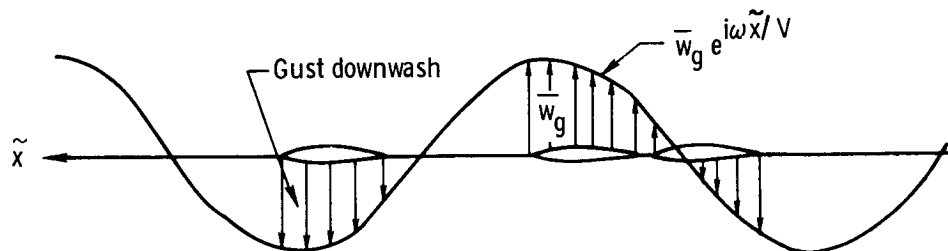


Figure 17.- Effect of penetration of gust field by wing of finite chord.

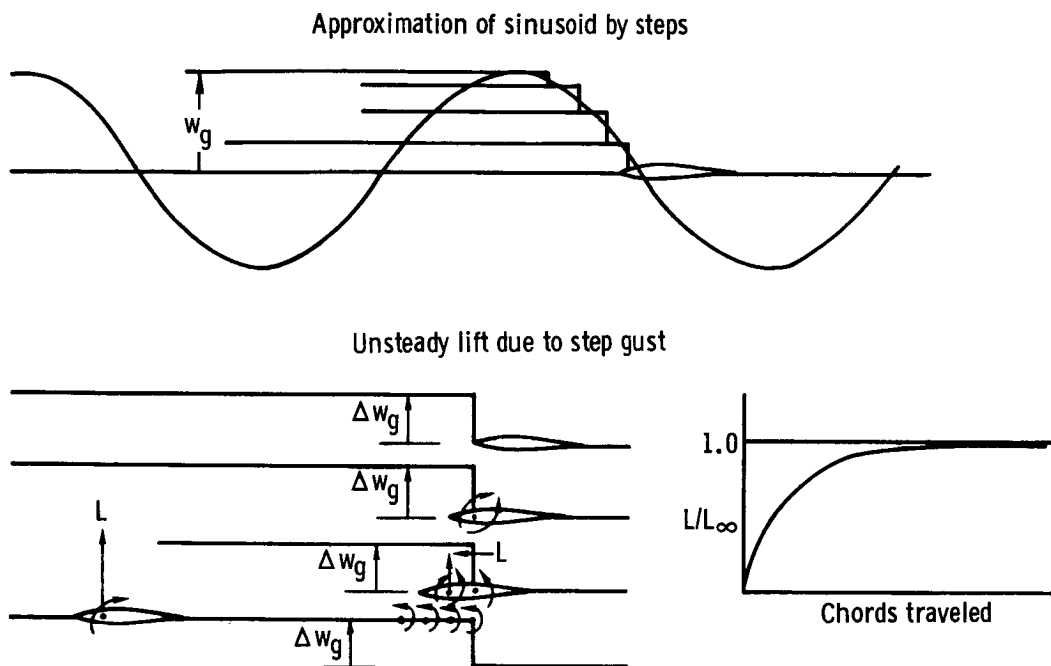


Figure 18.- Effect of gust penetration and wake in a harmonically oscillating airstream.

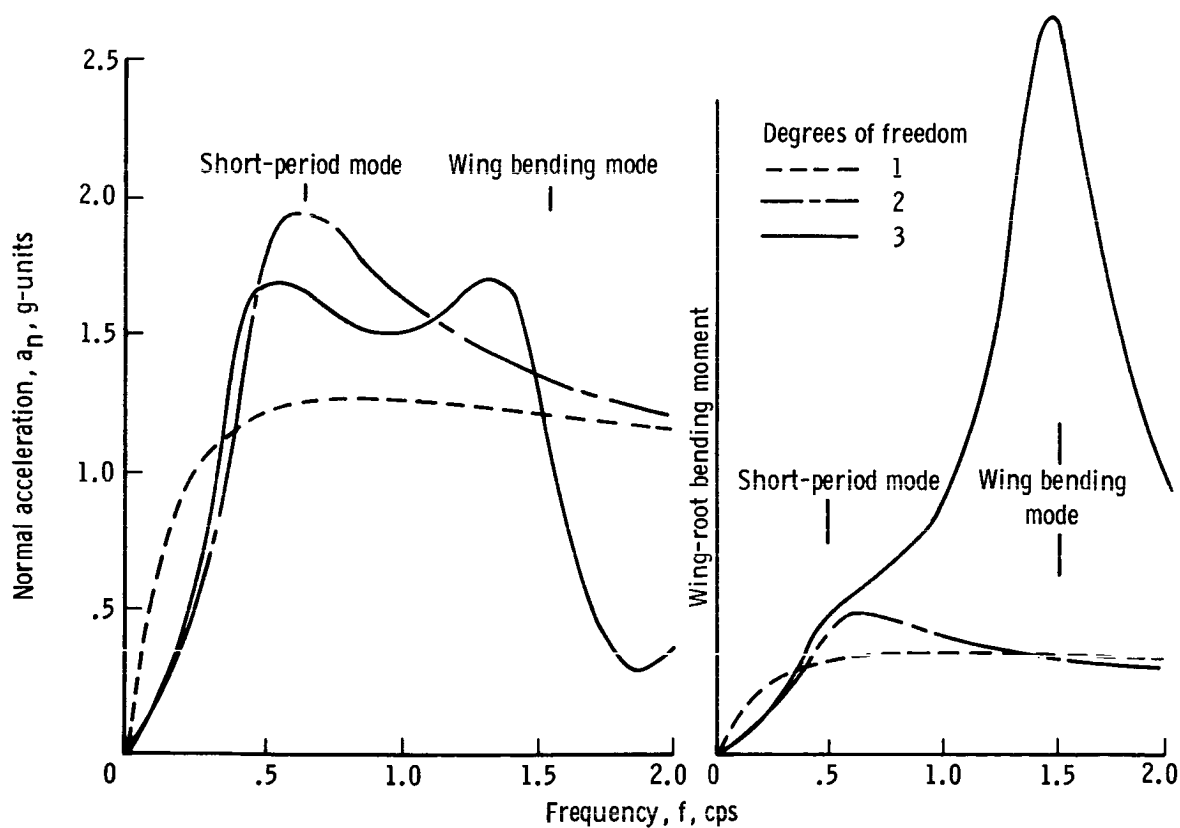


Figure 19.- Effect of various airplane motions and deformations on calculated frequency responses for swept-wing subsonic jet bomber.

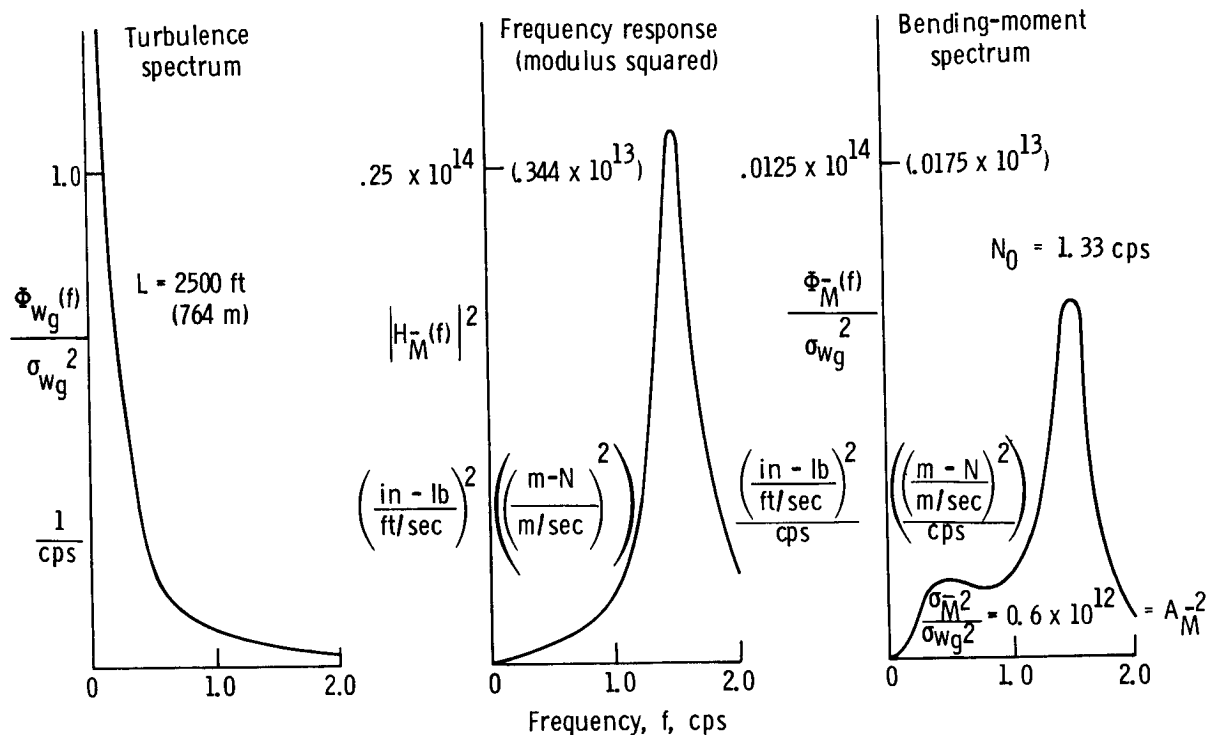


Figure 20.- Terms in input-output relation and statistical parameters for wing-bending-moment response of swept-wing subsonic jet bomber.

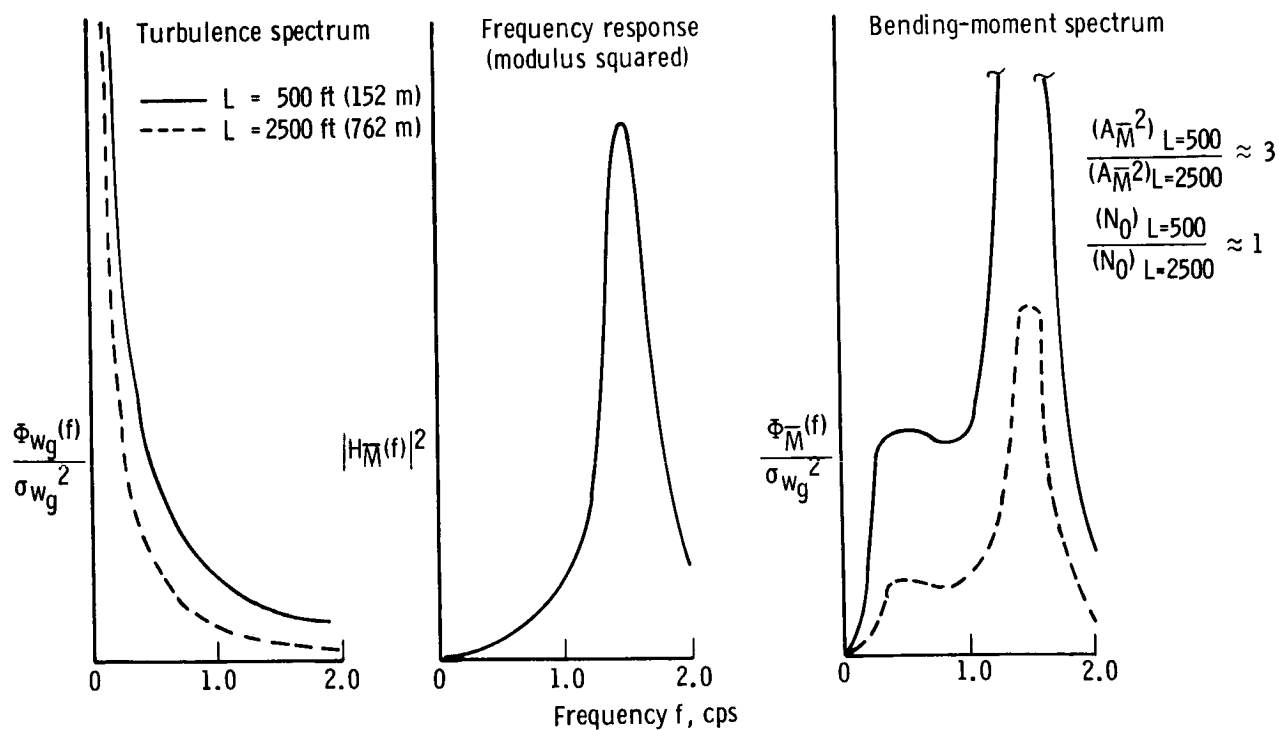


Figure 21.- Effect of variation in turbulence scale.

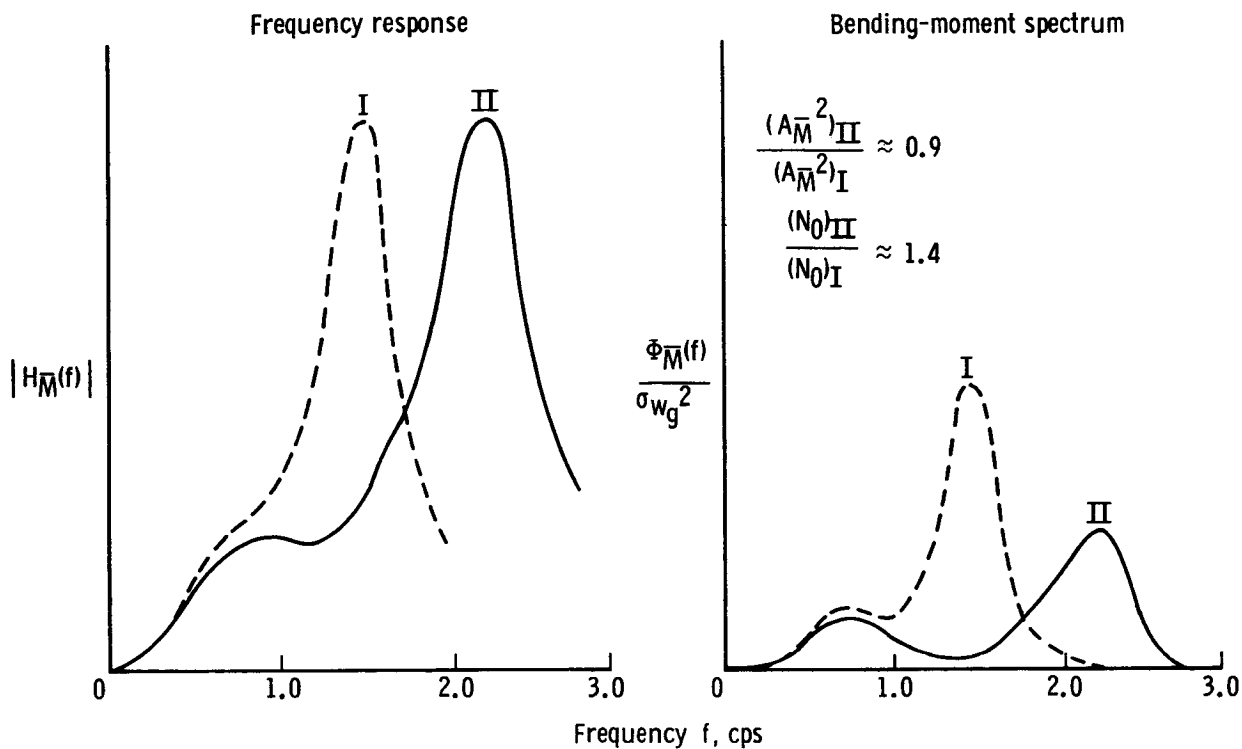


Figure 22.- Effect of variation in bending-mode frequency.

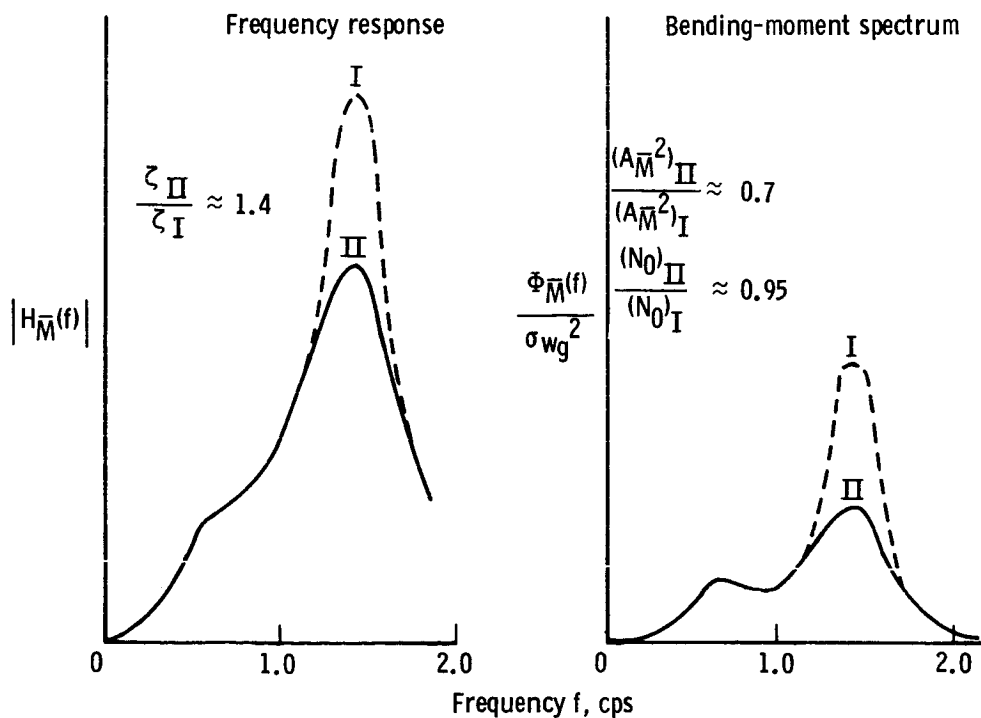


Figure 23.- Effect of variation in damping ratio of wing bending mode.

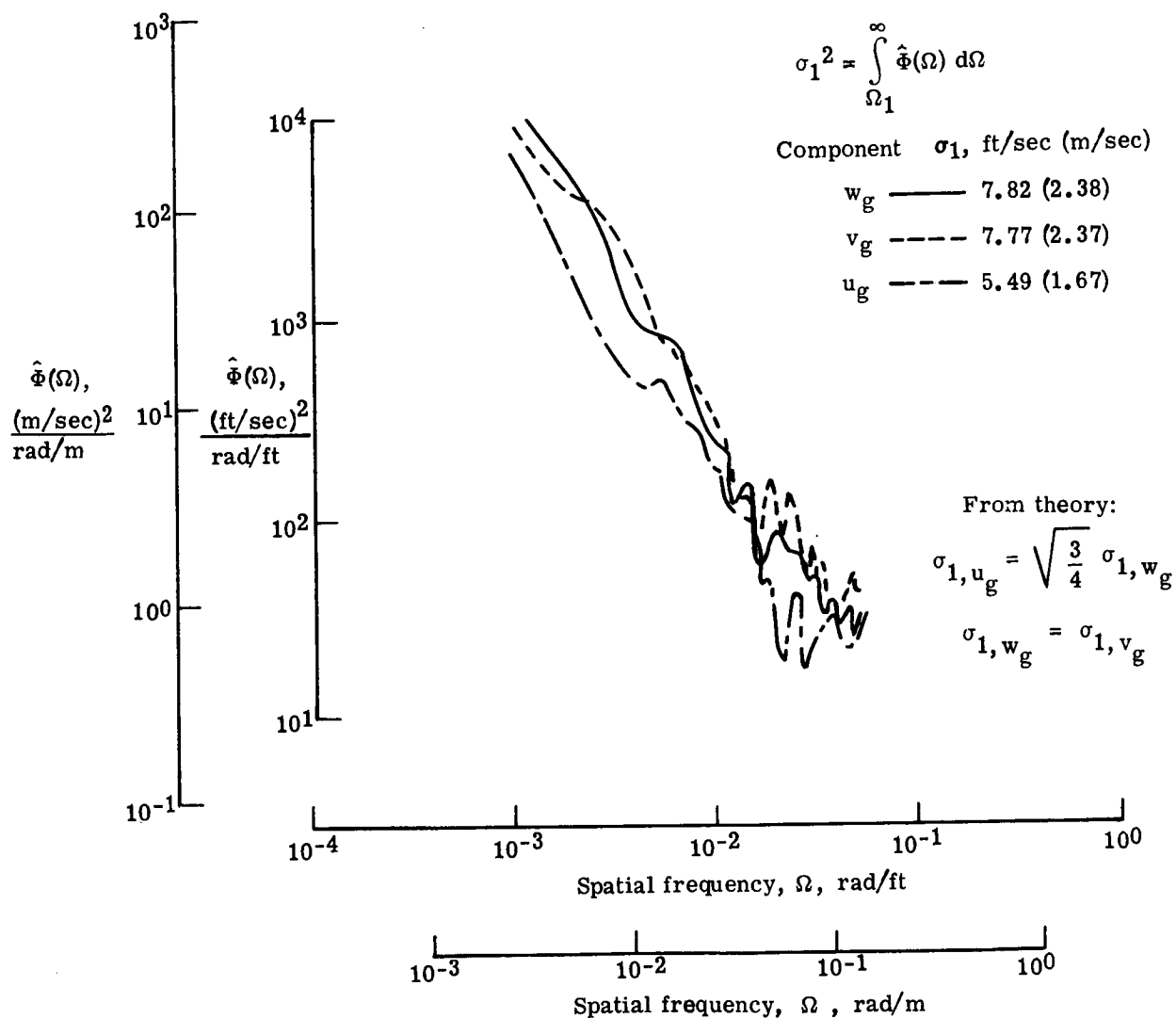


Figure 24.- Isotropy as determined from measurements during flight in a thunderstorm.

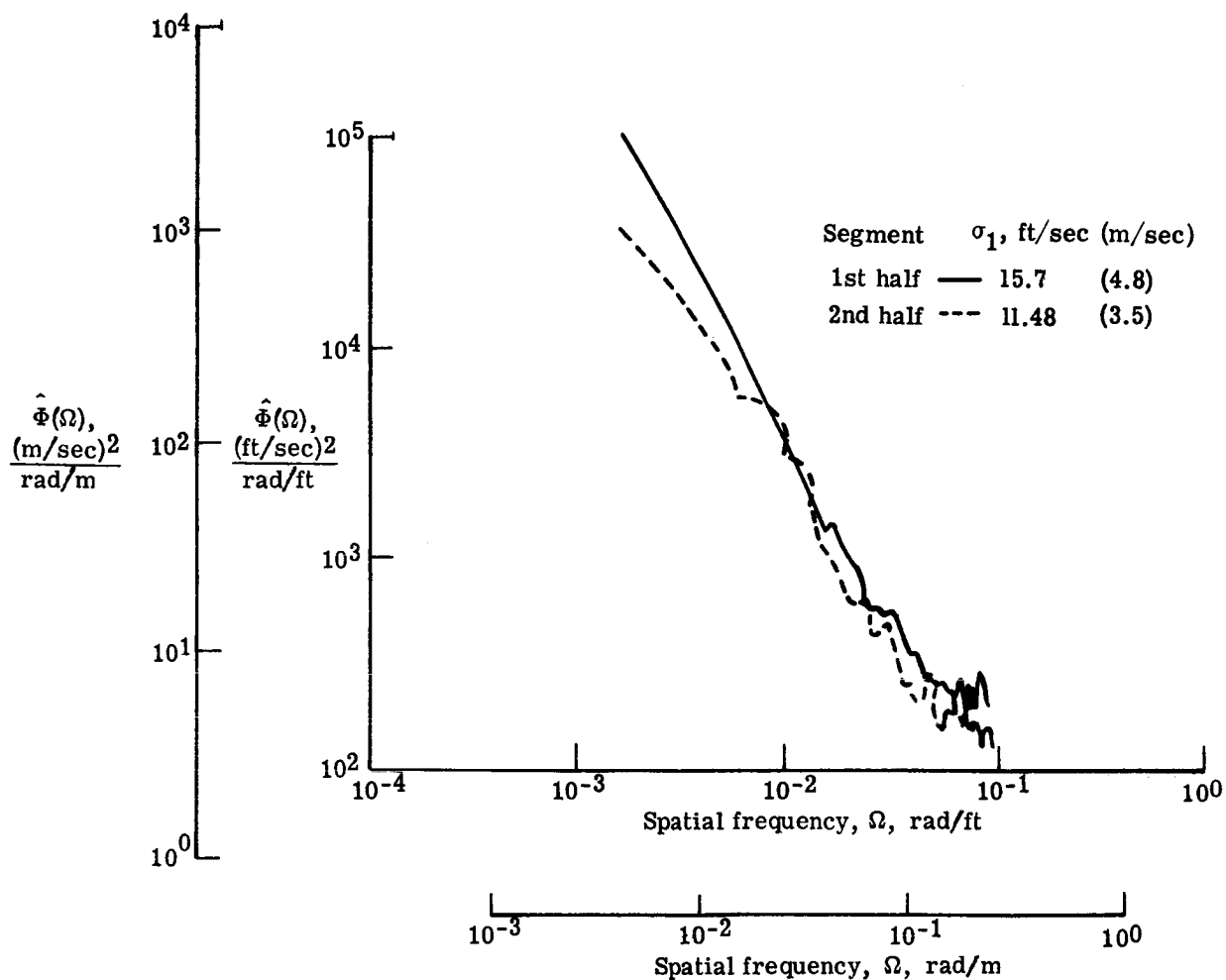
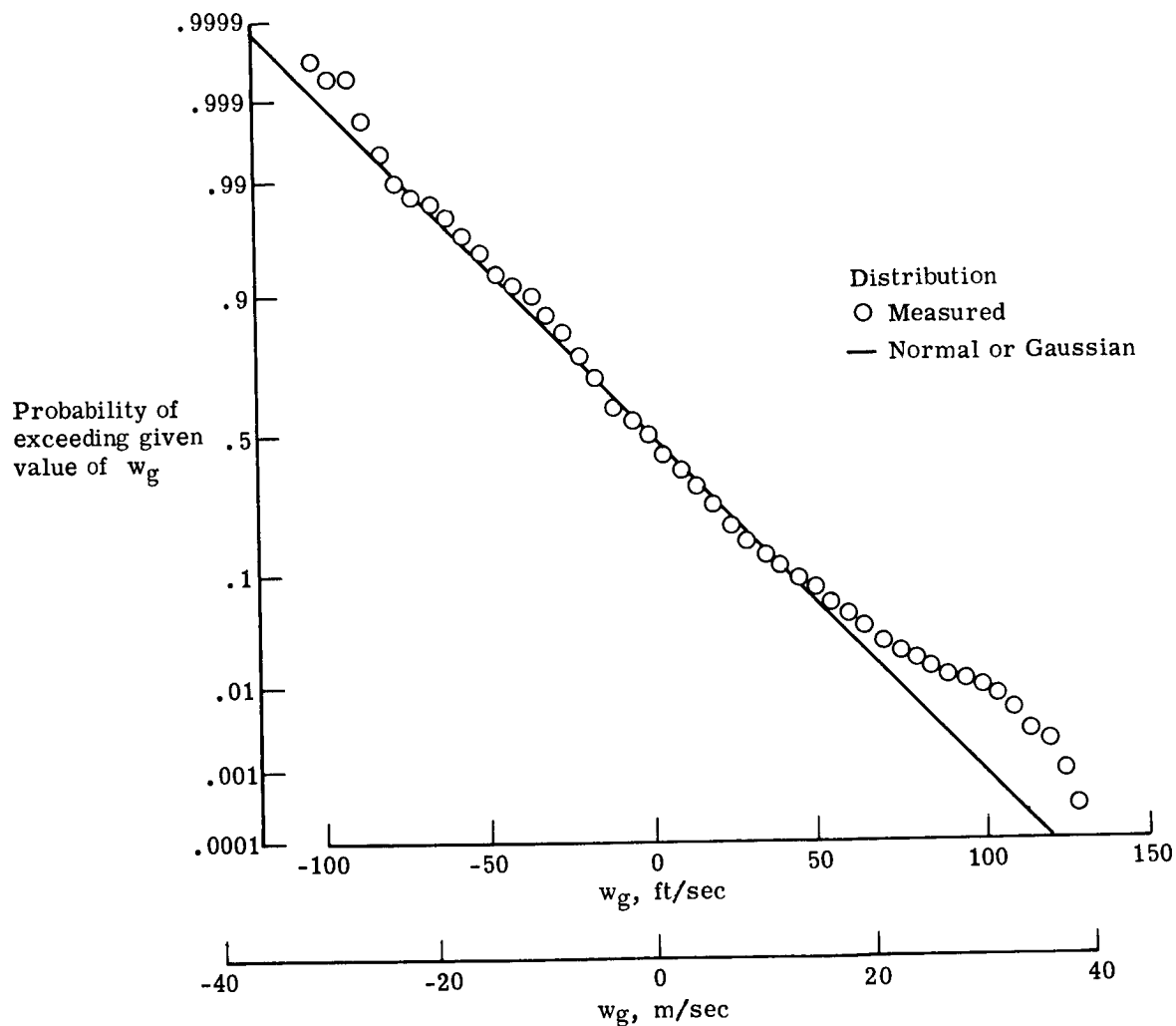


Figure 25.- Stationarity as determined during flight in a thunderstorm. (The length of total sample is 25 n. mi., and the time is 200 sec.)



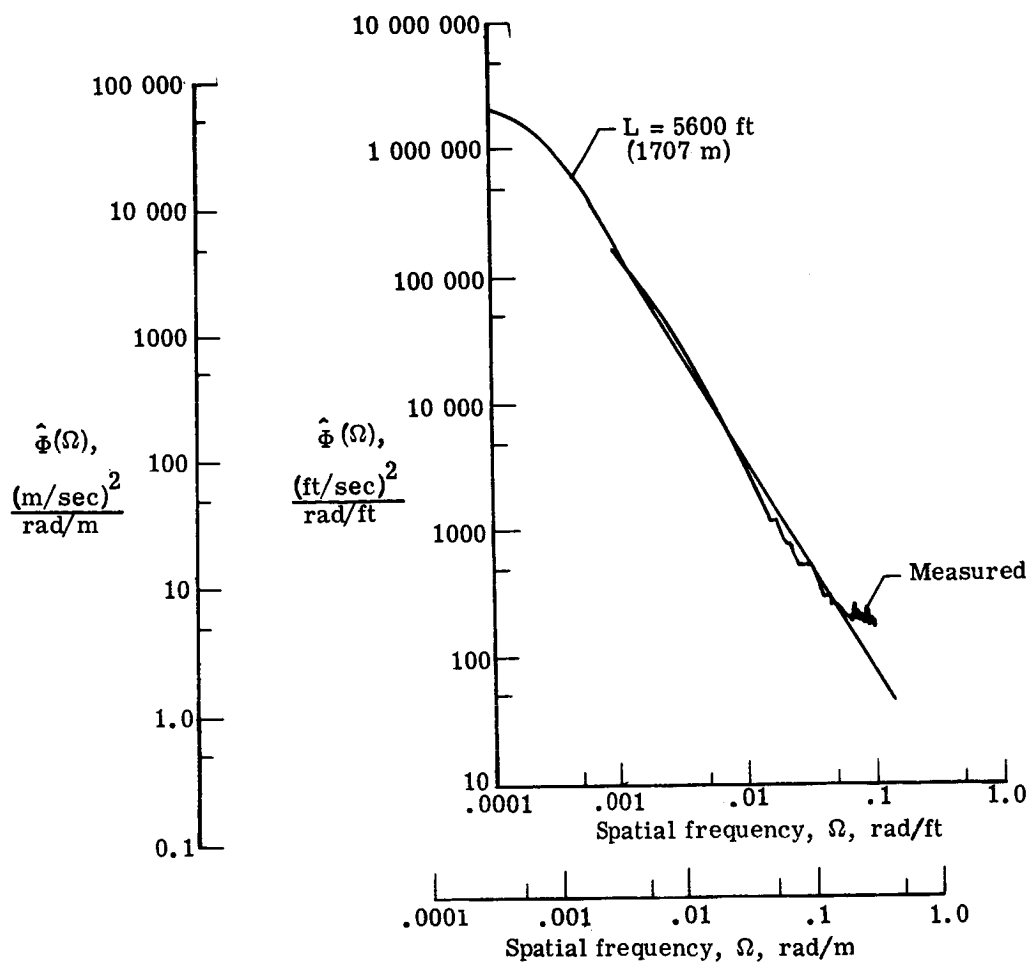


Figure 27.- Measured (from thunderstorm) and fitted spectra.



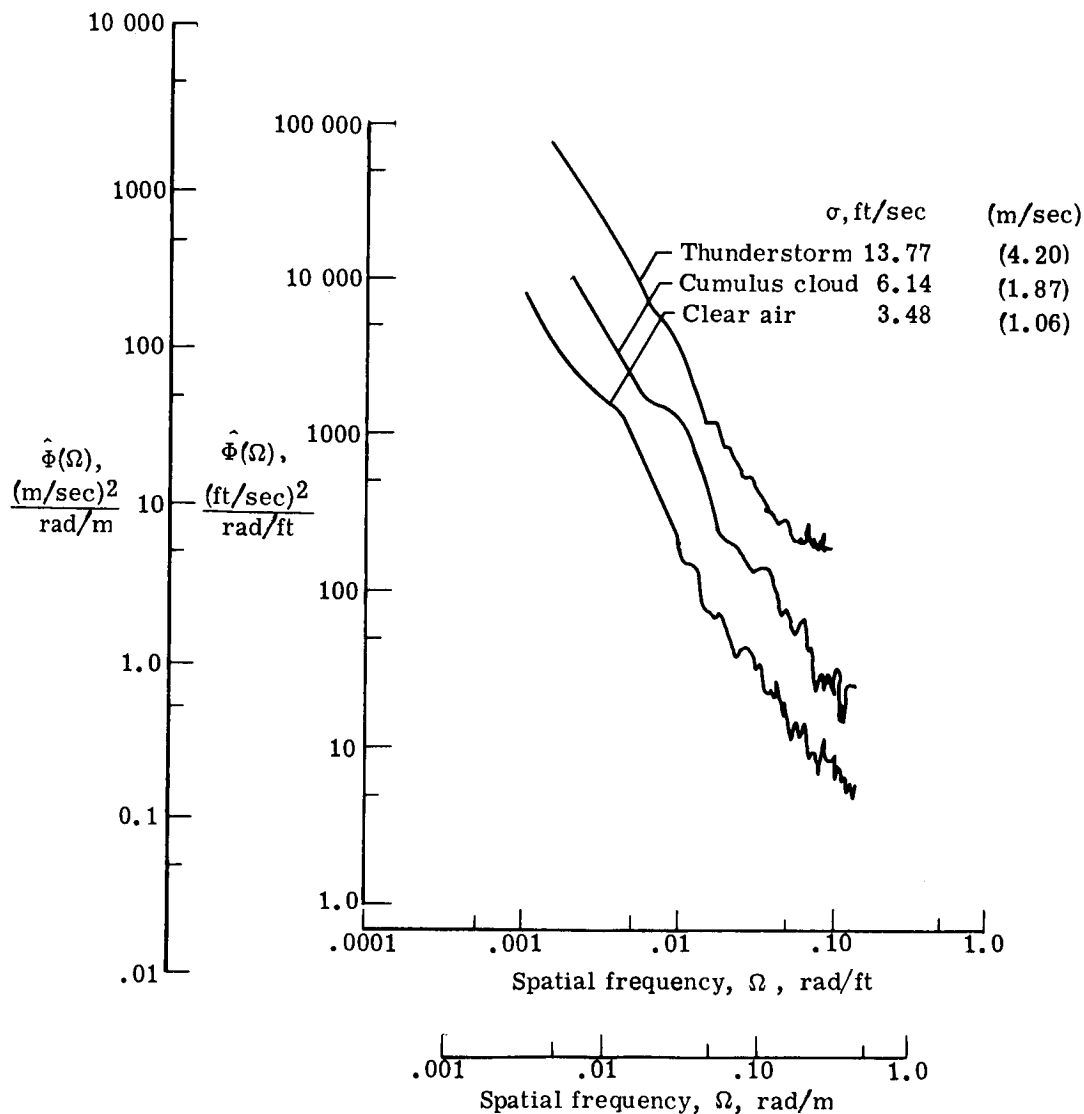


Figure 28.- Power spectra of turbulence for various weather conditions.

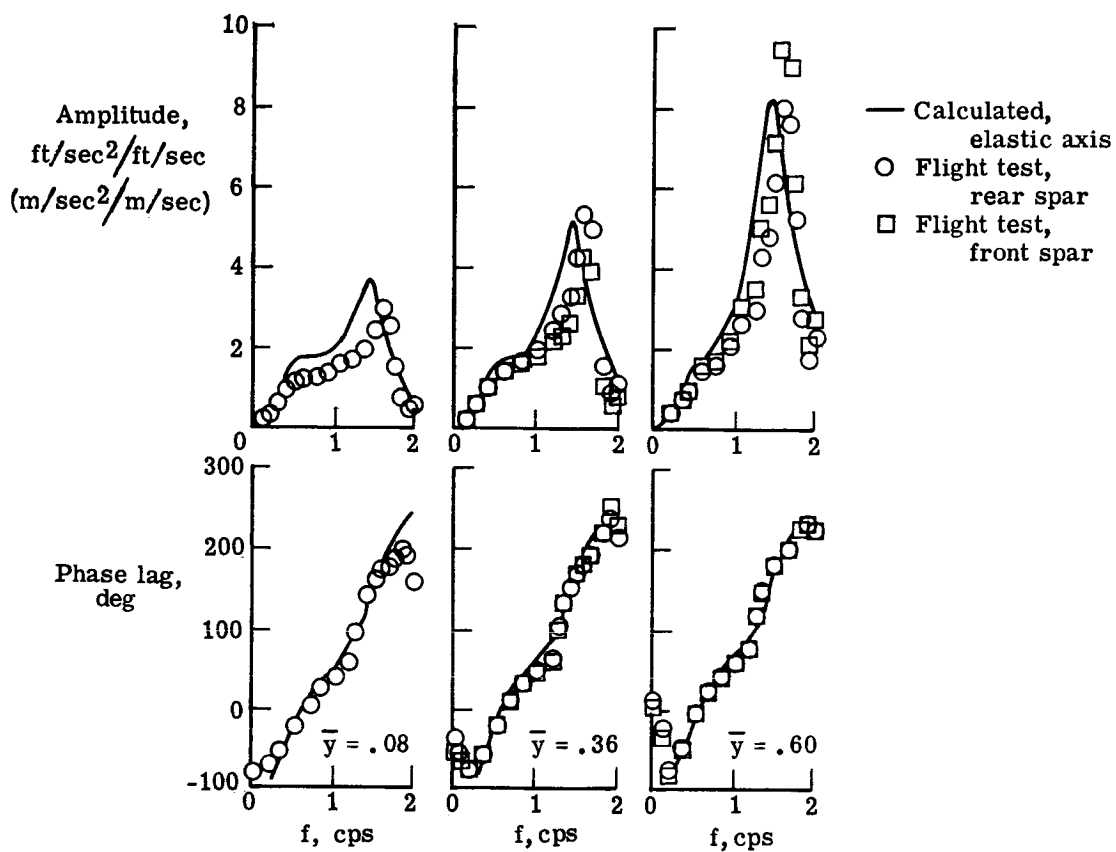


Figure 29.- Comparison of calculated and measured bending-moment transfer functions for B-47 airplane.

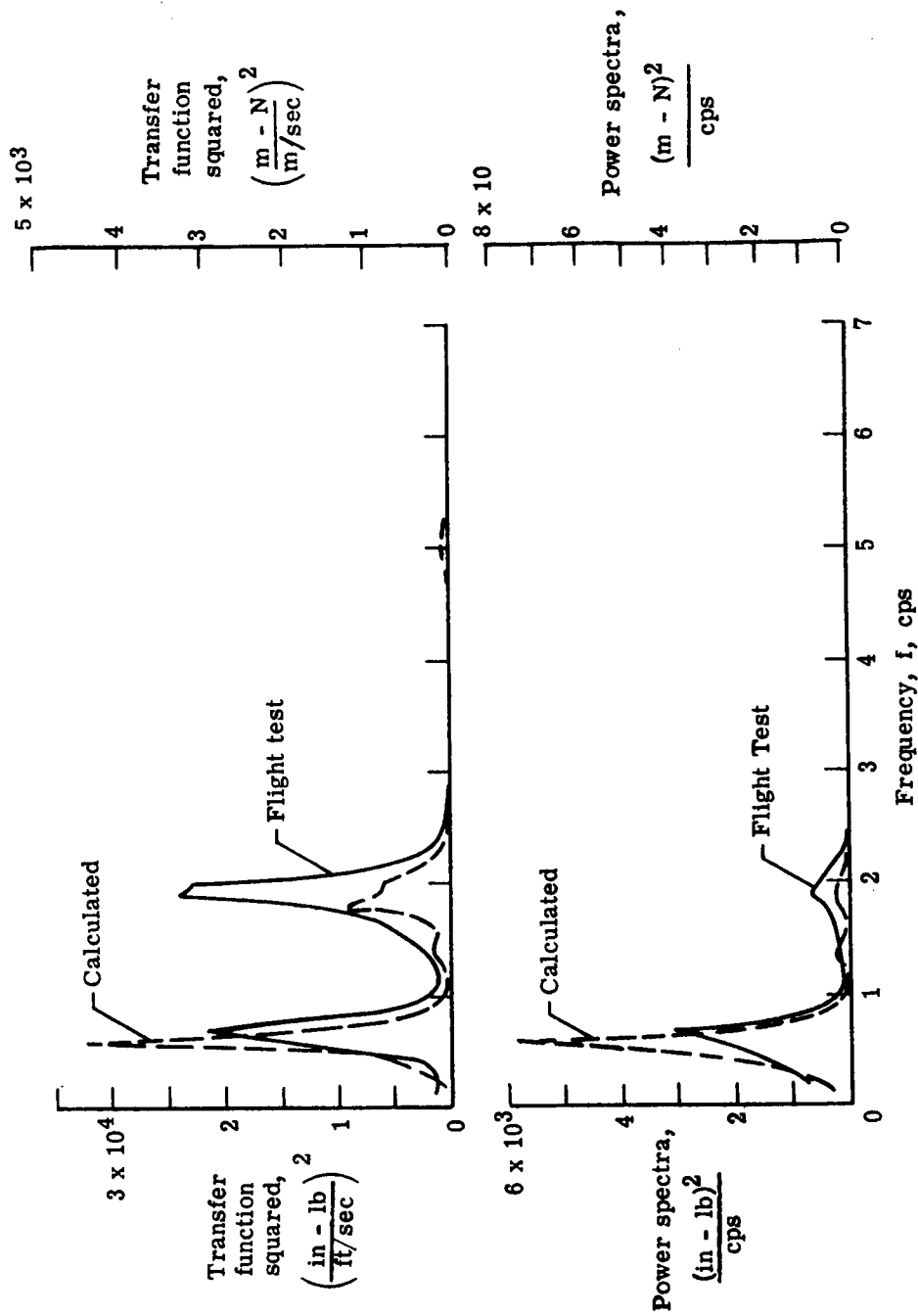


Figure 30.- Comparison of measured and calculated wing-bending-moment gust response for B-52 airplane.

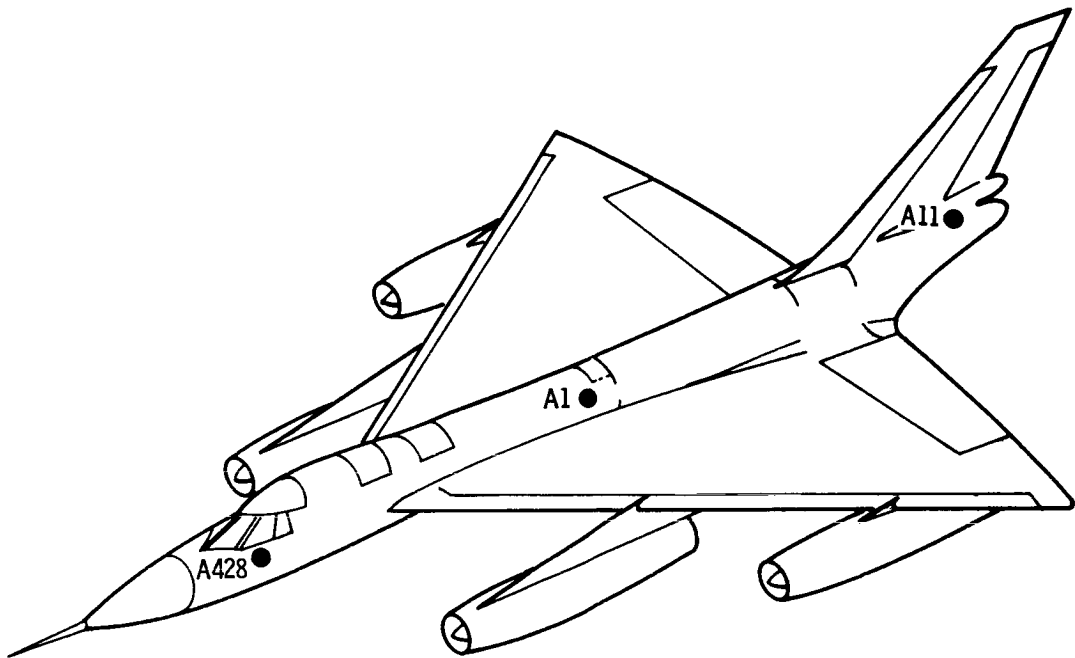


Figure 31.- B-58 airplane.

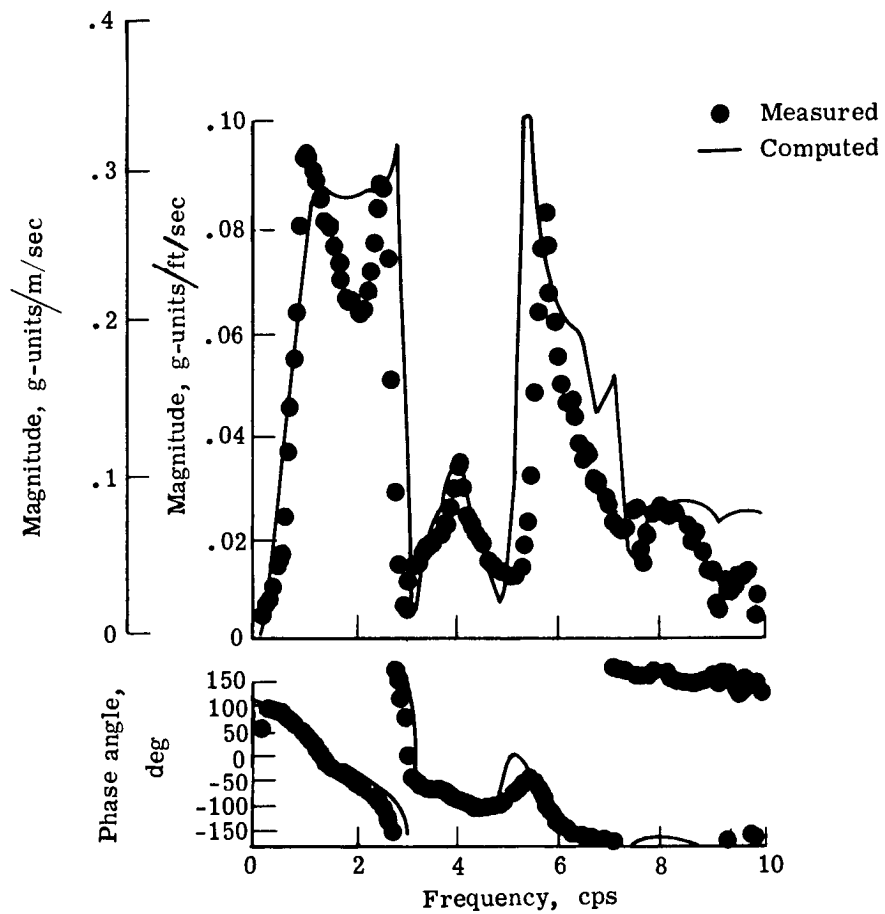


Figure 32.- Comparison of measured and computed frequency response functions for acceleration A1 (center of gravity) of B-58 airplane.

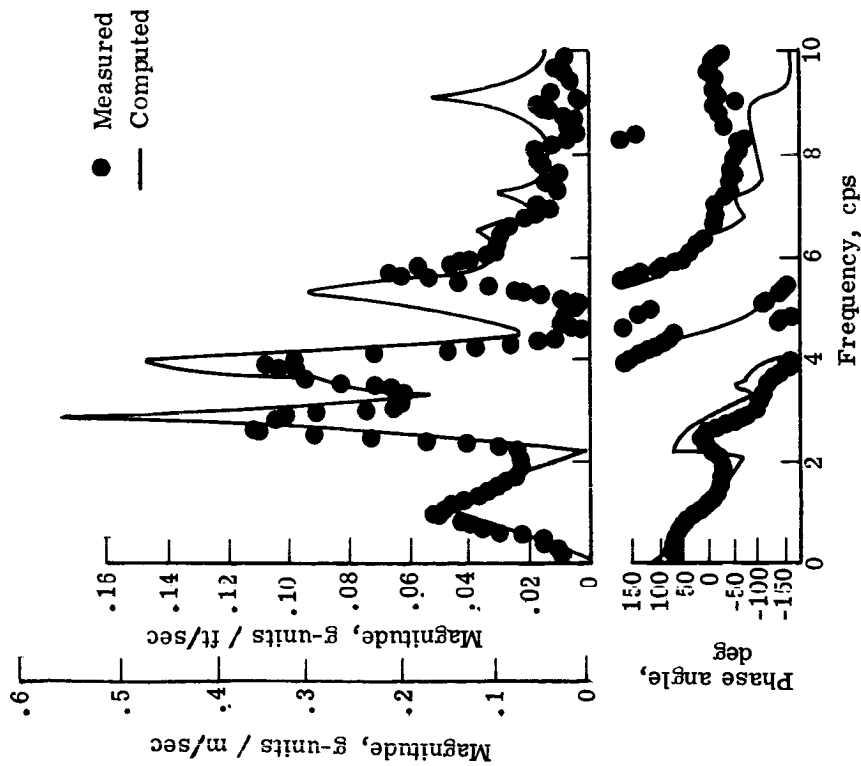


Figure 33.- Comparison of measured and computed frequency response functions for acceleration A428 (pilot's station) of B-58 airplane.

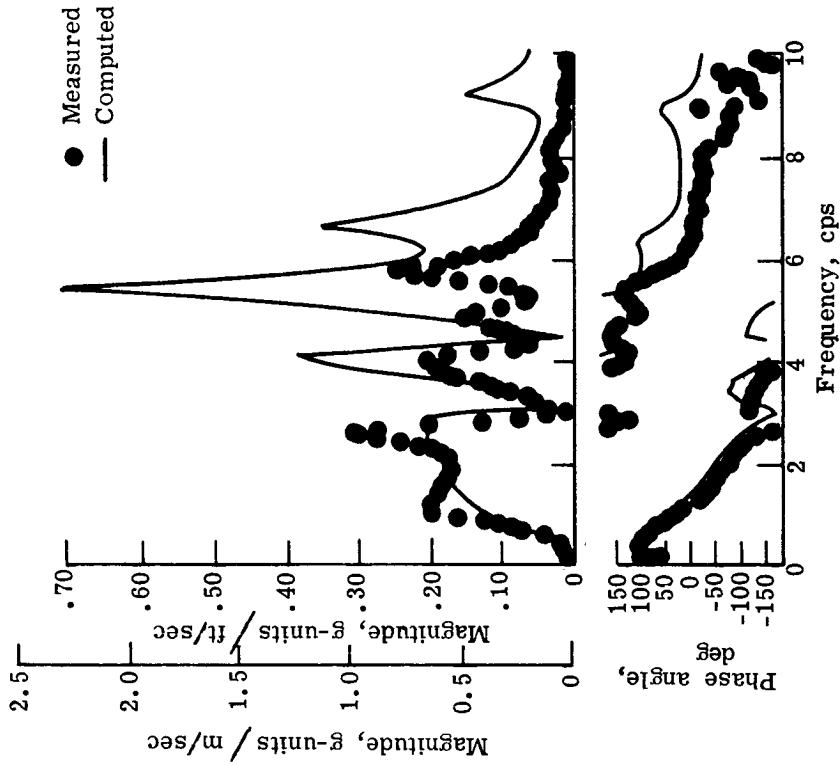


Figure 34.- Comparison of measured and computed frequency response functions for acceleration A11 (aft fuselage station) of B-58 airplane.

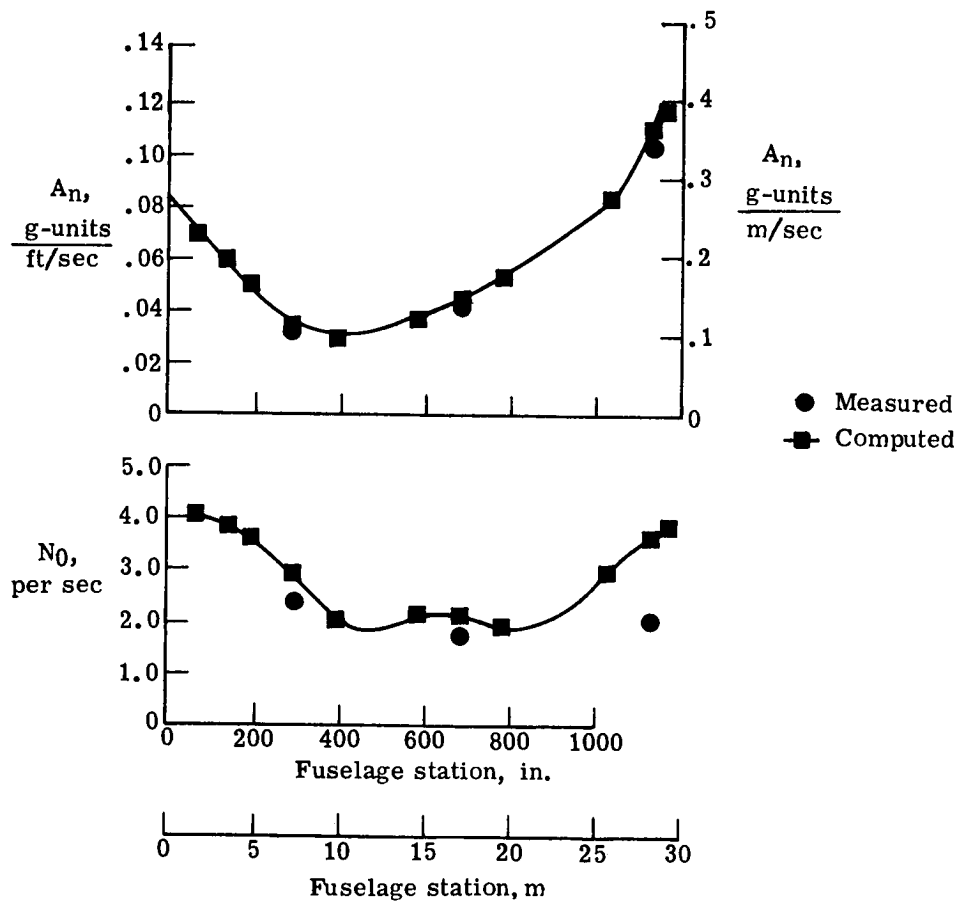


Figure 35.- Comparison of measured and computed values of  $A_n$  and  $N_0$  as functions of fuselage station for the B-58 airplane.

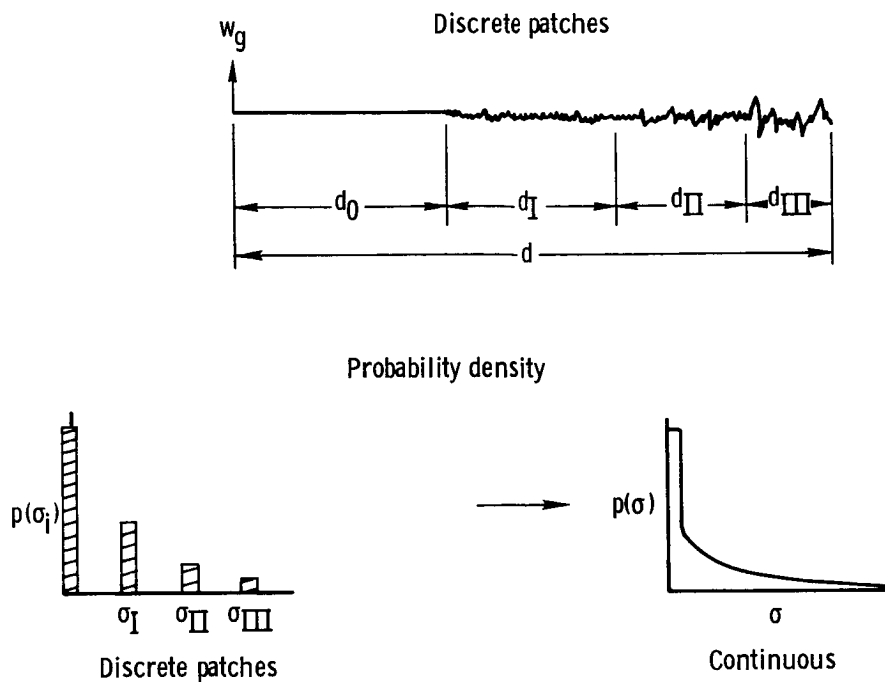


Figure 36.- Synthesis by patches.

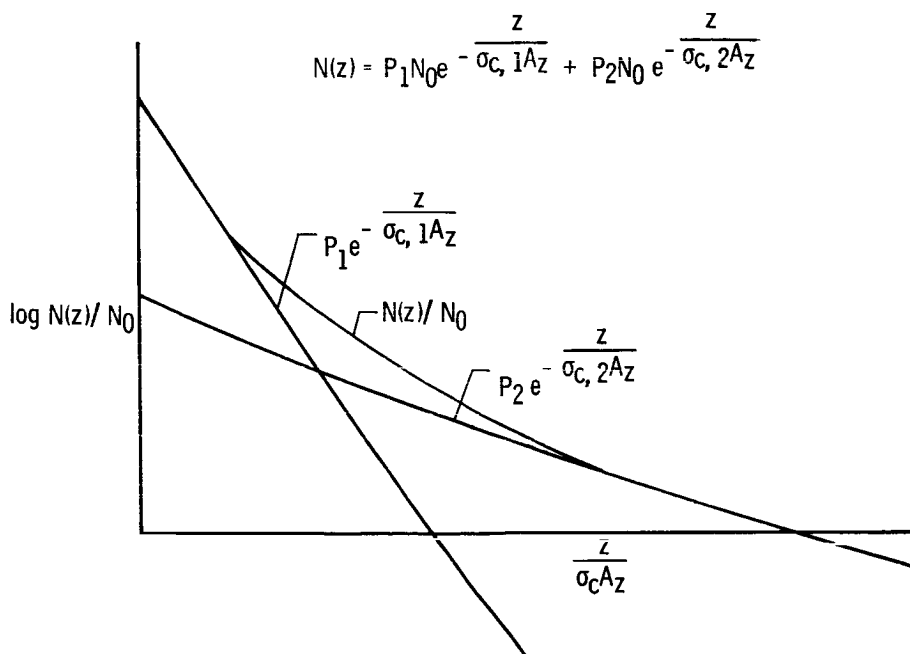


Figure 37.- Graphical illustration of  $N(z)$  at any given altitude.



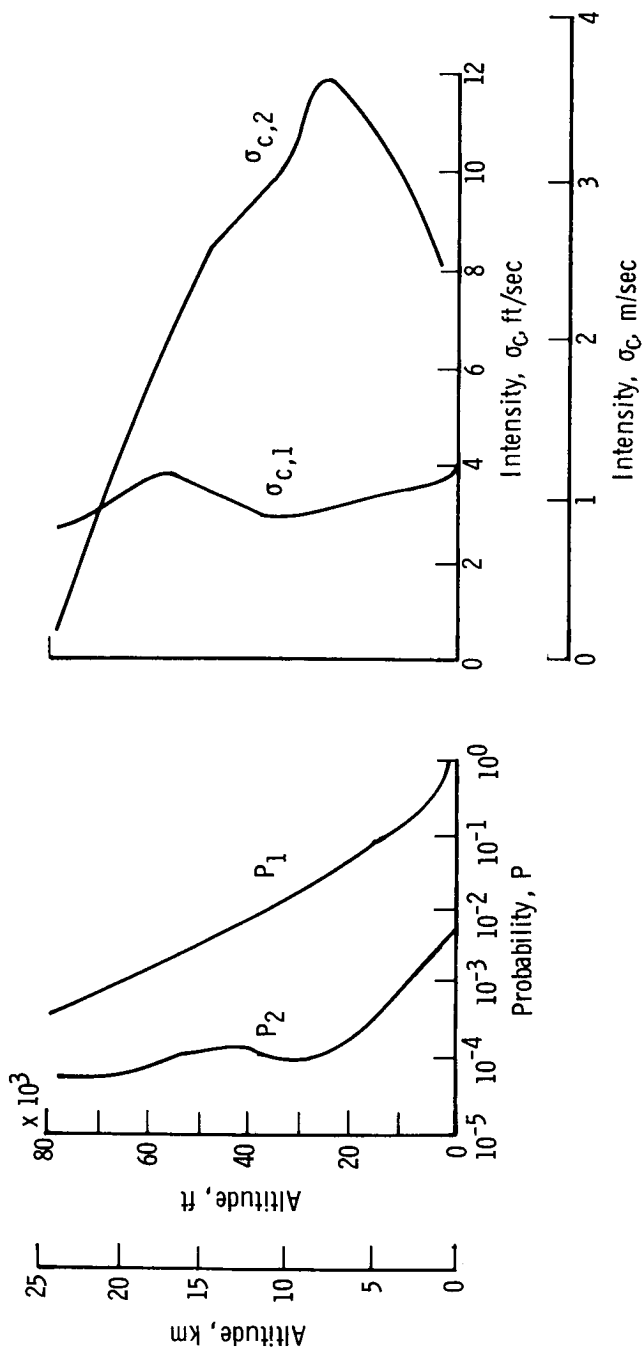


Figure 38.- Variations of probabilities and intensities with altitude.

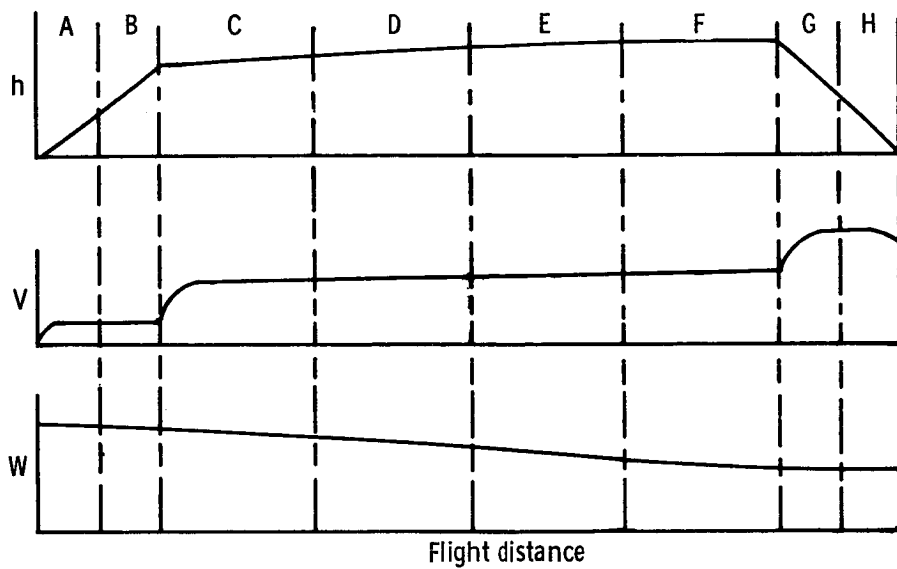


Figure 39.- Representative flight profile.

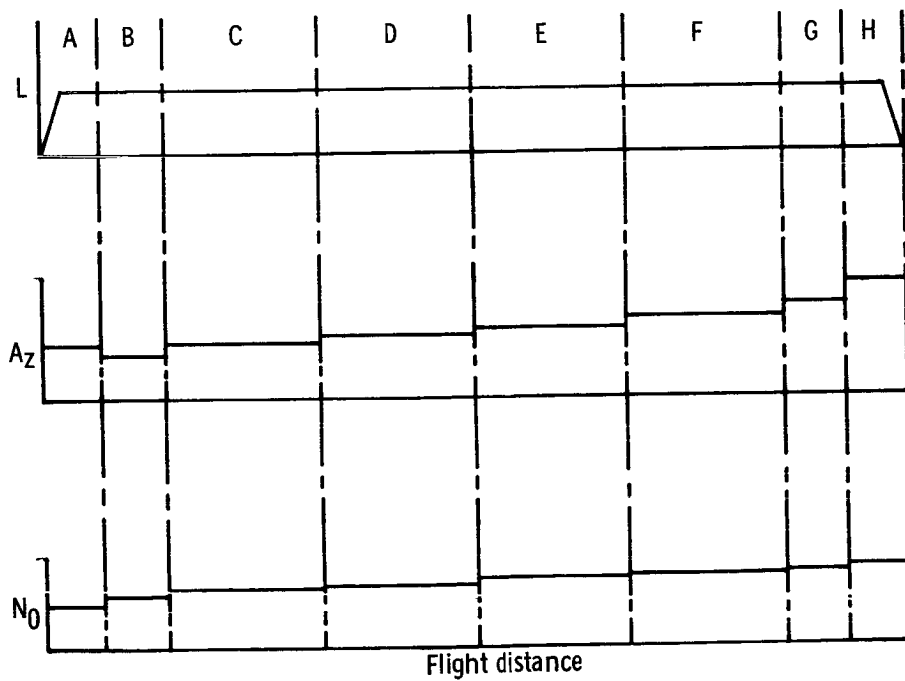


Figure 40.- Example of variations of  $L$ ,  $A_z$ , and  $N_0$  as determined in mission analysis for each stage of flight.

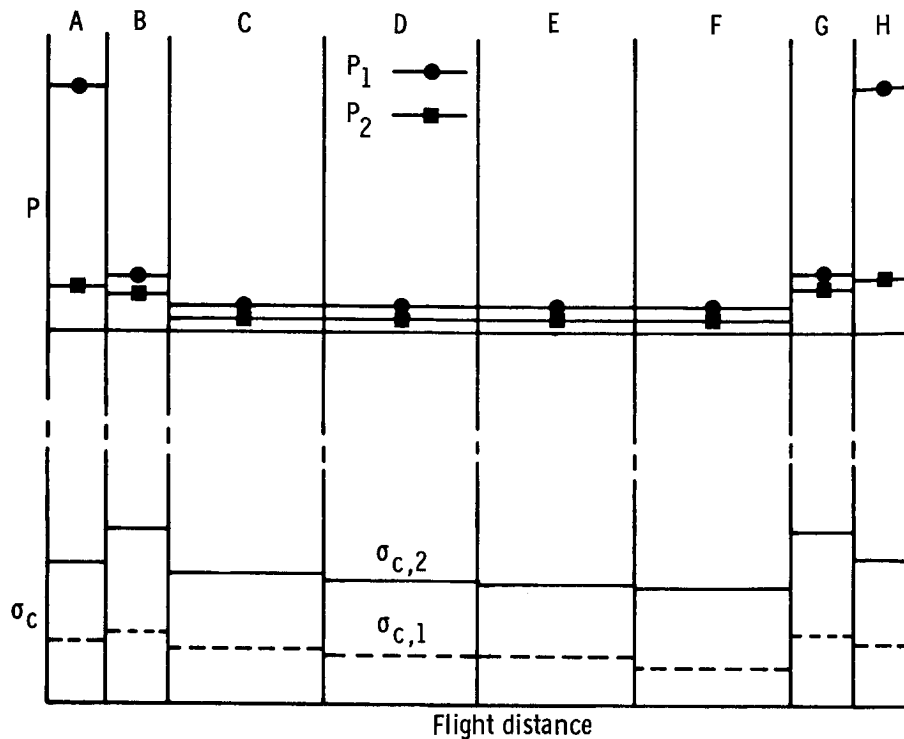


Figure 41.- Example of variations of  $P_1$ ,  $P_2$ ,  $\sigma_{c,1}$ , and  $\sigma_{c,2}$  as determined in mission analysis for each stage of flight.

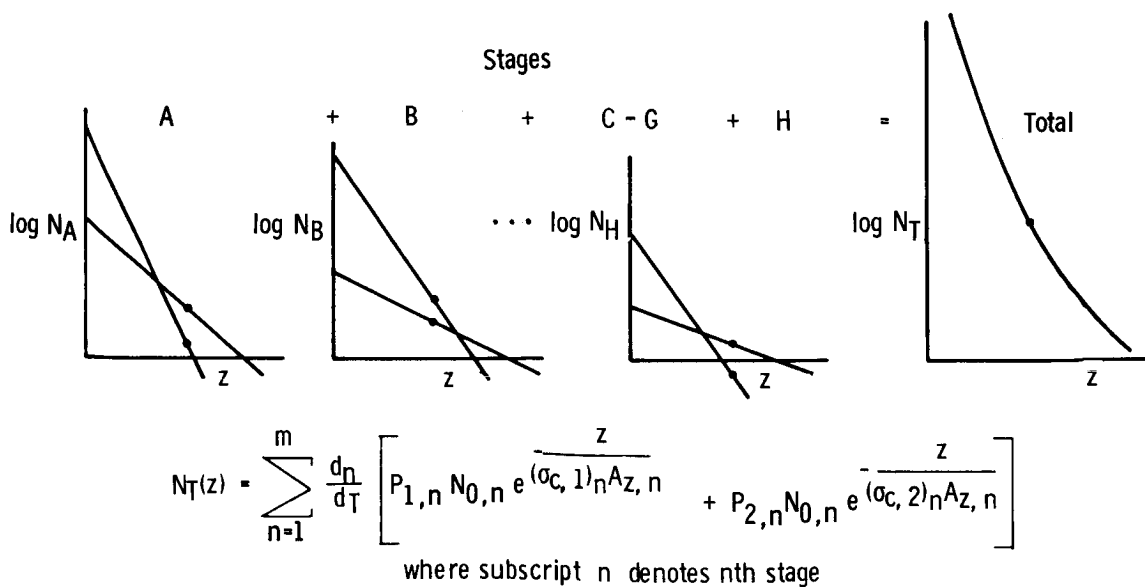


Figure 42.- Illustration of final step in mission analysis.

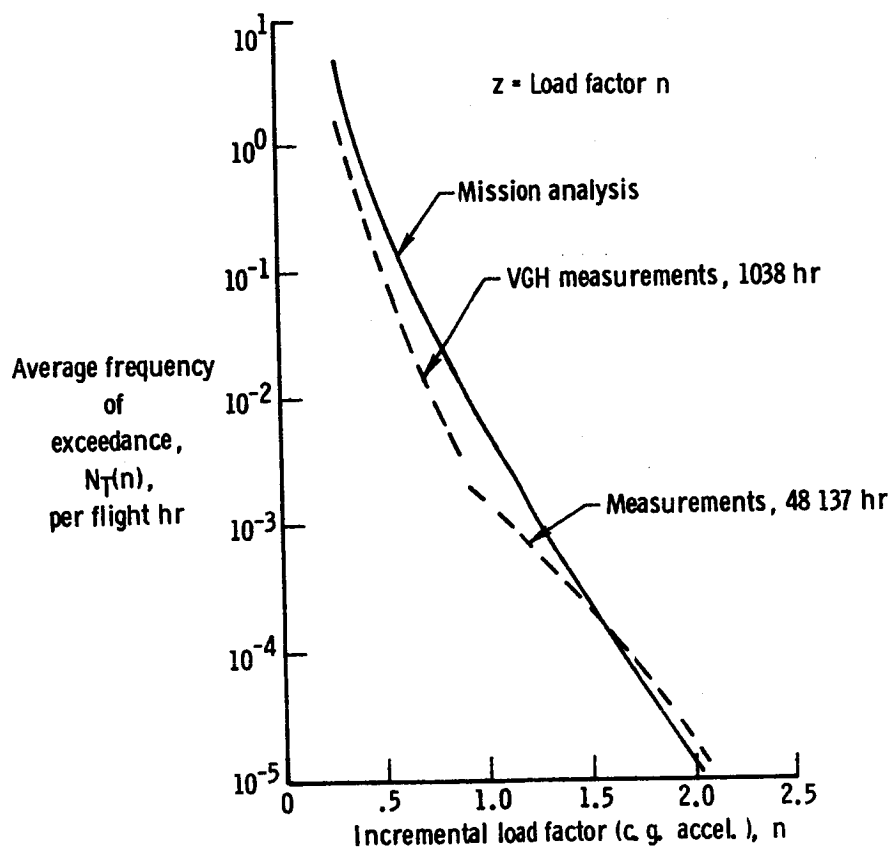


Figure 43.- Verification of calculated  $N_T(z)$ .



## 8. GUST ALLEVIATION

By William H. Phillips  
Langley Research Center

### ABSTRACT

A discussion is presented of the response of an airplane to turbulence, including techniques for the alleviation of lateral and longitudinal motions. A simplified theoretical treatment of the longitudinal response to vertical gusts, which allows calculation of the effects of various types of gust-alleviation systems, is presented. Flight experiments on various gust-alleviation systems are reviewed. A brief discussion is given of the application of these systems to different types of airplanes. Finally, methods of refinement of the simplified theory to include effects of horizontal gusts, unsteady lift effects, and isotropic turbulence are described.

### INTRODUCTION

The subject of gust alleviation has been a matter of concern to aeronautical engineers since the earliest days of aviation. Gusts are responsible for some of the more severe loading conditions on an airplane, and these conditions are usually the critical design conditions on transport or bomber types which are not intended for violent maneuvering. Also, many people are susceptible to airsickness during flight through rough air.

In recent years, with the trend in airplane design toward long, slender fuselages and thinner wings, structural oscillations have become a serious problem. These oscillations may cause fatigue of the structure and may even incapacitate the pilot, thereby causing loss of control. The adverse effects caused by gusts include the loads and stresses caused by a single extreme load and the fatigue damage caused by repeated loads. They also involve motions and deformations of the airplane which may cause upsets and loss of control and physiological effects resulting in deterioration of crew performance and passenger discomfort.

Despite the serious nature of gust-response problems, attempts to alleviate the effects of gusts have been rather rare in the past. Even at present, none of our existing commercial airplanes include any provisions for gust alleviation. The slow progress in this area may be attributed to the fact that many serious problems exist in the design of such systems. Techniques for analyzing such problems have in some cases been developed fairly recently. These techniques include random process theory and computerized techniques for calculating the dynamic response of systems with many degrees of freedom. Also, electronic devices and servomechanisms of the required reliability for use

in the primary flight control systems of airplanes are just now becoming available. The subject of gust alleviation is quite appropriate to illustrate how some of the more advanced analytical and computing techniques can help solve problems which have not been handled adequately in the past.

Some of the lack of interest in practical gust-alleviation systems may be attributed to the trend to flight at higher altitudes and the improved techniques for avoidance of bad weather made possible by turbojet power plants and weather radar systems.

In the design of recently proposed military airplanes, however, particularly those intended for high-speed flight at low altitudes where gust disturbances may be expected to be most severe, a great deal of effort has been put into the analysis of systems to alleviate these effects.

In the commercial airplane field, the probable future development of V/STOL types and the expansion of short-haul service may revive interest in gust alleviation for subsonic airplanes. Current interest in these problems is expected to lead to the eventual development of practical gust-alleviation systems for use on both military and commercial airplanes.

In this paper on gust alleviation, the nature of the disturbances caused by flight through turbulence is reviewed. A theoretical analysis is presented of the longitudinal response of a rigid airplane and of the effectiveness of various types of controls in reducing the response. Experimental studies of several types of gust-alleviation systems are recounted. Finally, a brief introduction to analytical techniques for the calculation of response of airplanes to a two-dimensional random turbulence field is given.

## SYMBOLS

b	wing span
c	mean aerodynamic chord of wing
$C_m$	pitching-moment coefficient, $\frac{M}{\frac{1}{2}\rho V^2 S c}$
$C_z$	vertical-force coefficient, $\frac{Z}{\frac{1}{2}\rho V^2 S}$
D	differential operator, $\frac{d}{ds}$

d	increment of distance along longitudinal axis
g	acceleration of gravity, 9.81 meters per second <sup>2</sup>
$k_y$	radius of gyration of airplane about Y-axis
$K_y$	nondimensional radius-of-gyration factor, $\frac{k_y}{c}$
K	ratio between flap deflection and quantity measured by gust detector with elevator fixed
L	lift
$L^*$	longitudinal integral scale of turbulence (see ref. 22)
$l$	ratio of tail length to mean aerodynamic chord of wing
$l_n$	ratio of distance between angle-of-attack vane and center of gravity to mean aerodynamic chord of wing
m	mass of airplane
M	pitching moment (positive nose-up)
n	normal acceleration
q	pitching velocity, $\dot{\theta}$
s	distance measured in chords, $\frac{tV}{c}$
S	wing area
t	time
$u_g$	horizontal velocity of gust (positive rearward)
V	velocity of center of gravity of airplane with respect to still air



$w$	velocity along Z-axis
$w_g$	vertical velocity of gust (positive upward)
$\overline{w}_g^2$	mean square value of vertical gust velocity
$x$	distance along longitudinal axis
$y$	distance along lateral axis
$Z$	vertical force (positive downward)
$\alpha$	angle of attack
$\alpha_g$	angle of attack due to gust, $\frac{w_g}{V}$ (see fig. 5)
$\alpha_0$	angle between X-axis and velocity vector $V$ (see fig. 5)
$\alpha_w$	angle of attack of wing
$\gamma(y)$	function expressing spanwise distribution of lift due to uniform angle of attack
$\delta_e$	elevator deflection
$\delta_f$	flap deflection
$\delta_v$	deflection of angle-of-attack vane
$\epsilon$	downwash angle at tail
$\theta$	angle of pitch relative to horizontal (see fig. 5)
$\mu$	relative-density factor, $\frac{m}{\rho S c}$
$\xi$	distance
$\rho$	air density

$\tau$	nondimensional time lag of servomechanism, expressed in chords traveled
$\phi_n$	power spectrum of normal acceleration
$\phi_{w_e}$	power spectrum of effective vertical gust velocity
$\phi_{w_g}$	power spectrum of vertical gust
$\psi$	correlation function
$\omega$	frequency
$\omega_n$	natural frequency of system

#### Subscripts:

e	elevator
H	due to horizontal gust
t	tail
V	due to vertical gust
w	wing

A dot over a quantity indicates differentiation with respect to time.

Stability derivatives are indicated by subscript notation; for example,  $C_{Z_\alpha} = \frac{dC_Z}{d\alpha}$ .

Rotary derivatives are defined as indicated by the following examples:

$$C_{Z_q} = \frac{\partial C_Z}{\partial \left( \frac{qc}{2V} \right)} \quad C_{Z_{D\dot{\delta}_f}} = \frac{\partial C_Z}{\partial \left( \frac{\dot{\delta}_f c}{2V} \right)} \quad C_{Z_{D^2\alpha}} = \frac{\partial C_Z}{\partial \left( \frac{\ddot{\alpha} c^2}{4V^2} \right)}$$

$$C_{Z_{Dq}} = \frac{\partial C_Z}{\partial \left( \frac{\dot{q} c^2}{4V^2} \right)} \quad C_{Z_{D\alpha}} = \frac{\partial C_Z}{\partial \left( \frac{\dot{\alpha} c}{2V} \right)}$$

A subscript following a stability derivative indicates component of airplane which contributes the derivative; for example,

$(C_{m\delta_f})_w$  variation of pitching-moment coefficient with flap deflection contributed by wing

$(C_{Z\delta_e})_t$  variation of vertical-force coefficient with elevator deflection contributed by tail

## NATURE AND EFFECTS OF RESPONSE TO TURBULENCE

In order to determine the most effective means of providing smooth flight, it is helpful to examine the motion of a typical airplane in rough air. A typical record of the accelerations and angular motions of an airplane in flight through rough air is shown in figure 1. This figure shows that the airplane is disturbed about all axes. The disturbance shown is for a particular magnitude of turbulence, but the relative amplitudes of the various quantities plotted would tend to remain the same for various intensities of turbulence. This figure shows that the quantity of most concern is the normal acceleration, inasmuch as the values reached (1.7g and -0.5g) are a relatively large percentage of the design limit load factors (typically for a transport airplane, 2.5g and -1.0g) and are also large enough to disturb passengers because of the physiological sensation of changes in body weight. The lateral acceleration is relatively much smaller. Corresponding angular displacements are only a few degrees and are comparable to those experienced in other modes of travel. Nevertheless, these angular motions may be a factor in inducing motion sickness because of the sensitivity of the inner ear to angular motions. The data of figure 1 also show that the motion is of an irregular oscillatory nature. This characteristic is of importance in determining the analytical technique required for study of the motion.

Little information is available as to the relative importance of various factors which might contribute to airsickness. Some research on this subject was conducted during World War II at Wesleyan University. In these tests a large number of men were subjected to vertical oscillations in a device similar to an elevator. Some of the results obtained in these tests are shown in figure 2. This figure shows the percentage of men who became sick within a period of 20 minutes when they were subjected to oscillations of various periods. These data appear to indicate that oscillations of 3- to 4-second periods are more likely to cause airsickness than oscillations of 1- to 2-second periods. In the design of a device to improve passenger comfort, therefore, it may not be necessary to emphasize the reduction of response to gusts of very short periods. Higher frequency disturbances, however, in the range from 1 to 10 cycles per second, may be

serious from the standpoint of structural fatigue and, if they are of sufficient amplitude, may interfere with the pilot's vision or control coordination because of resonant response of parts of the body.

## TECHNIQUES FOR LATERAL AND LONGITUDINAL GUST ALLEVIATION

Calculation of the response of airplanes is ordinarily simplified by separation of the complete equations of motion into a symmetric group (longitudinal motion) and an asymmetric group (lateral motion). (See ref. 1, ch. 4.) In flight through turbulence, as shown in figure 1, both longitudinal and lateral motions are excited simultaneously. Nevertheless, the justification for separation of the analysis of longitudinal and lateral motions remains valid provided the disturbed motions are sufficiently small to apply the usual assumptions of linearity.

### Lateral Motion

As shown previously in figure 1, the lateral acceleration experienced in flight through turbulence is much smaller than the normal acceleration. This difference results from the fact that the side force due to sideslip of a conventional airplane is ordinarily only about 10 percent of the normal force due to change in angle of attack. For this reason, the major emphasis in suppressing lateral response is placed on the elimination of angular motions in roll and yaw. These motions can be sensed by rate or displacement gyroscopes and controlled by the existing aileron and rudder control surfaces. Devices known as yaw dampers or stability augmentation systems provide this function on many existing airplanes. Existing autopilots on commercial airliners incorporate these features.

The lateral motions of an airplane in turbulence may be calculated by estimating the disturbing forces and moments (yawing moment, rolling moment, and side force) due to passage through random turbulence and applying them as forcing functions to the classical lateral-stability equations. Procedures for making these calculations are given in reference 2. The design of stability augmentation systems to suppress the angular motions is a problem in regulator theory which may be handled by techniques described in books on servomechanisms, as for example, reference 3. Because conventional techniques are capable of providing satisfactory systems for alleviating the lateral motions, these techniques are not discussed further herein.

### Longitudinal Motion

The longitudinal motion of an airplane in turbulence consists of changes in both pitch angle and normal acceleration. The use of the elevator control to reduce angular motions in pitch, however, does not eliminate the vertical accelerations, which result from the

direct effect of lift changes caused by variations in vertical gust velocity. In fact, maintaining the airplane at a constant angle of pitch increases the acceleration caused by low-frequency gusts because a stable airplane tends to relieve changes in acceleration by pitching into the gusts. In order to avoid the vertical accelerations due to rough air, the additional lift caused by a change in angle of attack from the steady flight condition must be eliminated. The gust disturbance must first be sensed by a suitable instrument; for example, an angle-of-attack vane or an accelerometer. The output of the sensor is then used to operate control surfaces to offset the effect of the gust.

The following methods might be considered to accomplish this result: (a) Pitching the whole airplane by use of the elevators to maintain a constant angle of attack during passage through gusts, (b) variation of wing incidence to maintain a constant angle of attack during passage through gusts, and (c) operation of flaps or other controls to offset the lift increments on the wing. In connection with methods (b) and (c), a problem of longitudinal control arises. Normally, control of the airplane by the elevator is accomplished by changing the angle of attack. If the lift increment due to change in angle of attack is eliminated, the elevators will be ineffective for producing a change in the direction of the flight path. The alleviation system must therefore incorporate means to restore this control capability.

## THEORETICAL ANALYSIS

In the past, many calculations of gust loads on airplanes, as well as analyses of gust-alleviation devices, were made by assuming some type of discrete gust such as a step gust or a ramp gust. In practice, however, as shown in figure 1, the actual gust variations are of an irregular, oscillatory nature. It is now well known that any such gust variation, either of the continuous or discrete type, may be expressed as the sum of sinusoidal waves or various frequencies and amplitudes. For this reason, the most general type of analysis may be made by calculating the response of the airplane to sinusoidal gusts of various frequencies. The actual distribution of gust amplitudes as a function of frequency which occurs in the atmosphere is known as the gust spectrum, and an analysis which takes into account such a distribution is known as a spectral analysis. In paper no. 7 by Kermit G. Pratt, the techniques for calculating the response of an airplane to turbulence by use of random process theory were described. As an example, the method for obtaining the output power spectrum of normal acceleration as the product of the power spectrum of vertical gusts and the square of the system frequency response is illustrated in figure 3. Some of the experimental results presented subsequently use this form of representation.

In order to obtain the system frequency response required by this technique, the response of the airplane is calculated to sinusoidal gusts of constant amplitude and

various frequencies. This response may be readily calculated from the transfer function relating the response and input variables.

### System Under Consideration

A simplified sketch of the type of vane-controlled acceleration alleviator analyzed herein is shown in figure 4. The servomechanism which operates the flap is assumed to require no force at its input. In practice, electrical signals generated by transducers at the vane and control stick would be applied as inputs to the flap servomechanism. The pilot's control input is fed to the flap as well as to the elevator to avoid the loss of longitudinal control which was stated previously to result if the lift due to change in angle of attack is eliminated.

### Assumptions Made in Analysis

The assumptions made in the analysis described herein are as follows:

- (1) Only longitudinal response is calculated.
- (2) Airspeed is assumed constant.
- (3) Only rigid-body motions of the airplane are included.
- (4) The airplane has a conventional straight-wing configuration, with tail surfaces aft of the wing.
- (5) Only vertical gusts are considered, and these gusts are assumed constant across the span at any instant.
- (6) Unsteady lift effects are not treated in full detail.

These assumptions restrict the scope of the analysis so that some of the aspects of gust alleviation discussed previously, such as structural oscillations, are neglected. The important problem of reducing the vertical accelerations of a conventional, subsonic airplane in cruising flight may, however, be investigated with adequate accuracy by this theory. The effects of relaxing some of these assumptions to allow consideration of a wider scope of problems are discussed subsequently.

### Reference Axes

A fundamental consideration in calculating response of an airplane to gusts is the selection of correct reference frames for the dynamic equations. All inertia forces resulting from acceleration of the airplane must be referred to an inertial coordinate system; that is, one which remains fixed in space. On the other hand, aerodynamic forces result from motion of the airplane with respect to the air mass in its vicinity which, under gusty conditions, is moving with respect to the inertial frame. These

considerations may be taken into account, when considering only vertical gusts, by a diagram such as figure 5. From this figure, certain relations for the angle of attack with respect to the air mass and with respect to the fixed inertial frame, the angle of attack of the wing, and the angle indicated by a free-floating vane mounted on a nose boom are as follows:

$$\alpha_g = \frac{w_g}{V}$$

$$\alpha_o = \frac{w}{V}$$

$$\alpha_w = \alpha_o + \alpha_g$$

$$\delta_v = -\alpha_o - \alpha_g e^{l_n D} + D \theta l_n$$

Similar relations may be derived for the angle of attack at the tail. In setting up the equations of motion, it is convenient to consider the contributions to the lift and moments of the wing and tail separately. In this way, the lag effects between the gust hitting the vane, wing, and tail, as well as lag in downwash, may be accounted for in a logical manner. Such effects are called "penetration effects." These effects should be taken into account for an accurate calculation of the dynamic motions of an airplane penetrating gusts.

#### Derivation of Equations

The derivation of the equations is based on a procedure similar to that used in the classical dynamic stability theory (ref. 1, ch. 4). Inasmuch as this derivation is described in reference 4, it is not repeated in full herein. The procedure used consists, first, in calculating the forces and moments produced by the wing and tail owing to small increments in total angle of attack and pitching velocity. The equations are formed by equating the force to the mass times vertical acceleration, and the moment to the pitching inertia times pitching angular acceleration. Contributions of the rigid-body motion and the gust velocity to the total angle of attack may then be separated, placing the gust-induced terms on the right-hand side of the equations as forcing functions. Finally, following nondimensionalization of the equations, the contributions of the wing and tail to the coefficient of each variable may be collected to obtain expressions for each stability derivative in terms of the wing and tail contributions. If a gust-alleviation system is incorporated into the airplane, effects of flap or elevator deflection resulting from operation of the system may be collected along with the rigid airplane wing and tail

contributions to the derivatives. The gust-alleviation system may therefore be treated by considering it to modify some of the stability derivatives of the basic airplane.

### Lag Effects

Basically, the classical dynamic stability theory depends on the assumption that all the aerodynamic forces and moments may be calculated from a knowledge of the state of the airplane at a given instant. By the state of the airplane is meant the instantaneous values of the variables which define its attitude and motion. For example, if the value of the angle of attack at a given instant is known, the associated pitching moment may be obtained from the derivative  $C_{m_{\dot{\alpha}}}$ . It was shown by Cowley and Glauert in 1921 (ref. 5) that only one aerodynamic lag effect is of sufficient importance to require consideration in calculating the short-period longitudinal motion. This effect is the lag of downwash which causes the appearance of a moment generated by the tail owing to the lift on the wing at a slightly earlier time; this time is that required for the downwash to travel from the wing to the tail. Cowley and Glauert showed how this effect could be approximated in the equations by introducing a moment proportional to the rate of change of angle of attack  $C_{m_{\dot{\alpha}}}$ . In this way, all the moments may still be calculated from the condition of the airplane at a given instant. This approximation may be shown to be very good provided the time lag involved is short compared to the natural period of the motion under consideration. This assumption is excellent in almost all cases of longitudinal motion inasmuch as the lag corresponds to the time for the airplane to travel one tail length, whereas the period of the short-period longitudinal mode typically corresponds to a distance traveled of from about 10 to 100 or more tail lengths.

In calculating the response of a gust-alleviation system, other lag (and lead) effects are introduced. For example, the gust encounters a vane or other sensor mounted ahead of the nose before it affects the wing. The subsequent effect of the gust on the tail lags the effect on the wing. A servomechanism introduced between the vane and the flap causes lag in the flap response. Rigorous treatment of these effects would introduce a great deal of complication in the equations. For example, including a constant time lead for encounter of the gust with the vane ahead of the wing changes the conventional differential equations into differential-difference equations, which have an infinite number of roots. Representation of the flap servomechanism by its complete equations of motion or transfer function would increase the order of the system of equations. These lag and lead effects, however, are all of the same order of magnitude as the lag of downwash for which the simple approximation introduced by Cowley and Glauert has been shown to be adequate. Therefore, the approximation of all of these lag effects as contributions to derivatives depending on the rate of change of the variables involved should be sufficiently accurate. In this way the gust-alleviation system may be analyzed without increasing the order of the basic airplane equations, and the physical effects of various design features



of the system may be seen by examining their contributions to the basic airplane stability derivatives.

### Effect of System on Stability Derivatives

Though the complete derivation of these equations is not presented herein, the final equations in nondimensional form are

$$\begin{aligned} 2\mu D(\alpha_0 - \theta) - \alpha_0 C_{Z\alpha} - \frac{1}{2} D\alpha_0 C_{Z_{D\alpha}} - \frac{1}{2} D\theta C_{Z_q} - \delta_f C_{Z_{\delta_f}} - \frac{1}{2} D\delta_f C_{Z_{D\delta_f}} \\ = \delta_e C_{Z_{\delta_e}} + \alpha_g C_{Z\alpha} + \frac{1}{2} D\alpha_g (C_{Z_{D\alpha}} - C_{Z_q}) \end{aligned}$$

$$\begin{aligned} 2\mu K_y^2 D^2 \theta - \alpha_0 C_{m\alpha} - \frac{1}{2} D\alpha_0 C_{m_{D\alpha}} - \frac{1}{2} D\theta C_{m_q} - \delta_f C_{m_{\delta_f}} - \frac{1}{2} D\delta_f C_{m_{D\delta_f}} \\ = \delta_e C_{m_{\delta_e}} + \alpha_g C_{m\alpha} + \frac{1}{2} D\alpha_g (C_{m_{D\alpha}} - C_{m_q}) \end{aligned}$$

The values of the derivatives in terms of the contributions of the tail and wing-fuselage combination are

$$C_{Z\alpha} = C_{Z_{\alpha_w}} + \left(1 - \frac{\partial \epsilon}{\partial \alpha}\right) C_{Z_{\alpha_t}}$$

$$C_{m\alpha} = C_{m_{\alpha_w}} + \left(1 - \frac{\partial \epsilon}{\partial \alpha}\right) C_{m_{\alpha_t}}$$

$$C_{Z_{D\alpha}} = 2l \frac{\partial \epsilon}{\partial \alpha} C_{Z_{\alpha_t}}$$

$$C_{m_{D\alpha}} = 2l \frac{\partial \epsilon}{\partial \alpha} C_{m_{\alpha_t}}$$

$$C_{Z_q} = 2l C_{Z_{\alpha_t}}$$

$$C_{m_q} = 2l C_{m_{\alpha_t}}$$

$$C_{Z_{\delta_f}} = (C_{Z_{\delta_f}})_w - \frac{\partial \epsilon}{\partial \delta_f} C_{Z_{\alpha_t}}$$

$$C_{m_{\delta_f}} = (C_{m_{\delta_f}})_w - \frac{\partial \epsilon}{\partial \alpha} C_{m_{\alpha_t}}$$

$$C_{Z_{D\delta_f}} = 2l \frac{\partial \epsilon}{\partial \delta_f} C_{Z_{\alpha_t}}$$

$$C_{m_{D\delta_f}} = 2l \frac{\partial \epsilon}{\partial \delta_f} C_{m_{\alpha_t}}$$

These equations refer to the basic airplane. The gust inputs appear as forcing terms on the right-hand side of the equations. The terms on the right-hand side involving the rotary derivatives  $C_{Z_{D\alpha}}$ ,  $C_{Z_q}$ , and so forth result from the penetration effects referred to previously.

A similar set of equations results when the action of a gust-alleviation system such as that shown in figure 4 is considered. The effect of the alleviation system may be considered simply to change the derivatives of the basic airplane. Expressions for these changed derivatives are rather lengthy but two of them are given as examples. First, make the following substitution for the flap deflection in the preceding equations:

$$\delta_f = K\delta_v e^{-\tau D}$$

The expressions for the derivatives then become

$$C_{Z\alpha} = C_{Z\alpha_w} + C_{Z\alpha_t} \left( 1 - \frac{\partial \epsilon}{\partial \alpha} + K \frac{\partial \epsilon}{\partial \delta_f} \right) - (C_{Z\delta_f})_w K$$

$$C_{ZD\alpha} = -2C_{Z\alpha_t} \left[ -l \frac{\partial \epsilon}{\partial \alpha} + K \frac{\partial \epsilon}{\partial \delta_f} (\tau + l) \right] + 2(C_{Z\delta_f})_w \tau K$$

Values of pitching-moment derivatives  $C_{m\alpha}$  and  $C_{mD\alpha}$  may be obtained by substituting  $C_m$  for  $C_Z$  in the preceding expression. These expressions make it clear that the system provides a powerful capability to modify the derivatives. By adjusting the gain constant  $K$ , the ratio of flap deflection to vane deflection, the effective lift-curve slope of the airplane  $C_{Z\alpha}$  may be reduced to zero. Similarly, the static stability  $C_{m\alpha}$  may be varied widely in either the stable or unstable direction, depending on the values of  $C_{m\delta_f}$  and  $\partial \epsilon / \partial \delta_f$ . If the flaps move up to counteract an upward gust and the resulting pitching moment due to the flaps is positive, the flaps will add an unstable increment to  $C_{m\alpha}$ . Neglect of these very powerful effects of a gust-alleviation system on airplane stability has been responsible for some of the disappointing results obtained in some of the experimental systems which have been tried.

#### Calculated Effects of Different Control Surfaces

In order to give a general idea of the effects of different types of gust-alleviation systems, some calculated results are now presented. For comparison with results to be presented subsequently, figure 6 shows the response of the basic airplane to sinusoidal gusts of various frequencies. These and subsequent calculations in this section have been made for an airplane similar to the Douglas DC-3 flying at 200 miles per hour (89.4 meters per second). The curves of figure 6 show that at very low frequencies the acceleration is reduced because the airplane, as a result of its static stability, tends to maintain a constant angle of attack with respect to the airstream. The curves approach a constant value at the higher frequencies plotted. This constant value results from the neglect of unsteady lift effects, structural oscillations, and the random variations of gust

velocity across the span. If these factors were taken into account, the response would be expected to reach the constant value shown (nearly equal to the acceleration caused by a steady angle-of-attack change equal to the gust amplitude) over some intermediate range of frequencies. Narrow peaks corresponding to excited structural modes might appear in the curve at higher frequencies, and the curves would eventually approach zero with increasing frequency because of unsteady lift effects and because of the reduction of average angle of attack due to random gust variations across the span.

### Elevators

In order to study the possibilities of different systems of acceleration alleviation, it is helpful to consider the control motions that would be required theoretically to produce zero acceleration of the center of gravity during flight through gusts. Elimination of the vertical accelerations does not necessarily avoid pitching of the airplane. Therefore, pitching motions occurring with the different methods of control are also of interest.

Figure 7 shows the elevator motion required to produce zero acceleration of the center of gravity in flight through gusts of various frequencies and the resulting pitching velocities. The elevator motion required increases almost linearly with frequency and reaches very large values at high frequencies. In addition, it is found that the phase angle of the elevator motion, not shown in the figure, must lead the angle-of-attack variation due to the gust by amounts increasing from  $90^\circ$  at low frequencies to  $160^\circ$  at high frequencies. Such large phase leads are difficult to obtain in practice and indicate the reason for the inability of a human pilot to counteract successfully the effects of gusts. The pitching velocities shown in figure 7 also reach very high values compared to those of the basic airplane. These high values of pitching velocity result from the fact that with elevator control it is necessary to rotate the whole airplane to maintain a constant angle of attack during passage through the gusts. These large pitching velocities are undesirable because of the changes in vertical acceleration which they cause at points some distance from the center of gravity. For example, in this case the vertical acceleration at a point 2 chord lengths from the center of gravity would be greater than that of the basic airplane with no acceleration alleviator at frequencies greater than 2 cycles per second. The use of elevator control, therefore, does not appear very promising as a means for producing smooth flight.

### Trailing-Edge Flaps on Wing

It might be thought that operation of the flaps to offset the lift increment due to gusts would overcome these objections because the flaps can produce lift increments without the necessity of rotating the entire airplane. Figure 8 shows the flap motion required to produce zero acceleration of the center of gravity and the resulting pitching velocity. For

these calculations it was assumed that the landing flaps were used as the acceleration-alleviation device. These results show that the pitching motions produced by the use of the flaps are even larger than those produced by the elevator. These large pitching motions result mainly from the action of the downwash from the flaps on the tail. This downwash acts in the same direction as the gusts and therefore produces large pitching motions of the airplane. Furthermore, in certain frequency ranges the phase relationship of these pitching motions is such that the angle-of-attack change of the airplane adds to that of the gusts and as a result still more flap deflection is required to offset the acceleration increments. These results indicate that the use of conventional trailing-edge flaps as an acceleration-alleviation device is not likely to prove successful.

The theory worked out previously may be used to show what flap characteristics would be required to eliminate accelerations and pitching motions of the airplane without use of the elevator. Consider again the airplane approaching a small gust disturbance. When the flap moves up to offset the gust, the pitching moment produced by the flap about the wing quarter-chord point should be zero. Then, when the tail penetrates the gusts, the downwash due to flap deflection combined with the downwash due to the wing lift should just offset the gust velocity at the tail. These characteristics are not obtainable with ordinary flap designs since the flap ordinarily produces a pitching moment about the wing quarter-chord point and produces downwash in the opposite direction from that required to offset the effect of the gust at the tail. The desired characteristics might be obtained, however, by some modifications to the usual flap design. The flap pitching moment could be reduced to zero by linking the flap directly to the elevator (or to a portion of the elevator). The reversed direction of downwash due to flap deflection might possibly be obtained by linking a small portion of the flap near the fuselage to deflect in the opposite direction from the main portion of the flap farther outboard.

Practical considerations may limit the alleviation produced by this system to something less than the complete elimination of airplane response, because complete alleviation effectively reduces the variation of pitching moment with angle of attack, or longitudinal stability, to zero. It is necessary to preserve some longitudinal stability so as to obtain desirable control characteristics. A considerable amount of acceleration alleviation may, however, be provided while maintaining satisfactory control characteristics. For example, figure 9 shows the response of an airplane to sinusoidal gusts when it is equipped with a vane-type acceleration alleviator. Characteristics have been adjusted to provide a stable value of  $C_{m\alpha}$ . The normal accelerations at all frequencies are reduced to about one-fifth of those for the basic airplane, while the pitching velocities remain low.

## Flaps and Elevators in Conjunction

Another possibility which might be considered is the use of the flaps and elevators in conjunction. By the use of these two controls it is theoretically possible to reduce both the accelerations and pitching motions due to gusts to zero. A physical picture of how this might be accomplished may be obtained as follows: Consider an airplane flying through a small gust disturbance. When the wing reaches the gust, the flaps must be deflected up to produce a lift increment opposing that from the angle of attack. This flap deflection produces a pitching moment which must be offset by an elevator motion. Then, when the airplane has moved to a position where the gust acts on the tail, the elevator must deflect in such a way as to counteract the effects of the gusts and the downwash due to the flap deflection. Since these downwash effects lag behind the flap motion, the elevator motion must also lag behind the flap motion by a phase lag which depends on the gust frequency. A servomechanism might be designed with the desired phase characteristics, but this method appears somewhat complicated. Another possibility is to use a closed-loop pitch control in which pitching disturbances of the airplane, regardless of their source, are sensed by a gyro and the elevator is moved to maintain the pitch angle constant.

### Response to Pilot's Control

As noted previously, the pilot's control in the vane-controlled alleviation system of figure 4 is connected to the flaps as well as the elevators so as to avoid the loss of control capability caused by the operation of the alleviation system.

When the pilot deflects the elevator, the resulting events may be described as follows: First, the flap moves down producing lift in the desired direction. Then, as the airplane rotates in response to the elevator, the angle of attack measured by the vane increases and causes the flaps to move back up to their neutral position. This type of control would therefore be expected to increase the speed of response of the airplane to elevator control motions. Figure 10 shows the response to a step motion of the elevator for the airplane with the vane-type acceleration alleviator as compared to the motion of the basic airplane. The response is seen to be much faster, but there is no tendency to oscillate or overshoot. This type of action has in recent years been termed "direct lift control" and has been found to be advantageous for maneuvers requiring accurate altitude control, such as landing approach.

### Control Characteristics Required for Complete Alleviation

The appropriate combination of flap effectiveness, pitching moments, and downwash characteristics should intuitively result in perfect gust alleviation. This condition occurs when the flap lift just offsets the lift increment on the wing due to the gust, the flap

pitching moment offsets the pitching moment on the wing due to the gust, and the flap downwash, trailing back in the airstream along with the gust, just offsets the gust velocity at the tail. This same conclusion is found directly from the preceding theoretical development. The values of the flap characteristics and gain constants required to satisfy this condition are

$$K = \frac{C_{Z\alpha_w}}{(C_{Z\delta_f})_w}$$

$$\tau = l_n$$

$$(C_{m\delta_f})_w = \frac{C_{m\alpha_w}(C_{Z\delta_f})_w}{C_{Z\alpha_w}}$$

$$\frac{\partial \epsilon}{\partial \delta_f} = \frac{-(C_{Z\delta_f})_w}{C_{Z\alpha_w}} \left( 1 - \frac{\partial \epsilon}{\partial \alpha} \right)$$

By substituting these values in the transfer functions giving the vertical and pitching response of the airplane owing to gust inputs, the numerator terms all go identically to zero. The agreement between intuitive reasoning and the results of the approximate analytical development lend confidence to the belief that the assumptions of the theory are sufficiently accurate for practical calculations, particularly in the case of a system designed to provide a high degree of gust alleviation.

## EXPERIMENTAL RESULTS

Many of the early methods employed in attempts at gust alleviation were devised without adequate analysis by their inventors. As an illustration of such early methods, an airplane built by Waterman about 1930 is shown in figure 11. In this airplane, the wings were attached to the fuselage by skewed hinges. In flight, the lift on the wings was balanced by the force of a pneumatic strut which acted as a spring and allowed the wings to deflect in flight through rough air. A similar effect is obtained automatically with swept-back wings since bending of a sweptback wing under a load reduces the angle of attack of the tips. These methods are seriously limited in their application, however, because they interfere with the provision of adequate lateral control. Deflection of the ailerons deflects the wing in a manner which produces a rolling moment opposing that from the ailerons. As a result, the lateral control effectiveness may be reduced and the reversal speed excessively lowered.

Several serious attempts have been made in the past to develop gust-alleviation systems and test them in flight. These projects are now described briefly and, where possible, comparison to theoretical predictions is made.

### British

In England, shortly after World War II, a large commercial airplane which incorporated a system to alleviate wing bending moments caused by gusts was designed. The ailerons were to deflect symmetrically in response to the output of some type of gust detector so as to reduce the wing loads. The designers hoped thereby to reduce the required weight and strength of the wing. As it turned out, this airplane never went into service, but the proposal stimulated interest in a flight project in which a system of this type was tried in a Lancaster aircraft (refs. 6 and 7). The system utilized a vane as a gust detector to operate the ailerons symmetrically through a hydraulic servomechanism. The system was built with little preliminary analysis, and when the pilot engaged the system for the first time, the flight in rough air seemed appreciably more bumpy than without the system. By reversing the sign of the gain constant relating aileron deflection to vane deflection, the ride was made somewhat smoother.

The explanation of these effects can be seen from the foregoing theory. The ailerons, in deflecting up for an up gust, would relieve the load on the tips as intended, but they would also produce a positive pitching moment, thereby reducing the static stability of the airplane and causing it to nose up more in response to an up gust. Furthermore, the reduced load on the tips gave a spanwise lift distribution which caused increased downwash at the tail, thereby adding to the noseup moment. The system, therefore, reduced the natural tendency of the airplane to nose into the gusts at low frequencies, and thereby increased the acceleration response in this range. As noted previously, the low-frequency accelerations are the ones most uncomfortable to the human occupants. The system actually reduced some of the response at higher frequencies, but at still higher frequencies the system destabilized the wing first symmetrical bending mode at 3 cycles per second. This condition further aggravated the roughness of the ride.

### Tests on C-47 Airplane

A second experimental program was conducted on a C-47 airplane (refs. 8 and 9). The objectives of this program were similar to those of the British experiment. The ailerons were arranged to deflect symmetrically upward with upward wing bending by means of a linkage system which added this component of deflection to that of the conventional aileron linkage. Since the wing deflection provides a large available driving force, no servomechanism was required, and as a result it was hoped that the system would be sufficiently reliable to use on service airplanes. This system suffers from the same objections as the British system. In addition, a further limitation was encountered

because the inertia of the ailerons, combined with the flexibility of the operating linkage, caused the aileron deflection to lag behind the wing deflection. Such a condition is very conducive to flutter. In order to avoid flutter, the gain between aileron deflection and wing bending had to be kept to a relatively low value. The system, with this limitation, was able to reduce the mean wing bending moments by only about 9 percent, and the effect on riding comfort was not noticeable.

## NACA

A third set of flight experiments was conducted by the NACA in the period from about 1952 to 1960. The results of this program may be found in references 10 to 14 which contain a complete discussion of the project. In the present paper, emphasis is placed on pointing out the various considerations, procedures, and analyses that enter into the design and testing of a system of this type.

The airplane used for the tests was a small twin-engine transport. The objective of the tests was to study various systems which had been previously analyzed in the theoretical work and to demonstrate the feasibility of a gust-alleviation system employing wing flaps and other control surfaces operated by a servomechanism.

Vane design.- Provision was made for testing the system with various combinations of the aerodynamic derivatives influencing the response, and with either a vane or accelerometer sensor. A picture of the airplane with the nose boom and vane installation is shown in figure 12. The vane was designed to follow the gust fluctuations as accurately as possible. It was constructed of balsa wood and, with its syncro pickup, was shown by wind-tunnel tests to have a natural frequency of 26 cycles per second and a damping ratio of 0.6 at an airspeed of 220 feet per second (67.06 meters per second). It was realized that the output of a vane measuring the gusts at one point would contain high-frequency fluctuations which, because of their small spatial extent, would probably not affect the entire wing of the airplane. This so-called "spanwise averaging effect" is important in designing a gust-alleviation system for best performance and is discussed more fully subsequently. For these tests, the decision was made to incorporate the necessary filtering of the vane output in the control mechanisms operating the flaps, rather than to incorporate any filtering in the dynamics of the vane itself. In this way, the vane data could also be used to obtain an accurate record of the gust input.

Control surfaces.- A photograph showing the modified control surfaces of the test airplane is shown in figure 13. Provision was made to connect a portion of the elevator to the flap through an adjustable linkage to vary  $(C_{m_{\delta_f}})_w$ . Since this section of the elevator moved in phase with the flap, it could be considered to add directly to the flap pitching moments. Provision was made to vary the downwash due to flap deflection



$\partial \epsilon / \partial \delta_f$  by splitting the trailing-edge flaps into two sections. The small inboard portion could be geared to the outboard section with a ratio between 0 and  $\pm 1.0$ . The outboard section of the landing flaps was connected to the ailerons so that in the alleviation mode the outboard flaps and ailerons moved together symmetrically for gust alleviation and differentially for lateral control. The flaps were redesigned structurally to allow full deflection in either direction at any speed within the capabilities of the test airplane. Landings were made with flaps up for the test program, but in case a practical gust alleviator should be designed, the additional problem of retaining the landing function of the flaps would have to be solved. The inboard portion of the elevator remained connected to the pilot's control stick. The critical requirement for elevator control was getting the tail down for landing with the alleviation system locked. The elevator of reduced area was adequate for this purpose with the center-of-gravity position used in the tests and was also satisfactory for control in flight with the alleviation system in operation.

Control system and safety provisions.- A two-stage electrohydraulic servomechanism was used to operate the flaps. The system operated essentially as shown in figure 4, but the electrical outputs of the vane, control stick, and accelerometer could be combined in any desired proportion as inputs to the servoamplifier. The flap position was proportional to the amplifier input under steady-state conditions.

Lateral control in the alleviation mode was supplied through an additional hydraulic servomechanism with mechanical input. The output of this system deflected the flap system asymmetrically through a mixing linkage.

A problem which must always be considered in installing modified control systems in an existing airplane is that of reversion to the original airplane system in case of any failure. In the system under consideration, the pilot's control wheel remained connected to the basic airplane controls through the original cable system. In the alleviation mode, the airplane was flown from the copilot's side, and the pilot's wheel simply followed the surface movements. In case of any malfunction, a separate hydraulic system was provided which could mechanically clamp the wing flaps in neutral and simultaneously disconnect the controls from the output of the hydraulic servomechanisms. Symmetrical deflection of the ailerons in the alleviation mode was permitted by allowing the hydraulic system to overpower preloaded spring struts in the aileron linkage of the basic airplane control system. These struts had sufficient preload to allow adequate manual control of the ailerons. When this system was being designed, electronic systems had a poor reputation for reliability, and elaborate safety precautions were necessary. With the present reliability and background of experience with electronic components, together with techniques of redundancy, sufficient reliability could probably be provided in a system of this type to avoid the need for these rather complex reversion systems.

Structural feedback considerations.- A complicated problem which requires consideration in the design of any automatic control system is the possibility that control movements will excite structural vibrations which, in turn, will be picked up by the sensors involved in the system and amplified through the servomechanisms to produce an increasing oscillation. Such a condition is often termed "structural feedback," and can lead to dangerous oscillations similar to control-surface flutter. Such a condition is particularly of concern in the case of a gust-alleviation system because the wing flaps produce a powerful aerodynamic force input, comparable in magnitude to that of a severe gust hitting the airplane. With the present state of the art of servomechanism and flutter analysis, an organization with sufficient resources could make a rational analysis of this problem by taking into account the numerous vibration modes of the structure as well as the rigid-body motions of the airplane. Such analyses, in fact, are made routinely for many of our modern airplanes. A frequent objective of such analyses is the design of "modal suppression systems," which serve to damp rather than amplify the structural modes. Some mention of these systems is made subsequently herein.

In the case of the gust-alleviation system under consideration, however, modern digital computing techniques did not exist, and safety could be assured only through conservative design techniques and cautious avoidance of potentially dangerous conditions. As will be seen, this approach placed a penalty on the performance of the system which could probably be avoided with a more complete analysis.

Ground vibration tests.- A rather complete set of ground vibration tests was made on the test airplane to determine the frequencies and mode shapes of the primary structural modes. The lowest natural frequency of the structure was the first wing bending mode at 8.0 cycles per second. Inasmuch as this frequency was considerably above the frequencies which might be suspected of producing motion sickness (see fig. 2), the flap servomechanism was designed to have its response highly attenuated at 8.0 cycles per second so that interaction with the structural mode would be unlikely. This attenuation was also increased by velocity saturation of the servo which would provide still more attenuation at larger input amplitudes. Thus, if any oscillation should start, its amplitude would be limited.

Frequency-response tests.- Rather complete frequency-response tests were also made on the control system. In these tests, a sinusoidal voltage simulating output of the vane synchro was applied to the servoamplifier. The resulting motion of the flaps, which were spring loaded to simulate the aerodynamic hinge moments acting in flight, was recorded. By combining the results of the ground vibration tests and the servo frequency-response tests, an approximate analysis could be made to determine the possibility of instability caused by structural feedback. For the vane-controlled system, this possibility was found to be remote because wing bending caused very little response of the structure

at the location of the vane. With an accelerometer pickup, however, a more rigorous analysis would be required to draw any definite conclusions. The acceleration at any point undergoing structural vibration increases as the amplitude and as the square of the frequency. For this reason, higher frequency modes which may appear to have small amplitude can result in a large accelerometer output. In conducting flight tests with the accelerometer-controlled system, the gain of the accelerometer signal was gradually increased from zero while the pilot applied pulse input disturbances to the flap system. The gain was then limited to a value which gave a well-damped response.

Measurement of aerodynamic parameters.- In order to calculate linkage ratios and gain settings to be used in the flight tests, rather complete aerodynamic data on the airplane were required. These data may be obtained most accurately by using a combination of flight tests and analytical procedures. In the case of the airplane under consideration, values of the derivatives  $C_{Z\alpha}$ ,  $C_{m\alpha}$ , and the sum of the damping derivatives  $C_{m\dot{q}} + C_{mD\dot{\alpha}}$  could be obtained by analyzing the records from abrupt pull-ups produced by step or pulse inputs to the elevator. The value of  $\partial\epsilon/\partial\alpha$  was obtained from available empirical data based on wind-tunnel measurements. A knowledge of this value allows separation of the values of  $C_{m\dot{q}}$  and  $C_{mD\dot{\alpha}}$ . In a similar manner, values of the flap lift and moment derivatives were obtained by applying step inputs to the full-span flap through the gust-alleviation servo. Again, estimates had to be made of the downwash due to the flaps  $\partial\epsilon/\delta_f$  and of the effects on downwash of the inboard flap gearing.

Method of flight testing.- Flight testing of a gust-alleviation system is difficult because the characteristics of the gust input are not under the control of the experimenter. If an isolated, reproducible gust could be found, the problem of flight testing would be simplified. Unfortunately, the atmospheric turbulence is of a random nature and stretches of continuous turbulence are rare, particularly in favorable weather conditions. In a conventional airplane, the pilot can give a subjective judgment of the severity of turbulence by noting the magnitude of accelerations experienced, but in testing a gust-alleviation system a smoother ride might result either from an effective system or a decrease in the intensity of turbulence. For these reasons, measurements of the turbulence input as well as the airplane response must be made. Vertical gust velocity is measured from the indications of an angle-of-attack vane corrected for motions of the airplane as measured by an accelerometer and pitching-velocity recorder.

Spectral-analysis techniques.- Because of the random nature of the turbulence, power-spectral analysis of the data is required. By this technique a time history of a randomly varying quantity, such as vertical gust velocity, is converted into a plot showing the square of the amplitude of each sinusoidal component of the quantity over a small range of frequencies against the frequency. In order to obtain an accurate power spectrum, the sample length should be about 20 times the wavelength of the lowest frequency

component being studied. Furthermore, the process is assumed to be stationary over this entire period; that is, the process producing the turbulence is assumed to remain constant over the sample period. Unfortunately, atmospheric turbulence is rarely a stationary process, and patches of smooth air or turbulence of different magnitudes are encountered at frequent intervals. As a result, power-spectral analysis rarely yields results having the degree of accuracy of more conventional flight measurements.

At the time the flight tests of the gust-alleviation system were started, power spectra were obtained by using an analog device which required transferring the flight data to magnetic tape and then running the tape as a continuous loop through a series of tuned filters to determine the frequency content. Later in the test program, digital computation techniques were used, though the computer time required for these analyses was quite long. More recently, improved methods of spectral analysis, sometimes called FFA (fast Fourier analysis), and higher speed digital computers make the determination of spectra considerably faster.

Characteristics of atmospheric turbulence.- A few typical results from the flight program are now shown. The power spectrum of atmospheric turbulence, as indicated by the gust angle of attack, is shown for two runs in figure 14. Typically, power spectra are plotted on log-log paper to allow coverage of a wide range of the variables under consideration and of frequency. The quantity of the ordinate scale, in this case degree<sup>2</sup>/cycle per second, is squared because the definition of power spectrum, which had its origin in the measurement of the resistive power loss of electric current in a resistor ( $I^2R$ ), requires that the square of the magnitude of the harmonic content be plotted. From the engineer's viewpoint, the log-log paper tends to mask differences between different spectra, whereas the squaring of the ordinate tends to exaggerate them. Thus, care is required in evaluating the true physical significance of quantities plotted in this way.

The data for the basic airplane cover a range of frequencies from 0.05 to 10 cycles per second, which at the test airspeed of 220 feet per second (67.06 meters per second), corresponds to a range of gust wavelengths of from about 4400 feet (1341.12 meters) down to 22 feet (6.71 meters). Over this entire range the power spectrum shows a negative slope of about -2. This value is typical of the spectrum of atmospheric turbulence. According to the theory of isotropic turbulence, the slope should be -5/3, but the accuracy of spectral determinations is not good enough to distinguish readily between the two values. The slope of -2 means, physically, that the actual amplitudes of gust velocities vary approximately inversely as their frequencies. This rapid decrease of input amplitude with increasing frequency furnishes another reason why, in the design of a gust-alleviation system, the low frequencies are often important and cannot, in any case, be neglected.

Flight test results.- A comparison of the power spectra for the normal acceleration for the basic airplane and for the airplane with a vane-type gust-alleviation system is

shown in figure 15. Note that these data are for slightly different atmospheric conditions and the results should not be compared directly. Also, the conditions are not those given in figure 14. Two points of interest are apparent, however. First, the alleviation system has little effect at frequencies above about 2 cycles per second. This result may be attributed to the attenuation of the response of the flap servomechanism at high frequencies. Second, the wing bending frequency shows up as a slight peak at 8 cycles per second. Because of the small magnitude of the gust input at this frequency, however, the response is quite small.

In order to compare the responses with the alleviation system on and off, the values of the power spectra of normal acceleration were divided by the values of power spectra of gust angle of attack at corresponding frequencies, and the square root of the result was taken. The result is a plot of the ratio of normal acceleration to gust angle of attack as a function of frequency, similar to that obtained from the frequency-response analysis. This result as well as similar data for pitching velocity are shown in figure 16. In the frequency range of greatest interest for passenger comfort, for example 0.2 to 0.5 cycle per second, the acceleration response was cut to about half that of the basic airplane. For the particular case shown, the pitching-velocity response of the basic airplane was reduced also.

The results shown are typical of those for various cases studied. In general, the trends in the results caused by varying the gearing between flaps and vane, inboard and outboard flaps, or between flaps and auxiliary elevators, were in good agreement with the predictions of the theory. The maximum alleviation obtained, however, was somewhat disappointing inasmuch as the theory indicated that the response could be reduced to a much lower value. The primary reason for this limitation in the effectiveness of the system is believed to be the attenuation of the flap response at high frequencies and, in particular, the velocity saturation characteristic which had been included as a safeguard against flutter. In detailed examination of the time histories of response to turbulence, the flaps could be seen to lag behind the desired motion whenever a particularly large gust input was encountered. The result of this lag was a peak in the acceleration response caused by the failure of the flap to offset the gust completely. In retrospect, it appears that a servomechanism with more nearly linear characteristics and higher frequency response could have been used with safety. The resulting alleviation would have more closely approached the theoretical predictions.

Work of René Hirsch in France. - No résumé of flight experience with gust-alleviation systems would be complete without mentioning the work of a Frenchman, René Hirsch, who has apparently devoted much of his life to this subject. About 1938, Hirsch completed a thesis on analysis and model tests of a gust-alleviating airplane. In this era, when servomechanisms were in an early state of development, Hirsch was forced to rely

on aerodynamic forces to actuate his system. He conceived the idea of using forces on the horizontal tail, which was mounted with freedom of vertical movement, to operate trailing-edge flaps on the wing through a direct mechanical linkage. The use of a surface aft of the wing to detect the gusts might at first seem illogical, but, as has been shown, the long-wavelength gusts are the ones of greatest importance. For these gusts, little difference in phase relationship exists between the flap motion and the gust whether the gust is sensed at the nose or tail of the airplane. The recognition of the importance of long-period disturbances was one area in which Hirsch showed greater insight than most of his contemporaries.

Hirsch also recognized the need to restore pilot control when the lift of the airplane was made insensitive to angle of attack. This ability followed naturally with his setup because, with conventional elevators on the horizontal tail, a rearward stick movement would raise the elevators, putting a down load on the tail, and thereby moving the flaps down. The effect was identical to that obtained in the vane-controlled system discussed previously by feeding a signal from the control stick to the flap servomechanism. Hirsch also showed how to design his system to give approximate compensation of horizontal gusts. As a bonus, as his airplane slowed down, the elevators would be raised and the flaps would automatically go down to their landing position. The same effect could be obtained on the vane-controlled system by spring loading the vane in the downward direction. Hirsch made a remarkably complete analysis of the static characteristics of his system by taking into account the hinge-moment derivatives due to deflection and due to angle of attack of the many movable surfaces on his design. At the time of this analysis, these concepts were quite new. In addition, he made a wind-tunnel test of a dynamic model of his airplane. The model was mounted in the tunnel with freedom to move vertically and was subjected to a gust produced by a venetian-blind arrangement ahead of the model. He showed that the model with surfaces fixed would bang against the top of the tunnel under the influence of the simulated gust, whereas the alleviated model was relatively undisturbed. This type of dynamic model testing of partly restrained models was years ahead of its time and has come into wide use more recently for flutter model testing.

Hirsch's work was apparently interrupted by World War II, but after the war he further demonstrated his concept by constructing a small clean twin-engine airplane which incorporated his system. A photograph of this airplane is shown in figure 17, and a line drawing showing the interior arrangement is shown in figure 18. Reports describing flight tests of the airplane are given in references 15 and 16. The proper operation of this system might be a subject of concern because of the number of hinged, moving, aerodynamically actuated parts. Hirsch used a double-hinged flap to obtain greater lift increments and linearity of hinge moments. This flap was actuated by the horizontal tail, which changed dihedral about chordwise hinges at the root. Not satisfied with alleviating vertical gusts, he also detected rolling gusts by hinging the wing tips

about a chordwise axis and using these surfaces to deflect the flaps asymmetrically. Finally, to restore aerodynamic damping in roll and pitch to the airplane, he incorporated large bellows-type actuators operated by dynamic pressure and controlled by wind-driven rate gyroscopes. Hirsch had such confidence in his system that he designed the airplane to a load factor of 2g, taking advantage of the saving in wing weight to improve performance.

Despite the complex-sounding features of the design, the system was well engineered and the airplane made many successful flights. Tests were made with recording instruments and the results, presented in the form of time histories, show that the degree of gust alleviation attained was very similar to that of the NACA airplane.

## RECENT DEVELOPMENTS

Despite the promising results obtained with two of the gust-alleviation systems described, no practical use of systems to reduce the accelerations associated with the rigid-body response of airplanes has been made. This lack of practical application in modern airplanes probably results from two considerations. First, as airplanes were designed for higher speeds and employed thinner wing sections, the structural frequencies decreased. The problem of providing adequate alleviation in the range of frequencies of interest for passenger comfort without exciting structural modes therefore became more difficult. Second, as jet airplanes flew at higher altitudes, they encountered turbulence less frequently and the problem was therefore less serious. Increased application of low-altitude flying for short-haul service, using STOL-type airplanes with light wing loading may bring about a revival of interest in this form of gust alleviation. At the other end of the speed range, the supersonic transport, because of its slender shape and thin surfaces, requires increased attention to the design of automatic control systems to improve the damping of structural modes of oscillation.

In recent years, the gust-response problems of high-speed military airplanes have received renewed attention. Fighter airplanes flying near sea level at high subsonic speeds, and therefore at high dynamic pressure, can subject the pilot to a very rough ride. The larger military airplanes, both bombers and transports, have suffered from fatigue problems, often as a result of service flying hours far exceeding the original design values. Since the life is largely determined by frequently repeated gust loads of all amplitudes, means have been sought to alleviate these loads. In some of the newer proposed supersonic aircraft designs, the long, slender fuselages have been found to contribute to excessive vibration at the pilot's station.

## Fighter Airplanes

Various methods have been studied and tested to help solve these problems. In the case of the subsonic fighter airplane, the relative density factor is so great that the short-period longitudinal oscillation has a relatively long wavelength, perhaps 1000 to 1500 feet (304.8 to 457.2 meters), where the gust input amplitude is becoming large. If the airplane has poor damping in pitch, resulting in a resonance peak at the short-period frequency, the use of a pitch damper may considerably reduce the response, both in pitch and in normal acceleration. The use of high wing loading and wings with low aspect ratio or high sweep angle to reduce the lift-curve slope may also be beneficial. These techniques can reduce the accelerations to only a certain point, however, before they start to interfere with other desired performance characteristics.

As a general rule, trailing-edge flaps, particularly on the outboard portion of the wing, are unsuitable for providing gust alleviation on a high-speed fighter airplane. At high-dynamic-pressure conditions, such surfaces are usually approaching their reversal speed. Even if they remained effective, they are generally so far aft of the center of gravity that they produce excessive pitching moments. Inboard flaps on a swept wing might avoid this problem, but on a low-aspect-ratio or delta-wing configuration they would still be likely to give excessive pitching moments. As shown previously, such pitching moments must be offset by deflection of the horizontal tail, which would largely offset their effectiveness by producing lift in the opposite direction. Perhaps the most promising method to provide effective gust alleviation on a high-speed fighter airplane would be to deflect the whole wing. A wing deflection of only  $1^\circ$  would, at a speed of 1000 feet per second (304.8 meters per second), be enough to offset the effect of a 17-foot-per-second (5.2-meter-per-second) gust.

The foregoing concept leads to the following arrangement which would appear to offer promise as a gust-alleviation system for a high-speed fighter airplane. A variable-incidence wing, operated through a rapid-response servomechanism in accordance with the output of a vane or similar sensor, would offset the effects of the gusts on the wing. The wing itself would produce small pitching moments about the center of gravity. To offset the gusts and downwash effects at the tail, the use of a highly effective pitch damper operating from a rate gyro would appear preferable to a device which varied the stabilizer incidence, with the appropriate lag, in response to the gust sensor signal. This arrangement would avoid critical dependence of the longitudinal stability on the tail-to-sensor gain constant. A system of this type has not yet, to the writer's knowledge, been analyzed. Any such analysis should, of course, include effects of structural modes which might be excited by the system.



## Large, Flexible Airplanes

Frequently, large bomber or transport airplanes are equipped with stability augmentation systems to improve the damping of the short-period longitudinal mode or the Dutch roll mode. These systems are designed to operate over a limited frequency range, or bandwidth, to avoid interaction with higher frequency structural modes. In some cases, however, excessive shaking of the cockpit has been experienced in flight through rough air, thereby making it difficult for the pilot to read his instruments. Also, as noted previously, fatigue damage to the structure has occurred because of repeated stresses caused by flying through mild or moderate turbulence. Several analytical and flight projects have been undertaken to develop systems to alleviate these effects. These projects have been given various acronyms, such as GASDSAS (gust alleviation and structural dynamic stability augmentation), LAMS (load alleviation and modal stabilization), and others, which may be seen in the literature (refs. 17 to 19).

The structural modes of a flexible airplane usually have very low damping, with the result that a spectrum of the response carried out to high frequencies will usually show a series of sharp peaks, one at each major structural mode. The object of modal suppression systems has been to improve the damping of these modes, thereby cutting down the peaks, without interfering with the rigid-body modes or the operation of the existing stability augmentation system.

Because the sensors and servos used in a modal suppression system must operate out to high frequencies, the probability of reducing the damping of a structural mode or producing flutter always exists. Such systems must therefore be analyzed in detail. The stability equations for such systems are systems of linear differential equations similar to those of the basic airplane, but of higher order and therefore more complicated. The need to provide satisfactory damping of the structural modes for widely varying flight conditions and aircraft loading further complicates the design problem. General rules for the design of such systems cannot be formulated because each airplane presents special problems. A few considerations which may aid in arriving at a preliminary design can, however, be presented.

In order to sense structural modes independently of the rigid-body motions of an airplane, it is possible to employ the difference in the outputs of two sensors. For example, by taking the difference between the outputs of accelerometers at the center of gravity and at the rear of the fuselage, the rigid-body normal acceleration may be eliminated, thereby leaving a signal proportional to pitching acceleration plus the contribution of structural modes. If the difference between the outputs of pitching accelerometers is used, the only signal remaining is that due to structural modes. Combinations of sensors at various locations may be used to emphasize the contributions of particular structural modes.

In order to be effective in damping a particular mode, both the sensor and the control surface must be affected by that mode. In other words, the force exerted by the control surface must move through a distance so as to perform work in damping a particular mode. This problem is illustrated in figure 19. The various modes have different nodal points and different directions of displacement at any given location. As a result, an instrument providing a stabilizing signal to one mode will most likely destabilize some other mode. This dilemma has resulted in the scheme called ILAF (identical location of accelerometer and force). By locating an acceleration sensor as close as possible to the control surface which it operates, at least the direction of the acceleration and the resulting damping effect on the structure will always be consistent, regardless of which mode is excited. If a given control surface is at the nodal point of some modes, however, it will be ineffective in damping these modes. The use of another control surface may therefore be required. Small auxiliary canard surfaces near the cockpit have been shown to be effective in damping fuselage vibrations. Such surfaces were tested in the XB-70 program.

## DISCUSSION OF ASSUMPTIONS OF THEORY

The assumptions made in the theoretical analysis were listed previously. The methods of extending the analysis to remove some of these assumptions are now discussed. Some remarks have been made previously on the methods for including lateral motions in the analysis and of the effects of variations in configuration and of structural flexibility. This section includes consideration of the effects of speed variations, horizontal gusts, unsteady lift effects, and isotropic turbulence.

### Speed Variations

The effect of including speed as an additional degree of freedom is the introduction of the long-period, or phugoid, mode in the airplane response. The phugoid mode has low damping and can be readily excited by gusts, but experience has shown that the human pilot with suitable instruments and external references has no difficulty in controlling this mode of motion. The pilot's ability to control this motion is likely to be equally good in the case of a gust-alleviated airplane when adequate means are provided to control the flight path. Furthermore, the changes in normal acceleration associated with this long-period mode are small. The omission of this degree of freedom, which is equivalent to the assumption that the speed is constrained to a constant value by the pilot, is therefore justified in studies primarily concerned with acceleration alleviation.

## Horizontal Gusts

The relative magnitudes of the lift increments due to horizontal and vertical gusts may be determined as follows: The lift may be expressed by the formula

$$L = \alpha C_{L\alpha} \frac{\rho}{2} V^2 S$$

For a vertical gust,  $\alpha_g = \frac{w_g}{V}$ ; the change in lift due to a gust of this magnitude is therefore

$$\Delta L_V = w_g C_{L\alpha} \frac{\rho}{2} S$$

For a horizontal gust, when the airplane is flown at the lift coefficient  $C_L$

$$\Delta L_H = C_L \frac{\rho}{2} 2V u_g S$$

The ratio of lift increments is therefore

$$\frac{\Delta L_H}{\Delta L_V} = \frac{2C_L}{C_{L\alpha}}$$

For cruising flight, with  $C_L \approx 0.25$  and  $C_{L\alpha} \approx 5.0$  per radian, the ratio  $\Delta L_H/\Delta L_V$  is about 0.1. The horizontal gusts are therefore relatively unimportant in this condition. In landing approach, with  $C_L \approx 1.0$ , the ratio may reach about 0.5. For a STOL airplane operating at  $C_L \approx 4.0$ , however, horizontal gusts become more important than vertical gusts in affecting the motion of the airplane.

## Unsteady Lift Effects

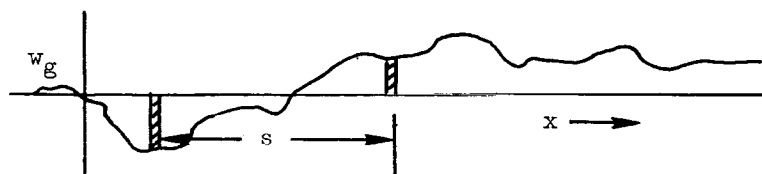
Though unsteady lift effects were neglected in the theory presented previously, early analyses of response to gusts placed undue emphasis on this aspect of the theory, often completely neglecting important factors such as the pitching response of the airplane. The reason for this trend was the desire to calculate response to discrete, sharp-edge gusts for determination of design loads. In the theory presented, lift is assumed to appear instantly when the angle of attack changes or the flap is deflected. The result of this assumption, from the frequency-response viewpoint, is to cause the transfer function relating normal acceleration to gust angle to maintain a constant value as the gust frequency approaches infinity (see fig. 6). In practice, the response would be attenuated at high frequencies because of the lag in buildup of lift. This attenuation does not become appreciable, however, until frequencies beyond those associated with the rigid-body

motion of the airplane are reached. In the case shown in figure 6, the response would not be reduced by 50 percent until a frequency of about 6 cycles per second. As shown subsequently, the effect of gust variations across the span causes the lift to be attenuated at a considerably lower frequency. The reduction in the input amplitude with increasing frequency in atmospheric turbulence further reduces the need for refinement of the calculations at high frequencies. It may be concluded, therefore, that for consideration of rigid-body motions, such effects may be safely neglected. In calculations involving higher frequency effects, such as flutter, penetration of sharp-edge gusts, excitation of structural modes, and so forth, unsteady lift effects should be considered.

### Isotropic Turbulence

When an airplane is flying through rough air, it has been found that the disturbances are similar whether the airplane flies on a north-south or east-west course. The mathematical model of turbulence of this type, called isotropic turbulence, is generally thought to be a good representation of actual atmospheric turbulence. A somewhat more exact description of this concept is therefore desirable.

In order to visualize the concept of isotropic turbulence, it is better to consider the observer to be at rest with respect to the general air mass, as if he were in a balloon, rather than flying through it as in an airplane. If the observer feels a gust, he would assume that for some small distance in his vicinity the gust velocity would be approximately the same. At a point a great distance away, however, the gust velocity would probably have no relation to the gust velocity that he was feeling. The relation between the two gust velocities as a function of the distance between the points of observation is known mathematically as the correlation function. The definition of the correlation function is shown in the following sketch:



$$\psi_{w_g} = \frac{1}{2S} \int_{-S}^S w_g(x) w_g(x+s) dx$$

$S \rightarrow \infty$

To be more exact, the gust velocity must be resolved into components along and perpendicular to the line joining the two points in question. The correlation function for the gust components along the line is called the longitudinal correlation function; that for gust components normal to the line and lying in the same plane is called the transverse correlation

function. The theory of isotropic turbulence shows that these two correlation functions are different but related. Return now to the definition of isotropic turbulence. The turbulence is said to be isotropic if these correlation functions depend only on the distance between the two points and not on the direction of the line joining the two points.

As shown in textbooks dealing with random processes (see ref. 20, for example), the correlation function is related to the power spectrum, the power spectrum being the Fourier transform of the correlation function. From the data on the power spectrum of atmospheric turbulence, therefore, the correlation function may be derived or vice versa.

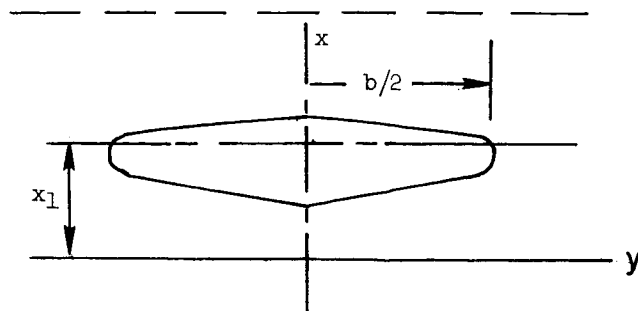
#### Calculation of Lift on a Wing in Isotropic Turbulence

The assumption that the gust velocity is constant across the wing span might be thought to be valid for gust wavelengths that are long compared to the span. For wavelengths that are short compared to the span, however, the probability is good that if the gust velocity is varying along the flight path, it will also be varying across the span. The resulting lift of the wing will be reduced in amplitude as compared to that calculated on the basis of a constant gust velocity across the span. The effect of the varying gust velocities across the span will be averaged by the wing, hence the term "spanwise averaging effect."

A rigorous calculation of the statistical or probable value of the lift variations on the wing as a function of gust wavelength in isotropic turbulence can be made by using formulations based on either power spectra or correlation functions. The power-spectral approach is explained in reference 1, chapter 10. It is thought, however, that the approach based on correlation functions is somewhat easier to understand. This method is therefore described.

The power spectra or correlation functions measured by a small sensor, such as a vane, traversing the atmosphere, have been called "point correlation functions." As an airplane flies through the air, it is influenced by gust velocities in a two-dimensional region defined by the flight path and the wing span. The power spectra or correlation functions for the wing lift variations have therefore been called "two dimensional." If considerations are again restricted to the effect of vertical gust velocities, the correlation function relating the gust velocities at any two points in this plane can be seen to be the transverse point correlation function. This is the correlation function which may be derived from vane measurements as the airplane flies through the turbulence, but in accordance with the assumptions of isotropic turbulence it is applied to obtain the correlation between gust velocities at any two points in the planar region swept out by the wing.

The expression for the lift on a wing subject to spanwise variations of vertical gust velocity at any point in a two-dimensional turbulence field is shown in the following sketch:



$$L(x_1) = \int_{-b/2}^{b/2} \gamma(y) w_g(x_1, y) dy$$

In this expression  $\gamma(y)$  is the spanwise lift distribution on the wing owing to a uniform angle of attack of unit magnitude. According to a theorem in linearized airfoil theory (ref. 21), the total lift on a wing with any arbitrary distribution of angle of attack may be obtained by multiplying the angle of attack at any spanwise station by the value of  $\gamma(y)$  at that station of the wing in reverse flow and integrating the result across the span. For an unswept wing, the reverse-flow provision may be omitted.

The method for determining the correlation function for the lift on a wing traversing a two-dimensional turbulence field is to write the expression for the lift at two points along the path. These expressions are then substituted into the formula for the correlation function to obtain the correlation function for the lift. By changing the order of integration, this expression may be shown to contain, as one term, the known transverse point correlation function for vertical gust velocity. With this knowledge, the resulting integral may be evaluated. These steps are

$$L(x) = \int_{-b/2}^{b/2} \gamma(y) w_g(x, y) dy$$

$$L(x + d) = \int_{-b/2}^{b/2} \gamma(y) w_g(x + d, y) dy$$

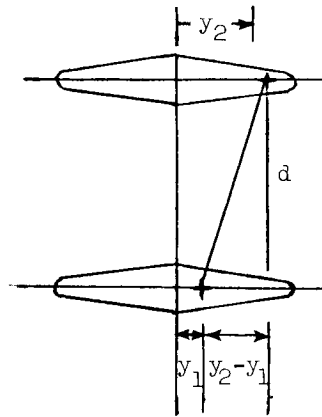
$$\begin{aligned} \psi_L(d) &= \frac{1}{2S} \int_{S \rightarrow \infty}^S L(x) L(x + d) dx \\ &= \frac{1}{2S} \int_{S \rightarrow \infty}^S \int_{-b/2}^{b/2} \gamma(y_1) w_g(x, y_1) dy_1 \int_{-b/2}^{b/2} \gamma(y_2) w_g(x + d, y_2) dy_2 dx \end{aligned}$$

By changing the order of integration

$$\psi_L(d) = \int_{-b/2}^{b/2} \int_{-b/2}^{b/2} \gamma(y_1) \gamma(y_2) \left[ \frac{1}{2S} \int_{S=-\infty}^S w_g(x, y_1) w_g(x + d, y_2) dx \right] dy_1 dy_2$$

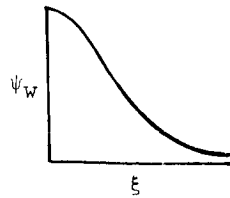
Note that the term in the brackets is the point correlation function for vertical gusts.

Perhaps the hardest point to understand in the derivation is the realization that the argument of the point correlation function appearing in the expression is the diagonal distance, or hypotenuse, of a triangle defined by points separated a distance  $d$  along the flight path and a lateral displacement  $y_2 - y_1$  across the wing span. As shown in the following sketch:



the two vertical gusts appearing in the correlation function are separated by the distance  $\sqrt{(y_2 - y_1)^2 + d^2}$ . If an expression for the point correlation function is assumed, such as

$\psi_w(\xi) = e^{-K\xi^2}$ , which may be plotted as shown in the following sketch,



then it is only necessary to substitute the expression for the hypotenuse as the argument of this function and to evaluate the integral involving this function. The point correlation function following this substitution is

$$\psi_w = e^{-K[(y_2 - y_1)^2 + d^2]}$$

Hence the correlation function for lift is

$$\psi_L(d) = \int_{-b/2}^{b/2} \int_{-b/2}^{b/2} \gamma(y_1) \gamma(y_2) e^{-K[(y_2 - y_1)^2 + d^2]} dy_1 dy_2$$

The power spectrum of wing lift may be derived from the correlation function if desired. This work has been carried out for various assumed point correlation functions and for several wing planforms in reference 22.

An example of these results is shown in figure 20. This figure shows the power spectra of effective vertical gust velocity  $\phi_{w_e}$  which, when considered constant across the span, will give the same lift as the actual randomly varying gust. The curves may therefore be considered proportional to the power spectra of wing lift. The curve for

$\frac{b}{L^*} = 0$  represents the point spectrum, inasmuch as the wing in this case has a span

approaching zero. The main effect of finite span is seen to be a more rapid decrease of the higher frequency components of the lift. The value of  $b/L^*$  of 0.25 (the smallest value shown), however, is probably much too large for actual airplanes in view of the large scale of atmospheric turbulence determined from flight measurements. A value of  $b/L^*$  of 0.05 would be more representative of actual conditions.

The calculation of the spanwise averaging effect has several implications for gust-alleviation systems. As stated previously, the lift reduction due to this effect may become important at a lower frequency than that due to unsteady lift effects. The effect is still small at the usual rigid-body frequencies, but it may be important in the range of wing structural frequencies. In calculations of structural response to gusts, therefore, the effects of isotropic turbulence should be taken into account.

While this paper has concentrated on longitudinal response, the lateral response of an airplane is also of interest. The assumption of constant gust velocity across the span may be adequate for the longitudinal analysis, but for calculations of lateral response it is obvious that the inputs due to rolling gusts would be missed completely by this assumption. Several reports are available in the literature showing how to take into account the effects of isotropic turbulence in calculating the rolling moments, yawing moments, and lateral forces acting on an airplane in flight through isotropic turbulence (refs. 2 and 23).

The consideration of the statistical nature of turbulence also makes it clear that perfect gust alleviation such as could be predicted by the simplified theory cannot be obtained in practice. The gust sensed by a vane on the center line of the airplane may differ from that acting on various parts of the wing and the resulting flap motion may not be exactly that required to counteract the gust. Some filtering of the high-frequency



inputs to the vane would be desirable because these gusts are less likely to be constant across the span. An interesting problem in optimal control theory, which to the writer's knowledge has not been solved, would be to calculate the filter characteristics to provide optimal gust alleviation, taking into account the location of the vane ahead of the wing, the spectrum of turbulence, and the dynamic characteristics of the airplane and gust-alleviation system.

## REFERENCES

1. Etkin, Bernard: Dynamics of Flight. John Wiley & Sons, Inc., c.1959.
2. Eggleston, John M.; and Phillips, William H.: The Lateral Response of Airplanes to Random Atmospheric Turbulence. NASA TR R-74, 1960. (Supersedes NACA TN 3954 by Eggleston and TN 4196 by Eggleston and Phillips.)
3. Truxal, John G.: Automatic Feedback Control System Synthesis. McGraw-Hill Book Co., Inc., 1955.
4. Phillips, William H.; and Kraft, Christopher C., Jr.: Theoretical Study of Some Methods for Increasing the Smoothness of Flight Through Rough Air. NACA TN 2416, 1951.
5. Cowley, W. L.; and Glauert, H.: The Effect of the Lag of the Downwash on the Longitudinal Stability of an Aeroplane and on the Rotary Derivative  $M_q$ . R. & M. No. 718, British A.R.C., 1921.
6. Zbrozek, J.; Smith, K. W.; and White, D.: Preliminary Report on a Gust Alleviator Investigation on a Lancaster Aircraft. R. & M. No. 2972, British A.R.C., 1957.
7. Zbrožek, J. K.: Theoretical Analysis of a Gust Alleviator Used on a Lancaster Aircraft and Comparison With Experiment. R. & M. No. 3326, British A.R.C., 1963.
8. Connor, Roger J.; Hawk, John; and Levy, Charles: Dynamic Analyses for the C-47 Airplane Gust Load Alleviation System. Rep. No. SM-14456, Douglas Aircraft Co., Inc., July 29, 1952.
9. Brooks, Billy S.; and Miller, Glenn C.: An Analysis of the Effectiveness of a Gust Alleviating Device. Tech. Note WCLS 53-52, Wright Air Develop. Center, U.S. Air Force, July 1, 1953.
10. Boucher, Robert W.; and Kraft, Christopher C., Jr.: Analysis of a Vane-Controlled Gust-Alleviation System. NACA TN 3597, 1956.
11. Kraft, Christopher C., Jr.: Initial Results of a Flight Investigation of a Gust-Alleviation System. NACA TN 3612, 1956.
12. Cooney, T. V.; and Schott, Russell L.: Initial Results of a Flight Investigation of the Wing and Tail Loads of an Airplane Equipped With a Vane-Controlled Gust-Alleviation System. NACA TN 3746, 1956.
13. Hunter, Paul A.; Kraft, Christopher C., Jr.; and Alford, William L.: A Flight Investigation of an Automatic Gust-Alleviation System in a Transport Airplane. NASA TN D-532, 1961.

14. Schott, Russell L.; and Hamer, Harold A.: Flight Investigation of Some Effects of a Vane-Controlled Gust-Alleviation System on the Wing and Tail loads of a Transport Airplane. NASA TN D-643, 1961.
15. Hirsch, René: Études et Essais d'un Avion Absorbeur de Rafales (Studies and Tests of an Airplane Gust Absorber). DOCAÉRO, no. 42, Jan. 1957.
16. Hirsch, R.: L'Absorption des Rafales sur Avions et Résultats des Essais en Vol d'un Appareil Expérimental (Gust-Absorption on Aircraft and Results of Flight Tests of an Experimental Device). Doc-Air-Espace, no. 105, July 1967, pp. 41-56.
17. Andrew, G. M.; Johnson, J. M., Jr.; and Gardner, F. H.: Gust Alleviator and Rigidity Augmentor for Supersonic Airplanes. Aerosp. Eng., vol. 21, no. 5, May 1962, pp. 72-73, 92-101.
18. Wykes, John H.; and Mori, Alva S.: An Analysis of Flexible Aircraft Structural Mode Control. AFFDL-TR-65-190, Pt. I, U.S. Air Force, June 1966. (Available from DDC as AD 486 794.)
19. Burris, P. M.; and Bender, M. A.: Aircraft Load Alleviation and Mode Stabilization (LAMS). AFFDL-TR-68-158, U.S. Air Force, Apr. 1969.
20. Lee, Y. W.: Statistical Theory of Communication. John Wiley & Sons, Inc., c.1960.
21. Sears, W. R., ed.: General Theory of High Speed Aerodynamics. Vol. VI of High Speed Aerodynamics and Jet Propulsion, Princeton Univ. Press, 1954, pp. 325-326.
22. Diederich, Franklin W.; and Drischler, Joseph A.: Effect of Spanwise Variations in Gust Intensity on the Lift Due to Atmospheric Turbulence. NACA TN 3920, 1957.
23. Eggleston, John M.; and Diederich, Franklin W.: Theoretical Calculations of the Power Spectra of the Rolling and Yawing Moments on a Wing in Random Turbulence. NACA Rep. 1321, 1957. (Supersedes NACA TN 3864.)

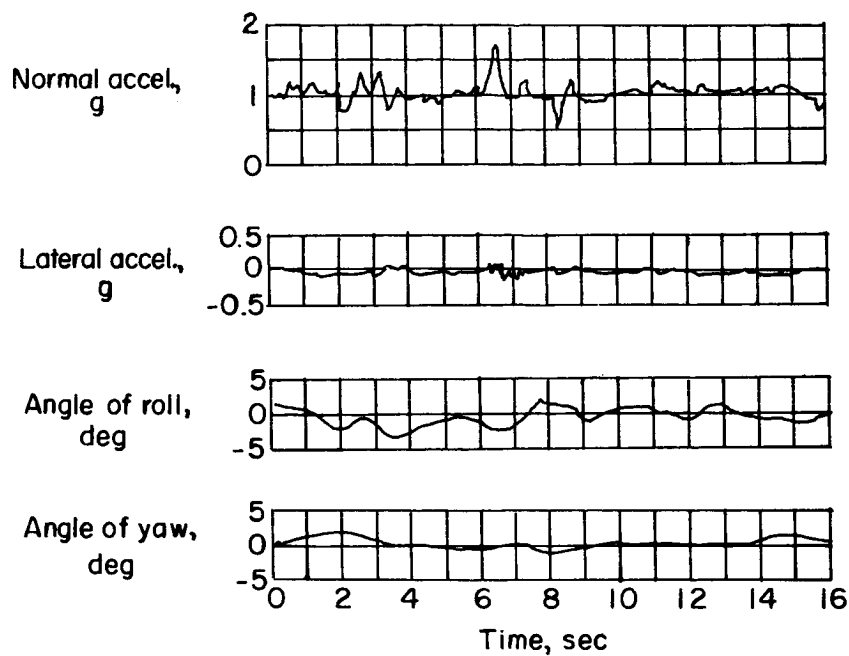


Figure 1.- Typical record of motions of an airplane in rough air.

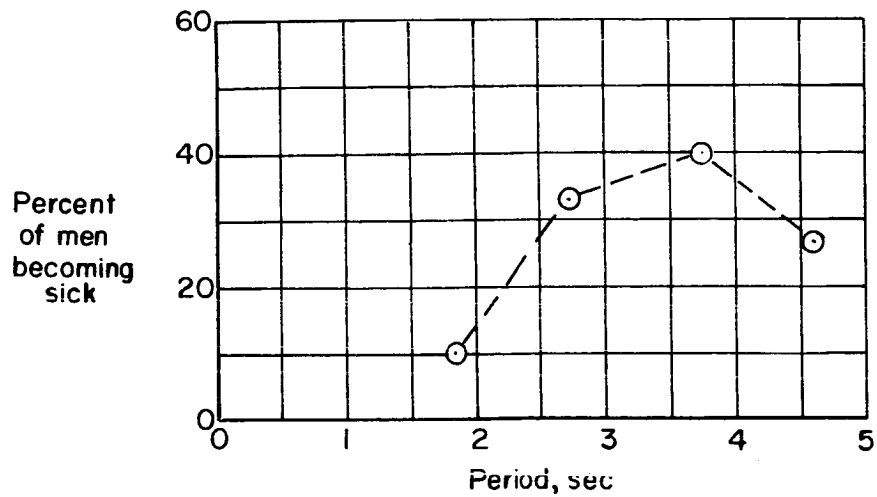


Figure 2.- Results of experiments on motion sickness.

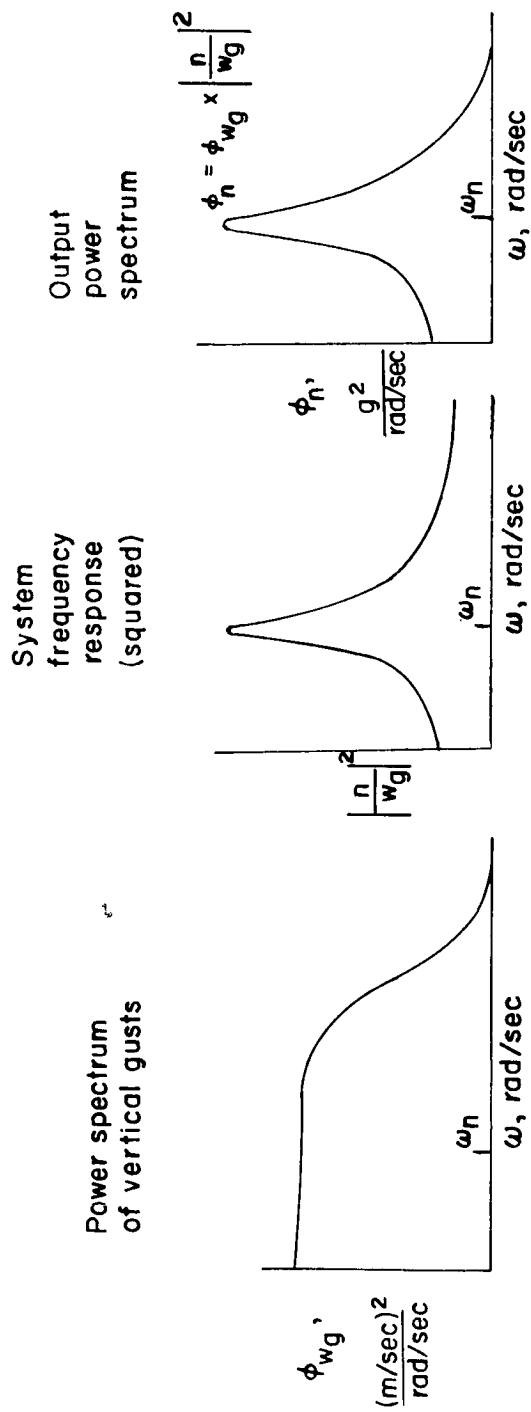


Figure 3.- Example of calculation of power spectrum of normal acceleration as product of power spectrum of vertical gusts and square of system frequency response relating normal acceleration to vertical gust velocity. Natural frequency of system is  $\omega_n$ .

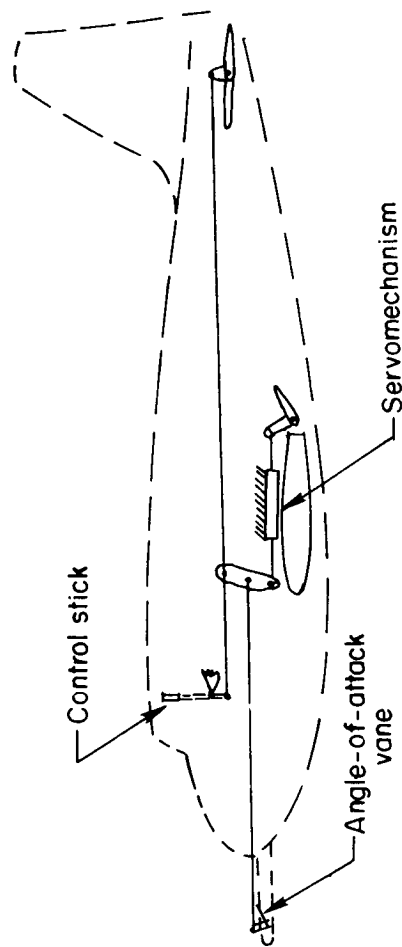


Figure 4.- Linkage for vane-controlled acceleration alleviator.



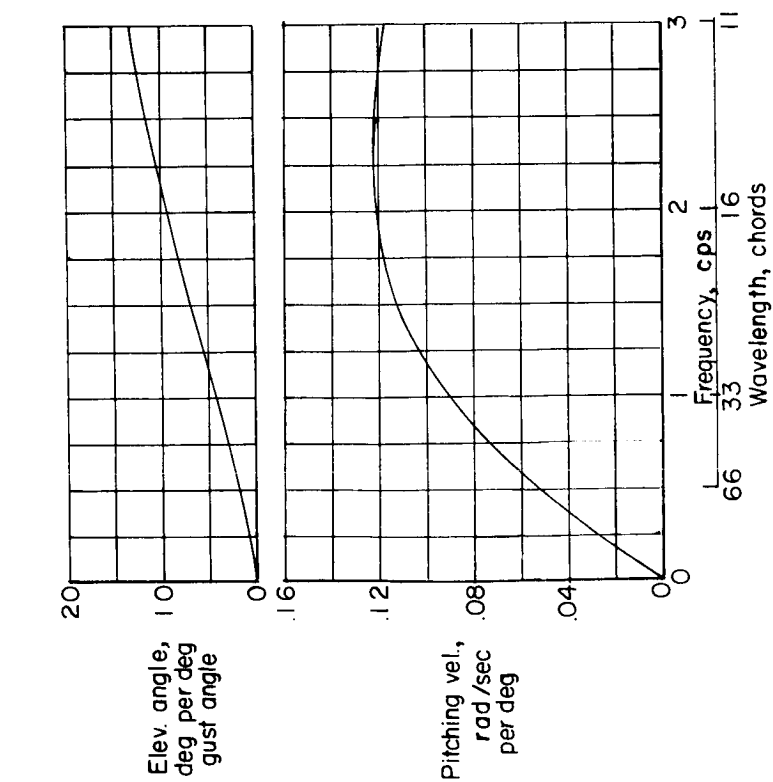


Figure 7.- Elevator motion to maintain zero acceleration; resulting pitching velocity.

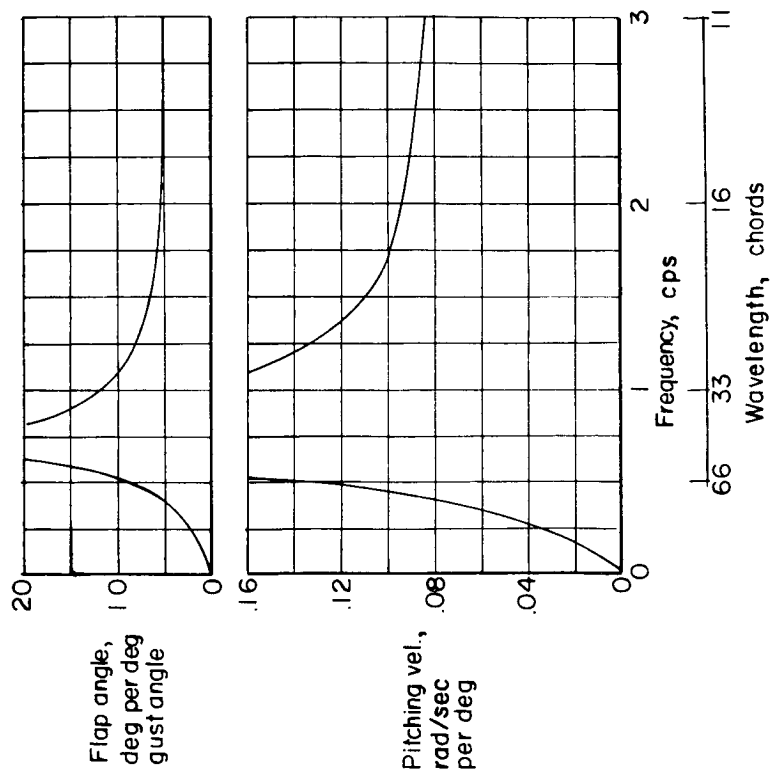


Figure 8.- Flap motion to maintain zero acceleration; resulting pitching velocity.

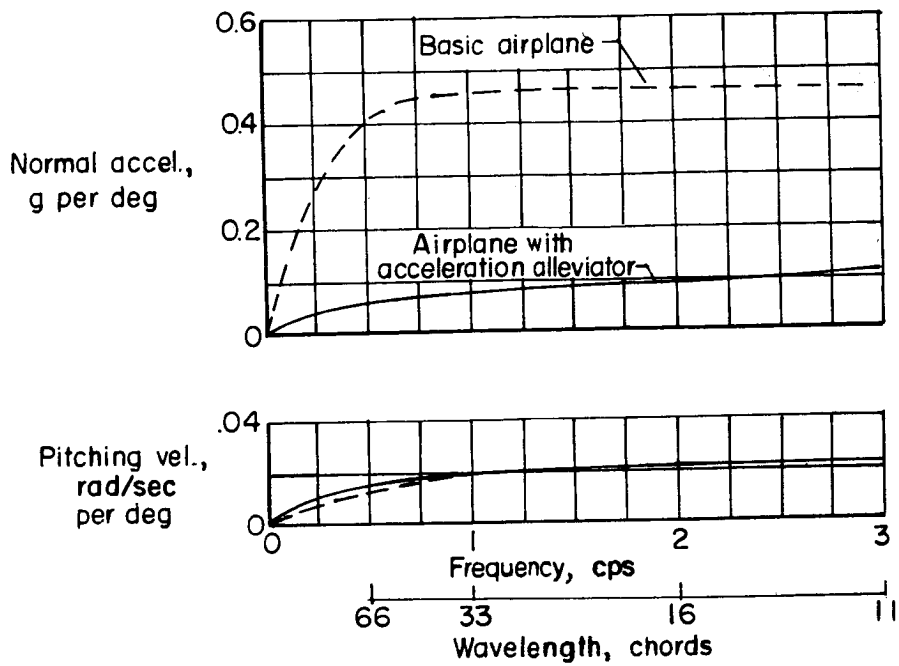


Figure 9.- Motions of airplane with vane-type acceleration alleviator owing to sinusoidal gust disturbance.

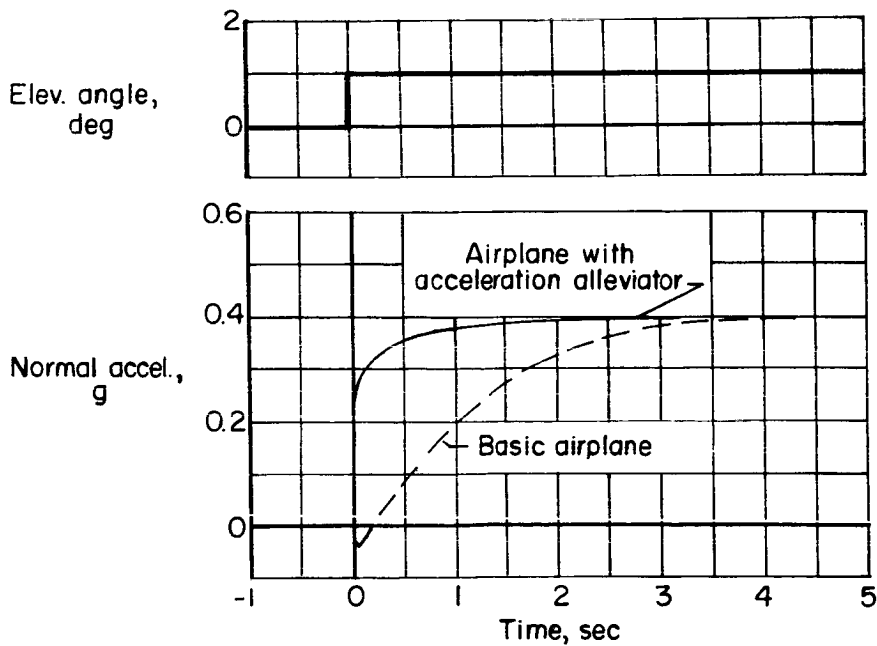


Figure 10.- Response to step motion of elevator.



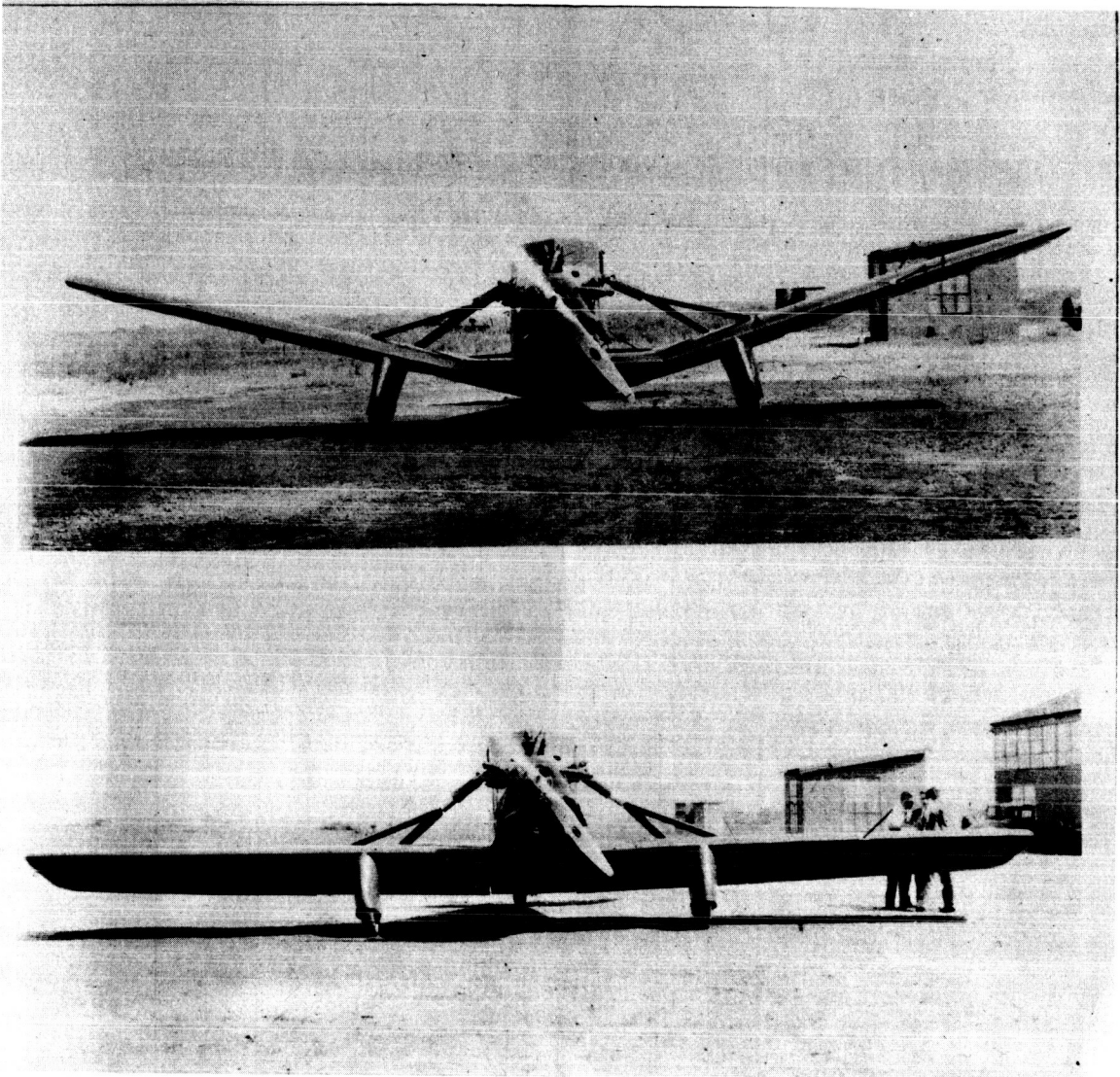


Figure 11.- Waterman's airplane incorporating wings attached to fuselage with skewed hinges. Pneumatic struts, shown in extended and compressed positions; balanced lift force in flight.

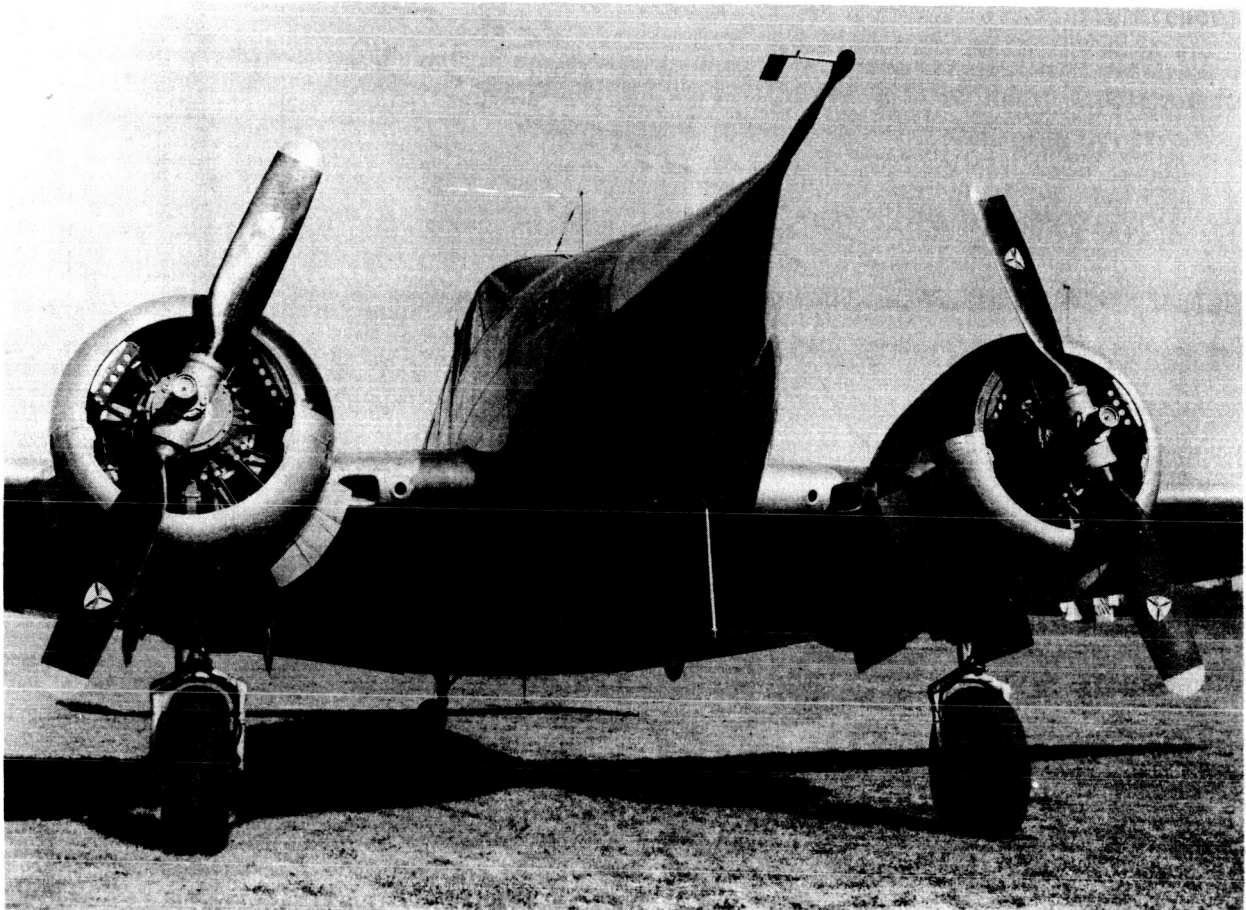


Figure 12.- Twin-engine transport airplane equipped for gust-alleviation studies.  
Nose boom and vane installation.



Figure 13.- Twin-engine transport airplane equipped for gust-alleviation studies.  
Modified control surfaces.

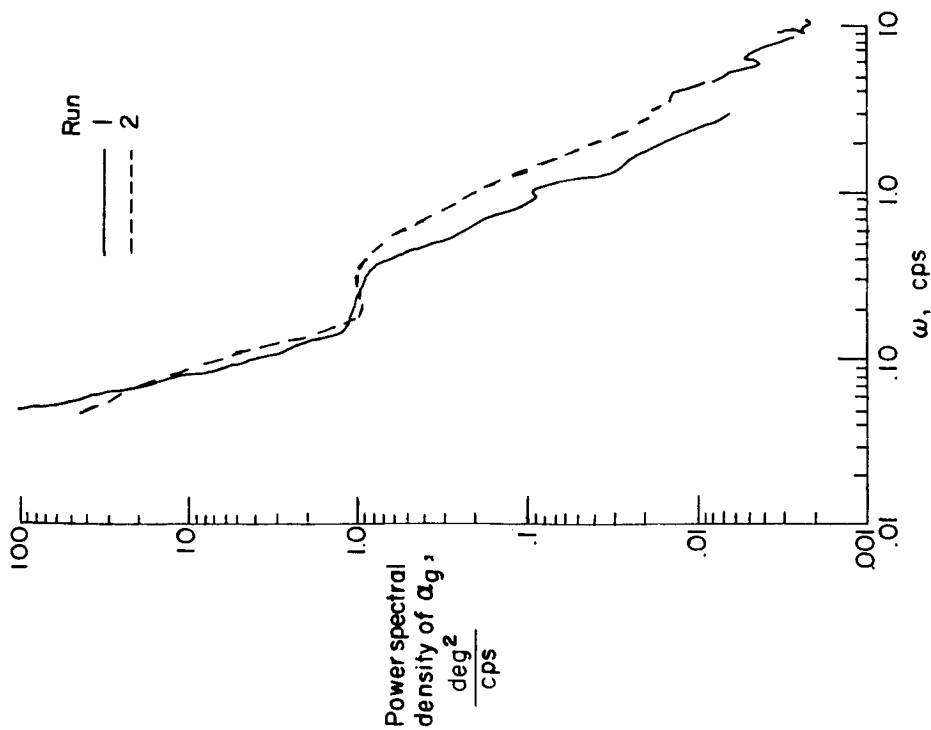


Figure 14.- Power spectra of gust angle of attack.

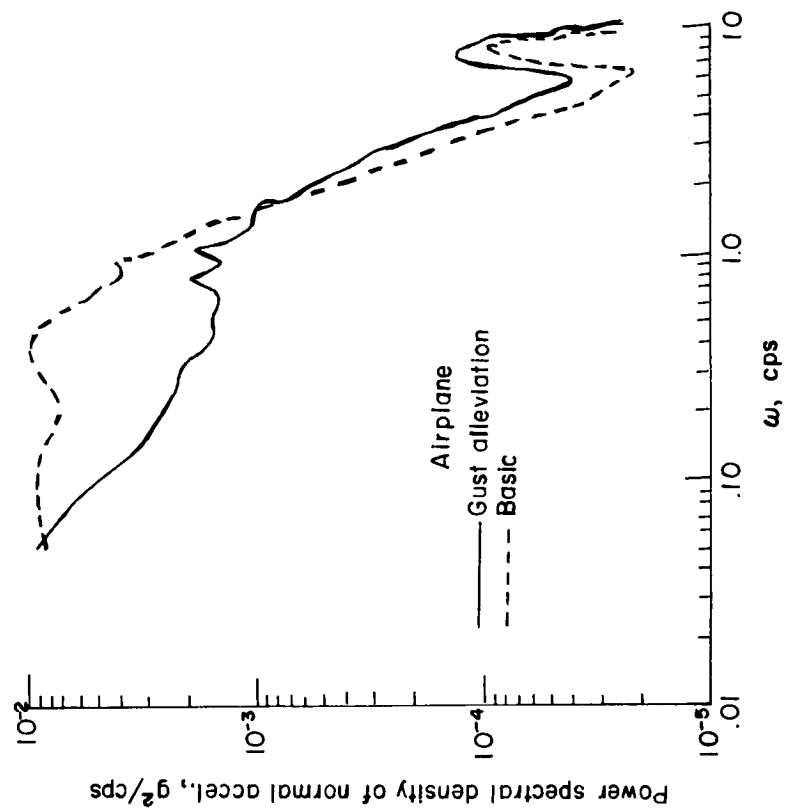


Figure 15.- Power spectra of normal acceleration.

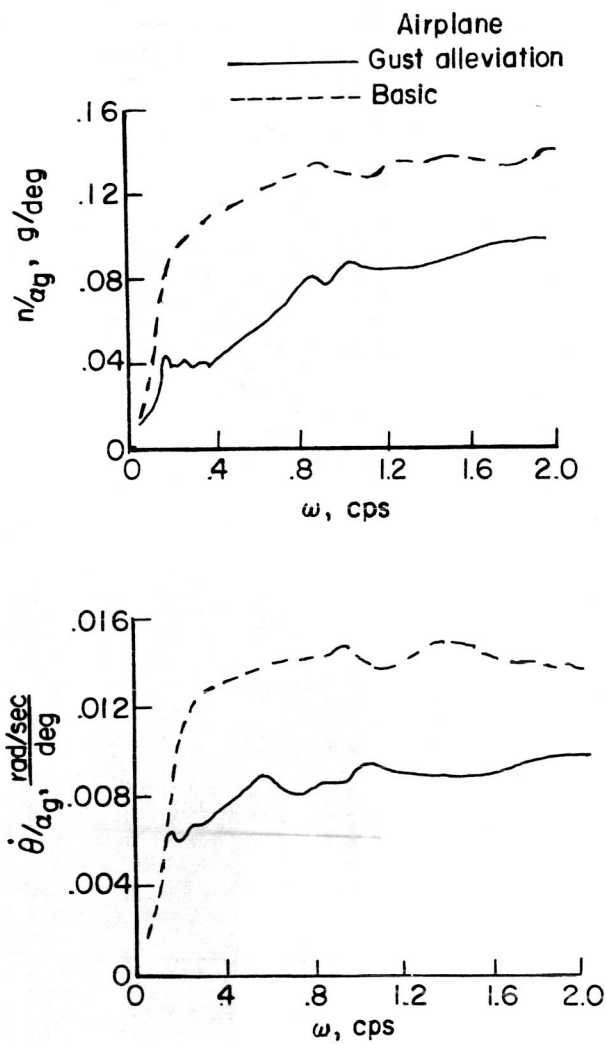


Figure 16.- Ratios of  $n$  and  $\dot{\theta}$  to gust angle of attack  $\alpha_g$ .

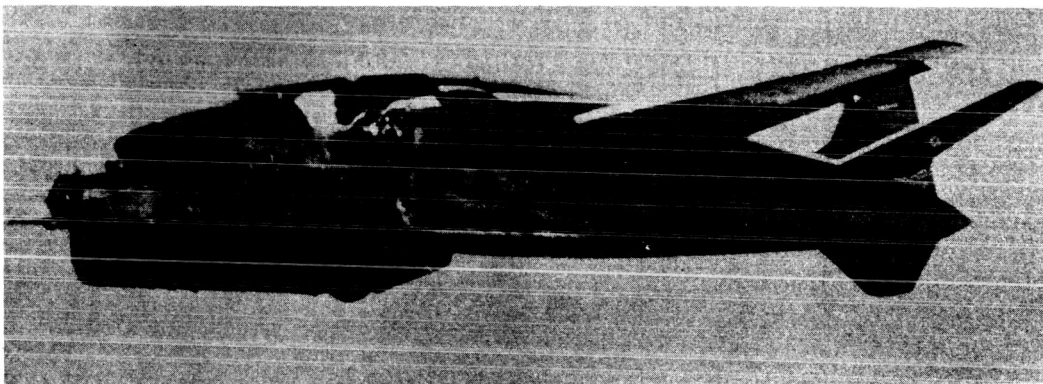


Figure 17.- Photograph of gust-alleviating airplane designed by René Hirsch.

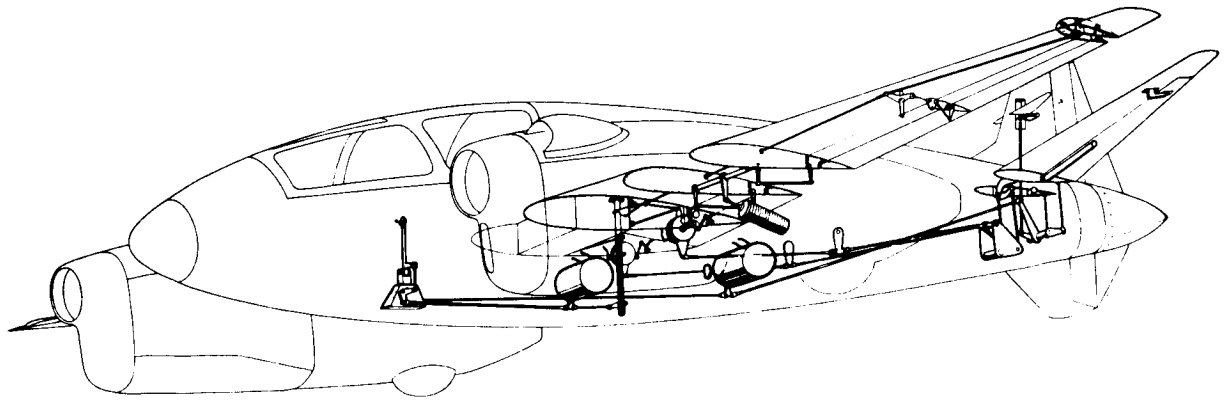


Figure 18.- Line drawing showing interior arrangement of airplane designed by René Hirsch.

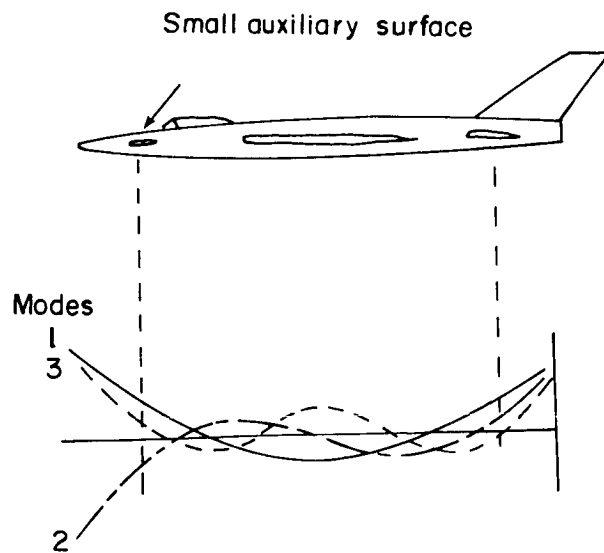


Figure 19.- Structural mode control.

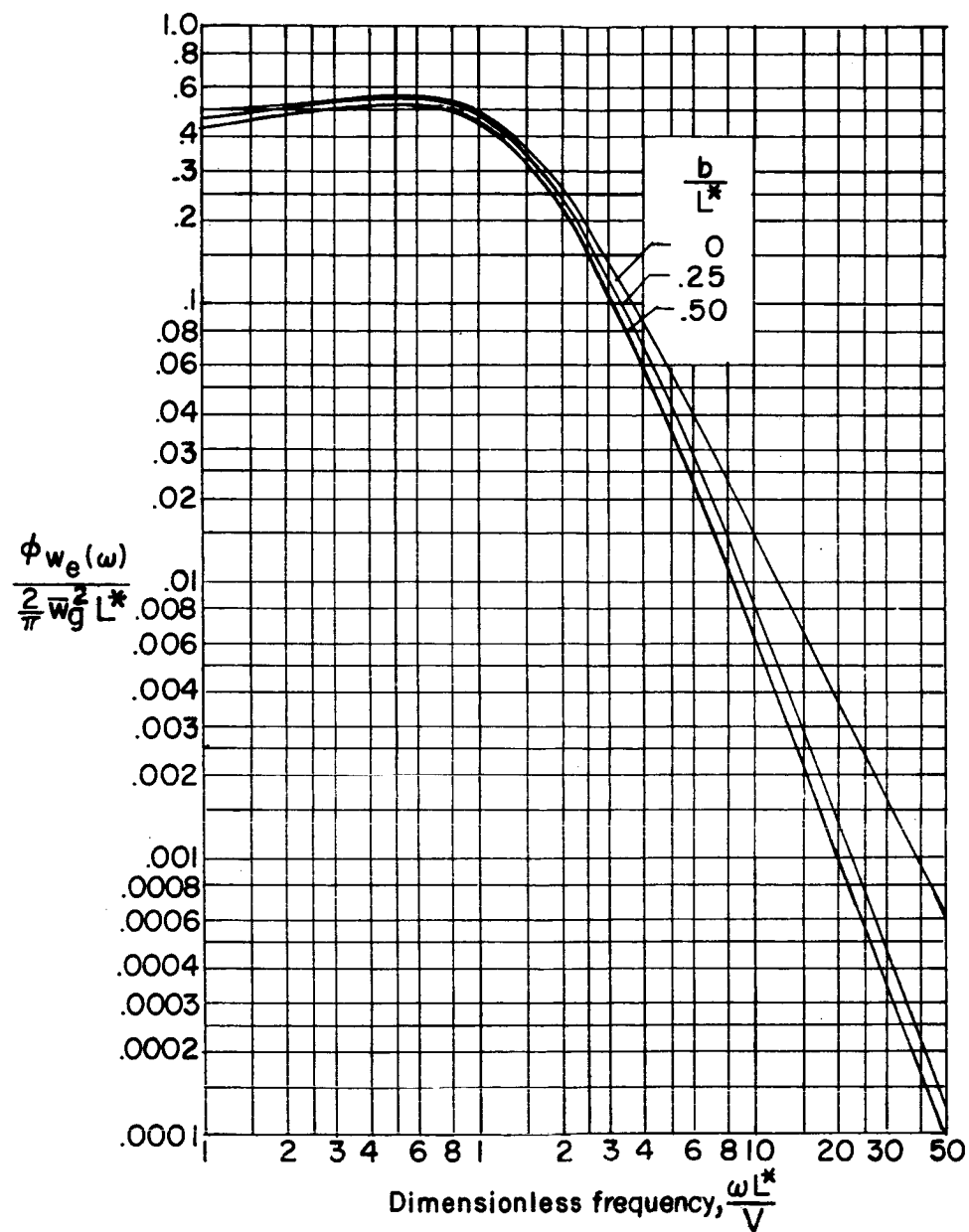


Figure 20.- Power spectra of effective vertical gust velocity for finite-span wings as a function of dimensionless frequency (ref. 22).



## 9. HUMAN RESPONSE IN CLOSED-LOOP CONTROL OF DYNAMIC SYSTEMS

By James J. Adams  
Langley Research Center

### ABSTRACT

This lecture describes a model matching method which has been used to determine human response in controlling a wide range of vehicles. The use of the resulting models of human response to determine the complete pilot plus vehicle system response is discussed. The implications of the results on system performance are discussed, and several examples in which the answers to engineering problems are obtained are presented.

### INTRODUCTION

The area of research known as human factors covers many topics. Some specialized topics, which are studied by psychologists, are studies of control compatibility, reflex time, the effects of lighting on human performance, proper display arrangement, and the corresponding eye movements of the subject. Other studies have a medical aspect and cover detailed studies of muscle control, eye control, and the sensing ability of organs such as the eye and the semicircular canals. In contrast to these detailed investigations, there are studies of a much broader nature that attempt to define a man's decision-making processes and the trade-off that he will make between utility and cost.

In the present study, an engineering view is taken of human response as related to all of the topics listed previously, but it does not treat them with the same detail as does the psychological approach. What is presented and defined is a linear transfer function that describes a pilot's control movements in controlling a vehicle to some position or direction which he has decided to be desirable.

The measurement of these transfer functions is first described in some detail. Next, samples of these transfer functions are presented to illustrate their nature. Finally, several examples of the application of these transfer functions to obtain answers to engineering problems are presented.

The use of linear functions to describe pilot response is maintained throughout the discussion so as to allow the use of linear analysis methods. The advantage of being able to use the very powerful and thoroughly developed linear methods of analysis is believed to be greater than the small advantage that might be derived from using nonlinear representations of pilot response, which would provide only a slight improvement in the representation of the pilot.



## SYMBOLS

I	inertia, slug-ft <sup>2</sup> (kilogram-meter <sup>2</sup> )
g	gravity, ft/sec <sup>2</sup> (meters/sec <sup>2</sup> )
h	distance between pilot center of gravity and vehicle center of gravity, ft (meters)
K	gain (or coefficient)
m	mass, slugs (kilograms)
s	Laplace operator, per second
T	thrust, lb (newtons)
t	time, sec
X	body reference axis
x	displacement, ft (meters)
$\alpha$	general pilot gain
$\delta$	control deflection, radians
$\epsilon$	displayed error, volts
$\zeta$	damping ratio
$\theta$	attitude angle, radians
$\tau$	pilot lag coefficient, radians/sec
$\omega$	frequency, radians/sec

**Subscripts:**

c            command

P            pilot

V            vehicle

1,2          particular gains, as noted in text

Dots over symbols denote differentiation with respect to time.

**REVIEW**

A review of linear analysis is given by considering a simple problem. Given is a single-degree-of-freedom body, with inertia  $I$  and a pointing requirement as illustrated in figure 1. The line labeled  $\theta_c$  represents the line to some target at which the vehicle axis  $X$  must point. The first element of the control system to be considered is illustrated with a spring, which is assumed to be adjusted so that the vehicle will tend to point toward the target. The dynamic equation of motion of the system is then

$$\begin{aligned}\text{Torque} &= I\ddot{\theta} \\ &= K(\theta_c - \theta)\end{aligned}$$

where  $K$  is a spring constant. The equation can be written in Laplace notation, where the operator is used to denote differentiation

$$Is^2\theta = K(\theta_c - \theta)$$

or rewritten as

$$\theta(Is^2 + K) = K\theta_c$$

The term in parentheses is known as the auxiliary equation, or the system characteristic equation. The time-domain solution of the differential equation is known to be

$$\theta = \sin\sqrt{\frac{K}{I}} t$$

However, the usual approach is to determine the roots of the characteristic equation. An imaginary root indicates an oscillatory system for which the frequency is given by

$$\omega = \sqrt{\frac{K}{I}}$$

This system undamped natural frequency is an excellent indicator of the nature of the system response and is often used in engineering discussions to describe the system.

A time history of the system response to an initial error is given in figure 2. Since the motion of the system does not damp out, it is not a satisfactory system, and damping must be added. The addition of damping is illustrated in figure 3 with a dashpot.

The system equation is now

$$Is^2\theta = K(\theta_c - \theta) + K_2(\dot{\theta}_c - \dot{\theta})$$

where  $K_2$  is the damping coefficient. The system characteristic equation is now

$$s^2 + \frac{K_2}{I}s + \frac{K}{I} = 0$$

The characteristic that is determined from this equation for engineering discussion is the damping ratio  $\zeta$ , where

$$\zeta = \frac{K_2/I}{2\omega}$$

The ideal damping ratio is 0.7, which is a compromise between a system response that is too oscillatory and one that is too sluggish. A time history of system response to an initial error when the system damping ratio is 0.7 is illustrated in figure 4.

From consideration of performance (that is, for a system that provides a quick response to commands and has the lowest possible error in the presence of external disturbances), it is desirable to have as high a system frequency as possible as well as a damping ratio of 0.7. However, practical considerations usually limit the system frequency that can be achieved. One of these considerations is control lag.

In a practical system, static stability and damping are not supplied by springs and dashpots such as were used for illustration in the preceding paragraphs. Rather, control-torque-producing mechanisms which supply torque as a function of error and rate are used. These mechanisms do not usually supply torque as a simple function of error and rate but have some lag associated with their operation. The effect that such lags can have on system response is illustrated by considering a system which has no damping:

$$s^2 + 0s + 1 = 0$$

If the control is applied with a controller that is not perfect in its response but rather responds with a first-order lag with a time constant of 1 second, the system characteristic equation becomes

$$s^2 + \frac{0s + 1}{s + 1} = 0$$

or

$$s^3 + s^2 + 0s + 1 = 0 \quad (1)$$

which factors to

$$(s + 1.5)(s^2 - 0.5s + 0.7)$$

and the quadratic factor indicates that the system is unstable, as shown by the negative coefficient on  $s$ . This system would respond to a command or an external disturbance with a divergent oscillation.

This example illustrates, in an exaggerated case, the effect of control lag on system response. In a practical situation, where some damping was provided, the control coefficients, or gains, would be adjusted so that the system would be stable but the system frequency would be restricted.

The system characteristic set down above is usually derived in a more mathematical manner. The equation-of-motion derivation is as follows:

The vehicle equation is

$$s^2\theta = K_c\delta$$

where  $K_c$  is the control coefficient and  $\delta$  is control deflection.

The control equation is

$$s\delta = K_1(\delta_c - \delta)$$

The command equation is

$$\delta_c = K_2(\theta_c - \theta)$$

The characteristic determinant is then:

$$\begin{vmatrix} s^2 & -K_c & 0 \\ 0 & s + K_1 & -K_1 \\ K_2 & 0 & 1 \end{vmatrix} = s^2(s + K_1) + K_c K_1 K_2$$

$$= s^3 + K_1 s^2 + K_c K_1 K_2$$

which can be seen to be equivalent to the example set down in equation (1).

From a block-diagram and transfer-function approach, the system characteristic is derived as follows. The block diagram of the example system, with a first-order lag in the controller and with no damping function provided, is shown in figure 5.

The system response is

$$\frac{\theta}{\theta_c} = \frac{K_2 \left( \frac{K_1}{s + K_1} \right) \frac{K_c}{s^2}}{1 + K_2 \left( \frac{K_1}{s + K_1} \right) \frac{K_c}{s^2}} = \frac{K_2 K_1 K_c}{s^2(s + K_1) + K_2 K_1 K_c} = \frac{K_2 K_1 K_c}{s^3 + K_1 s^2 + K_2 K_1 K_c}$$

and it can be seen that the denominator is equivalent to the system characteristic equation set down in equation (1). The system characteristics expressed by the denominator are known as the system closed loop characteristics.

## HUMAN-MODELING TECHNIQUE

A human model should contain all of the control concepts discussed in the previous paragraphs. A suitable model in transfer function form is

$$\frac{\text{Output}}{\text{Displayed error}} = \frac{\delta}{\theta_c - \theta} = \frac{K_1 + K_2 s}{(s + \tau)^2}$$

The numerator of this transfer function indicates that the model assumes a linear response to displayed error and error rate. The second-order lag function indicated by the denominator of the transfer function is predicated on the fact that the subsystem

being described (namely, the pilot's arm and control stick) does have inertia and therefore a second-order type of response is required. The assumption of critical damping that is implicit in the perfect-square form is made because it is the simplest reasonable assumption that can be selected.

An analog diagram of the model is presented in figure 6. This compact analog arrangement provides the following transfer function, which is slightly different from the transfer function presented at the beginning of the section, but is not changed essentially:

$$\frac{\delta}{\epsilon} = \frac{K_1\tau + K_1K_2s}{(s + \tau)^2}$$

This model was matched to human pilots by automatically adjusting the gains  $K_1$ ,  $K_2$ , and  $\tau$  in the following manner. In a suitable experimental setup, which provided a given, measurable error signal to the pilot, this same error signal was used as the input to the model. The pilot's output (his control stick deflection) was summed with the output of the model to form a difference. To determine whether this difference was due to the incorrect setting of any one of the gains in the model, the signal at that gain was taken, transformed into the output form by the use of an approximate representation of the remainder of the pilot's transformation, and compared with the difference to see whether it was correlated with the difference. This correlation was performed by multiplying the particular signal and the difference. If a correlation existed (the signal and the difference were in phase), the multiplier would have a biased output. This output was then integrated, and the output of the integrator was used to provide an incremental change in the particular gain. In this manner the gain settings are caused to run to a value that minimizes the difference between the model and the pilot, and when the minimum is achieved the best possible representation of the human has been obtained.

A mathematical derivation of this identification process is as follows: First it is necessary to form a suitable function of the difference (diff) between the pilot and the model which will have a minimum value for some particular value of a given gain, which is called the gain  $\alpha$  for the moment. A suitable function is:

$$f(\text{diff}) = \frac{(\text{diff})^2}{2}$$

A plot of the variation of this function of the difference with  $\alpha$  is shown in figure 7: A steepest descent method can now be used to find the lowest point on this curve. The method satisfies the equation

$$\dot{\alpha} = -K \frac{\partial f(\text{diff})}{\partial \alpha}$$

which indicates that if  $\alpha$  is caused to change at a rate proportional to the slope of the curve, then  $\alpha$  will seek the point where the slope is zero, and thus the minimum value of the difference will be found.

The operational form of the steepest descent equation is obtained if the following two transformations are made:

$$\dot{\alpha} = -K \frac{\partial f(\text{diff})}{\partial(\text{diff})} \frac{\partial(\text{diff})}{\partial \alpha}$$

$$\dot{\alpha} = -K(\text{diff}) \frac{\partial(\text{diff})}{\partial \alpha}$$

To illustrate the particular form of the last equation, take for example, the gain  $K_2$  of the model

$$\frac{\partial(\text{diff})}{\partial K_2} = \frac{(K_1 s) \epsilon}{(s + \tau)^2}$$

However, for the model signal at  $K_2$ , which is called  $\delta'$  (fig. 6)

$$\frac{\delta'}{\epsilon} = \frac{K_1 s}{(s + \tau)^2}$$

Then, a substitution can be made

$$\frac{\partial(\text{diff})}{\partial K_2} = \frac{K_1 s}{(s + \tau)^2} \frac{(s + \tau)^2}{K_1 s} \delta' = \delta'$$

Thus, it can be seen that taking the model signal at  $K_2$  and multiplying by the difference gives a value for  $\dot{K}_2$ . The value for  $\dot{K}_2$  can be used to adjust  $K_2$  to give the best possible match to the human subject. Similar adjustment loops for  $K_1$  and  $\tau$  can be provided, and all three gains can be adjusted at the same time. A block diagram of the gain-adjustment loops is shown in figure 8. A more detailed description is also given in reference 1.

## EXPERIMENTS

The automatic model-matching scheme described in the preceding section was used to determine pilot response in a series of compensatory-tracking tasks. A block diagram

of the task is shown in figure 9. A random disturbance was injected into the system as shown. The pilot's task was to keep the moving indicator on his display alined as nearly as possible with a fixed reference mark. This experimental arrangement was used to determine the effect of vehicle dynamics on pilot response. The different vehicle dynamics tested are listed in table I. Also listed in the table to illustrate what these different dynamics mean are the maximum acceleration, velocity, and displacement that would result with each dynamics for a step-control input.

TABLE I.- PLANT DYNAMICS

Vehicle transfer function	Maximum values for a 10-volt step-control input		
	Acceleration, volts/sec	Velocity, volts/sec	Displacement, volts/sec
1	$\infty$	$\infty$	10
$\frac{1}{s+1}$	$\infty$	10	10
$\frac{10}{s^2+3s+10}$	100	17	10
$2/s$	$\infty$	20	$\infty$
$\frac{10}{s(s+1)}$	100	100	$\infty$
$\frac{10}{s^2}$	100	$\infty$	$\infty$
$\frac{10}{s^2(s+1)}$	100	$\infty$	$\infty$

These dynamics are progressively more difficult to control for successive functions in the list. The last one,  $\frac{10}{s^2(s+1)}$ , represents a boundary for stable closed-loop control for a human controller.

## RESULTS

Typical gains measured in these experiments and the closed-loop-system characteristics obtained by using the linear pilot model transfer function together with the linear



transfer for the plant are presented in table II. The important points to notice from this table are that for successive items down the list of vehicle dynamics, the pilot's lag coefficient  $\tau$  increases, and the closed-loop oscillatory mode of motion frequency  $\omega$  and damping ratio  $\zeta$  decrease. The decrease in  $\omega$  and  $\zeta$  indicates that system performance is deteriorating, and the normalized error  $\epsilon/\text{disturbance}$  measured in the experiments verifies this deterioration.

TABLE II. - MEASURED PILOT GAINS AND CLOSED-LOOP CHARACTERISTICS

Dynamics	Measured gains			Closed-loop characteristics			$\epsilon/\text{disturbance}$
	$K_1$	$\tau$ , rad/sec	$K_2$	$\omega$ , rad/sec	$\zeta$	Real roots	
$2/s$	6.5	4	0	4.0	0.4	-7.68	0.26
$\frac{10}{s(s+1)}$	5	10	3	3.0	0.3	-6.3, -13.0	0.50
$\frac{10}{s^2}$	8	15	5	2.5	0.2	-10.0, -20.0	0.75
$\frac{10}{s^2(s+1.5)}$	12	28	30	$\begin{cases} 2.5 \\ 28.4 \end{cases}$	$\begin{matrix} 0 \\ .99 \end{matrix}$	-1.0	1.0

If these pilot response data are to be applied to other dynamics which may be similar to, but not exactly like, the examples tested, the following rules must be followed. Consider the pilot-transfer function rearranged to the following form:

$$\frac{\zeta}{\epsilon} = \frac{\frac{K_1}{\tau} \left( 1 + \frac{K_2}{\tau} s \right)}{\left( \frac{s}{\tau} + 1 \right)^2}$$

Determine the dynamics given in table II that is most nearly similar to the dynamics to be studied. Take the corresponding value of  $\tau$  and lead time constant  $K_2/\tau$  for use in the model. Then adjust the static gain  $K_1/\tau$  to provide the system-closed-loop frequency indicated in the table. This model may then be used for whatever analytical study it is desired to perform.

Factors other than the vehicle dynamics in the closed-loop system were also studied for their effect on pilot response. These other factors are control sensitivity, display sensitivity, and disturbance frequency. It was found that these factors had to be varied to

extreme values in order to have a noticeable effect on pilot response. Additional information on these factors can be found in reference 1.

In addition to the single-axis tasks, measurements of pilot response were also made for multiaxis control tasks. In these multiaxis tasks, the pilot had to control pitch, roll, and yaw attitude angles by using a two-degree-of-freedom control stick and rudder pedals. As before, the pilot's gains were measured, and then the closed-loop-system characteristics for each individual axis were determined. The vehicle dynamics used in these tests were  $K/s^2$  on each axis. The significant result of these experiments was that as additional axes of control were added to the pilot's task, he altered his response so that the system-closed-loop frequency was reduced. Some typical values for the pitch-axis closed-loop natural frequency are presented in table III to illustrate this point.

TABLE III. - MULTIAxis-CLOSED-LOOP  
OSCILLATORY CHARACTERISTICS

	$\omega$ , rad/sec	$\zeta$
Pitch axis alone . . . . .	3.3	0.36
Pitch axis in combination with roll . . . . .	2.5	0.47
Pitch axis in combination with roll and yaw . . . . .	2.1	0.68

Additional information on these experiments can be found in reference 2.

To proceed to even more realistic and difficult control tasks, multiloop control situations were studied. The translation control of a jet supported lunar module or helicopter is an example of the multiloop type of control situation. The variables involved are shown in figure 10. In this situation translation  $x$  is controlled by manipulation of pitch angle  $\theta$ . Pitch angle, in turn, is controlled by operation of the attitude control system. Thus, attitude control forms an inner loop around which an outer loop for translation is closed. Consequently, the name multiloop task is appropriate. It has been determined that pilot response in a multiloop-control task can be represented by two transfer functions, located in series, with one transfer function in each loop. The block diagram of the system is shown in figure 11.

It was found that the pilot transfer functions such as were measured in the multiaxis tasks were suitable for the inner-loop pilot response. Then, by a trial-and-error matching of time histories of translation response to a step change command, the outer-loop pilot transfer function was determined. Typical pilot transfer functions, together with the

vehicle transfer functions, for a multiloop lunar-module translation task are:

Inner loop:

Vehicle

$$\frac{\theta}{\delta} = \frac{0.5}{s(s + 0.5)}$$

Pilot

$$\frac{\delta}{\epsilon} = \frac{2.67(1 + 0.41s)}{(1 + 0.167s)^2}$$

Outer loop:

Vehicle

$$\frac{x}{\theta} = \frac{5.36}{s^2}$$

Pilot

$$\frac{\theta_c}{\epsilon} = \frac{0.009(1 + 9.2s)}{(1 + 0.1s)^2}$$

The system characteristics for the complete system are two oscillatory modes of motion and four real roots, as shown in table IV.

TABLE IV.- MULTILoop SYSTEM CHARACTERISTICS

Oscillatory		Real roots
$\omega$ , rad/sec	$\zeta$	
1.11	0.046	-0.167, -0.336, -4.75
10.2	.99	-6.85

The high-frequency oscillatory root and the two large real roots are control modes of motion and are not important to an understanding of the response of the system. The low-frequency oscillatory root is the attitude mode of motion. The two low real roots are the translation mode of motion, and they can be thought of as representing an overdamped oscillatory mode of motion with a frequency of 0.24 radian per second. When the translation mode of motion is referred to in this manner, and its frequency is compared with the frequency of the attitude mode of motion, it can be seen that translation is controlled at a much lower frequency than is attitude.

Closing the outer loop around the inner loop also affects the characteristics of the inner loop. If the inner loop alone is considered, its characteristics include an oscillatory mode of motion with a frequency of 1.0 radian per second and a damping ratio of 0.26. When the outer loop is closed around this inner loop, the attitude mode of motion is an oscillatory mode of motion with a frequency of 1.1 radians per second and a damping ratio of 0.046. Thus, it can be seen that in the complete system, the damping of the attitude mode of motion is greatly reduced.

It was also found necessary to include a limiter on the output of the outer-loop pilot model in order to represent the pilot properly. Both this limiter and the low frequency of the translation mode of motion are reflections of the lack of tight (or precise) control of translation as compared with control of attitude.

## APPLICATIONS

### Damper Failure Problem

If the pilot transfer functions which have been measured are correct, they should be able to predict system performance. The closed-loop system characteristics, which were calculated by using the measured transfer functions, are certainly very reasonable and indicate that the measurements are correct. A further check of these measurements has been made by using the transfer functions to predict system response in new situations. Some of these applications are presented to demonstrate that the models can be used to provide engineering data and to illustrate how the applications are made.

The first application was in the use of the pilot models to confirm the system instability that occurs following a damper failure. The control task was the translation control of a lunar module. Damping stability augmentation was included in the vehicle attitude-control loop and, at a time unknown to the pilot, this augmentation was removed so that a damper failure was simulated. The situation is illustrated in the block diagram of figure 12, where the switch shown in the inner loop was used to simulate the damper failure. When human subjects were presented with this type of damper failure during a 1000-foot (305-meter) translation, as presented with a simplified simulator, the pilot-vehicle system became unstable. An example time history is shown in figure 13. A divergent oscillation occurred after the damper failure, and the divergence continued for approximately 15 seconds.

For the purpose of applying pilot models to an analysis of this situation, it was assumed that the pilot would continue, for some length of time after damper failure, controlling with the same transfer function that he had been using before failure. The system was initially stable, of course, with system characteristics similar to those presented in the previous section on multiloop control tasks. When the inner-loop-vehicle transfer function was changed from that representing a vehicle with damping augmentation  $\frac{K}{s(s + 0.5)}$  to one with no damping  $K/s^2$ , the computed system characteristics indicated an unstable attitude mode of motion. Further, when the inner-loop pilot model was then changed to correspond to measured pilot response with a vehicle with no damping, the system again became stable.

The fact that analysis made by using the pilot models does confirm the changes from stable to unstable system response noted in simulator experiments with human subjects shows that the models are correct and can be used in engineering analyses.

### Langley Lunar Landing Research Facility

This section describes the application of pilot models to the design of a large, full-scale, simulator to be used in the study of lunar-landing problems. The simulator was designed to support 5/6 of the weight of the vehicle by means of an overhead cable, thus simulating lunar gravity. It was necessary to keep the cable directly over the vehicle in order to simulate lunar gravity properly. This simulation was to be accomplished by use of a servomechanism to drive an overhead bridge in such a way that the cable angle would always be controlled to zero. It was in the design study of this overhead drive system that the pilot models were used. The block diagram of the system (fig. 14) shows the multiloop translation-control system mentioned previously along with an additional block representing the servo drive mechanism which would be present in the simulator.

Initial studies of the drive system by itself indicated that it could be adjusted to have an oscillatory response which would have either a poorly damped 2.5-second period or a well-damped 4-second period. The question that needed to be answered was whether these characteristics would be in a range that would affect the response of the complete man-vehicle-simulator system, and, if so, which would be the better to use.

Accordingly, the response of the complete system, in which models were used for the pilot, was computed for a configuration in which no drive-system dynamics was included and for the two configurations in which the drive system mentioned previously was used. The response to a 200-foot (61-meter) change in position command is shown in figure 15. Using the pilot-vehicle combination response as a standard for comparison, it can be seen that both drive system configurations do affect the response of the system, and that the high-gain system (the 2.5-second period characteristic system) affects the response the least. From these results it was concluded that the drive system should be adjusted to have as high a frequency as possible, and that, even so, the simulator would be slightly more difficult to control than the actual vehicle.

When the simulator was put into operation, the results of the design computations were checked by making test runs with each of the two drive system characteristics. The experiments confirmed the computations in that the response with the low-gain system showed a clear deterioration in damping of the attitude mode of motion, and the pilots reported that the system was definitely more difficult to control than the high-gain system.

## Kinesthetic Control

Another method of control for which it was desired to obtain some insight is that of kinesthetic control. With this method the operator controls vehicle attitude by shifting his center of gravity. Usually, the vehicles considered as candidates for this type of control are very small, and the acceleration of the operator, as he moves about, reacts with the vehicle in a manner that could be significant. Thus, the system has many additional coupling terms that are not present in a conventional control system. Therefore, an analysis was made by using pilot models to determine the effects of these additional coupling terms.

Since the system does have these additional coupling terms, it is much more convenient to describe the system by using equations of motion rather than transfer functions. In this type of description the pilot transfer function is split up, with the numerator being included in the command equation and the denominator being included in the control equation. The equations are, then

Vehicle equations:

$$(I_V + I_P + m_P h^2) \ddot{\theta}_V + (I_P + m_P h^2) \ddot{\theta}_P + m_P h \ddot{x} = m_P g h (\theta_P + \theta_V)$$

$$m_P h \ddot{\theta}_V + m_P h \ddot{\theta}_P + (m_P + m_V) \ddot{x} = T \theta_V$$

Control equation:

$$(I_P + m_P h^2) \ddot{\theta}_V + (I_P + m_P h^2) \ddot{\theta}_P + m_P h \ddot{x} = m_P g h (\theta_P + \theta_V) + \tau_1 (\theta_{P,c} - \theta_P) + \tau_2 \dot{\theta}_P$$

Command equation:

$$\theta_{P,c} = K_1 (\theta_{V,c} - \theta_V) + K_2 (\dot{\theta}_{V,c} - \dot{\theta}_V)$$

The variables are defined in figure 16, along with a block diagram of the system. The outer-loop pilot model, which is not included in the system equations presented above, is the same as mentioned in the section "Langley Lunar Landing Research Facility."

As the first step in determining the gains of the pilot model, the gains  $\tau_1$  and  $\tau_2$  were adjusted to provide the proper control response characteristics; that is, a frequency of 10 radians per second and a damping ratio of 1.0. These values were taken as being representative values for control response when the vehicle is of the acceleration type  $K/s^2$ . The adjustment was made by using a single degree of freedom in control-deflection

response to control-deflection command. In this particular case, the unstable nature of the controller (the inverted pendulum configuration of the pilot) was taken into account. This state gain  $\tau_1$  was made large enough to give the controller a stable characteristic with a frequency of 10 radians per second. Then these controller gains were used in the complete, coupled system to determine the characteristics of the system response to a commanded control deflection. It was found that the control response characteristics were improved by the coupling terms. The frequency increased to 15 radians per second, and the damping ratio increased to 1.4.

Next, the gains  $K_1$  and  $K_2$  were adjusted to provide the proper pitch-angle response (a frequency of 1.0 radian per second and a damping ratio of 0.3, as has been shown to be typical for an inner attitude loop in a multiloop control task). Again, these gains were established by using a single-degree-of-freedom response to a pitch-angle command. When these gains were combined with the complete, coupled system, the pitch-angle response was degraded. The frequency dropped to 0.78 radian per second, and, more significant, the damping ratio dropped to 0.16. When the outer loop was closed around this pitch-angle system, the multiloop system became unstable. These results indicate that the kinesthetic control system will be more difficult for a pilot than the conventional type of system.

Kinesthetic control also suffers from a rather severe restriction on maximum control power. The pilot can shift his center of gravity only so far – any further and he will topple over. Use of a computer to solve the nonlinear equations also showed that this limitation in control power would also lead to system instability. Therefore, this factor adds an additional restriction to the potential application of kinesthetic control.

## REFERENCES

1. Adams, James J.; and Bergeron, Hugh P.: Measured Variation in the Transfer Function of a Human Pilot in Single-Axis Tasks. NASA TN D-1952, 1963.
2. Adams, James J.; Bergeron, Hugh P.; and Hurt, George J., Jr.: Human Transfer Functions in Multi-Axis and Multi-Loop Control Systems. NASA TN D-3305, 1966.

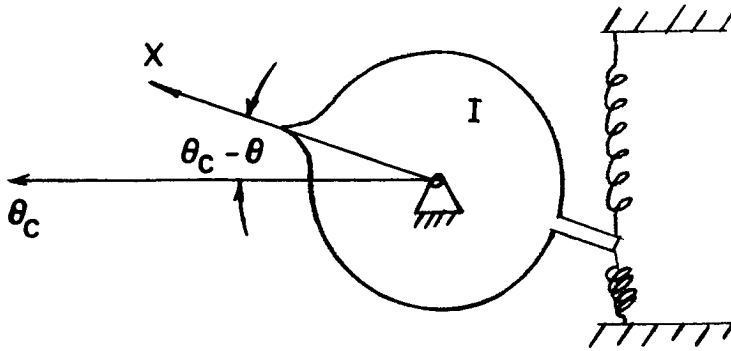


Figure 1.- Spring-inertia system.

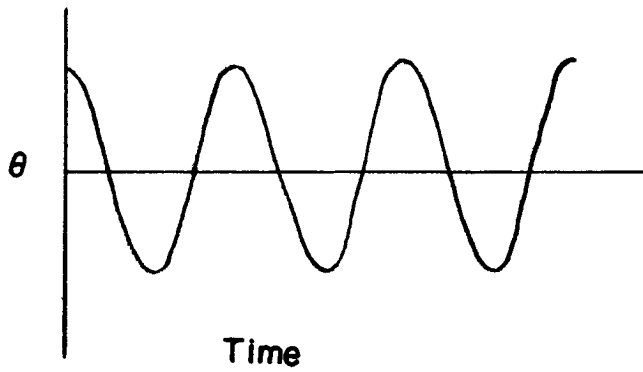


Figure 2.- Response of spring-inertia system.

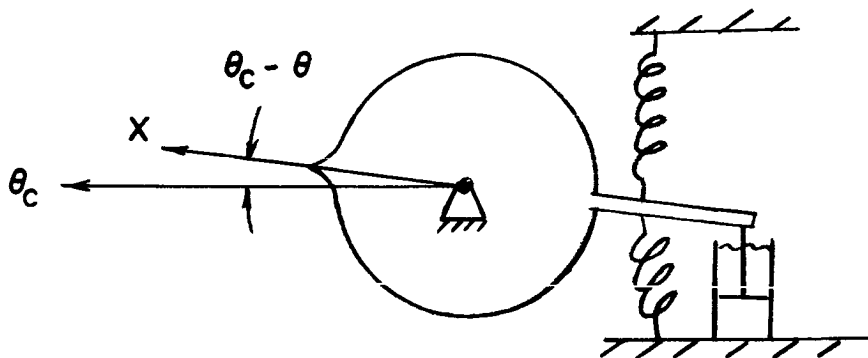


Figure 3.- Spring-dashpot inertia system.



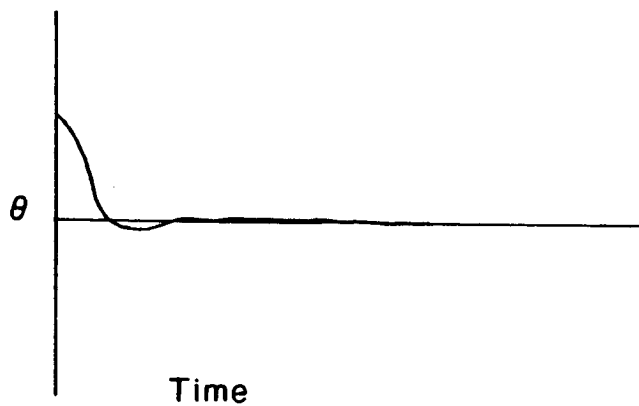


Figure 4.- Response of spring-dashpot inertia system.

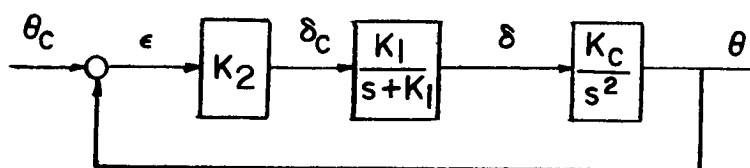


Figure 5.- Block diagram of example system.

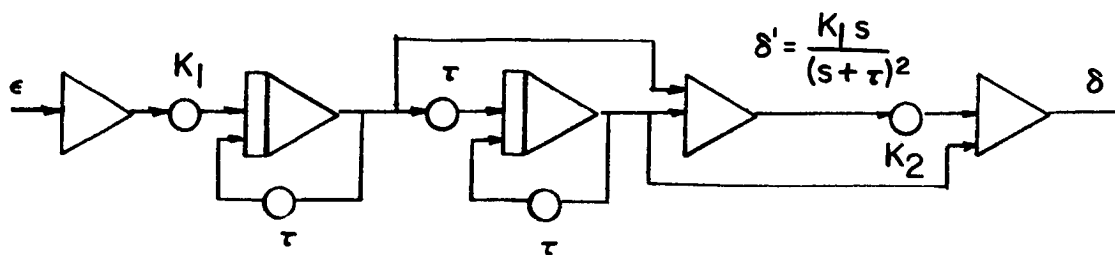


Figure 6.- Analog-computer diagram of pilot model.

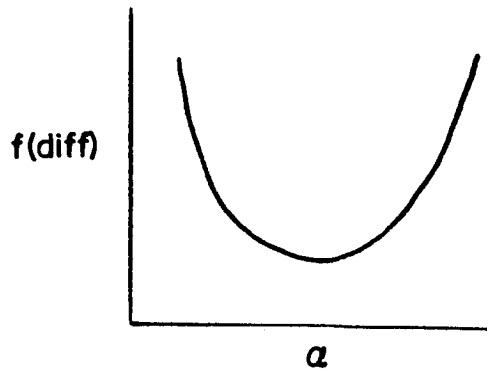


Figure 7.- Variation of  $f(\text{diff})$  with  $\alpha$ .

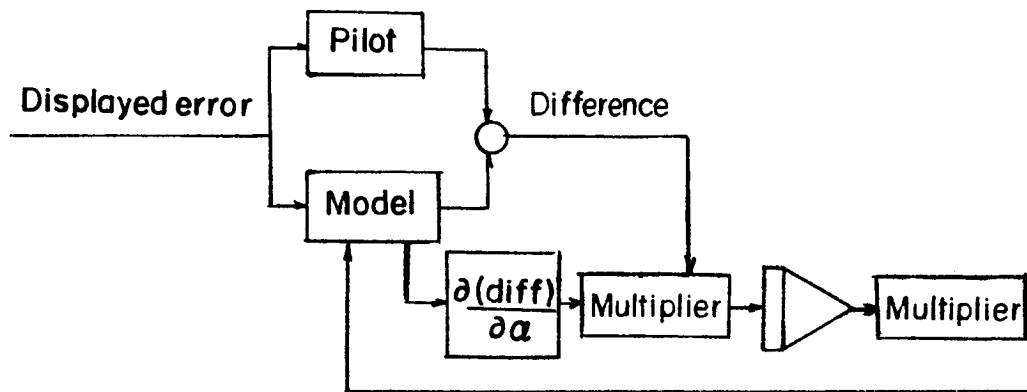


Figure 8.- Diagram of model-gain-adjustment loops.

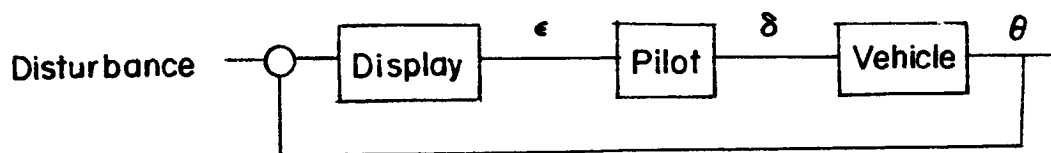


Figure 9.- Diagram of compensatory-tracking task.

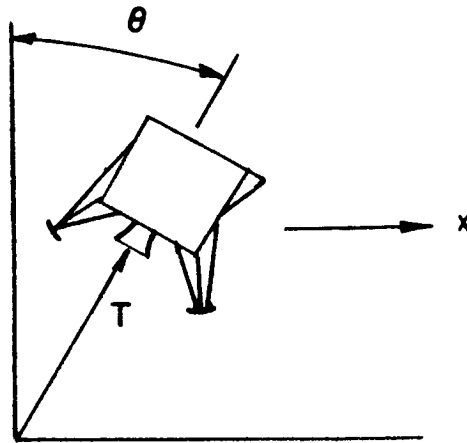


Figure 10.- Multiloop control task variables.

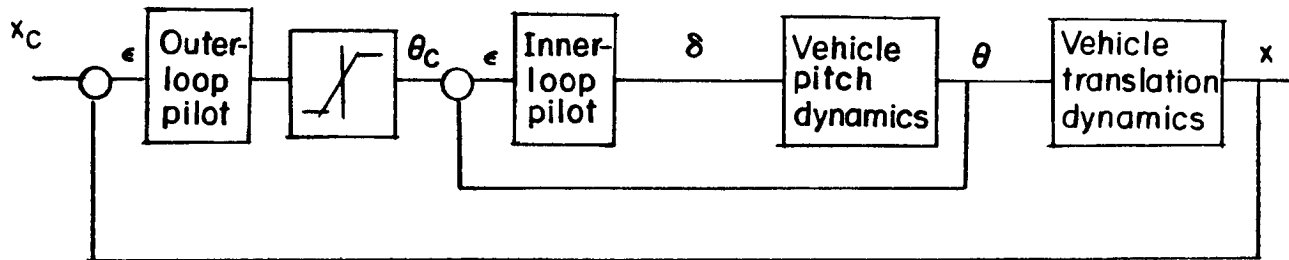


Figure 11.- Block diagram of multiloop control task.

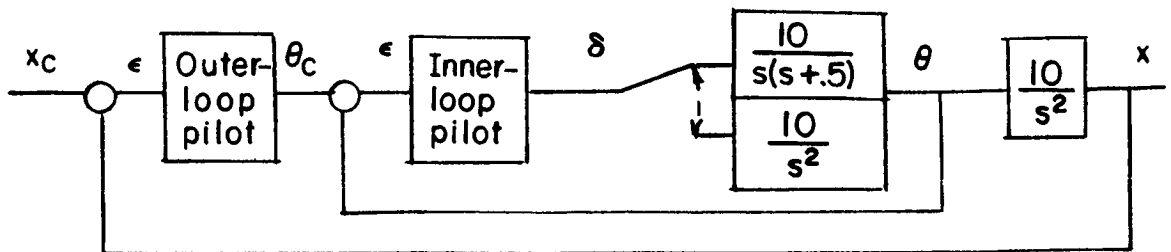


Figure 12.- Diagram of damper failure problem.

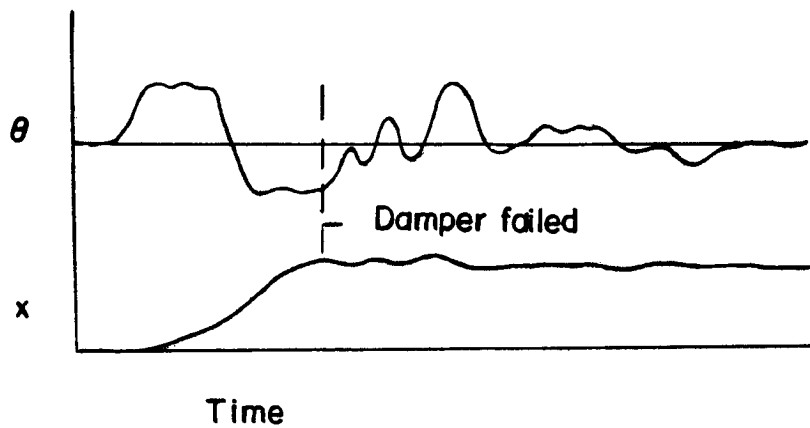


Figure 13.- Multiloop control task with unexpected damper failure.

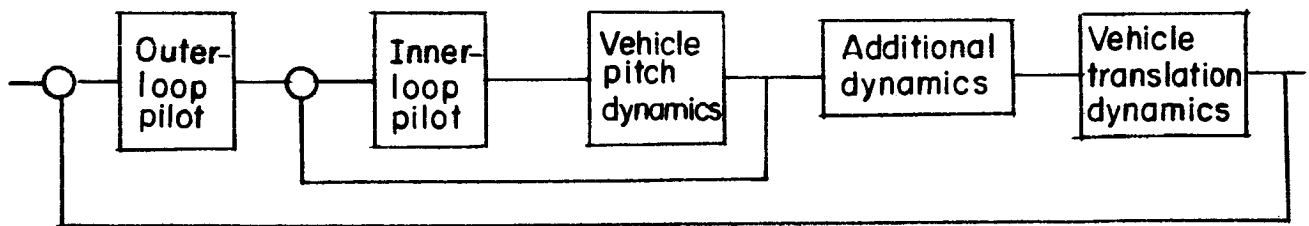
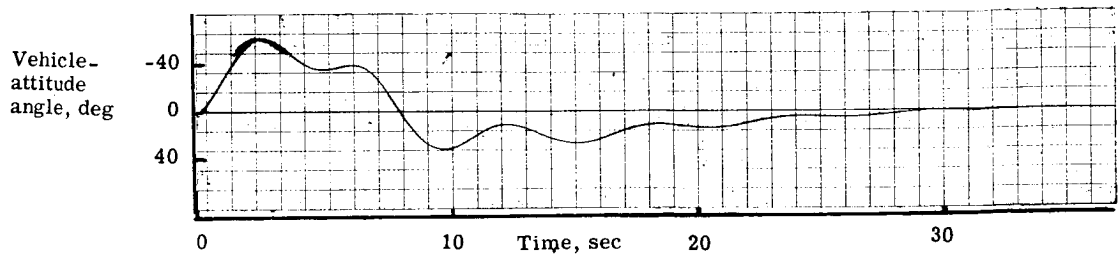
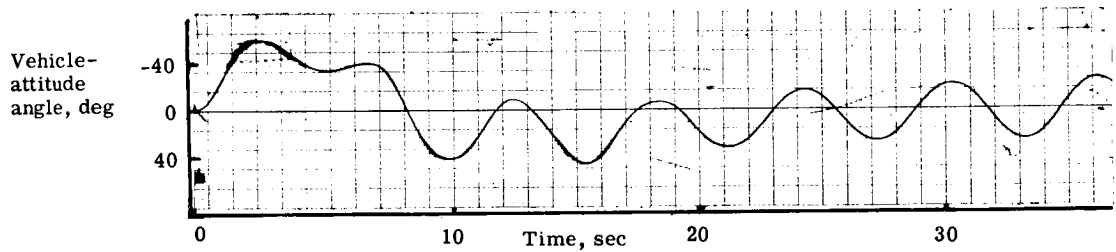


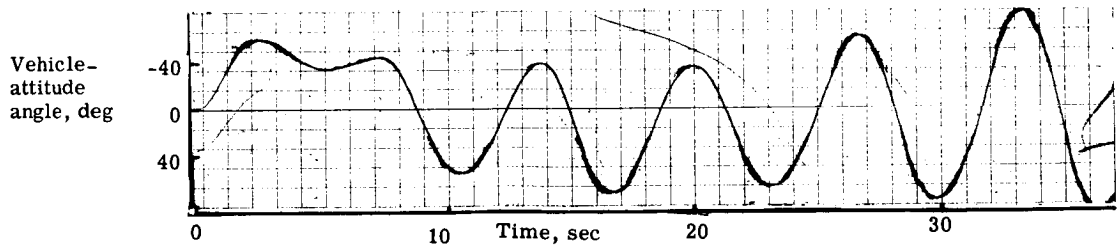
Figure 14.- Diagram of lunar-landing-simulator problem.



(a) Pilot-vehicle combination.



(b) Pilot-vehicle-simulator combination  
with high-gain simulator.



(c) Pilot-vehicle-simulator combination  
with low-gain simulator.

Figure 15.- Calculated vehicle attitude response to a  
200-foot (61-meter) step translation command.

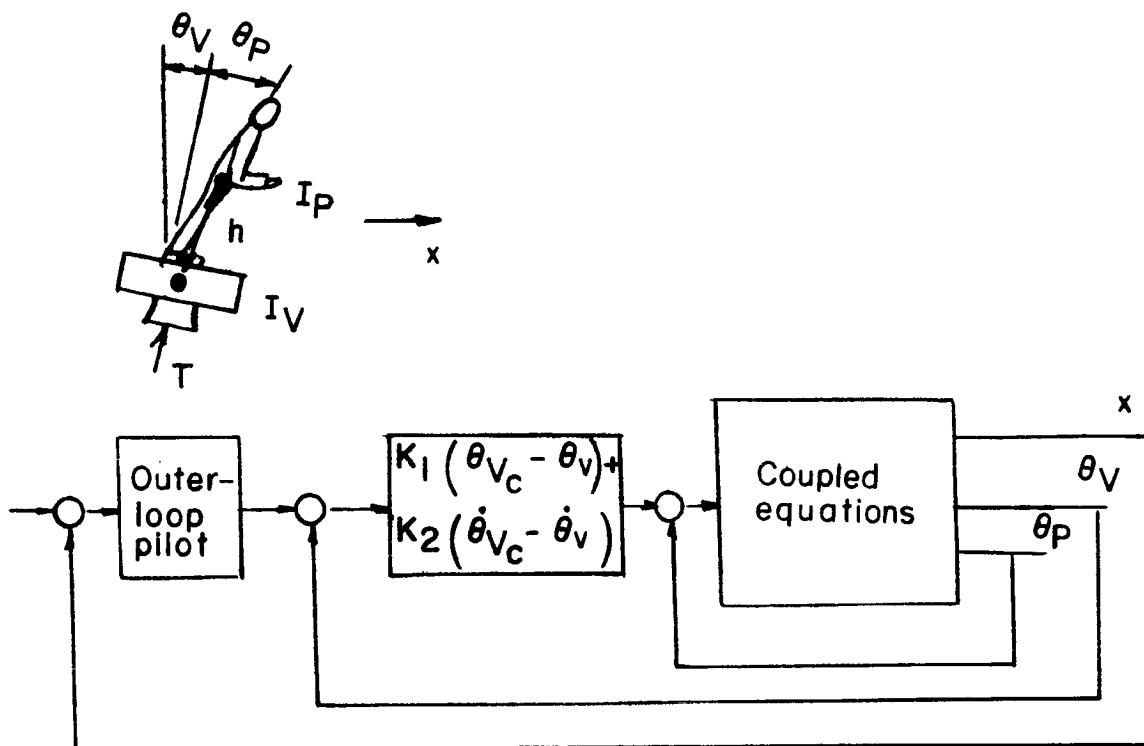


Figure 16.- Kinesthetic-control problem.



# 10. INTRODUCTION TO LINEAR SYSTEM ANALYSIS AND DESIGN BY USE OF STATE VECTOR APPROACH

By Raymond C. Montgomery  
Langley Research Center

## ABSTRACT

This paper is concerned with the analysis and synthesis of linear feedback-control systems by using the state vector approach. The analysis of linear systems is first considered. Here, both autonomous and time-varying solutions of linear systems are studied. In particular the stability of linear time-invariant systems is characterized, as is the stability of periodic time-varying systems (Floquet theory). Next, control in linear systems is studied. First, concepts of the controllability and observability are explained, together with their relation to the determination of state-variable feedback gains and construction of state-variable estimators. Then a practical method for calculation of feedback gains to obtain prespecified control-system characteristics is presented (differential synthesis). The paper is concluded with an example of determination of state-variable feedback gains for a lifting-body entry vehicle and the design of a state estimator for a simple spring-mass system.

## INTRODUCTION

The physical systems which are dealt with are often described in the form of a differential equation

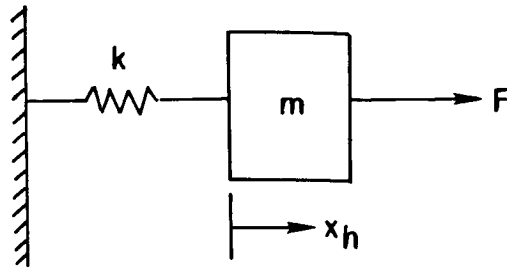
$$\dot{\mathbf{x}} = \mathbf{f}(\mathbf{x}, \mathbf{u})$$

with time  $t$  as the independent variable where  $\mathbf{x}$  is an  $n$ -dimensional state vector,  $\mathbf{u}$  is an  $m$ -dimensional control vector, and  $\mathbf{f}(\mathbf{x}, \mathbf{u})$  is an  $n$ -dimensional vector function of  $\mathbf{x}$  and  $\mathbf{u}$ . In this section a superscript  $t$  will imply the transpose of a vector or matrix. As used herein, "state" means a set of quantities related to the system such that if it is known at any instant, then the behavior of the system is determined as a functional of the control vector  $\mathbf{u}(t)$  alone. In many cases these differential equations are either linear in  $\mathbf{x}$  and  $\mathbf{u}$  or can be approximated by a set of linear differential equations. In such cases the governing equations of motion of the system can be written in the form

$$\dot{\mathbf{x}} = \mathbf{A}\mathbf{x} + \mathbf{B}\mathbf{u} \quad (\mathbf{x}(0) = \mathbf{x}^0) \quad (1)$$



As an example of the state vector formulation of a problem consider the harmonic oscillator shown in the following sketch:



The equation of motion for this system is

$$\ddot{x}_h + \frac{k}{m} x_h = \frac{F}{m}$$

An appropriate state vector representation of this system can be made with  $x_1 = x_h$  and  $x_2 = \dot{x}_h$ . The resulting equation of motion in state vector form of equation (1) is

$$\dot{\mathbf{x}} = \begin{bmatrix} \dot{x}_1 \\ \dot{x}_2 \end{bmatrix} = \begin{bmatrix} 0 & 1 \\ -\frac{k}{m} & 0 \end{bmatrix} \begin{bmatrix} x_1 \\ x_2 \end{bmatrix} + \begin{bmatrix} 0 \\ 1 \end{bmatrix} u$$

where  $u = \frac{F}{m}$  is taken as the control. Note that although the particular state selected is acceptable, it is not the only acceptable one. Indeed any vector  $y = Tx$  where  $T$  is a nonsingular matrix would be a suitable state. However  $y = x_h$  is not a suitable state since initial conditions for both  $x_h$  and  $\dot{x}_h$  are required along with the control input  $u$  so as to define the motion. Other examples of systems which can be written in state vector form according to equation (1) are the longitudinal and lateral linearized equations of motion of aircraft with  $\mathbf{x}^t = (u, \alpha, \theta, q)$  where  $u$  is incremental forward speed,  $\alpha$  is incremental angle of attack,  $\theta$  is incremental pitch attitude, and  $q$  is pitch rate for the longitudinal case and  $\mathbf{x}^t = (\beta, p, r, \phi)$  where  $\beta$  is sideslip angle,  $p$  is roll rate,  $r$  is yaw rate, and  $\phi$  is the bank angle for the lateral case.

This paper is designed to be an introduction to the analysis and design of linear control systems by using the state vector approach. As such even within the framework of state vector methods some important exclusions must be made. One exclusion is the analysis and synthesis of linear systems by using optimal control theory for which reference 1 provides a suitable introduction; another is decoupling design which is the subject of reference 2. These subjects are important and a thorough understanding of them is essential to the control systems engineer; however, they are beyond the scope of an introductory lecture. A major portion of this paper is devoted to linear systems analysis. Some of the fundamental aspects of linear systems analysis in the state variable

form are presented. A more detailed discussion of this subject is included in reference 3. One useful design method presented consists of the synthesis of linear systems with virtual state vector feedback by means of differential synthesis as developed by Montgomery and Hatch (ref. 4) coupled with the state estimator design approach presented by Luenberger (ref. 5).

## SYMBOLS

$A$	differential transition matrix
$A_\phi$	leading coefficient of numerator of transfer function $\phi/\delta_a$
$a$	real scalar
$a(t)$	forcing function
$B$	input matrix
$B(s)$	matrix polynomial in $s$
$B_k$	matrix coefficient of term $s^{n-k}$ in $B(s)$
$b$	input vector
$C$	output matrix
$C_{l_p}$	damping-in-roll coefficient
$C_{l_r}$	rolling-moment coefficient due to yaw rate
$C_{l_\beta}$	rolling-moment coefficient due to sideslip
$C_{l_{\delta_a}}$	aileron rolling-moment coefficient
$C_{l_{\delta_r}}$	rudder rolling-moment coefficient
$C_{n_p}$	yawing-moment coefficient due to roll rate
$C_{n_r}$	damping-in-yaw coefficient

$C_{n\beta}$	static directional-stability coefficient
$C_{n\delta_a}$	aileron yawing-moment coefficient
$C_{n\delta_r}$	rudder yawing-moment coefficient
$C_{y_p}$	lateral-force coefficient due to rolling velocity
$C_{y_r}$	lateral-force coefficient due to yawing velocity
$C_{y\beta}$	lateral-force coefficient due to sideslip
$C_{y\delta_a}$	lateral-force coefficient due to aileron deflection
$C_{y\delta_r}$	lateral-force coefficient due to rudder deflection
$c(\sigma)$	forced variation in transfer-function parameters
$c_{ik}$	coefficient of $k$ th power of $A$ in $A^i$
$c^1$	desired values of transfer-function parameters
$D$	matrix defined by equations (42)
$d(s)$	characteristic polynomial of system
$d_k$	coefficient of $s^{n-k}$ in $d(s)$
$d(i)$	$i$ th column of $D$
$d_A(s)$	augmented system characteristic polynomial
$e^{At}$	solution of equation (11) for constant $A$
$F$	control interconnect matrix
$F_{ij}$	elements of $F$
$f(g)$	function relating gain parameters $g$ to transfer-function parameters $c$ according to $c = f(g)$

$f(t)$	forcing function for method of variation of parameters
$f(x,u)$	vector function of $x$ and $u$
$G$	gain matrix or Gram matrix
$g_i(t)$	time functions defined according to equation (41)
$H$	system output matrix
$I$	commensurable identity matrix
$I_x$	rolling moment of inertia
$I_z$	yawing moment of inertia
$I_{xz}$	product of inertia
$K$	augmented input matrix
$k$	integer or spring constant of harmonic oscillator
$L(X)$	Laplace transform of $X$ as shown in equation (5)
$M$	matrix defined by equations (43)
$m$	mass of harmonic oscillator or dimension of control vector $u$
$m_i$	multiplicity of $\lambda_i$
$n$	dimension of $x$
$\bar{0}$	null matrix
$P$	differential transition matrix for state estimator
$P(c,q)$	function relating flying-quality parameters $q$ to transfer-function parameters $c$ according to $P(c,q) = 0$

$P(t, t_0)$	function defined by equation (36)
$p$	roll rate
$Q$	u-input matrix for state observer
$q$	flying-quality parameters
$R$	y-input matrix for state observer
$r$	yaw rate or radial distance
$S(a)$	hypersphere of radius $a$
$s$	Laplace variable
$T$	transformation matrix or period of periodically time-varying system
$t, t_0, t_1, t_2, t_3$	time
$\text{tr}$	trace
$\text{tr}A$	sum of principle diagonal elements of matrix $A$
$u$	input vector
$u_p$	augmented input vector
$v$	augmented input vector
$v(s)$	Laplace transform of $v$
$W$	weighting matrix
$X(t)$	fundamental matrix of system
$x$	state vector
$\tilde{x}$	estimated state vector

$x_h$	position of harmonic oscillator
$Y_{ij}$	matrices resulting from partial fraction expansion of $\frac{B(s)}{d(s)}$
$y$	system output
$\alpha$	angle of attack
$\alpha_i(t)$	scalar functions defined by equations (40)
$\alpha_{ijk}$	coefficient of $s^{n-k}$ in transfer function $x_i/u_j$
$\beta$	sideslip angle
$\Delta$	scalar step size
$\delta_a$	aileron deflection
$\delta_r$	rudder deflection
$\zeta_\phi$	damping coefficient of numerator quadratic of transfer function $\phi/\delta_a$
$\zeta_d$	damping coefficient of Dutch roll mode
$\theta$	pitch angle
$\lambda_i$	eigenvalues of system
$\mu_i$	unit vector with zero in all but $i$ th position
$\sigma$	dummy variable of integration used in method of conversion to differential form
$\tau$	dummy variable of integration
$\tau_r$	roll-mode time constant
$\tau_s$	spiral-mode time constant

$\tau_z$	time constant of state estimator
$\tau_{\phi_1}, \tau_{\phi_2}$	real zeros of characteristic polynomial for lateral aircraft dynamics other than $-1/\tau_S$ and $-1/\tau_R$
$\Phi(t, t_0)$	state transition matrix
$\tilde{\Phi}(s)$	Laplace transform of $\Phi$
$\phi(t)$	forcing function
$\phi_{ij}$	elements of $\Phi$
$\Psi$	state transition matrix for adjoint system
$\omega$	natural frequency of harmonic oscillator
$\omega_d$	natural frequency of Dutch roll mode
$\omega_\phi$	natural frequency of numerator quadratic of transfer function $\phi/\delta_a$

## LINEAR SYSTEMS ANALYSIS

### Solutions of Autonomous Equations

Now consider representing solutions of equation (1) for the case where the matrices  $A$  and  $B$  are constant in time. Consider first the zero input or homogeneous solutions of equation (1). Owing to the similarity of equation (1) and the scalar equation  $\dot{x} = ax$  the solution of which is known to be of the form  $x = x_0 e^{at}$  where the function  $e^{at}$  is defined by

$$e^{at} = 1 + at + \frac{(at)^2}{2!} + \dots + \frac{(at)^k}{k!} + \dots$$

a solution of equation (1) of the form

$$x(t) = X(t) x(0) = X(t) x^0$$

is sought where

$$X(t) = I + At + \frac{(At)^2}{2!} + \dots + \frac{(At)^k}{k!} + \dots$$

Since the later two series expressions are remarkably similar, the matrix function  $X(t)$  is most often written in literature as  $e^{At}$ . Solutions of equation (1) are therefore sought of the form

$$\left. \begin{aligned} x(t) &= e^{At}x^0 \\ e^{At} &= I + At + \frac{(At)^2}{2!} + \dots + \frac{(At)^k}{k!} + \dots \end{aligned} \right\} \quad (2)$$

First note that the series expression for  $e^{At}$  converges absolutely and uniformly for all finite intervals in  $t$  and its differentiated series

$$\frac{d}{dt}(e^{At}) = A + A(At) + A\frac{(At)^2}{2!} + \dots + A\frac{(At)^k}{k!} + \dots$$

also converges absolutely and uniformly (ref. 5). It follows that  $x(t)$  as defined by equations (2) satisfies

$$\dot{x}(t) = \frac{d}{dt}(e^{At})x^0 = (Ae^{At})x^0 = A(e^{At}x^0) = Ax$$

and also satisfies the condition

$$x(0) = e^{A0}x^0 = Ix^0 = x^0$$

Hence, owing to the uniqueness of the solutions of equation (1) passing through the initial point  $x(0) = x^0$ , equations (2) provide the solution of equation (1) for  $u(t) = 0$ .

For the forced response of  $x(t)$  to  $u(t)$  defined by equation (1), again note that the solution of the scalar equation  $\dot{x} = ax + \phi(t)$  is expressible in the form of

Duhamel's integral  $x(t) = x_0e^{at} + \int_0^t e^{a(t-\tau)}\phi(\tau) d\tau$  and therefore assumes a solution of equation (1) of the form

$$x(t) = e^{At}x^0 + \int_0^t e^{A(t-\tau)}Bu(\tau) d\tau \quad (3)$$

The fact that this assumed form of the solution of equation (1) is the solution may be verified by direct substitution. In the process of substitution equation (3) must be differentiated with respect to  $t$ . This differentiation proceeds as



$$\dot{x}(t) = A e^{At} x^0 + e^{A(t-\tau)} B u(\tau) \Big|_{\tau=t} + \int_0^t A e^{A(t-\tau)} B u(\tau) d\tau$$

so that

$$\dot{x}(t) = A \left[ e^{At} x^0 + \int_0^t e^{A(t-\tau)} B u(\tau) d\tau \right] + B u(t)$$

Since the basic properties of the function  $e^{At}$  are quite useful in the practical application of linear system theory, some of these properties are set down here although their proof is deferred until the discussion on time-varying linear systems. These properties are

$$\left. \begin{aligned} |e^{At}| &= e^{(\text{tr} A)t} \\ e^{At_1} e^{At_2} &= e^{A(t_1+t_2)} \\ (e^{At_1})^{-1} &= e^{-At_1} \end{aligned} \right\} \quad (4)$$

where  $|e^{At}|$  indicates the determinant of the matrix  $e^{At}$  and  $\text{tr} A$  indicates the trace of the matrix  $A$ , that is, the sum of its diagonal elements.

One important use of the properties of  $e^{At}$  is the rapid calculation of the free-motion response of  $x(t)$  defined by the solution to equation (1) where  $u(t) \equiv 0$ . One popular numerical integration scheme is the fourth-order Runge-Kutta numerical integration process. Another useful technique is to express the function  $e^{At}$  in terms of elementary functions (a process to be presented subsequently). Another technique is to use the series definition of  $e^{At}$  and the relation  $x(t) = e^{A(t-t_0)} x^0$  to provide a rapid and accurate method of calculating the free motion. Suppose that the free motion of equation (1) with  $x(0) = x^0$  at the discrete time intervals  $t_k = k\Delta$  ( $k = 1, 2, \dots$ ) is desired. The series definition of  $e^{At}$  can be used to obtain

$$e^{A\Delta} = I + A\Delta + \frac{(A\Delta)^2}{2!} + \dots$$

or a fourth-order Runge-Kutta numerical integration process may be employed on the system

$$\dot{X} = AX \quad (X(0) = I)$$

to obtain the value of  $e^{A\Delta} = X(\Delta)$ . This process need be done only once for

$$\begin{aligned}x(0) &= x^0 \\x(\Delta) &= x^1 = e^{A\Delta}x^0 \\x(2\Delta) &= x^2 = e^{A\Delta}x^1 \\&\vdots \\x(k\Delta) &= x^k = e^{A\Delta}x^{k-1}\end{aligned}$$

Note that these formulas are an exact quadrature and their accuracy depends only on the desired accuracy in obtaining the numerical value of  $e^{A\Delta}$ . For the general forced response, equation (1) must be satisfied with an approximate quadrature. One approximate quadrature which is useful is

$$x[(k+1)\Delta] = e^{A\Delta}x(k\Delta) + (e^{-A\Delta})^{n-1}Bu(k\Delta)\Delta$$

As previously mentioned one method for calculation of the free-motion response of a linear system is to expand  $e^{At}$  in terms of elementary functions. To do this, the Laplace transform is employed. The Laplace transform  $L(X)$  of a function  $X(t)$  defined on the interval  $[0, \infty)$  is defined by

$$L(X) = \int_0^\infty e^{-st}X(t) dt \quad (5)$$

For differentiable functions  $X$

$$L(\dot{X}) = \int_0^\infty e^{-st}\dot{X}(t) dt = -X(0) + sL(X)$$

If  $\Phi(t) \equiv e^{At}$ , then

$$\dot{\Phi}(t) = A\Phi(t)$$

$$\Phi(0) = I$$

By applying the Laplace transform to this last differential equation the function  $\Phi(t)$  must satisfy

$$sL(\Phi) - I = AL(\Phi)$$

so that

$$(sI - A)L(\Phi) = I$$

and hence the Laplace transform  $\tilde{\Phi}(s) = L(\Phi)$  of the function  $\Phi(t)$  is given by

$$\tilde{\Phi}(s) = (sI - A)^{-1}$$

By Cramer's rule the function  $\tilde{\Phi}(s)$  can be written in the form

$$\tilde{\Phi}(s) = \frac{B(s)}{d(s)} \quad (6)$$

where

$$\left. \begin{aligned} B(s) &= B_1 s^{n-1} + B_2 s^{n-2} + \dots + B_n \\ d(s) &= s^n + d_1 s^{n-1} + d_2 s^{n-2} + \dots + d_n \end{aligned} \right\} \quad (7)$$

In equations (7) the quantities  $B_k$  are  $n$ -square matrices and the quantities  $d_k$  are scalars. The procedure for calculating the matrix coefficients  $B_k$  and the polynomial coefficients  $d_k$ , which appear in equations (7) by Cramer's rule, is not computationally efficient. This difficulty is somewhat diminished by a procedure using the Leverrier algorithm

$$\left. \begin{aligned} B_1 &= I & d_1 &= -\text{tr} A \\ B_2 &= IA + d_1 I & d_2 &= -\frac{1}{2} \text{tr}(B_2 A) \\ \vdots & & \vdots & \\ \vdots & & \vdots & \\ B_k &= B_{k-1} A + d_{k-1} I & d_k &= -\frac{1}{k} \text{tr}(B_k A) \\ \vdots & & \vdots & \\ \vdots & & \vdots & \\ B_n &= B_{n-1} A + d_{n-1} I & d_n &= -\frac{1}{n} \text{tr}(B_n A) \\ \bar{0} &= B_n A + d_n I & & \end{aligned} \right\} \quad (8)$$

To prove this algorithm, first note that by the definition of a matrix inverse

$$B(s)(sI - A) = d(s)I = (sI - A)B(s)$$

so that

$$s^n I + \sum_{k=1}^n s^{n-k} d_k I = s \sum_{k=1}^n s^{n-k} B_k - A \sum_{k=1}^n s^{n-k} B_k$$

or

$$s^n I + \sum_{k=1}^n s^{n-k} d_k I = B_1 s^n + \sum_{k=1}^{n-1} s^{n-k} B_{k+1} - A \sum_{k=1}^n s^{n-k} B_k$$

Rearrangement of the last expression yields

$$0 = s^n (I - B_1) + \sum_{k=1}^{n-1} s^{n-k} (-B_{k+1} + B_k A + d_k I) + (d_n I + A B_n) s^0$$

from which the matrix relations on the left-hand side of equations (8) are immediately obtained.

To validate the right-hand side of the algorithm, equations (8), first note that

$$\frac{d}{ds} [d(s)] = \frac{d}{ds} |sI - A|$$

Now, by following the law for differentiation of determinants,  $\frac{d}{ds} |sI - A|$  is the sum of the  $n$ -determinants obtained by successively replacing different columns of the matrix  $(sI - A)$  by the derivative of the column to be replaced with respect to  $s$ . A typical term for the  $k$ th column is

$$\begin{vmatrix} s - a_{11} & -a_{12} & \dots & -a_{1,k-1} & 0 & -a_{1,k+1} & \dots & -a_{1n} \\ -a_{21} & s - a_{22} & \dots & -a_{2,k-1} & 0 & -a_{2,k+1} & \dots & -a_{2n} \\ \vdots & \vdots & & \vdots & \vdots & \vdots & & \vdots \\ -a_{k1} & -a_{k2} & \dots & -a_{k,k-1} & 1 & -a_{k,k+1} & \dots & -a_{kn} \\ \vdots & \vdots & & \vdots & \vdots & \vdots & & \vdots \\ -a_{n1} & -a_{n2} & \dots & -a_{n,k-1} & 0 & -a_{n,k+1} & \dots & s - a_{nn} \end{vmatrix}$$

Now, since  $B(s)$  is the adjoint matrix of  $(sI - A)$  the  $k$ th term is precisely the element  $(k,k)$  of  $B(s)$ . It is therefore concluded that

$$\frac{d}{ds} [d(s)] = \text{tr} B(s) \quad (9)$$

From equation (9)

$$ns^{n-1} + (n-1)d_1s^{n-2} + \dots + d_{n-1} = s^{n-1}\text{tr} B_1 + s^{n-2}\text{tr} B_2 + \dots + \text{tr} B_n$$

identically in  $s$  so that

$$(n-k)d_k = \text{tr} B_{k+1} \quad (k = 1, 2, \dots, n-1)$$

By using the left-hand side of equations (8)

$$B_{k+1} = B_k A + d_k I$$

so that

$$(n-k)d_k = \text{tr} B_k A + d_k \text{tr} I \quad (k = 1, 2, \dots, n-1)$$

The last expression directly yields

$$d_k = -\frac{1}{k} \text{tr} B_k A \quad (k = 1, 2, \dots, n-1)$$

Extension of this last result to include  $k = n$  follows from the trace of the last equation on the left-hand side of equations (8) which yields  $0 = \text{tr} B_n A + nd_n$ . This concludes the proof of the Leverrier algorithm.

In order to expand  $e^{At}$  in terms of elementary functions it is advantageous to reduce the algebraic equation for  $(sI - A)^{-1}$  to the form

$$(sI - A)^{-1} = \frac{B(s)}{d(s)} = \sum_{i=1}^{\sigma} \sum_{j=0}^{m_i-1} \frac{Y_{ij}}{(s - \lambda_i)^{j+1}}$$

where the values of  $\lambda_i$  for  $i = 1, 2, \dots, \sigma$  are the distinct eigenvalues of  $A$ . This expansion can be made by the method of partial fractions and is explained in reference 3.

Once the expansion is made the function  $e^{At}$  is

$$e^{At} = L^{-1}[(sI - A)^{-1}] = \sum_{i=1}^{\sigma} e^{\lambda_i t} \sum_{j=0}^{m_i-1} Y_{ij} \frac{t^j}{j!}$$

### Solutions of Time-Varying Equations

The analysis of time-varying linear systems has risen to importance not only because of its application to optimization techniques (in particular to direct iterative methods) but also because it can account for the large variations in aerodynamic derivatives and control effectivenesses which occur during the execution of large-scale maneuvers of aircraft. An example of this is the transition period during take-off and landing of VTOL vehicles. Only elementary properties of time-varying linear systems are of concern here. Consider then solutions of the system

$$\left. \begin{aligned} \dot{x}(t) &= A(t)x(t) + a(t) \\ x(t_0) &= x^0 \end{aligned} \right\} \quad (10)$$

where  $A(t)$  and  $a(t)$  are defined over the time interval over which the solution  $x(t)$  is required. This interval is presumed to include  $t_0$ .

Owing to the linearity of equations (10) in  $x(t)$ , if a state transition matrix  $\Phi(t, t_0)$  is defined by the expressions

$$\left. \begin{aligned} \frac{\partial \Phi}{\partial t}(t, t_0) &= A(t) \Phi(t, t_0) \\ \Phi(t_0, t_0) &= I \end{aligned} \right\} \quad (11)$$

then the general solution of

$$\frac{dX}{dt}(t) = A(t)X(t) \quad (12)$$

with  $X(t_1)$  given is

$$X(t) = \Phi(t, t_1) X(t_1) \quad (13)$$

If  $X(t)$  is nonsingular at any time, then  $X(t)$  is said to be a fundamental matrix of  $A(t)$ . Equation (13) may be verified by direct substitution noting the fact that  $\Phi(t, t_1)$  satisfies equations (11). Aside from the fact that the state transition matrix satisfies equations (11) and provides the solution to equation (12) by equation (13), this special matrix has other useful properties. Some other properties of  $\Phi(t, t_0)$  are

$$\Phi(t_1, t_2) \Phi(t_2, t_3) = \Phi(t_1, t_3) \quad (14)$$

$$\Phi^{-1}(t_1, t_2) = \Phi(t_2, t_1) \quad (15)$$

$$\frac{\partial}{\partial t} |\Phi(t, t_0)| = \text{tr} A(t) |\Phi(t, t_0)| \quad (16)$$

$$|\Phi(t, t_0)| = e^{\int_{t_0}^t \text{tr} A(\tau) d\tau} \quad (17)$$

Equation (14) follows by defining  $X(t) = \Phi(t, t_3)$  and by using equation (12) in the following way

$$X(t_1) = \Phi(t_1, t_2) X(t_2) = \Phi(t_1, t_2) \Phi(t_2, t_3)$$

so that

$$X(t_1) = \Phi(t_1, t_3) = \Phi(t_1, t_2) \Phi(t_2, t_3)$$

Equation (15) follows from applying equation (14) in the following way

$$I = \Phi(t_1, t_1) = \Phi(t_1, t_2) \Phi(t_2, t_1)$$

and, by using the definition of the matrix inverse equation (16), follows from the application of the formula for differentiation of a determinant as follows

$$\frac{\partial}{\partial t} |\Phi(t, t_0)| = \begin{vmatrix} \frac{\partial \phi_{11}}{\partial t} & \frac{\partial \phi_{12}}{\partial t} & \dots & \frac{\partial \phi_{1n}}{\partial t} \\ \phi_{21} & \phi_{22} & & \\ \vdots & & \ddots & \\ \phi_{n1} & & & \phi_{nn} \end{vmatrix} + \begin{vmatrix} \phi_{11} & \phi_{12} & \dots & \phi_{1n} \\ \frac{\partial \phi_{21}}{\partial t} & \frac{\partial \phi_{22}}{\partial t} & & \\ \vdots & & \ddots & \\ \phi_{n1} & & & \phi_{nn} \end{vmatrix} + \dots + \begin{vmatrix} \phi_{11} & \phi_{12} & \dots & \phi_{1n} \\ \phi_{21} & \phi_{22} & & \\ \vdots & & \ddots & \\ \frac{\partial \phi_{n1}}{\partial t} & & & \frac{\partial \phi_{nn}}{\partial t} \end{vmatrix}$$

Then by using the relations  $\frac{\partial \Phi}{\partial t}(t, t_0) = A(t) \Phi(t, t_0)$ , the first term of the last series can be written as

$$\begin{vmatrix} a_{11}\phi_{11} + a_{12}\phi_{21} + \dots + a_{1n}\phi_{n1} & a_{11}\phi_{12} + a_{12}\phi_{22} + \dots + a_{1n}\phi_{n2} & \dots & a_{11}\phi_{1n} + a_{12}\phi_{2n} + \dots + a_{1n}\phi_{nn} \\ \phi_{21} & \phi_{22} & & \phi_{2n} \\ \vdots & & \ddots & \\ \phi_{n1} & \phi_{n2} & & \phi_{nn} \end{vmatrix}$$

By multiplication of the  $i$ th row by  $a_{1i}$  ( $i \neq 1$ ) and by adding the negative of the result to the first row for all  $i = 2, 3, \dots, n$ , the preceding determinant is reduced to

$$\begin{vmatrix} a_{11}\phi_{11} & a_{11}\phi_{12} & \dots & a_{11}\phi_{1n} \\ \phi_{21} & \phi_{22} & & \\ \vdots & & \ddots & \\ \phi_{n1} & & & \phi_{nn} \end{vmatrix}$$

which is  $a_{11} |\Phi(t, t_0)|$ . By applying this procedure to each term of the series,

$$\frac{\partial}{\partial t} |\Phi(t, t_0)| = a_{11}(t) |\Phi(t, t_0)| + \dots + a_{nn}(t) |\Phi(t, t_0)|$$

is obtained. Hence

$$\frac{\partial}{\partial t} |\Phi(t, t_0)| = \text{tr} A |\Phi(t, t_0)|$$

Equation (17) follows directly from the integration of equation (16) with the initial condition  $|\Phi(t_0, t_0)| = 1$ .

Now consider the forced response of equations (10). A solution of the form

$$x(t) = \Phi(t, t_0) f(t) \quad (18)$$

is assumed where  $f(t)$  is a function to be determined. Substitution of equation (18) into equations (10) yields

$$\frac{\partial \Phi}{\partial t}(t, t_0) f(t) + \Phi(t, t_0) \dot{f}(t) = A(t) \Phi(t, t_0) f(t) + a(t)$$

which reduces to

$$\Phi(t, t_0) \dot{f}(t) = a(t)$$

by using equations (11) and (14). Hence

$$\dot{f}(t) = \Phi(t_0, t) a(t) \quad (19)$$



Integration of equation (19) yields

$$f(t) = f(t_0) + \int_{t_0}^t \Phi(t_0, \tau) a(\tau) d\tau$$

From the initial condition  $x(t_0) = x^0$ , it is seen that  $f(t_0) = x^0$ , and hence the solution of equation (10) is generally of the form

$$x(t) = \Phi(t, t_0) \left[ x^0 + \int_{t_0}^t \Phi(t_0, \tau) a(\tau) d\tau \right] \quad (20)$$

or

$$x(t) = \Phi(t, t_0) x^0 + \int_{t_0}^t \Phi(t, \tau) a(\tau) d\tau \quad (21)$$

The representation of the solutions of equations (10) obtained by using either of the forms of equations (20) or (21) is inconvenient when applied to iterative optimization schemes. This inconvenience is offset by using properties of the system adjoint to equations (10). By defining the adjoint of the state transition matrix  $\Phi(t, t_0)$  of  $A(t)$  for all  $(t, t_0)$  according to the expression

$$\Psi^t(t, t_0) = \Phi^{-1}(t, t_0) \quad (22)$$

where  $\Psi(t, t_0)$  is the adjoint matrix, it is seen that

$$\Psi^t(t, t_0) \Phi(t, t_0) \equiv I$$

so that

$$\frac{\partial \Psi^t}{\partial t}(t, t_0) \Phi(t, t_0) + \Psi^t(t, t_0) \frac{\partial \Phi}{\partial t}(t, t_0) \equiv 0$$

Hence

$$\left[ \frac{\partial \Psi^t}{\partial t}(t, t_0) + \Psi^t(t, t_0) A(t) \right] \Phi(t, t_0) \equiv 0$$

Since  $\Phi(t, t_0)$  is never singular

$$\left. \begin{aligned} \frac{\partial \Psi}{\partial t}(t, t_0) &= -A^t(t) \Psi(t, t_0) \\ \Psi(t_0, t_0) &= I \end{aligned} \right\} \quad (23)$$

Note that if  $x(t)$  is a homogeneous solution of equations (10) and  $y(t)$  satisfies

$$\dot{y}(t) = -A^t(t) y(t) \quad (24)$$

then

$$\frac{d}{dt}(x^t y) = \frac{dx^t}{dt} y + x^t \frac{dy}{dt} = 0$$

so that

$$x^t(t) y(t) = x^t(t_0) y(t_0) \quad (25)$$

Also note that the solutions of equations (20) and (21) for  $x(t)$  can be written, by using the adjoint matrix, as

$$x(t) = \Phi(t, t_0) x(t_0) + \int_{t_0}^t \Psi^t(\tau, t) a(\tau) d\tau \quad (26)$$

Equation (26) is of particular use in trajectory optimization problems using the method of steepest descent.

### Stability of Linear Systems

One of the most important considerations in systems analysis is system stability. Generally stability can be defined as the absence of undesirable behavior. For purposes of analysis, however, this definition is too vague to be useful. There are many definitions of stability which are useful in systems analysis (Lyapunov, Lagrange, orbital, and so forth). Each of the definitions of stability infers certain properties of the system to which it is applied and stability in one sense does not usually infer stability in other senses. In this paper only stability in the sense of Lyapunov is considered.

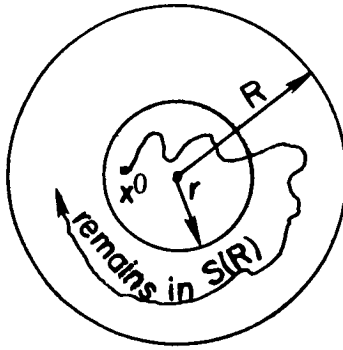
In giving a definition of Lyapunov stability, use is made of the notion of the hypersphere  $S(a)$  of  $n$ -dimensional space defined by

$$S(a) = \left\{ x \mid \|x\| \leq a \right\}$$

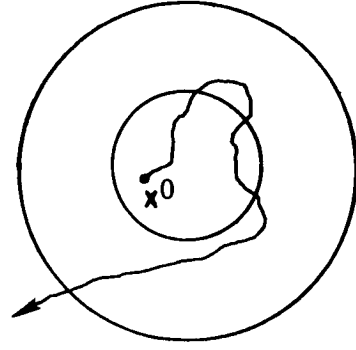
where  $x$  is an  $n$ -dimensional vector and  $\|x\| = \sqrt{x_1^2 + \dots + x_n^2}$ .

A system is said to be stable in the sense of Lyapunov if given  $R > 0$  it can be determined that an  $r > 0$  exists such that all system responses initiating within  $S(r)$

at any time  $t_0$  remain for all  $t > t_0$  within  $S(R)$ . Geometrically this is shown in the following sketches:



Stable



Unstable

If, in addition to being stable, all solutions initiating within  $S(r)$  satisfy  $\lim_{t \rightarrow \infty} x(t) = \bar{0}$  for all  $(t_0, x^0 \in S(r))$ , then the system is said to be asymptotically stable. Any system that is not stable is said to be unstable.

Before proceeding with the characterization of stability a definition of the norm of a matrix is presented. A more detailed discussion of matrix norms is contained in reference 6. Given the  $n \times n$  matrix  $A$ , the norm of  $A$ ,  $\|A\|$ , is defined by

$$\|A\| = \inf \left\{ k \mid \|Ax\| \leq k\|x\| \right\} \quad (27)$$

where  $\inf \{ \}$  implies the infimum. Since  $\|A\alpha x\| = \alpha\|Ax\| \leq k\|\alpha x\| = \alpha k\|x\|$  for  $\alpha > 0$  implies that  $\|Ax\| \leq k\|x\|$ , it is seen that the infimum of equation (27) may be performed over the unit sphere  $\|x\| = 1$ . Hence an equivalent definition of  $\|A\|$  is

$$\|A\| = \sup_{\|x\|=1} \|Ax\| \quad (28)$$

From equation (27) it is also deduced that if  $C = AB$ , then

$$\|C\| \leq \|A\| \cdot \|B\| \quad (29)$$

$$\|Ax\| \leq \|A\| \cdot \|x\| \quad (30)$$

Equation (30) follows immediately from equation (27), whereas equation (29) follows from equation (30) by

$$\|ABx\| \leq \|A\| \cdot \|Bx\| \leq \|A\| \cdot \|B\| \cdot \|x\|$$

Similarly the triangle inequality

$$\|A + B\| \leq \|A\| + \|B\| \quad (31)$$

holds.

Now it can be stated and proved that, for a linear system with state transition matrix  $\Phi(t, t_0)$ , the zero state is stable in the sense of Lyapunov if and only if there exists a constant  $M$  such that  $\|\Phi(t, t_0)\| \leq M$  for all  $(t, t_0)$ . If in addition  $\|\Phi(t, t_0)\| \rightarrow 0$  as  $t \rightarrow \infty$  for all values of  $t_0$ , then the system is asymptotically stable.

Proof:

If  $\|\Phi(t, t_0)\| \leq M$  for all  $(t, t_0)$  and given any  $R > 0$ , then  $r = \frac{R}{M}$  suffices to show that

$$\|x^0\| \leq r \implies \|x(t)\| = \|\Phi(t, t_0)x^0\| \leq \|\Phi(t, t_0)\| \cdot \|x^0\| \leq M \left(\frac{R}{M}\right)$$

Hence the system is stable in the sense of Lyapunov.

Conversely, suppose that the system is stable in the sense of Lyapunov and that  $\|\Phi(t, t_0)\|$  has no upper bound. Since  $\|\Phi(t, t_0)\|$  is not bounded from above, at least one of its elements, for example,  $|\phi_{ij}(t, t_0)|$ , has no upper bound. By selecting an initial condition  $x^0 = \epsilon u^{(j)}$ , where  $\epsilon > 0$  and  $u^{(j)}$  is a unit vector with zero in all but the  $j$ th position, it can be seen that no matter how small  $\epsilon = \|x^0\|$  that  $x_i(t)$  is unbounded. The zero state is hence unstable which is a contradiction. This completes the proof of the statement.

For time-invariant systems,  $\Phi(t, t_0)$  can be expressed in the form

$$e^{At} = \sum_{i=1}^{\sigma} \sum_{j=0}^{m_i-1} t^j e^{\lambda_i t} Y_{ij} \quad (32)$$

Since

$$\|e^{At}\| \leq \sum_{i=1}^{\sigma} \sum_{j=0}^{m_i-1} |t^j e^{\lambda_i t}| \|Y_{ij}\|$$

the stability of time-invariant systems is directly related to the eigenvalues of  $A$ ,  $\lambda_i$ , and the multiplicity  $m_i$  of those eigenvalues. Indeed the system is stable if and only if

all eigenvalues of  $A$  have nonpositive real parts and those with zero real parts are simple eigenvalues of  $A$ . For asymptotic stability all eigenvalues of  $A$  must have negative real parts.

Now consider some aspects of stability for periodic time-varying systems of the form

$$\dot{x} = A(t)x \quad (A(t) = A(t+T)) \quad (33)$$

In literature this stability analysis is called Floquet theory. Let  $\Phi(t, t_0)$  be the state transition matrix for  $A(t)$ :

(1) Note that  $\Phi(t+T, t_0)$  is a fundamental matrix of  $A(t)$ . This is seen by defining  $X(t, t_0) = \Phi(t+T, t_0)$ . Hence,

$$\frac{\partial X}{\partial t}(t, t_0) = \frac{\partial \Phi}{\partial t}(t+T, t_0) = A(t+T) \Phi(t+T, t_0) = A(t) X(t, t_0)$$

and since  $X(t_0, t_0) = \Phi(t_0+T, t_0)$  is nonsingular, it follows that  $X(t, t_0)$  is a fundamental matrix of  $A(t)$ .

(2)  $\Phi(t+T, t_0) = \Phi(t, t_0) \Phi(t_0+T, t_0)$ . This follows since the solution  $X(t)$  of a linear system can be expressed as  $X(t) = \Phi(t, t_0) X(t_0)$ . By using  $\Phi(t+T, t_0)$  as  $X(t)$ , it follows that

$$X(t) \triangleq \Phi(t+T, t_0) = \Phi(t, t_0) X(t_0) = \Phi(t, t_0) \Phi(t_0+T, t_0)$$

Now define a matrix  $B$  as

$$e^{BT} = \Phi(t_0+T, t_0) \quad (34)$$

Then from statement (2)

$$\Phi(t+T, t_0) = \Phi(t, t_0) e^{BT} \quad (35)$$

Consider the function  $P(t, t_0)$  defined by

$$P(t, t_0) = \Phi(t, t_0) e^{-B(t-t_0)} \quad (36)$$

Note that  $P(t, t_0)$  is periodic in  $t$  since

$$P(t+T, t_0) = \Phi(t+T, t_0) e^{-B(t-t_0)-BT} = \left[ \Phi(t+T, t_0) e^{-BT} \right] e^{-(t-t_0)B} = \Phi(t, t_0) e^{-(t-t_0)B}$$

(from eq. (35)). Hence the fundamental matrix  $\Phi(t, t_0)$  can be written in the form

$$\Phi(t, t_0) = P(t, t_0) e^{B(t-t_0)} \quad (37)$$

where  $P(t, t_0)$  is periodic in  $t$  with period  $T$  and where  $B$  is defined by equation (34). Since  $P(t, t_0)$  is periodic, the stability of the system can be related to the stability of the invariant system

$$\dot{y} = By \quad (38)$$

The eigenvalues of  $B$  are called the "characteristic exponents" of  $A(t)$ . Solutions of equations (33) and (38) are related by  $x(t) = P(t, t_0) y(t)$ . Since  $P(t, t_0)$  is nonsingular, the initial condition of  $y$  is given by  $y(t_0) = P(t_0, t_0) x(t_0) = x(t_0)$ .

## CONTROL IN LINEAR SYSTEMS

### Concepts of Controllability and Observability

Before stating the definitions of controllability and observability, some facts concerning time-invariant systems not previously mentioned that have a strong influence on both controllability and observability of time-invariant systems are demonstrated. One of the most useful results of matrix theory is the Caley-Hamilton theorem. From the Leverrier algorithm

$$B_1 = I, \dots, B_k = B_{k-1}A + d_{k-1}I, \dots, \bar{0} = B_nA + d_nI$$

the following sequence is constructed

$$\begin{aligned} \bar{0} &= B_nA + d_nI = (B_{n-1}A + d_{n-1}I)A + d_nI \\ \bar{0} &= B_{n-1}A^2 + d_{n-1}A + d_nI = (B_{n-2}A + d_{n-2}I)A^2 + d_{n-1}A + d_nI \\ &\vdots \\ \bar{0} &= B_{n-k}A^{k+1} + d_{n-k+1}A^k + d_{n-k+2}A^{k-1} + \dots + d_nI \end{aligned}$$

and finally

$$\bar{0} = A^n + d_1 A^{n-1} + \dots + d_n A^0$$

The last result is the famous Caley-Hamilton theorem; that is, a matrix  $A$  satisfies its own characteristic equation. From this theorem it is obvious that any power of  $A$  can be written as a linear combination of the powers of  $A$  between zero and  $n-1$ ; that is,

$$A^i = \sum_{k=0}^{n-1} c_{ik} A^k \quad (i = 0, 1, \dots) \quad (39)$$

It also follows that, since  $e^{At} = \sum_{k=0}^{\infty} A^k \frac{t^k}{k!}$ ,

$$e^{At} = \sum_{i=0}^{n-1} \left( \sum_{j=0}^{\infty} c_{ij}(t) \right) A^i$$

or

$$e^{At} = \sum_{i=0}^{n-1} \alpha_i(t) A^i \quad (40)$$

By using this expression, general solutions of equation (1) can be written as

$$x(t) = e^{At} \left[ x^0 + \int_0^t e^{-A\tau} B u(\tau) d\tau \right]$$

or

$$x(t) = e^{At} \left[ x^0 + \sum_{i=0}^{n-1} A^i B \int_0^t g_i(\tau) u(\tau) d\tau \right] \quad (41)$$

Controllability and observability are now defined. In the following, controllability and observability are used to infer what is called complete controllability and complete observability, respectively, in the technical literature. A more detailed discussion of all aspects of controllability and observability is provided in reference 3. A time-invariant linear system is herein said to be controllable if given an arbitrary  $x^0$  there is a finite time  $T$  and a control  $u(t)$  ( $0 \leq t \leq T$ ) such that  $x(0) = x^0$  and  $x(T) = \bar{0}$ . To define observability, first introduce the notion of system output. The following equations

describe a linear system

$$\left. \begin{aligned} \dot{x} &= Ax + Bu \\ y &= Cx + Du \end{aligned} \right\} \quad (42)$$

where  $x$ ,  $y$ , and  $u$  are vectors of dimensions  $n$ ,  $p$ , and  $m$ , respectively. Here it has been assumed that the state  $x$  is not directly obtainable and knowledge of the system can only be obtained through a measurement of  $y$  and a knowledge of  $u$ . The concept of observability relates to being able to determine the state of the system from measurements of  $y$  and  $u$  over an interval in time. If a system is not observable, then it may undergo internal motion with no input or output and this motion be hence undetectable. A time-invariant system of equations (42) is said to be observable if given the output  $y(t)$  and input  $u(t)$  over the interval  $0 \leq t \leq T$  the initial state  $x(0)$  of the system can be determined uniquely.

In order to characterize controllability of a system, equation (41) and the definition of controllability are used to obtain that in some finite  $T$

$$\bar{0} = e^{AT} \left[ x^0 + \sum_{i=0}^{n-1} A^i B \int_0^T g_i(\tau) u(\tau) d\tau \right]$$

or since  $e^{AT}$  is nonsingular

$$\sum_{i=0}^{n-1} A^i B \int_0^T g_i(\tau) u(\tau) d\tau = -x^0$$

By using the definitions

$$\left. \begin{aligned} M &= [A^0 B, A^1 B, A^2 B, \dots, A^{n-1} B] \\ v &= \int_0^T \begin{bmatrix} g_0(t) u(t) \\ g_1(t) u(t) \\ \vdots \\ g_{n-1}(t) u(t) \end{bmatrix} dt \end{aligned} \right\} \quad (43)$$

it is seen that  $v$  must satisfy

$$Mv = -x^0 \quad (44)$$



for all values of  $x^0$  so that  $M$  must possess  $n$  linearly independent column vectors for the system to be controllable. The condition that  $M$  has  $n$  linearly independent column vectors is both necessary and sufficient for the system to be controllable. To check the system of equations (42) for controllability, determine the rank of  $M$ , and the system is controllable if and only if

$$\text{rank } M = \text{rank} [A^0 B, A^1 B, \dots, A^{n-1} B] = n \quad (45)$$

For observability no generality is lost by considering the system of equations (42) with no input. The resulting output satisfies

$$y(t) = C e^{At} x^0$$

or

$$y(t) = \sum_{k=0}^{n-1} \alpha_k(t) C A^k x^0$$

Hence by denoting  $D \triangleq C^t$  and by letting  $d_{(i)}$  be the  $i$ th column of  $D$

$$\sum_{k=0}^{n-1} (\alpha_i, \alpha_k) d_{(j)}^t A^k x^0 = (\alpha_i, y_j)$$

where the inner product  $(f_1, f_2) \equiv \int_0^T f_1(t) f_2(t) dt$  is used. Since the functions

$\alpha_i(t)$  ( $i = 0, 1, \dots, n-1$ ) are linearly independent, the Gram matrix  $G$ , the matrix  $G$  whose elements  $G_{ij}$  are  $(\alpha_i, \alpha_j)$ , is nonsingular. The last set of equations thus has a solution

$$\begin{bmatrix} d_{(j)}^t A^0 x^0 \\ d_{(j)}^t A^1 x^0 \\ \vdots \\ d_{(j)}^t A^{n-1} x^0 \end{bmatrix} = G^{-1} \begin{bmatrix} (\alpha_0, y_j) \\ (\alpha_1, y_j) \\ \vdots \\ (\alpha_{n-1}, y_j) \end{bmatrix}$$

Note that the quantities on the right-hand side are components of  $x^0$  projected on the vectors  $A^k d_{(j)}$ . Hence this set of vectors must span the vector space of  $x^0$  so that  $x^0$  can be uniquely determined. It follows that observability of the system may be

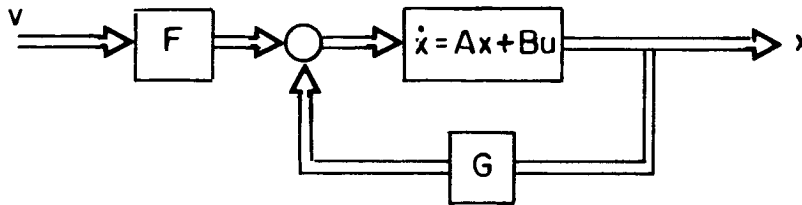
determined by evaluation of the rank of the matrix  $[A^t{}^0D, A^t{}^1D, \dots A^t{}^{n-1}D]$  which must be  $n$  if the system is to be observable.

### Feedback Control

If the system characteristics are unacceptable it is sometimes possible to favorably alter the basic system characteristics using feedback control. If the feedback system is linear

$$u = Gx + Fv \quad (46)$$

as illustrated in the following sketch:



The system characteristics are altered so that they behave according to the modified equation

$$\dot{x} = (A + BG)x + BFv \quad (47)$$

and the system transfer functions are altered according to

$$x(s) = (sI - A - BG)^{-1}BFv(s) \quad (48)$$

For the special case where  $B$  is a vector  $b$  and  $G$  is a vector transposed  $g^t$ , equation (48) is particularly useful since the characteristic of the system can be written

$$\begin{aligned} (sI - A - bg^t) &= (sI - A) \left[ I - (sI - A)^{-1}bg^t \right] \\ &= (sI - A) \left[ I - \frac{B(s)}{d(s)}bg^t \right] \end{aligned}$$

where  $B(s)$  is used as the adjoint of  $(sI - A)$  and  $d(s)$  is used as the characteristic polynomial of  $A$ . From known properties of determinants

$$\begin{aligned}\det [sI - A - bg^t] &= d(s) \det \left[ I - \frac{B(s)}{d(s)} bg^t \right] \\ &= d(s) \left[ 1 - \frac{g^t B(s) b}{d(s)} \right]\end{aligned}$$

where  $\det [M]$  denotes the determinant of a square matrix  $M$  and where the identity

$$\det [I + ab^t] = 1 + b^t a$$

is used. Hence if  $d_A(s)$  is the augmented characteristic polynomial and  $d(s)$  is the unaugmented one, they are related through the expression

$$d_A(s) = d(s) - g^t B(s) b \quad (49)$$

Equating coefficients of powers of  $s$  in equation (49) gives

$$d_{A_k} - d_k = -g^t B_k b \quad (k = 1, 2, \dots, n)$$

or

$$b^t B_k^t g = d_k - d_{A_k}$$

which are  $n$  equations for the  $n$  gains of  $g$ . If the matrix  $\begin{bmatrix} b^t B_1^t \\ b^t B_2^t \\ \vdots \\ b^t B_n^t \end{bmatrix}$  is nonsingular

equation (49) has a unique solution for arbitrary differences  $d_k - d_{A_k}$ . This condition is equivalent to  $\text{rank} [A^0 b, A^1 b, \dots, A^{n-1} b] = n$ . Hence, if the system is controllable, the characteristic roots of the closed-loop system may be arbitrarily specified through state variable feedback.

### State Variable Reconstruction

In many control problems, where it is desirable to utilize state variable feedback, the state is not available and only some restricted output quantity can be measured. In such cases it is possible to design an estimator of the state provided the output is observable. Consider the linear system

$$\left. \begin{array}{l} \dot{x} = Ax + Cu \\ y = Hx \end{array} \right\} \quad (50)$$

The assumption is made that this system is observable through the output  $y$ . Augment the expression  $y = Hx$  with an auxiliary equation  $z = Tx$  such that  $\begin{bmatrix} H \\ T \end{bmatrix}$  is a square matrix. Here  $z$  will be the state of the observer or state estimator. Assume that the state estimator satisfies a linear set of equations

$$\dot{z} = Pz + Qu + Ry \quad (51)$$

(Note that  $u$  and  $y$ , which are available measurements, are used as inputs to this state estimator.) Now see which conditions need be placed on  $P$ ,  $Q$ ,  $R$ , and  $T$  to construct the observer.

The identity  $z = Tx$  must be satisfied for all  $x$  and  $u$ . Also  $\dot{z} \equiv T\dot{x}$  implies that

$$PTx + Qu + RHx = TA x + TCu$$

or

$$(TA - PT - RH)x + (TC - Q)u \equiv 0$$

for all  $(x, u)$ . Hence the observer must satisfy the expressions

$$TA = PT + RH \quad (52)$$

$$Q = TC \quad (53)$$

Generally  $A$ ,  $P$ ,  $RH$ , and  $C$  in equations (52) and (53) are specified and both  $T$  and  $Q$  are determined. Sequentially postmultiplying equation (52) by  $A$  gives

$$TA = PT + RH$$

$$TA^2 = P^2T + RHA + PRH$$

$$TA^3 = P^3T + RHA^2 + PRHA + P^2RH$$

$$\vdots$$

$$TA^n = P^nT + RHA^{n-1} + PRHA^{n-2} + \dots + P^{n-1}RHA^0$$

If the values of  $d_k$  are the coefficients of the power  $n - k$  of  $s$  in the characteristic equation of  $A$ , multiply the equations by these coefficients and collect terms on adding to obtain

$$\begin{aligned} & T(A^n + d_1 A^{n-1} + \dots + d_n A^0) - T d_n A^0 \\ &= (P^n + d_1 P^{n-1} + \dots + d_n P^0)T - P^0 d_n T + \phi(P, R, H, A) \end{aligned}$$

or, since  $A$  satisfies its own characteristic equation,

$$(P^n + d_1 P^{n-1} + \dots + d_n P^0)T = -\phi(P, R, H, A)$$

Hence, determining  $T$  rests on the singularity of the matrix polynomial  $P^n + d_1 P^{n-1} + \dots + d_n P^0$ . If eigenvalues of  $A$  and  $P$  are required to be distinct, then this assures the nonsingularity of the matrix of these coefficients. On the other hand if eigenvalues of  $P$  are allowed to be those of  $A$ , the solution of  $T$  cannot be assured.

### Synthesis of Feedback Control

For a linear system of the form

$$\dot{x} = Ax + Cu \quad (54)$$

the character of the response of the system to control input is specified by a set of transfer functions. The transfer functions are derived by taking the Laplace transform of equation (54) with the initial conditions set to zero; therefore

$$x(s) = (sI - A)^{-1}Cu(s) \quad (55)$$

Hence, the transfer function between the  $i$ th component of  $x$  and the  $j$ th component of  $u$  is of the form

$$\frac{x_i}{u_j} = \frac{\alpha_{ij1}s^{n-1} + \alpha_{ij2}s^{n-2} + \dots + \alpha_{ijn}}{s^n + d_1 s^{n-1} + d_2 s^{n-2} + \dots + d_n} \quad (56)$$

where the coefficients  $d_k$  can be obtained from equations (8) and the coefficients  $\alpha_{ijk}$  can be computed from the expression

$$\alpha_{ijk} = \mu_i^t B_k C \mu_j \quad (57)$$

where  $\mu_i$  and  $\mu_j$  are commensurable unit vectors with zero in all but the  $i$ th and  $j$ th positions, respectively. The pole-zero configuration of the transfer function (eq. (56)) is implicitly determined by the coefficients  $\alpha_{ijk}$  and  $d_k$ .

In order to alter the transfer-function coefficients and thus the pole-zero configuration a feedback control system is introduced as schematically illustrated in figure 1. The system has the form

$$u = Gx + Fu_p \quad (58)$$

where

$F$   $m \times m$  control interconnect matrix

$G$   $m \times n$  linear feedback gain matrix

$u_p$   $m$ -dimensional input vector

When equation (58) is substituted into equation (1) the system becomes

$$\dot{x} = Hx + Ku_p \quad (59)$$

where

$$\left. \begin{aligned} H &\triangleq A + CG \\ K &\triangleq CF \end{aligned} \right\} \quad (60)$$

The system transfer function becomes

$$x(s) = (sI - H)^{-1}Ku_p(s) \quad (61)$$

The transfer function between the component  $x_i$  of  $x$  and the component  $u_{pj}$  of  $u_p$  has the same form as equation (56) where the coefficients  $\alpha_{ijk}$  and  $d_k$  have been obtained by substitution of  $H$  for  $A$  in equations (8) and  $K$  for  $C$  in equation (57).

The problem considered here is to determine a gain matrix  $G$  and an interconnect matrix  $F$  that result in a specific set of coefficients  $\alpha_{ijk}$  and  $d_k$  corresponding to the transfer function of interest  $x_i/u_j$ .

One way to determine the matrices  $G$  and  $F$  is, after substituting equation (9) into equations (4) and (6), to expand equations (8) and (57) in terms of the elements of  $G$  and  $F$  and construct a set of nonlinear algebraic equations of the form

$$f(g) = c \quad (62)$$

Here the transfer-function coefficients  $c$  are

$$c^t = (d_1, \dots, d_n, \alpha_{ij1}, \dots, \alpha_{ijn}) \quad (63)$$

and the vector of independent variables  $g$  is

$$g^t = (g_{11}, \dots, g_{1n}, \dots, g_{mn}, f_{11}, \dots, f_{1m}, \dots, f_{mm}) \quad (64)$$

and  $f(g)$  is the set of nonlinear functions representing the relationship between the elements of  $g$  and  $c$ . Equation (62) must then be solved for a set of gain and interconnect matrix elements that result in a specified  $c = c^1$ .

For a complex set of equations such as those representing aircraft dynamics, equation (62) is difficult to construct and not generally easy to solve. In order to avoid these difficulties the method of solution proposed here is to convert the nonlinear algebraic set of equations into a set of implicit differential equations with known initial conditions.

In order to best explain the method of conversion to differential form for solving nonlinear algebraic equations, consider the scalar equation

$$f(g) = g^2 - 3g + 2 = c \quad (65)$$

The graph of  $f(g)$  against  $g$  satisfying equation (65) is presented in figure 2. Assume that the object is to determine a value of  $g$  that satisfies  $f(g) = 0$ . First, let both  $g$  and  $c$  be functions of a dummy variable  $\sigma$  which varies between 0 and 1; that is,  $c = c(\sigma)$  and  $g = g(\sigma)$ . The basic idea is to choose an arbitrary  $g^0 = g(0)$  and select a variation  $g(\sigma)$  such that it passes through the point  $c(0) = f(g^0)$  and the desired point  $c(1) = 0$ . A typical curve  $c(\sigma)$  satisfying these requirements is the straight line illustrated in figure 3. Here  $c(0)$  was calculated by substituting  $g = g^0 = 0$  into equation (65). Then the variation in  $g(\sigma)$  required by the identity  $f[g(\sigma)] \equiv c(\sigma)$  is determined by using a differential form of equation (65)

$$\frac{\partial f}{\partial g} [g(\sigma)] \frac{dg}{d\sigma}(\sigma) = \frac{dc}{d\sigma}(\sigma)$$

For the particular example using the straight-line variation indicated in figure 3 for  $c(\sigma)$ , the derivative  $dg/d\sigma$  must satisfy

$$\frac{dg}{d\sigma}(\sigma) = \frac{-2}{2g - 3} \quad (66)$$

Equation (66) may be integrated numerically over the interval  $0 \leq \sigma \leq 1$  by using the chosen initial condition  $g(0) = 0$ . The value of  $g$  at  $\sigma = 1$  satisfied  $f[g(1)] = c(1) = 0$  and a solution to the equation  $f(g) = 0$  is obtained.

It is obvious that for this simple example it is easier to solve the nonlinear algebraic equation by using the quadratic formula than to apply a conversion to differential form. However for complex linear systems a conversion to differential form has advantages which are discussed subsequently.

Conversion to differential form can be applied to the synthesis of linear systems by solving equation (62) in a manner similar to that used for the scalar equation (65).

Assume that the object is to select a vector  $c^1$  consisting of desired transfer-function coefficients and determine a gain and interconnect vector  $g^1$  that satisfies  $f(g^1) = c^1$ . Let  $c$  and  $g$  be functions of the dummy variable  $\sigma$  and select  $c(\sigma)$  such that it satisfies  $c(0) = c^0$  where  $c^0 \triangleq f(g^0)$ ,  $c(1) = c^1$ , and is differentiable on the interval  $0 \leq \sigma \leq 1$ . The linear function

$$c(\sigma) = c^0 + \sigma(c^1 - c^0) \quad (67)$$

is an example. The variation in  $g(\sigma)$  required by the identity  $f[g(\sigma)] = c(\sigma)$  must satisfy the equation

$$\text{grad}_g f[g(\sigma)] \frac{dg}{d\sigma}(\sigma) = \frac{dc}{d\sigma}(\sigma) \quad (68)$$

which is equation (62) converted to differential form. Here  $\text{grad}_g f[g(\sigma)] = \frac{\partial f[g(\sigma)]}{\partial g}$ .

Equation (68) is a set of implicit differential equations which are linear in the derivatives  $dg/d\sigma$  and which can usually be integrated numerically over the interval  $0 \leq \sigma \leq 1$  by using the initial conditions  $g(0) = g^0$ . The right-hand side of the equation (that is,  $dc/d\sigma$ ) can be thought of as a forcing function requiring  $g(\sigma)$  to follow some path which preserves the identity  $f[g(\sigma)] = c(\sigma)$ . Therefore the value of  $g(\sigma)$  at  $\sigma = 1$  should satisfy the equation  $f[g(1)] = c^1$  and a gain and interconnect vector  $g^1$  is obtained that results in a vector  $c^1$  of desired transfer-function coefficients. During integration of equation (68) singularities may arise because of the implicit nature of these differential equations. A discussion of these singular situations is now presented.

An advantage of this synthesis technique is that the vector  $c$  and the matrix  $\text{grad}_g f[g(\sigma)]$  can be easily formulated by using Leverrier's algorithm and a differentiated form of this algorithm. Thus the complicated nonlinear algebraic functions  $f(g)$



need not be expanded into scalar form and equation (68) can be constructed as well as solved by using a digital computer. The method of calculating  $\text{grad}_g f[g(\sigma)]$  is now presented.

In order to obtain a suitable forcing function  $dc(\sigma)/d\sigma$ , the function  $c(\sigma)$  must be determined. As previously stated  $c(\sigma)$  must pass through the initial and desired vectors of transfer-function coefficients. The vector of initial coefficients is calculated by assuming some initial gain vector  $g$  which is made up of the elements of the gain matrix  $G$  and the interconnect matrix  $F$ . Usually, suitable initial conditions are  $G = 0$  and  $F = I$  which are equivalent to the open-loop system without control augmentation. However, in some cases when the off diagonal elements of  $F$  are to be changed, their initial values should be nonzero to avoid computational difficulties. The selection of desirable coefficients can be accomplished for the aircraft from established flying-qualities parameters. These parameters are determined by the desired transfer-function pole-zero locations. For other applications similar criteria would have to be obtained to establish a desired value  $c^1$ .

The first function  $c(\sigma)$  to be used was the linear variation of equation (67). It was found that with the resulting forcing function

$$\frac{dc(\sigma)}{d\sigma} = c^1 - c^0 \quad (69)$$

integration errors which occur during integration of equation (68) were not reduced but remained uncorrected. However the effect of integration errors is reduced by modifying equation (69) so that the slope  $dc(\sigma)/d\sigma$  is continuously updated. The modified linear forcing function which accomplishes this updating is

$$\frac{dc}{d\sigma} = \frac{c^1 - f(g)}{1 - \sigma} \quad (70)$$

This function has been used successfully in many applications. This closed-loop forcing function greatly improves the computational accuracy of obtaining the desired  $c^1$  and thus  $g^1$ . Equations (69) and (70) are the only two forcing functions which have been used; however, others may be satisfactory.

In some applications it is desirable to determine the gain vector  $g$  required to specify functions of the transfer-function polynomial coefficients instead of the coefficients directly. These functions can be the parameters obtained when the polynomials are factored. To do this requires a modification of the forcing function as well as the gradient matrix. Consider then the problem of specifying a set of parameters  $q$  that are algebraically related to the elements  $d_k$  and  $\alpha_{ijk}$  of the vector  $c$  by the equation

$$P(c, q) = 0 \quad (71)$$

By using the same concept developed to specify  $c$ , equation (71) is formally differentiated to yield

$$\text{grad}_q P \frac{dq}{d\sigma} + \text{grad}_c P \frac{dc}{d\sigma} = 0$$

Hence from equation (68) a relation between the variations in  $q$  and the gain and inter-connect matrix variations is established

$$\text{grad}_c P \text{grad}_g f \frac{dg}{d\sigma} = -\text{grad}_q P \frac{dq}{d\sigma} \quad (72)$$

In equation (72) the quantity  $dq/d\sigma$  on the right-hand side acts as the forcing term and is selected arbitrarily. Equation (72) is then numerically integrated to obtain the vector  $g(\sigma)$  required to obtain the variation selected  $q(\sigma)$ . The application of equation (72) follows along the same line as that of equation (68).

To construct the matrix  $\text{grad}_g f(g)$  first consider the partial derivatives of  $f(g)$  with respect to the gain matrix elements. Let  $dG$  represent an infinitesimal change in the gain matrix  $G$ . This change causes infinitesimal changes in the matrices  $B_k$  and the coefficients  $d_k$  of equations (8) when  $H$  is substituted for  $A$ . These matrices and coefficients obey the equations

$$\left. \begin{aligned} dB_1 &= 0 \\ dB_k &= (dB_{k-1})H + B_{k-1}CdG + Id(d_{k-1}) \\ d(d_k) &= -\frac{1}{k} \text{trace} \left[ (dB_k)H + B_kCdG \right] \end{aligned} \right\} \begin{aligned} &(d(d_1) = -\text{trace}(CdG)) \\ & \\ &(k = 2, 3, \dots, n) \end{aligned} \quad (73)$$

where  $dB_k$  and  $d(d_k)$  are infinitesimal changes in the matrices  $B_k$  and coefficients  $d_k$ . Equations (73) are linear in the matrix  $dG$  so that by setting all the elements  $dG$  to zero, except  $dG_{pq}$  which is set to unity ( $dG = \mu_p \mu_q^t$ ), the result is that  $d(d_k) = \partial d_k / \partial g_{pq}$  and  $dB_k = \partial B_k / \partial g_{pq}$ . The partial derivatives  $\partial d_k / \partial g_{pq}$  are elements of one column of  $\text{grad}_g f(g)$ . To obtain the elements  $\partial \alpha_{ijk} / \partial g_{pq}$  of the same column the partial derivatives  $\partial B_k / \partial g_{pq}$  are used in a differential form of equation (57)

$$\frac{\partial \alpha_{ijk}}{\partial g_{pq}} = \mu_i^t \frac{\partial B_k}{\partial g_{pq}} K \mu_j \quad (74)$$

Thus by repeated substitution the gradient matrix elements related to  $G$  can be obtained.

Now consider elements of  $\text{grad}_g f(g)$  which are partial derivatives of  $f(g)$  with respect to the interconnect matrix elements  $f_{pq}$ . Note that the coefficients  $d_k$  and the matrices  $B_k$  are independent of the matrix  $K$  so that  $\partial d_k / \partial f_{pq} = 0$  and  $\partial B_k / \partial f_{pq} = 0$ . Hence from equations (57) and (60)

$$\frac{\partial \alpha_{ijk}}{\partial f_{pq}} = \mu_i^t \frac{\partial B_k}{\partial f_{pq}} K \mu_j^t + \mu_i^t B_k C \frac{\partial F}{\partial f_{pq}} \mu_j = \mu_i^t B_k C \mu_p \mu_q^t \mu_j$$

by using

$$\frac{\partial F}{\partial f_{pq}} = \mu_p \mu_q^t$$

Thus

$$\frac{\partial \alpha_{ijk}}{\partial f_{pq}} = \begin{cases} \mu_i^t B_k C \mu_p & (j = q) \\ 0 & (j \neq q) \end{cases} \quad (75)$$

Again by repeated substitution the gradient matrix columns related to  $F$  can be obtained. This entire process can be accomplished by using a digital computer.

During the integration of equation (68) there may be instances in which the determinant of  $\text{grad}_g f[g(\sigma)]$  goes to zero. At these singular situations there is a restricted set of variations in  $c(\sigma)$  that can be realized by variations in  $g(\sigma)$ ; that is, the variations in  $c(\sigma)$  are not completely arbitrary and in some instances the desired  $c^1$  may not be obtainable. A thorough investigation of these singular situations has not been undertaken; however, it is known that they arise when  $g(\sigma)$  passes through a local maxima or minima of the elements of  $f(g)$  or when the poles or zeros of the transfer functions being altered change from pairs of complex roots to pairs of real roots and vice versa. Two techniques have been used to avoid or bypass these singularities. These techniques are applicable only when the number of transfer-function coefficients being varied is less than the total number of gain and interconnect matrix elements available. In order to explain these techniques first assume that only feedback gains can be altered. Further assume that there are eight gains available and only six transfer-function coefficients are to be altered. Conceptually only six gains should be required to alter six coefficients but in order to avoid singularities seven gains are allowed to vary.

The first technique used to avoid singularities is based on minor determinants of  $\text{grad}_g f(g)$ . During each integration step any six of the seven chosen gains are allowed to vary with the seventh remaining constant at its last value. The combination of six gains can change from step to step and is chosen at the beginning of each step by determining

which of the seven possible six-by-six gradient matrices has the largest determinant. By using this procedure, gain combinations which result in gradients with determinants near zero are avoided and thus singularities are avoided. This technique is easily programmed in the computer and is used for all the examples presented in the application section.

The second technique used to avoid singularities utilizes optimum methods to calculate  $dg(\sigma)/d\sigma$ . The performance index

$$\left[ \frac{dg^t(\sigma)}{d\sigma} \right] \frac{W}{2} \left[ \frac{dg(\sigma)}{d\sigma} \right]$$

is minimized subject to the constraint of equation (68). By applying basic optimization techniques

$$\frac{dg}{d\sigma}(\sigma) = W^{-1} \left[ \text{grad}_g f(g) \right]^t \left\{ \text{grad}_g f(g) W^{-1} \left[ \text{grad}_g f(g) \right]^t \right\}^{-1} \frac{dc}{d\sigma}(\sigma)$$

Here all seven of the chosen gains vary during each integration step but the weighting matrix  $W$  can be used to place more or less emphasis on a particular gain. This technique has been used successfully in all applications attempted.

It should be noted that the solutions for  $g$  obtained by this synthesis technique are not unique as illustrated by the example of figure 2. The result of integrating equation (66) with the initial condition  $g(0) = 0$  leads to the solution  $g(1) = 1$ . However the initial condition  $g(0) = 3$  is also appropriate for equation (66), but it leads to the result  $g(1) = 2$ . The two techniques used to bypass singularities also have nonunique results. In these cases, however, the solution obtained represents only one of a complete family of possible solutions.

#### An Illustrative Example of Gain Determination

The differential synthesis technique developed in the preceding section was applied to determining feedback gains and control interconnect ratios to obtain various pole-zero configurations for the transfer functions related to the lateral response of a lifting-body entry vehicle. A flight condition at a Mach number of 1.8, an altitude of 60 000 feet (18.288 kilometers), and an angle of attack of  $15^\circ$  was used in this study. Table I contains the vehicle configuration and aerodynamic data used. The linearized aircraft lateral equations of motion used can be found in reference 7 and were formulated according to equation (1) with

$$x^t \triangleq (x_1, x_2, x_3, x_4) = (p, \phi, r, \beta)$$

and

$$u^t \triangleq (u_1, u_2) = (\delta_a, \delta_r)$$

One of the important indicators of the quality of lateral response is the bank angle to aileron transfer function. Flight and simulator experience has shown that seven flying-quality parameters in this transfer function influence pilot opinion of lateral response. These are  $A_\phi$ ,  $\zeta_\phi$ ,  $\omega_\phi$ ,  $\tau_s$ ,  $\tau_r$ ,  $\zeta_d$ , and  $\omega_d$  which appear in the bank angle to aileron transfer function

$$\frac{\phi}{\delta_a} = \frac{A_\phi (s^2 + 2\zeta_\phi \omega_\phi s + \omega_\phi^2)}{\left(s + \frac{1}{\tau_s}\right) \left(s + \frac{1}{\tau_r}\right) (s^2 + 2\zeta_d \omega_d s + \omega_d^2)} \quad (76)$$

When written in the form of equation (56), equation (76) is

$$\frac{\phi}{\delta_a} = \frac{x_2}{u_1} = \frac{\alpha_{212}s^2 + \alpha_{213}s + \alpha_{214}}{s^4 + d_1s^3 + d_2s^2 + d_3s + d_4} \quad (77)$$

If the flying-quality parameters are unsatisfactory, the coefficients  $d_k$  and  $\alpha_{ijk}$  can be adjusted so that desired flying-quality parameters are obtained. Desirable flying-quality parameters for the transfer function  $\phi/\delta_a$  were selected from information contained in references 8 and 9 which indicate that pole-zero cancellation is desirable in order to obtain good response. Numerical values of the desired flying-quality parameters used in the study as well as those of the basic vehicle are listed in table II. The lateral response of the basic vehicle is unacceptable at this flight condition because of roll reversal indicated by the negative value of  $\omega_\phi^2$ . Also the value of  $1/\tau_r$  indicates that the roll subsidence damping is too low, and the value of  $\zeta_d$  indicates that the Dutch roll mode damping is too low. This basic case has been selected since it demonstrates some design problems that may be encountered.

The objective of this example was to determine a gain matrix  $G$  required to obtain particular values of all the numerator and denominator coefficients except  $\alpha_{212}$  of equation (77) by using a control interconnect matrix of  $F = I$ . Thus six coefficients were changed and the vector  $c$  was of the form

$$c^t = (d_1, d_2, d_3, d_4, \alpha_{213}, \alpha_{214})$$

Since only six coefficients were to be changed, in concept only six gain matrix elements should have been required. However to avoid singularities in the gradient matrix of

equation (68), seven feedback gains were employed. Hence for this example all gain matrix elements were used except  $\delta_r/\phi$  and equation (68) was implemented with

$$g^t = (g_{11}, g_{12}, g_{13}, g_{14}, g_{21}, g_{23}, g_{24})$$

For this example the initial conditions at  $\sigma = 0$  corresponded to the unaugmented aircraft with  $G = 0$  and  $F = I$ . The closed-loop form of the forcing function on the right-hand side of equation (68)

$$\frac{dc}{d\sigma} = \frac{c^1 - f(g)}{1 - \sigma}$$

was used with  $c^1$  taken as the list of desired coefficients contained in table II. Equation (68) was then numerically integrated from  $\sigma = 0$  to  $\sigma = 1$  in steps of 0.1 by using a fourth-order Runge-Kutta integration process. The variation of the coefficients (components of  $c$ ) with  $\sigma$  is illustrated in figure 4 which shows that the selected linear variation in  $c(\sigma)$  with  $\sigma$  was followed very closely by  $f(g)$  and that the components of  $c$  at  $\sigma = 1$  were equal to the components of  $c^1$ . Figure 4 also illustrates the variation of the associated flying-quality parameters with  $\sigma$  that results from the linear variation of the coefficients. Note that at  $\sigma = 0$ , the numerator polynomial has two real zeros  $1/\tau_{\phi_1}$  and  $1/\tau_{\phi_2}$ . As  $\sigma$  increases, the real zeros meet and then break away into a pair of complex zeros at  $\sigma = 0.22$ .

The gain variations that were calculated to establish the coefficient variations of figure 4 are shown in figure 5. From  $\sigma = 0$  to  $\sigma = 0.2$ , six gains were varied and the gain  $\delta_a/r$  was held constant at zero. In the neighborhood of  $\sigma = 0.22$ , a singularity occurred in the gradient matrix because of the change in analytic form of the numerator polynomial and the integration process could not continue holding  $\delta_a/r = 0$ . However this singularity was avoided and the integration step was completed by holding the gain  $\delta_r/p$  constant and allowing the remaining six gains to vary. The numerical integration process may be slightly inaccurate in the neighborhood of this singularity; however, because of the closed-loop programming of the coefficient variations this inaccuracy has little effect on the outcome of the integration process at  $\sigma = 1$ . From  $\sigma = 0.3$  to  $\sigma = 0.7$ , the gain  $\delta_a/r$  was again held constant. Another type of singularity occurred in the neighborhood of  $\sigma = 0.7$ . This singularity was due to the rapidly increasing gain  $\delta_r/p$ . By holding  $\delta_r/p$  constant and allowing the remaining six gains to vary, the integration process was continued to  $\sigma = 1$ . At  $\sigma = 1$ , the gains that yield the desired numerator and denominator coefficients of equation (77) were obtained. Although in this case seven gains were used to change six coefficients, in some cases the additional gain may not be necessary. A Control Data Corporation 6600 series digital computer was used to obtain the results for this case and the run time was 8 seconds.

The time histories of the responses of the aircraft to 5° step aileron inputs presented in figures 6 and 7 clearly illustrate the effect of using a feedback control system. Figure 6 illustrates the response of the basic vehicle, and figure 7 illustrates that of the augmented vehicle. The surging and reversal of the bank-angle response have been corrected; however, there still remains an undesirable steady-state sideslip. By using other combinations of feedback gains it is practically possible to eliminate this undesirable effect.

### An Illustrative Example of State Reconstruction

An illustration of the application of Luenburger's state estimator to feedback control systems design is now presented. Here it is assumed that the state variable feedback gains which yield desired characteristics of the closed-loop system have been obtained by differential synthesis or some other method. A system is designed by using Luenburger's approach to estimate the actual system state, thus allowing use of this estimated state in the feedback loop. The inputs to this state estimator are restricted to allowable system measurements – the actual system output and the state of the estimator.

Consider the problem of designing a feedback control system for the harmonic oscillator discussed in the introduction. The equations of motion of the oscillator are

$$\dot{\mathbf{x}} = \mathbf{A}\mathbf{x} + \mathbf{C}u$$

where

$$\mathbf{A} = \begin{bmatrix} 0 & 1 \\ -\omega^2 & 0 \end{bmatrix}$$

and

$$\mathbf{C} = \begin{bmatrix} 0 \\ 1 \end{bmatrix}$$

with  $\omega^2 = \frac{k}{m}$  and  $u = \frac{F}{m}$ . The predetermined feedback system is

$$u = \mathbf{G}\tilde{\mathbf{x}} + \mathbf{F}u_p$$

where  $\tilde{\mathbf{x}}$  is the estimated state and  $u_p$  is the closed-loop system input. The matrices  $\mathbf{G} = (g_1, g_2)$  and  $\mathbf{F} = f$  are assumed previously determined. As an output of the actual system assume that only the position of the oscillator can be measured; that is,  $y = \mathbf{H}\mathbf{x}$  where  $\mathbf{H} = (1, 0)$ .

The state estimator will be a system similar to that of equation (51) according to

$$\dot{\mathbf{z}} = \mathbf{P}\mathbf{z} + \mathbf{Q}\mathbf{u} + \mathbf{R}y$$

and the estimator's state  $\mathbf{z}$  is related to the estimated state  $\tilde{\mathbf{x}}$  according to

$$\mathbf{z} = \mathbf{T}\mathbf{x}$$

The matrices  $\mathbf{T} = (t_1, t_2)$  and  $\mathbf{Q} = q$  must satisfy equations (52) and (53). These matrix equations yield the following scalar relations that  $\mathbf{T}$  and  $\mathbf{Q}$  must satisfy

$$-\omega^2 t_2 + \frac{1}{\tau_z} t_1 = r$$

$$\frac{1}{\tau_z} t_2 + t_1 = 0$$

$$q = t_2$$

The solution to the last set of equations is

$$\mathbf{T} = t \left( -\frac{1}{\tau_z}, 1 \right)$$

$$\mathbf{Q} = q = t$$

where  $t = \frac{-r}{\omega^2 + \frac{1}{\tau_z^2}}$ . Hence the estimated state of the actual system is given by

$$\tilde{\mathbf{x}} = \begin{bmatrix} \mathbf{H} \\ \mathbf{T} \end{bmatrix}^{-1} \begin{bmatrix} y \\ z \end{bmatrix} = \begin{bmatrix} 1 & 0 \\ \frac{1}{\tau_z} & \frac{1}{t} \end{bmatrix} \begin{bmatrix} y \\ z \end{bmatrix}$$

and the feedback control system is

$$u = \mathbf{G}\tilde{\mathbf{x}} + \mathbf{F}u_p = \left( g_1 + \frac{g_2}{\tau_z} \right) y + \frac{g_2}{t} z + fu_r$$

When this control system is employed in the actual system, the new system has three states – the position and velocity of the oscillator and the state of the estimator. The transfer functions between these three state variables and the control input  $u_p$  are



$$\frac{x_1}{u_p} = \left(s + \frac{1}{\tau_z}\right) \frac{f}{\Delta}$$

$$\frac{x_2}{u_p} = s \left(s + \frac{1}{\tau_z}\right) \frac{f}{\Delta}$$

$$\frac{z}{u_p} = \left(s^2 - \frac{1}{\tau_z^2}\right) \frac{tf}{\Delta}$$

where  $\Delta = \left(s + \frac{1}{\tau_z}\right) \left(s^2 - g_2 s + \omega^2 - g_1\right)$ . Note that the factor  $s + \frac{1}{\tau_z}$  appears in each of these transfer functions as well as in the total-system characteristic polynomial.

## REFERENCES

1. Athans, Michael; and Falb, Peter L.: Optimal Control – An Introduction to the Theory and Its Applications. McGraw-Hill Book Co., Inc., c.1966.
2. Falb, Peter L.; and Wolovich, William A.: Decoupling in the Design and Synthesis of Multivariable Control Systems. NASA TN D-4219, 1967.
3. Zadeh, Lotfi A.; and Desoer, Charles A.: Linear System Theory. The State Space Approach. McGraw-Hill Book Co., Inc., c.1963.
4. Montgomery, Raymond C.; and Hatch, Howard G., Jr.: Application of Differential Synthesis to Design of Multiaxis Stability Augmentation Systems. J. Aircraft, vol. 6, no. 4, July-Aug. 1969, pp. 336-343.
5. Luenberger, David G.: Observing the State of a Linear System. IEEE Trans. Mil. Electron., vol. MIL-8, no. 2, Apr. 1964, pp. 74-80.
6. Householder, A. S.: On Norms of Vectors and Matrices. ORNL 1756, U.S. At. Energy Comm., Sept. 14, 1954.
7. Woodcock, Robert J.; and Drake, Douglas E.: Estimation of Flying Qualities of Piloted Airplanes. AFFDL-TR-65-218, U.S. Air Force, Apr. 1966. (Available from DDC as AD 483 622.)
8. Ashkenas, I. L.: A Consolidation of Lateral-Directional Handling Qualities. AIAA Pap. No. 65-314, July 1965.
9. Taylor, Lawrence W., Jr.; and Iliff, Kenneth W.: Fixed-Base Simulator Pilot Rating Surveys for Predicting Lateral-Directional Handling Qualities and Pilot Rating Variability. NASA TN D-5358, 1969.

TABLE I.- VEHICLE CONFIGURATION AND AERODYNAMIC DATA<sup>a</sup>

Mass, kg . . . . .	4536
$I_x$ , kg-m <sup>2</sup> . . . . .	2318
$I_z$ , kg-m <sup>2</sup> . . . . .	10 301
$I_{xz}$ , kg-m <sup>2</sup> . . . . .	678
Wing span, m . . . . .	4.648
Wing area, m <sup>2</sup> . . . . .	16.722
$C_{l_p}$ . . . . .	-0.15
$C_{l_r}$ . . . . .	0
$C_{l_\beta}$ . . . . .	-0.05
$C_{l_{\delta_a}}$ . . . . .	-0.015
$C_{l_{\delta_r}}$ . . . . .	0.005
$C_{n_p}$ . . . . .	0
$C_{n_r}$ . . . . .	-0.2
$C_{n_\beta}$ . . . . .	0.05
$C_{n_{\delta_a}}$ . . . . .	0.02
$C_{n_{\delta_r}}$ . . . . .	-0.02
$C_{y_p}$ . . . . .	0
$C_{y_r}$ . . . . .	0
$C_{y_\beta}$ . . . . .	-0.8
$C_{y_{\delta_a}}$ . . . . .	0
$C_{y_{\delta_r}}$ . . . . .	0.04

<sup>a</sup>Body-axis aerodynamic coefficients are in radian measure.

TABLE II. - COEFFICIENTS AND FLYING-QUALITY PARAMETERS  
FOR TRANSFER FUNCTION  $\phi/\delta_a$

Coefficients	Basic	Desired	Flying-quality parameters	Basic	Desired
$d_1$ . . . . .	0.57	2.41	$1/\tau_s$ . . . . .	0.013	0.01
$d_2$ . . . . .	11.17	10.37	$1/\tau_r$ . . . . .	0.296	1.5
$d_3$ . . . . .	3.43	13.60	$\zeta_d$ . . . . .	0.039	0.15
$d_4$ . . . . .	0.043	0.14	$\omega_d$ . . . . .	3.33	3.0
$\alpha_{212}$ . . . . .	-7.14	(a)	$A_\phi$ . . . . .	-7.14	(a)
$\alpha_{213}$ . . . . .	-1.32	-6.43	$\zeta_\phi$ . . . . .	(b)	0.15
$\alpha_{214}$ . . . . .	17.89	-64.30	$\omega_\phi$ . . . . .	(b)	3.0
			$\omega_\phi^2/\omega_d^2$ . . . . .	-0.226	1.0

<sup>a</sup>Not specified.

<sup>b</sup>For basic case, numerator quadratic in transfer function  $\phi/\delta_a$  has two real zeros:  $1/\tau_{\phi 1} = 1.68$  and  $1/\tau_{\phi 2} = -1.5$ .

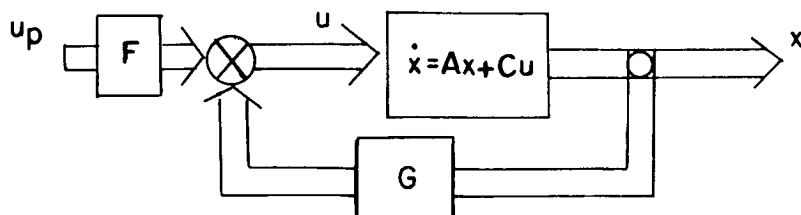


Figure 1.- System block diagram.

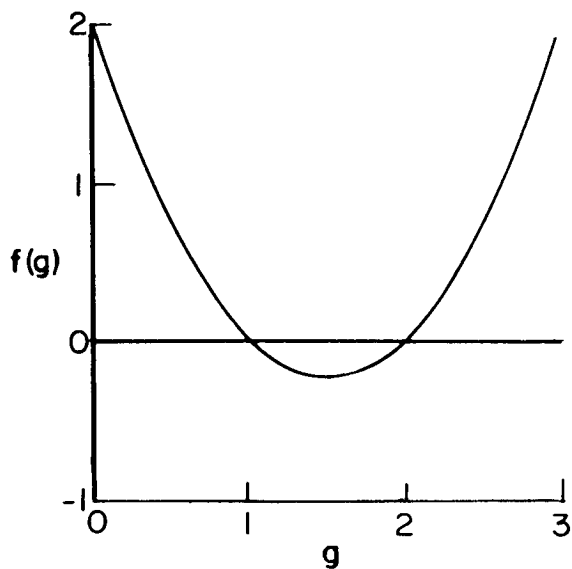


Figure 2.- Graph of scalar function defined by equation (65).

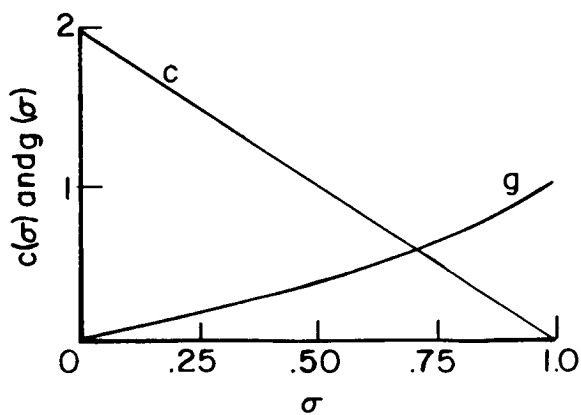


Figure 3.- Graph of selected variation  $c(\sigma)$  and variation  $g(\sigma)$  which result from solution of equation (66).

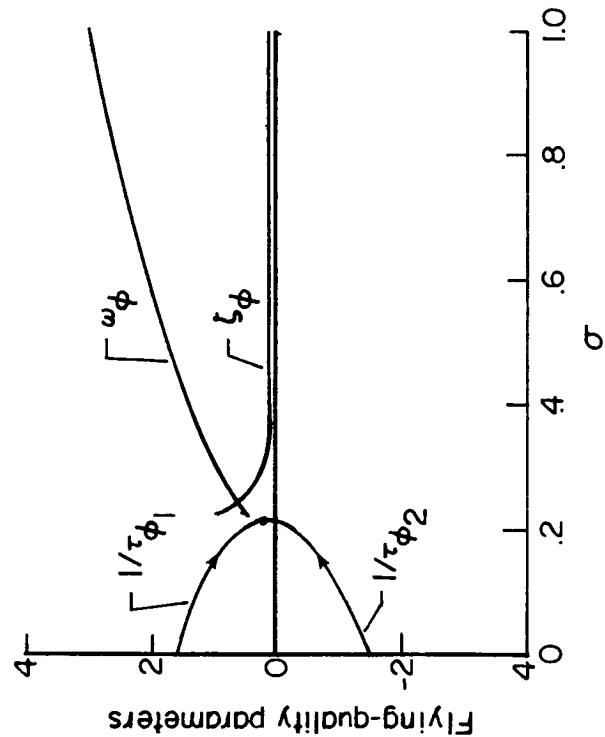
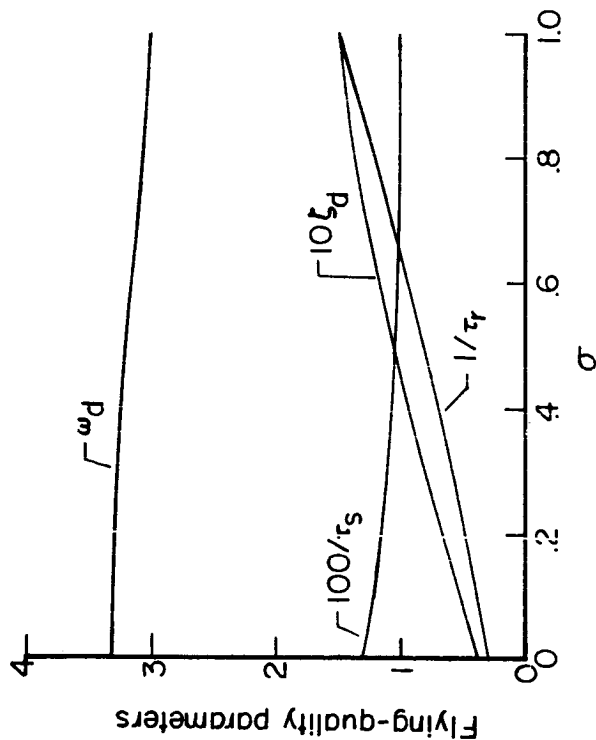
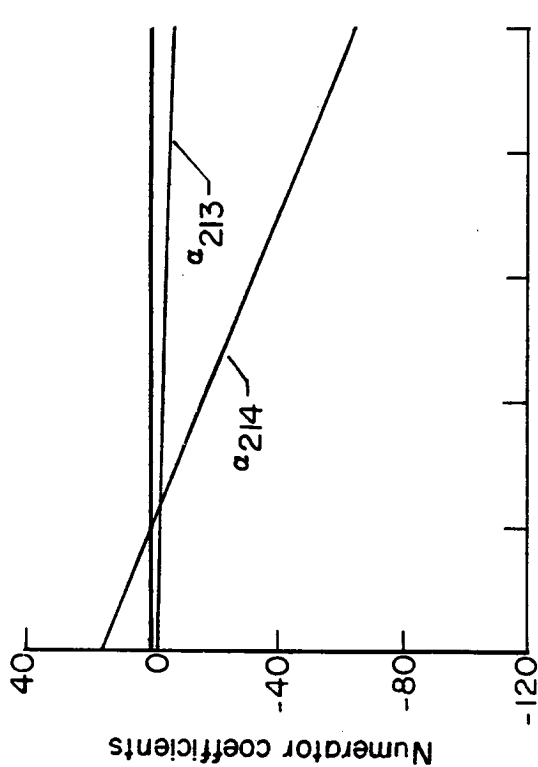
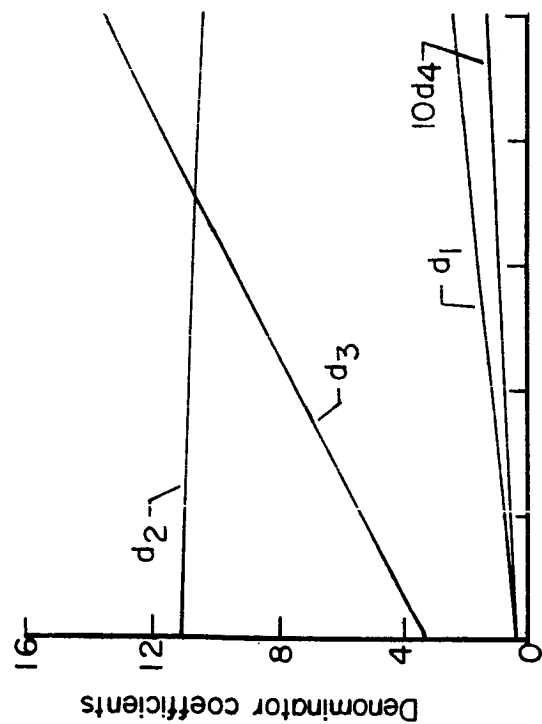
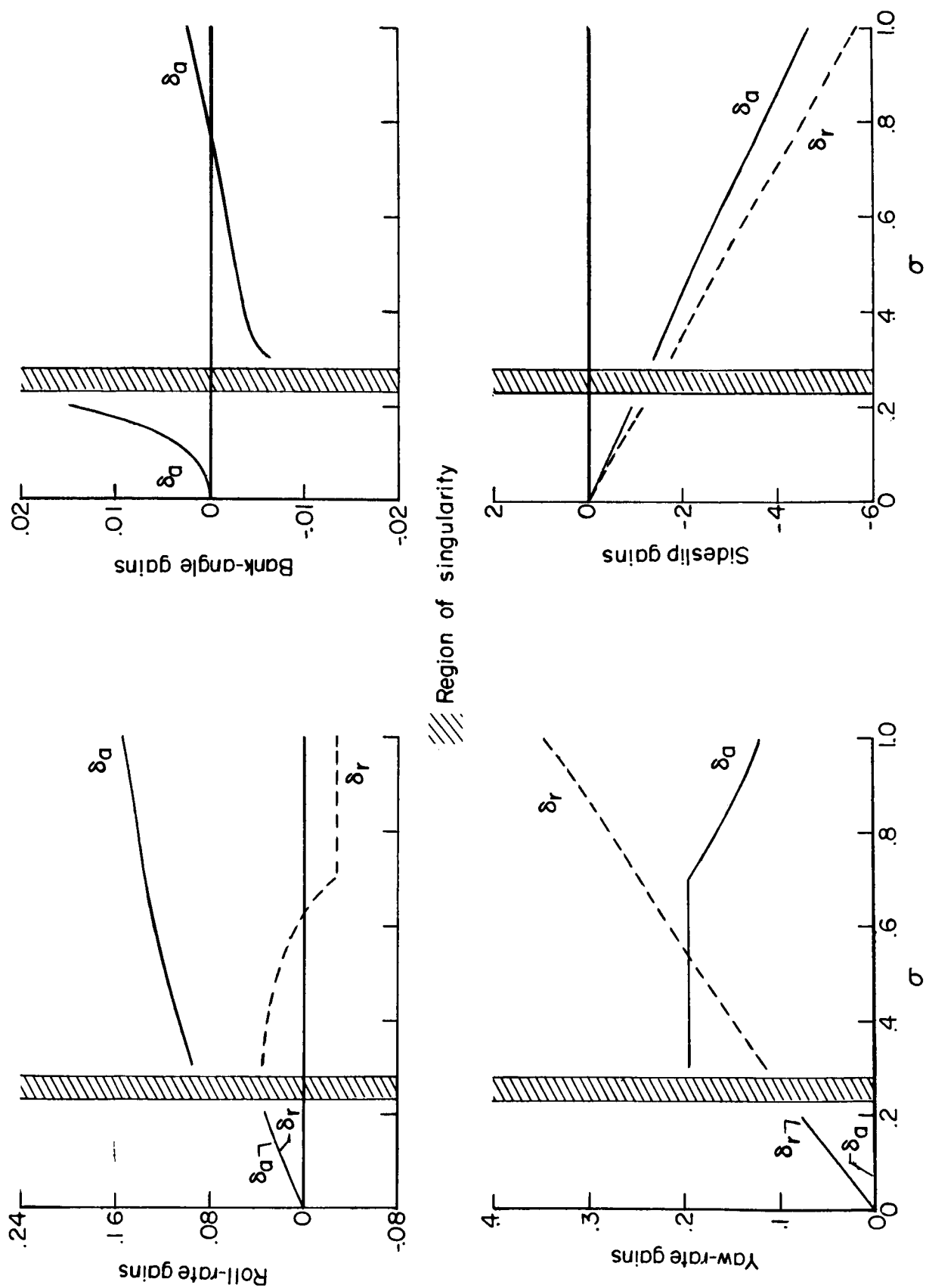


Figure 4.- Variation of transfer-function coefficients  $\phi/\delta_a$  and flying-quality parameters with  $\sigma$ .

Figure 5.- Variation of feedback gains with  $\sigma$ .

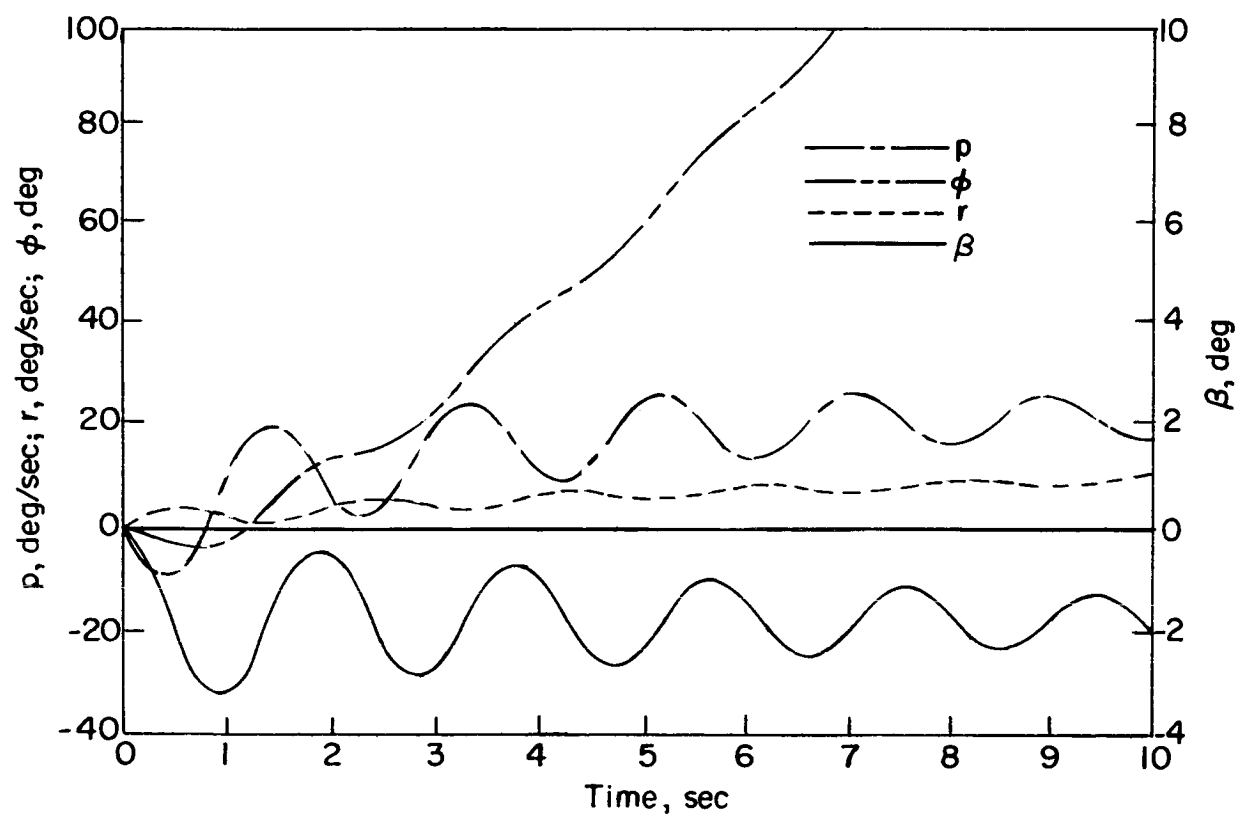


Figure 6.- Time history of response of basic vehicle to 5° step aileron input.



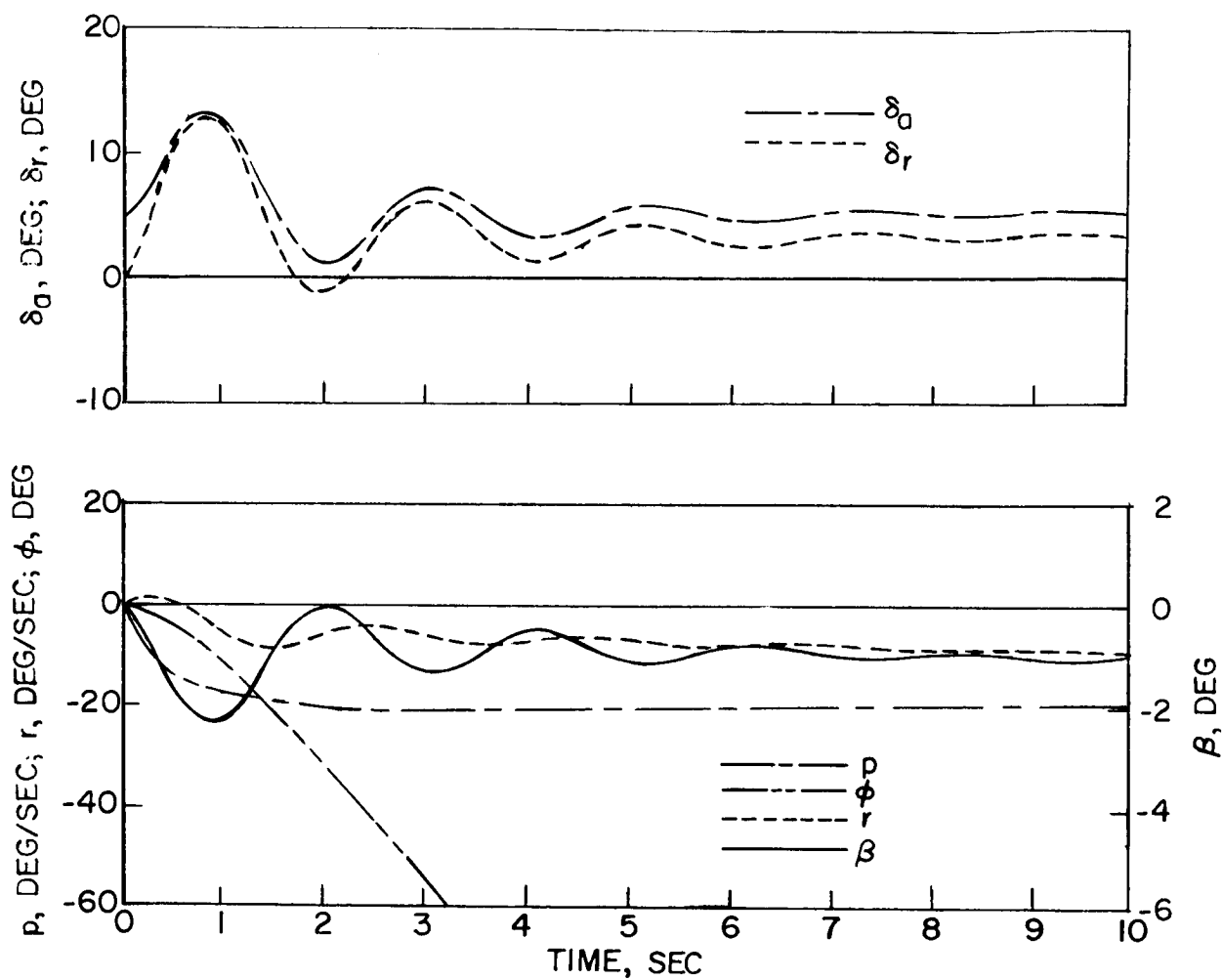


Figure 7.- Time history of response of augmented vehicle to 5° step aileron input.

## 11. OPTIMIZATION TECHNIQUES

By Ernest S. Armstrong  
Langley Research Center

### ABSTRACT

A brief introduction to some of the important concepts of deterministic optimal control theory is presented. The optimization of functions is treated by the methods of mathematical programming, and the optimization of definite integrals is treated by optimal control theory. Sequential and nonsequential methods are considered.

### INTRODUCTION

A brief introduction to some of the important concepts of deterministic optimization theory is presented. Optimization herein means either the maximization or minimization of a scalar function or a functional (meaning a definite integral of a function or its equivalent). No loss of generality occurs when minimization is considered in place of maximization because the process of the maximization of  $J$  is equivalent to the minimization of  $-J$  and the maximum of  $J$  equals minus the minimum of  $-J$  where  $J$  is either a function or a functional.

Both functions and functionals may be optimized by either sequential or nonsequential methods. Nonsequential optimization methods seek the optimizing quantity (a constant vector for a function or a function for a functional) by means of satisfying necessary and/or sufficient conditions for optimality. Sequential methods seek the optimizing quantity by means of constructing sequences which converge to a quantity effecting the optimization. Sequential and nonsequential methods are also referred to as direct and indirect methods (ref. 1), respectively.

The first part of this paper contains some mathematical preliminaries. The optimization of functions and functionals is next treated from both the sequential and nonsequential viewpoints. The optimization of functionals is treated through optimal control theory. Finally some uses of function minimization techniques in optimal control theory are considered.

### SYMBOLS

Inasmuch as this paper is mathematical in nature, an effort has been made to define each symbol at its introduction. Certain generalities of the notations are presented as follows:

$$a(\tau^-) = \lim_{\substack{t \rightarrow \tau \\ t < \tau}} a(t)$$

$f(\bar{x})$  scalar-valued function of vector  $\bar{x}$

$\bar{f}(\bar{x})$  vector-valued function of vector  $\bar{x}$

$\nabla_{\bar{x}} f(\bar{x})$  gradient vector

$\frac{\partial \bar{f}(\bar{x})}{\partial \bar{x}}, \bar{f}_{\bar{x}}(\bar{x})$  Jacobian matrix

$\frac{\partial^2 f(\bar{x})}{\partial \bar{x}^2}$  Hessian matrix

max maximum

min minimum

' prime denotes matrix transpose

. between vectors implies inner product; over a variable denotes first derivative

-1 over a matrix denotes inverse

| | absolute value of

|| || Euclidean norm

- approaches in the limit

- bar over a variable denotes vector

\* optimum value

$\delta$  increment

$\approx$  approximately equal to

$\subset$  is a subset of

$\epsilon$  is an element of

$\geq$  greater than or equal to zero when applied to a scalar; positive semidefinite when applied to a matrix

$>$  greater than zero when applied to a scalar; positive definite when applied to a matrix

$\Rightarrow$  implies

## MATHEMATICAL PRELIMINARIES

Some mathematical topics which are needed for a modern discussion of optimization are briefly presented in this section. A more thorough discussion may be found in reference 2.

### Matrix Algebra

The symbol  $R^n$  is used to denote the space of all elements (called vectors) of the form

$$\bar{x} = \begin{pmatrix} x_1 \\ x_2 \\ \vdots \\ x_n \end{pmatrix} = \text{col } (x_i) \quad (i = 1, \dots, n)$$

where the  $x_i$  are real numbers. If  $\bar{x}$  is an element of  $R^n$ , the notation is  $\bar{x} \in R^n$ .

Let

$$\bar{v} = \text{col } (v_i) \quad (i = 1, 2, \dots, n)$$

$$\bar{w} = \text{col } (\bar{w}_i) \quad (i = 1, 2, \dots, n)$$

then the scalar

$$\sum_{i=1}^n v_i \bar{w}_i = \bar{v}' \bar{w} = \bar{w}' \bar{v}$$

is called an inner (or scalar) product of  $\bar{v}$  and  $\bar{w}$  and is written  $\bar{v} \cdot \bar{w}$ . Let  $\bar{w} = A\bar{x}$  where  $A$  is an  $n \times n$  matrix. Then  $\bar{v} \cdot A\bar{x}$  is called a "bilinear form" on  $R^n$  and  $\bar{x} \cdot A\bar{x}$  is called a quadratic form on  $R^n$ . Note that  $\bar{v} \cdot A\bar{x} = A\bar{x} \cdot \bar{v} = \bar{x} \cdot A'\bar{v}$ . Given an  $n \times n$  matrix  $A$ , if  $\bar{x} \cdot A\bar{x} \geq 0$  for all  $\bar{x}$ , then  $A$  is said to be positive semidefinite (negative semidefinite) with notation  $A \geq 0$  ( $\leq 0$ ). If  $\bar{x} \cdot A\bar{x} > 0$  for all  $\bar{x} \neq \bar{0}$ , then  $A$  is said to be positive definite (negative definite) with notation  $A > 0$  ( $< 0$ ). If  $A = -A'$  (that is,  $A$  is skew symmetric), then  $\bar{x} \cdot A\bar{x} = 0$ , since  $\bar{x} \cdot A\bar{x} = A\bar{x} \cdot \bar{x} = \bar{x} \cdot A'\bar{x} = -\bar{x} \cdot A\bar{x}$  whereby  $2\bar{x} \cdot A\bar{x} = 0$ . In examining a nonsymmetric matrix for definiteness the symmetric matrix  $\frac{A + A'}{2}$  may be examined since  $A$  can always be written as

$$A = B + C$$

where

$$B = B' = \frac{A + A'}{2}$$

and

$$C = \frac{A - A'}{2} = -C'$$

and, since  $C$  is skew symmetric,

$$\bar{x} \cdot A\bar{x} = \bar{x} \cdot B\bar{x} + \bar{x} \cdot C\bar{x} = \bar{x} \cdot B\bar{x}$$

Given a square  $n$ th-order matrix  $A$ , the matrix  $\lambda I - A$  is the characteristic matrix of  $A$  where  $I$  is an  $n \times n$  identity matrix and  $\lambda$  is a scalar. The determinant of  $\lambda I - A$  set equal to zero is the characteristic equation of  $A$ . The roots of the characteristic equation are called the eigenvalues of  $A$ . Given  $A = A'$ , let  $\lambda_i$  ( $i = 1, 2, \dots, n$ ) be the eigenvalues of  $A$ . All eigenvalues of symmetric matrix are real. If for all  $i = 1, 2, \dots, n$ :  $\lambda_i \geq 0$ , then  $A$  is positive semidefinite;  $\lambda_i \leq 0$ , then  $A$  is negative semidefinite;  $\lambda_i > 0$ , then  $A$  is positive definite;  $\lambda_i < 0$ , then  $A$  is negative definite.

The vector space  $R^n$  with inner product

$$\bar{x} \cdot \bar{y} = \sum_{i=1}^n x_i y_i \quad (\bar{x} \in R^n, \bar{y} \in R^n)$$

is an example of a Euclidean space. The quantity  $\|\bar{x}\| = (\bar{x} \cdot \bar{x})^{1/2}$  is called a Euclidean norm of  $\bar{x} \in R^n$  and is a measure of the magnitude of  $\bar{x}$ . Given  $\bar{x} = \text{col}(x_i)$  and  $\bar{y} = \text{col}(y_i)$  ( $i = 1, 2, \dots, n$ ), if  $\bar{x} \cdot \bar{y} = 0$ , then  $\bar{x}$  and  $\bar{y}$  are said to be orthogonal. If  $A' = A^{-1}$ , then the matrix  $A$  is said to be orthogonal.

The vectors  $\bar{x}_i$  ( $i = 1, 2, \dots, m$ ), where  $m$  is a finite natural number, are said to be linearly independent if the only  $a_i$  ( $i = 1, 2, \dots, m$ ) satisfying

$$\sum_{i=1}^m a_i \bar{x}_i = \bar{0}$$

where  $\bar{0}$  is the null vector (a vector with all zero elements) of the same dimension as  $\bar{x}$ , is  $a_i = 0$ . In  $R^n$ ,  $n$  linearly independent vectors, such that each vector in  $R^n$  can be written as a linear combination of the vectors, are termed basis vectors for  $R^n$ . The only vector in  $R^n$  which is orthogonal to a set of basis vectors is the null vector of dimension  $n$ .

### Matrix Analysis

Define

$$\bar{f} = \text{col} (f_i) \quad (i = 1, 2, \dots, m)$$

$$\bar{x} = \text{col} (x_i) \quad (i = 1, 2, \dots, n)$$

Define  $\bar{f}(\bar{x})$  as a vector-valued function of  $\bar{x}$ . Let  $\frac{\partial f_i(\bar{x})}{\partial x_j}$  ( $i = 1, 2, \dots, m$ ;  $j = 1, 2, \dots, n$ ) exist.

The  $m \times n$  matrix

$$\left( \frac{\partial f_i(\bar{x})}{\partial x_j} \right) = \begin{pmatrix} \frac{\partial f_1}{\partial x_1}, & \frac{\partial f_1}{\partial x_2}, & \dots & \frac{\partial f_1}{\partial x_n} \\ \frac{\partial f_2}{\partial x_1}, & \frac{\partial f_2}{\partial x_2}, & \dots & \frac{\partial f_2}{\partial x_n} \\ \cdot & \cdot & \cdot & \cdot \\ \cdot & \cdot & \cdot & \cdot \\ \cdot & \cdot & \cdot & \cdot \\ \frac{\partial f_m}{\partial x_1}, & \frac{\partial f_m}{\partial x_2}, & \dots & \frac{\partial f_m}{\partial x_n} \end{pmatrix}$$

is called the Jacobian matrix of  $\bar{f}(\bar{x})$  with respect to  $\bar{x}$  and denoted by  $\frac{\partial \bar{f}(\bar{x})}{\partial \bar{x}}$  or  $\bar{f}_{\bar{x}}(\bar{x})$ .

Example:

Given

$$\bar{f}(\bar{x}) = A\bar{x}$$

where  $A$  is a constant matrix, then

$$\frac{\partial \bar{f}(\bar{x})}{\partial \bar{x}} = A$$

Example:

Given

$$\bar{f}(\bar{x}) = \begin{pmatrix} x_1^2 + x_2 \\ x_3^2 - x_2 \end{pmatrix}$$

then

$$\frac{\partial \bar{f}(\bar{x})}{\partial \bar{x}} = \begin{bmatrix} 2x_1 & 1 & 0 \\ 0 & -1 & 2x_3 \end{bmatrix}$$

Let  $f(\bar{x})$  be a scalar-valued function of the vector  $\bar{x}$ . The gradient of  $f(\bar{x})$  with respect to  $\bar{x}$  is defined as the column vector

$$\begin{bmatrix} \frac{\partial f(\bar{x})}{\partial x_1} \\ \frac{\partial f(\bar{x})}{\partial x_2} \\ \cdot \\ \cdot \\ \cdot \\ \frac{\partial f(\bar{x})}{\partial x_n} \end{bmatrix}$$

with notation  $\nabla_{\bar{x}} f(\bar{x})$ .

The matrix

$$\frac{\partial}{\partial \bar{x}} \nabla_{\bar{x}} f(\bar{x}) = \left( \frac{\partial^2 f}{\partial x_i \partial x_j} \right)$$

is the Hessian matrix of  $f(\bar{x})$ . Note that

$$\nabla_{\bar{x}} f(\bar{x}) = \frac{\partial f'(\bar{x})}{\partial \bar{x}}$$

**Example:**

Given

$$f(\bar{x}) = \bar{x} \cdot A \bar{x}$$

then

$$\nabla_{\bar{x}} f(\bar{x}) = (A + A') \bar{x} = 2A \bar{x}$$

if  $A = A'$ .

Given the composite function  $f[\bar{x}(t)]$ , then

$$\frac{d}{dt} f[\bar{x}(t)] = \nabla_{\bar{x}} f(\bar{x}) \cdot \frac{d\bar{x}(t)}{dt}$$

if all derivatives exist. A Taylor series about the point  $\bar{x}_0 \in R^n$  can be written as

$$f(\bar{x} + \bar{x}_0) = f(\bar{x}_0) + \nabla_{\bar{x}} f(\bar{x}_0) \cdot \bar{x} + \frac{1}{2} \bar{x} \cdot \frac{\partial^2 f}{\partial \bar{x}^2}(\bar{x}_0) \bar{x} + \text{Higher order terms}$$

Convexity (ref. 3)

An  $n$ -dimensional region  $S$  is said to be convex if, whenever  $(x_1, x_2, \dots, x_n)'$  and  $(y_1, y_2, \dots, y_n)'$  belong to  $S$ , their convex combination

$$[\theta x_1 + (1 - \theta)y_1, \dots, \theta x_n + (1 - \theta)y_n]'$$
( $0 \leq \theta \leq 1$ )

also belongs to  $S$ .



Example:

The set  $S = \{\bar{x} : \bar{x} \in R^n, \|\bar{x}\| < \rho\}$  is convex. Since

$$\|\theta\bar{x} + (1 - \theta)\bar{y}\| \leq \theta\|\bar{x}\| + (1 - \theta)\|\bar{y}\| < \theta\rho + (1 - \theta)\rho = \rho$$

Geometrically convexity means that the straight line connecting any two points of a convex region belongs to the region.

A function of a single variable  $f(x)$  is convex (also concave upward) on an interval, if for any two points  $x_1$  and  $x_2$  on the interval  $x_1 < x_2$ , it satisfies Jensen's inequality

$$f\left(\frac{x_1 + x_2}{2}\right) \leq \frac{f(x_1) + f(x_2)}{2}$$

Geometrically this indicates that the value of the function of a point which is the average of  $x_1$  and  $x_2$  is less than its average value at the two points. This condition may also be stated as

$$f[(1 - \theta)x_1 + \theta x_2] \leq (1 - \theta)f(x_1) + \theta f(x_2) \quad (0 \leq \theta \leq 1)$$

The function  $f(x)$  is strictly convex if only the inequality holds. A twice differentiable function  $f(x)$  on an open interval (not necessarily including the endpoints of the interval) is convex if and only if  $\frac{d^2f}{dx^2} \geq 0$  on the interval. This definition may be generalized to a function of several variables. If  $D$  is a convex set of the points  $x_1, \dots, x_n$ , a real-valued function in  $D$  is convex if for  $\bar{x}$  and  $\bar{y}$  in  $D$  the following holds:

$$f[(1 - \theta)\bar{x} + \theta\bar{y}] \leq (1 - \theta)f(\bar{x}) + \theta f(\bar{y}) \quad (0 \leq \theta \leq 1)$$

It is strictly convex if the strict inequality holds for  $0 < \theta < 1$  and  $\bar{x}$  and  $\bar{y}$  are distinct points in  $D$ . A function  $f(\bar{x})$  is concave (strictly concave) if  $-f(\bar{x})$  is convex (strictly convex). If  $f(\bar{x})$  is a twice continuously differentiable function on an open convex set  $D$ , it is convex in  $D$  if and only if the quadratic form (in  $\bar{y}$ )

$$\bar{y} \cdot \frac{\partial^2 f(\bar{x})}{\partial \bar{x}^2} \bar{y} \geq 0$$

for every  $\bar{x}$  in  $D$ ; that is,  $\frac{\partial^2 f(\bar{x})}{\partial \bar{x}^2}$  is positive semidefinite for every  $\bar{x}$  in  $D$ . The function is strictly convex if  $\frac{\partial^2 f(\bar{x})}{\partial \bar{x}^2} > 0$ . If  $f(\bar{x})$  is differentiable and convex, then

$$f(\bar{x}) \geq f(\bar{x}^*) + \nabla_{\bar{x}} f(\bar{x}^*) \cdot (\bar{x} - \bar{x}^*)$$

### The Newton-Raphson Method

The Newton-Raphson method (ref. 3) for computing the root of an equation is a successive approximation procedure.

For an equation in a single independent variable

$$y = f(x)$$

start with an estimate of  $x$ , for example  $x^{(0)}$ , near the root of

$$f(x) = 0$$

which is to be determined. Then compute the intersection of the tangent line to the graph at this estimate with the  $x$ -axis and use the intersection as the abscissa of the new estimate. This gives the new estimate, denoted by  $x^{(1)}$ , as

$$x^{(1)} = x^{(0)} - \frac{f[x^{(0)}]}{\frac{df}{dx}[x^{(0)}]}$$

For the second iteration

$$x^{(2)} = x^{(1)} - \frac{f[x^{(1)}]}{\frac{df}{dx}[x^{(1)}]}$$

and for the  $n$ th iteration

$$x^{(n)} = x^{(n-1)} - \frac{f[x^{(n-1)}]}{\frac{df}{dx}[x^{(n-1)}]}$$

Next consider finding a root  $\bar{x} = \text{col}(x_i) \quad (i = 1, 2, \dots, n)$  of the system of equations

$$f_1(\bar{x}) = 0$$

$$f_2(\bar{x}) = 0$$

.

.

.

$$f_n(\bar{x}) = 0$$

The Newton-Raphson iteration sequence in this case is generated by

$$\bar{x}^{(n+1)} = \bar{x}^{(n)} - \left\{ \frac{\partial \bar{f}}{\partial \bar{x}} [\bar{x}^{(n)}] \right\}^{-1} \bar{f} [\bar{x}^{(n)}] \quad (n = 0, 1, \dots)$$

where

$$\bar{f} = \text{col}(f_i) \quad (i = 1, 2, \dots, m)$$

Conditions for the convergence of both the scalar and vector versions of the Newton-Raphson algorithm are given in reference 3.

### OPTIMIZATION OF FUNCTIONS

Consider the mathematical programming problem I of minimizing a scalar-valued function  $f(\bar{x})$  ( $\bar{x} \in R^n$ ) subject to the constraint functions

$$g_i(\bar{x}) \geq 0 \quad (i = 1, 2, \dots, m)$$

$$h_j(\bar{x}) = 0 \quad (j = 1, 2, \dots, p < n)$$

When  $f$ ,  $g_i$ , and  $h_j$  are linear, the problem is called a linear programming problem (ref. 4). If any of the functions are nonlinear, the problem is called a nonlinear programming problem (ref. 5). The case where  $f(\bar{x})$  is a positive semidefinite quadratic form and the constraints are linear is called a quadratic programming problem (ref. 6). The case where  $f(\bar{x})$  is convex,  $g_i(\bar{x})$  is concave, and  $h_j(\bar{x})$  is linear is called a convex programming problem (ref. 7). The convexity conditions assure that the feasible

region (the set of points satisfying the constraints) is convex and that any local solution is also a global solution. Other forms of the optimization problem (such as, separable and factorable) are discussed in reference 7.

The solution (assuming it exists) of the optimization problem I, denoted by  $\bar{x}^*$ , can be sought by either sequential or nonsequential methods. Some of these methods are presented subsequently herein. The treatment of the problem constraints varies according to the purpose of the discussion. In general, an inequality constraint of the form

$$k_1 \leq g(\bar{x}) \leq k_2$$

where  $k_1$  and  $k_2$  are constants, may be transformed into an equality constraint by the introduction of a new (real) variable  $y$  and setting

$$[g(\bar{x}) - k_1][k_2 - g(\bar{x})] - y^2 = 0$$

This method is attributed to Valentine (ref. 8). Likewise an equality constraint

$$h(\bar{x}) = 0$$

may be written as

$$0 \leq h(\bar{x}) \leq 0$$

and treated as an inequality constraint.

General methods exist for solving constrained optimization problems as though they were unconstrained (penalty functions primarily) and for treating constraints directly (projection methods). See reference 7 for a summary of these methods.

### Nonsequential Methods

Varying amounts of information about the solution of problem I can be obtained depending on the properties of  $f(\bar{x})$ ,  $g_i(\bar{x})$ , and  $h_j(\bar{x})$ . First-order necessary conditions are presented when the functions are differentiable. Second-order necessary and sufficient conditions are given when the functions are twice differentiable. Cases where the functions are not necessarily differentiable nor even continuous are considered in reference 9, and a method for minimization without computing derivatives is given in reference 10.

First-order necessary conditions.- In problem I assume that the functions  $f(\bar{x})$ ,  $g_i(\bar{x})$  ( $i = 1, 2, \dots, m$ ), and  $h_j(\bar{x})$  ( $j = 1, 2, \dots, p$ ) are differentiable. References 11 and 12 show that if  $\bar{x}^*$  is the optimal solution to  $\min_{\bar{x}} f(\bar{x})$

$$g_i(\bar{x}) \geq 0 \quad (i = 1, 2, \dots, m)$$

$$h_j(\bar{x}) = 0 \quad (j = 1, 2, \dots, p < n)$$

then there exist scalars  $\lambda_i$  ( $i = 0, 1, \dots, m$ ) and  $\psi_j$  ( $j = 1, 2, \dots, p$ ) not all zero and satisfying at  $\bar{x}^*$  the following conditions:

$$(1) \quad g_i(\bar{x}^*) \geq 0 \quad (i = 1, 2, \dots, m)$$

$$(2) \quad h_j(\bar{x}^*) = 0 \quad (j = 1, 2, \dots, p)$$

$$(3) \quad \lambda_i g_i(\bar{x}^*) = 0 \quad (i = 1, 2, \dots, m)$$

$$(4) \quad \lambda_i \geq 0 \quad (i = 0, 1, \dots, m)$$

(5) With

$$L(\bar{x}, \bar{\lambda}, \bar{\psi}) = \lambda_0 f(\bar{x}) - \sum_{i=1}^m \lambda_i g_i(\bar{x}) + \sum_{j=1}^p \psi_j h_j(\bar{x})$$

then

$$\nabla_{\bar{x}} L(\bar{x}^*, \bar{\lambda}, \bar{\psi}) = \bar{0}$$

The quantities  $\lambda_i$  ( $i = 0, 1, \dots, m$ ) and  $\psi_j$  ( $j = 1, 2, \dots, p$ ) are called dual variables or generalized Lagrange multipliers. The foregoing statement of conditions (1) to (5) can be regarded as an existence theorem for a set of Lagrange multipliers for problem I to be sought, along with  $\bar{x}^*$ , from conditions (1) to (5).

The condition  $\lambda_0 \geq 0$  means that it is legitimate, if necessary to obtain a solution, to have  $\lambda_0 = 0$ . This situation however is abnormal since, for  $\lambda_0 = 0$ ,  $\bar{x}^*$  would be determined only by the constraining relations. Conditions which guarantee the existence of a set of Lagrange multipliers with  $\lambda_0 \neq 0$  are now of concern. Such a set

is known to exist if the constraints of problem I satisfy the Kuhn-Tucker first-order constraint qualification (ref. 13). Let  $\bar{x}^{(0)}$  be a point satisfying  $g_i[\bar{x}^{(0)}] \geq 0$  and  $h_j[\bar{x}^{(0)}] = 0$ . The first-order constraint qualification holds at  $\bar{x}^{(0)}$  if for any nonzero vector  $\bar{z}$ , such that  $\bar{z} \cdot \nabla_{\bar{x}} g_i[\bar{x}^{(0)}] \geq 0$  for all  $i$  such that  $g_i[\bar{x}^{(0)}] = 0$  and  $\bar{z} \cdot \nabla_{\bar{x}} h_j[\bar{x}^{(0)}] = 0$  ( $j = 1, 2, \dots, p$ ),  $\bar{z}$  is tangent to a once differentiable arc emanating from  $\bar{x}^{(0)}$  and contained in the feasible region (ref. 7). With this constraint qualification met at  $\bar{x}^*$ , then necessary conditions that  $\bar{x}^*$  be a local minimum of problem I are that there exist  $\lambda_i$  ( $i = 0, 1, 2, \dots, m$ ) and  $\psi_j$  ( $j = 1, 2, \dots, p$ ) satisfying conditions (1) to (5) with  $\lambda_0 = 1$ .

Two other conditions, each independently guaranteeing the existence of a set of multipliers with  $\lambda_0 \neq 0$  for problem I, also exist (ref. 7):

(i) If at a feasible point  $\bar{x}^*$  there exists a vector  $\bar{z}$  such that  $\bar{z} \cdot \nabla_{\bar{x}} g_i(\bar{x}^*) > 0$  for all  $i$  such that  $g_i(\bar{x}^*) = 0$ ,  $\bar{z} \cdot \nabla_{\bar{x}} h_j(\bar{x}^*) = 0$  ( $j = 1, \dots, p$ ) and if the  $\nabla_{\bar{x}} h_j(\bar{x}^*)$  are linearly independent, then a necessary condition that  $\bar{x}^*$  be a local minimum of problem I is that there exist  $\lambda_i$  and  $\psi_j$  satisfying conditions (1) to (5) with  $\lambda_0 = 1$ .

(ii) A sufficient condition that the first-order constraint qualification holds at a point  $\bar{x}^{(0)}$  satisfying the constraints of problem I is that the gradients  $\nabla_{\bar{x}} g_i[\bar{x}^{(0)}]$  for all  $i$  such that  $g_i[\bar{x}^{(0)}] = 0$  and  $\nabla_{\bar{x}} h_j[\bar{x}^{(0)}]$  ( $j = 1, 2, \dots, p$ ) be linearly independent.

Conditions (i) and (ii) are more useful than the original statement of the Kuhn-Tucker constraint qualification because they can be tested. The Kuhn-Tucker constraint qualification is sufficient but possibly not necessary to guarantee multipliers with  $\lambda_0 \neq 0$ . It is still questionable whether a weaker condition can be found.

It follows from conditions (1) to (5) that if problem I is unconstrained, then for  $\bar{x}^*$  to be a local minimum of the differentiable function  $f(\bar{x})$ , it is necessary that

$$\nabla_{\bar{x}} f(\bar{x}^*) = \bar{0}$$

The foregoing results are called first order because they involve only first partial derivatives. If  $f(\bar{x})$ ,  $g_i(\bar{x})$  ( $i = 1, 2, \dots, m$ ), and  $h_j(\bar{x})$  ( $j = 1, 2, \dots, p$ ) are assumed twice differentiable, then a more complete characterization of  $\bar{x}^*$  can be given.

Second-order necessary conditions.— Let  $\bar{x}^{(0)}$  be a point satisfying the constraints of problem I. The second-order constraint qualification holds at  $\bar{x}^{(0)}$  if the following is true. Let  $\bar{y}$  be any nonzero vector such that  $\bar{y} \cdot \nabla_{\bar{x}} g_i[\bar{x}^{(0)}] = 0$  for all  $i$  such that  $g_i[\bar{x}^{(0)}] = 0$  and such that  $\bar{y} \cdot \nabla_{\bar{x}} h_j[\bar{x}^{(0)}] = 0$  ( $j = 1, 2, \dots, p$ ). Then  $\bar{y}$  is tangent to a

twice differentiable arc emanating from  $\bar{x}^{(0)}$  and contained in the region along which  $g_i(\bar{x}) \equiv 0$  (i such that  $g_i[\bar{x}^{(0)}] = 0$ ) and  $h_j(\bar{x}) \equiv 0$  ( $j = 1, 2, \dots, p$ ).

If the first- and second-order constraint qualifications hold at a point  $\bar{x}^*$ , then necessary conditions that  $\bar{x}^*$  be a local minimum of problem I are that there exist Lagrange multipliers with  $\lambda_0 \neq 0$  such that conditions (1) to (5) hold and such that for every nonzero vector  $\bar{y}$ , where  $\bar{y} \cdot \nabla_{\bar{x}} g_i(\bar{x}^*) = 0$  (i such that  $g_i(\bar{x}^*) = 0$ ) and  $\bar{y} \cdot \nabla_{\bar{x}} h_j(\bar{x}^*) = 0$  ( $j = 1, 2, \dots, p$ ) it follows that

$$\bar{y} \cdot \frac{\partial^2 L}{\partial \bar{x}^2}(\bar{x}^*, \bar{\lambda}, \bar{\psi}) \bar{y} \geq 0$$

A sufficient condition that the second-order constraint qualification be satisfied at a point  $\bar{x}^*$  satisfying the constraints of problem I is that the vectors  $\nabla_{\bar{x}} g_i(\bar{x}^*)$  (i such that  $g_i(\bar{x}^*) = 0$ ) and  $\nabla_{\bar{x}} h_j(\bar{x}^*)$  ( $j = 1, 2, \dots, p$ ) be linearly independent.

Necessary conditions that a twice continuously differentiable function have a local unconstrained minimum at a point  $\bar{x}^*$  are

$$\nabla_{\bar{x}} f(\bar{x}^*) = \bar{0}$$

and

$$\bar{y} \cdot \frac{\partial^2 f(\bar{x}^*)}{\partial \bar{x}^2} \bar{y} \geq 0$$

for all  $\bar{y}$ .

Second-order sufficiency conditions.— Sufficient conditions that a point  $\bar{x}^*$  be an isolated (unique locally) local minimum of problem I, where  $f(\bar{x})$ ,  $g_i(\bar{x})$ , and  $h_j(\bar{x})$  are twice differentiable functions, are that there exist  $\lambda_i$  ( $i = 1, \dots, m$ ) and  $\psi_j$  ( $j = 1, \dots, p$ ) such that  $\bar{x}^*$ ,  $\lambda_i$ , and  $\psi_j$  satisfy conditions (1) to (5) with  $\lambda_0 = 1$  and for every nonzero  $\bar{y}$  satisfying

$$\bar{y} \cdot \nabla_{\bar{x}} g_i(\bar{x}^*) = 0$$

for all i such that  $\lambda_i > 0$

$$\bar{y} \cdot \nabla_{\bar{x}} g_k(\bar{x}^*) \geq 0$$

for all k such that  $g_k(\bar{x}^*) = 0$  and  $\lambda_k = 0$  and

$$\bar{y} \cdot \nabla_{\bar{x}} h_j(x^*) = 0 \quad (j = 1, \dots, p)$$

it follows that

$$\bar{y} \cdot \frac{\partial^2 L}{\partial \bar{x}^2}(x^*, \bar{\lambda}, \bar{\psi}) \bar{y} > 0$$

Sufficient conditions that a point  $\bar{x}^*$  be an isolated local unconstrained minimum of the twice differentiable function  $f(\bar{x})$  are that

$$\nabla_{\bar{x}} f(\bar{x}^*) = 0$$

and

$$\bar{y} \cdot \frac{\partial^2 f(\bar{x}^*)}{\partial \bar{x}^2} \bar{y} > 0$$

for all nonzero  $\bar{y}$ .

### Sequential Methods

In considering sequential minimization it is beneficial to be able to treat the optimization problem I in unconstrained form even though the problem is constrained. To this extent consider a method called penalty functions for solving constrained optimization problems as though they were unconstrained. Interior and exterior penalty methods as presented in reference 7 are discussed herein.

Assume that an unconstrained minimization problem can be solved either by the nonsequential methods previously presented or by the unconstrained sequential methods to be presented in this section after the discussion of penalty methods.

An interior penalty-function technique considers problem II of the form  $\min_{\bar{x}} f(\bar{x})$  subject to

$$g_i(\bar{x}) \geq 0 \quad (i = 1, \dots, m)$$

Equality constraints are not allowed. Let  $I(\bar{x})$  be a scalar-valued function of  $\bar{x}$  such that:

- (1)  $I(\bar{x})$  is continuous in  $\bar{x}$  for all  $\bar{x}$  satisfying  $g_i(\bar{x}) > 0$  ( $i = 1, \dots, m$ ).
- (2)  $I(\bar{x}) \rightarrow \infty$  as any  $g_i(\bar{x}) \rightarrow 0$ .



Let  $s(r)$  be a scalar-valued function of a real variable  $r$  such that, if  $r_1 > r_2 > 0$ , then  $s(r_1) > s(r_2) > 0$  and  $s(r) \rightarrow 0$  as  $r \rightarrow 0$ .

Example:

$$I(\bar{x}) = \sum_{i=1}^m \frac{1}{g_i(\bar{x})}$$

or

$$I(\bar{x}) = - \sum_{i=1}^m \log g_i(\bar{x})$$

and

$$s(r) = r^i \quad (i = 1, 2, \dots)$$

The interior penalty-function method proceeds as follows: Define  $U(\bar{x}, r) = f(\bar{x}) + s(r) I(\bar{x})$ . For a sequence of  $r_i$ , where  $r_{i+1} < r_i$  ( $i = 1, 2, \dots$ ), minimize the unconstrained function  $U(\bar{x}, r_i)$  obtaining a sequence  $\bar{x}(r_1), \bar{x}(r_2), \dots, \bar{x}(r_i), \dots$  as  $r_i \rightarrow 0$ . Conditions under which  $\bar{x}(r_i)$  converges to a solution  $\bar{x}^*$  of problem II as  $r_i \rightarrow 0$  are discussed in reference 7. The term  $s(r)I(\bar{x})$  may be regarded as a penalty term added to the function  $f(\bar{x})$  ensuring that a minimum of  $U(\bar{x}, r)$  is achieved in the interior of the feasible region by balancing the avoidance of the boundaries and the minimization of  $f(\bar{x})$ . The solution  $\bar{x}^*$  is approached from the interior of the feasible region - hence the name "interior" method. The point  $\bar{x}^*$  may lie on the boundary of the feasible region in the limit as  $r_i \rightarrow 0$ . It now becomes evident why equality constraints were omitted in problem II since, for equalities treated as inequalities, no interior points exist.

Equality constraints as well as inequality constraints may be treated by the exterior penalty-function technique. Consider problem II as before except that the inequality constraints may now include equalities treated as inequalities.

Let  $p(t)$  be a scalar-valued function of a variable  $t$  with properties that if  $0 < t_1 < t_2$ , then  $0 < p(t_1) < p(t_2)$ , and as  $t \rightarrow \infty$ ,  $p(t) \rightarrow \infty$ . Let  $O(\bar{x})$  be a continuous scalar-valued function of  $\bar{x}$  with properties such that  $O(\bar{x}) = 0$  if  $g_i(\bar{x}) \geq 0$  ( $i = 1, 2, \dots, m$ ) and  $O(\bar{x}) > 0$  otherwise.

Example:

$$O(\bar{x}) = \frac{1}{2} \sum_{i=1}^m \left[ g_i(\bar{x}) - |g_i(\bar{x})| \right]^2$$

and

$$p(t) = t^i \quad (i = 1, 2, \dots)$$

The exterior penalty-function method proceeds as follows: Define  $T(\bar{x}, t) = f(\bar{x}) + p(t) O(\bar{x})$ . For a sequence of  $t_i$ , where  $t_{i+1} > t_i$  ( $i = 1, 2, \dots$ ), minimize the unconstrained function  $T(\bar{x}, t_i)$  obtaining a sequence  $\bar{x}(t_1), \bar{x}(t_2), \dots, \bar{x}(t_i), \dots$  as  $t_i \rightarrow \infty$ . Conditions under which  $\bar{x}(t_i)$  converges to a solution  $\bar{x}^*$  of problem I are discussed in reference 7. The intuitive basis for the exterior method is as follows. If  $\bar{x}$  strays too far from the feasible region, the penalty term  $p(t) O(\bar{x})$  becomes large when  $t$  is large. Thus as  $t \rightarrow \infty$  the tendency is to draw the unconstrained minima toward the feasible region so as to minimize the value of the penalty term. This algorithm is termed "exterior" because the movement of  $\bar{x}(t)$  is, in general, from the outside or infeasible region toward the inside of the feasible region.

Now turn to the problem of sequential minimization of an unconstrained function  $f(\bar{x})$ . The function  $f(\bar{x})$  may actually be unconstrained or it may be that a constrained problem is being solved by unconstrained methods; for example, penalty functions. Here a set of  $\bar{x}^{(i)}$  ( $i = 0, 1, \dots$ ) is sought such that

$$f[\bar{x}^{(i+1)}] < f[\bar{x}^{(i)}]$$

and the sequence converges to a point  $\bar{x}^*$  which minimizes  $f(\bar{x})$ . One way of generating such a sequence may be through the gradient method (ref. 3). In the gradient method an  $\bar{x}^{(0)}$  is assumed and  $\bar{x}^{(0)}$  is corrected by

$$\delta \bar{x}^{(0)} = \bar{x}^{(1)} - \bar{x}^{(0)} = -\alpha_0 \nabla_{\bar{x}} f[\bar{x}^{(0)}] \quad (\alpha_0 > 0)$$

thus producing

$$\bar{x}^{(1)} = \bar{x}^{(0)} + \delta \bar{x}^{(0)} = \bar{x}^{(0)} - \alpha_0 \nabla_{\bar{x}} f[\bar{x}^{(0)}]$$

The parameter  $\alpha_0$  is chosen by

$$\min_{\alpha_0 > 0} \left( f\left\{ \bar{x}^{(0)} - \alpha_0 \nabla_{\bar{x}} f[\bar{x}^{(0)}] \right\} - f[\bar{x}^{(0)}] \right)$$

for which a necessary condition is

$$\nabla_{\bar{x}} f[\bar{x}^{(1)}] \cdot \nabla_{\bar{x}} f[\bar{x}^{(0)}] = 0$$

In general the gradient sequence is

$$\bar{x}^{(i+1)} = \bar{x}^{(i)} + \delta \bar{x}^{(i)} = \bar{x}^{(i)} - \alpha_i \nabla_{\bar{x}} f[\bar{x}^{(i)}]$$

where the parameter  $\alpha_i > 0$  is chosen by

$$\min_{\alpha_i > 0} \left( f\left\{ \bar{x}^{(i)} - \alpha_i \nabla_{\bar{x}} f[\bar{x}^{(i)}] \right\} - f[\bar{x}^{(i)}] \right)$$

or

$$\nabla_{\bar{x}} f[\bar{x}^{(i+1)}] \cdot \nabla_{\bar{x}} f[\bar{x}^{(i)}] = 0 \quad (i = 0, 1, \dots)$$

The term "gradient" is used since  $\delta \bar{x}^{(i)} = -\alpha_i \nabla_{\bar{x}} f[\bar{x}^{(i)}]$  is in the negative gradient direction of  $f(\bar{x})$  at  $\bar{x}^{(i)}$ . The gradient method is first order in that it makes use of only first derivatives of  $f(\bar{x})$ .

Another way of determining the minimum of  $f(\bar{x})$  by constructing sequences is the direct application of the Newton-Raphson method to the necessary condition at  $\bar{x}^*$

$$\nabla_{\bar{x}} f(\bar{x}^*) = \bar{0}$$

By the Newton-Raphson algorithm find a root, hopefully  $\bar{x}^*$ , of

$$\nabla_{\bar{x}} f(\bar{x}) = \bar{0}$$

In this way an  $\bar{x}^{(0)}$  is assumed to begin the process and form new  $\bar{x}^{(i)}$  by

$$\begin{aligned} \bar{x}^{(i+1)} &= \bar{x}^{(i)} + \delta \bar{x}^{(i)} \\ &= \bar{x}^{(i)} - \left\{ \frac{\partial^2 f[\bar{x}^{(i)}]}{\partial \bar{x}^2} \right\}^{-1} \nabla_{\bar{x}} f[\bar{x}^{(i)}] \end{aligned}$$

Although it does not occur in the Newton-Raphson algorithm, a parameter  $\alpha_i$  multiplying  $\delta \bar{x}^{(i)}$  may be inserted and determined as in the gradient method. The Hessian

matrix  $\frac{\partial^2 f[\bar{x}^{(i)}]}{\partial \bar{x}^2}$  must at each stage be nonsingular and, if  $\bar{x}^{(i)}$  is to approach the minimum  $f(\bar{x})$ , must approach positive definiteness as  $i \rightarrow \infty$ . If  $f(\bar{x})$  is strictly convex, then these requirements are guaranteed. This Newton-Raphson method is termed second order because it requires second derivatives of  $f(\bar{x})$ . The Newton-Raphson method is often called the "Taylor series" method because it occurs from

$$\min_{\delta \bar{x}^{(i)}} \left\{ f[\bar{x}^{(i)} + \delta \bar{x}^{(i)}] \right\}$$

with  $f[\bar{x}^{(i)} + \delta \bar{x}^{(i)}]$  approximated by a second-order Taylor series in  $\delta \bar{x}^{(i)}$  about  $\bar{x}^{(i)}$ ; that is,

$$f[\bar{x}^{(i)} + \delta \bar{x}^{(i)}] \approx f[\bar{x}^{(i)}] + \nabla_{\bar{x}} f[\bar{x}^{(i)}] \cdot \delta \bar{x}^{(i)} + \frac{1}{2} \delta \bar{x}^{(i)} \cdot \frac{\partial^2 f[\bar{x}^{(i)}]}{\partial \bar{x}^2} \delta \bar{x}^{(i)}$$

Conditions for the convergence of the gradient and Newton-Raphson algorithms are found in reference 3.

Now see how the gradient and Newton-Raphson methods behave when  $f(\bar{x})$  is a quadratic function

$$f(\bar{x}) = a + \bar{b} \cdot \bar{x} + \frac{\bar{x} \cdot C \bar{x}}{2}$$

where the scalar  $a$ , the vector  $\bar{b}$ , and the matrix  $C = C' > 0$  are constants. First apply nonsequential methods to determine  $\bar{x}^*$ . The first-order necessary condition is

$$\nabla_{\bar{x}} f(\bar{x}) = \bar{0}$$

which gives

$$\bar{x} = -C^{-1} \bar{b}$$

Since  $\frac{\partial^2 f(\bar{x})}{\partial \bar{x}^2} = C > 0$ ,  $\bar{x}^* = -C^{-1} \bar{b}$ . By the gradient method

$$\begin{aligned} \bar{x}^{(i+1)} &= \bar{x}^{(i)} - \alpha_i \nabla_{\bar{x}} f[\bar{x}^{(i)}] \\ &= \bar{x}^{(i)} - \alpha_i [\bar{b} + C \bar{x}^{(i)}] \\ &= (I - \alpha_i C) \bar{x}^{(i)} - \alpha_i \bar{b} \end{aligned} \quad (i = 0, 1, \dots)$$

where  $\alpha_1$  minimizes  $f\left\{\bar{x}^{(i)} - \alpha_1 \nabla_{\bar{x}} f\left[\bar{x}^{(i)}\right]\right\} - f\left[\bar{x}^{(i)}\right]$  or satisfies

$$\nabla_{\bar{x}} f\left[\bar{x}^{(i+1)}\right] \cdot \nabla_{\bar{x}} f\left[\bar{x}^{(i)}\right] = 0$$

yielding

$$\left[\bar{b} + C\bar{x}^{(i+1)}\right] \cdot \left[\bar{b} + C\bar{x}^{(i)}\right] = 0$$

or

$$\alpha_1 = \frac{\left[\bar{b} + C\bar{x}^{(i)}\right] \cdot \left[\bar{b} + C\bar{x}^{(i)}\right]}{\left[\bar{b} + C\bar{x}^{(i)}\right] \cdot C\left[\bar{b} + C\bar{x}^{(i)}\right]}$$

Reference 3 shows that the sequence defined by the gradient method converges for arbitrary  $\bar{x}^{(0)}$  when

$$f(\bar{x}) = a + \bar{b} \cdot \bar{x} + \frac{\bar{x} \cdot C\bar{x}}{2} \quad (C = C' > 0)$$

The convergence may not, however, be in a finite number of steps.

Now apply the Newton-Raphson algorithm. The sequence is generated by

$$\bar{x}^{(i+1)} = \bar{x}^{(i)} - \left\{ \frac{\partial^2 f\left[\bar{x}^{(i)}\right]}{\partial \bar{x}^2} \right\}^{-1} \nabla_{\bar{x}} f\left[\bar{x}^{(i)}\right] \quad (i = 0, 1, \dots)$$

with

$$\nabla_{\bar{x}} f(\bar{x}) = \bar{b} + C\bar{x}$$

and

$$\frac{\partial^2 f(\bar{x})}{\partial \bar{x}^2} = C$$

or

$$\bar{x}^{(i+1)} = \bar{x}^{(i)} - C^{-1}[\bar{b} + C\bar{x}^{(i)}]$$

On the first iteration ( $i = 0$ )

$$\begin{aligned}
\bar{x}^{(1)} &= \bar{x}^{(0)} - C^{-1}[\bar{b} + C\bar{x}^{(0)}] \\
&= \bar{x}^{(0)} - C^{-1}\bar{b} - \bar{x}^{(0)} \\
&= -C^{-1}\bar{b} \\
&= \bar{x}^*
\end{aligned}$$

Thus the Newton-Raphson method converges in one step to  $\bar{x}^*$  from arbitrary  $\bar{x}^{(0)}$  when  $f(\bar{x})$  is a quadratic function as defined.

For the quadratic function the gradient method produces a sequence which ultimately converges and requires only first-order information. However a very high number of iterations may be required before the limit point is recognized; this is a disadvantage in the gradient method. The Newton-Raphson method converges rapidly but has the disadvantage of requiring second-order information and a matrix inverse to exist. A method which requires only first-order information and converges in a finite number of steps for the defined quadratic function is the conjugate direction method which is now discussed (ref. 14).

Define

$$\bar{g}^{(i)} = \nabla_{\bar{x}} f[\bar{x}^{(i)}]$$

and consider an arbitrary sequence

$$\bar{x}^{(i+1)} = \bar{x}^{(i)} + \alpha_i \bar{p}^{(i)} \quad (i = 0, 1, \dots)$$

where the scalar  $\alpha_i$  minimizes  $f[\bar{x}^{(i+1)}] - f[\bar{x}^{(i)}]$  which implies that

$$\bar{g}^{(i+1)} \cdot \bar{p}^{(i)} = 0$$

for all  $i$  and  $\bar{p}^{(i)}$  is an unspecified vector function of  $\bar{x}^{(i)}$ . By repeated use of the correction formula

$$\bar{x}^{(n)} = \bar{x}^{(j+1)} + \sum_{i=j+1}^{n-1} \alpha_i \bar{p}^{(i)}$$

where  $\bar{x}$  is of dimension  $n$ . For the quadratic function

$$\bar{q}^{(i)} = \bar{b} + C\bar{x}^{(i)}$$

and

$$\begin{aligned}
 \bar{g}^{(n)} &= \bar{b} + C\bar{x}^{(n)} \\
 &= \bar{b} + C \left[ \bar{x}^{(j+1)} + \sum_{i=j+1}^{n-1} \alpha_i \bar{p}^{(i)} \right] \\
 &= \bar{g}^{(j+1)} + \sum_{i=j+1}^{n-1} \alpha_i C\bar{p}^{(i)}
 \end{aligned}$$

Form the inner product  $\bar{g}^{(n)} \cdot \bar{p}^{(j)}$  yielding

$$\bar{g}^{(n)} \cdot \bar{p}^{(j)} = \bar{g}^{(j+1)} \cdot \bar{p}^{(j)} + \sum_{i=j+1}^{n-1} \alpha_i \bar{p}^{(j)} \cdot C\bar{p}^{(i)}$$

The term  $\bar{g}^{(j+1)} \cdot \bar{p}^{(j)}$  is zero. Let  $\bar{p}^{(i)}$  ( $i = 0, 1, \dots, n-1$ ) be chosen such that

$$\bar{p}^{(i)} \cdot C\bar{p}^{(j)} = 0 \quad (i \neq j)$$

Such vectors are said to be C-conjugate. In this case, for  $C > 0$ , it can be shown that  $\bar{p}^{(0)}, \bar{p}^{(1)}, \dots, \bar{p}^{(n-1)}$  are linearly independent and form a basis of the space  $R^n$ . With  $\bar{p}^{(i)}$  ( $i = 0, \dots, n-1$ ) chosen to be C-conjugate functions of  $\bar{x}^{(i)}$

$$\bar{g}^{(n)} \cdot \bar{p}^{(j)} = 0 \quad (j = 0, 1, \dots, n-1)$$

Since the  $\bar{p}^{(j)}$  form a basis of  $R^n$

$$\bar{g}^{(n)} = \bar{0}$$

or

$$\bar{b} + C\bar{x}^{(n)} = 0$$

or

$$\bar{x}^{(n)} = -C^{-1}\bar{b} = \bar{x}^*$$

Thus the method of conjugate directions presented minimizes the quadratic function in  $n$ -steps where  $n$  is the dimension of  $\bar{x}$ .

If  $\bar{p}^{(i)} = A\bar{g}^{(i)}$ , where  $A$  is a positive definite matrix, the method of conjugate directions is referred to as the method of conjugate gradients. A particularly useful conjugate-gradient method is the Fletcher-Powell (ref. 15) reformulation of the Davidon method (ref. 16). Here

$$\bar{p}^{(i)} = -H^{(i)}\bar{g}^{(i)}$$

where  $H^{(0)}, H^{(1)}, \dots$  is a sequence of symmetric positive definite matrices. The matrix  $H^{(0)}$  is arbitrary but is usually taken to be the identity matrix and subsequent matrices are determined by

$$H^{(i+1)} = H^{(i)} + \frac{\bar{p}^{(i)}\bar{p}^{(i)'}}{\bar{p}^{(i)} \cdot C\bar{p}^{(i)}} - \frac{H^{(i)}\bar{v}^{(i)}\bar{v}^{(i)'}H^{(i)}}{\bar{v}^{(i)} \cdot H^{(i)}\bar{v}^{(i)}}$$

where

$$\bar{v}^{(i)} = \bar{g}^{(i+1)} - \bar{g}^{(i)}$$

It is shown in reference 15 that as  $\bar{x}^{(i)}$  reaches  $\bar{x}^*$ ,  $H^{(i)}$  becomes  $C^{-1}$ .

The first-order methods of gradients and conjugate directions and the second-order Newton-Raphson method have been introduced and their behavior has been examined when the function to be minimized is quadratic. For functions not necessarily quadratic the gradient, conjugate direction, Newton-Raphson, and other methods (ref. 17) are still applied. Usually convergence is not guaranteed but it is hoped that a guess  $\bar{x}^{(0)}$  can be made sufficiently close to  $\bar{x}^*$  so that the methods behave quadratically; this means that they converge in a finite number of steps. The choice of  $\alpha_i$  is often made by search methods (ref. 18).

## OPTIMIZATION OF FUNCTIONALS

The optimization of functionals (a general functional is a mapping of a function into a real number) lies in the domain of functional analysis (ref. 19). A subdivision of functional analysis treating the optimization of functionals in the form of definite integrals (or equivalent representations) is called the calculus of variations (ref. 20). An extension of the calculus of variations is found in the modern subject of optimal control theory (ref. 21). Excellent survey articles on optimal control theory are



given in references 22 and 23. References 24 and 25 demonstrate how calculus of variations problems may be solved by optimal control methods. For a modern approach the optimization of definite integrals (or equivalent representations) are considered herein by the methods of optimal control theory. As in the case of function optimization, optimal control theory may be formulated either sequentially or nonsequentially.

### The Basic Optimal Control Problem

Let a controllable dynamic system be described by a set of vector differential equations of the form

$$\dot{\bar{x}}(t) = \bar{f}[\bar{x}(t), \bar{u}(t), t] \quad (\bar{x}(t_0) = \bar{x}_0)$$

where

$\bar{x}_0$             initial value of  $\bar{x}(t)$

$t \in [t_0, t_1]$

$\bar{x} \in R^n$

$\bar{f} \in R^n$

$\bar{u} \in R^m$

$t$             time

$t_0$             initial time

$t_1$             final time

$\bar{x}(t)$             state variable of system

$\bar{x} = \text{col } (x_i) \quad (i = 1, 2, \dots, n)$

$\bar{u}(t)$             control variable

$\bar{u} = \text{col } (u_i) \quad (i = 1, 2, \dots, m)$

Controls which are piecewise continuous functions of  $t$  and for each  $t$  satisfy  $u(t) \in U^m \subset R^m$  are herein called admissible.

Examples of  $U$ :

- (a) If  $\bar{u}$  is unconstrained, then  $U = R^m$ .
- (b) If  $\|\bar{u}\| = 1$ , then  $U$  is the boundary of a unit hypersphere with center at the origin.
- (c) If  $|u_i| \leq 1$  ( $i = 1, 2, \dots, m$ ), then  $U$  is the interior and boundary of a unit hypercube centered at the origin in  $R^m$ .

Assume a performance functional exists in the form of a definite integral of a function  $f_0(\bar{x}, \bar{u}, t)$  denoted by

$$J = \int_{t_0}^{t_1} f_0[\bar{x}(t), \bar{u}(t), t] dt$$

For two controls  $\bar{u}_1$  and  $\bar{u}_2$ ,  $\bar{u}_1$  is said to be better than  $\bar{u}_2$  if

$$J(\bar{u}_1) < J(\bar{u}_2)$$

Also let there be target sets  $S_0$  and  $S_1$  in  $R^n$  such that the control  $\bar{u}$  with  $\dot{\bar{x}} = \bar{f}(\bar{x}, \bar{u}, t)$  must take  $\bar{x}(t)$  from  $\bar{x}(t_0) = \bar{x}_0 \in S_0$  to  $\bar{x}(t_1) \in S_1$ . The time  $t_1$  is the first time  $\bar{x}(t)$  enters  $S_1$ .

The basic optimal control problem is as follows: For all  $\bar{u} \in U$  which take  $\bar{x}_0 \in S_0$  to  $\bar{x}(t_1) \in S_1$  through

$$\dot{\bar{x}} = \bar{f}(\bar{x}, \bar{u}, t)$$

find the control (or controls, if any exist) which minimizes

$$J = \int_{t_0}^{t_1} f_0[\bar{x}(t), \bar{u}(t), t] dt$$

Such controls are called optimal.

#### Discussion

An optimal control (or controls) exists if a control (or controls) can be found which takes  $\bar{x}_0$  to  $\bar{x}(t_1)$  such that, if  $\bar{u}^*$  is an optimal control,  $J(\bar{u}^*) \leq J(\bar{u})$  for all  $\bar{u} \in U$ .

Based on the assumption of the existence of an optimal control (or controls) necessary conditions that a given control in  $U$  be optimal can be established for a wide class of problems. The most general set of necessary conditions is the Pontryagin maximum principle (ref. 21). If a control fails the necessary conditions, then it is not optimal. Conversely, all the controls in  $U$  which satisfy the necessary conditions need not be optimal (unless the necessary conditions are both necessary and sufficient). Those controls satisfying the necessary conditions are called "extremal controls." If an optimal control exists and is unique, then it follows from the necessary conditions. If no control can be found to satisfy the necessary conditions, then no optimal control exists.

Next consider some sufficient conditions for optimality. If a control fails a given set of sufficient conditions, the control may still be optimal (unless the sufficient conditions are also necessary). Sufficient conditions can be naturally divided into two classes: local and global.

Local sufficiency.- If  $\hat{u} \in U$  satisfies certain conditions, then  $J(\hat{u}) \leq J(\bar{u})$  for all  $\bar{u}$  belonging to some neighborhood of  $\hat{u}$  and not necessarily all of  $U$ .

Global sufficiency.- If  $\hat{u} \in U$  satisfies certain conditions, then  $J(\hat{u}) \leq J(\bar{u})$  for all  $\bar{u} \in U$ . Global sufficiency implies existence. Necessary conditions are generally derived by assuming that an optimal control  $\bar{u}^*$  exists and by examining properties of the problem in a neighborhood of  $\bar{u}^*$ . Necessary conditions derived in this manner are local conditions. A sufficiency condition for the continuous optimal control problem is the Hamilton-Jacobi-Bellman theory (ref. 2).

#### Other Forms of the Optimal Control Problem

Some other forms of the optimal control problem are now presented. The basic optimal control problem as stated appears in a nonautonomous form; that is, the independent variable  $t$  appears explicitly in the equations. This problem can be transformed to an autonomous problem by the introduction of a new state variable  $x_{n+1}$  such that

$$\dot{x}_{n+1} = 1 \qquad (x_{n+1}(t_0) = t_0; \quad x_{n+1}(t_1) = t_1)$$

The problem as stated is in Lagrange form (from the Lagrange problem of the calculus of variations) and can be changed to Mayer form by the introduction of a new variable  $x_0$  such that

$$\dot{x}_0 = f_0(\bar{x}, \bar{u}) \qquad (x_0(t_0) = 0)$$

The problem is then to minimize  $x_0(t_1)$ .

The problem may have been stated in Bolza form; that is, minimize

$$l[\bar{x}(t_1)] + \int_{t_0}^{t_1} f_0(\bar{x}, \bar{u}) dt \quad \text{where } l[\bar{x}(t_1)] \text{ is a function evaluated at } \bar{x}(t_1). \text{ For a}$$

Lagrange problem, introduce a new variable  $x_{n+1}$  and a new control  $u_{m+1}$  such that

$$\dot{x}_{n+1} = u_{m+1} \quad (x_{n+1}(t_0) = 0; \quad x_{n+1}(t_1) = l[\bar{x}(t_1)])$$

and then minimize  $\int_{t_0}^{t_1} [f_0(\bar{x}, \bar{u}) + u_{m+1}] dt.$

A free-end time problem,  $t_1$  unspecified, may be transformed into a fixed-end time problem by the introduction of a new variable  $\tau$  where

$$0 \leq \tau \leq 1$$

and by making the transformation

$$t = t_0 + (t_1 - t_0)\tau$$

The unknowns  $t_1$  and  $t_0$  can be eliminated by treating them as parameters. In this way new state variables  $x_{n+1}$  and  $x_{n+2}$  are defined such that

$$\dot{x}_{n+1} = 0$$

$$\dot{x}_{n+2} = 0$$

and  $t_0$  is replaced by  $x_{n+1}$  and  $t_1$  by  $x_{n+2}$  in the equations (if  $t_0$  is also unspecified).

A fixed-end time ( $t_1$  specified) may be treated as a free-end time problem by introducing the new state variable  $x_{n+1}$  with

$$\dot{x}_{n+1} = 1 \quad (x_{n+1}(t_0) = t_0; \quad x_{n+1}(t_1) = t_1)$$

Transformations of these types are given in reference 24.

## Constraints

Constraints, including the state differential equations, may be treated in optimal control theory in much the same way as in the optimization of functions.

Given  $\int_{t_0}^{t_1} h(\bar{x}, \bar{u}) dt = c$ , where  $c$  is a given constant, introduce a new variable  $x_{n+1}$  defined as

$$\dot{x}_{n+1} = h(\bar{x}, \bar{u}) \quad (x_{n+1}(t_0) = 0; \quad x_{n+1}(t_1) = c)$$

to place the integral constraint in the form of a state equation.

Given  $k_1 \leq y(\bar{x}, \bar{u}) \leq k_2$ , Valentine's method (ref. 8) may be directly applied to convert the inequality into an equality.

Given  $g(\bar{x}, \bar{u}) = 0$  over  $[t_0, t_1]$  the following approaches may be used:

(1) Introduce a new variable  $x_{n+1}$  defined as

$$\dot{x}_{n+1} = g^2(\bar{x}, \bar{u}) \quad (x_{n+1}(t_0) = 0; \quad x_{n+1}(t_1) = 0)$$

(2) Apply Lagrange multipliers as in the calculus of variations (ref. 20).

(3) Apply penalty functions as shown in references 26 to 28. In reference 28 the state equations are included in the penalty terms.

Consider  $\int_{t_0}^{t_1} \varphi(\bar{x}, \bar{u}) dt \leq M$ , where  $\varphi(\bar{x}, \bar{u}) \geq 0$ . Since  $\int_{t_0}^t \varphi(\bar{x}, \bar{u}) dt$  for  $t \in [t_0, t_1]$  is monotone increasing in  $t$ , the problem may be divided into two separate problems:

(a) Solve with  $\int_{t_0}^{t_1} \varphi(\bar{x}, \bar{u}) dt = M$ .

(b) Solve without the constraint eliminating those results causing  $\int_{t_0}^{t_1} \varphi(\bar{x}, \bar{u}) dt > M$ .

Comparing the results of (a) and (b) and selecting the best result solves the original problem.

See also reference 29 on constraints.

## Nonsequential Methods

Necessary conditions.- From the foregoing transformations consider a restatement of the problem in autonomous form: For all  $\bar{u} \in U$  which take  $\bar{x}_0 \in S_0$  to  $\bar{x}(t_1) \in S_1$  through

$$\dot{\bar{x}} = \bar{f}(\bar{x}, \bar{u})$$

find the control (or controls, if any exist) which minimize

$$J(\bar{u}) = \int_{t_0}^{t_1} f_0(\bar{x}, \bar{u}) dt$$

Change to a Mayer problem by introducing  $x_0$ . Both  $\bar{f}(\bar{x}, \bar{u})$  and  $f_0(\bar{x}, \bar{u})$  are continuous in  $\bar{x}$  and  $\bar{u}$  and continuously differentiable in  $\bar{x}$ . Consider  $t_1 - t_0$  as unspecified. Pontryagin's maximum principle may now be stated as follows. If  $\bar{u}^*$ ,  $t_0 \leq t \leq t_1$ , is an optimal control, then there exists a nonzero (not identically zero) continuous  $n+1$  dimensional vector  $\bar{\lambda}(t) = (\lambda_0, \lambda_1, \dots, \lambda_n)'$  the elements of which satisfy

$$\frac{d}{dt} \lambda_j = - \sum_{i=0}^n \frac{\partial f_i(\bar{x}, \bar{u})}{\partial x_j} \lambda_i \quad (j = 0, 1, \dots, n)$$

such that.

- (a)  $\max_{\bar{u} \in U} H(\bar{x}, \bar{u}, \bar{\lambda}) = H(\bar{x}, \bar{u}^*, \bar{\lambda}) \quad (t \in [t_0, t_1])$  with  $H = \sum_{i=0}^n \lambda_i f_i(\bar{x}, \bar{u}) = \lambda_0 f_0(\bar{x}, \bar{u}) + \bar{\lambda} \cdot \bar{f}(\bar{x}, \bar{u})$
- (b)  $H[\bar{x}(t), \bar{u}^*(t), \bar{\lambda}(t)] \equiv 0 \quad (t \in [t_0, t_1])$
- (c)  $\lambda_0(t) = \text{Constant} \leq 0$
- (d) The vector  $(\lambda_1, \dots, \lambda_n)'$  is perpendicular to  $S_0$  and  $S_1$  at  $t_0$  and  $t_1$ , respectively. This is called the transversality condition.

With the introduction of  $H$ , the state ( $x_i$ ) and auxiliary variable ( $\lambda_i$ ) equations can be written in canonical form

$$\frac{dx_i}{dt} = \frac{\partial H}{\partial \lambda_i}(\bar{x}, \bar{u}, \bar{\lambda}) \quad (i = 0, 1, \dots, n)$$

$$\frac{d\lambda_i}{dt} = - \frac{\partial H}{\partial x_i}(\bar{x}, \bar{u}, \bar{\lambda}) \quad (i = 0, 1, \dots, n)$$

The maximum principle generates extremal controls. Given the existence of an optimal control, the best extremal control is optimal. In using the maximum principle try to ensure that an optimal control exists for the problem, find all extremal controls,

and select the best. Neither of these steps are easy (ref. 30). Particular difficulties of the maximum principle known as singular and abnormal problems are discussed in reference 31.

Example:

Consider an optimal control problem with variables  $\bar{x} = (x_1, x_2)'$  and  $\bar{\lambda} = (\lambda_1, \lambda_2)'$ . Let the trajectory at  $t_1$  be required to intersect the surface  $x_1^2 + x_2^2 = 1$ . The transversality condition states that  $\lambda(t_1)$  is colinear with the normal to the terminal surface. Thus

$$S_1 = \left\{ \begin{array}{l} \bar{x} : \theta_1(\bar{x}) = x_1^2 + x_2^2 - 1 \\ \phantom{\bar{x} : } = 0 \end{array} \right\}$$

and

$$\nabla_{\bar{x}} \theta_1(\bar{x}) = \begin{pmatrix} 2x_1 \\ 2x_2 \end{pmatrix}$$

is the normal. Thus

$$\bar{\lambda}(t_1) = \alpha \begin{bmatrix} x_1(t_1) \\ x_2(t_1) \end{bmatrix}$$

with  $\alpha$  a scalar.

Example:

Consider a system the state equations of which are

$$\dot{x}_1 = x_2$$

$$\dot{x}_2 = u$$

with control variable constraint

$$|u| \leq 1$$

whereby

$$U = [-1, 1]$$

Transfer the system from a given initial state  $S_0 = [x_1(t_0), x_2(t_0)]$  to the rest state  $S_1 = [0, 0]$  in minimum time. Thus

$$J = \int_{t_0}^{t_1} dt = t_1 - t_0$$

An existence theorem applies to this problem. (See appendix B of ref. 24.) The best extremal control is then the optimal in the sense of minimum time.

To deduce the extremal control invoke the necessary conditions of the maximum principle whereby

$$H = \lambda_0 + \lambda_1 x_2 + \lambda_2 u$$

$$\dot{\lambda}_1 = -\frac{\partial H}{\partial x_1} = 0$$

$$\dot{\lambda}_2 = -\frac{\partial H}{\partial x_2} = -\lambda_1$$

$$\lambda_1(t) = \lambda_1(t_1)$$

$$\lambda_2(t) = \lambda_2(t_1) + \lambda_1(t_1)(t_1 - t)$$

Therefore

$$H = \lambda_0 + c_1 x_2 + (c_2 - c_1 t)u$$

where

$$c_1 = \lambda_1(t_1) = \text{Constant}$$

$$c_2 = \lambda_1(t_1)t_1 + \lambda_2(t_1)$$

The control which maximizes  $H$  is

$$u^* = \text{sgn}(c_2 - c_1 t)$$

where

$$\text{sgn } a(t) = \begin{cases} 1 & (a(t) > 0) \\ -1 & (a(t) < 0) \\ a(\tau^-) & (a(\tau) = 0) \end{cases}$$



If  $c_2 = c_1 = 0$ , then  $\lambda_1 = \lambda_2 = 0$  and  $H = \lambda_0$ . Condition (b) implies that  $\lambda_0 = 0$  or  $\bar{\lambda} = \begin{pmatrix} \lambda_0 \\ \lambda_1 \\ \lambda_2 \end{pmatrix} = \bar{0}$ . However the maximum principle states that  $\bar{\lambda} \neq \bar{0}$  which is a contradiction. Therefore on an optimal trajectory either  $c_1$  or  $c_2 \neq 0$ . The control  $u^*$  changes sign at most once. The argument of  $\text{sgn}$  in  $u^*$

$$\sigma(t) = c_2 - c_1 t$$

is called a "switching function." Forming

$$\frac{\frac{dx_1}{dt}}{\frac{dx_2}{dt}} = \frac{x_2}{u^*} \Rightarrow \frac{dx_1}{dx_2} = \frac{x_2}{u^*}$$

or

$$x_2 dx_2 = u^* dx_1 \quad (u^* = \pm 1)$$

whereby the extremal trajectories satisfy

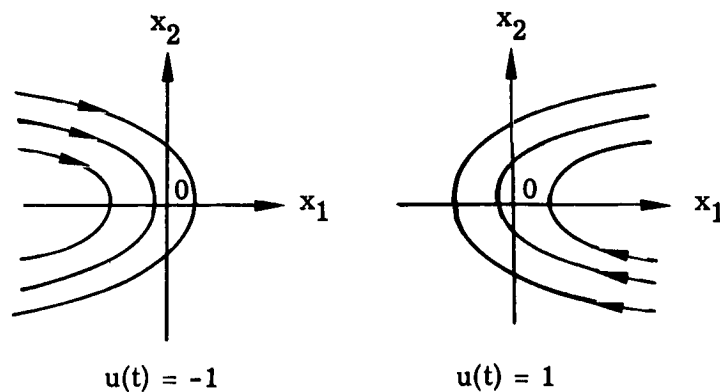
$$\frac{x_2^2}{2} = \pm x_1 + k$$

(where  $k$  is an integration constant) where

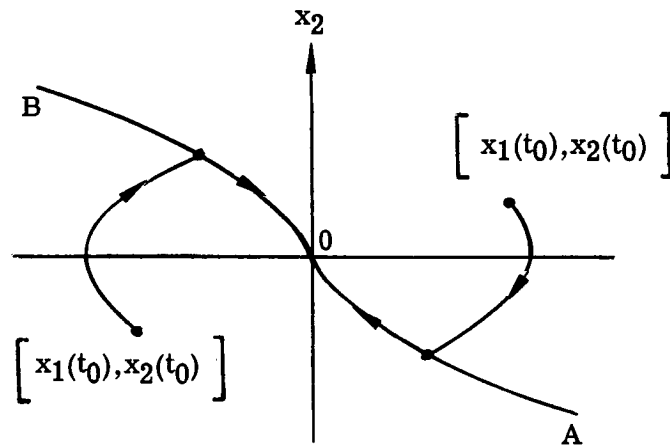
$$\frac{dx_2}{dt} > 0 \quad (u^* = 1)$$

$$\frac{dx_2}{dt} < 0 \quad (u^* = -1)$$

is shown in the following sketch:



Since there can be at most one switch, an extremal path consists of at most two parabolic arcs. Furthermore, since an extremal path terminates at the origin, the terminal arc; that is, the second arc if there is more than one, belongs to one of the two half parabolas  $x_2^2 = 2x_1$  ( $\dot{x}_2 > 0$ ) or  $x_2^2 = -2x_1$  ( $\dot{x}_2 < 0$ ). These half parabolas, denoted by A0 and B0 in the following sketch, compose the switching curve in state space; that is, the locus of states at which an extremal control switches:



The switching curve divides state space into two open half spaces. Extremal paths which start below the switching curve correspond to extremal control sequence  $1 \rightarrow -1$ , and conversely those originating above the switching curve correspond to extremal control sequence  $-1 \rightarrow 1$ . If the initial point of an extremal path belongs to the switching curve, there is no switch.

Two observations follow:

- (1) For initial state  $[x_1(t_0), x_2(t_0)]$  extremal control is unique, hence, optimal.
- (2) There exists an optimal path from every point in state space  $R^2$ .

Since  $S_1$  and  $S_2$  are points, the transversality conditions are automatically satisfied. To show this, for the terminal manifold

$$S_1 = \begin{cases} \theta_1 = x_1 = 0 \\ \theta_2 = x_2 = 0 \end{cases}$$

(where  $S_1$  is the intersection of  $\theta_1$  and  $\theta_2$ )

$$\bar{\lambda} = \begin{pmatrix} \lambda_1 \\ \lambda_2 \end{pmatrix}$$

is normal to any vector in the tangent plane of  $S_1$ . A vector  $\begin{pmatrix} \alpha_1 \\ \alpha_2 \end{pmatrix}$  lies in the tangent plane of  $S_1$  if and only if it is orthogonal to  $\nabla_{\bar{x}}^{\theta_1}$  and  $\nabla_{\bar{x}}^{\theta_2}$ . Since

$$\nabla_{\bar{x}}^{\theta_1} = \begin{pmatrix} 1 \\ 0 \end{pmatrix}$$

$$\nabla_{\bar{x}}^{\theta_2} = \begin{pmatrix} 0 \\ 1 \end{pmatrix}$$

then  $\begin{pmatrix} \alpha_1 \\ \alpha_2 \end{pmatrix} \cdot \nabla_{\bar{x}}^{\theta_1} = 0$  yields  $\alpha_1 = 0$  and  $\begin{pmatrix} \alpha_1 \\ \alpha_2 \end{pmatrix} \cdot \nabla_{\bar{x}}^{\theta_2} = 0$  yields  $\alpha_2 = 0$ . Therefore the only vector in the tangent plane of  $S_1$  is the null vector which is orthogonal to all  $\bar{\lambda}$ .

Sufficient conditions.— A statement of the Hamilton-Jacobi-Bellman method is presented in this section. Further information is given in references 2 and 31 to 36. The discrete form of this method is better known as dynamic programming (ref. 33).

**Theorem:** Consider the control process in  $R^n$

$$\dot{\bar{x}} = \bar{f}(\bar{x}, \bar{u}, t)$$

with initial state  $\bar{x}(t_0)$  and terminal set  $S_1 \subset R^n$ . Admissible controllers are all piecewise continuous functions  $\bar{u}(t)$  on  $t_0 \leq t \leq t_1$  with values in the restraint set  $U \subset R^m$ , steering the response  $\bar{x}(t)$  from  $\bar{x}(t_0) = \bar{x}_0$  to  $\bar{x}(t_1) \in S_1$ . The functional is

$$J(\bar{u}) = l[\bar{x}(t_1)] + \int_{t_0}^{t_1} f_0[\bar{x}(t), \bar{u}(t), t] dt$$

where  $l$ ,  $\bar{f}$ , and  $f_0$  are functions continuously differentiable in all arguments. Assume there exists a continuously differentiable control  $\bar{u}^*(\bar{\lambda}, \bar{x}, t)$  so that

$$\begin{aligned} H^*(\bar{\lambda}, \bar{x}, t) &= \max_{\bar{u} \in U} [-f_0(\bar{x}, \bar{u}, t) + \bar{\lambda} - \bar{f}(\bar{x}, \bar{u}, t)] \\ &= H[\bar{\lambda}, \bar{x}, t, \bar{u}^*(\bar{\lambda}, \bar{x}, t)] \end{aligned}$$

Let  $C(\bar{x}, t)$  for  $\bar{x} \in R^n$  and  $t \leq t_1$  be a continuously differentiable function of second order which is a solution of the Hamilton-Jacobi-Bellman equation

$$\frac{\partial C(\bar{x}, t)}{\partial t} + H^*(\nabla_{\bar{x}} C, \bar{x}, t) = 0$$

with  $C[\bar{x}(t_1), t_1] = -l[\bar{x}(t_1)]$  for  $\bar{x}(t_1) \in S_1$ . Assume that the control law

$$\bar{u}(\bar{x}, t) = \bar{u}^*(\nabla_{\bar{x}} C, \bar{x}, t)$$

determines a response  $\bar{x}(t)$  steering  $(\bar{x}_0(t_0), t_0)$  to  $(S_1, t_1)$ ; then  $\bar{u}$  is an optimal control (provided it lies in  $U$ ) with optimal response  $\bar{x}(t)$ , and with

$$J(\bar{u}) = -C[\bar{x}(t_0), t_0]$$

**Example:**

Consider the linear time-varying system described by

$$\dot{\bar{x}} = A(t)\bar{x} + B(t)\bar{u} \quad (\bar{x}(t_0) = \bar{x}_0)$$

and the functional

$$J = \frac{1}{2} \bar{x}(t_1) \cdot F \bar{x}(t_1) + \frac{1}{2} \int_{t_0}^{t_1} [\bar{x}(t) \cdot Q(t) \bar{x}(t) + \bar{u}(t) \cdot R(t) \bar{u}(t)] dt$$

where  $t_1 - t_0$  is given,  $\bar{u}(t)$  is unconstrained,  $\bar{u}(t) \in R^m$ ,  $\bar{x}(t_1)$  is unspecified,  $\bar{x}(t_1) \in S_1 = R^n$ ,  $F$  is a constant  $n \times n$  positive semidefinite matrix ( $\geq 0$ ),  $R(t)$  is a continuous matrix ( $> 0$ ),  $Q(t)$  is a continuous matrix, ( $\geq 0$ ),  $A(t)$  is a continuous  $n \times n$  matrix, and  $B(t)$  is a continuous  $n \times m$  matrix. The problem is to find  $\bar{u}$  to minimize  $J$ . With regard to the sufficiency theorem

$$l[\bar{x}(t_1)] = \frac{1}{2} \bar{x}(t_1) \cdot F \bar{x}(t_1)$$

$$H^*(\bar{\lambda}, \bar{x}, t) = \max_{\bar{u} \in R^m} H(\bar{x}, \bar{\lambda}, \bar{u}, t)$$

$$= \max_{\bar{u} \in R^m} \left[ -\frac{1}{2} (\bar{x} \cdot Q \bar{x} + \bar{u} \cdot R \bar{u}) + \bar{\lambda} \cdot (A \bar{x} + B \bar{u}) \right]$$

The first partial derivative of  $H(\bar{\lambda}, \bar{x}, \bar{u}, t)$  with respect to  $\bar{u}$  set equal to zero gives

$$-R\bar{u} + B'\bar{\lambda} = \bar{0}$$

or

$$\bar{u} = R^{-1}B'\bar{\lambda}$$

This  $\bar{u}$  maximizes  $H(\bar{\lambda}, \bar{x}, \bar{u}, t)$  since the second partial with respect to  $\bar{u}$  gives  $-R < 0$ . Thus

$$H^*(\bar{\lambda}, \bar{x}, t) = -\frac{1}{2}\bar{x} \cdot Q\bar{x} + \frac{1}{2}\bar{\lambda} \cdot BR^{-1}B'\bar{\lambda} + \bar{\lambda} \cdot A\bar{x}$$

Look for a solution of the Hamilton-Jacobi-Bellman equation

$$\frac{\partial C}{\partial t} + H^*(\nabla_{\bar{x}}C, \bar{x}, t) = \frac{\partial C}{\partial t} + \frac{1}{2}\nabla_{\bar{x}}C \cdot BR^{-1}B'\nabla_{\bar{x}}C - \frac{1}{2}\bar{x} \cdot Q\bar{x} + \nabla_{\bar{x}}C \cdot A\bar{x} = 0$$

where at  $t_1$

$$C[\bar{x}(t_1), t_1] = -l[\bar{x}(t_1)] = -\frac{1}{2}\bar{x}(t_1) \cdot F\bar{x}(t_1)$$

Try a solution of the form

$$C(\bar{x}, t) = -\frac{1}{2}\bar{x}(t) \cdot K(t)\bar{x}(t)$$

where  $K(t)$  is an arbitrary differentiable  $n \times n$  matrix. Assume that  $K(t) = K'(t)$  and let  $K(t_1) = F$  satisfy the boundary condition. With

$$\frac{\partial C}{\partial t} = -\frac{1}{2}\bar{x} \cdot \dot{K}(t)\bar{x}$$

and

$$\nabla_{\bar{x}}C = -K(t)\bar{x}$$

the Hamilton-Jacobi-Bellman equation becomes

$$-\frac{1}{2}\bar{x} \cdot \dot{K}\bar{x} + \frac{1}{2}K\bar{x} \cdot BR^{-1}B'K\bar{x} - \frac{1}{2}\bar{x} \cdot Q\bar{x} - K\bar{x} \cdot A\bar{x} = 0$$

Write  $K\bar{x} \cdot A\bar{x}$  as  $\frac{1}{2}(\bar{x} \cdot KA\bar{x} + \bar{x} \cdot A'K\bar{x})$ . The Hamilton-Jacobi-Bellman equation

$$\frac{1}{2} \bar{\dot{x}} \cdot (-\dot{K} + KBR^{-1}B'K - Q - KA - A'K) \bar{x} = 0$$

is identically satisfied for  $K(t)$  satisfying

$$\dot{K}(t) = K(t)BR^{-1}B'K(t) - K(t)A - A'K(t) - Q \quad (K(t_1) = F)$$

which is the matrix Riccati equation often referred to in optimal control theory. The theorem guarantees the optimality of

$$\bar{u}^*(t) = R^{-1}(t)B'(t)\nabla_{\bar{x}}C(\bar{x},t) = -R^{-1}(t)B'(t)K(t)\bar{x}(t)$$

with

$$J(\bar{u}^*) = -C(\bar{x}_0, t_0) = \frac{1}{2} \bar{x}_0 \cdot K(t_0) \bar{x}_0$$

Maximum principle and sufficiency.- With some conditions added to the basic optimal control problem the maximum principle becomes sufficient as well as necessary. A formulation of this result is found in references 36 and 37.

### Sequential Methods

The optimization of functionals in the form of an optimal control problem may also be treated by sequential methods. Here try to form a sequence of admissible controls  $\bar{u}^{(i)}(t)$  ( $i = 0, 1, \dots$ ) which yield  $\bar{x}^{(i)}(t)$  through the differential equations

$$\dot{\bar{x}}^{(i)}(t) = \bar{f}[\bar{x}^{(i)}, \bar{u}^{(i)}]$$

and generate a monotone decreasing sequence of values  $J^{(i)}$  of the performance index  $J$  which converge to a minimum value of  $J$ . As in the sequential optimization of functions, there exist the methods of gradients (refs. 1 and 38), conjugate gradients (ref. 39), and second-order variations (ref. 40). A form of the Newton-Raphson process exists for optimal control problems in the same sense as in function optimization problems in that it seeks to satisfy iteratively the necessary conditions of the nonsequential methods (refs. 41 and 42). For a summary of these methods see reference 43.

In order to illustrate the general approach of the sequential methods, a simple form of the gradient method is presented. Consider the problem of finding an unconstrained control  $\bar{u}(t)$  which minimizes

$$J = \phi[\bar{x}(t_1)]$$

where  $\bar{x}(t)$  is determined through  $\dot{\bar{x}} = \bar{f}(\bar{x}, \bar{u})$ ,  $t \in [t_0, t_1]$ ,  $\bar{x}(t_0) = \bar{x}_0$ , and  $t_1 - t_0$  is specified. Try to construct a sequence  $\bar{u}^{(i)}(t)$  so as to minimize  $J$ . Assume a control function  $\bar{u}^{(0)}(t)$  and solve for  $\bar{x}^{(0)}(t)$ , the solution of

$$\dot{\bar{x}} = \bar{f}[\bar{x}, \bar{u}^{(0)}] \quad (\bar{x}(t_0) = \bar{x}_0)$$

Writing the variational equations for

$$\dot{\bar{x}} = \bar{f}(\bar{x}, \bar{u})$$

around  $[\bar{x}^{(0)}(t), \bar{u}^{(0)}(t)]$  yields

$$\frac{d}{dt} \delta \bar{x}^{(0)} = \frac{\partial \bar{f}[\bar{x}^{(0)}, \bar{u}^{(0)}]}{\partial \bar{x}} \delta \bar{x}^{(0)} + \frac{\partial \bar{f}[\bar{x}^{(0)}, \bar{u}^{(0)}]}{\partial \bar{u}} \delta \bar{u}^{(0)} \quad (\delta \bar{x}^{(0)} = \bar{0})$$

Introduce  $\bar{\lambda}^{(0)}(t)$ , unspecified for the moment, and differentiate with respect to  $t$ ,  $\bar{\lambda}^{(0)}(t) \cdot \delta \bar{x}^{(0)}(t)$ , to obtain

$$\frac{d}{dt} \bar{\lambda}^{(0)}(t) \cdot \delta \bar{x}^{(0)}(t) = \left\{ \dot{\bar{\lambda}}^{(0)} + \frac{\partial \bar{f}'[\bar{x}^{(0)}, \bar{u}^{(0)}]}{\partial \bar{x}} \bar{\lambda}^{(0)} \right\} \cdot \delta \bar{x}^{(0)} + \frac{\partial \bar{f}'[\bar{x}^{(0)}, \bar{u}^{(0)}]}{\partial \bar{u}} \bar{\lambda}^{(0)} \cdot \delta \bar{u}^{(0)}$$

Define  $\bar{\lambda}^{(0)}(t)$  as the solution of

$$\dot{\bar{\lambda}}^{(0)}(t) = - \frac{\partial \bar{f}'[\bar{x}^{(0)}, \bar{u}^{(0)}]}{\partial \bar{x}} \bar{\lambda}^{(0)}(t)$$

whereby

$$\frac{d}{dt} \bar{\lambda}^{(0)}(t) \cdot \delta \bar{x}^{(0)}(t) = \frac{\partial \bar{f}'[\bar{x}^{(0)}, \bar{u}^{(0)}]}{\partial \bar{u}} \bar{\lambda}^{(0)} \cdot \delta \bar{u}^{(0)}$$

or

$$\bar{\lambda}^{(0)}(t_1) \cdot \delta \bar{x}^{(0)}(t_1) = \int_{t_0}^{t_1} \frac{\partial \bar{f}'[\bar{x}^{(0)}, \bar{u}^{(0)}]}{\partial \bar{u}} \bar{\lambda}^{(0)} \cdot \delta \bar{u}^{(0)} dt$$

Define

$$\bar{\lambda}^{(0)}(t_1) = \nabla_{\bar{x}} \varphi[\bar{x}^{(0)}(t_1)]$$

whereby

$$\begin{aligned}\bar{\lambda}^{(0)}(t_1) \cdot \delta \bar{x}^{(0)}(t_1) &= \nabla_{\bar{x}} \varphi[\bar{x}^{(0)}(t_1)] \cdot \delta \bar{x}^{(0)}(t_1) = \delta \varphi[\bar{x}^{(0)}(t_1)] \\ &\approx \varphi[\bar{x}^{(0)}(t_1) + \delta \bar{x}^{(0)}(t_1)] - \varphi[\bar{x}^{(0)}(t_1)]\end{aligned}$$

The quantity  $\delta \bar{u}^{(0)}(t)$  is undetermined. In the gradient method  $\delta \bar{u}^{(0)}(t)$  is determined by solving the following optimal control problem:

Find  $\delta \bar{u}^{(0)}$  so as to minimize

$$\delta \varphi[\bar{x}^{(0)}(t_1)] = \int_{t_0}^{t_1} \frac{\partial \bar{f}'[\bar{x}^{(0)}, \bar{u}^{(0)}]}{\partial \bar{u}} \bar{\lambda}^{(0)} \cdot \delta \bar{u}^{(0)} dt$$

subject to the constraint  $P^2 = \int_{t_0}^{t_1} \delta \bar{u}^{(0)}(t) \cdot W(t) \delta \bar{u}^{(0)}(t) dt$  where  $W(t)$  is a positive definite symmetric matrix and  $P$  is a positive constant. The  $P^2$  constraint is introduced so that the magnitude of  $\delta \bar{u}^{(0)}(t)$  can be controlled to insure the validity of the foregoing linearization process. The matrix  $W(t)$  is added for weighting purposes. The solution of this problem (easily obtained by the use of nonsequential methods) is

$$\delta \bar{u}^{(0)}(t) = -\frac{W(t)^{-1}}{\alpha} \frac{\partial \bar{f}'[\bar{x}^{(0)}(t), \bar{u}^{(0)}(t)]}{\partial \bar{u}} \bar{\lambda}^{(0)}(t)$$

with

$$\alpha = \left[ \frac{\int_{t_0}^{t_1} \frac{\partial \bar{f}'}{\partial \bar{u}} \bar{\lambda}^{(0)} \cdot W^{-1} \frac{\partial \bar{f}'}{\partial \bar{u}} \bar{\lambda}^{(0)} dt}{P^2} \right]^{1/2}$$

and

$$\delta \varphi[\bar{x}^{(0)}(t_1)] = -P \int_{t_0}^{t_1} \left[ \frac{\partial \bar{f}'}{\partial \bar{u}} \bar{\lambda}^{(0)} \cdot W^{-1} \frac{\partial \bar{f}'}{\partial \bar{u}} \bar{\lambda}^{(0)} \right]^{1/2} dt$$

In practice  $W$  and  $P^2$  are specified by the user.

Replacing  $\bar{u}^{(0)}(t)$  by  $\bar{u}^{(0)}(t) + \delta \bar{u}^{(0)}(t)$  gives a new control  $\bar{u}^{(1)}(t)$  yielding  $J^{(1)} = \varphi[\bar{x}^{(1)}(t_1)]$  (to first order) differing from  $J^{(0)} = \varphi[\bar{x}^{(0)}(t_1)]$  by

$-P \int_{t_0}^{t_1} \left[ \frac{\partial \bar{f}'}{\partial \bar{u}} \bar{\lambda}^{(0)} \cdot W^{-1} \frac{\partial \bar{f}'}{\partial \bar{u}} \bar{\lambda}^{(0)} \right]^{1/2} dt$ . A correction to  $\bar{u}^{(1)}(t)$  is obtained by treating



$\bar{u}^{(1)}(t)$  as  $\bar{u}^{(0)}(t)$  and repeating the process. Repetitive application yields the sequence  $\bar{u}^{(i)}(t)$  ( $i = 0, 1, \dots$ ) determined by

$$\delta \bar{u}^{(i)}(t) = \frac{-W^{-1}(t)}{\alpha_i} \frac{\partial \bar{f}'[\bar{x}^{(i)}, \bar{u}^{(i)}]}{\partial \bar{u}} \bar{\lambda}^{(i)}(t)$$

with  $\bar{\lambda}^{(i)}$  determined from backward integration of

$$\dot{\bar{\lambda}}^{(i)}(t) = \frac{-\partial \bar{f}'[\bar{x}^{(i)}, \bar{u}^{(i)}]}{\partial \bar{x}} \bar{\lambda}^{(i)}(t) \quad \left( \bar{\lambda}^{(i)}(t_1) = \nabla_{\bar{x}} \phi[\bar{x}^{(i)}(t_1)] \right)$$

and  $\bar{x}^{(i)}$  determined from forward integration of

$$\dot{\bar{x}}^{(i)}(t) = \bar{f}[\bar{x}^{(i)}(t), \bar{u}^{(i)}(t)] \quad (\bar{x}^{(i)}(t_0) = \bar{x}_0)$$

and

$$\alpha_i = \left[ \frac{\int_{t_2}^{t_1} \frac{\partial \bar{f}'[\bar{x}^{(i)}, \bar{u}^{(i)}]}{\partial \bar{u}} \bar{\lambda}^{(i)} \cdot W^{-1} \frac{\partial \bar{f}'[\bar{x}^{(i)}, \bar{u}^{(i)}]}{\partial \bar{u}} \bar{\lambda}^{(i)} dt}{P^2} \right]^{1/2}$$

$$\begin{aligned} \delta J^{(i)} &= \int_{t_0}^{t_1} \frac{\partial \bar{f}'[\bar{x}^{(i)}, \bar{u}^{(i)}]}{\partial \bar{u}} \bar{\lambda}^{(i)} \cdot \delta \bar{u}^{(i)} dt \\ &= -P \int_{t_0}^{t_1} \left\{ \frac{\partial \bar{f}'[\bar{x}^{(i)}, \bar{u}^{(i)}]}{\partial \bar{u}} \bar{\lambda}^{(i)} \cdot W^{-1} \frac{\partial \bar{f}'[\bar{x}^{(i)}, \bar{u}^{(i)}]}{\partial \bar{u}} \bar{\lambda}^{(i)} \right\}^{1/2} dt \end{aligned}$$

The gradient of  $J^{(i)}$  with respect to the magnitude of  $\delta u^{(i)}$  is given by  $\delta J^{(i)}/P$ .

For appropriate values of  $W$  and  $P^2$  this process generates a sequence of  $\bar{u}^{(i)}(t)$  providing a decreasing sequence of  $J^{(i)}$ . At each stage it may be necessary to readjust  $W$  and  $P^2$  to retain convergence.

Ideally the process converges to a point where

$$\delta \bar{u}^{(i)}(t) = \frac{-W^{-1}(t)}{\alpha_i} \frac{\partial \bar{f}'[\bar{x}^{(i)}(t), \bar{u}^{(i)}(t)]}{\partial \bar{u}} \bar{\lambda}^{(i)}(t) \equiv \bar{0}$$

or where

$$\frac{\partial \bar{f}'[\bar{x}^{(i)}(t), \bar{u}^{(i)}(t)]}{\partial \bar{u}} \bar{\lambda}^{(i)}(t) \equiv \bar{0}$$

For the original optimization problem (not the one determining  $\delta \bar{u}^{(0)}(t)$ )

$$H(\bar{x}, \bar{\lambda}, \bar{u}) = \bar{\lambda} \cdot \bar{f}(\bar{x}, \bar{u})$$

and

$$\nabla_{\bar{u}} H(\bar{x}, \bar{\lambda}, \bar{u}) = \frac{\partial \bar{f}'(\bar{x}, \bar{u})}{\partial \bar{u}} \bar{\lambda}$$

whereby

$$\delta \bar{u}^{(i)}(t) = \frac{-W^{-1}(t)}{\alpha_i} \nabla_{\bar{u}} H[\bar{x}^{(i)}, \bar{\lambda}^{(i)}, \bar{u}^{(i)}]$$

Hence the term "gradient" is used for this sequential method. Convergence is then to a local extremum of  $H(\bar{x}, \bar{\lambda}, \bar{u})$ , that is, where  $\nabla_{\bar{u}} H(\bar{x}, \bar{\lambda}, \bar{u}) = \bar{0}$ . The convergence point may not be the global maximum of  $H(\bar{x}, \bar{\lambda}, \bar{u})$  with respect to  $\bar{u}$  as the Pontryagin maximum principle requires. The gradient method has been found to be highly effective in atmospheric trajectory problems.

## FUNCTION OPTIMIZATION AND OPTIMAL CONTROL THEORY

Function optimization theory may be applied to optimal control problems. If the state equations are in the form of difference equations (rather than differential) or if a continuous problem has been discretized (ref. 44) and the performance index is a finite sum, then function optimization techniques can be directly applied (ref. 45). A discrete form of the maximum principle appears in reference 46. Function optimization methods can also be applied to optimal control problems in another way as discussed in this section.

An unfortunate by-product of applying Pontryagin's maximum principle (or the calculus of variations) to some optimal control problems is a two-point boundary-value problem. A large class of these boundary-value problems involves a vector differential equation of the form:

$$\dot{\bar{y}} = \bar{g}(\bar{y}, \text{sgn } \bar{z}, \bar{\alpha}, t) \quad (t \in [t_0, t_1], \bar{y}(\bar{\alpha}, t_0) = \bar{y}_0) \quad (1)$$

where

$$\bar{y} = \text{col } (y_i) \quad (i = 1, 2, \dots, 2n)$$

$$\bar{z} = \text{col } (z_i) \quad (i = 1, 2, \dots, l)$$

$$\text{sgn } \bar{z} = \text{col } (\text{sgn } z_i) \quad (i = 1, 2, \dots, l)$$

and

$$\bar{\alpha} = \text{col } (\alpha_i) \quad (i = 1, 2, \dots, m)$$

The elements of the vector  $\bar{y}$  are the state  $(x_j)$  ( $j = 1, \dots, n$ ) and the auxiliary variables  $(\lambda_j)$  ( $j = 1, \dots, n$ ) of the control theory with the  $\alpha_i$  unknown constants usually corresponding to some of the initial values of the  $y_i$  and/or the final time  $t_1$ . The vector  $\bar{z} = \bar{z}(\bar{y}, \alpha, t)$  is made up of functions termed "switching functions" in control theory. The two-point boundary-value problem arises when the optimal-control theory requires that  $\bar{\alpha}$  be determined to satisfy terminal conditions of the form

$$\bar{e}[\bar{y}(\bar{\alpha}, t_1), \bar{\alpha}, t_1] = \bar{0} \quad (2)$$

where  $\bar{y}(\bar{\alpha}, t)$  is the solution of equation (1) for given  $\bar{\alpha}$ .

For example, in an optimal control problem where the initial state is specified and the terminal state unspecified, the transversality conditions yield no information about  $\lambda_i(t_0)$  ( $i = 1, 2, \dots, n$ ) but require  $\lambda_i(t_1) = 0$  ( $i = 1, \dots, n$ ). This problem could be put into the form of equation (2) by identifying

$$\alpha_i = \lambda_i(t_0) \quad (i = 1, \dots, n)$$

as constants to be found such that

$$\bar{e}[\bar{y}(\bar{\alpha}, t_1), \bar{\alpha}, t_1] = \text{col } [\lambda_i(\bar{\alpha}, t_1)] = \bar{0} \quad (i = 1, \dots, n)$$

The terminal conditions represented by equation (2) can be viewed as an implicit system of equations in  $\bar{\alpha}$ . From this viewpoint a solution of equation (2) may be sought directly by the Newton-Raphson method. Alternatively, let a positive definite function be formed in the vector  $\bar{e}$ . The minimum of this function with respect to  $\bar{\alpha}$  is

$$\bar{e} = \bar{0}$$

Thus equations (1) and (2) can be solved by finding an  $\bar{\alpha}$  which minimizes a positive definite function in  $\bar{e}$  to zero. With this viewpoint any of the sequential function minimization methods may be applied. The application of these methods to solve boundary-value problems in optimal control is discussed in references 47 to 49.

## REFERENCES

1. Leitmann, George, ed.: Optimization Techniques. Academic Press, Inc., c.1962.
2. Athans, Michael; and Falb, Peter L.: Optimal Control. McGraw-Hill Book Co., Inc., c.1966.
3. Saaty, Thomas L.; and Bram, Joseph: Nonlinear Mathematics. McGraw-Hill Book Co., Inc., c.1964.
4. Dantzig, George B.: Linear Programming and Extensions. Princeton Univ. Press, 1963.
5. Abadie, J., ed.: Nonlinear Programming. North-Holland Pub. Co. (Amsterdam), 1967.
6. Boot, John C. G.: Quadratic Programming. Rand McNally & Co., 1964.
7. Fiacco, Anthony V.; and McCormick, Garth P.: Nonlinear Programming: Sequential Unconstrained Minimization Techniques. John Wiley & Sons, Inc., c.1968.
8. Valentine, Frederick Albert: The Problem of Lagrange With Differential Inequalities as Added Side Conditions. Contributions to the Calculus of Variations - 1933-1937, Univ. of Chicago Press, 1965, pp. 403-447.
9. Moore, James C.: Some Extensions of the Kuhn-Tucker Results in Concave Programming. NASA Grant NGR 26-004-012, Bus. Public Admin. Res. Center, Univ. of Missouri, Aug. 14, 1967.
10. Powell, M. J. D.: A Method for Minimizing a Sum of Squares of Non-Linear Functions Without Calculating Derivatives. Computer J., vol. 7, no. 4, Jan. 1965, pp. 303-307.
11. John, Fritz: Extremum Problems With Inequalities as Subsidiary Conditions. Studies and Essays, Courant Anniversary Volume, Interscience Publ., Inc., 1948, pp. 187-204.
12. Mangasarian, O. L.; and Fromovitz, S.: The Fritz John Necessary Optimality Conditions in the Presence of Equality and Inequality Constraints. J. Math. Anal. Appl., vol. 17, no. 1, Jan. 1967, pp. 37-47.
13. Kuhn, H. W.; and Tucker, A. W.: Nonlinear Programming. Proceedings of the Second Berkeley Symposium on Mathematical Statistics and Probability, Jerzy Neyman, ed., Univ. of California Press, 1951, pp. 481-492.
14. Fletcher, R.; and Reeves, C. M.: Function Minimization by Conjugate Gradients. Computer J., vol. 7, no. 2, July 1964, pp. 149-154.

15. Fletcher, R.; and Powell, M. J. D.: A Rapidly Convergent Descent Method for Minimization. *Computer J.*, vol. 6, 1963-1964, pp. 163-168.
16. Davidon, William C.: Variable Metric Method for Minimization. ANL-5990 Rev. (Contract W-31-109-eng-38), Argonne Nat. Lab., Nov. 1959.
17. Kowalik, J.; and Osborne, M. R.: Methods for Unconstrained Optimization Problems. Amer. Elsevier Pub. Co., Inc., 1968.
18. Wilde, Douglas J.: Optimum Seeking Methods. Prentice-Hall, Inc., c.1964.
19. Luenberger, David G.: Optimization by Vector Space Methods. John Wiley & Sons, Inc., c.1969.
20. Gelfand, I. M.; and Fomin, S. V. (Richard A. Silverman, transl.): Calculus of Variations. Prentice-Hall, Inc., c.1963.
21. Pontryagin, L. S.; Boltyanskii, V. G.; Gamkrelidze, R. V.; and Mishchenko, E. F.: The Mathematical Theory of Optimal Processes. Interscience Publ., Inc., c.1962.
22. Athans, Michael: The Status of Optimal Control Theory and Applications for Deterministic Systems. *IEEE Int. Conv. Record*, vol. 14, pt. 6, 1966, pp. 100-124.
23. Paiewonsky, Bernard: Optimal Control: A Review of Theory and Practice. *AIAA J.*, vol. 3, no. 11, Nov. 1965, pp. 1985-2006.
24. Leitmann, George: An Introduction to Optimal Control. McGraw-Hill Book Co., Inc., c.1966.
25. Hestenes, Magnus R.: Calculus of Variations and Optimal Control Theory. John Wiley & Sons, Inc., c.1966.
26. Jones, Arnold P.; and McCormick, Garth P.: Penalty Methods in Optimal-Control Theory. Tech. Pap. RAC-TP-371 (Contract DAHC 19-69-C-0017), Res. Anal. Corp., July 1969.
27. Lasdon, L. S.; Waren, A. D.; and Rice, R. K.: An Interior Penalty Method for Inequality Constrained Optimal Control Problems. 1967 Joint Automatic Control Conference, Lewis Winner, June 1967, pp. 538-548.
28. Balakrishnan, A. V.: On a New Computing Technique in Optimal Control and Its Application to Minimal-Time Flight Profile Optimization. *J. Optimization Theory Appl.*, vol. 4, no. 1, July 1969, pp. 1-21.
29. Bryson, Arthur E., Jr.; and Ho, Yu-Chi: Applied Optimal Control. Blaisdell Pub. Co., c.1969.
30. Neustadt, Lucien W.: The Existence of Optimal Controls in the Absence of Convexity Conditions. *J. Math. Anal. Appl.*, vol. 7, no. 1, Aug. 1963, pp. 110-117.

31. Hsu, Jay C.; and Meyer, Andrew U.: Modern Control Principles and Applications. McGraw-Hill Book Co., Inc., c.1968.
32. Lee, E. B.; and Markus, L.: Foundations of Optimal Control Theory. John Wiley & Sons, Inc., c.1967.
33. Bellman, Richard E.; and Dreyfus, Stuart E.: Applied Dynamic Programming. Princeton Univ. Press, 1962.
34. Kalman, R. E.: The Theory of Optimal Control and the Calculus of Variations. Mathematical Optimization Techniques, Richard Bellman, ed., Univ. of California Press, 1963, pp. 309-331.
35. Tchamran, A.: On Bellman's Functional Equation and a Class of Time-Optimal Control Systems. J. Franklin Inst., vol. 280, no. 6, Dec. 1965, pp. 493-505.
36. Boltyanskii, V. G.: Sufficient Conditions for Optimality and the Justification of The Dynamic Programming Method. SIAM J. Contr., vol. 4, no. 2, May 1966, pp. 326-361.
37. Mangasarian, O. L.: Sufficient Conditions for the Optimal Control of Nonlinear Systems. SIAM J. Contr., vol. 4, no. 1, Feb. 1966, pp. 139-152.
38. Bryson, A. E.; and Denham, W. F.: A Steepest-Ascent Method for Solving Optimum Programming Problems. Trans. ASME, Ser. E: J. Appl. Mech., vol. 29, no. 2, June 1962, pp. 247-257.
39. Sinnott, J. F., Jr.; and Luenberger, D. G.: Solution of Optimal Control Problems by the Method of Conjugate Gradients. 1967 Joint Automatic Control Conference, Lewis Winner, June 1967, pp. 566-574.
40. Breakwell, John V.; Speyer, Jason L.; and Bryson, Arthur E.: Optimization and Control of Nonlinear Systems Using the Second Variation. J. Soc. Ind. Appl. Math. Contr., ser. A, vol. 1, no. 2, 1963, pp. 193-223.
41. McGill, Robert; and Kenneth, Paul: Solution of Variational Problems by Means of a Generalized Newton-Raphson Operator. AIAA J., vol. 2, no. 10, Oct. 1964, pp. 1761-1766.
42. Lee, E. Stanley: Quasilinearization and Invariant Embedding. Academic Press, Inc., 1968.
43. Kopp, Richard E.; and Moyer, H. Gardner: Trajectory Optimization Techniques. Advances in Control Systems - Theory and Applications, vol. 4, C. T. Leondes, ed., Academic Press, Inc., 1966, pp. 103-155.

44. Daniel, James W.: On the Convergence of a Numerical Method for Optimal Control Problems. Tech. Rep. No. 44 (Contract N00014-67-A-0128-0004), Computer Sci. Dep., Univ. of Wisconsin, Sept. 1968.
45. Canon, Michael D.; Cullum, Clifton D., Jr.; and Polak, Elijah: Theory of Optimal Control and Mathematical Programming. McGraw-Hill Book Co., Inc., c.1970.
46. Holtzman, Jack M.: Convexity and the Maximum Principle For Discrete Systems. IEEE Trans. Automat. Contr., vol. AC-11, no. 1, Jan. 1966, pp. 30-35.
47. Armstrong, Ernest S.: A Combined Newton-Raphson and Gradient Parameter Correction Technique for Solution of Optimal-Control Problems. NASA TR-293, 1968.
48. Armstrong, Ernest S.; and Markos, Athena, T.: A Computational Method for Time-Optimal Space Rendezvous. NASA TN D-5017, 1969.
49. Straeter, Terry A.: A Comparison of Gradient Dependent Techniques for the Minimization of an Unconstrained Function of Several Variables. AIAA Pap. No. 69-951, Sept. 1969.